Studies of human genetic diseases and developmental processes with the frog *Xenopus laevis*

Dissertation for Obtaining the Doctoral Degree
of Natural Sciences (Dr. rer. nat.)

Faculty of Natural Sciences
University of Hohenheim

Institute of Biology, Dept. of Zoology (190z)

submitted by
Tim Ott

from Pforzheim
2020

Dean:	Prof. Dr. Uwe Beifuss
1st reviewer:	Prof. Dr. Martin Blum
2nd reviewer:	Prof. Dr. Heinz Breer
Submitted on:	08.06.2020
Oral examination on:	29.07.2020

Affidavit according to Sec. 7(7) of the University of Hohenheim doctoral degree regulations for Dr. rer. nat.

1. For the dissertation submitted on the topic

   Studies of human genetic diseases and developmental processes with the frog *Xenopus laevis*

   I hereby declare that I independently completed the work.

2. I only used the sources and aids documented and only made use of permissible assistance by third parties. In particular, I properly documented any contents, which I used – either by directly quoting or paraphrasing – from other works.
3. I did not accept any assistance from a commercial doctoral agency or consulting firm.
4. I am aware of the meaning of this affidavit and the criminal penalties of an incorrect or incomplete affidavit.

I hereby confirm the correctness of the above declaration: I hereby affirm in lieu of oath that I have, to the best of my knowledge, declared nothing but the truth and have not omitted any information.

_____ _____

Place and Date Signature

Abstract

Next generation sequencing is a driving force behind the identification of genes and alleles that are suspected to cause human genetic diseases. *In silico* tools are routinely used in the clinical everyday life to characterize unknown genotypes. However, these tools have a limited predictive accuracy and can only provide a first-line assessment. Especially un- or less studied genes require in every case predictive *in vivo* model systems that allow conclusions about disease associations. Classically, mice and zebrafish are utilized for such research, which concomitantly deepens the understanding of the involved developmental processes. In this collection of studies, the African clawed frog *Xenopus laevis* was used to explore and promote its suitability for the analysis of potential human disease genes, variants and their associated developmental processes.

The first chapters covers potential candidate genes for primary ciliary dyskinesia (PCD), a condition that result in respiratory symptoms, misoriented visceral organs, also known as laterality defects, and other symptoms. Therefore, the orthologues of *flagella associated protein 34* (*CFAP43*), *cilia and flagella associated protein 157* (*CFAP157*), *cilia and flagella associated protein 206* (*CFAP206*) and *family with sequence similarity 183 member B* (*FAM183B*) were studied, which all most likely encode scaffolding proteins. These genes presented with distinct ciliary loss of function phenotypes despite all being broadly expressed in motile ciliated tissues. This strengthens a potential PCD link for the candidate genes and indicates that they are trapped in a synexpression group.

The second chapter addresses if an actin based motor protein and a novel metzincin peptidase, encoded by *myosin ID* (*MYO1D*) and *leishmanolysin like peptidase 2*

(*LMLN2*)/*tout-de-travers* (*TDT*), respectively, are potentially causative for PCD independent laterality defects. Loss of function studies confirmed an involvement in the process of laterality determination for both genes. Myo1d interacts with the planar cell polarity pathway to polarize cilia of the left-right organizer (LRO), which generate the leftward fluid flow, the initial cue for asymmetric development. Tdt, in contrast, works downstream of flow and is required for its interpretation by sensor cells. It will be discussed that these results point to ancestral actomyosin dependent mode for symmetry breakage and to a proteolytic cleavage event that is only necessary for species with a fluid flow producing LRO.

The third chapter deals with two candidates for neurodevelopmental disorders, namely *hyaluronan mediated motility receptor* (*HMMR*) and *progesterone immunomodulatory binding factor 1* (*PIBF1*). Initial findings were verified that the loss of function phenotype of the microtubule binding protein Hmmr resembles a subtype of human holoprosencephaly. Further, variants of the centrosomal protein PIBF1 from a patient with Joubert syndrome were confirmed to be deleterious.

These studies reflect the versatile use of *Xenopus laevis* as a model organism for the analysis of human disease genes, variants and the underlying developmental processes.

Zusammenfassung

Next generation sequencing ist eine treibende Kraft hinter der Identifizierung von Genen und Allelen, die mutmaßlich humane Erbkrankheiten verursachen. Im klinischen Alltag werden routinemäßig *in silico* Methoden eingesetzt, um unbekannte Genotypen zu charakterisieren. Diese Methoden haben jedoch eine limitierte Vorhersagegenauigkeit und ermöglichen nur eine erste Beurteilung. Besonders spärlich oder nicht analysierte Gene erfordern in jedem Fall aussagekräftige *in vivo* Modellsysteme, die Schlüsse über etwaige Krankheitsassoziationen zulassen. Klassischer Weise werden für solche Forschungsbemühungen, die beiläufig auch das Verständnis der daran beteiligten Entwicklungsprozesse vertieft, Mäuse oder Zebrabärblinge verwendet. In dieser hier vorliegenden Studienkollektion wurde der Afrikanische Krallenfrosch *Xenopus laevis* verwendet, um dessen Eignung für die Analyse potentieller humaner Krankheitsgene, -genvarianten und deren assoziierten Entwicklungsprozesse zu ergründen und dies herauszustellen.

Im ersten Kapitel werden Kandidatengene der primären ciliären Dyskinesie (PCD), eine Krankheit die sich in respiratorischen Symptomen, fehlorientierten viszeralen Organen, sogenannten Lateralitätsdefekte, und in weiteren Symptomen äußern kann, besprochen. Dafür wurden die Orthologe des *flagella associated protein 34* (*CFAP43*), *cilia and flagella associated protein 157* (*CFAP157*), *cilia and flagella associated protein 206* (*CFAP206*) und *family with sequence similarity 183 member B* (*FAM183B*) untersucht, die vermutlich alle für Gerüstproteine codieren. Diese Gene wiesen verschiedenartige ciliäre Funktionsverlust-Phänotypen auf, obwohl sie alle in breitem Maße in motil-cilierten Geweben exprimiert waren. Dies untermauerte eine potentielle PCD Assoziation der Kandidatengene und impliziert, dass sie in einer Synexpressionsgruppe gefangen sind.

Das zweite Kapitel behandelt die Frage ob ein Aktin basierendes Motorprotein und eine neue Metzinkin Peptidase, jeweils von *myosin ID* (*MYO1D*) und *leishmanolysin like peptidase 2* (*LMLN2*)/*tout-de-travers* (*TDT*) codiert, potentiell für PCD unabhängige Lateralitätsdefekte verantwortlich sein könnten. Funktionsverlust-Experimente bestätigten eine Rolle im Prozess der Lateralitätsdeterminierung für beide Gene. Myo1d interagiert mit dem planaren Zellpolaritätsweg um die Cilien des Links-Rechts-Organisators (LRO) zu polarisieren, die wiederum einen linksgerichteten Flüssigkeitsstrom kreieren, der den initialen Reiz für die asymmetrische Entwicklung darstellt. Im Gegensatz dazu agiert Tdt stromabwärts des Flüssigkeitsstroms und wird für dessen Wahrnehmung durch Sensorzellen benötigt. Es wird diskutiert werden, dass diese Ergebnisse auf eine anzestralen Aktomyosin-abhängigen Mechanismus des Symmetriebruchs hindeuten und auf ein proteolytisches Spaltungsereignis, welches nur in Spezies mit einem Flüssigkeitsstrom-produzierenden LRO benötigt wird.

Das dritte Kapitel befasst sich mit zwei Kandidaten für neurologische Entwicklungsstörungen, namentlich *hyaluronan mediated motility receptor* (*HMMR*) und *progesterone immunomodulatory binding factor 1* (*PIBF1*). Hierbei konnten initiale Beobachtungen verifiziert werden, dass der Phänotyp nach Verlust des Mikrotubuli-assoziierten Proteins Hmmr einem Subtyp der Holoprosenzephalie gleicht. Des Weiteren konnten Varianten des zentrosomalen Proteins PIBF1, von einem Patienten mit Joubert Syndrom, als schadhaft bestätigt werden.

Diese Studien veranschaulichen den vielseitigen Nutzen von *Xenopus laevis* als Modellorganismus für die Analyse humaner Krankheitsgene, -genvarianten und deren zugrundeliegenden Entwicklungsprozessen.

Directory

Introduction

Challenges for human genetic disease studies

Human diseases are considered rare in the US if they affect less than 200 000 citizens, which currently corresponds to a prevalence of 6.1 / 10 000 or less, matching closely the EU definition with a cut-off at a prevalence of 5 / 10 000. Orphanet, the European reference database of rare diseases lists more than 6 000 disorders with unique identifiers, affecting between 3.5–5.9 % of the world's population at any given time point, which equals 263–433 million individuals in total (Nguengang Wakap et al., 2019). Approximately 70 % of these rare diseases have been linked to specific gene variants in the past decades. All of these cases are part of the fast-expanding group of so-called genetic diseases, which in addition include more frequently occurring conditions.

Generally, genetic diseases can be referred to as being monogenic, with only one gene affected, or polygenic when they involve multiple genes. The underlying alterations of the genome arise spontaneously, like in the context of DNA replication, or can be induced by any number of DNA damaging agents, such as for example ionizing radiation. Single nucleotide variants, small insertions and deletions, commonly referred to as indels, affecting less than 50 nucleotides, or structural variants of 50 bases and beyond are continuously being identified.

Next generation sequencing (NGS) is the driving force of this identification process, which is widely adopted in clinical diagnosis laboratories and displaced Sanger sequencing of single loci as the gold standard (Di Resta et al., 2018). Although the role of falling costs of NGS might be overestimated (Schwarze et al., 2018), transition from

whole exome sequencing to whole genome sequencing for diagnostic reasons will be applied on a broader scale in the near future.

The limiting factor for profound diagnostics lays at the end of the high-throughput bioinformatics pipeline, were newly identified gene variants need to be assessed for their pathogenicity. Missense variants constitute the largest group of variants that are associated with monogenetic diseases (Ma et al., 2015). However, the interpretation of missense variants is an extremely challenging task. *In silico* prediction tools such as Sorting Intolerant From Tolerant (SIFT) (Vaser et al., 2016) or Polymorphism Phenotyping v2 (PolyPhen-2) (Adzhubei et al., 2010) are typically utilized to uncover deleterious missense variants and to discriminate them from benign ones, in accordance with the recommendations made by the American College of Medical Genetics and Genomics (ACMG) (Richards et al., 2015). These programs test amino acid substitutions based on single or multiple features such as sequence conservation, physico-chemical properties or structural elements (Niroula and Vihinen, 2016). As all available tools are limited in their predictive capacity, several programs or ensemble methods like Combined Annotation-Dependent Depletion (CADD) (Rentzsch et al., 2019) or Rare Exome Variant Ensemble Learner (REVEL) (Ioannidis et al., 2016), which combine multiple algorithms, are commonly used. Although undeniably useful, a high variability in the recognition performance and high rates of false-positive hits have raised concerns about the reliability of such programs (Niroula and Vihinen, 2019). Hence, clinical consequences should never exclusively rely on results gained from *in silico* methods. Rather, animal model systems are needed to assess genetic variants in an *in vivo* context.

The chronicle of *Xenopus* in research

The African clawed frog *Xenopus laevis* has a long and well documented history in biological and biomedical research, as comprehensively reviewed in depth by John Gurdon and Nick Hopwood (Gurdon and Hopwood, 2000). In brief, *Xenopus* made its first appearance on the scientific landscape, at the time as *Bufo laevis*, with its description by François Daudin at the beginning of the 19th century (Daudin, 1802/03). In the following decades, *Xenopus* was occasionally used in comparative anatomical studies and in physiological research by the 1920s. The foundation for its widespread use as a laboratory animal was set by Lancelot Hogbens endocrinological studies around 1930, in which he demonstrated that injections of pituitary extracts induced ovulation in *Xenopus* females (Hogben et al., 1931). Harry Zwarenstein and Hillel Shapiro first reported its capacity as a biological pregnancy test, in which urine from pregnant women containing chorionic gonadotropin induced spawning only hours after injection into the dorsal lymph sac (Shapiro and Zwarenstein, 1934). The ease and reliability of this pregnancy test was superior to other assays at that time and led to the rapid establishment of laboratory colonies of *Xenopus* around the world. Hormone preparations of chorionic gonadotropin were already commercially available in the early 1930s, principally enabling developmental biologists to induce egg laying at will, granting access to large amounts of biological material and to overcome the seasonal character of amphibian embryological studies. However, it took until the 1950s that *Xenopus* was used to examine embryological problems and only in the 1960s it out-competed other amphibian model systems based on the number of published studies per year.

A vast number of scientific studies that made use of *Xenopus* contributed extensively to our current knowledge. Plenty of these studies discovered fundamental principles of

cellular and developmental processes in humans and non-human animals, which are also key for the understanding of distinct disease states.

In 1962, John Gurdon reported his pioneer work on nuclear reprogramming for which he utilized *Xenopus* (Gurdon, 1962). By transferring nuclei from differentiated intestinal epithelial cells into enucleated oocytes, he created embryos, which developed into normal tadpoles, thereby demonstrating the totipotency of the nucleus and the reprogramming capacity of the egg. The first isolation of a eukaryotic gene was achieved by Max Birnstiel and colleagues, who published their results of the *Xenopus* DNA that includes the tracts for the ribosomal 18S and 28S RNA in 1966 (Birnstiel et al., 1966). The first eukaryotic transcription factor, namely general transcription factor IIIA (Gtf3a), was also isolated from *Xenopus*, as reported by David Engelke and colleagues in 1980 (Engelke et al., 1980). Andrew Murray and Marc Kirschner established in 1991, that the cell cycle progression is ultimately regulated via the level of cyclin B1 (Ccnb1), using an elegant *in vitro* system from *Xenopus* egg extracts (Murray and Kirschner, 1989).

The above-mentioned historical studies are representative for many scientific ‘firsts’ that have been achieved with *Xenopus*. The potential of this model system, however, is far bigger, and it is especially well-suited for the assessment of human genetic disease alleles.

The versatile use of *Xenopus*

Xenopus as a model system historically meant *Xenopus laevis* for a long time, an allotetraploid species that emerged from a hybridization event between two diploid progenitors approximately 17–18 million years ago (Session et al., 2016). Since the

1990s, scientists also utilize the closely related diploid *Xenopus tropicalis* (Grainger, 2012), which split from the progenitors of *Xenopus laevis* about 49 million years ago (Session et al., 2016). Marc Kirschner introduced this new species of the genus *Xenopus* for more convenient genetic work. Outbred *Xenopus* animals can be commercially obtained from multiple suppliers. Sequenced inbreed lines, the *Xenopus laevis* J strain and the *Xenopus tropicalis* Nigerian strain, are available to the community through the National *Xenopus* Resource, the European *Xenopus* Resource Centre and the National Bioresource Project of Japan. Both species vary only slightly with respect to husbandry conditions, with *Xenopus tropicalis* generally preferring warmer temperatures of 24–26 °C, in contrast to *Xenopus laevis* with its preference at 18–20 °C. Their different temperature optima are also reflected by the shorter generation time of 5–8 month for *Xenopus tropicalis* versus 6–12 month for *Xenopus laevis*. However, free swimming pre-metamorphic tadpoles of both species are already convenient for most assays, as they develop their various organ systems, depending on temperature, in less than a week. As previously mentioned, large clutches of eggs are available at any time, which - when fertilized *in vitro* - give rise to hundreds of tightly synchronized embryos. Their large egg size with a diameter of approximately 1 mm for *Xenopus laevis* and 0.5 mm for *Xenopus tropicalis* make them ideally suited for all kinds of manipulations.

Various well-established methods for altering gene expression, for example of disease candidate genes, exist and can be applied to both species via microinjections. Gene loss-of-function studies can be rapidly achieved via synthetic morpholino antisense oligomers (MOs) (Heasman et al., 2000) or via clustered regularly short palindromic repeats (CRISPR)/CRISPR-associated (Cas) systems for genome editing (Blitz et al., 2013; Moreno-Mateos et al., 2017; Nakayama et al., 2013).

MOs are short-chained nucleic acid analogs usually consisting of about 18–30 subunits that exert their function through binding with high affinity to complementary RNA molecules. A steric blocking mechanism inhibits translation or splicing of the targeted mRNA, if directed to the start codon or to splice sites, respectively. The same principle also allows inhibition of other RNA species like miRNAs or lncRNAs (Moulton, 2016). Suboptimal MO doses can be used to mimic situations in which haploinsufficiency is presented or can reveal interactions, if more than one MO is applied. This knock-down method turned out to be highly useful, especially as RNA interference was never widely adopted by the *Xenopus* community, due to the lack of the RNA-induced silencing complex (RISC) associated nuclease argonaute RISC catalytic component 2 (Ago2) (Lund et al., 2011).

Different CRISPR/Cas systems have dramatically simplified the way how gene knock-outs can be achieved in *Xenopus* (Blitz et al., 2013; Moreno-Mateos et al., 2017; Nakayama et al., 2013), thereby replacing zinc finger nucleases and transcription activator-like effector nucleases (TALENs). The most commonly used and best-implemented CRISPR/Cas system is CRISPR/Cas9 (Cong et al., 2013; Mali et al., 2013). This dichotomous system consists of an engineered chimeric so-called single guide RNA (sgRNA) that mediates sequence specificity and directs the endonuclease Cas9 via complexing to the targeted genomic region. If a target sequence is identified, Cas9 cuts precisely within the recognition motif of the sgRNA leaving a DNA double-strand break for repair. In early *Xenopus* embryos, the error-prone but fast responsive non-homologous end joining machinery for DNA double-strand break repair is favored over other repair pathways, which results in mutagenesis of the target locus via indels. The resulting F0 specimens are mosaic but can be directly analyzed due to the high

penetrance of the method, or can be raised and subsequently crossed to establish a defined knock-out.

Besides its use for knock-out studies, the CRISPR/Cas9 system offers a novel way of generating precise knock-in lines (Aslan et al., 2017; Shi et al., 2015; Suzuki et al., 2018), as an alternative to more random insertions via restriction enzyme mediated integration (Kroll and Amaya, 1996), phiC31 integrase (Allen and Weeks, 2005), I-SceI meganuclease (Fong et al., 2006) or transposons (Sinzelle et al., 2006). DNA base editing (Shi et al., 2019) suited for the introduction of all four transition mutations and the recently developed prime editing method (Anzalone et al., 2019), allowing the additional eight transversion mutations as well as defined small insertions or deletions, are also based on CRISPR/Cas9, but the latter has not yet been applied to *Xenopus*.

Misexpression of genes of interest is also straightforward in *Xenopus*, as *in vitro* synthesized mRNAs are rapidly translated (Krieg and Melton, 1984). As an alternative to mRNA injections, the introduction and expression from plasmids (Bendig, 1981) or artificial chromosomes (Fish et al., 2012) is also feasible. These DNA constructs can additionally harbor cis-regulatory elements to achieve a defined spatiotemporal expression pattern.

A precise cell lineage map of the 32-cell stage (Moody, 1987) makes it possible to apply all of the above-mentioned tools in a virtually tissue-specific manner, limiting the need for expensive and time consuming conditional methods. Unilateral manipulations, leaving one side of the embryo as an internal control, is an additional merit of the *Xenopus* system, since the position of the left-right body axis can be deduced from the pigment distribution and the cell size at the 4-cell stage already.

The combination of the above-mentioned tools with the fast extra-corporeal development of *Xenopus*, which is an ancestral trait of amphibians, allows to dissect

and to tightly trace all processes from fertilization, via gastrulation and neurulation to organogenesis. This is of utmost importance, as genetic diseases usually affect these early developmental processes by which the later phenotype manifests itself.

Xenopus genetic diseases models

The above-mentioned tools have been applied to study a great variety of human genetic diseases in *Xenopus*. To reflect the possible impact of such work, recently published studies will be highlighted.

Bruno Reversade and his team described a series of recessive variants of the Wnt signaling enhancer *R-spondin 2* (*RSPO2*) in fetuses with tetra-amelia syndrome (Szenker-Ravi et al., 2018). Hallmark of this disease is the absence of all four limbs. By mutating *rspo2* unilaterally via CRISPR/Cas9 in *Xenopus tropicalis*, the authors recapitulated the loss of both fore- and hindlimbs seen in tetra-amelia syndrome. An additional TALEN-mediated double loss of the direct interacting ubiquitin ligases *ring finger protein 43* (*rnf3*) and *zinc and ring finger 3* (*znrf3*) surprisingly resulted in supernumerary limbs. Hence, the authors proposed an antagonistic interaction of RSPO2 with RNF3 and ZNRF3, which helped to clarify the etiology of tetra-amelia syndrome.

In a remarkable recent study, Yonglong Chen and colleagues impressively modeled Holt-Oram syndrome (HOS) as well as oculocutaneous albinism type 1A (OCA1A) in *Xenopus tropicalis* using base editing of *T-box transcription factor 5* (*tbx5*) and *tyrosinase* (*tyr*), respectively (Shi et al., 2019). HOS is an autosomal dominant disease usually leading to cardiac and forelimb defects. Patients with OCA1A, which is inherited in an autosomal recessive manner, lack any pigmentation, experience

nystagmus and visual impairment. Introduction of so far uncharacterized missense variants from both *TBX5* or *TYR* via base editor 3 in the *Xenopus* orthologues mimicked in each case the clinical presentation, with defective forelimbs and albinism.

In the last and most recent case presented here, Mustafa Khokha and colleagues revisited variants of the endoplasmic reticulum (ER) membrane protein complex (EMC) component *ER membrane protein complex subunit 1* (*EMC1*) from patients with a broad spectrum of birth defects, including congenital heart disease, craniofacial abnormalities and neurodevelopmental defects (Marquez et al., 2020). Functionally, the EMC acts as a transmembrane domain insertase for a subset of transmembrane proteins. MO or CRISPR/Cas9 based depletion of Ecm1 in *Xenopus tropicalis* recapitulated many aspects of the patients' phenotypes, indicative of compromised neural crest cells (NCCs). Intriguingly, embryos displayed defective NCC development upon loss of *ecm1*. An unbiased proteomic approach identified several EMC-dependent pathways, most prominently Wnt signaling, which turned out to be causative for the previously observed NCC phenotype. Hence, the authors used NCCs to test the potential disease causing *EMC1* variants in rescue experiments, which revealed that most of them were indeed loss-of-function alleles.

Aim of this work

The functional studies presented hereafter were designed to address a complex consisting of uncharacterized or less studied potential human disease genes or variants and to deepen the understanding of the developmental processes in which they are involved. Three different parts cover primary ciliary dyskinesia (PCD), PCD independent laterality defects as well as neurodevelopmental disorders.

PCD is clinical condition caused by immotile or dyskinetic cilia, which can result in respiratory symptoms and misoriented visceral organs, commonly referred to as laterality defect, among other symptoms. The group of Achim Gossler identified potential PCD candidate genes in a murine target gene screen for the master regulator of motile cilia *forkhead box J1* (*Foxj1*). A positive hit collection consisting of *cilia and flagella associated protein 34* (*Cfap43*), *cilia and flagella associated protein 157* (*Cfap157*), *cilia and flagella associated protein 206* (*Cfap206*) and *family with sequence similarity 183 member B* (*Fam183b*) were selected to be studied in a collaborative effort with the Gossler group.

Two genes, *myosin ID* (*MYO1D*) and *leishmanolysin like peptidase 2* (*LMLN2*)/*tout-de-travers* (*TDT*) are potentially involved in PCD independent laterality defects and possess a remarkable evolutionary relevance. Ancestral deuterostomes establish laterality via a ciliary driven leftward fluid flow during neurulation. In contrast, the protostome *Drosophila melanogaster* uses a yet not fully understood mechanism that involves interaction of the *MYO1D* orthologue *Myosin 31DF* (*Myo31DF*) with the planar cell polarity (PCP) pathway on protein level. With respect to the instructive capacity of PCP signaling for the cilia orientation that directs the deuterostome leftward fluid flow, an evolutionary conserved laterality module could exist among bilaterians. However, within deuterostomes the leftward fluid flow was independently lost in two taxa along with a functional *TDT* orthologue, a gene that was recently identified by the group of Bruno Reversade to be mutated in patients with laterality defects. Therefore, analysis of *myo1d* and *tdt* together with the groups of Stéphane Noselli and Bruno Reversade, respectively, could not only reveal so far undiscovered pathomechanisms but also shield light on the evolution of laterality in bilaterians.

Candidates for neurodevelopmental disorders were studied with the *Xenopus hyaluronan mediated motility receptor* (*hmmr*) and the human *progesterone immunomodulatory binding factor 1* (*PIBF1*). Findings by the group of Kerstin Feistel implicated that loss of *hmmr* resulted in embryonic forebrain defects, which may resemble human holoprosencephaly (HPE). Christina Evers group found potential deleterious variants of *PIBF1* in a patient with Joubert syndrome (JS), which manifests as a typical set of mid- and hindbrain malformations. Further work with the groups of Kerstin Feistel and Christina Evers could deepen our understanding of the HPE etiology and will allow us to assess the pathogenicity of the novel PIBF1 variants, respectively.

Original research chapter I:

Primary ciliary dyskinesia (PCD)

CFAP157 is a murine downstream effector of FOXJ1 that is specifically required for flagellum morphogenesis and sperm motility

© 2016. Published by The Company of Biologists Ltd | Development (2016) 143, 4736-4748 doi:10.1242/dev.139626

RESEARCH ARTICLE

CFAP157 is a murine downstream effector of FOXJ1 that is specifically required for flagellum morphogenesis and sperm motility

Marina Weidemann[1], Karin Schuster-Gossler[1], Michael Stauber[1], Christoph Wrede[2], Jan Hegermann[2], Tim Ott[3], Karsten Boldt[4], Tina Beyer[4], Katrin Serth[1], Elisabeth Kremmer[5], Martin Blum[3], Marius Ueffing[4] and Achim Gossler[1,*]

ABSTRACT

Motile cilia move extracellular fluids or mediate cellular motility. Their function is essential for embryonic development, adult tissue homeostasis and reproduction throughout vertebrates. FOXJ1 is a key transcription factor for the formation of motile cilia but its downstream genetic programme is only partially understood. Here, we characterise a novel FOXJ1 target, *Cfap157*, that is specifically expressed in motile ciliated tissues in mouse and *Xenopus* in a FOXJ1-dependent manner. CFAP157 protein localises to basal bodies and interacts with tubulin and the centrosomal protein CEP350. *Cfap157* knockout mice appear normal but homozygous males are infertile. Spermatozoa display impaired motility and a novel phenotype: *Cfap157*-deficient sperm exhibit axonemal loops, supernumerary axonemal profiles with ectopic accessory structures, excess cytoplasm and clustered mitochondria in the midpiece regions, and defective axonemes along the flagella. Our study thus demonstrates an essential sperm-specific function for CFAP157 and suggests that this novel FOXJ1 effector is part of a mechanism that acts during spermiogenesis to suppress the formation of supernumerary axonemes and ensures a correct ultrastructure.

KEY WORDS: Cfap157, Ciliogenesis, Axoneme, Spermiogenesis, Male infertility

INTRODUCTION

Motile cilia are slender protrusions of the surface of eukaryotic cells. Their core, the axoneme, consists of nine peripheral microtubular doublets and typically two central microtubules. The axoneme carries dynein arms and originates at the basal body, a centriolar structure anchored to the cell cortex. Motile cilia move extracellular fluids, mediate cellular motility and play essential roles during development, tissue homeostastis and reproduction (reviewed by Choksi et al., 2014b; Gerdes et al., 2009; Nigg and Raff, 2009). In vertebrate embryos, motile cilia in the left-right organiser rotate and generate a leftward flow of the extracellular fluid, which is translated into left-right asymmetry of visceral organs (reviewed by Blum et al., 2014; Nonaka et al., 1998; Takeda et al., 1999). Coordinated beating of motile cilia on epithelia of the lung is required for airway clearance (Jain et al., 2010; Stannard and O'Callaghan, 2006). Motile cilia on ependymal cells lining the brain ventricles secure normal cerebrospinal fluid flow (Banizs et al., 2005; Jacquet et al., 2009; Lee, 2013; Spassky et al., 2005) and motile cilia in the fallopian tube contribute to movement of eggs (Lyons et al., 2006). Motility of the sperm flagellum is essential for sperm function (Afzelius and Eliasson, 1983). Consequently, human primary ciliary dyskinesia (PCD), which is caused by dysfunction of motile cilia, is associated with situs randomisation, respiratory problems, male infertility and, less frequently, with female infertility and hydrocephalus (reviewed by Praveen et al., 2015).

Whereas cells of respiratory epithelia and ependyma form multiple motile cilia, spermatozoa carry one flagellum, a specialised motile cilium with specific accessory structures. The flagellum consists of: the connecting piece, which links it to the sperm head and holds the centriole from which the axoneme nucleates; the midpiece, which contains nine outer dense fibres (ODFs) and peripheral mitochondria; the principal piece, which possesses both ODFs and a peripheral fibrous sheath; and the end piece (reviewed by Eddy, 2006). The flagellum develops during differentiation of spermatids in seminiferous tubules of testes. Concomitantly, the sperm head reshapes and the acrosome, which is a sperm-specific secretory vesicle, forms (reviewed by Fléchon, 2016). Most of the cytoplasm is removed via a residual body that detaches from the neck region and, via a cytoplasmic droplet that is shed at the midpiece-principal piece boundary, the annulus (reviewed by Hermo et al., 2010). Spermatozoa are stored in the cauda epididymis, where they undergo further maturation (reviewed by Buffone et al., 2012; Cornwall, 2009).

FOXJ1 is a key transcription factor for the formation of motile cilia throughout vertebrates (Alten et al., 2012; Brody et al., 2000; Chen et al., 1998; Stubbs et al., 2008; Vij et al., 2012; Yu et al., 2008). FOXJ1 targets include: structural, motor and accessory proteins of the axoneme; intraflagellar and vesicular transport proteins; and basal body components (reviewed by Santos and Reiter, 2008). Additional proteins are thought to be involved in the function of cilia (Andersen et al., 2003; Gerdes et al., 2009; Gherman et al., 2006; McClintock et al., 2008). Comparing the transcriptomes of fetal respiratory epithelia before and after motile ciliogenesis, and heterozygous with homozygous *Foxj1* mutant

[1]Institute for Molecular Biology, OE5250, Hannover Medical School, Carl-Neuberg-Str. 1, Hannover 30625, Germany. [2]Institute of Functional and Applied Anatomy, OE8840, Hannover Medical School, Carl-Neuberg-Str. 1, Hannover 30625, Germany. [3]Institute of Zoology, University of Hohenheim, Garbenstraße 30, Stuttgart 70593, Germany. [4]Institute of Ophthalmic Research, Center for Ophthalmology, University of Tübingen, Röntgenweg 11, Tübingen 72076, Germany. [5]Institute of Molecular Immunology, Helmholtz Zentrum München, German Research Center for Environmental Health (GmbH), Core Facility Monoclonal Antibodies, Marchioninistr. 25, München 81377, Germany.

*Author for correspondence (gossler.achim@mh-hannover.de)

A.G., 0000-0002-9103-9116

Received 13 May 2016; Accepted 9 November 2016

RESEARCH ARTICLE Development (2016) 143, 4736-4748 doi:10.1242/dev.139626

lungs, we identified a few hundred candidates for FOXJ1 effectors during ciliogenesis. Here, we describe the analysis of one candidate, *Cfap157*, that encodes a basal body protein of unknown function. *Cfap157* transcription correlates with the presence of motile cilia and depends on FOXJ1. Despite its expression in many cell types with motile cilia, loss of *Cfap157* function in mice specifically affects flagellum morphogenesis and sperm motility.

RESULTS

Expression and localisation of *Cfap157*

Cfap157 (GeneID 227736) encodes a 523 amino acid protein that lacks known motifs, except for a PEST domain (http://bioinf.cs.ucl.ac.uk/psipred/), is conserved among chordates and shares sequence identity of variable extent with proteins of various other eukaryotes, including the green algae *Chlamydomonas* (Table S1). Mouse *Cfap157* expression detected by RT-PCR was essentially confined

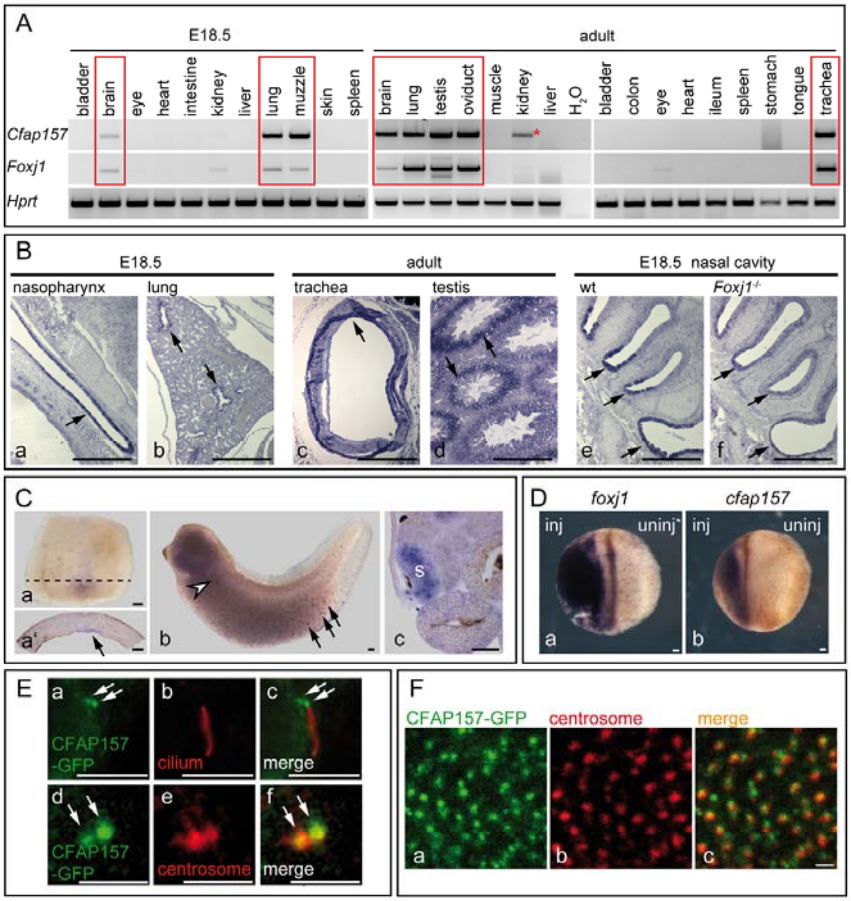

Fig. 1. Expression and localisation of *Cfap157* RNA and protein. (A) RT-PCR with primers in exons 1 and 3 of *Cfap157*, in exons 2 and 3 of *Foxj1*, and in exons 7 and 9 of *Hprt* on RNA isolated from E18.5 and adult wild-type mouse tissues. Boxes indicate co-expression of *Cfap157* and *Foxj1* in tissues carrying motile cilia. Asterisk indicates *Cfap157* PCR product in kidney that was not consistently detected by RT-PCR (see Fig. 3D). (B) Section *in situ* hybridisation with a full-length *Cfap157* cDNA probe on E18.5 and adult wild-type mouse tissues, as well as E18.5 *Foxj1* wild-type (wt) and *Foxj1*-deficient ($Foxj1^{-/-}$) sagittal nose sections. Arrows indicate expression domains. Scale bars: 500 µm in a-c,e,f; 250 µm in d. (C) Whole-mount *in situ* hybridisation of *Xenopus laevis* embryos with a full-length *cfap157* cDNA probe at stage 16 (a, dorsal explant; a′, transverse section along plane shown in a; arrow, gastrocoel roof plate), stage 35 (b; arrowhead, nephrostomes; arrows, multiciliated epidermal cells) and stage 45 (c; transverse section of tadpole; s, stomach). Scale bars: 100 µm. (D) Whole-mount *in situ* hybridization with a full-length cDNA *foxj1* probe (a) or a *cfap157* probe (b) on stage 20 *Xenopus* embryos after left-sided injection of *foxj1* mRNA (n=37). Scale bars: 100 µm. (E) Localisation of CFAP157-GFP protein at the basal body of IMCD3 cells co-stained with acetylated tubulin (a-c) or γ-tubulin (d-f). Arrows, CFAP157-GFP. Scale bars: 5 µm in a-c; 2 µm in d-f. (F) Localisation of CFAP157-GFP protein to basal bodies of motile cilia on cells of stage 30 *Xenopus* larval epidermis co-stained with γ-tubulin. Scale bar: 1 µm.

RESEARCH ARTICLE

Development (2016) 143, 4736-4748 doi:10.1242/dev.139626

to tissues containing motile cilia correlating with the expression of *Foxj1* (Fig. 1A, boxes). Section *in situ* hybridisation showed *Cfap157* expression in epithelia known to carry motile cilia and spermatogenic cells in testes (Fig. 1Ba-d, arrows). *Cfap157* was downregulated in airway epithelial cells of *Foxj1*-null mutants (Fig. 1Be,f, arrows), confirming that *Cfap157* transcription depends on FOXJ1 in these cells. Whole-mount *in situ* hybridisation of *Xenopus* embryos revealed *cfap157* (GeneID 780234) expression in cells carrying motile cilia (Fig. 1C). Consistent with the transcriptional dependence of *Cfap157* on FOXJ1 in mice, overexpression of *foxj1* induced ectopic expression of *cfap157* in *Xenopus* embryos (Fig. 1D).

We analysed the subcellular localisation of CFAP157 in inner medullary collecting duct 3 (IMCD3) cells, which express endogenous *Cfap157* and form non-motile cilia, by expressing GFP fusions (because our anti-CFAP157 antibodies did not detect endogenous CFAP157). In IMCD3 cells induced to form cilia CFAP157-GFP was enriched in two adjacent dots near the ciliary base (Fig. 1Ea-c) that co-stained with γ-tubulin (Fig. 1Ed-f), indicating localisation at the basal body. Consistently, GFP-labelled CFAP157 expressed in *Xenopus* embryos showed multiple dots subapical to the membrane that overlapped with γ-tubulin in multiciliated epidermal cells, also indicating localisation to basal bodies of motile cilia (Fig. 1F).

Identification of potential protein interaction partners of CFAP157

To identify interaction partners of CFAP157, SF-TAP-tagged (Gloeckner et al., 2007) full-length CFAP157 or CFAP157ΔPEST (lacking the C-terminal PEST domain) was expressed in HEK293T cells and purified by Strep-FLAG tandem affinity purification. The eluates were analysed by liquid chromatography fractionation and mass spectrometry (LC-MS). Interesting candidate interaction partners in HEK293T cells included the two tubulins TUBA4A and TUBB5, basigin, and the centrosomal proteins CEP350 and SSNA1 (Table S2). SSNA1 was also significantly enriched among proteins pulled down from testis lysates using purified SF-TAP-tagged CFAP157ΔPEST, in addition to various other proteins (Table S3). Co-immunoprecipitation assays using CHO cells co-expressing full-length HA-tagged CFAP157ΔPEST and myc- or flag-tagged versions of potential interaction partners thus far confirmed the interaction of CFAP157 with TUBA4A, TUBB5 and CEP350 (Fig. 2A, boxes) but not with basigin and SSNA1. Assays using HA-tagged full-length CFAP157, which is expressed at lower levels than the ΔPEST-version, produced similar results (data not shown). A direct or indirect interaction of CFAP157 with tubulins and CEP350 is consistent with the localisation of CFAP157 at ciliary basal bodies and with the co-expression of *Cfap157* and *Cep350* in brain, lung and testis (Fig. 2B).

Generation of *Cfap157^{lacZ}* and *Cfap157^{Δex2}* knockout mice

To analyse the physiological function of CFAP157, we generated mutant mice (Fig. 3A) using the EUCOMM ESC clone G05 (*1700019L03Rik$^{tm1a(EUCOMM)Hmgu}$*) and validated them using PCR and Southern blot analysis (Fig. 3B,C). In these mice, a *lacZ* gene and a *neo* cassette were inserted into intron 1, and exon 2 was flanked by loxP sites (*Cfap157^{lacZneo}*). Additional loxP and FRT sites allowed for removal of *neo* and exon 2 to generate a null allele with a *lacZ*-reporter (*Cfap157^{lacZ}*) or for removal of *lacZ* and *neo* to generate a conditional allele (*Cfap157^{ex2flox}*). Deletion of exon 2 (*Cfap157^{Δex2}*) causes a frameshift and termination of translation in exon 3 and/or nonsense-mediated mRNA decay. These alleles were generated using Zp3-Cre (de Vries et al., 2000) or flp-deleter mice (Rodríguez et al., 2000) and verified by using PCR.

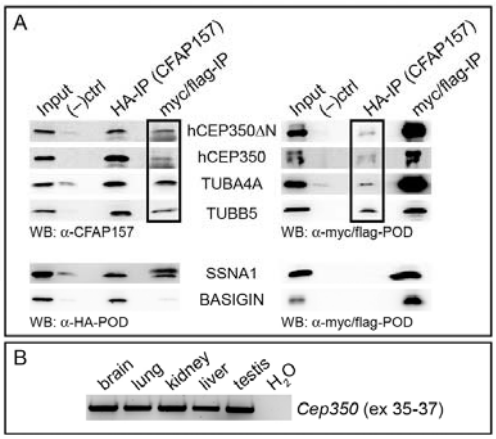

Fig. 2. Analysis of putative CFAP157 protein interaction partners identified by tandem affinity purification/mass spectrometry (TAP/MS). (A) Co-immunoprecipitation (IP) of HA-CFAP157ΔPEST and myc- or flag-tagged potential interaction partners: myc-hCEP350; myc-hCEP350ΔN (Yan et al., 2006); TUBA4A-flag; TUBB5-flag; SSNA1-flag; BASIGIN-myc; (−)ctrl, IP performed without antibodies. CO-IP bands are boxed. (B) *Cep350* RT-PCR on RNA isolated from adult mouse tissues; H_2O, control without cDNA.

Homozygous *Cfap157^{lacZ}* or *Cfap157^{Δex2}* mice were born at Mendelian ratios (Table S4) and were indistinguishable from wild-type mice. *Cfap157* transcripts were not detected in RNA from homozygous brain and lung (Fig. 3D, Fig. S1). However, RT-PCR on testis RNA of homozygous *Cfap157^{Δex2}* mice amplified fragments of transcripts lacking either exon 2 or both exon 2 and exon 3 (Fig. 3E, asterisk and arrowhead), which is probably caused by alternative splicing and stabilisation of mRNA that can occur during spermatogenesis due to removal of destabilising 3′UTR sequences (Kleene, 2005; Li et al., 2016). The latter transcript could be translated into a CFAP157 protein lacking 142 amino acids. qRT-PCR suggested significant expression of this transcript (Fig. S2). However, northern blot analysis with a full-length *Cfap157* cDNA probe detected no transcripts in *Cfap157^{lacZ}* and *Cfap157^{Δex2}* testis RNA (Fig. 3F). Importantly, no CFAP157 protein could be precipitated from homozygous *Cfap157^{lacZ}* and *Cfap157^{Δex2}* testis lysates (Fig. 3G, arrowheads and bracket; direct detection of CFAP157 in lysates using western blots was precluded by high background) using antibodies raised against peptides encoded by exons 1 and 7. These results demonstrated that *Cfap157^{lacZ}* and *Cfap157^{Δex2}* are null alleles.

Analysis of reporter expression in *Cfap157^{lacZ}* mice and dependence of *Cfap157* transcription on FOXJ1

β-Galactosidase staining of *Cfap157^{lacZ}* embryonic and fetal tissues revealed *lacZ* expression in the node of E8 embryos, in the fourth ventricle of the brain at E12.5 and in the airways at E18.5 (Fig. 4A, arrows). In adults, *lacZ* was expressed in the airways of the lung, the ependymal layer of the ventricles and the seminiferous tubules of testis (Fig. 4B). On a *Foxj1*-null background (Brody et al., 2000), reporter expression from the *Cfap157^{lacZ}* allele was lost (e.g. fetal

DEVELOPMENT

RESEARCH ARTICLE Development (2016) 143, 4736-4748 doi:10.1242/dev.139626

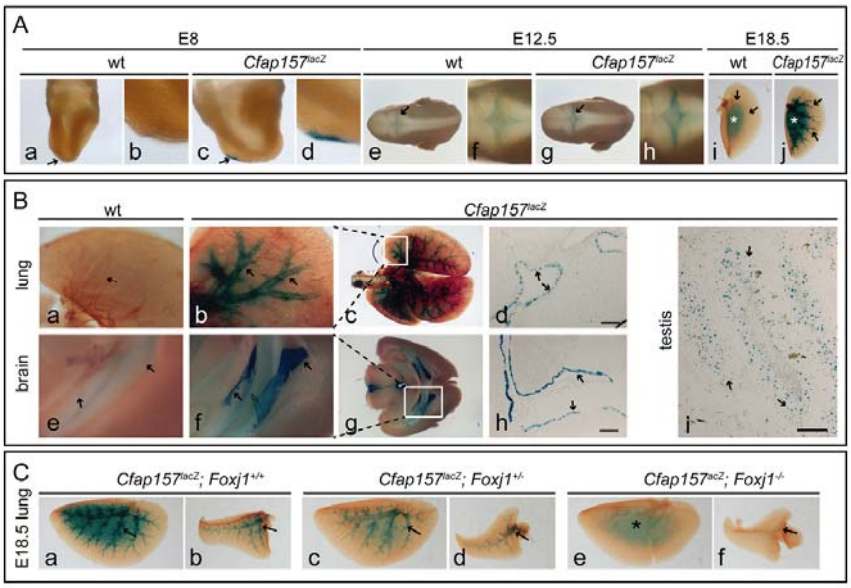

Fig. 4. FOXJ1-dependent reporter expression in *Cfap157*^{lacZ} mice. (A) *lacZ* expression in *Cfap157*^{lacZ} E8 (a-d) and E12.5 (e-h) embryos, and E18.5 lungs (i,j). (B) *lacZ* expression in *Cfap157*^{lacZ} adult lung (b-d), brain (f-h) and testis (i); wild type (wt; a,e), negative control. Lungs were cleared with benzyl alcohol:benzyl benzoate (a-c). (d,h,i) Cryosections. (b,f) Higher magnifications of boxed areas in c,g. Scale bars: 100 µm in d,h,i. (C) β-Galactosidase expression in E18.5 lung lobes of *Cfap157*^{lacZ} mice that were *Foxj1*$^{+/+}$ (a,b; *n*=4), *Foxj1*$^{+/-}$ (c,d; *n*=2) or *Foxj1*$^{-/-}$ (e,f; *n*=5). Arrows indicate the node (in Aa,c), ventricle/ependyma (in Ae,g, Be-h), airways (in Ai,j, Ba-d,Ca-d,f) or spermatogenic cells (Bi). Asterisks indicate background staining.

Cfap157$^{\Delta ex2}$ homozygous males) but never generated pregnancies. In addition, continuous matings (3-5 months) with homozygous *Cfap157*^{lacZ} (*n*=16) or *Cfap157*$^{\Delta ex2}$ (*n*=7) males produced no offspring. Collectively, these analyses indicated a CFAP157 function that is distinctly required for sperm function.

Cfap157 functions in sperm motility and flagellum morphogenesis

Cfap157 mutant sperm dissected from the cauda epididymis ('cauda sperm') displayed a reduced and abnormal motility, often resulting in twitching or local circular movement (Movies 1 and 2). Most *Cfap157* spermatozoa contained a bulge in the proximal flagellum next to a dislocated head (see below). Computer assisted sperm analysis (CASA; Yániz et al., 2015) of *Cfap157* mutant cauda sperm showed a severely reduced motility rate (Fig. 6A, Table S6) and a significantly lower concentration (Fig. 6B, Table S6).

Cauda sperm of 4- to 6-month-old *Cfap157* mutant males bound eggs inefficiently and hardly moved them, in contrast to wild-type sperm (Fig. 6C, *n*>12 eggs; Movies 3 and 4). *In vitro* fertilisation (IVF) assays showed that *Cfap157* mutant sperm are essentially unable to fertilise eggs even when in close contact: 143/211 (68%) wild-type eggs incubated with sperm from fertile heterozygous *Cfap157*$^{lacZ/+}$ males developed pronuclei, indicating fertilisation, whereas only 13/488 (2.7%) wild-type eggs incubated with sperm from homozygous *Cfap157*$^{lacZ/lacZ}$ males were fertilised (Table S7). Likewise, the development of blastocysts occurred in only 4/1111 (0.4%) and 1/810 (0.1%) wild-type eggs incubated with cauda sperm from *Cfap157*$^{lacZ/lacZ}$ and *Cfap157*$^{\Delta ex2/\Delta ex2}$ males, respectively, whereas incubation with wild-type sperm produced blastocysts in 260/437 (58%) eggs (Fig. 6D, Table S8). As IVF with both wild-type and mutant sperm resulted in a lower percentage of blastocysts than fertilised eggs, the loss of embryos appears unrelated to the CFAP157 mutation.

Staining various structures in cauda sperm of ~6-month-old *Cfap157* mutant males revealed morphological abnormalities in the midpiece region in 95% of sperm cells that were identical for both alleles (*n*=125 *Cfap157*^{lacZ}; *n*=129 *Cfap157*$^{\Delta ex2}$ spermatozoa; Fig. 7A-E). Ninety-three percent (235/254) of sperm cells showed an axonemal loop of the midpiece (Fig. 7Ac,d,g,h, Bc,d,g,h) and 6% (14/254, some also with a loop) contained a bulge (Fig. 7Ae,f). Seventy-five percent (191/254) of sperm heads were bent abnormally (Fig. 7Ac,g, Bc,g) and 12% (31/254) were missing (Fig. 7Be). The loop appeared to contain excess cytoplasm (Fig. 7Ac,g, Bc,g). Haematoxylin and Eosin staining of *Cfap157* sperm cells confirmed that surplus cytoplasm incorporated the loop completely in some, and partially in other spermatozoa (not shown). Co-staining of the annulus at the midpiece–principal piece boundary using anti-septin 7 antibodies revealed that the axonemal loop was restricted to the midpiece (*n*=45; Fig. 7Bd,f,h). Staining of acetylated tubulin showed that 76/180 spermatozoa contained a connecting microtubular link that appeared to fix the loop (Fig. 7Bd,h, arrows). The rest did not show such a link, perhaps obscured by twisted or narrow loops (Fig. 7Ad,h). Staining with AKAP3 antibodies showed the presence of ectopic fibrous sheath in the midpiece region close to the sperm head in 111/139 spermatozoa (arrows and arrowheads in Fig. 7Cd,f,h) and much less in the principal piece. Ten out of 139 mutant sperm cells had no AKAP3-

RESEARCH ARTICLE Development (2016) 143, 4736-4748 doi:10.1242/dev.139626

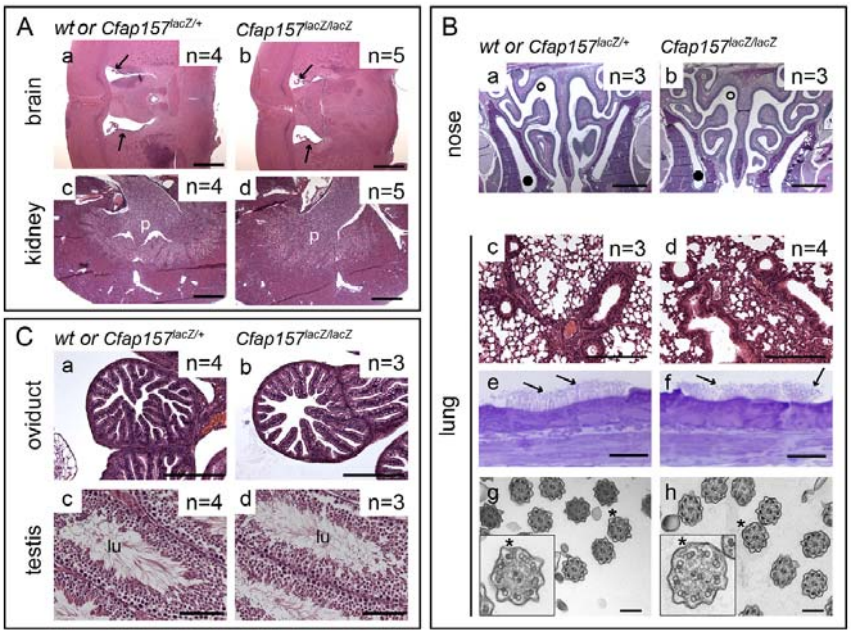

Fig. 5. *Cfap157*$^{lacZ/lacZ}$ tissues without phenotypic alteration. (A) HE-stained adult brain (a,b; coronal sections; arrows, lateral ventricles) and kidney (c,d; p, renal pelvis; one homozygous kidney completely sectioned to check for micro-cysts but none were found). Arrows indicate ventricles. (B) Periodic acid-Schiff (PAS) staining of coronal nose sections (a,b; open circle, lumen; filled circle, sinus), HE-stained lung sections (c,d), light microscopy of thin lung sections (e,f; arrows, cilia), TEM of pulmonary cilia (g,h; asterisks, axonemal profiles magnified in insets). (C) HE-stained oviduct (a,b) and testis sections (c,d; lu, lumen of seminiferous tubule). Scale bars: 1 mm in A; 1 mm in Ba,b; 250 µm in Bc,d and Ca,b; 10 µm in Be,f; 200 nm in Bg,h; 100 µm in Cc,d.

labelled fibrous sheath, and 18/139 looked like wild-type sperm, which contained fibrous sheath exclusively in the principal piece (n=34; Fig. 7Cb). Staining with MitoTracker revealed an accumulation of mitochondria near the axonemal link but not along the axoneme of the looped midpiece (n=75; Fig. 7Dd). The length of the looped midpiece (*Cfap157*$^{lacZ/lacZ}$, 23±1 µm, n=6; *Cfap157*$^{\Delta ex2/\Delta ex2}$, 23±1 µm, n=17; *Cfap157*$^{lacZ/+}$, 23±1 µm, n=8) and of the remaining flagellum (*Cfap157*$^{lacZ/lacZ}$, 94±7 µm, n=16; *Cfap157*$^{\Delta ex2/\Delta ex2}$, 93±4 µm, n=13; *Cfap157*$^{lacZ/+}$, 93±4 µm, n=6) was similar to wild type and consistent with previous wild-type measurements (Cummins and Woodall, 1985). Nuclei (n=147) and acrosomes (n=65) of *Cfap157* sperm stained with DAPI and lectin appeared normal (Fig. 7Ab,d,f,h). Collectively, these analyses show that CFAP157 is required for the normal organisation of the midpiece axoneme, for the transport/localisation of the fibrous sheath and mitochondria, as well as for elimination of excess cytoplasm, processes that occur in the seminiferous tubules prior to spermiation. CFAP157 is absent from epididymal sperm (Fig. S5), perhaps reflecting the disintegration of centrioles in mature sperm (Eddy, 2006) or the overall loss of proteins during sperm maturation (Skerget et al., 2015). This indicates that CFAP157 is no longer present in mature sperm and supports a function exclusively in the testis.

To monitor the development of the *Cfap157* phenotype in testes, we analysed sections of seminiferous tubules at all stages of spermatogenesis, which we identified by the size and shape of acrosomes and nuclei (Ahmed and de Rooij, 2009; Meistrich and Hess, 2013) that were indistinguishable between wild type and *Cfap157* mutants (n=3) at all stages (total of 246 mutant tubule sections). Consistent with previous observations (Zhang et al., 2012), mitochondria (stained using anti-COX IV antibodies) aligned in wild-type midpieces of spermatids beginning at stage 14/15 (arrowheads in Fig. 8Aa,a′,b,b′; Fig. S6Ac,c′) and formed slender threads projecting from the sperm heads into the lumen at stage 16 (arrowheads in Fig. 8Ac,c′; Fig. S6Ad-g,d′-g′). As in wild type, *Cfap157*-null tubules displayed aligned mitochondria beginning at stage 14/15 (arrowheads in Fig. 8Ad-f′; Fig. S6An,n′). At stage 16, mitochondrial threads appeared less regular, partly kinky and bulky (arrows Fig. 8Af,f′; Fig. S6Ar,r′), and sperm heads lining the lumen were not well oriented (Fig. 8Af,f′; Fig. S6Ao-r, o-r′). There was no evidence for the strong accumulation of mitochondria observed in cauda sperm (Fig. 7), suggesting that clustering of mitochondria occurs after spermiation. Prior to stage 12, the fibrous sheath marker AKAP3 was diffusely distributed in the cytoplasm of developing spermatids. As previously described (Sakai et al., 1986), fibre-like structures appeared first in spermatids at stage 13 (arrows in Fig. S6Ba,a′,l,l′) and were prominent thereafter (arrows in Fig. 8Ba,a′,c,c′). Fibres were present at a distance from the sperm heads in mature wild-type sperm (Fig. 8Bc,c′; Fig. S6Bg,g′), resulting in a zone devoid of AKAP3 staining between the sperm heads lining the lumen and the principal pieces (arrowheads in Fig. 8B; Fig. S6Bf,f′,g,g′). By

RESEARCH ARTICLE Development (2016) 143, 4736-4748 doi:10.1242/dev.139626

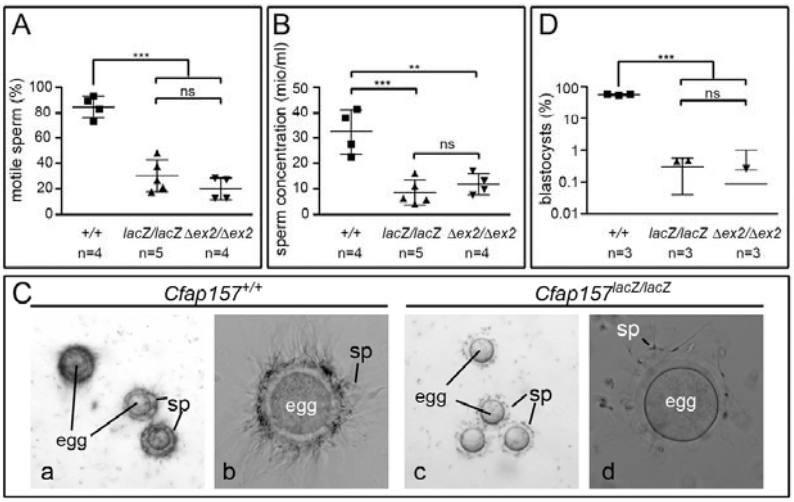

Fig. 6. Motility and fertility of *Cfap157* sperm. (A,B) Analysis of motility (A) and sperm number (B) of wild-type, homozygous *Cfap157*$^{lacZ/lacZ}$ and *Cfap157*$^{\Delta ex2/\Delta ex2}$ cauda sperm isolated from adult mice (>2 months old). (C) Pictures taken from Movies 3 and 4 performed during IVF of wild-type eggs with wild-type (a,b) and *Cfap157*$^{lacZ/lacZ}$ (c,d) sperm (sp). (D) Percentage of wild-type eggs that developed into blastocysts after IVF with wild-type or mutant sperm [logarithmic scale; three data points (zero values) are not shown]. Data are mean±s.d.; ns, not significant; $^{**}P<0.01$; $^{***}P<0.001$; *n*, number of males analysed.

contrast, fibrous, dotted and diffuse AKAP3 staining in *Cfap157* mutant sperm was found in abnormal positions and in the vicinity of sperm heads (asterisks in Fig. 8Bd,d′-f,f″; Fig. S6Bn-r,n′-r′), suggesting that ectopic accumulation of fibrous sheaths develops during late stages of spermiogenesis.

Ultrastructural defects in CFAP157-deficient sperm

TEM of *Cfap157*$^{lacZ/lacZ}$ cauda epididymis sections showed fewer sperm in the mutant than in the wild type (Fig. 9A) and expanded structures probably representing the abnormal *Cfap157*-null midpieces observed by light microscopy (Fig. 9Ab, blue arrows). Cell membranes around some of these structures were fragmented (Fig. 9Ab, yellow arrow), indicating reduced stability.

Longitudinal sections of *Cfap157*$^{lacZ/lacZ}$ sperm (Fig. 9Ca,b,g) revealed a dislocated sperm head (bent by 180° in Fig. 9Ca) and a large cytoplasmic remnant (arrow). Although microtubule fibres were not visible in this section, ODFs continuous in midpiece branches and the principal piece (Fig. 9Cb, arrows; Fig. S7Ae,f) suggested the fusion of two midpiece axonemes to form a single principal piece axoneme, i.e. an axonemal fork. The axonemal loop, visible by the ODFs, ran along the edge of the cell, encircling the excess cytoplasm (Fig. 9Cg, arrow).

Cfap157$^{lacZ/lacZ}$ midpiece regions contained irregular arrangements of mitochondria clustered around a central axonemal profile (Fig. 9Cc; stars, red arrow) and additional peripheral axoneme profiles (Fig. 9Cc, yellow arrows) that were surrounded by a fibrous sheath (Fig. 9Cd, hexagon) consistent with the enrichment of fibrous sheath in the midpieces of isolated cauda sperm (Fig. 7C). Peripheral axonemes were not surrounded by individual plasma membranes and are therefore unlikely to represent sections through folded or clustered flagella. The presence of similar groups of peripheral axonemes on opposite sides of the cell implied that bundles of a varying number of axonemes formed the axonemal loops, consistent with the lack of mitochondria attached to them (Fig. 7Dd, Fig. 9Cc,d).

Finally, we observed defective axonemes in *Cfap157* mutant sperm missing or displaying dislocated microtubule doublets at various flagellar levels [compare Fig. 9Bc,d with 9Cc,d,f (arrowheads) and Fig. 9Be with 9Ce (arrowheads); Fig. S7] in about one out of three mutant axoneme profiles. Profiles of coupled axonemes confirmed the presence of axoneme bundles in *Cfap157* mutant sperm (Fig. 9Cf). The mirror image of the incomplete axonemes and ODFs of this example (Fig. 9Cf, arrowheads and asterisks) suggested that both profiles belonged to the same folded axoneme. Defective axonemes typically possessed a central microtubule pair, suggesting that they were assembled incompletely rather than split after assembly, although we cannot exclude other mechanisms. Microtubules of mutant axonemes possessed inner and outer dynein arms (Fig. S8), indicating that *Cfap157* is not required for dynein arm assembly.

DISCUSSION

We identified *Cfap157* from microarray screens of FOXJ1-dependent genes in the mouse fetal lung (Stauber et al., 2016). *Cfap157* also appeared in several other screens that suggested activation by FOXJ1 (Choksi et al., 2014a), involvement in ciliogenesis (Hoh et al., 2012; Ivliev et al., 2012; McClintock et al., 2008) and association with human PCD (Geremek et al., 2011, 2014). Here, we show that CFAP157 is a novel FOXJ1 effector that is expressed in various motile ciliated tissues but essential only during spermatogenesis.

Cfap157: a FOXJ1 target with a sperm-specific function

Cfap157 expression correlated with *Foxj1* expression and the presence of motile cilia in mouse and frog, and endogenous *Cfap157* expression in mice depended on FOXJ1. Despite its

RESEARCH ARTICLE

Development (2016) 143, 4736-4748 doi:10.1242/dev.139626

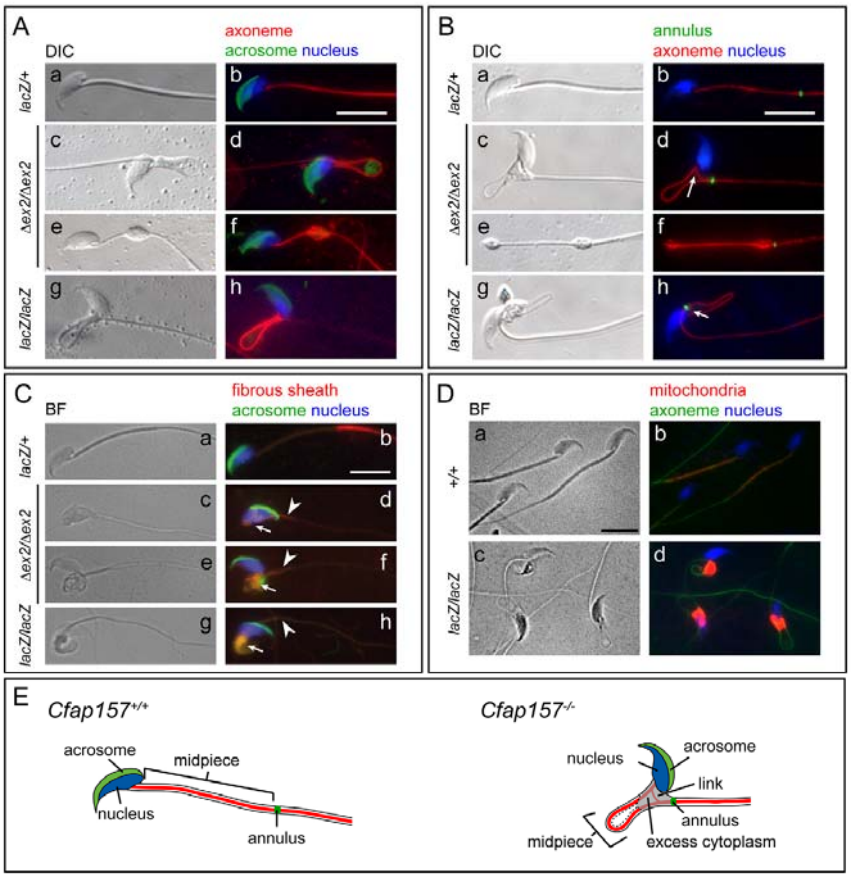

Fig. 7. Phenotypic analysis of *Cfap157* mutant sperm. (A) Cauda sperm from *Cfap157*$^{lacZ/+}$ (a,b), *Cfap157*$^{\Delta ex2/\Delta ex2}$ (c-f) and *Cfap157*$^{lacZ/lacZ}$ (g,h) mice stained for axonemes (red), nuclei (blue) and acrosomes (green). (B) Sperm of the same genotypes as in A stained for axonemes (red), nuclei (blue) and annuli (green); arrows indicate axonemal linker at the base of the midpiece loop. (C) Sperm of the same genotypes as in A stained for fibrous sheaths (red), nuclei (blue) and acrosomes (green); arrows indicate abnormal localisation of fibrous sheath material close to the sperm head; arrowheads indicate straight midpiece region. (D) Wild-type and *Cfap157*$^{lacZ/lacZ}$ sperm stained for mitochondria (red), nuclei (blue) and axonemes (green). (E) Schematic drawing depicting the *Cfap157* phenotype observed by immunocytochemistry; fibrous sheath and mitochondria are not shown (compare with D). DIC, differential interference contrast; BF, bright field. Scale bars: 10 µm.

expression in several tissues, both mutant *Cfap157* alleles specifically affected only the formation and function of the sperm flagellum, although we cannot rule out minor defects in other motile cilia without obvious functional consequences. Possibly, CFAP157 function is compensated for in some motile cilia after gene disruption, as described in *Cep131* mutant mice (Hall et al., 2013) and in zebrafish mutants (Rossi et al., 2015). However, the identity of any compensating factor remains undetermined and it appears plausible that the sperm flagellum with its unique accessory structures has requirements that differ from other motile cilia. This presumption is supported by mutations of other ciliogenesis factors that distinctly affect sperm cells: e.g. disruption of *Spef2* causes disorganised flagellar axonemes and male infertility but normal tracheal axonemes (Sironen et al., 2011). In contrast to *Cfap157*, *Spef2*-deficient mice still exhibit sinusitis and hydrocephalus, putatively due to a reduction of the beat frequency of the respective motile cilia (Sironen et al., 2011). Conservation of mouse and human CFAP157 protein (Table S1) suggests that human CFAP157 may play a similar role in male fertility and that mutations would result in a similar phenotype.

A unique sperm phenotype in *Cfap157* mutants

Impaired sperm motility, reduced sperm numbers and inefficient attachment of mutant spermatozoa to the zona pellucida (collectively observed in all 13 *Cfap157*$^{lacZ/lacZ}$ and 8 *Cfap157*$^{\Delta ex2/\Delta ex2}$ males analysed) can be explained by the expanded and disorganised midpiece and dislocated head, supernumerary axonemes and a disrupted axonemal arrangement.

RESEARCH ARTICLE Development (2016) 143, 4736-4748 doi:10.1242/dev.139626

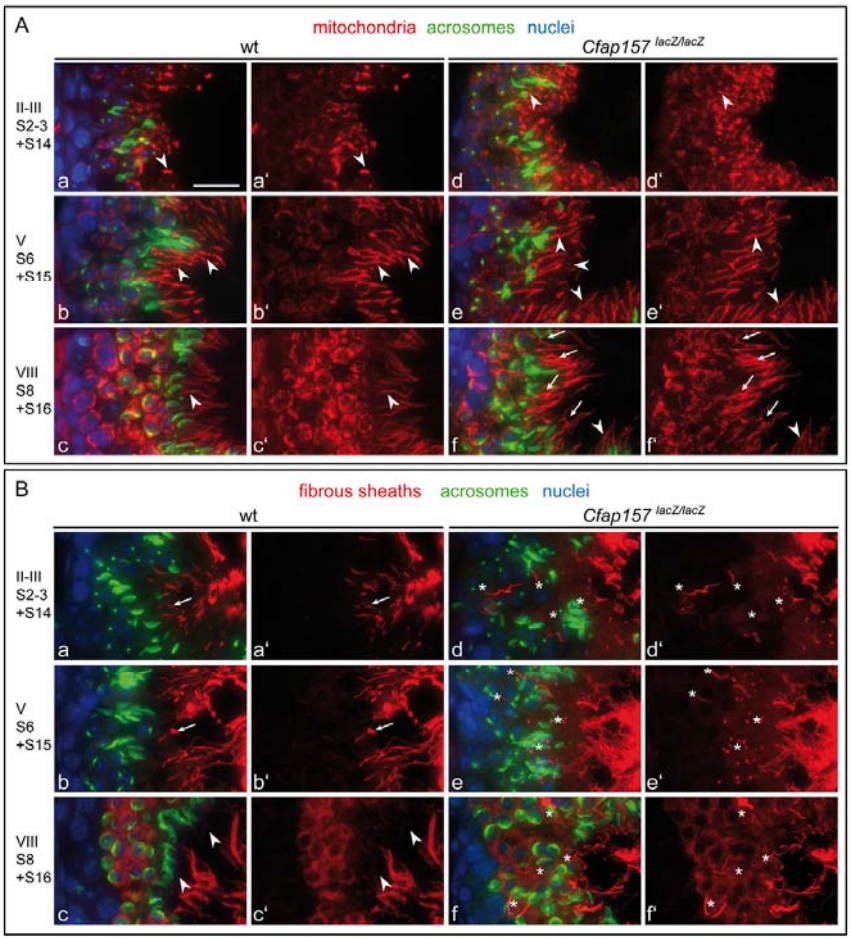

Fig. 8. Phenotypic analysis of *Cfap157* mutant testes. Sections of wild-type (Aa-c',Ba-c') and *Cfap157*$^{lacZ/lacZ}$ mutant (Ad-f',Bd-f') testes stained for acrosomes (green) and nuclei (blue), and (A) mitochondria (red; 155 analysed mutant tubule sections) or (B) fibrous sheaths (red; 91 analysed mutant tubule sections). Roman numbers indicate the stage of the epithelial cycle; arabic numbers indicate the stage of spermatogenesis. (A) Arrowheads indicate mitochondria aligning in threads; arrows indicate abnormally arranged mitochondria. (B) Arrows indicate forming fibres; arrowheads indicate normal midpiece regions devoid of fibrous sheath; asterisks indicate abnormally located fibrous sheath material. Scale bars: 25 µm. Lumen is towards the right.

Cfap157-deficient sperm heads are bent with respect to the flagellar axis; consequently, flagellar beating does not drive spermatozoa into the egg but along the surface, away from the egg. This and sterical hindrance may have caused the reduced binding to eggs and the failure to penetrate the zona pellucida that requires the impetus of the sperm (Buffone et al., 2012). The reduced sperm concentration is unlikely to contribute to infertility because a similar reduction in sperm numbers in *Arl4*-null mice did not affect fertility (Schürmann et al., 2002).

The most peculiar aspect of the phenotype was the looped axoneme in the disorganised midpiece region containing multiple axonemal profiles. The additional axonemal profiles could be derived either from ectopic nucleation of several axonemes or from fragmented or broken axonemes. However, tubulin staining showed continuous axonemes throughout the flagellum (e.g. Fig. 7A,B,D) and localisation of CFAP157 to basal bodies would be consistent with a centriolar function, arguing in favour of ectopic nucleation. Fibrous sheath normally occurs only in the principal piece and its formation progresses from distal to proximal up to the annulus (Irons and Clermont, 1982). The presence of fibrous sheath around *Cfap157*-deficient midpiece axonemes suggests that an apparently normal annulus may not be sufficient to prevent the formation of fibrous sheath in the midpiece. Immunocytochemical analysis suggested that the abnormal distribution of fibrous sheath occurs during late stages of spermiogenesis and that mitochondrial clustering develops

RESEARCH ARTICLE Development (2016) 143, 4736-4748 doi:10.1242/dev.139626

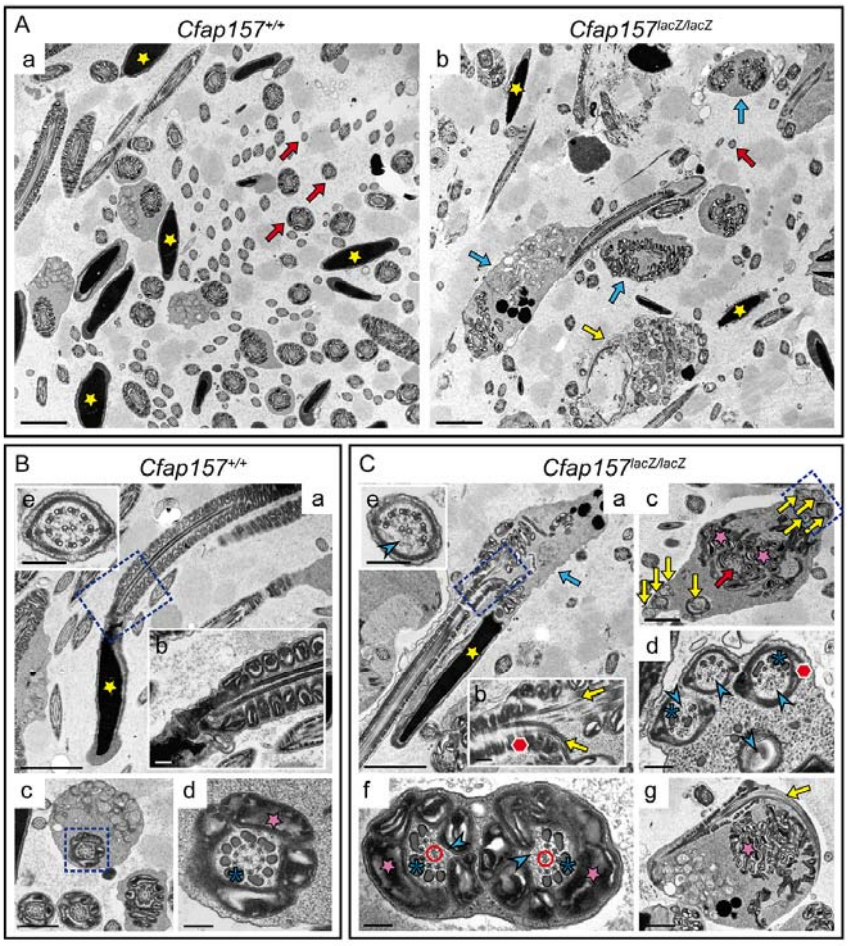

Fig. 9. Electron microscopy analysis of wild-type and *Cfap157*$^{lacZ/lacZ}$ sperm in the cauda epididymis. (A) Overviews of wild-type (a) and *Cfap157*$^{lacZ/lacZ}$ sections (b): yellow stars, sperm heads; red arrows, flagella. (B,C) Detailed images for wild type (B) and mutant (C). (a) Longitudinal section of a sperm cell: yellow stars, head; blue arrow, expanded midpiece. (b) Magnification of area boxed in a: yellow arrows, ODFs; hexagon, fibrous sheath. (c) Cross-section at the midpiece level; the wild-type section contains a cytoplasmic droplet. Red arrow indicates central axoneme; yellow arrows indicate peripheral axonemes; pink stars indicate mitochondria. (d) Magnification of the boxed area in c: pink star, mitochondria; asterisks, ODFs; blue arrowheads, missing microtubule doublets; hexagon, fibrous sheath. (e) Cross-sections of an axial filament: blue arrowhead, missing microtubule doublets. (f) Cross-section of a paired *Cfap157*^{lacZ} axoneme: pink star, mitochondria; asterisks, ODFs; blue arrowheads, missing microtubule doublets; red circles, central pairs. (g) Longitudinal section of a *Cfap157*^{lacZ} spermatozoon at the level of the axonemal loop: pink star, mitochondria. Scale bars: 2 µm in A; 2 µm in Ba,Ca; 0.2 µm in Bb,Cb; 1 µm in Bc,Cc; 0.2 µm in Bd,Cd; 0.2 µm in Be,Ce; 0.2 µm in Cf; 1 µm in Cg.

even after spermiation (Fig. 8). Formation of the sperm tail is essentially complete at spermiogenesis stage 12 (Vernet et al., 2016), preceding the alignment of mitochondria and formation of fibrous sheaths. This implies that the axonemal defects, including supernumerary axonemes develop prior to stage 12 and thus are the primary phenotype of *Cfap157*-null sperm cells. As differentiation of the sperm tail is difficult to assess in testis sections (Vernet et al., 2012), further ultrastructural analyses of testes and epididymis will clarify this issue.

Various mouse mutations that affect sperm morphology and motility have been identified (de Boer et al., 2015; reviewed by Escalier, 2006; Naz et al., 2009) but none of them resemble the *Cfap157* phenotype. Superficially, the structural defects of *Cfap157* mutant sperm showed some similarity to *Spem1*. In spermatozoa lacking *Spem1*, the midpiece wraps around the head, which is bent backwards and kept in this position by remnants of the cytoplasm (Zheng et al., 2007). *Cfap157* mutant sperm also contains excess cytoplasm; however, the axonemal loop of the midpiece appears to

RESEARCH ARTICLE Development (2016) 143, 4736-4748 doi:10.1242/dev.139626

be fixed by a small axonemal link that may emerge from an axonemal fork, the flagellum is not wrapped around the head, and the head is bent in smaller angles in isolated sperm. The presence of multiple flagellar axonemes in the proximal tail region and looped midpiece axonemal bundles has to the best of our knowledge not been previously described.

The localisation of CFAP157 in spermatozoa is currently unknown because we were unable to detect endogenous CFAP157 with our mouse antibodies and commercially available antibodies applying various fixation and staining protocols. Two anti-C9ORF117 antibodies produced and applied by the Human Protein Atlas both detect ciliary protein in human bronchus and nasopharynx (Ivliev et al., 2012) but show no or low diffuse cytoplasmic staining in human testis and epididymis (http://www.proteinatlas.org). This may indicate distinct localisation in different tissues or species, or be due to the inability of these antibodies to detect CFAP157 in developing spermatozoa.

Our data suggest CFAP157 localisation and function at basal bodies. An entry point into the biochemical characterisation of CFAP157 may be the validated interaction with CEP350, a centrosomal protein that binds microtubules (Hoppeler-Lebel et al., 2007; Patel et al., 2005). It controls microtubule stability and thereby plays a role in procentriole assembly, centriole elongation and Golgi organisation (Hoppeler-Lebel et al., 2007; Le Clech, 2008). Requirement of CEP350 for microtubule docking to the centrosome is controversial (Hoppeler-Lebel et al., 2007; Yan et al., 2006). CFAP157 could be involved in any of these processes. Intriguingly, CEP350 also targets proteins to the centrosome and is therefore required for ciliogenesis. An example is CYLD, a deubiquitinating enzyme that is anchored to the centrosome by CEP350, where it is required for migration and docking of basal bodies to the plasma membrane (Eguether et al., 2014).

In conclusion, we have identified a gene, *Cfap157*, that is expressed downstream of FOXJ1 in cell types carrying motile cilia with a pivotal function only in male germ cells. Our analyses suggest that CFAP157 is part of a novel mechanism that acts specifically in developing mammalian spermatozoa to ensure the formation of a single ultrastructurally correct flagellar axoneme and of a functional midpiece.

MATERIALS AND METHODS

Ethics statement, generation and husbandry of mice

Mouse and *Xenopus laevis* handling was in accordance with the German laws (Tierschutzgesetz), and was approved by the ethics committee of Lower Saxony for care and use of laboratory animals (LAVES) and by the Regional Government Stuttgart, Germany (A379/12 Zo 'Molekulare Embryologie'). Mice were housed in the animal facility of Hannover Medical School (ZTL) as approved by the responsible Veterinary Officer of the City of Hannover. Animal welfare was supervised and approved by the Institutional Animal Welfare Officer.

Cfap157^{lacZneo} mice were generated with EUCOMM ESC clone G05 [*1700019L03Rik*$^{tm1a(EUCOMM)Hmgu}$ https://www.eummcr.org/]. Other mouse strains were Zp3:Cre (de Vries et al., 2000), FLPe (Rodríguez et al., 2000), *Foxj1*$^{-}$ (Brody et al., 2000) and CD-1 or CD-1//129/Sv hybrid as wild type. Mice were genotyped by PCR as described in the supplementary Materials and Methods.

Computer-assisted sperm analysis (CASA) and *in vitro* fertilisation (IVF)

For CASA, sperm were isolated from the cauda epididymis in 150 µl HTF medium and capacitated for 90 min at 37°C. Sperm suspension (3 µl) were analysed in a Leja Standard Count 4 Chamber Slide under an Olympus CX41 (Zuber Optik) using the QualiSperm (Biophos optimised for human sperm) software that automatically measures motility rates and concentration of sperm. For IVF, sperm isolated from the cauda epididymis in HTF was capacitated for 2 h at 37°C and 5% CO_2. Eggs were isolated from superovulated wild-type females, incubated in HTF in groups of 40 with sperm for 6 h at 37°C under oil, washed and incubated in HTF. The presence of pronuclei was checked between 10 and 12 h after incubation with sperm. Development of blastocysts was checked after culture in KSOM from day 3.5 to 7.5 after IVF. Statistical analysis was performed using Prism (GraphPad) and one-way ANOVA.

Xenopus experiments

Xenopus microinjections, histological analyses and RNA *in situ* hybridisation were carried out essentially as described previously (Belo et al., 1997; Tingler et al., 2014). Full details are provided in the supplementary Materials and Methods.

Analysis of subcellular localisation of CFAP157-GFP in IMCD3 cells

CFAP157-GFP fusion proteins were transiently expressed in IMCD3 cells and analysed for GFP fluorescence. IMCD3 cells were also stained using acetylated and γ-tubulin. For further details, including the antibodies used, see the supplementary Materials and Methods.

Identification and validation of protein interaction partners

Tandem StrepII-Flag-tagged CFAP157 was transiently expressed in HEK293T cells and CFAP157 complexes were isolated (Gloeckner et al., 2007). Moreover, proteins from testis lysates were pulled down using purified StrepII-Flag-tagged CFAP157. Isolated CFAP157 complexes were analysed by LC-MS/MS as described previously (Boldt et al., 2011). Selected candidate interaction partners identified by MS were further analysed by co-immunoprecipitation. Details of constructs, SF-TAG purification, MS analysis and coimmunoprecipitation are provided in the supplementary Materials and Methods.

Histological methods

Immunofluorescence staining of testis sections and isolated sperm, section *in situ* hybridisation, β-galactosidase and Hematoxylin and Eosin staining were performed using standard procedures. Further details, including the antibodies used, can be found in the supplementary Materials and Methods.

Transmission electron microscopy (TEM)

Caudae epididymis and lungs were dissected from adult, 3-month-old wild-type and homozygous *Cfap157*^{lacZ} littermates, fixed, embedded and analysed as described previously (Rudat et al., 2014).

Southern and northern blot analysis

Southern and northern blot hybridisations were carried out according to standard procedures. Details on the probes and conditions used can be found in the supplementary Materials and Methods.

LR-PCR and (q)RT-PCR

Correct targeting of the *Cfap157* locus was confirmed by PCR on genomic DNA isolated from liver with the Expand Long Range Kit (Roche) according to the manufacturer's instructions. RT-PCR was performed on cDNA generated from total RNA isolated from various tissues of different genotypes. Details of PCR conditions, primers and fragment lengths can be found in the supplementary Materials and Methods.

Immunoprecipitation of CFAP157 from testis lysates

The generation of the monoclonal and polyclonal antibodies against CFAP157 is described in detail in the supplementary Materials and Methods. For immunoprecipitation, testes and epididymides were homogenised in 1 ml/100 mg RIPA buffer containing protease inhibitor (Roche). Lysate (500 µl) was incubated with 10 µl polyclonal antibody or monoclonal antibody 3B9 against CFAP157 for 4 h at 4°C and incubated with 20 µl prewashed protein G Sepharose (GE) overnight at 4°C. Beads were washed in RIPA buffer and resuspended in 2× sample buffer.

RESEARCH ARTICLE Development (2016) 143, 4736-4748 doi:10.1242/dev.139626

Precipitated proteins were detected using monoclonal antibody 3B9 (1:100) or polyclonal antibody (1:5000).

Acknowledgements
We thank EUCOMM for the targeted *CFAP157* ESCs; E. Nigg (Biozentrum, Basel, Switzerland) for the Myc-CEP350 plasmids; S. Brody (Washington University, St Louis, MO, USA) for *Foxj1* mice; M. Menon and M. Gaestel (Institute for Physiological Chemistry, MHH, Hanover, Germany) for Septin antibodies and MitoTracker; D. Conrad, C. Schippert and P. Hillemanns (Department of Gynaecology and Obstetrics, MHH, Hanover, Germany) for access to their CASA instruments and their help; and Georg Witman (University of Massachusetts, Worcester, MA, USA) for advice on the *Chlamydomonas* FAP157 sequence.

Competing interests
The authors declare no competing or financial interests.

Author contributions
M.W. designed and performed *in vivo* and *in vitro* experiments, validated knockout mice and antibodies, performed (co)immunoprecipitations, analysed data and wrote the paper; K.S.-G. established knockout mouse lines and performed *in vitro* fertilisations; M.S. participated in design and performance of some mouse experiments, analysed data and wrote the paper; C.W. and J.H. designed and performed electron microscopy, and analysed data; T.O. and M.B. designed and performed *Xenopus* experiments, and analysed data; K.B., T.B. and M.U. designed and performed tandem affinity purification and mass spectrometry, and analysed data; K.S. performed some immunoprecipitations, and stained, staged and analysed testis sections and mutant sperm; E.K. designed peptides and generated monoclonal antibodies; A.G. designed experiments, analysed data and wrote the paper; all authors read and approved the manuscript prior to submission.

Funding
This work was financially supported by the State of Lower Saxony (Israel.-Gemeinschaftsvorhaben ZN2630 to A.G.) and by the Deutsche Forschungsgemeinschaft Cluster of Excellence 'REBIRTH' to A.G. M.U. and K.B. were supported by a grant from the Tistou and Charlotte Kerstan Foundation. T.O. was supported by a PhD fellowship from the Landesgraduiertenförderung Baden-Württemberg.

Supplementary information
Supplementary information available online at
http://dev.biologists.org/lookup/doi/10.1242/dev.139626.supplemental

References

Afzelius, B. A. and Eliasson, R. (1983). Male and female infertility problems in the immotile-cilia syndrome. *Eur. J. Respir. Dis. Suppl.* **127**, 144-147.
Ahmed, E. A. and de Rooij, D. G. (2009). Staging of mouse seminiferous tubule cross-sections. *Methods Mol. Biol.* **558**, 263-277.
Alten, L., Schuster-Gossler, K., Beckers, A., Groos, S., Ulmer, B., Hegermann, J., Ochs, M. and Gossler, A. (2012). Differential regulation of node formation, nodal ciliogenesis and cilia positioning by Noto and Foxj1. *Development* **139**, 1276-1284.
Andersen, J. S., Wilkinson, C. J., Mayor, T., Mortensen, P., Nigg, E. A. and Mann, M. (2003). Proteomic characterization of the human centrosome by protein correlation profiling. *Nature* **426**, 570-574.
Banizs, B., Pike, M. M., Millican, C. L., Ferguson, W. B., Komlosi, P., Sheetz, J., Bell, P. D., Schwiebert, E. M. and Yoder, B. K. (2005). Dysfunctional cilia lead to altered ependyma and choroid plexus function, and result in the formation of hydrocephalus. *Development* **132**, 5329-5339.
Belo, J. A., Bouwmeester, T., Leyns, L., Kertesz, N., Gallo, M., Follettie, M. and De Robertis, E. M. (1997). Cerberus-like is a secreted factor with neutralizing activity expressed in the anterior primitive endoderm of the mouse gastrula. *Mech. Dev.* **68**, 45-57.
Blum, M., Schweickert, A., Vick, P., Wright, C. V. E. and Danilchik, M. V. (2014). Symmetry breakage in the vertebrate embryo: when does it happen and how does it work? *Dev. Biol.* **393**, 109-123.
Boldt, K., Mans, D. A., Won, J., van Reeuwijk, J., Vogt, A., Kinkl, N., Letteboer, S. J. F., Hicks, W. L., Hurd, R. E., Naggert, J. K. et al. (2011). Disruption of intraflagellar protein transport in photoreceptor cilia causes Leber congenital amaurosis in humans and mice. *J. Clin. Invest.* **121**, 2169-2180.
Brody, S. L., Yan, X. H., Wuerffel, M. K., Song, S.-K. and Shapiro, S. D. (2000). Ciliogenesis and left-right axis defects in forkhead factor HFH-4-null mice. *Am. J. Respir. Cell Mol. Biol.* **23**, 45-51.
Buffone, M. G., Ijiri, T. W., Cao, W., Merdiushev, T., Aghajanian, H. K. and Gerton, G. L. (2012). Heads or tails? Structural events and molecular mechanisms that promote mammalian sperm acrosomal exocytosis and motility. *Mol. Reprod. Dev.* **79**, 4-18.
Chen, J., Knowles, H. J., Hebert, J. L. and Hackett, B. P. (1998). Mutation of the mouse hepatocyte nuclear factor/forkhead homologue 4 gene results in an absence of cilia and random left-right asymmetry. *J. Clin. Invest.* **102**, 1077-1082.
Choksi, S. P., Babu, D., Lau, D., Yu, X. and Roy, S. (2014a). Systematic discovery of novel ciliary genes through functional genomics in the zebrafish. *Development* **141**, 3410-3419.
Choksi, S. P., Lauter, G., Swoboda, P. and Roy, S. (2014b). Switching on cilia: transcriptional networks regulating ciliogenesis. *Development* **141**, 1427-1441.
Cornwall, G. A. (2009). New insights into epididymal biology and function. *Hum. Reprod. Update* **15**, 213-227.
Cummins, J. M. and Woodall, P. F. (1985). On mammalian sperm dimensions. *J. Reprod. Fertil.* **75**, 153-175.
de Boer, P., de Vries, M. and Ramos, L. (2015). A mutation study of sperm head shape and motility in the mouse: lessons for the clinic. *Andrology* **3**, 174-202.
de Vries, W. N., Binns, L. T., Fancher, K. S., Dean, J., Moore, R., Kemler, R. and Knowles, B. B. (2000). Expression of Cre recombinase in mouse oocytes: a means to study maternal effect genes. *Genesis* **26**, 110-112.
Eddy, E. M. (2006). The spermatozoon. In *Knobil and Neills Physiology of Reproduction*, 3rd edn. (ed. J. D. Neill, T. M. Plant, D. W. Pfaff, J. R. G. Challi, D. M. de Kretser, J. S. Richards and P. M. Wassarman), pp. 1-52. London: Academic Press.
Eguether, T., Ermolaeva, M. A., Zhao, Y., Bonnet, M. C., Jain, A., Pasparakis, M., Courtois, G. and Tassin, A.-M. (2014). The deubiquitinating enzyme CYLD controls apical docking of basal bodies in ciliated epithelial cells. *Nat. Commun.* **5**, 4585.
Escalier, D. (2006). Knockout mouse models of sperm flagellum anomalies. *Hum. Reprod. Update* **12**, 449-461.
Fléchon, J.-E. (2016). The acrosome of eutherian mammals. *Cell Tissue Res.* **363**, 147-157.
Gerdes, J. M., Davis, E. E. and Katsanis, N. (2009). The vertebrate primary cilium in development, homeostasis, and disease. *Cell* **137**, 32-45.
Geremek, M., Bruinenberg, M., Zietkiewicz, E., Pogorzelski, A., Witt, M. and Wijmenga, C. (2011). Gene expression studies in cells from primary ciliary dyskinesia patients identify 208 potential ciliary genes. *Hum. Genet.* **129**, 283-293.
Geremek, M., Ziętkiewicz, E., Bruinenberg, M., Franke, L., Pogorzelski, A., Wijmenga, C. and Witt, M. (2014). Ciliary genes are down-regulated in bronchial tissue of primary ciliary dyskinesia patients. *PLoS ONE* **9**, e88216.
Gherman, A., Davis, E. E. and Katsanis, N. (2006). The ciliary proteome database: an integrated community resource for the genetic and functional dissection of cilia. *Nat. Genet.* **38**, 961-962.
Gloeckner, C. J., Boldt, K., Schumacher, A., Roepman, R. and Ueffing, M. (2007). A novel tandem affinity purification strategy for the efficient isolation and characterisation of native protein complexes. *Proteomics* **7**, 4228-4234.
Hall, E. A., Keighren, M., Ford, M. J., Davey, T., Jarman, A. P., Smith, L. B., Jackson, I. J. and Mill, P. (2013). Acute versus chronic loss of mammalian Azi1/Cep131 results in distinct ciliary phenotypes. *PLoS Genet.* **9**, e1003928.
Hermo, L., Pelletier, R.-M., Cyr, D. G. and Smith, C. E. (2010). Surfing the wave, cycle, life history, and genes/proteins expressed by testicular germ cells. Part 3: developmental changes in spermatid flagellum and cytoplasmic droplet and interaction of sperm with the zona pellucida and egg plasma membrane. *Microsc. Res. Tech.* **73**, 320-363.
Hoh, R. A., Stowe, T. R., Turk, E. and Stearns, T. (2012). Transcriptional program of ciliated epithelial cells reveals new cilium and centrosome components and links to human disease. *PLoS ONE* **7**, e52166.
Hoppeler-Lebel, A., Celati, C., Bellett, G., Mogensen, M. M., Klein-Hitpass, L., Bornens, M. and Tassin, A.-M. (2007). Centrosomal CAP350 protein stabilises microtubules associated with the Golgi complex. *J. Cell Sci.* **120**, 3299-3308.
Irons, M. J. and Clermont, Y. (1982). Kinetics of fibrous sheath formation in the rat spermatid. *Am. J. Anat.* **165**, 121-130.
Ivliev, A. E., 't Hoen, P. A. C., van Roon-Mom, W. M. C., Peters, D. J. M. and Sergeeva, M. G. (2012). Exploring the transcriptome of ciliated cells using in silico dissection of human tissues. *PLoS ONE* **7**, e35618.
Jacquet, B. V., Salinas-Mondragon, R., Liang, H., Therit, B., Buie, J. D., Dykstra, M., Campbell, K., Ostrowski, L. E., Brody, S. L. and Ghashghaei, H. T. (2009). FoxJ1-dependent gene expression is required for differentiation of radial glia into ependymal cells and a subset of astrocytes in the postnatal brain. *Development* **136**, 4021-4031.
Jain, R., Pan, J., Driscoll, J. A., Wisner, J. W., Huang, T., Gunsten, S. P., You, Y. and Brody, S. L. (2010). Temporal relationship between primary and motile ciliogenesis in airway epithelial cells. *Am. J. Respir. Cell Mol. Biol.* **43**, 731-739.
Kleene, K. C. (2005). Sexual selection, genetic conflict, selfish genes, and the atypical patterns of gene expression in spermatogenic cells. *Dev. Biol.* **277**, 16-26.
Le Clech, M. (2008). Role of CAP350 in centriolar tubule stability and centriole assembly. *PLoS ONE* **3**, e3855.
Lee, L. (2013). Riding the wave of ependymal cilia: genetic susceptibility to hydrocephalus in primary ciliary dyskinesia. *J. Neurosci. Res.* **91**, 1117-1132.
Li, W., Park, J. Y., Zheng, D., Hoque, M., Yehia, G. and Tian, B. (2016). Alternative cleavage and polyadenylation in spermatogenesis connects chromatin regulation with post-transcriptional control. *BMC Biol.* **14**, 6.

Development (2016) 143, 4736-4748 doi:10.1242/dev.139626

Lyons, R. A., Saridogan, E. and Djahanbakhch, O. (2006). The reproductive significance of human fallopian tube cilia. *Hum. Reprod. Update* **12**, 363-372.
McClintock, T. S., Glasser, C. E., Bose, S. C. and Bergman, D. A. (2008). Tissue expression patterns identify mouse cilia genes. *Physiol. Genomics* **32**, 198-206.
Meistrich, M. L. and Hess, R. A. (2013). Assessment of spermatogenesis through staging of seminiferous tubules. *Methods Mol. Biol.* **927**, 299-307.
Naz, R. K., Engle, A. and None, R. (2009). Gene knockouts that affect male fertility: novel targets for contraception. *Front. Biosci.* **14**, 3994-4007.
Nigg, E. A. and Raff, J. W. (2009). Centrioles, centrosomes, and cilia in health and disease. *Cell* **139**, 663-678.
Nonaka, S., Tanaka, Y., Okada, Y., Takeda, S., Harada, A., Kanai, Y., Kido, M. and Hirokawa, N. (1998). Randomization of left-right asymmetry due to loss of nodal cilia generating leftward flow of extraembryonic fluid in mice lacking KIF3B motor protein. *Cell* **95**, 829-837.
Patel, H., Truant, R., Rachubinski, R. A. and Capone, J. P. (2005). Activity and subcellular compartmentalization of peroxisome proliferator-activated receptor alpha are altered by the centrosome-associated protein CAP350. *J. Cell Sci.* **118**, 175-186.
Praveen, K., Davis, E. E. and Katsanis, N. (2015). Unique among ciliopathies: primary ciliary dyskinesia, a motile cilia disorder. *F1000Prime Rep.* **7**, 36.
Rodríguez, C. I., Buchholz, F., Galloway, J., Sequerra, R., Kasper, J., Ayala, R., Stewart, A. F. and Dymecki, S. M. (2000). High-efficiency deleter mice show that FLPe is an alternative to Cre-loxP. *Nat. Genet.* **25**, 139-140.
Rossi, A., Kontarakis, Z., Gerri, C., Nolte, H., Hölper, S., Krüger, M. and Stainier, D. Y. R. (2015). Genetic compensation induced by deleterious mutations but not gene knockdowns. *Nature* **524**, 230-233.
Rudat, C., Grieskamp, T., Röhr, C., Airik, R., Wrede, C., Hegermann, J., Herrmann, B. G., Schuster-Gossler, K. and Kispert, A. (2014). Upk3b is dispensable for development and integrity of urothelium and mesothelium. *PLoS ONE* **9**, e112112.
Sakai, Y., Koyama, Y.-I., Fujimoto, H., Nakamoto, T. and Yamashina, S. (1986). Immunocytochemical study on fibrous sheath formation in mouse spermiogenesis using a monoclonal antibody. *Anat. Rec.* **215**, 119-126.
Santos, N. and Reiter, J. F. (2008). Building it up and taking it down: the regulation of vertebrate ciliogenesis. *Dev. Dyn.* **237**, 1972-1981.
Schürmann, A., Koling, S., Jacobs, S., Saftig, P., Krauss, S., Wennemuth, G., Kluge, R. and Joost, H.-G. (2002). Reduced sperm count and normal fertility in male mice with targeted disruption of the ADP-ribosylation factor-like 4 (Arl4) gene. *Mol. Cell. Biol.* **22**, 2761-2768.
Sironen, A., Kotaja, N., Mulhern, H., Wyatt, T. A., Sisson, J. H., Pavlik, J. A., Miilunieml, M., Fleming, M. D. and Lee, L. (2011). Loss of SPEF2 function in mice results in spermatogenesis defects and primary ciliary dyskinesia. *Biol. Reprod.* **85**, 690-701.
Skerget, S., Rosenow, M. A., Petritis, K. and Karr, T. L. (2015). Sperm proteome maturation in the mouse epididymis. *PLoS ONE* **10**, e0140650.
Spassky, N., Merkle, F. T., Flames, N., Tramontin, A. D., García-Verdugo, J. M. and Alvarez-Buylla, A. (2005). Adult ependymal cells are postmitotic and are derived from radial glial cells during embryogenesis. *J. Neurosci.* **25**, 10-18.
Stannard, W. and O'Callaghan, C. (2006). Ciliary function and the role of cilia in clearance. *J. Aerosol. Med.* **19**, 110-115.
Stauber, M., Weidemann, M., Dittrich-Breiholz, O., Lobschat, K., Alten, L., Mai, M., Beckers, A., Kracht, M. and Gossler, A. (2016). Identification of FOXJ1 effectors during ciliogenesis in the foetal respiratory epithelium and embryonic left-right organiser of the mouse. *Dev. Biol.* (in press).
Stubbs, J. L., Oishi, I., Izpisúa Belmonte, J. C. and Kintner, C. (2008). The forkhead protein Foxj1 specifies node-like cilia in Xenopus and zebrafish embryos. *Nat. Genet.* **40**, 1454-1460.
Takeda, S., Yonekawa, Y., Tanaka, Y., Okada, Y., Nonaka, S. and Hirokawa, N. (1999). Left-right asymmetry and kinesin superfamily protein KIF3A: new insights in determination of laterality and mesoderm induction by kif3A-/- mice analysis. *J. Cell Biol.* **145**, 825-836.
Tingler, M., Ott, T., Tözser, J., Kurz, S., Getwan, M., Tisler, M., Schweickert, A. and Blum, M. (2014). Symmetry breakage in the frog Xenopus: role of Rab11 and the ventral-right blastomere. *Genesis* **52**, 588-599.
Vernet, N., Mahadevaiah, S. K., Ellis, P. J. I., de Rooij, D. G. and Burgoyne, P. S. (2012). Spermatid development in XO male mice with varying Y chromosome short-arm gene content: evidence for a Y gene controlling the initiation of sperm morphogenesis. *Reproduction* **144**, 433-445.
Vernet, N., Mahadevaiah, S. K., Decarpentrie, F., Longepied, G., de Rooij, D. G., Burgoyne, P. S. and Mitchell, M. J. (2016). Mouse Y-encoded transcription factor Zfy2 is essential for sperm head remodelling and sperm tail development. *PLoS ONE* **11**, e0145398.
Vij, S., Rink, J. C., Ho, H. K., Babu, D., Eitel, M., Narasimhan, V., Tiku, V., Westbrook, J., Schierwater, B. and Roy, S. (2012). Evolutionarily ancient association of the FoxJ1 transcription factor with the motile ciliogenic program. *PLoS Genet.* **8**, e1003019.
Yan, X., Habedanck, R. and Nigg, E. A. (2006). A complex of two centrosomal proteins, CAP350 and FOP, cooperates with EB1 in microtubule anchoring. *Mol. Biol. Cell* **17**, 634-644.
Yániz, J. L., Soler, C. and Santolaria, P. (2015). Computer assisted sperm morphometry in mammals: a review. *Anim. Reprod. Sci.* **156**, 1-12.
Yu, X., Ng, C. P., Habacher, H. and Roy, S. (2008). Foxj1 transcription factors are master regulators of the motile ciliogenic program. *Nat. Genet.* **40**, 1445-1453.
Zhang, Y., Ou, Y., Cheng, M., Saadi, H. S., Thundathil, J. C. and van der Hoorn, F. A. (2012). KLC3 is involved in sperm tail midpiece formation and sperm function. *Dev. Biol.* **366**, 101-110.
Zheng, H., Stratton, C. J., Morozumi, K., Jin, J., Yanagimachi, R. and Yan, W. (2007). Lack of Spem1 causes aberrant cytoplasm removal, sperm deformation, and male infertility. *Proc. Natl. Acad. Sci. USA* **104**, 6852-6857.

The evolutionary conserved FOXJ1 target gene *Fam183b* is essential for motile cilia in Xenopus but dispensable for ciliary function

www.nature.com/scientificreports

SCIENTIFIC REPORTS

OPEN

The evolutionary conserved FOXJ1 target gene *Fam183b* is essential for motile cilia in *Xenopus* but dispensable for ciliary function in mice

Received: 16 April 2018
Accepted: 20 September 2018
Published online: 02 October 2018

Anja Beckers[1], Tim Ott[2], Karin Schuster-Gossler[1], Karsten Boldt[3], Leonie Alten[1], Marius Ueffing[3], Martin Blum[2] & Achim Gossler[1]

The transcription factor FOXJ1 is essential for the formation of motile cilia throughout the animal kingdom. Target genes therefore likely constitute an important part of the motile cilia program. Here, we report on the analysis of one of these targets, *Fam183b*, in *Xenopus* and mice. *Fam183b* encodes a protein with unknown function which is conserved from the green algae *Chlamydomonas* to humans. *Fam183b* is expressed in tissues harbouring motile cilia in both mouse and frog embryos. FAM183b protein localises to basal bodies of cilia in mIMCD3 cells and of multiciliated cells of the frog larval epidermis. In addition, FAM183b interacts with NUP93, which also localises to basal bodies. During frog embryogenesis, *Fam183b* was dispensable for laterality specification and brain development, but required for ciliogenesis and motility of epidermal multiciliated cells and nephrostomes, i.e. the embryonic kidney. Surprisingly, mice homozygous for a null allele did not display any defects indicative of disrupted motile ciliary function. The lack of a cilia phenotype in mouse and the limited requirements in frog contrast with high sequence conservation and the correlation of gene expression with the presence of motile cilia. This finding may be explained through compensatory mechanisms at sites where no defects were observed in our FAM183b-loss-of-function studies.

Cilia are microtubule-based organelles that protrude from the cell surface. Cilia are categorised as non-motile (also called primary) or motile[1]. Virtually every vertebrate cell carries at some point a primary cilium, which is critical for sensing of external stimuli and signal transduction (reviewed in[2,3]). In contrast, motile cilia are present on specialised cell types; they either move cells through the surrounding medium or extracellular fluids along the cell surface (e.g.[4–6]). Motile cilia are essential for normal embryonic development and for function of a multitude of tissues. Single motile cilia on cells of the left-right organiser (LRO) of vertebrate embryos rotate and thereby generate a leftward fluid flow, which is essential for the asymmetric development of visceral organs[7–9]. Multiple motile cilia that are present on the surface of epithelial cells of the respiratory tract, the fallopian tube, or on ependymal cells lining the ventricles, beat in a coordinated manner. They thereby clear the airways from inhaled particles or pathogens[5,10], support the movement of eggs into the ampulla of the oviduct and towards the uterus[11], or contribute to the cerebrospinal fluid flow[6,12–14]. The highly specialised motile cilium of the sperm cell, the flagellum, is essential for sperm motility and fertilisation[4]. Dys- or impaired function of motile cilia in humans lead to a condition referred to as primary cilia dyskinesia (PCD). PCD patients suffer from impaired mucociliary clearance and respiratory problems. Accompanying defects may include organ situs randomisation associated with cardiac malformations, male infertility, and - less frequently - reduced female fertility and hydrocephalus (reviewed in[15]), although the latter is frequently found in mouse models of PCD[14]. Mucociliary epithelia are

[1]Institute for Molecular Biology, OE5250, Hannover Medical School, Carl-Neuberg-Str. 1, 30625, Hannover, Germany. [2]Institute of Zoology, University of Hohenheim, Garbenstraße 30, 70593, Stuttgart, Germany. [3]Institute of Ophthalmic Research, Center for Ophthalmology, University of Tübingen, Röntgenweg 11, 72076, Tübingen, Germany. Anja Beckers and Tim Ott contributed equally. Correspondence and requests for materials should be addressed to M.B. (email: martin.blum@uni-hohenheim.de) or A.G. (email: gossler.achim@mh-hannover.de)

also encountered outside of the airways. For example, as a first line of defense, multiciliated cells (MCCs) in the *Xenopus* tadpole skin move mucus across the epithelium to keep it free from pathogens[16].

In vertebrates, the development of motile cilia depends critically on the transcription factor FOXJ1[17–23]. FOXJ1 activates the transcription of numerous known ciliary genes[6,20,21,24–28] and acts downstream of NOTO in the mouse LRO[18,29]. Genes with unknown function that act downstream of FOXJ1 are likely also required for the formation or function of motile cilia. In microarray screens for FOXJ1 target genes, we have identified *Fam183b* as one such candidate gene[28].

Here, we describe the expression and functional analysis of *Fam183b* in frog embryos and mice. In both species, expression was correlated with the presence of motile cilia. FAM183b protein localised to the basal body and interacted with nucleoporin NUP93, which also localises to the basal body. Knockdown of the *Fam183b* ortholog in *Xenopus* embryos resulted in severely impaired ciliary movement in the tadpole skin. Surprisingly, a null allele in mice had no obvious cilia-related phenotypes, suggesting the presence of mechanisms that effectively compensate the loss of FAM183b in mice.

Results

Expression and subcellular localisation of *Fam183b*. *Fam183b* encodes a protein of 137 amino acids with unknown biochemical function. FAM183b is homologous to the flagellar associated protein FAP144 (ACJ06133.1) of *Chlamydomonas* and highly conserved from cnidarians to mammals (Supplementary Table S1). Most vertebrate genomes harbor one Fam183 gene, which in the mouse is called *Fam183b*, while in all other species it is referred to as *Fam183a*. The human genome is the only case in which two Fam183 genes have been annotated (Fig. 1A), which are referred to as FAM183A (hgnc_id = HGNC:34347) and FAM183B (hgnc_id = HGNC:34511). The latter represents a pseudogene (https://www.genenames.org/cgi-bin/search?search_type=all&search=fam183b&submit=Submit). Thus, the mouse *Fam183b* gene constitutes the ortholog of *Fam183a* genes in other vertebrates and humans (http://www.informatics.jax.org/marker/MGI:1922679).

In early mouse embryos, *Fam183b* expression, detected by whole mount *in situ* hybridisation (WISH), was confined to the LRO at E7.75 (node; arrowhead in Fig. 1Ba). In *Noto*-mutant E7.75 embryos, transcripts were not detected (Fig. 1Bb), indicating that *Fam183b* acts downstream of NOTO. Absence of *Fam183b* transcripts may result from down-regulation of *Foxj1* in *Noto* mutants, as NOTO acts upstream of FOXJ1 in the LRO[18] and *Fam183b* is down-regulated in the *Foxj1*-mutant foetal respiratory epithelium[28]. In adult mice, strong *Fam183b* expression was detected by RT-PCR in tissues carrying motile cilia, while lower transcript levels were found in a few additional tissues such as eye and heart (Fig. 1C). Strong expression in cells carrying motile cilia was consistently seen upon *in situ* hybridisation of histological tissue sections, i.e. in spermatogenetic cells in the testis (Fig. 1Da, arrows in a'), multiciliated cells of the fallopian tube (arrows in Fig. 1Db'), the respiratory tract (Fig. 1Dc, arrow in c', d, arrows in d', d") as well as the choroid plexus (CP; Fig. 1De) and ependymal layer of the brain (Fig. 1De, arrow in e'). Notable exceptions from this correlation were found in developing follicles in the ovary (arrows in Fig. 1Db) and in the eye, where photoreceptor cells and cells of the inner nuclear and ganglion cell layers of the retina displayed *Fam183b* mRNA staining (Fig. 1Df,f'). *In situ* hybridisation of *Xenopus laevis* embryos revealed *fam183a* expression at stage 20 in the gastrocoel roof plate (GRP; Fig. 1Ea,a'), i.e. the *Xenopus* LRO[30] and in the floor plate of the neural tube (FP; Fig. 1Ea'). At stage 34, transcripts were detected in the ciliated nephrostomes (white arrows in Fig. 1Eb) and epidermal MCCs (black arrows in Fig. 1Eb). Stage 45 tadpoles revealed *fam183a* gene expression in the sub-commissural organ, the zona limitans intrathalamica and the floor plate of the brain (SCO, ZLI, and FP; Fig. 1Ec'), in the dorsal epithelium of the branchial chambers (inset in Fig. 1Ec and Fig. 1Ec"), and in the stomach (Fig. 1Ec"'). Overexpression of *foxj1* on the left side of *Xenopus* embryos induced ectopic expression of *fam183a* (Fig. 1F), corroborating the requirement of FOXJ1 for *Fam183b* expression in mice (Fig. 1B and[28]) and further supporting the notion that FAM183b acts downstream of FOXJ1 and NOTO.

Antibodies generated against a peptide of mouse FAM183b did not detect the endogenous protein by indirect immunofluorescence in cells or on tissue sections (not shown). In order to investigate the subcellular localisation of FAM183b, we expressed N-terminally GFP-tagged mouse FAM183b in *Xenopus* embryos and observed that tagged FAM183b localised to basal bodies, as shown by co-staining with centrin4 (*Xenopus*, Fig. 2A). In contrast, C- and N-terminally Flag-tagged FAM183b expressed in mIMCD3 cells, which were induced to form (primary) cilia, only partially colocalised with the centrosome/basal body marker γ-tubulin (Fig. 2B), and individual mIMCD3 cells with strong overexpression of FAM183b displayed staining throughout the cell (Fig. 2Bc,c',d,d'). Collectively, these data demonstrate that expression of FAM183b in tissues carrying motile cilia is conserved between mouse and frog, suggesting a conserved ciliary function in these two vertebrate model organisms.

***Fam183b* interaction partners.** In a first attempt to approach the unknown biochemical function of FAM183b, we set out to identify interaction partners. To that end, a yeast-two-hybrid (Y2H) screen was performed using a testis library. In addition, SF-TAP-tagged[31] FAM183b was expressed in HEK293 cells, affinity purified, and analysed by liquid chromatography fractionation in combination with mass spectrometry (LC-MS). Non-promiscuous candidate interaction partners identified in the Y2H screen were NUP93, TMEM269 and ANKRD36 (Supplementary Table S2). NUP93 was identified by LC-MS as well, in addition to chaperones, mitochondrial, ribosomal and other proteins not related to motile cilia or centrosomes (Supplementary Table S3). Co-immunoprecipitation (IP) assays using CHO cells co-expressing Flag-tagged FAM183b and Myc-tagged NUP93 confirmed the interaction of FAM183b with NUP93 (Fig. 2C). The centrosomal localisation of endogenous NUP93 in mIMCD3 cells further supported this notion (Fig. 2D). Localisation of FAM183b was not observed at the nuclear envelop of mIMCD3 cells, even in cells strongly overexpressing Flag-tagged-FAM183b (Fig. 2Bc,d). These data suggested that interaction of NUP93 with FAM183b was confined to the centrosome.

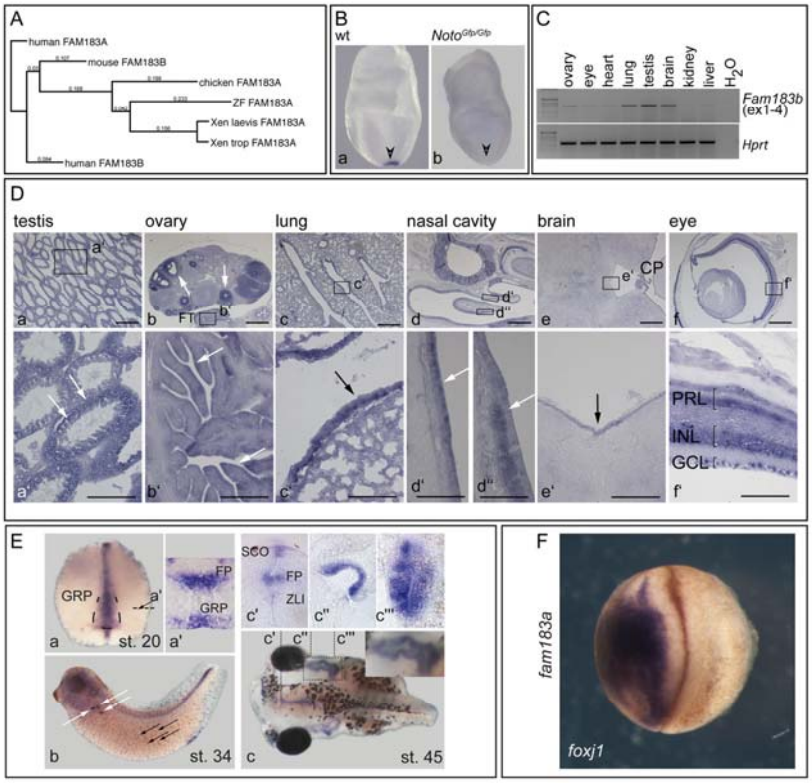

Figure 1. Expression of *Fam183b*. (**A**) Phylogram of vertebrate *Fam183* genes rooted on human *FAM183A*. Sequences used for alignment and phylogenetic analysis: human, HGNC-34347 and HGNC-34511; mouse, Q5NC57; chicken, F1P3Y5; Xen. tropicalis, XP_004914015; Xen. laevis, XP_018113781; zebrafish, ZDB-GENE-111103-1. (**B**) WISH of E7.75 wild type (wt) (a) and *Noto*$^{Gfp/Gfp}$ (b) mutant embryos shows NOTO-dependent expression of *Fam183b* in the LRO. (**C**) Analysis of *Fam183b* expression by RT-PCR of RNA from adult organs, as indicated. Full size gel is shown in Supplementary Figure S1. (**D**) SISH analysis of adult tissues, as indicated. Boxed areas in a–f outline regions shown at higher magnification in a'–f'. Arrows point to sites of expression. FT: fallopian tube; CP: choroid plexus; PRL: photoreceptor layer; INL: inner nuclear layer; GCL: ganglion cell layer. (**E**) Expression of *fam183a* in *Xenopus laevis*. *Fam183a* mRNA was found at stage 20 in the floor plate (FP) and LRO (GRP; a,a'); at stage 34 in MCCs and nephrostomes (b); and at stage 45 (c) in the sub-commissural organ (SCO), the zona limitans intrathalamica (ZLI) and the floor plate of the brain (c'), in the dorsal lining of the branchial chamber (inset in c and c"), and the stomach (c""). (**F**) *Fam183a* is a *foxj1* target gene. Embryos were unilaterally injected on the left side with a *foxj1 mRNA* and analysed for *fam183a* expression. *foxj1*, injected side. Scale bars: Da–f = 500 μm, a'–f' = 100 μm.

Functional analysis of *fam183a* in *Xenopus laevis*. To assess the physiological function of FAM183a in *Xenopus* embryos, we interfered with protein translation using morpholino oligonucleotides (MO) to block translation (TBMO) or splicing of exon 1 (SBMO), respectively. MOs were unilaterally injected into the epidermal lineage at the 4-cell stage, such that the uninjected side served as an internal control. Treated specimens were cultured to stage 33 and analysed for ciliary motility of the epidermal MCCs. Tadpoles at that stage glide across the agar layer of culture dishes using the motility of skin MCCs[32]. Gliding behaviour was pronounced on the uninjected side, while no motility was detectable when specimens were flipped over to the injected side (not shown), indicating that ciliogenesis or ciliary motility were impaired. To assess cilia and their motility directly, high-speed video microscopy was performed on control and injected sides of morphant tadpoles at stage 33. Compared to wild type specimens (Movie S1), ciliation and ciliary motility were severely impaired ($p < 0.0001$, respectively) on the MO-injected side, with both MOs yielding comparable results (Movies S2, S3). Ciliation of skin MCCs was impaired, with fewer and shorter cilia on morphant MCCs (Fig. 3A). Additional phenotypes observed in the morphants include frequent pericardial edema (arrow head in Fig. 3Bb, $p < 0.0001$), which could be due to

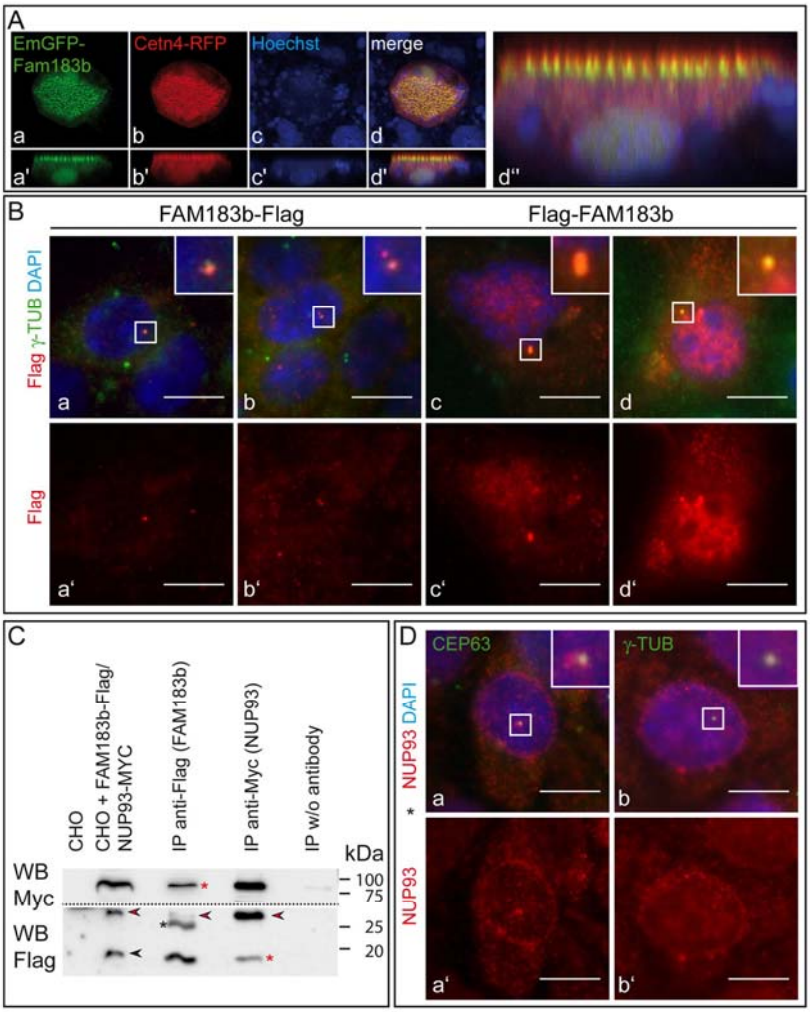

Figure 2. Subcellular localisation of FAM183B. (**A**) Co-localisation of mouse FAM183b-GFP with centrin4 in stage 33 *Xenopus* embryos. (**B**) Detection of C- and N-terminally Flag-tagged FAM183b in mIMCD3 cells by indirect immunofluorescence showing partial overlap with γ-tubulin. (**C**) Co-IP of tagged FAM183b and NUP93, indicating interaction. Red asterisks: co-IP; black asterisk: anti-Flag light chain detected by secondary antibody; black arrowhead: FAM183b at the expected apparent molecular weight; red arrowheads: background band detected in transfected CHO cells and IPs. Full size Western blots are shown in Supplementary Figure S2. (**D**) Co-localisation of endogenous NUP93 with CEP63 and γ-tubulin at centrosomes. Scale bars: Ba–d,a'–d', Da,b,a',b' = 10 µm.

defective motility of nephrostome cilia or alternatively cardiac or lymphatic dysfunction[33]. In contrast, we did not detect evidence of cardiac/gut looping defects or hydrocephalus (Fig. 3C,D, and data not shown; median values for ventricle profiles: WT = 238269 µm², TBMO = 25909 µm² and SBMO = 24454 µm²). This may suggest that cilia in the LRO are functioning normally despite the dramatic ciliary phenotype in the embryonic epidermis. However, given that pericardial edema may complicate ascertainment of the cardiac loop, to be certain that global LR patterning is normal would require additional molecular marker analysis or an examination of cilia in the LRO. In addition, the evolution of hydrocephalus in *Xenopus* due to cilia dysfunction is not well understood, so whether normal ventricle size is indicative of normal cilia function remains unclear.

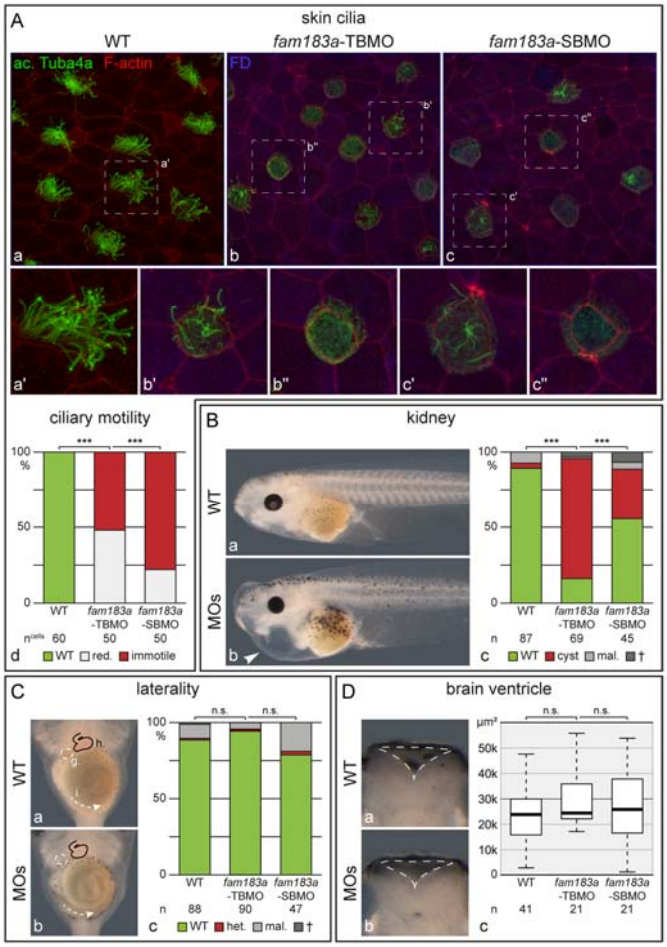

Figure 3. Functional analysis of *fam183a* in *Xenopus laevis*. (**A**) Embryos at the 4-cell stage were injected with *fam183a*-TBMO (b) or -SBMO (c), cultured to stage 33 and analysed for epidermal MCC ciliation (a–c) and ciliary beating (d). Note that cilia were reduced in length and number in MCCs of morphant specimens. Stippled boxes in (a–c) indicate the regions shown enlarged (a'–c"). Edemata (**B**), organ situs (**C**) and hydrocephalus (**D**) were analyzed at stage 45. Note that epidermal cilia defects and cardial edemata, were encountered in a statistically significant proportion of specimens, while rare LR defects and hydrocephalus were not significant. White arrowhead in (**B**b) highlights cardial edema; arrangement of inner organs and gut coiling in (**C**a,b) was illustrated by outlines and arrows, respectively; ventricular margins in (**D**a,b) were depicted by strippled outlines. FD: fluorescin dextran; g: gall bladder; h: heart; het., heterotaxia; i: intestine; mal: malformed; red. reduced; Sa: situs ambiguus; Si: situs inversus; Ss: situs solitus; +: dead.

Functional analysis of *Fam183b* in the mouse. To analyse the physiological function of FAM183b in mammals, we generated a conditional allele in mice. To that end, two loxP sites were introduced, 1.5 kb upstream of the transcriptional start site into a region of minimal sequence conservation across species, and downstream of exon 1, respectively (Fig. 4A). Cre-mediated recombination deletes the promoter region and transcriptional and translational start sites (*Fam183b*$^{\Delta ex1}$) and thus should prevent the translation of FAM183b protein. To generate mice lacking FAM183b in all tissues, we deleted the floxed region of the *Fam183b* locus in the female germ line using *ZP3:Cre* mice[34]. Homozygous *Fam183b*$^{\Delta ex1}$ mice were born at Mendelian ratio (7/30) and showed no obvious abnormalities. Loss of *Fam183b* expression was assessed at the RNA level by RT-PCR, Northern blot hybridisation and WISH of early embryos. No transcripts containing exon 1, and only very low amounts of

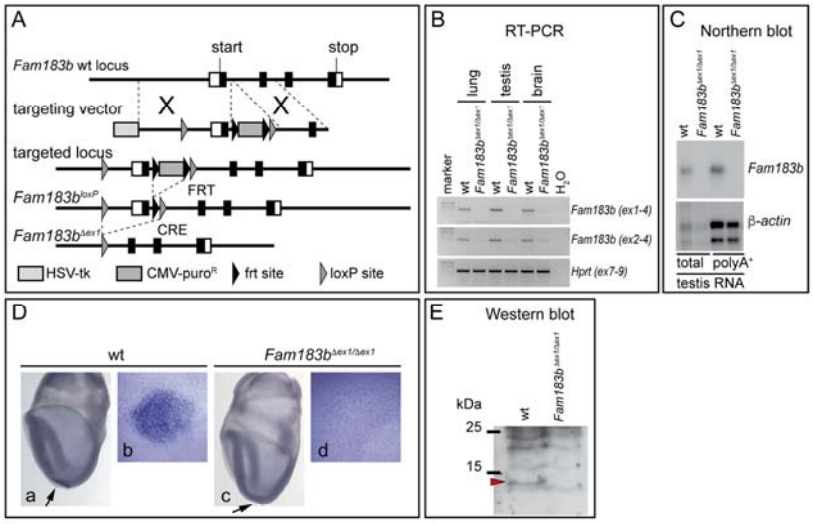

Figure 4. Generation and validation of a *Fam183b*-null allele. (**A**) Schematic drawing depicting the structure of the wild type locus, targeting vector and mutated allele. (**B**) RT-PCR with primers binding in *Fam183b* exon 1 and 4, *Fam183b* exon 2 and 4, and *Hprt* exon 7 and 9 on RNA from adult tissues. Full size gel is shown in Supplementary Figure S3. (**C**) Northern blot of total and polyA$^+$ RNA from wt and *Fam183b*-mutant testes. Full size Northern blots are shown in Supplementary Figure S4. (**D**) WISH of E7.75 wt (a,b) and *Fam183b*$^{\Delta ex1/\Delta ex1}$ (c,d) embryos. (b,d) higher magnification of ventral views of the LRO. (**E**) Western blot analysis of testis lysates from wt and *Fam183b*$^{\Delta ex1/\Delta ex1}$ testes. The full size Western blot is shown in Supplementary Figure S5.

transcripts harbouring exons 2–4 were detected by RT-PCR prepared from various mutant tissues (Fig. 4B). No transcripts were detected in RNA purified from mutant testis by Northern blot hybridisation using a full length *Fam183b* probe (Fig. 4C). *Fam183b* mRNA was not observed by WISH in the LRO of embryos homozygous for the *Fam183b* deletion (Fig. 4D). Our polyclonal anti-FAM183b antibodies, which were directed against a peptide encoded by exon 2, detected a protein of the expected size in the unsoluble fraction of wild type testis lysates (in addition to several background bands), which was missing in lysates from homozygous mutant males (arrowhead in Fig. 4E). Together, these analyses indicated that the *Fam183b*$^{\Delta ex1}$ mutation effectively abolished *Fam183b* mRNA transcription and the generation of FAM183b protein, and thus represented a functional null allele.

Male infertility due to immotile spermatozoa, perturbed left-right asymmetry, hydrocephalus and mucus accumulation in the respiratory tract are frequently found in mice with impaired function of motile cilia, whereas female infertility is less common[15]. Homozygous *Fam183b* mutants of both sexes were fertile and showed no externally visible abnormalities over an extended observation period of 12 months (n = 20). Early postnatal lethality that could possibly be caused by cardiac malformations due to situs randomisation was not observed in 10 litters of homozygous breeding pairs. Likewise, inspection of inner organs of 27 homozygous *Fam183b*$^{\Delta ex1}$ mice showed no evidence of left-right defects (data not shown). Serially sectioned brains of 6 months old *Fam183b*$^{\Delta ex1}$ homozygotes (n = 4) did not reveal enlarged ventricles that might be indicative of hydrocephalus (Fig. 5Cb,b',d,d',d"). Likewise, HE-stained sections of the lung (Fig. 5Cf,f') or PAS stained sections of the nasal cavities (n = 4) did not show obvious morphological alterations or accumulation of mucus (Fig. 5Ch,h',j).

Taken together, our functional analyses of *Fam183a/b* in *Xenopus* and mouse revealed striking differences: while the orthologous genes were found to be highly conserved, both in sequence and expression pattern, phenotypic defects were only observed in the frog, where they were restricted to tissues harbouring multiciliated cells.

Discussion

The ciliation and ciliary motility phenotype encountered upon gene knockdown of *fam183a* in the frog tadpole mucociliary epithelium identifies this novel *Foxj1* target as a potential PCD candidate gene. The lack of a corresponding defect in airway epithelia of knockout mice apparently contradicts this notion. However, this result does not predict in any way whether or not a *Fam183a* null mutation would be causing PCD in human patients. For example, it has been suggested that the phenotypic severity of ciliopathies is a function of the total mutational load in ciliary genes[3]. An inbred mouse strain such as the one used here to create a knockout line in this respect differs greatly from the human population, in which large differences exist with respect to the inter-individual mutational load. It is not unprecedented that mutations in orthologous genes result in different arrays of phenotypes, depending on the model organism in question. For example, null mutations of *Noto* in zebrafish (floating head, *flh*) cause the complete absence of the notochord along the entire anterior-posterior

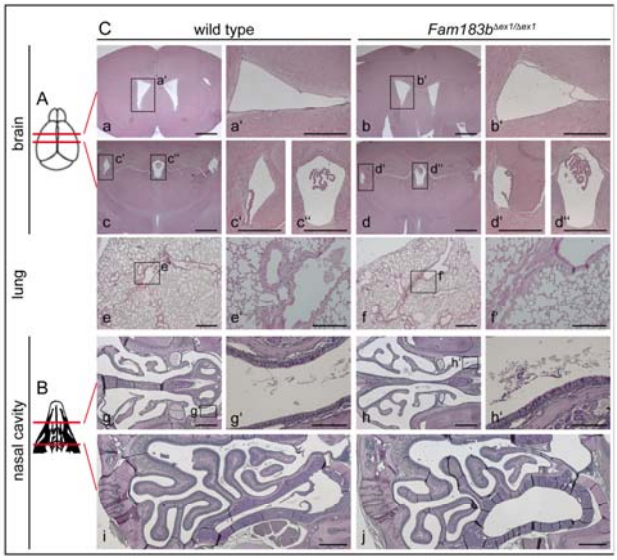

Figure 5. Histological analysis of *Fam183b*-mutant tissues. (**A**) Schematic drawing showing the planes of sections shown in (**C**a–d). (**B**) Scheme depicting planes of sections shown in (**C**g–j). (**C**a–d) Representative sections of wild type (a,c) and *Fam183b*$^{\Delta ex1}$ mutant brains (b,d) at the two horizontal levels indicated in (**A**). Boxed areas indicate the regions shown at higher magnification in a',b',c',c'',d' and d''. (**C**e,f) Representative sections of wild type (e) and *Fam183b*$^{\Delta ex1}$ mutant (f) lungs. Boxed areas indicate the regions shown at higher magnification in e',f'. (**C**g–j) Representative sections of wild type (g,i) and *Fam183b*$^{\Delta ex1}$ mutant (h,j) nasal cavities at the two horizontal levels indicated in (**B**). Boxed areas indicate the regions shown at higher magnification in g' and h'. Scale bars: a,b,c,d: 1 mm; a', b',c',c'',d',d'': 500 µm; e,f: 500 µm; e',f': 200 µm; g–j: 500 µm; g',h': 100 µm.

body axis and severe associated patterning defects[35] whereas *Noto* null-mutant mice show highly variable mild notochord defects restricted to the posterior region[36]. Likewise, various genes that are essential for early steps in neural crest development in non-mammalian vertebrates appear to be dispensable for the corresponding steps in the mouse (reviewed in[37]). Finally, the loss of a functional *Fam183b* allele might be compensated for in the mouse, but not in other vertebrates such as frogs and humans.

Compensation of (germ line) mutations is a phenomenon that is increasingly being observed in various species, the underlying mechanisms being largely unclear (reviewed in[38]). One potential explanation for the lack of an obvious *Fam183b*$^{\Delta ex1}$ motile cilia phenotype could be the presence of (a) redundant gene(s) in the mouse. However, we did not find any evidence for the presence of a *Fam183b* paralog in mouse. In zebrafish, *egfl7*-morphants exhibited severe vascular defects while *egfl7*-mutants showed no obvious phenotypes, which was attributed to gene expression changes and consequent compensation in mutant but not knockdown animals[39]. A similar compensatory mechanism might act in mice since siRNA-mediated knock down of *Azi1/Cep131* in embryonic fibroblasts interfered with ciliogenesis, whereas ciliogenesis in *Azi1/Cep131* null-mutant mice as well as null mutant embryonic fibroblasts occurred normally[40]. Given the importance of (motile) cilia for development and maintenance of tissue homeostasis, it seems likely that the function of a number of cilia genes is buffered by compensatory mechanisms to provide genetic robustness. The conditional knockout mouse generated in this study may provide an opportunity to investigate compensatory mechanisms, particularly in the lung.

A direct or indirect interaction of FAM183b with NUP93 is consistent with the localisation of both proteins to basal bodies (Fig. 2B,D) and the reported localisation of NUP93-GFP to the ciliary base[41]. Several nucleoporins including NUP93 have been described to be part of a presumed ciliary pore complex that regulates protein transport into cilia[41] raising the possibility that FAM183b is involved in this process. Alternatively, nucleoporins may function as scaffolding proteins at the ciliary base, according to a recent study on NUP188 and NUP93, which showed that the nuclear pore was intact in *Xenopus* morphants while biogenesis of motile cilia was impaired[42]. In any case, the identification and verification of NUP93 as a FAM183b interaction partner is in line with a function of this poorly characterised protein in a ciliary context.

It remains to be seen whether human PCD patients with mutations in FAM183A exist or whether humans like mice are able to compensate for the loss of this protein. The high sequence conservation throughout the animal kingdom strongly argues for a function of this gene at least at some of its expression sites. As more examples of transcriptional adaptation to gene loss in the germ line become known, it also becomes increasingly clear that

candidate genes for human disease need to be analysed in more than one model organism and using more than one loss-of-function approach. The use of MOs in *Xenopus laevis* may prove to be one such possibility[43].

Methods

Generation and husbandry of animals. Animal experiments were performed in accordance with the German regulations (Tierschutzgesetz). For mice experiments were approved by the ethics committee of Lower Saxony for care and use of laboratory animals (LAVES, Niedersächsisches Landesamt für Verbraucherschutz und Lebensmittelsicherheit), for frogs by the Regional Government Stuttgart, Germany (A379/12 Zo 'Molekulare Embryologie'). Mice were housed in the animal facility of Hannover Medical School (ZTL), as approved by the responsible Veterinary Officer of the City of Hannover. Animal welfare was supervised and approved by the Institutional Animal Welfare Officer. Frogs were kept at the appropriate condition (pH = 7.7, 20 °C) at a 12 h light cycle in the animal facility of the Institute of Zoology at the University of Hohenheim. Animal welfare was supervised and approved by the Institutional Animal Welfare Officer. Female frogs (4–20 years old) were stimulated with 25–75 units of human chorionic gonadotropin (hCG; Sigma), depending on weight and age, that was injected subcutaneously one week prior to oviposition. On the day prior to ovulation. female frogs were injected with 300–700 units of hCG. Eggs were collected into a petri dish by careful squeezing of the females, followed by *in vitro* fertilization. Sperm of male frogs was obtained by dissecting of testes that were stored at 4 °C in 1x MBSH (Modified Barth's Saline with HEPES).

Fam183b^{loxP} mice were generated by Artemis Taconics (Neurather Ring 1, 51063 Köln, Germany). C57BL/6 BAC DNA was used for the generation of the targeting construct. The targeting strategy was based on *Fam183b* NCBI transcript NM_029283_1. Exon 1 (containing the translation initiation codon) and approx. 1.5 kb of sequence upstream of exon 1 (promoter region) was flanked by loxP sites (size of loxP-flanked region: approx. 3.0 kb). The positive selection marker (Puromycin resistance - PuroR) was inserted into intron 1 flanked by FRT sites and was removed by crossing to ACTB::FLPe mice. The phenotype of *Fam183b*$^{\Delta ex1}$ mice was analysed on a C57BL/6 (N9) background. Other mouse strains have been described previously: ZP3::Cre[34], ACTB::FLPe[44], *Noto*^{Gfp}[29].

Genotyping of *Fam183b*^{loxP} and *Fam183b*$^{\Delta ex1}$ mice. *Fam183b*$^{\Delta ex1/\Delta ex1}$ mice were genotyped by PCR with allele-specific primer pairs:

wild type allele: Fam183b_35: CAAACAAACCATGTTGCTTGG.
Fam183b_36: AGTAGAGGCAGGTATGTGTTT 259 bp product.
Fam183b^{loxP} allele: Fam183b_35: CAAACAAACCATGTTGCTTGG.
Fam183b_36: AGTAGAGGCAGGTATGTGTTT 315 bp product.
Fam183b$^{\Delta ex1}$ allele: Fam183b_35: CAAACAAACCATGTTGCTTGG.
Fam183b KO 41 R:GAAGGTGAATGGCCTAAATGG 293 bp product.

Gene knockdown in *Xenopus* embryos. Embryos were injected at the 4 cell stage with *fam183a*-TBMO or *fam183a*-SBMO to target the MCCs (B1/B2 lineage), kidney (C3 lineage), LRO (C1/C2 lineage) and anterior neural tube (A1/A2 lineage). Sequences of MOs were TBMO: 5′-TTAGGCTCGTTTCCAGGGCAACCAT-3′ and SBMO: 5′-TGCCCTCATTCATTACCCTTCCGAT-3′. The following MO-doses were used, which were compatible in all cases with normal development: MCC-injections (TBMO 8 pmol, SBMO 4 pmol); kidney (TBMO 2 pmol, SBMO 1 pmol); LRO (TBMO 2 pmol, SBMO 1 pmol); neural tube (TBMO 2 pmol, SBMO 1 pmol).

Generation of FAM183b-antibodies and Western blot detection of endogenous FAM183b. A polyclonal anti-FAM183b-antibody was raised in rabbits by immunisation with peptide CTRKPMSWHDNLEEPE (residues 51–65 encoded by exon 2 of mouse FAM183b) and affinity purified by standard procedures. FAM183b-antibodies recognise overexpressed and endogenous protein on Western blots but do not detect FAM183b by immunohistochemistry. For Western blot analyses, one adult testis was lysed in 1 ml RIPA buffer, the non-soluble fraction was sonicated in sample buffer supplemented with 200 mM DTT and 10 mM iodoacetamid and the equivalent of half a testis was loaded into one slot of a 20% PAGE-SDS gel, separated and transferred to Immobilon-P membrane (Merck). Purified antibodies were diluted 1:1000 in 5% milk / 0.5% Tween20 in PBS. Secondary antibodies: anti-rabbit-HRP (GE Healthcare, 1:10000).

Subcellular localisation of FLAG-tagged FAM183b and endogenous NUP93. N- or C-terminally flag-tagged FAM183b was transiently expressed (Lipofectamine® 2000 Transfection Reagent, Invitrogen) in mIMCD-3 cells (ATCC® CRL-2123™), according to the manufacturer's instructions. Transfected cells were cultured on gelatinised (0.1% gelatine) cover slips for 16 hrs, fixed with ice-cold methanol and washed three times for 10 min each with PBS. Unspecific antibody binding was blocked for 60 min with 5% FCS in PBS. Cells were incubated with antibodies against flag (mouse anti-flag; Sigma F3165; 1:1000) and γ-tubulin (rabbit anti-γ-tubulin; abcam ab11317; 1:4000). As secondary antibodies, mouse ALEXA-555 (Invitrogen A-31570, 1:200) and rabbit ALEXA-488 (Invitrogen A-11034, 1:200) were used; nuclei were counter-stained with DAPI (0.5µg/ml, Applichem). Slides were mounted with Prolong Gold Antifade Reagent (Invitrogen) and analysed under a Leica microscope DMI6000 B (100 x oil objective) using LAS AF software. Localisation of mouse NUP93 in mIMCD3 cells was analysed using mouse anti-NUP93 antibody (abcam ab53750; 1:100). Cells were co-stained with rabbit anti-CEP63 (Millipore #06-1292; 1:100) or rabbit anti-γ-tubulin (abcam ab11317; 1:4000). Secondary antibodies used were as described above.

Subcellular localisation of GFP-tagged FAM183b in *Xenopus*. N-terminally GFP-tagged mouse *Fam183b* (Fam183b in pcDNA6.2/N-EmGFP-Dest; Invitrogen, Gateway system) and cetn4-RFP (cetn4-RFP in pCS2+, to stain basal bodies) plasmids were co-injected into the epidermal lineage of 4-cell frog embryos.

Injected specimens were cultured to stage 33, fixed with PFA, counterstained with Hoechst 33342 to highlight nuclei, and analysed for GFP and RFP using a Zeiss LSM-700.

Section and whole-mount *in situ* hybridisation (SISH and WISH). SISH was performed on 10 µm paraffin sections of formaldehyde-fixed (4% PFA) organs with a digoxigenin (DIG) antisense riboprobe derived from *Fam183b* cDNA (Fantom clone; FANTOM Consortium and RIKEN Genome Exploration Research Group Phase I & II Team[45]) essentially as described[46]. WISH of mutant and wild type mouse embryos were performed in parallel under identical conditions following standard procedures. Mouse SISH and WISH results were documented with a Leica DM5000B microscope using Leica Firecam software. WISH of staged wild type and morphant *Xenopus* embryos was performed as described[47].

Reverse transcription (RT-) PCR from total RNA. Total RNA was isolated from dissected mouse tissues using TriReagent (Zymo Research), cDNA synthesised using SuperScriptII Reverse Transcriptase (Invitrogen), following the manufacturer's instructions. PCR was performed using the following primer pairs:

Fam183b Ex1-F:	ATCTTGCGGGAACTCTTTC	
Fam183b Ex4-B:	AGAGTGATGTCGTGGTAGAC	308 bp product (4 exon transcript)
5′HPRT:	CACAGGACTAGAACACCTGC	
3′HPRT:	GCTGGTGAAAAGGACCTCT	248 bp product

Isolation of polyA$^+$ RNA and Northern Blot hybridisation. Total RNA was isolated from testis using TriReagent (Zymo Research), polyA$^+$ RNA was isolated from adult wild type and *Fam183b*$^{\Delta ex1/\Delta ex1}$ testis using magnetic Oligo dT beads (Dynal, Novagen). Northern blot hybridisation was carried out according to standard procedures. Integrity of loaded RNAs was verified by hybridisation with a β-actin probe (633 bp SalI-XbaI fragment from ZX00177K09 clone; Riken fantom II cDNA book).

Histological methods. Immunofluorescence staining, Hematoxylin and Eosin (HE) staining and Periodic acid–Schiff (PAS) staining were performed using standard procedures.

Sources of cDNAs and generation of expression vectors. Mouse *Fam183b* cDNA clones were obtained from the FANTOM DNA book (3 exon transcript, clone 3100002J23; Rearray ID: ZX00144L01) and from RZPD (IRALp962H0945Q, clone Image ID 6703357, Source BioScience; 4 exon transcript). Expression vectors were produced using LR clonase (Invitrogen®) according to the manufacturer's instructions. The Fam183b ORF (4 exons), without and with STOP sequence, were PCR-amplified with primers pairs Fam183b-KpnI-ENTR1A-for (ggtaccGAATGGCCATGGCAGGACGTGTG) and Fam183boS-EcoRI-rev (gaattcTTCTGGTGATCGTCTTCCCCCAAG), or Fam183b-KpnI-ENTR1A-for (ggtaccGAATGGCCATGGCAGGACGTGTG) and Fam183bmS-EcoRI-ENTR-rev (gaattcTACTTCTGGTGATCGTCTTCCCC), cloned in pENTR™1A using the KpnI/EcoRI sites following transfer into the Gateway expression vectors pCDNA6.2-N-GFP, pCDNA6.2-C-GFP (Invitogen®) and modified FLAG-vectors inwhich the GFP-ORF in pCDNA6.2-N-GFP and pCDNA6.2-C-GFP was replaced by the flag sequence. For co-IP experiments N-flag-*Fam183b* (4Exons) was cloned into pCAGGS-FLPe vector (Gene Bridges, GmbH, Heidelberg, Germany) by replacing the FLP gene of this vector by the flag-tagged *Fam183b* sequence. A mouse *Nup93* cDNA was obtained from the FANTOM DNA book (clone B230111C05; Rearray ID: PX00938F16). An expression vector for C-terminally Myc-tagged NUP93 was generated by inserting a XhoI-BlpI fragment from B230111C05 into a synthesised Nup93 cDNA fragment (accggtATGGATACTGAGGGGTTTGGTGAGCTCCTTCAGCAAGCTGAACAGCTTGCTGCTGAGACTGAAGGCATCTCTGAGCTTCCACATGTAGAACGAAATTTACAGGAGATCCAGCAAGCTGGTGAGCGCCTGCGTTCCCGTACCCTCACACGCACATCCCAGGAGACAGCAGATGTCAAGGCATCAGTTCTTCTCGGGTCAAGGGGACTTGACATATCCCATATCTCCCAGAGACTGGAGAGTCTGAGCGCAGCCACCACTTTTGAACCTCTCGAGACAAGCTGCTAAGCCCTGTTGTCCCACAGATCAGCGCCCCACAGTCTAACAAAGAAAGGCTGAAGAACATGGCCCTCTCCATTGCGGAGAGGTACAGAGCTCAGGGAATAAGTGCAAATAAGTTTGTGGACTCTACATTCTATCTCCTCTTGGACCTGATCACCTTTTTTGACGAGTATCACAGTGGTCATATTGACAGAGCCTTTGATATTATTGACCGCTTGAAGCTGGTGCCTCTGAATCAGGAGAGTGTGGAAGAAAGGGTGGCTGCCTTCAGAAACTTCAGTGATGAAATCAGACACAACCTCTCAGAAGTTCTTCTCGCCACCATGAACATCCTGTTCACACAGTTTAAGAGGCTCAAAGGAACAAGTCCATCTTCAGCAACCAGGCCCCAGCGAGTCATTGAAGACCGTGACTCTCAACTCCGAAGTCAAGCCAGAGCCCTGATTACCTTTGCTGGGATGATACCGTACCGGACGTCGGGGGACACTAATGCCAGGCTGGTGCAGATGGAGGTCCTCATGAATGCATCAGAGCAGAAGCTGATCTCAGAGGAGGACCTGCAgcggccgc) and cloning the Nup93-Myc coding sequence as AgeI-NotI fragment into pIRESpuro3 (Clontech #631619). For the Y2H screen, the ORF of *Fam183b* was flanked by EcoRI and SalI sites by PCR using primers Fam183b-EcoRI-Y2H#2431-for (gaattcATGGCCATGGCAGGACGTGTGGGGC) and Fam183b-SalI-Y2H#2431-rev (gtcgacTCACTTCTGGTGATCGTCTTCCCCC) and cloned into the bait-vector pGBT9 DNA-BD (Clontech #K1605-A). Expression vectors for Strep/Flag-tagged FAM183b were generated by flanking the Fam183b ORF (4 Exon transcript) with KpnI and EcoRI, or NheI and XhoI sites by PCR using primers C-SF-Fam183b-KpnI-for (ggtaccCATGGCCATGGCAGGACGTGTGGGGC) and C-SF-Fam183b-EcoRI-rev (gaattcTCGAGCTTCTGGTGATCGTCTTCCCCC) and N-SF-Fam183b-NheI-for (gctagcATGGCCATGGCAGGACGTGTGGGGC) and N-SF-Fam183b-XhoI-rev (ctcgagCTACTTCTGGTGATCGTCTTCCCCC), respectively, and cloned into N-SF-TAP pcDNA3 and C-SF-TAP pcDNA3[31]. All constructs were sequence-verified.

Yeast-two-Hybrid Screening. The Yeast-two-Hybrid screen was performed by the DKFZ Protein-Protein Interaction Screening Facility as described[48]. As bait, the ORF of *Fam183b* (3 exon transcript) fused to the GAL4

DNA binding domain was used to screen a mouse testis prey library (Clontech) in histidine/adenine free medium in the presence of 2 mM amino-triazole.

Affinity purification and mass spectrometry. N- and C-terminally tandem StrepII-Flag-tagged FAM183b (4 exon variant) was transiently expressed in HEK293T cells, FAM183b complexes were isolated[31] and analysed by LC-MS/MS as described[49]. Selected candidate interaction partners identified by MS were further analysed by Co-IP.

Co-IP of overexpressed proteins from CHO cells. Expression plasmids for Flag-tagged FAM183b (in pCAG-IRESpuro) and Myc-tagged NUP93 (in pIRESpuro3) were co-transfected into CHO cells (ATCC® CCL-61™), using PerFectin transfection reagent (Genlantis) according to the manufacturer's instructions. Cells were harvested 16 hrs after transfection, washed on ice with cold PBS, covered by lysis buffer (50 mM Tris-Hcl pH7,5, 150 mM NaCl, 1 mM EDTA, 1% NP-40, 1% Triton X-100, 1% BSA, 1x Complete EASY proteinase inhibitor (Roche, #04693159001, 500 µl per 10 cm dish), and incubated for 5 min on ice. Cells were scraped off the dish and genomic DNA was sheared by pulling through a cannula (BRAUN-9186166), incubated for 20 min on ice, and centrifuged 15 min at 4 °C and 3000 rpm. 25 µl Protein G-Sepharose beads (Amersham, #17-0618-01) was added to the supernatant and incubated for 1 h at 4 °C with continuous inversion for preclearing. The preclearing step was repeated once and beads were pelleted by centrifugation (2 min at 3000 rpm). 50 µl supernatant was removed as input control, the remainder distributed equally to three vials and filled up to 1 ml with 20 mM NaPi pH7,0 (with proteinase inhibitor). Vials were incubated with either 8 µl mouse anti-Myc 9E10 (Sigma, M5546, 6,1 mg/ml) or mouse anti-Flag M2 (Sigma, F3165, 4,2 mg/ml) or without antibody 1,5–3 h on a turning wheel at 4 °C. 25 µl Protein G-beads (GE healthcare, 17-0618-01) per IP were preincubated 1,5–3 h in 1 ml 20 mM NaPi pH7,0 with 1% BSA (with proteinase inhibitor) on a turning wheel at 4 °C, harvested by centrifugation, added to each IP sample and incubated on a turning wheel at 4 °C overnight. IPs were washed three times for 20 min on a turning wheel with wash buffer (50 mM Tris-HCl pH8.5, 500 mM NaCl, 5 mM EDTA, 0,05% NP-40, 0,1% BSA, 1x proteinase inhibitor), the supernatant was completely removed from beads, 40 µl 2x sample buffer added (125 mM Tris-HCl pH 6,8, 20% glycerol, 4% SDS, 0,04% Bromphenol Blue, 2% β-mercaptoethanol, 200 mM DTT, 10 mM Iodoacetamid), heated 5 min to 95 °C and 20 µl loaded on SDS-PAGE. Western blots were performed according to standard procedures. Membrane was cut horizontally at the 50 kDa marker band. Protein on the upper part was detected with anti-Myc-POD (Sigma, A5598) on the lower part with anti-Flag-POD (Sigma, A8592) 1:10000 in 5% milk/0,1% Tween20 in PBS. Pictures were obtained in a Fuji LAS4000 chemiluminescence reader.

High-speed video microscopy of epidermal cilia. Wild type or morphant specimens were analysed for epidermal ciliary beat patterns at stage 33. Embryos were mounted on a slide containing a rectangular chamber constructed from duct tape. Ciliary beating was recorded using a high-speed Hamamatsu video camera Orca flash 4.0 at 600 frames per second.

Measurements and statistics. Measurements were performed in ImageJ (https://imagej.nih.gov/ij/). p-values for ordinal data were calculated using the two-sided Fisher's exact test (https://www.graphpad.com/quickcalcs/contingency1/). p-values for metric data were determined using the Mann-Whitney U test in R (https://www.r-project.org/). Significance was scored as follows: $p \geq 0.05$: not significant; $*p < 0.05$: $**p < 0.01$: $***p < 0.001$.

Multiple sequence alignments and phylogenetic analysis. Sequences were aligned using ClustalW (v1.83; multiple sequence alignment; Pairwise Alignment Mode: Slow; Pairwise Alignment Parameters: Open Gap Penalty = 10.0, Extend Gap Penalty = 0.1, Similarity Matrix: gonnet; Multiple Alignment Parameters: Open Gap Penalty = 10.0, Extend Gap Penalty = 0.2, Delay Divergent = 30%, Gap Distance = 4; Similarity Matrix: gonnet). The phylogenetic tree was build by Neighbor joining, Best Tree Mode (systematic tie breaking). Distances were estimated and gaps distributed proportionally. The tree was rooted to human FAM183A.

Data Availability

The data generated or analysed during this study are included in this published article (and its Supplementary Information files), the full mass spectrometry proteomics data have been deposited to the ProteomeXchange Consortium via the PRIDE[50] partner repository with the dataset identifier PXD009409 (Username: reviewer22871@ebi.ac.uk Password: UVNiVt93).

References

1. Takeda, S. & Narita, K. Structure and function of vertebrate cilia, towards a new taxonomy. *Differentiation* **83**, S4–11 (2012).
2. Berbari, N. F., Connor, A. K. O., Haycraft, C. J. & Yoder, B. K. The Primary Cilium as a Complex Signaling Review Center. *Curr Biol* **19**, R526–R535 (2009).
3. Gerdes, J. M., Davis, E. E. & Katsanis, N. The vertebrate primary cilium in development, homeostasis, and disease. *Cell* **137**, 32–45 (2009).
4. Afzelius, B. A. & Eliasson, R. Male and female infertility problems in the immotile-cilia syndrome. *Eur J Respir Dis Suppl* **127**, 144–147 (1983).
5. Stannard, W. & O'Callaghan, C. Ciliary function and the role of cilia in clearance. *J Aerosol Med* **19**, 110–115 (2006).
6. Jacquet, B. V. *et al.* FoxJ1-dependent gene expression is required for differentiation of radial glia into ependymal cells and a subset of astrocytes in the postnatal brain. *Development* **136**, 4021–4031 (2009).
7. Blum, M., Schweickert, A., Vick, P., Wright, C. V. E. & Danilchik, M. V. Symmetry breakage in the vertebrate embryo: When does it happen and how does it work? *Dev Biol* **393**, 109–123 (2014).
8. Hirokawa, N., Tanaka, Y. & Okada, Y. Cilia, KIF3 molecular motor and nodal flow. *Current Opinion in Cell Biology* 1–9, https://doi.org/10.1016/j.ceb.2012.01.002 (2012).

9. Pennekamp, P., Menchen, T., Dworniczak, B. & Hamada, H. Situs inversus and ciliary abnormalities: 20 years later, what is the connection? *Cilia* **4**, 1 (2015).
10. Jain, R. *et al.* Temporal relationship between primary and motile ciliogenesis in airway epithelial cells. *Am J Respir Cell Mol Biol* **43**, 731–739 (2010).
11. Lyons, R. A., Saridogan, E. & Djahanbakhch, O. The reproductive significance of human Fallopian tube cilia. *Hum. Reprod. Update* **12**, 363–372 (2006).
12. Banizs, B. *et al.* Dysfunctional cilia lead to altered ependyma and choroid plexus function, and result in the formation of hydrocephalus. *Development* **132**, 5329–5339 (2005).
13. Spassky, N. *et al.* Adult ependymal cells are postmitotic and are derived from radial glial cells during embryogenesis. *Neurosci* **25**, 10–18 (2005).
14. Lee, L. Riding the wave of ependymal cilia: genetic susceptibility to hydrocephalus in primary ciliary dyskinesia. *J. Neurosci. Res.* **91**, 1117–1132 (2013).
15. Praveen, K., Davis, E. E. & Katsanis, N. Unique among ciliopathies: primary ciliary dyskinesia, a motile cilia disorder. *F1000Prime Rep* **7**, 36 (2015).
16. Walentek, P. & Quigley, I. K. What we can learn from a tadpole about ciliopathies and airway diseases: Using systems biology in *Xenopus* to study cilia and mucociliary epithelia. *Genesis* **55**, e23001 (2017).
17. Brody, S. L., Yan, X. H., Wuerffel, M. K., Song, S. K. & Shapiro, S. D. Ciliogenesis and left-right axis defects in forkhead factor HFH-4-null mice. *Am J Respir Cell Mol Biol* **23**, 45–51 (2000).
18. Alten, L. *et al.* Differential regulation of node formation, nodal ciliogenesis and cilia positioning by Noto and Foxj1. *Development* **139**, 1276–1284 (2012).
19. Chen, J., Knowles, H. J., Hebert, J. L. & Hackett, B. P. Mutation of the mouse hepatocyte nuclear factor/forkhead homologue 4 gene results in an absence of cilia and random left-right asymmetry. *J. Clin. Invest.* **102**, 1077–1082 (1998).
20. Stubbs, J. L., Oishi, I., Izpisúa Belmonte, J. C. & Kintner, C. The forkhead protein Foxj1 specifies node-like cilia in Xenopus and zebrafish embryos. *Nat Genet* **40**, 1454–1460 (2008).
21. Yu, X., Ng, C. P., Habacher, H. & Roy, S. Foxj1 transcription factors are master regulators of the motile ciliogenic program. *Nat Genet* **40**, 1445–1453 (2008).
22. Vij, S. *et al.* Evolutionarily ancient association of the FoxJ1 transcription factor with the motile ciliogenic program. *PLoS Genet* **8**, e1003019 (2012).
23. Boon, M. *et al.* MCIDAS mutations result in a mucociliary clearance disorder with reduced generation of multiple motile cilia. *Nat Commun* **5**, 1–8 (2014).
24. Choksi, S. P., Babu, D., Lau, D., Yu, X. & Roy, S. Systematic discovery of novel ciliary genes through functional genomics in the zebrafish. *Development* **141**, 3410–3419 (2014).
25. Didon, L. *et al.* RFX3 modulation of FOXJ1 regulation of cilia genes in the human airway epithelium. *Respir. Res.* **14**, 70 (2013).
26. Gomperts, B. N., Gong-Cooper, X. & Hackett, B. P. Foxj1 regulates basal body anchoring to the cytoskeleton of ciliated pulmonary epithelial cells. *J Cell Sci* **117**, 1329–1337 (2004).
27. Newton, F. G. *et al.* Forkhead Transcription Factor Fd3F Cooperates with Rfx to Regulate a Gene Expression Program for Mechanosensory Cilia Specialization. *Dev Cell* **22**, 1221–1233 (2012).
28. Stauber, M. *et al.* Identification of FOXJ1 effectors during ciliogenesis in the foetal respiratory epithelium and embryonic left-right organiser of the mouse. *Dev Biol* **423**, 170–188 (2017).
29. Beckers, A., Alten, L., Viebahn, C., Andre, P. & Gossler, A. The mouse homeobox gene Noto regulates node morphogenesis, notochordal ciliogenesis, and left right patterning. *Proc. Natl. Acad. Sci. USA* **104**, 15765–15770 (2007).
30. Schweickert, A. *et al.* Cilia-driven leftward flow determines laterality in Xenopus. *Curr Biol* **17**, 60–66 (2007).
31. Gloeckner, C. J., Boldt, K., Schumacher, A., Roepman, R. & Ueffing, M. A novel tandem affinity purification strategy for the efficient isolation and characterisation of native protein complexes. *Proteomics* **7**, 4228–4234 (2007).
32. Vick, P. *et al.* Flow on the right side of the gastrocoel roof plate is dispensable for symmetry breakage in the frog Xenopus laevis. *Dev Biol* **331**, 281–291 (2009).
33. Getwan, M. & Lienkamp, S. S. Toolbox in a tadpole: Xenopus for kidney research. *Cell Tissue Res* **369**, 143–157 (2017).
34. de Vries, W. N. *et al.* Expression of Cre recombinase in mouse oocytes: a means to study maternal effect genes. *Genesis* **26**, 110–112 (2000).
35. Talbot, W. S. *et al.* A homeobox gene essential for zebrafish notochord development. *Nature* **378**, 150–157 (1995).
36. Abdelkhalek, H. B. *et al.* The mouse homeobox gene Not is required for caudal notochord development and affected by the truncate mutation. *Genes Dev* **18**, 1725–1736 (2004).
37. Barriga, E. H., Trainor, P. A., Bronner, M. & Mayor, R. Animal models for studying neural crest development: is the mouse different? *Development* **142**, 1555–1560 (2015).
38. El-Brolosy, M. A. & Stainier, D. Y. R. Genetic compensation: A phenomenon in search of mechanisms. *PLoS Genet* **13**, e1006780 (2017).
39. Rossi, A. *et al.* Genetic compensation induced by deleterious mutations but not gene knockdowns. *Nature* **524**, 230–233 (2015).
40. Hall, E. A. *et al.* Acute versus chronic loss of mammalian Azi1/Cep131 results in distinct ciliary phenotypes. *PLoS Genet* **9**, e1003928 (2013).
41. Kee, H. L. *et al.* A size-exclusion permeability barrier and nucleoporins characterize a ciliary pore complex that regulates transport into cilia. *Nat Cell Biol* **14**, 431–437 (2012).
42. del Viso, F. *et al.* Congenital Heart Disease Genetics Uncovers Context-Dependent Organization and Function of Nucleoporins at Cilia. *Dev Cell* **38**, 478–492 (2016).
43. Blum, M., De Robertis, E. M., Wallingford, J. B. & Niehrs, C. Morpholinos: Antisense and Sensibility. *Dev Cell* **35**, 145–149 (2015).
44. Rodríguez, C. I. *et al.* High-efficiency deleter mice show that FLPe is an alternative to Cre-loxP. *Nat Genet* **25**, 139–140 (2000).
45. Kawai, J. & Hayashizaki, Y. DNA book. *Genome Research* **13**, 1488–1495 (2003).
46. Moorman, A. F., Houweling, A. C., de Boer, P. A. & Christoffels, V. M. Sensitive nonradioactive detection of mRNA in tissue sections: novel application of the whole-mount *in situ* hybridization protocol. *J. Histochem. Cytochem.* **49**, 1–8 (2001).
47. Belo, J. A. *et al.* Cerberus-like is a secreted factor with neutralizing activity expressed in the anterior primitive endoderm of the mouse gastrula. *Mech Dev* **68**, 45–57 (1997).
48. Mohr, K. & Koegl, M. High-throughput yeast two-hybrid screening of complex cDNA libraries. *Methods Mol. Biol.* **812**, 89–102 (2012).
49. Boldt, K. *et al.* An organelle-specific protein landscape identifies novel diseases and molecular mechanisms. *Nat Commun* **7**, 11491 (2016).
50. Vizcaíno, J. A. *et al.* 2016 update of the PRIDE database and its related tools. *Nuc Acids Res* **44**, D447–56 (2016).

Acknowledgements

We thank S. Brody (Washington University, St. Louis) for *Foxj1*-mutant mice and members of our laboratories for suggestions and discussions. This work was financially supported by the DFG Cluster of Excellence "REBIRTH" to A.G.

Author Contributions

A.B., K.S.-G. and L.A. performed experiments in mouse and tissue cultures. K.B. analysed FAM183b interaction partners by MS. T.O. analysed *fam183a* in the frog *Xenopus laevis*. M.U., M.B. and A.G. designed experiments. All authors evaluated results. A.G. and M.B. wrote the paper, which was edited and approved by all authors.

Additional Information

Supplementary information accompanies this paper at https://doi.org/10.1038/s41598-018-33045-2.

Competing Interests: The authors declare no competing interests.

Publisher's note: Springer Nature remains neutral with regard to jurisdictional claims in published maps and institutional affiliations.

CFAP43 modulates ciliary beating in mouse and *Xenopus*

ARTICLE IN PRESS

Developmental Biology xxx (xxxx) xxx

Contents lists available at ScienceDirect

Developmental Biology

journal homepage: www.elsevier.com/locate/developmentalbiology

CFAP43 modulates ciliary beating in mouse and *Xenopus*

Ev Rachev [a], Karin Schuster-Gossler [a], Franziska Fuhl [b], Tim Ott [b], Lena Tveriakhina [a], Anja Beckers [a], Jan Hegermann [c], Karsten Boldt [d], Michaela Mai [a,2], Elisabeth Kremmer [e,1], Marius Ueffing [d], Martin Blum [b,*], Achim Gossler [a,**]

[a] Institute for Molecular Biology, OE5250, Hannover Medical School, Carl-Neuberg-Str. 1, 30625, Hannover, Germany
[b] Institute of Zoology, University of Hohenheim, Garbenstraße 30, 70593, Stuttgart, Germany
[c] Institute of Functional and Applied Anatomy, Research Core Unit Electron Microscopy, Hannover Medical School, Carl-Neuberg-Str. 1, 30625, Hannover, Germany
[d] Institute of Ophthalmic Research, Center for Ophthalmology, University of Tübingen, Röntgenweg 11, 72076, Tübingen, Germany
[e] Institute of Molecular Immunology, Helmholtz Zentrum München, German Research Center for Environmental Health (GmbH), Core Facility Monoclonal Antibodies, Marchioninistr. 25, 81377, München, Germany

ARTICLE INFO

Keywords:
CFAP43
Ciliogenesis
Cilia
Hydrocephalus
Mucociliary clearance
Male infertility
Xenopus laevis
Mouse

ABSTRACT

Malfunctions of motile cilia cause a variety of developmental defects and diseases in humans and animal model organisms. Defects include impaired mucociliary clearance of the airways, sperm immotility, hydrocephalus and organ laterality. Here, we characterize the evolutionary conserved *Cfap43* gene by loss-of-function experiments in the mouse and the frog *Xenopus laevis*. *Cfap43* is expressed in tissues carrying motile cilia and acts as a target gene of the transcription factor FOXJ1, which is essential for the induction of motile ciliogenesis. We show that CFAP43, a protein of unknown biochemical function, localizes to the ciliary axoneme. CFAP43 is involved in the regulation of the beating frequency of tracheal cilia and loss of CFAP43 causes severe mucus accumulation in the nasal cavity. Likewise, morphant and crispant frog embryos revealed impaired function of motile cilia of the larval epidermis, a model for airway mucociliary epithelia. CFAP43 participates in the formation of flagellar axonemes during spermatogenesis as mice mutant for *Cfap43* display male infertility, consistent with observations in male sterile patients. In addition, mice mutant for *Cfap43* display early onset hydrocephalus. Together, these results confirm the role of CFAP43 in the male reproductive tract and pinpoint additional functions in airway epithelia mucus clearance and brain development.

1. Introduction

Cilia project from the surface of many eukaryotic cells into the extracellular space and are pivotal for normal development and tissue homeostasis (Gerdes et al., 2009; Praveen et al., 2015). Their core, the axoneme, is composed of nine peripheral microtubule doublets, with or without attached motor proteins, and possesses two central microtubules or not. Cilia are classified as motile or not, and cells bearing motile cilia may be mono- or multiciliated (reviewed in Takeda and Narita, 2012). Cells with motile cilia either propel themselves, such as for example the sperm cell, or move fluids along the cell surface. During early mammalian and amphibian development, motile monocilia at the left-right organizer (LRO) generate a leftward fluid flow that is essential for the establishment of the asymmetric arrangement of visceral organs (Blum and Ott, 2018a; Yoshiba and Hamada, 2014). The coordinated beating of hundreds of motile cilia on epithelial cells of the respiratory tract in mice or the epidermis of *Xenopus* larvae (multiciliated cells, MCCs) is essential for mucociliary clearance (Jain et al., 2010; Stannard and O'Callaghan, 2006). MCCs lining the brain ventricles generate flow of the cerebrospinal fluid (CF), which is required for brain development and function (Banizs et al., 2005; Jacquet et al., 2009; Lee, 2013; Spassky et al., 2005). In fallopian tubes, MCCs move egg cells into the ampulla and preimplantation embryos towards the uterus (Lyons et al., 2006). Motile cilia in the pronephric ducts of frog embryos propel urine from the pronephros to the cloaca, contributing to urine excretion and water homeostasis (reviewed in Getwan and Lienkamp, 2017).

* Corresponding author.
** Corresponding author.
E-mail addresses: martin.blum@uni-hohenheim.de (M. Blum), gossler.achim@mh-hannover.de (A. Gossler).
[1] present address: Department of Biology II, Ludwig-Maximilians University, Großhaderner Straße 2, 82,152 Martinsried, Germany.
[2] present address: DMSG Bundesverband, Krausenstr. 50, 30,171 Hannover, Germany.

https://doi.org/10.1016/j.ydbio.2019.12.010
Received 16 September 2019; Received in revised form 14 December 2019; Accepted 18 December 2019
Available online xxxx
0012-1606/

Please cite this article as: Rachev, E. et al., CFAP43 modulates ciliary beating in mouse and *Xenopus*, Developmental Biology, https://doi.org/10.1016/j.ydbio.2019.12.010

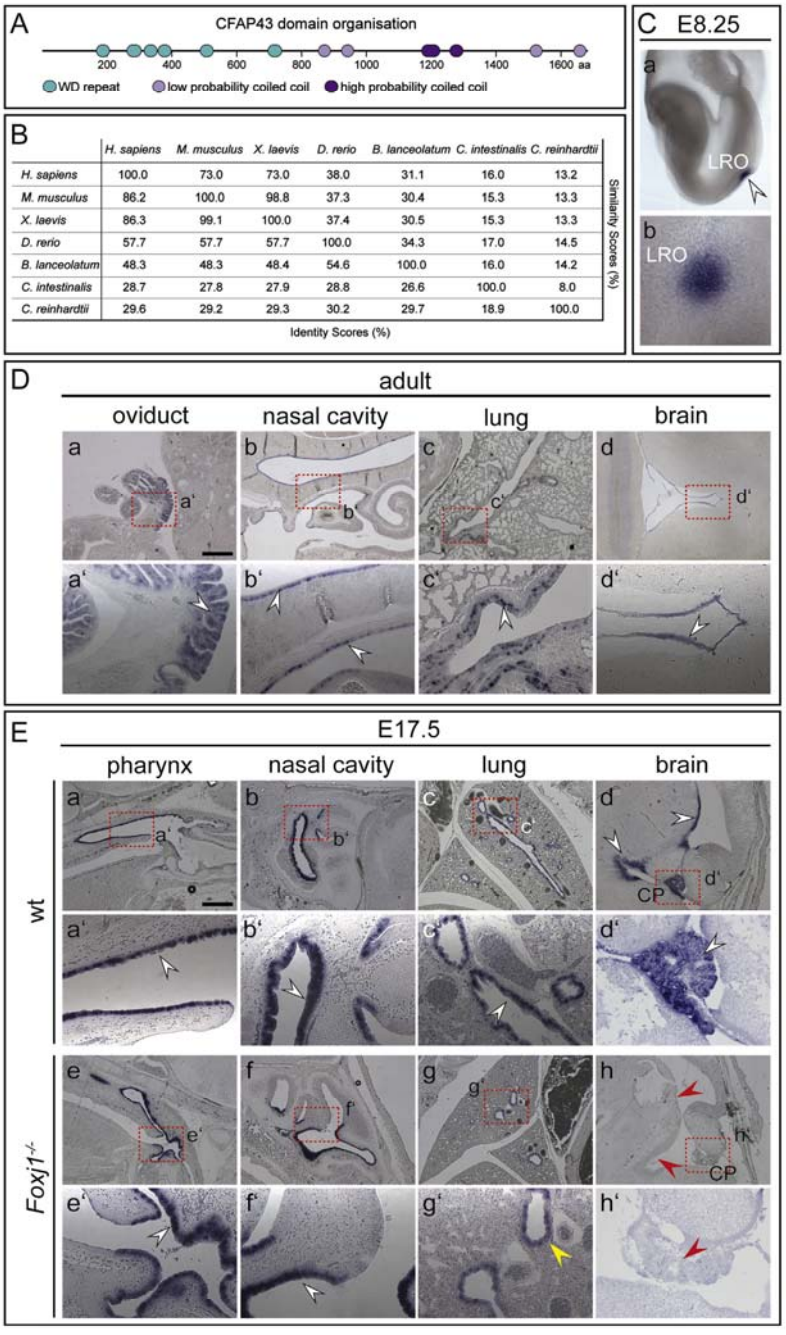

	H. sapiens	M. musculus	X. laevis	D. rerio	B. lanceolatum	C. intestinalis	C. reinhardtii
H. sapiens	100.0	73.0	73.0	38.0	31.1	16.0	13.2
M. musculus	86.2	100.0	98.8	37.3	30.4	15.3	13.3
X. laevis	86.3	99.1	100.0	37.4	30.5	15.3	13.3
D. rerio	57.7	57.7	57.7	100.0	34.3	17.0	14.5
B. lanceolatum	48.3	48.3	48.4	54.6	100.0	16.0	14.2
C. intestinalis	28.7	27.8	27.9	28.8	26.6	100.0	8.0
C. reinhardtii	29.6	29.2	29.3	30.2	29.7	18.9	100.0

Fig. 1. Murine *Cfap43* is expressed in tissues carrying multiciliated cells. **(A)** Murine CFAP43 protein contains 6 WD-repeats in the N-terminal part (Uniprot, (https://www.uniprot.org/uniprot/E9Q7R9), whereas the C-terminus contains six coiled-coil domains, as predicted by Multicoil (http://cb.csail.mit.edu/cb/multicoil/cgi-bin/multicoil.cgi). **(B)** Similarity matrix of CFAP43 amino acid sequences from different species reveals high evolutionary conservation. **(C)** *Cfap43* is expressed in the left-right organizer (LRO, arrowhead) at E8.25 (lateral (a) and ventral view (b)) as detected by WISH. **(D)** *Cfap43* expression in wt adult mouse tissues was detected by SISH (a-d; red boxes are magnified in a'-d'). White arrowheads in (a'-d') point to regions of expression. **(E)** *Cfap43* expression in E17.5 wt (a-d; red boxes are magnified in a'-d') and *Foxj1*$^{-/-}$ (e-h; red boxes are magnified in e'-h') tissues was detected by SISH (marked by white arrowheads). Note that *Cfap43* expression was reduced in the lung epithelium (g, yellow arrowhead in g') and absent in the ependymal layer and choroid plexus (CP) of *Foxj1*$^{-/-}$ specimens (red arrowheads in h, h'). Scale bars: Da-d, Ea-h = 500 μm.

Impaired or disrupted cilia motility leads, depending on the affected cilia type and species, to reduced mucociliary clearance and respiratory malfunctions, abnormal asymmetric arrangement of the inner organs, male and female infertility as well as hydrocephalus (Lee, 2013; reviewed in Praveen et al., 2015). We identified *Cfap43* in microarray screens for genes that were up-regulated during the differentiation of ciliated cells in the fetal mouse lung and down-regulated in *Foxj1* mutants (Stauber et al., 2017). Patients heterozygous for a truncated CFAP43 protein were reported to develop normal pressure hydrocephalus (Morimoto et al., 2019), and homozygous missense and nonsense mutations in *CFAP43* were identified in sterile male patients with 'multiple morphological abnormalities of the sperm flagella' (MMAF (Coutton et al., 2018; Sha et al., 2017; Tang et al., 2017)). Other symptoms related to non-functional motile cilia were not reported from such patients. In mice, nonsense mutations of *Cfap43* resulted in a comparable sperm phenotype, again without reported additional defects in tissues carrying motile cilia (Coutton et al., 2018; Sha et al., 2017; Tang et al., 2017). Here we show that *Cfap43* expression correlates with the presence of motile cilia in mouse and frog embryos, as well as in adult mouse tissues. Endogenous CFAP43 protein localizes to the ciliary axoneme. Furthermore, we demonstrate that CFAP43 loss-of-function affects not only mouse sperm, but also brain ventricle development and ciliary beat frequencies in multiciliated cells of both the mouse airways and *Xenopus* embryonic skin: knockout mice as well as morphant and crispant frog embryos reveal defects in mucociliary clearance.

2. Results

2.1. Expression and localization of Cfap43 mRNA and protein in mouse and frog

Cfap43 encodes an evolutionary conserved protein of 1682 amino acids, which contains 6 predicted WD repeats in its N-terminal and 6 low/high probability coiled coil domains in its C-terminal region (UniProt Consortium, 2019; Wolf et al., 1997) (Fig. 1A, B). During embryonic mouse development, *Cfap43* mRNA was detected in the left-right organizer (LRO) at E8.25 (LRO; Fig. 1C). High expression levels of *Cfap43* correlated with the presence of motile cilia in adult tissues (Fig. 1D, and Fig. S1) and in E17.5 embryos (Fig. 1Ea-d, a'-d'). *Cfap43* transcripts were detected in epithelial cells lining the respiratory tract, in brain ependymal cells and the choroid plexus (Fig. 1D, Ea-d, a'-d'). In *Foxj1*-mutant E17.5 embryos (n=3), *Cfap43* mRNA was reduced in the large airways of the lung (yellow arrowhead in Fig. 1Eg'), and not detectable in ependymal cells and the choroid plexus (red arrowheads in Fig. 1Eh, h'). Surprisingly, no reduction was seen in MCCs of the nasal cavity and the upper respiratory tract (Fig. 1Ee, f, white arrows in e', f'). Similar to mouse, *cfap43* mRNA transcription correlated with *foxj1* expression and the presence of motile cilia in *Xenopus laevis* embryos (Fig. 2). Transcripts were detected in the LRO (gastrocoel roof plate, GRP), floor plate (FP), MCCs of the larval epidermis, nephrostomes, branchial chambers (BC), and stomach (stom.), but not clearly detectable in the brain (zona limitans intrathalamica, ZLI; subcommissural organ, SCO) (Fig. 2Ab-h''''). The dependence on *foxj1* was demonstrated in gain- and loss-of-function experiments: ectopic *cfap43* staining was seen on the injected side of stage 19 embryos unilaterally injected with *foxj1* mRNA (100% penetrance in 3 independent experiments with 15 injected embryos each; typical specimen shown in Fig. 2B). To investigate whether *foxj1* was strictly required for *cfap43* transcription, a sgRNA was designed to target the *foxj1* locus (Fig. S2). Crispant specimens revealed that *cfap43* transcripts were drastically reduced (Fig. 2C), with residual staining retained in the proctodeum (black arrowhead in Fig. 2Cb). Reductions were observed in every crispant analyzed (3 experiments; 15 specimens each). Of note, formation of externally visible hydrocephalus was not recorded in *foxj1* crispants up to stage 45, i.e. before tadpoles start feeding and metamorphosis commences.

To study expression and localization of CFAP43 protein, we generated

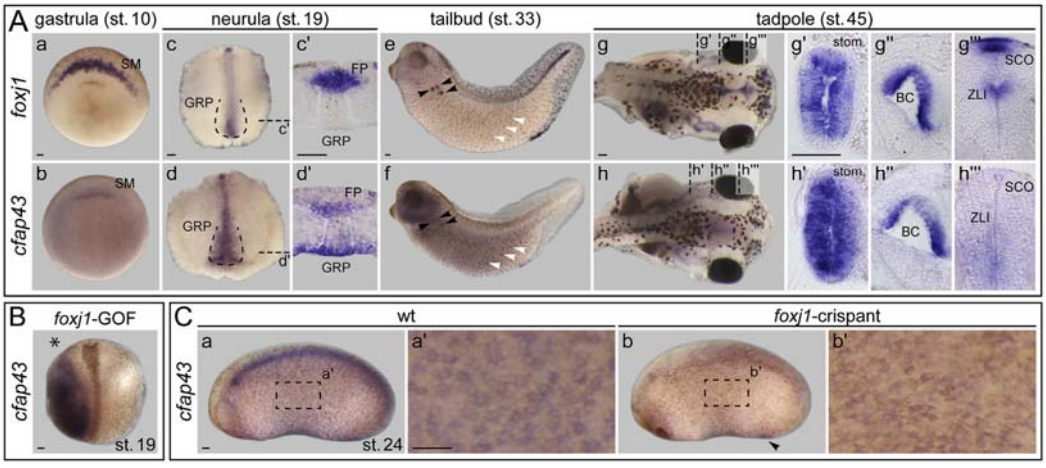

Fig. 2. Expression of *cfap43* in wt and *foxj1*-manipulated *Xenopus* embryos.
(A) *Foxj1* and *cfap43* are co-expressed as shown by comparative analysis of *foxj1* and *cfap43* mRNA expression in staged embryos using specific antisense RNA probes. (a, b) *foxj1* expression, but not *cfap43* was shown in the precursor of the left-right organizer (LRO), the superficial mesoderm (SM) of stage 10 gastrula embryos. (c, d) Dorsal explants and transversal histological sections (c', d') through neurula embryos at stage 19 revealed mRNA transcription of both genes in the floor plate (FP), and *cfap43* mRNA in addition in the LRO (GRP; outlined by dashed lines), where expression is induced already at stage 15 (not shown). (e, f) Co-expression in the nephrostomes (black arrowheads) and MCCs (white arrowheads) of stage 33 larvae. (g, h) Staining of stage 45 tadpoles in whole-mounts demonstrated strong neural expression of *foxj1* in the sub-commissural organ (SCO), zona limitans intrathalamica (ZLI) and the FP, which was absent for *cfap43* (g'', h''). Non-neural expression was found in the dorsal lining of the branchial chamber (BC) (g'', h'') and in the stomach (stom.) (g', h'). **(B)** *Cfap43* is a *foxj1* target gene. Embryos were unilaterally injected with *foxj1* mRNA and analyzed for *cfap43* expression. *, injected side. **(C)** *Foxj1* F0 crispant embryos (b, b') lacked detectable *cfap43* expression except for the proctodeum (black arrowhead). Scale bars = 100 μm.

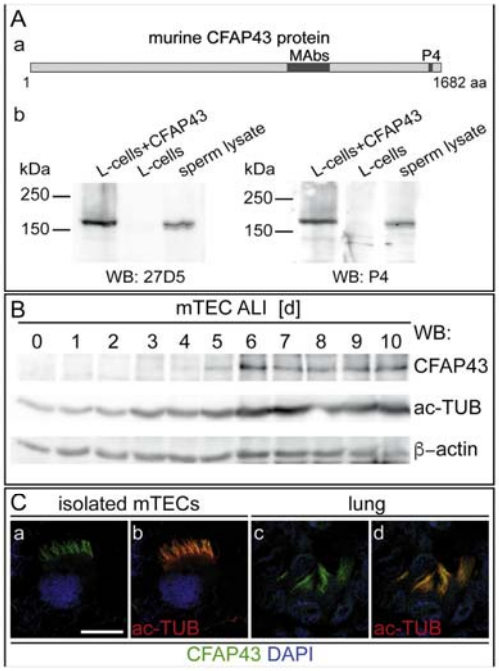

Fig. 3. Detection and subcellular localization of murine CFAP43.
(A) (a) A schematic representation of mouse CFAP43 protein showing regions used for immunization marked by dark gray boxes. (b) Western blot analyses of lysates from L-cells overexpressing CFAP43, untransfected L-cells, and wt mouse sperm lysates probed with monoclonal antibody 27D5 (left) or polyclonal antibody P4 (right). **(B)** Western blot analyses of mouse tracheal epithelial cells (mTECs) at various time points after initiation of air liquid interface (ALI) cultures probed for CFAP43 (27D5), acetylated α-tubulin (ac-TUB), and β-actin show upregulation of CFAP43 during ciliogenesis. **(C)** CFAP43 localizes to cilia in isolated mTECs (a, b) and lung sections (c, d), which were co-stained with monoclonal antibody 22A11 and acetylated α-tubulin (ac-TUB). Full size Western blots for Ab and B are shown in Figs. S9A and B. Scale bar in C = 10 μm.

specific antibodies directed against mouse CFAP43. Polyclonal rabbit antibodies were raised against a C-terminal peptide (P4, amino acids 1633–1647), while monoclonal rat and mouse antibodies (MAbs) were directed against a bacterially expressed polypeptide encompassing amino acids 1053–1226 (Fig. 3Aa). Western blot analyses detected CFAP43 in extracts from L-cells over-expressing the protein as well as endogenous protein in lysates of mouse sperm cells isolated from the cauda epididymis at the expected molecular weight of approximately 190 kDa (Fig. 3Ab). Endogenous CFAP43 was also detected in air-liquid interphase (ALI) cultures of mouse tracheal epithelial cells (mTECs), following the induction of ciliogenesis (Fig. 3B), consistent with the upregulation of *Cfap43* expression during fetal lung development (Stauber et al., 2017). In isolated mTECs (Fig. 3Ca, b) and in epithelial cells lining the lung airways (Fig. 3Cc, d), CFAP43 co-localized with acetylated-α-tubulin (ac-TUB), indicating localization of CFAP43 to motile cilia. This result is consistent with the localization of *Chlamydomonas* FAP43 to the inner dynein arm-associated tether and tether head complex (Fu et al., 2018; Kubo et al., 2018). In *Xenopus*, the polyclonal and monoclonal antibodies directed against mouse CFAP43 showed no specific signals (not shown). In summary, our expression analyses of *Cfap43* in mouse and frog demonstrate a tight correlation with motile cilia as well as a dependence on the transcription factor *Foxj1* at most of its expression sites.

2.2. Ciliary defects in Xenopus morphants and crispants

Cfap43 function was investigated in *Xenopus* embryos following gene knock-down using morpholino oligomers (MOs) and by genome editing using CRISPR/Cas9. Both translation and splice blocking MOs were used, referred to as TBMO and SBMO, respectively. MOs were injected at the 4-cell stage and targeted specifically to ciliated tissues and organs, namely the LRO, nephrostomes, skin, and brain. Targeting was controlled by co-injection of lineage tracer Alexa Fluor 488 dextran and pre-selection of correctly targeted specimens prior to phenotypic analysis. Both SBMO and TBMO resulted in a majority of embryos developing edema around the heart (tadpole cysts; Fig. S3A; raw data in Table S2), which can result from defective cardiac, lymphatic or nephrostome function (del Viso and Khokha, 2012). As *cfap43* was expressed in the developing nephrostomes (Fig. 2Af; raw data in Table S2), edema can be indicative of malfunctioning nephrostome cilia. The *Xenopus* tadpole skin harbors MCCs and mucus-producing cells and serves as a first line of defense against infections by MCC-driven mucus transport along the tadpole head-tail axis, functionally resembling MCCs of the mammalian airway epithelium (Blum and Ott, 2018b; Dubaissi and Papalopulu, 2011; Dubaissi et al., 2014; Walentek and Quigley, 2017). Hovering of tadpoles caused by ciliary beating of skin MCCs was reduced in tadpoles injected with TBMO, suggesting impaired ciliary function (Movie S1). Hydrocephalus and laterality defects were not observed in morphant specimens (Fig. S3B-E; raw data in Table S2).

Supplementary video related to this article can be found at https://doi.org/10.1016/j.ydbio.2019.12.010.

Because rescue experiments of morphant phenotypes, using HA-, GFP- or untagged mouse and *Xenopus* full-length constructs, failed, two guide RNAs (sgRNA1 and 2) were designed to edit the *cfap43* gene locus by CRISPR/Cas9 (Fig. S4). F0 specimens were analyzed for genome editing and ciliary phenotypes. LR defects, edemas and hydrocephalus were not observed (Fig. S3A, B, C). However, crispants displayed altered MCC motility (Movie S2). Remarkably, ciliary beat frequencies were markedly increased in morphant and crispant specimens, while cilia-driven transport of fluorescent beads along the anterior-posterior axis of stage 32 larvae was considerably reduced (Fig. 4A, B; Movies S2, S3; raw data in Table S1). IF staining of basal bodies and basal feet in skin MCCs revealed no differences between wildtype and crispant embryos (Fig. 4D). The lack of edemas in crispant specimens compared to morphants (Fig. S3A) could be the result of genetic compensation triggered by mutant mRNA degradation (El-Brolosy et al., 2019), which – however – has not been reported in *Xenopus* so far. In line with this formal possibility, *cfap43* transcripts were greatly reduced in crispant specimens (Fig. 4C). Genome editing thus confirmed a function of *cfap43* in the mucociliary epithelium of the tadpole skin, while additional motile cilia defects in morphant nephrostomes were either unspecific or compensated in crispants.

Supplementary video related to this article can be found at https://doi.org/10.1016/j.ydbio.2019.12.010.

2.3. Mucus accumulation, immobile sperm, and enlarged ventricles in Cfap43 knockout mice

To analyze the function of CFAP43 in mouse, we generated a conditional allele by flanking exon 3 (*ex3*) with loxP sites (Fig. 5A; Fig. S5). Deletion of exon 3 by Cre-mediated recombination results in a frame shift and termination of translation in exon 4 (*ex4*). Mutant mRNA, which might be degraded by nonsense-mediated decay, could still result in translation of an N-terminal polypeptide of 122 aa, encoded by exons 1 and 2 and followed by an additional 16 aa encoded by the shifted reading frame. To delete CFAP43 in all tissues we excised exon 3 in the female germ line ($Cfap43^{\Delta ex3}$) using ZP3:Cre mice (de Vries et al., 2000). Upon mating of heterozygous animals, homozygous $Cfap43^{\Delta ex3}$ mice were

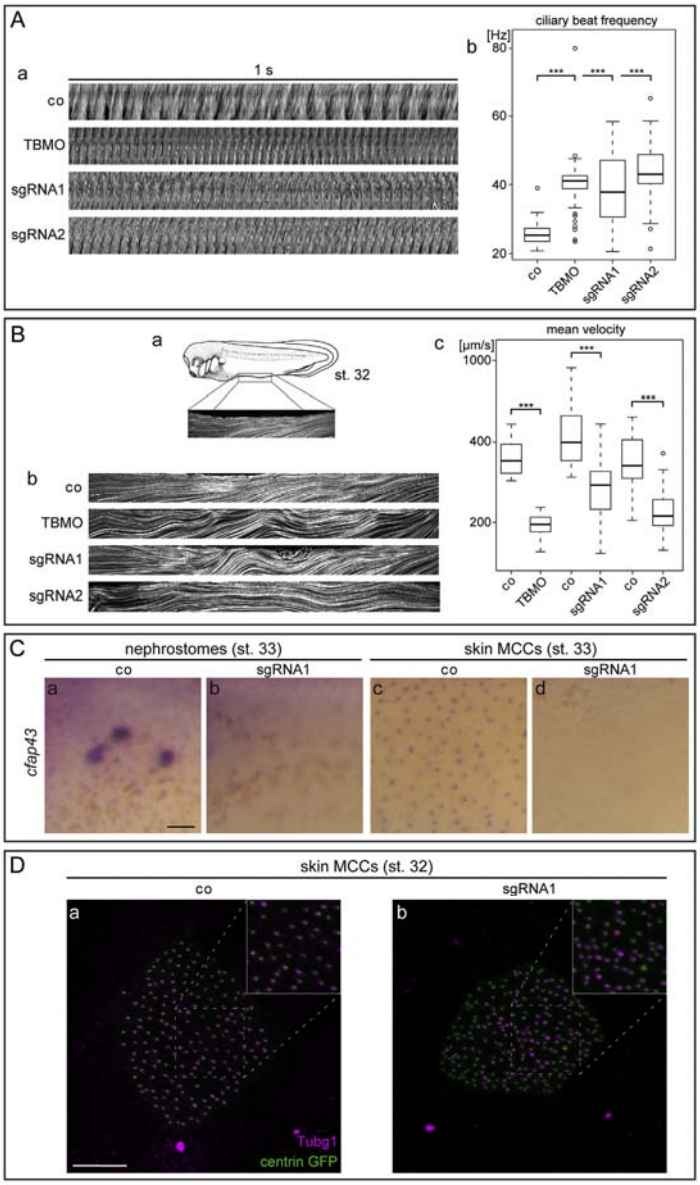

Fig. 4. Ciliary defects in *Xenopus cfap43* morphant and crispant larval skin.
(A) (a) Kymographs of ciliary motility of single MCCs were generated from control (co) wt, TBMO-, sgRNA1-and sgRNA2-injected specimens. (b) Statistical evaluation of results from 3 independent experiments with 15 embryos each and 5 analyzed MCCs per embryo revealed elevated ciliary beat frequencies upon *cfap43* loss-of-function. **(B)** (a) Schematic depiction of the region used for flow analysis in control wt and manipulated stage 32 embryos. Embryo scheme taken from https://www.xenbase.org/anatomy/alldev.do. (b) Maximum intensity projections of single control wt, TBMO-, sgRNA1-and sgRNA2-injected specimens represent cilia-generated flow. (c) Evaluation of bead transport from 3 independent experiments with 8 analyzed specimens each shows reduced mean velocities in *cfap43* morphants and crispants. **(C)** *cfap43* mRNA transcripts were reduced in *cfap43* crispant embryos (b, d) at stage 33, with a focus on nephrostomes (a, b) and MCCs (c, d). Morphant Embryos were injected with 0.5 pmol TBMO. **(D)** IF staining of basal bodies (centrin GFP) and basal feet (Tubg1) in skin MCCs of stage 32 wildtype and crispant specimens. Scale bars: C = 100 µm, D = 10 µm ***, $p<0.001$.

obtained at the expected Mendelian ratio (62 or 28.6% wt, 104 or 47.9% heterozygotes, 51 or 23.5% homozygotes). Except for three mice, which developed a cranial vault around weaning indicative of hydrocephalus, no externally visible abnormalities were detected in >100 adult mutants.

Next, we analyzed the presence or absence of CFAP43 protein in knockout mice. We were unable to isolate sufficient *Cfap43*$^{\Delta ex3/\Delta ex3}$ sperm cells from the cauda epididymis for Western blot analysis, and crude testis lysates gave rise to high background on Western blots. However, immunoprecipitation of CFAP43 from testis lysates detected CFAP43 in wt but failed to detect full length CFAP43 protein in testis lysates of homozygous *Cfap43*$^{\Delta ex3}$ males, using the polyclonal P4 or the monoclonal 27D5 antibody (Fig. 5B). Also, a predicted shorter variant with an apparent molecular weight of 172 kDa, which potentially could result from splicing of exon 2 into exon 7, restoring the reading frame,

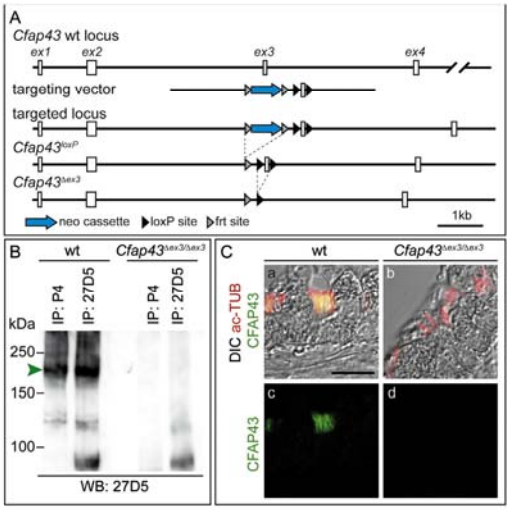

Fig. 5. Generation and validation of a *Cfap43* null allele in the mouse. **(A)** *Cfap43* wt locus, targeting vector, and targeted alleles (*Cfap43* targeted locus, $Cfap43^{loxP}$, and $Cfap43^{\Delta ex3}$). **(B)** Western blot analysis of CFAP43 following IP with polyclonal antibody P4 or MAb 27D5 from testes lysates shows absence of CFAP43 protein in $Cfap43^{\Delta ex3/\Delta ex3}$ mutants. The green arrowhead points to CFAP43 protein. **(C)** Indirect IF staining of lung sections of wt and $Cfap43^{\Delta ex3/\Delta ex3}$ mutants using monoclonal antibody 5B1 co-stained with acetylated α-tubulin (ac-TUB) shows CFAP43 in cilia in wt, but its absence in $Cfap43^{\Delta ex3/\Delta ex3}$ lungs. Full size Western blot for B is shown in Fig. S9C. Scale bar in C = 10 μm.

was not detected (Fig. 5B). Consistently, staining of cilia on epithelial cells lining the airways of the lung was lost in $Cfap43^{\Delta ex3/\Delta ex3}$ mice (Fig. 5C). Deletion of exon 3 thus prevented the translation of CFAP43 protein, indicating that $Cfap43^{\Delta ex3}$ in all likelihood represented a *bona fide* null allele.

Left-right defects were not observed in 21 homozygous $Cfap43^{\Delta ex3}$ mutants, as assessed by the analysis of organ situs, consistent with the results in *Xenopus* morphants and crispants.

Expression in multiciliated cells of the respiratory tract suggested a potential function of CFAP43 for cilia motility and mucociliary clearance. Indeed, mucus accumulation was observed by PAS staining of histological sections in the nasal cavities of three months (n=3) and one year old (n=6) mutant mice (Fig. 6A). Mucus-producing goblet cells were present in equal numbers in wt and *Cfap43* knockout specimens (Fig. S6, Table S3), and CFAP43 was exclusively present on wt airway MCCs (n=3, Fig. 6B), strongly suggesting that mucus accumulation was caused by MCC defects. Analysis of trachea sections of 6–7 weeks old mice showed that cilia on mutant MCCs were present, and marker proteins of outer and inner dynein arms as well as radial spokes were detected as in wt (Fig. 6C). Likewise, TEM analysis of lung sections showed no obvious alterations in axonemal structures or rotational polarization of cilia (Fig. 6D), Additionally, and cilia length was unaltered in isolated $Cfap43^{\Delta ex3}$ mTECs as compared to wt (Fig. 6E). Mutant tracheal MCC cilia were motile and – at first glance – appeared indistinguishable from wt (Movie S4). However, quantitative analyses of ciliary beat frequencies (CBF) in tracheal cilia of 6–9 months old wt and knockout mice, revealed a significant increase in CBF from on average of 10 Hz in wt to about 16 Hz in mutants (Fig. 6Fa, b; Fig. S7; raw data in Table S4). To analyze the functional consequences of altered CBF, fluorescent beads were added to tracheal epithelial explants (Fig. S7C). Despite the increase in CBF, bead transport was markedly reduced in mutant samples (Fig. 6Fc; Movie S5, raw data in Table S5), corroborating the results obtained in frog tadpole skin (cf. Fig. 4A, B; Movies S2, S3).

Supplementary video related to this article can be found at https://doi.org/10.1016/j.ydbio.2019.12.010.

$Cfap43^{\Delta ex3/\Delta ex3}$ females bred and raised their offspring normally, whereas males (n=6) were infertile when mated to wt or mutant females, due to severe sperm defects (Fig. 7A; Movie S6), in agreement with findings in humans (Tang et al., 2017). In correlation with the differentiation of sperm cells during the first round of spermatogenesis, upregulation of *Cfap43* expression was detected starting at d15 (Fig. 7B). *Cfap43* loss in mutant males did not impair the structure of seminiferous tubules and lumina contained sperm cells (Fig. 7Ca, b, e, f). However, flagella were not present in the center of the lumina but appeared dispersed in $Cfap43^{\Delta ex3/\Delta ex3}$ mutants (Fig. 7Ce, f). In the cauda epididymis of mutants, only few tubules were filled with sperm cells as compared to wt (Fig. 7Cc, c', g, g', d, d', h, h'), while tubules themselves appeared normal (Fig. 7Cc, g). In mutant tubules that contained sperm cells, staining of axonemes with acetylated α-Tubulin (ac-TUB) appeared reduced (Fig. 7Cd, d', h, h'). Isolated epididymal sperm cells frequently showed short flagella (442/489) that contained coiled (188/489) or split (80/489) axonemes (Fig. 8B, Table S6). The midpiece was severely shortened, as indicated by localization of mitochondria (visualized by COXIV staining; Fig. 8Ba-c) and position of the annulus (visualized by SEPT7 staining; Fig. 8Bd-f). Fibrous sheath material (visualized by AKAP3 staining) was not associated with microtubules but concentrated between split or coiled axonemes, or was absent (Fig. 8Bg-j).

Supplementary video related to this article can be found at https://doi.org/10.1016/j.ydbio.2019.12.010.

Ultrastructural analysis of $Cfap43^{\Delta ex3/\Delta ex3}$ epididymis sections by transmission electron microscopy (TEM) showed fewer sperm nuclei (red asterisks in Fig. 8Ca, b) and flagellar cross sections (red arrows in Fig. 8Cb) as well as large and partly fragmented cytoplasmic structures (arrowheads in Fig. 8Cb), as compared to wt specimens (Fig. 8Ca). Cross sections of mutant axonemes showed variable but severe axonemal malformations: at the level of the midpiece (indicated by the presence of peripheral mitochondria, yellow triangles in Fig. 8Cc, f), we observed few and abnormally located disorganized microtubules (small red arrows in Fig. 8Cf) and dislocation of outer dense fibers (ODF pink star; large red arrow in Fig. 8Cf). Sections through the principal piece (indicated by the absence of peripheral mitochondria, Fig. 8Cd, e, g-i) showed single (large red arrows in Fig. 8Cg) or fragmented microtubules (small red arrows in Fig. 8Cg). They possibly represented isolated A- and B-tubules of microtubule doublets, rather than intact doublets. Further, mutant sperm displayed supernumerary (or fragmented) ODFs (pink stars, Fig. 8Cg, h), ODFs located peripheral to the fibrous sheath (red arrowhead in Fig. 8Ch), or lacked the fibrous sheath (Fig. 8Ci).

Histological analysis of $Cfap43^{\Delta ex3/\Delta ex3}$ brains (n=11) from mice not displaying external signs of hydrocephalus showed enlarged ventricles in all cases at 6–13 weeks of age (arrowhead in Fig. 9Af). Enlarged ventricles were invariably observed in brains from homozygous mutants at day P7 (n=4/4), P5 (n=3/3) and P3 (4/4), as well as in 3/5 brains analyzed at P1 (Fig. 9Ag-j). Sagittal sections of P5 $Cfap43^{\Delta ex3/\Delta ex3}$ brains (n=5) revealed no evidence for aqueduct obstruction (arrowheads in Fig. 9B; Fig. S8A). Immunofluorescence staining of P7 brain sections detected glutamylated-tubulin (Glu-TUB) in cilia similar to wt (Fig. 9C). In agreement with the observed early onset of dilated ventricles in $Cfap43^{\Delta ex3/\Delta ex3}$ brains at P1, *Cfap43* expression was detected in the ependymal cells lining the lateral and medial walls of the lateral ventricles, in the aqueduct (AQ), and in the choroid plexus (CP) of E16.5 fetuses (Fig. 9D). High-speed video microscopy showed that *Cfap43* mutant ependymal cilia of the lateral walls were motile and moved fluorescent beads at a slightly reduced, though not significantly slower rate compared to wt littermates (Fig. S8B; Movie S7; raw data in Table S7).

Supplementary video related to this article can be found at https://

ARTICLE IN PRESS

E. Rachev et al. Developmental Biology xxx (xxxx) xxx

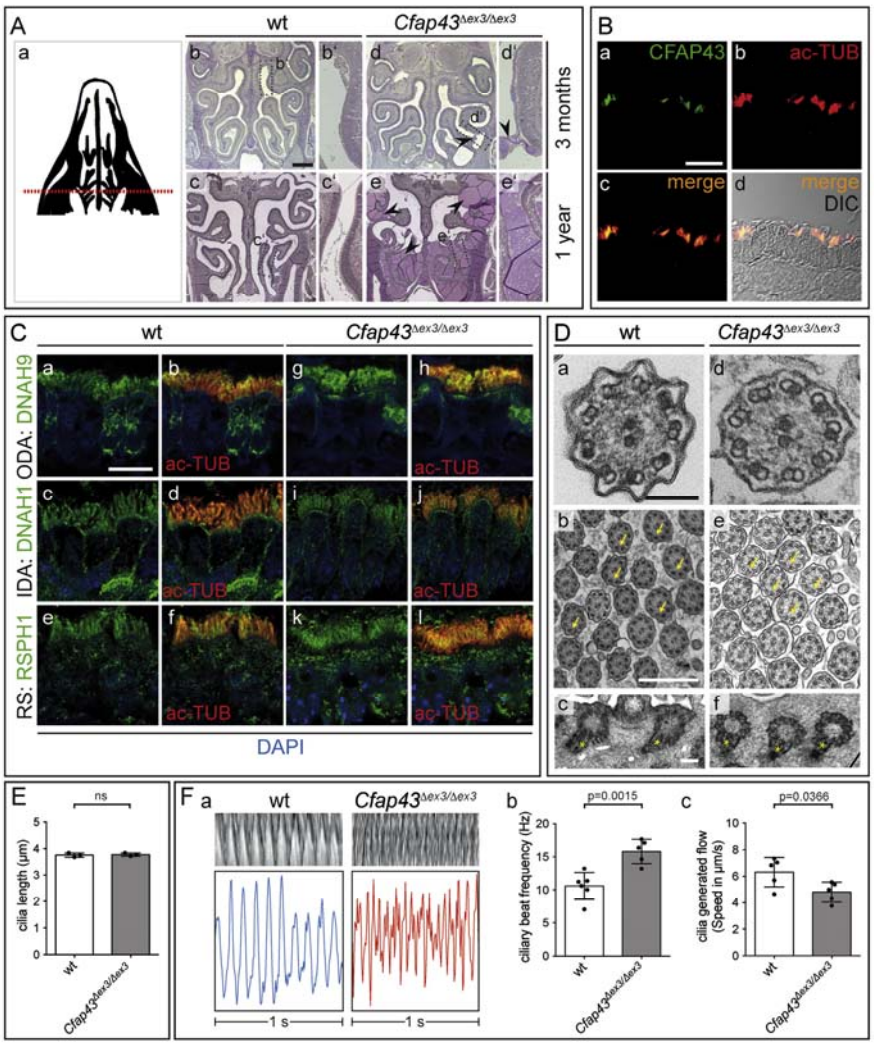

Fig. 6. Airway cilia morphology and function in wt and *Cfap43* knockout mice.
(A) PAS staining of frontal sections (at level indicated in (a)) from nasal cavities of 3 months (b, d) and 1 year (c, e) old wt (b, c) and *Cfap43*$^{\Delta ex3/\Delta ex3}$ (d, e) mice show mucus accumulations in mutants (black arrowheads in (d, e)). Dashed boxes outline areas of higher magnification in (b'-e'). **(B)** IF staining of wt lung sections with monoclonal antibody 5B1 highlights CFAP43 localization exclusively to cilia of epithelial cells, which were co-stained with acetylated α-tubulin (ac-Tub). **(C)** Outer dynein arms (ODA, DNAH9: a, b, g, h), inner dynein arms (IDA, DNAH1: c, d, i, j), and radial spokes (RS, RSPH1: e, f, k, l) are present in wt (a–f) and *Cfap43*$^{\Delta ex3/\Delta ex3}$ (g–l) tracheal cilia. **(D)** TEM analyses of wt (a–c) and *Cfap43*$^{\Delta ex3/\Delta ex3}$ (d–f) lung cilia axonemes demonstrate normal arrangement of 9 + 2 axonemes (a, d) and normal rotational polarization of cilia, as indicated by orientation of central microtubule pairs (yellow arrows in b and e) and basal feet (yellow asterisks in c and f). **(E)** Cilia length is comparable in wt and *Cfap43*$^{\Delta ex3/\Delta ex3}$ tracheas. Each dot represents the average cilia length from one individual. **(F)** (a) Representative kymographs (above) and plotted values (bellow) of wt (blue) and *Cfap43*$^{\Delta ex3/\Delta ex3}$ (red) tracheal cilia motility (t = 1 s) depict ciliary beat frequency (CBF). (b) CBF is enhanced in *Cfap43*$^{\Delta ex3/\Delta ex3}$ as compared to wt tracheal cilia. Each dot represents the average CBF of one specimen (n≥11 cells analyzed). (c) Cilia generated flow is reduced in *Cfap43*$^{\Delta ex3/\Delta ex3}$ versus wt tracheas. Each dot represents the average ciliary flow per specimen from n≥3 recordings. More details concerning CBF and ciliary flow measurement are shown in Fig. S7. Scale bars: A = 1 mm; B = 20 µm; C = 10 µm; Da, d = 100 nm; Db, e = 500 nm; Dc, f = 100 nm.

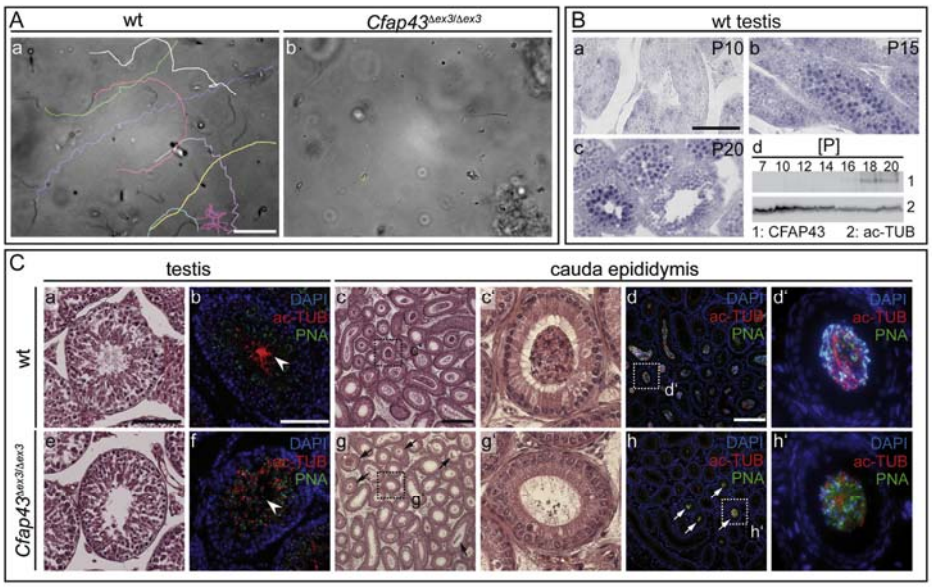

Fig. 7. *Cfap43* expression during spermiogenesis and sperm defects in *Cfap43*$^{\Delta ex3/\Delta ex3}$ males.
(A) Representative trajectories of wt and *Cfap43*$^{\Delta ex3/\Delta ex3}$ sperm motility reveal immobility of sperm from mutant mice (cf. Movie S6). **(B)** SISH on wt testis (a–c) and WB analysis of wt testis lysates (d) show upregulation of *Cfap43* expression from postnatal (P) day P15 on. Full size Western blot is shown in Fig. S9D. **(C)** Histological (HE) (a, c, c', e, g, g') and immunostained (b, f, d, d', h, h') sections show wt (a-d') and *Cfap43*$^{\Delta ex3/\Delta ex3}$ (e-h') testes (a, b, e, f) and cauda epididymides (c-d', g-h'). In immunostainings the acrosome was marked by PNA (green) and the sperm flagella were labelled using acetylated α-tubulin (ac-TUB, red). DAPI was used to stain nuclei (blue). Scale bars: A = 50 μm, Ba-c = 100 μm; Ca, b, e, f = 100 μm; Cc, d, g, h = 200 μm.

doi.org/10.1016/j.ydbio.2019.12.010.

In summary, our analyses of *Cfap43* null mutant mice demonstrated that CFAP43 function was not limited to sperm flagella, but also required in airway epithelia and brain ependyma, tissues carrying and requiring motile cilia function.

3. Discussion

Originally, we identified *Cfap43* as a gene acting downstream of FOXJ1 in the fetal respiratory epithelium of the mouse lung (Stauber et al., 2017). The conserved nature of this regulation became obvious in wt *Xenopus* embryos, where both genes were largely co-expressed, as well as in gain- and loss-of-function scenarios. In the mouse, *Cfap43* expression was consistently reduced in epithelial cells lining the large airways of the lung, and absent in ependymal cells and the choroid plexus of *Foxj1*$^{-/-}$ fetuses (Fig. 1E). Surprisingly, however, *Cfap43* expression was unaffected in the upper respiratory tract of mouse *Foxj1*$^{-/-}$ knockout specimens and only moderately reduced at the frog larval proctodeum (Fig. 2C), suggesting differential regulation of *Cfap43* in the various cell populations carrying motile cilia. Members of the RFX family of transcription factors can act downstream (ventral node; Alten et al., 2012) or upstream (ependymal cells; Zein et al., 2009) of FOXJ1, or in a redundant manner (floor plate; Cruz et al., 2010); they might therefore contribute to tissue-dependent differences of *Cfap43* transcription in *Foxj1* mutants. However, in MCCs RFX proteins rather act as scaffolding proteins (Quigley and Kintner, 2017), suggesting that additional tissue-specific factors maintain *Cfap43* transcription in the absence of FOXJ1.

As an evolutionarily highly conserved component of motile cilia, *Cfap43* has been studied before in humans, mice, trypanosomes, and the single-cell green algae *Chlamydomonas reinhardtii*. In humans, mutations in *CFAP43* were causative for a rare type of male infertility, namely MMAF (multiple morphological abnormalities of the sperm flagella). No additional health problems were reported in sterile male patients (Coutton et al., 2018; Sha et al., 2017; Tang et al., 2017). Likewise, no cilia-related defects other than sperm flagellum malformation were reported for the *Cfap43* mutant mice generated by Tang et al. (2017) and Coutton et al. (2018). The null allele that we created in the mouse confirmed both human and mouse sperm phenotypes: sperm were immobile and the morphological and ultrastructural flagella defects observed in patients (Coutton et al., 2018; Sha et al., 2017; Tang et al., 2017) were highly similar to malformations described here. Therefore, the human mutations, which resulted in premature stop codons and splicing defects, likely represent null alleles as well. During spermatogenesis, the material for outer dense fibers and the fibrous sheath is transported along the growing axoneme (Irons and Clermont, 1982a, 1982b), which could explain the mis-arranged accessory structures of the flagellum after loss of CFAP43. Since the flagella appeared distorted in the seminiferous tubules of the testis, defects likely occurred during axoneme formation and were not acquired during later stages of spermatogenesis or in the maturation process. Whether sperm defects arise in frogs as well was not addressed, as raising sexually mature adult frogs is time-consuming. We would, however, anticipate that CFAP43 is required for sperm flagella formation throughout the vertebrates.

Our descriptive and functional investigation of mucociliary epithelia in postnatal mutant mouse and embryonic frog morphant and crispant specimens uncovered a novel function of CFAP43 in motile cilia. Mucus accumulation, as found in *Cfap43* knockout mice, can be caused by alterations of ciliary structure or beating. Ciliary length and rotational polarity, as well as mucus production (inferred from the unchanged number of mucus-producing cells) were apparently not affected by loss of *Cfap43*. However, loss of CFAP43 increased the ciliary beat frequency (CBF) which was accompanied by reduced velocity of cilia generated

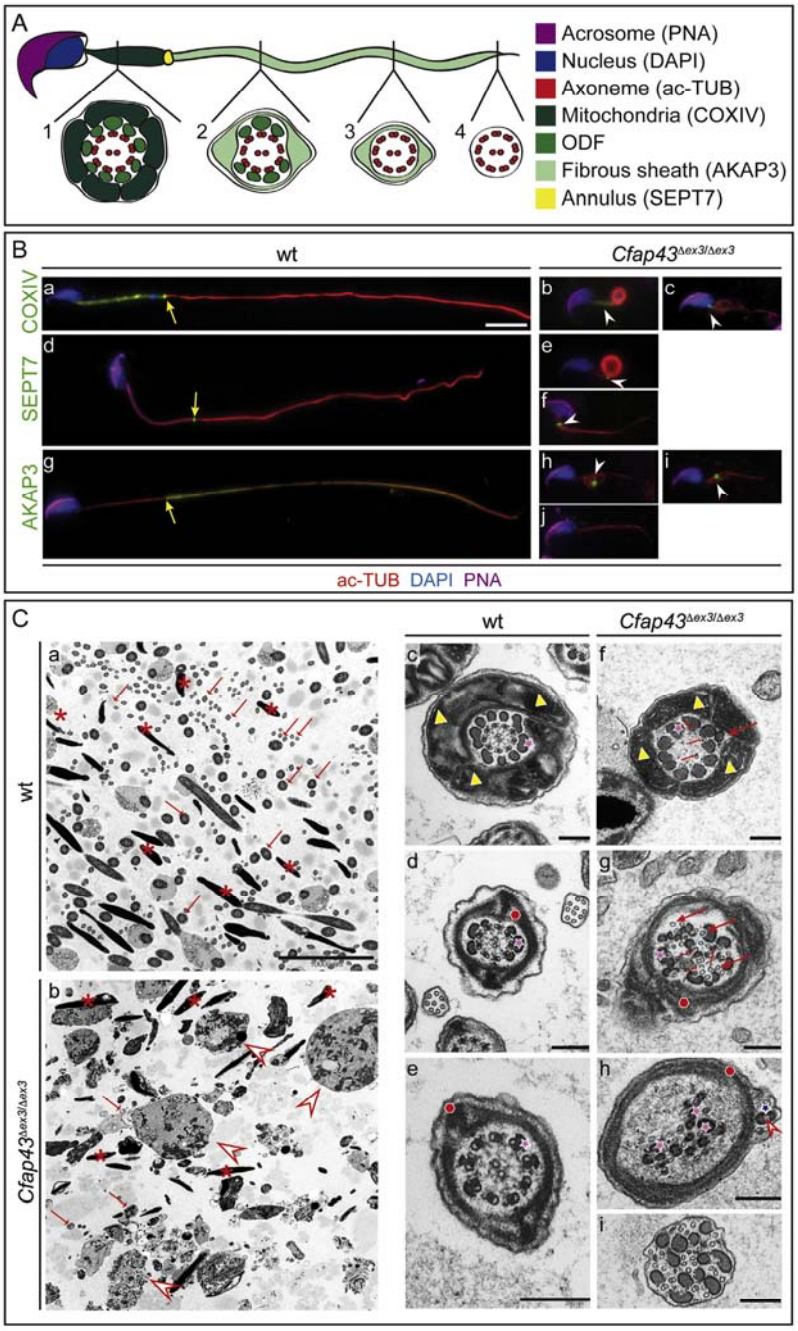

Fig. 8. Subcellular and electron microscopic analysis of *Cfap43*$^{\Delta ex3/\Delta ex3}$ mouse sperm.

(A) Schematic overview indicating the sperm architecture. In the midpiece (1) the axoneme is surrounded by outer dense fibers (ODF) and mitochondria. The annulus is located at the border between the midpiece and the principal piece (yellow). ODFs are continuing in the principal piece (2), surrounded by the fibrous sheath. In the proximal part (3) of the principal piece the ODFs are discontinuous. In the end piece (4) only the axoneme is maintained. **(B)** Characterization of cauda sperm from wt (a, d, g) and *Cfap43*$^{\Delta ex3/\Delta ex3}$ (b, c, e, f, h-j) males. Mutant sperms show a shortened midpiece and malformed axoneme. Axonemes were stained for acetylated α-tubulin (ac-TUB, red), nuclei were visualized using DAPI (blue), and acrosomes were marked by PNA (purple). (a–c) Mitochondria are shown by COXVI (green). (d–f) The annulus is marked by SEPT7 (green). (g–j) AKAP3 was stained to highlight fibrous sheath (green). Yellow arrows point to midpiece/principal piece border in wt; white arrowheads point to shortened midpiece region containing mitochondria in (b, c), to annuli abnormally close to the sperm head in (e, f) of *Cfap43*$^{\Delta ex3/\Delta ex3}$ mutant sperm, and to abnormal localization of fibrous sheath material between coiled or split axonemes close to the sperm head (h, i). In some cases no fibrous sheath was detected in *Cfap43*$^{\Delta ex3/\Delta ex3}$ mutant sperm (j). **(C)** Overviews of wt (a) and *Cfap43*$^{\Delta ex3/\Delta ex3}$ (b) sections show large, partly fragmented cytoplasmic structures in *Cfap43*$^{\Delta ex3/\Delta ex3}$ (b, arrowheads). Red asterisks indicate sperm heads, red small arrows point to flagellar cross sections. (c, f) Detail images show flagellar cross sections of wt (c) and *Cfap43*$^{\Delta ex3/\Delta ex3}$ (f) sperms at the midpiece level as indicated by the presence of peripheral mitochondria (yellow triangles). Pink stars mark outer dense fibers (ODFs); the large red arrow points to a dislocated ODF; small red arrows point to abnormally located microtubules. (d-e, g-i) Detail images show flagellar cross sections of wt (d, e) and *Cfap43*$^{\Delta ex3/\Delta ex3}$ (g–i) principal pieces as indicated by the absence of mitochondria and the presence of fibrous sheath (red hexagons). (h) Arrowhead points to ODFs (blue star) peripheral to the fibrous sheath. (i) Detail image of flagellar principle piece cross section of *Cfap43*$^{\Delta ex3/\Delta ex3}$ lacking fibrous sheath material. Scale bars: B = 10 μm; Ca, b = 10 μm; Cc-h = 200 nm.

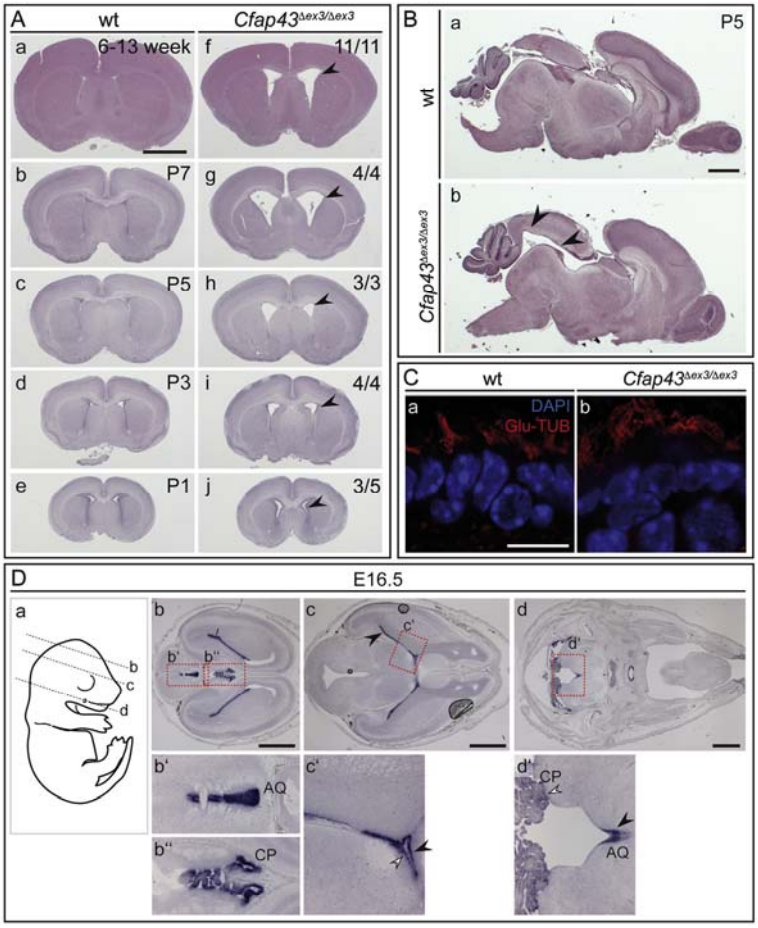

Fig. 9. Brain defects in *Cfap43*$^{\Delta ex3/\Delta ex3}$ mouse mutants.
(A) HE stained frontal sections of wt (a–e) and *Cfap43*$^{\Delta ex3/\Delta ex3}$ (f–j) mouse brains at different postnatal days show dilated ventricles (arrowheads) in mutant mice. **(B)** Mid-sagittal sections of P5 wt (a) and *Cfap43*$^{\Delta ex3/\Delta ex3}$ (b) mouse brains show no obstruction of the aqueduct (arrowheads). **(C)** Ependymal cilia are present in P7, as demonstrated by IF staining of brain sections for glutamylated-tubulin (Glu-TUB, red) in wt (a) and *Cfap43*$^{\Delta ex3/\Delta ex3}$ (b) mouse brains. Nuclei are marked by DAPI staining (blue). **(D)** (b–d) *Cfap43* transcripts are expressed in mouse embryonic brain at E16.5. SISH of transverse sections (section planes are indicated in a); red boxes are magnified in b', b'', c' and d'. Black arrowheads in (c) and (c') point to *Cfap43* expression in the lateral wall of the lateral ventricles, white arrowhead in (c') highlights expression at the medial wall. Black arrowhead in (d') points to *Cfap43* expression in the AQ, white arrowhead in (d') highlights *Cfap43* expression in the CP of the fourth ventricle. AQ: aqueduct; CP: choroid plexus. Scale bars: A = 2 mm; B = 1 mm; C =10 μm; D = 1 mm.

flow (CGF). Such an - at first glance - counter-intuitive observation is not unprecedented and was for example also found in knockout mice of *Ttll1*, a gene encoding a tubulin glutamylating enzyme (Ikegami et al., 2010). *Ttll1* mutant cilia were characterized by a loss of beating asymmetry, i.e. the velocities of the effective (transport of mucus) and recovery stroke (restoring the initial position) where similar (Ikegami et al., 2010). Reduced CGF in *Cfap43*-mutant tracheal cells, despite increased CBF, could therefore be caused by alterations of velocities of effective or recovery stroke, changes in wave form or ciliary bending, parameters that we could not resolve in our analyses. The observed mucus accumulation in the upper airways of mutant mice likely arise as a consequence of this defect. Incidentally, *Ttll1* knockout mice displayed mucociliary clearance defects as well (Ikegami et al., 2010). The larval skin of the frog tadpole did not show mucus accumulation, most likely because the mucociliary epithelium exists only for a short interval of about three days (roughly stages 20–40). Mucociliary defects in human patients were not reported, but may have gone unnoticed.

Our reasoning that CFAP43 impacts on ciliary motility in a rather subtle way is further supported by analyses of the CFAP43 orthologues FAP43 in *Tetrahymena* and *Chlamydomonas*. In both organisms, FAP43 is a component of the tether/tether head complex that together with FAP44 links the inner dynein arm (IDA) subspecies f (I1 dynein) motor head to the A-tubule of the outer microtubule doublet (Fu et al., 2018; Kubo et al., 2018; Urbanska et al., 2018). The two-headed IDA I1 has been suggested to impact on the wave form through modulation of cilia bending, rather than on microtubule sliding (Kubo et al., 2018; Urbanska et al., 2018). In *Tetrahymena*, loss of FAP43 affected the ciliary wave form, beat stroke and swimming velocity (Urbanska et al., 2018), whereas subtle flagellar beating defects were seen upon loss of FAP43 in *Chlamydomonas* (Kubo et al., 2018). Using STED microscopy and immunogold labelling, tagged CFAP43 was located between the axoneme and paraflagellar rod of *T. brucei* (Coutton et al., 2018). An evolutionary conserved localization of CFAP43 (together with CFAP44) to a bridge between axonemal microtubule doublets 5 and 6 was proposed and discussed to restrict ciliary and flagellar movement to a planar beating form (Afzelius, 1959; Lin et al., 2012; Lindemann et al., 1992). Further studies and improved tools to analyze, dissect and describe ciliary beating of airway epithelial and ependymal cells are needed to unravel the functional consequences of CFAP43 loss for the wave form of cilia on multiciliated cells in vertebrates. Likewise, further studies will be

required to elucidate the biochemical function of CFAP43. Towards this aim we identified potential interaction partners by immunoprecipitation of CFAP43 from adult mouse testes and subsequent mass spectrometric analysis, which led to a number of candidate proteins (Table S8) that, when validated, should provide entry points for further biochemical analyses.

Most *Cfap43* mutant mice showed dilated ventricles at P1, before full maturation of ependymal epithelia, but after onset of multiciliogenesis on the ventromedial wall of the lateral ventricles (Abdelhamed et al., 2018; Ibañez-Tallon et al., 2004). The observed phenotype was fully penetrant by P7, concomitant with the maturation of ependymal cilia, but progressed only in rare cases to externally visible hydrocephalus. Therefore, the detected hydrocephalus upon loss of CFAP43 in mice may be caused by early defects in choroid plexus cilia (Banizs et al., 2005), medial wall cilia (Abdelhamed et al., 2018), impaired ependyma, or a combination thereof. Ependymal cilia were motile both in mouse and frog, and ependymal flow in mouse brains was apparently unaltered. Recently, a heterozygous mutation in *Cfap43* was described in a Japanese family with normal pressure hydrocephalus (NPH) (Morimoto et al., 2019). NPH constitutes a variant of hydrocephalus that develops past the age of 40 and is characterized by excess cerebrospinal fluid production. However, the progression of NPH contrasts with the early-onset hydrocephalus found in our knockout mice. In-depth studies, beyond the scope of the present investigation, are needed to unravel the molecular mechanism of hydrocephalus formation in mutant mice. It is tempting to speculate, however, that a choroid plexus ciliary defect results in excess CF, which causes early onset hydrocephalus in mouse and NPH in humans, although the presumed dominant-negative mode of action of the described human mutation (Morimoto et al., 2019) needs to be confirmed and mechanistically evaluated. The lack of hydrocephalus in mutant frog embryos may be due to the much earlier time point of analysis, before the onset of metamorphosis. It may be worthwhile to generate a mutant line in *Xenopus tropicalis*, in order to assess *cfap43* function in the developing and adult brain, with a focus on CF production in the choroid plexus.

Male infertility, mucociliary clearance defects of the airways, and hydrocephalus are hallmarks of primary ciliary dyskinesia (PCD) in humans and mouse models of this disease. In that sense, the knockout mouse fulfils some criteria of PCD. PCD patients generally are characterized by immobile cilia. *Cfap43*, therefore, does not qualify as a PCD gene. Also, besides infertility, no other defects have been described in human male MMAF patients. It may, however, be useful to re-evaluate patients for NPH and subtle mucociliary clearance defects. If such pathologies were detected, *Cfap43* may represent a gene for a PCD subtype that accounts for more subtle phenotypes.

4. Conclusions

CFAP43 is a highly conserved axonemal protein of motile cilia. Besides the known function in mammalian sperm cells, CFAP43 is required in the brain and respiratory tract of mice, as well as in skin MCCs in frog embryos. Airway mucus accumulation in mice occurs most likely due to changed beating of multiciliated epithelial cells of the respiratory tract leading to reduced velocity of the generated mucus flow. Changes in the ependymal flow were not observed as a cause for hydrocephalus formation, suggesting that more subtle ciliary or other defects underlie the development of this phenotype.

5. Materials and methods

Multiple protein sequence alignment: Sequences were aligned using ClustalW (v1.83; multiple sequence alignment; Pairwise Alignment Mode: Slow; Pairwise Alignment Parameters: Open Gap Penalty = 10.0, Extend Gap Penalty = 0.1, Similarity Matrix: gonnet; Multiple Alignment Parameters: Open Gap Penalty = 10.0, Extend Gap Penalty = 0.2, Delay Divergent = 30%, Gap Distance = 4; Similarity Matrix: gonnet).

Ethics approval: Animals were handled in accordance with the German regulations (Tierschutzgesetz) and for mice approved by the ethics committee of Lower Saxony for care and use of laboratory animals (LAVES, Niedersächsisches Landesamt für Verbraucherschutz und Lebensmittelsicherheit), for frogs by the Regional Government Stuttgart, Germany (A379/12 Zo 'Molekulare Embryologie'). Mice were kept in the central animal facility of Hannover Medical School (ZTL) and maintained as approved by the responsible Veterinary Officer of the City of Hannover.

5.1. Mouse methods

Experimental animals: Cfap43 mutant mice were generated and genotyped as described below. Other mouse lines used were described previously: *Foxj1* mutants (*Foxj1*^{tm2Zhu}) (Brody et al., 2000), Zp3:Cre (de Vries et al., 2000), and FLPe (Rodríguez et al., 2000).

Generation of a conditional Cfap43 allele: A targeting vector containing exon 3 flanked by loxP sites and approximately 1 kb of intron 2 and 3, respectively, and a neomycin resistance cassette flanked by frt sites inserted upstream of exon 3 was generated by standard cloning procedures. Linearized targeting vector DNA and CRISPR-Cas plasmid pX330 (Cong et al., 2013) containing the guide sequence 5′-GTCAT CTGGATGTGACAGTCC-3′ were introduced into ES cells by electroporation. ES cells were screened for homologous recombination by PCR using the following primer pairs: 5′flank: (5′-AAGTACGAGAAGGAGGT AGTAAGGC-3′, 5′-GGCTGGACGTAAACTCCTCTTCAGA-3′); 3′flank: (5′-GAGATTGGAAAACATTTTACCAGTGAAGT-3′, 5′-GAGATTGGAAAA CATTTTACCAGTGAAGT-3′). The presence of both loxP sites in positive clones was ascertained using primer pairs (5′-AATAGCAGG-CATGCTGGGGATG, GGGACTTACCAGAGGGCCAGC-3′) and (5′-GGATC CGACAGTCCTGGATTGTGTCTT-3′, 5′-GAAAGTTAACCTTCCCATCAT CCCCTG-3′), respectively. PCR positive clones were further characterized by Southern blot hybridization. Southern probes were generated from genomic DNA (5′ probe: genomic *Cfap43* DNA from bp 4149–5325 (start ATG set as bp 1); primers: 5′-AAGTACGAGAAGGAGGTAGTAAGGC-3′, 5′-TAGATCACACGAAGTGTTCTGTCC-3′; 3′ probe: genomic DNA from bp 8636–9203, primers 5′-TAAATAAGGATTGCGATCTTTTTAGGA-3′, 5′-GGCCATGGGGTCTGCTCAC-3′) and labelled using Prime-It II Random primer labelling kit (Agilent). Southern blotting and hybridization were performed following standard procedures. Correctly targeted ES-cells were injected into CD1 morulae or blastocysts. The neomycin cassette of mutant mice was excised by breeding with FLPe mice (Rodríguez et al., 2000), and exon 3 was excised by crossing with ZP3:Cre mice (de Vries et al., 2000). Mice resulting from integration of the targeting construct were genotyped by PCR using primers 5′-GCTCTATG GCTTCTGAGGCGG-3′ and 5′-GGGACTTACCAGAGGGCCAGC-3′ (mutant product 291 bp, no wt product), and mice containing floxed *Cfap43* exon 3 (*Cfap43*^{loxP}) without the neomycin cassette were genotyped using primers 5′-TCACCCGGCCTCCCCAAG-3′ and 5′-TCCAGGACTGTCG-GATCCACCT-3′ (mutant product 687 bp, wt product 602 bp). *Cfap43*$^{\Delta ex3}$ mice were genotyped using primers 5′-GCCAGTCACTAGGG AAAGGGAAGC-3′ and 5′-TCCGGTGAAACCAGGGGTCAG-3′, which give rise to a 271 bp wt and a 193 bp mutant product, respectively.

Collection, embedding, and sectioning of mouse tissues: For tissue collection mice were killed by cervical dislocation. Tissues were dissected, fixed overnight at 4 °C in 4% PFA or 100% methanol, if necessary decalcified in 0.5 M EDTA for 2 weeks exchanging EDTA every other day, dehydrated, and embedded in paraffin according to standard procedures. Embedded tissues were sectioned at 5 or 10 μm.

Transmission electron microscopy (TEM): Epididymides and lungs were dissected from 3-month-old wt and *Cfap43*$^{\Delta ex3/\Delta ex3}$ littermates. Tissues were fixed, embedded, and analyzed as previously described (Rudat et al., 2014).

Section in situ hybridizations (SISH): SISH were performed on 10 μm sections of PFA fixed and paraffin-embedded tissues as described in Moorman et al. (2001). DIG-labelled RNA probe was produced from

FANTOM plasmid PX00616F12 (Kawai and Hayashizaki, 2003) using the Roche DIG RNA labelling system.

Whole mount in situ hybridization (WISH): WISH were performed on E8.25 old embryos as described in (Stauber et al., 2017). DIG-labelled RNA probe was produced from FANTOM plasmid PX00616F12 (Kawai and Hayashizaki, 2003) using the Roche DIG RNA labelling system.

Histology on tissue sections: Histological staining was performed on 10 μm sections of PFA fixed and paraffin-embedded tissues. Hematoxylin and eosin (HE) staining was performed according to standard procedures. PAS staining was carried out using the Periodic Acid-Schiff (PAS) Kit (Sigma Aldrich) according to manufacturer's instructions.

Isolation and processing of sperm cells: For isolation of sperm, epididymides were collected and cut into 1–3 mm fragments in HTF medium (101.65 mM NaCl, 4.7 mM KCl, 199.5 μM $MgSO_4$, 370.5 μM KH_2PO_4, 25 mM $NaHCO_3$, 2.7 mM $CaCl_2$, 2.8 mM glucose, 0.33 mM sodium pyruvate, 18.3 mM sodium lactate, Pen/Strep, 0.0002% phenol red, 4 mg/ml BSA) containing 0.5% methyl-cellulose for video-microscopy or PBS for other applications, and shaken 15 min at 600 rpm. For video-microscopy, sperm was incubated in HTF for 1 h before documentation. Sperm cells in PBS were spread on glass slides and dried before further processing.

Isolation of murine tracheal epithelial cells (mTECs): Multiciliated cells of the airways were collected by tracheal brushing, suspended in PBS, spread on glass slides, and air-dried before further processing.

Cell culture: L-cells allowing for inducible CFAP43 expression under control of the Tet ON/OFF system (Clontech) were maintained in DMEM/F12 (Gibco) containing 10% FCS, Pen/Strep, and 2 mM Glutamax. For induction of CFAP43 expression, 1 μg/ml doxycycline was added to the medium for 24 h. Murine tracheal epithelial cells (mTECs) were isolated and cultured at air liquid interface (ALI) as described in (You and Brody, 2013). CHO cells were cultured in DMEM/F12 containing 10% FCS, Pen/Strep, and 2 mM Glutamax (Gibco). Transfections were performed using Perfectin (Genlantis) according to manufacturer's instructions.

RNA isolation and RT-PCR: RNA was isolated using TriReagent (Geyer), cDNA was produced using the Superscript-II Reverse Transcriptase kit (Thermo Fisher Scientific), and PCRs were performed using the Expand High Fidelity PCR system (Roche) using the following primer combinations: mouse *Hprt* (5′-GCTGGTGAAAAGGACCTCT-3′; 5′-CACAGGACTAGAACACCTGC-3′), mouse *Cfap43* (5′-TCTACGGGAAGAACTGGTGG-3′; 5′-AGCTTGCTGCTTGGAGATGT-3′), mouse *Foxj1* (5′-CTTCTGCTACTTCCGCCATGC-3′; 5′-TCCTCCTGGGTCAGCAGTAAGG-3′).

Generation of antibodies: The rabbit polyclonal antibody against epitope CEKIARERYDNQLKQ (P4) was generated by Biogenes (BioGenes GmbH, Berlin) and affinity purified using P4-coupled SulfoLink Coupling Gel columns (Pierce). Monoclonal antibodies against CFAP43 were generated by immunization of rats and mice with a fragment of CFAP43 containing amino acids 1053–1226 expressed as MBP fusion protein (MBP-CFAP43) in bacteria. MBP-CFAP43 mainly remained in the insoluble fraction of harvested bacteria, thus inclusion bodies were purified as described (O'Callaghan et al., 1998). Insoluble inclusion bodies were resuspended in PBS and 50 μg were injected intraperitoneally (i.p.) and subcutaneously (s.c.) into LOU/C rats or C57/BL6 mice using incomplete Freund's adjuvant supplemented with 5 nmol CpG 2006 (rats) or CpG 1668 (mice, TIB MOLBIOL, Berlin, Germany). After a six-week interval, a final boost with 50 μg MBP-CFAP43 and CpG was injected i.p. and s.c. three days before fusion. Fusion of the myeloma cell line P3X63.Ag8.653 with the immune spleen cells was performed according to standard procedures. Hybridoma supernatants were tested in a solid-phase immunoassay with MBP-CFAP43 or an irrelevant maltose binding protein coated to ELISA plates. Antibodies from tissue culture supernatant bound to the ELISA plates were detected with HRP conjugated mAbs against the rat IgG isotypes (TIB173 IgG2a, TIB174 IgG2b, TIB170 IgG1 all from ATCC, R-2c IgG2c homemade), thus avoiding mAbs of IgM class. HRP was visualized with ready to use TMB (1-StepTM Ultra TMB-ELISA, Thermo). MAbs that reacted specifically with CFAP43 were further analyzed by Western blots and indirect immunofluorescence. Anti-CFAP43 22A11 (rat IgG2b), anti-CFAP43 5B1 (rat IgG2b), and anti-CFAP43 27D5 (mouse IgG2b) were used in this study.

Immunofluorescence staining: Paraffin sections were deparaffinized, rehydrated and antigens were unmasked by 20 min boiling in 10 mM Tris-HCl pH 9.5, 1 mM EDTA. Dried sperm and tracheal cells were washed in PBS. Unspecific binding was blocked by 5% FCS in PBS. Primary antibodies were incubated at 4 °C overnight, secondary antibodies for 1 h at room temperature. For lung sections primary antibodies were incubated sequentially: First anti-CFAP43 1B5 (overnight at 4 °C), followed by anti-acetylated α-tubulin (1 h at room temperature). Antibodies were diluted in blocking solution: anti-acetylated α-tubulin (ac-TUB) (axoneme, Sigma Aldrich T6793) 1:1000, anti-CFAP43 (22A11) 1:50, anti-CFAP43 (5B1) 1:5, anti-AKAP3 (fibrous sheath, Proteintech 13,907-1-AP) 1:200, anti-CoxIV (mitochondria, Abcam ab202554) 1:200, anti-Septin7 (annulus, IBL international #18991) 1:200, anti-glutamylated-tubulin (Glu-TUB) (AdipoGen AG-20B-0020-C100) 1:500, anti-mouse-Alexa555 (Invitrogen A21424) 1:500, anti-rat-Alexa488 (Invitrogen A11006) 1:500, and anti-rabbit-Alexa488 (Invitrogen A11034) 1:500. DAPI (1 μg/ml, Applichem) and PNA-lectin Alexa467 (2 μg/ml, Thermo Fisher L32460) were incubated together with secondary antibodies.

Immunoprecipitation (IP): For immunoprecipitation, 1 testis was lysed in 1 ml lysis buffer (50 mM Tris-HCl pH 7.5, 500 mM NaCl, 5 mM EDTA, 0.05% NonidetP40, Roche Complete protease inhibitor, and 0.1% BSA), sonicated, debris pelleted at 800×g for 10–20 min, and the supernatant was transferred into fresh tubes. Half a testis was used for each IP. 25 μl washed UltraLink beads (Perbio) and anti-CFAP43 antibodies (10 μl P4 or 500 μl 27D5) were added and incubated for 4h at 4 °C. Subsequently, beads were washed 3 times for 20 min in wash buffer (50 mM Tris pH 8.5, 500 mM NaCl, 5 mM EDTA, 0.05% NonidetP40, Roche Complete protease inhibitor, and 0.1% BSA) before analysis by Western blotting.

Western blot analysis: SDS-PAGE and Western blotting were carried out according to standard procedures. Antibodies were used at the following dilutions: anti-acetylated α-tubulin (Sigma Aldrich T6793) 1:1 000, anti-CFAP43 (27D5) 1:10, anti-CFAP43 (P4) 1:100, and anti-β-actin (MP Biomedicals 69,100) 1:1 000 000. Primary antibodies were detected using POD-labelled secondary antibodies: anti-mouse-POD (Amersham NA931), anti-rabbit-POD (Amersham NA934), and anti-rat-POD (Amersham NA935). Western blots were developed using WesternBright Quantum (Advansta).

Determination of cilia length in multiciliated cells of the trachea: Tracheas of each three 4 months old wt and *Cfap43*$^{\Delta ex3}$ mice were dissected and mTECs isolated and stained using anti-acetylated α-tubulin as described above. Cells were imaged using a confocal microscope (Leica TCS SP8 AOBS) and cilia length was determined using FIJI (Schindelin et al., 2012) by measuring the length of the ciliary tuft of each cell at three locations and averaging the measurements. For each individual, twenty cells were analyzed.

Analysis of ciliary beat frequency (CBF) and cilia-generated flow in mouse trachea: Tracheas of 6–9 months old mice were dissected as shown in Fig. S7A and described in Francis and Lo, (2013) (Francis and Lo, 2013). Two reinforcing rings (AVERY, Zweckform) were pasted into the middle of a 35 mm glass bottom Petri dish (MatTek, P35G-1.5-20-C) creating a chamber for recordings. Trachea samples were placed luminal side down into the chamber filled with Leibovitz's L-15 (Gibco) medium and covered with a 15 mm cover glass. Multiciliated cells were recorded using the Andor sCMOS Zyla camera and Nikon Spinning Disk confocal microscope (Nikon Eclipse Ti, Yokogawa/Andor) using the 100x objective. DIC optics was used to image ciliary beating for 9 s at frame rates of 156–168 fps (frames per second) at 24–27 °C. CBF was determined using FIJI as described in (Drummond, 2009). A line was set parallel to the cell membrane (Fig. S7Ba, c; Movie S4) and gray values underneath the line were represented in a single row of pixels in a kymograph (Fig. S7Bb, d) using the FIJI KymoResliceWide plugin (https://imagej.net/KymoResliceWide). The values for each pixel were plotted and imported to MATLAB (MathWorks). The Fast Fourier Transform algorithm of

MATLAB was used to extract the frequency responses of the measured signals. The double-sided magnitude of the transform was computed and normed to the length of the input signal. The single-sided spectrum of the symmetrical FFT outcome was used and multiplied by two to calculate the signals amplitudes. The highest peak amplitude in the power spectrum between 0 Hz and half the frequency of acquisition (frame rate) was used to determine the CBF. Beads (1:1000, Polysciences, Inc., Fluorespbrite Multifluorescent Microspheres 0.5 micron) were added to the trachea explants and the bead flow was recorded at 5 fps for 10 s at 24–27 °C using fluorescent microscopy. CGF in the determined region of interest (ROI) (Fig. S7C) was analyzed using the IMARIS (bitplane) 2D particle tracking tool.

Determination of ciliary flow in lateral ventricles: Brains were explanted at P7 and placed into Leibovitz's L-15 medium (Invitrogen) supplemented with FBS (Invitrogen). For analysis of ciliary flow at the floor of the lateral ventricles, the brain hemispheres exposing the lateral ventricles were transferred in medium enriched with 1 μm yellow-green FluoSpheres carboxylate (1:1000, Invitrogen). Flow was recorded for 30 s at 200 fps. Analysis of particle speed was performed using IMARIS (bitplane) using the 2D particle tracking tool.

Statistical analyses: Statistical analyses (students's t-test, One-way ANOVA) were performed using Prism (Graphpad). Data are given as mean ± SD.

Liquid chromatography fractionation and mass spectrometry: CFAP43 was immunoprecipitated from mouse testis using the Thermo Scientific Pierce crosslink IP kit with antibody P4. Immunoprecipitated CFAP43 complexes were isolated, purified, and subsequently analyzed by LC-MS/MS as described previously (Beyer et al., 2018). The full mass spectrometry proteomics data have been deposited to the ProteomeXchange Consortium via the PRIDE (Vizcaíno et al., 2016) partner repository with the dataset identifier PXD015425.

5.2. Xenopus methods

Microinjections: Xenopus laevis embryos were bilaterally injected into the neural (hydrocephalus), axial mesoderm (laterality), paraxial mesoderm (kidney) or epidermal cell lineage at the 4 cell stage. Drop size was calibrated to 4 nl per injection and *Alexa Fluor* 488 dextran (MW 70,000 or 10,000, respectively, 0.5–1 μg/μl, Thermo Fisher Scientific) was added as lineage tracer. Two different *cfap43* morpholino oligomers were used, targeting the translation start site (TBMO; 5′-CAGAGCACAGCCGGAGTTTTCCATC-3′) or the splice donor site of exon 1 (SBMO; 5′-TATTACTTTAGTCTGCCGGTTTACC-3′).

In situ hybridization in whole mounts (WISH) and on histological sections: WISH was performed using standard procedures as described elsewhere (Kawai and Hayashizaki, 2003). For histological sections, embryos were embedded in a gelatin-albumin mix and sectioned with a vibratome (Leica) at 30 μm.

Statistical analysis of Xenopus phenotypes: All measurements were performed using FIJI. Statistical calculation of organ situs defects and cyst analysis was performed using chi square (http://www.physics.csbsju.edu/stats/contingency_NROW_NCOLUMN_form.html). p-values of ventricular perimeter were calculated via Wilcoxon-Match-Pair test in RStudio.

CRISPR/Cas9 mediated genome editing: Single guide RNAs (sgRNAs) were designed using the CRISPRscan algorithm (Moreno-Mateos et al., 2015). sgRNAs targeting exon 4 and 5 were transcribed using the MEGAshortscript T7 Kit (Invitrogen) from synthetic DNA oligomers and purified with the MEGAclear Transcription Clean-Up Kit (Invitrogen). Embryos were injected with 1 ng Cas9 (PNA Bio) and 300 pg sgRNA at the 1-cell stage. Following injections, embryos were cultivated at room temperature. Direct sequencing of PCR products was applied to confirm genome editing. Groups of 10 embryos each were pooled at stage 45, DNA was isolated and gene-specific primers were used to amplify targeted sequences of *foxj1* and *cfap43*, respectively. Knockout efficiency was calculated using Synthego ICE online tool (("https://tools.synthego.com/#/," n.d.).

High-speed video microscopy of Xenopus laevis epidermal cilia: Control, morphant or crispant specimens were analyzed for epidermal ciliary beating patterns at stage 32. Embryos were mounted on a slide containing a rectangular chamber constructed from duct tape. Ciliary beating was recorded for 1 s at the most ventral proportion of the embryos using a high-speed Hamamatsu video camera Orca flash 4.0 at 800 fps (frames per second). For analysis of ciliary flow, 1 μm fluorescent beads (Invitrogen FluoSpheres; 1:2000) were added to the culture medium and specimens were imaged using a Zeiss Axiocam HSm camera at 175 fps. Evaluation of CBF and ciliary flow was as described in the respective mouse methods.

Immunofluoresence staining: Embryos were fixed at stage 32 in 4% PFA in PBS for 2 h at RT and washed before immunostaining. Basal feet and basal bodies were marked using anti-Tubg1 (γ-Tubulin, clone GTU-88, mouse IgG1, 1:1000) and centrin GFP DNA. Pictures were taken with a Zeiss LSM710 confocal microscope.

Determination of ventricle perimeter: Xenopus embryos were fixed in MEMFA at stage 45 or stage 48. After fixation, embryos were washed in PBS and bisected in the middle of the 4th ventricle. Ventricle perimeter were determined using FIJI.

Critical materials and resources are provided in the key resource table.

Reagent or resource	Source	Identifier
Antibodies		
acetylated α-tubulin	Sigma Aldrich	Cat.#T6793; RRID: AB_477585
AKAP3	Proteintech	Cat.#13907-1-AP; RRID:AB_2273887
β-Actin	MP Biomedicals	Cat.#69100
CoxIV	Abcam	Cat.#ab202554
Septin7	IBL international	Cat.#18991; RRID:AB_10705434
Glutamylated tubulin	AdipoGen	Cat.#AG-20B-0020-C100
Mouse-Alexa555	Invitrogen	Cat.#A21424; RRID:AB_141780
Rat-Alexa555	Invitrogen	Cat.#A11006; RRID:AB_2534074
Rabbit-Alexa488	Invitrogen	Cat.#11034; RRID:AB_2576217
Mouse-POD	Amersham	

(continued on next page)

(continued)

Reagent or resource	Source	Identifier
Rabbit-POD	Amersham	Cat.#NA931; RRID:AB_772210
Rat-POD	Amersham	Cat.#NA934; RRID:AB_772206
CFAP43 5B1 (monoclonal)	This paper	Cat.#NA935; RRID:AB_772207
CFAP43 22A11 (monoclonal)	This paper	N/A
CFAP43 27D5 (monoclonal)	This paper	N/A
CFAP43 P4 (polyclonal)	This paper	N/A
gamma tubulin (Tubg1)	Sigma Aldrich	Prod.#T6557-100UL
Bacterial and Virus Strains		
E.coli XL1 blue for cloning		
E.coli BL21(DE3) for protein recombinant expression		
Chemicals, Peptides, and Recombinant Proteins		
MBP-CFAP43 aa1053-1226 (generation of monoclonal ABs)	This paper	N/A
CEKIARERYDNQLKQ (generation of polyclonal AB)	This paper	N/A
DAPI	AppliChem	Cat.#A4099
PNA-lectin	Invitrogen	Cat.#L32460
Pfu DNA Polymerase	Promega	M7741
Taq DNA Polymerase	Promega	M3001
FluoSpheres carboxylate 1.0 μM yellow-green (505/515)	Invitrogen	F8823
Cas9 protein from Streptococcus pyogenes with NLS	PNA Bio	CP01
Critical Commercial Assays		
Superscript IV Reverse Trancriptase	Invitrogen	Cat.#18090050
TriReagent	SigmaAldrich	Cat.#T9424
PAS staining kit	SigmaAldrich	Cat.#1016460001
DIG RNA labelling kit	Roche	Cat.#11175025910
Prime-It II Random primer labelling	Agilent	Cat.#300385
Expand High Fidelity PCR system	Roche	Cat.#11732641001
MEGAclear Transcription Clean-Up Kit	Invitrogen	AM1908
MEGAshortscrip T7 Transcription Kit	Invitrogen	AM1354
Deposited Data		
Mass spectrometry results	This Paper	ProteomeXchange Consortium: PXD015425
Experimental Models: Cell Lines		
Hamster: CHO cells	ATCC	CRL-11268
Mouse: L-cells	ATCC	CRL-2648
Mouse: L-cells (inducible CFAP43 expression)	This paper	N/A
Mouse: ES cells	Own laboratory	N/A
Experimental Models: Organisms/Strains		
Mouse: CD1	Charles River Laboratories	N/A
Mouse: 129Sv/CD1 hybrids	Own colony	N/A
Mouse: C57/BL6		
Mouse: FLPe	Rodríguez et al. (2000)	MGI:2448985
Mouse: ZP3:Cre	De Vries et al. (2000)	MGI:2176187
Mouse: *Cfap43Δex3*	This paper	N/A
Rat: LOU/C		
Xenopus laevis	Nasco	LM00715/LM00535
Oligonucleotides		
Cfap RT-PCR fwd: TCTACGGGAAGAACTGGTGG	This paper	N/A
Cfap RT-PCR rev: AGCTTGCTGCTTGGAGATGT	This paper	N/A
Foxj1 RT-PCR fwd: CTTCTGCTACTTCCGCCATGC	This paper	N/A
Foxj1 RT-PCR rev: TCCTCCTGGGTCAGCAGTAAGG	This paper	N/A
Hprt RT-PCR fwd: GCTGGTGAAAAGGACCTCT	This paper	N/A

(continued on next page)

(continued)

Reagent or resource	Source	Identifier
Hprt RT-PCRrev: CACAGGACTAGAACACCTGC	This paper	N/A
gRNA fwd: CACCGTCATCTGGATGTGACAGTCC	This paper	N/A
gRNArev: AAACGGACTGTCACATCCAGATGAC	This paper	N/A
Screen loxP sites fwd1: AATAGCAGGCATGCTGGGGATG	This paper	N/A
Screen loxP sites rev1: GGGACTTACCAGAGGGCCAGC	This paper	N/A
Screen loxP sites fwd2: GGATCCGACAGTCCTGGATTGTGTCTT	This paper	N/A
Screen loxP sites rev2: GAAAGTTAACCTTCCCATCATCCCCTG	This paper	N/A
5′ southern probe generation fwd: AAGTACGAGAAGGAGGTAGTAAGGC	This paper	N/A
5′ southern probe generation rev: TAGATCACACGAAGTGTTCTGTCC	This paper	N/A
3′ southern probe generation fwd: TAAATAAGGATTGCGATCTTTTTAGGA	This paper	N/A
3′ southern probe generation rev: GGCCATGGGGTCTGCTCAC	This paper	N/A
Genotyping mice + targeting construct fwd: GCTCTATGGCTTCTGAGGCGG	This paper	N/A
Genotyping mice + targeting construct rev: GGGACTTACCAGAGGGCCAGC	This paper	N/A
Genotyping mice *Cfap43*^{loxP} fwd: TCACCCGGCCTCCCCAAG	This paper	N/A
Genotyping mice *Cfap43*^{loxP} rev: TCCAGGACTGTCGGATCCACCT	This paper	N/A
Genotyping mice *Cfap43*^{dex3} fwd: GCCAGTCACTAGGGAAAGGGAAGC	This paper	N/A
Genotyping mice *Cfap43*^{dex3} rev: TCCGGTGAAACCAGGGGTCAG	This paper	N/A
Morpholino: cfap43 TBMO CAGAGCACAGCCGGAGTTTTCCATC	This paper	N/A
Morpholino: cfap43 SBMO TATTACTTTAGTCTGCCGGTTTACC	This paper	N/A
sgRNA template reverse oligo AAAAGCACCGACTCGGTGCCACTTTTTCAAGTTGATAACGGACTAGCCTTA TTTTAACTTGCTATTTCTAGCTCTAAAAC	This paper	N/A
cfap43 sgRNA1 template forward oligo CCTCACTGGGAAGTTTGACTGGC	This paper	N/A
cfap43 sgRNA1 forward primer AACAGTTCGCGACATCTCTAC	This paper	N/A
cfap43 sgRNA1 reverse primer AAATTGTTGGGGTGCATACGA	This paper	N/A
cfap43 sgRNA2 template forward oligo CCAGTGAGAGATCTCTTACTGTG	This paper	N/A
cfap43 sgRNA2 forward primer AGATCTCCGCTTCATCATCACCCA	This paper	N/A
cfap43 sgRNA2 reverse primer GCATTCTGCCAAGATTTCACCT	This paper	N/A
foxj1.S/L sgRNA template forward oligo GCAGCTAATACGACTCACTATAGGGATACATACCTGCCAGGTGTTTTAGAGCTAGAAATAGCAAG	This paper	N/A
foxj1.L forward primer CGTGGGTAAGACGCCTTCAT	This paper	N/A
foxj1.L reverse primer GGGCAAAGCAGCACGTTTAT	This paper	N/A
foxj1.S forward primer CTCCCATGGTTACAGGCAGC	This paper	N/A
foxj1.S reverse primer CCTCAGCACTACAAAAGCAGC	This paper	N/A
Recombinant DNA		
Cfap43 FANTOM plasmid (*in situ* probe generation)	Kawai and Hayashizaki (2003)	PX00616F12
pTet-On Advanced vector (inducible expression in L-cells)	Clontech	Cat.#631069
pTRE-Tight vector (inducible expression in L-cells)	Clontech	Cat.#631059
Cas9 Caspase (pX330) (ES-cell targeting)	Addgene, Cong et al., 2013	Cat.#44230
	This paper	N/A

(continued on next page)

(continued)

Reagent or resource	Source	Identifier
Cfap43 targeting vector derived from pBluescript		
pMAL-C (Recombinant protein expression in *E. coli*)	NEB	Cat.#N8108S
Software and Algorithms		
FIJI (ImageJ)	Schindelin et al. (2012)	RRID:SCR_002285
Prism	GraphPad	RRID:SCR_002798
Imaris	Bitplane	RRID:SCR_007370
MATLAB	MathWorks	RRID:SCR_001622
MacVector	MacVector	RRID:SCR_015700
Photoshop	Adobe	RRID:SCR_014199
Illustrator	Adobe	RRID:SCR_010279
Chi-square		http://www.physics.csbsju.edu/stats/contingency_NROW_NCOLUMN_form.html
Synthego ICE	Synthego	https://ice.synthego.com/
Other		

Authors' contributions

ER, AB, and LT performed experiments in mice and cell culture, KSG generated and analyzed mutant mice, TO and FF performed experiments in *Xenopus*, and - together with AB and LT - the analysis of ciliary motility of mutant mouse ventricles at P7. JH performed the TEM analyses. KB and MU performed the mass spectrometric analysis, MM characterized polyclonal antibodies and generated cell line with inducible CFAP43 expression, EK generated monoclonal antibodies. AG and MB planned and supervised experiments, analyzed data together with ER, AB, TO, FF and LT, and wrote the manuscript with suggestions from all authors.

Acknowledgements

We thank S. Brody (Washington University, St. Louis) for *Foxj1* mice; Feng Zhang for plasmid pX330; R. Bauerfeind for the introduction into the Nikon Spinning Disk and the help with cilia recordings; J. Gieseke for help with MATLAB (MathWorks). This work was financially supported by DFG grant GO 449/14-1 and BL 285/14-1 to AG and MB as well as by the DFG Cluster of Excellence "REBIRTH" to AG. TO was the recipient of a Ph.D. fellowship from the Landesgraduiertenförderung Baden-Württemberg. MU was supported by the Tistou & Charlotte Kerstan Stiftung.

Appendix A. Supplementary data

Supplementary data to this article can be found online at https://doi.org/10.1016/j.ydbio.2019.12.010.

References

Abdelhamed, Z., Vuong, S.M., Hill, L., Shula, C., Timms, A., Beier, D., Campbell, K., Mangano, F.T., Stottmann, R.W., Goto, J., 2018. A mutation in Ccdc39 causes neonatal hydrocephalus with abnormal motile cilia development in mice. Development 145, dev154500. https://doi.org/10.1242/dev.154500.

Afzelius, B., 1959. Electron microscopy of the sperm tail; results obtained with a new fixative. J. Biophys. Biochem. Cytol. 5, 269–278.

Alten, L., Schuster-Gossler, K., Beckers, A., Groos, S., Ulmer, B., Hegermann, J., Ochs, M., Gossler, A., 2012. Differential regulation of node formation, nodal ciliogenesis and cilia positioning by Noto and Foxj1. Development 139, 1276–1284. https://doi.org/10.1242/dev.072728.

Banizs, B., Pike, M.M., Millican, C.L., Ferguson, W.B., Komlosi, P., Sheetz, J., Bell, P.D., Schwiebert, E.M., Yoder, B.K., 2005. Dysfunctional cilia lead to altered ependyma and choroid plexus function, and result in the formation of hydrocephalus. Development 132, 5329–5339. https://doi.org/10.1242/dev.02153.

Beyer, T., Bolz, S., Junger, K., Horn, N., Moniruzzaman, M., Wissinger, Y., Ueffing, M., Boldt, K., 2018. CRISPR/Cas9-mediated genomic editing of cluap1/IFT38 reveals a new role in actin arrangement. Mol. Cell. Proteom. 17, 1285–1294. https://doi.org/10.1074/mcp.RA117.000487.

Blum, M., Ott, T., 2018a. Animal left-right asymmetry. Curr. Biol. 28, R301–R304. https://doi.org/10.1016/j.cub.2018.02.073.

Blum, M., Ott, T., 2018b. Xenopus: an undervalued model organism to study and model human genetic disease. Cells Tissues Organs 205, 303–313. https://doi.org/10.1159/000490898.

Brody, S.L., Yan, X.H., Wuerffel, M.K., Song, S.K., Shapiro, S.D., 2000. Ciliogenesis and left-right axis defects in forkhead factor HFH-4-null mice. Am. J. Respir. Cell Mol. Biol. 23, 45–51. https://doi.org/10.1165/ajrcmb.23.1.4070.

Cong, L., Ran, F.A., Cox, D., Lin, S., Barretto, R., Habib, N., Hsu, P.D., Wu, X., Jiang, W., Marraffini, L.A., Zhang, F., 2013. Multiplex genome engineering using CRISPR/Cas systems. Science 339, 819–823. https://doi.org/10.1126/science.1231143.

Consortium, UniProt, 2019. UniProt: a worldwide hub of protein knowledge. Nucleic Acids Res. 47, D506–D515. https://doi.org/10.1093/nar/gky1049.

Coutton, C., Vargas, A.S., Amiri-Yekta, A., Kherraf, Z.-E., Ben Mustapha, S.F., Le Tanno, P., Wambergue-Legrand, C., Karaouzène, T., Martinez, G., Crouzy, S., Daneshipour, A., Hosseini, S.H., Mitchell, V., Halouani, L., Marrakchi, O., Makni, M., Latrous, H., Kharouf, M., Deleuze, J.-F., Boland, A., Hennebicq, S., Satre, V., Jouk, P.-S., Thierry-Mieg, N., Conne, B., Dacheux, D., Landrein, N., Schmitt, A., Stouvenel, L., Lorès, P., Khouri, El, E., Bottari, S.P., Fauré, J., Wolf, J.-P., Pernet-Gallay, K., Escoffier, J., Gourabi, H., Robinson, D.R., Nef, S., Dulioust, E., Zouari, R., Bonhivers, M., Touré, A., Arnoult, C., Ray, P.F., 2018. Mutations in CFAP43 and CFAP44 cause male infertility and flagellum defects in Trypanosoma and human. Nat. Commun. 9, 686. https://doi.org/10.1038/s41467-017-02792-7.

Cruz, C., Ribes, V., Kutejova, E., Cayuso, J., Lawson, V., Norris, D., Stevens, J., Davey, M., Blight, K., Bangs, F., Mynett, A., Hirst, E., Chung, R., Balaskas, N., Brody, S.L., Marti, E., Briscoe, J., 2010. Foxj1 regulates floor plate cilia architecture and modifies the response of cells to sonic hedgehog signalling. Development 137, 4271–4282. https://doi.org/10.1242/dev.051714.

de Vries, W.N., Binns, L.T., Fancher, K.S., Dean, J., Moore, R., Kemler, R., Knowles, B.B., 2000. Expression of Cre recombinase in mouse oocytes: a means to study maternal effect genes. Genesis 26, 110–112.

del Viso, F., Khokha, M., 2012. Generating diploid embryos from Xenopus tropicalis. Methods Mol. Biol. 917, 33–41. https://doi.org/10.1007/978-1-61779-992-1_3.

Drummond, I., 2009. Studying cilia in zebrafish. Methods Cell Biol. 93, 197–217. https://doi.org/10.1016/S0091-679X(08)93011-9.

Dubaissi, E., Papalopulu, N., 2011. Embryonic frog epidermis: a model for the study of cell-cell interactions in the development of mucociliary disease. Disease Models & Mechanisms 4, 179–192. https://doi.org/10.1242/dmm.006494.

Dubaissi, E., Rousseau, K., Lea, R., Soto, X., Nardeosingh, S., Schweickert, A., Amaya, E., Thornton, D.J., Papalopulu, N., 2014. A secretory cell type develops alongside multiciliated cells, ionocytes and goblet cells, and provides a protective, anti-infective function in the frog embryonic mucociliary epidermis. Development 141, 1514–1525. https://doi.org/10.1242/dev.102426.

El-Brolosy, M.A., Kontarakis, Z., Rossi, A., Kuenne, C., nther, S.G.X., Fukuda, N., Kikhi, K., Boezio, G.L.M., Takacs, C.M., Lai, S.-L., Fukuda, R., Gerri, C., Giraldez, A.J., Stainier, D.Y.R., 2019. Genetic compensation triggered by mutant mRNA degradation. Nature 1–26. https://doi.org/10.1038/s41586-019-1064-z.

Francis, R., Lo, C., 2013. Ex vivo method for high resolution imaging of cilia motility in rodent airway epithelia. J Vis Exp e50343. https://doi.org/10.3791/50343.

Fu, G., Wang, Q., Phan, N., Urbanska, P., Joachimiak, E., Lin, J., Wloga, D., Nicastro, D., 2018. The I1 dynein-associated tether and tether head complex is a conserved regulator of ciliary motility. Mol. Biol. Cell mbc.E18-02-0142. https://doi.org/10.1091/mbc.E18-02-0142.

Gerdes, J.M., Davis, E.E., Katsanis, N., 2009. The vertebrate primary cilium in development, homeostasis, and disease. Cell 137, 32–45. https://doi.org/10.1016/j.cell.2009.03.023.

Getwan, M., Lienkamp, S.S., 2017. Toolbox in a tadpole: Xenopus for kidney research [WWW Document], n.d Cell Tissue Res. 369, 143–157. https://doi.org/10.1007/s00441-017-2611-2. WWW Document. https://tools.synthego.com/#/. https://tools.synthego.com/#/. https://tools.synthego.com/#/.

Ibañez-Tallon, I., Pagenstecher, A., Fliegauf, M., Olbrich, H., Kispert, A., Ketelsen, U.-P., North, A., Heintz, N., Omran, H., 2004. Dysfunction of axonemal dynein heavy chain Mdnah5 inhibits ependymal flow and reveals a novel mechanism for hydrocephalus formation. Hum. Mol. Genet. 13, 2133–2141. https://doi.org/10.1093/hmg/ddh219.

Ikegami, K., Sato, S., Nakamura, K., Ostrowski, L.E., Setou, M., 2010. Tubulin polyglutamylation is essential for airway ciliary function through the regulation of beating asymmetry. Proc. Natl. Acad. Sci. U.S.A. 107, 10490–10495. https://doi.org/10.1073/pnas.1002128107.

Irons, M.J., Clermont, Y., 1982a. Formation of the outer dense fibers during spermiogenesis in the rat. Anat. Rec. 202, 463–471. https://doi.org/10.1002/ar.1092020405.

Irons, M.J., Clermont, Y., 1982b. Kinetics of fibrous sheath formation in the rat spermatid. Am. J. Anat. 165, 121–130. https://doi.org/10.1002/aja.1001650204.

Jacquet, B.V., Salinas-Mondragon, R., Liang, H., Therit, B., Buie, J.D., Dykstra, M., Campbell, K., Ostrowski, L.E., Brody, S.L., Ghashghaei, H.T., 2009. FoxJ1-dependent gene expression is required for differentiation of radial glia into ependymal cells and a subset of astrocytes in the postnatal brain. Development 136, 4021–4031. https://doi.org/10.1242/dev.041129.

Jain, R., Pan, J., Driscoll, J.A., Wisner, J.W., Huang, T., Gunsten, S.P., You, Y., Brody, S.L., 2010. Temporal relationship between primary and motile ciliogenesis in airway epithelial cells. Am. J. Respir. Cell Mol. Biol. 43, 731–739. https://doi.org/10.1165/rcmb.2009-0328OC.

Kawai, J., Hayashizaki, Y., 2003. DNA book. Genome Res. 13, 1488–1495. https://doi.org/10.1101/gr.914203.

Kubo, T., Hou, Y., Cochran, D.A., Witman, G.B., Oda, T., 2018. A microtubule-dynein tethering complex regulates the axonemal inner dynein(I1). Mol. Biol. Cell mbc.E17-11-0689. https://doi.org/10.1091/mbc.E17-11-0689.

Lee, L., 2013. Riding the wave of ependymal cilia: genetic susceptibility to hydrocephalus in primary ciliary dyskinesia. J. Neurosci. Res. 91, 1117–1132. https://doi.org/10.1002/jnr.23238.

Lin, J., Heuser, T., Song, K., Fu, X., Nicastro, D., 2012. One of the nine doublet microtubules of eukaryotic flagella exhibits unique and partially conserved structures. PLoS One 7, e46494. https://doi.org/10.1371/journal.pone.0046494.

Lindemann, C.B., Orlando, A., Kanous, K.S., 1992. The flagellar beat of rat sperm is organized by the interaction of two functionally distinct populations of dynein bridges with a stable central axonemal partition. J. Cell Sci. 102 (Pt 2), 249–260.

Lyons, R.A., Saridogan, E., Djahanbakhch, O., 2006. The reproductive significance of human Fallopian tube cilia. Hum. Reprod. Update 12, 363–372. https://doi.org/10.1093/humupd/dml012.

Moorman, A.F., Houweling, A.C., de Boer, P.A., Christoffels, V.M., 2001. Sensitive nonradioactive detection of mRNA in tissue sections: novel application of the whole-mount in situ hybridization protocol. J. Histochem. Cytochem. 49, 1–8.

Moreno-Mateos, M.A., Vejnar, C.E., Beaudoin, J.-D., Fernandez, J.P., Mis, E.K., Khokha, M.K., Giraldez, A.J., 2015. CRISPRscan: designing highly efficient sgRNAs for CRISPR-Cas9 targeting in vivo. Nat. Methods 12, 982–988. https://doi.org/10.1038/nmeth.3543.

Morimoto, Y., Yoshida, S., Kinoshita, A., Satoh, C., Mishima, H., Yamaguchi, N., Matsuda, K., Sakaguchi, M., Tanaka, T., Komohara, Y., Imamura, A., Ozawa, H., Nakashima, M., Kurotaki, N., Kishino, T., Yoshiura, K.-I., Ono, S., 2019. Nonsense mutation in CFAP43 causes normal-pressure hydrocephalus with ciliary abnormalities. Neurology. https://doi.org/10.1212/WNL.0000000000007505.

O'Callaghan, C.A., Tormo, J., Willcox, B.E., Blundell, C.D., Jakobsen, B.K., Stuart, D.I., McMichael, A.J., Bell, J.I., Jones, E.Y., 1998. Production, crystallization, and preliminary X-ray analysis of the human MHC class Ib molecule HLA-E. Protein Sci. 7, 1264–1266. https://doi.org/10.1002/pro.5560070525.

Praveen, K., Davis, E.E., Katsanis, N., 2015. Unique among ciliopathies: primary ciliary dyskinesia, a motile cilia disorder. F1000Prime Rep 7, 36. https://doi.org/10.12703/P7-36.

Quigley, I.K., Kintner, C., 2017. Rfx2 stabilizes Foxj1 binding at chromatin loops to enable multiciliated cell gene expression. PLoS Genet. 13, e1006538 https://doi.org/10.1371/journal.pgen.1006538.

Rodríguez, C.I., Buchholz, F., Galloway, J., Sequerra, R., Kasper, J., Ayala, R., Stewart, A.F., Dymecki, S.M., 2000. High-efficiency deleter mice show that FLPe is an alternative to Cre-loxP. Nat. Genet. 25, 139–140. https://doi.org/10.1038/75973.

Rudat, C., Grieskamp, T., Röhr, C., Airik, R., Wrede, C., Hegermann, J., Herrmann, B.G., Schuster-Gossler, K., Kispert, A., 2014. Upk3b is dispensable for development and integrity of urothelium and mesothelium. PLoS One 9, e112112. https://doi.org/10.1371/journal.pone.0112112.

Schindelin, J., Arganda-Carreras, I., Frise, E., Kaynig, V., Longair, M., Pietzsch, T., Preibisch, S., Rueden, C., Saalfeld, S., Schmid, B., Tinevez, J.-Y., White, D.J., Hartenstein, V., Eliceiri, K., Tomancak, P., Cardona, A., 2012. Fiji: an open-source platform for biological-image analysis. Nat. Methods 9, 676–682. https://doi.org/10.1038/nmeth.2019.

Sha, Y.-W., Wang, X., Xu, X., Su, Z.-Y., Cui, Y., Mei, L.-B., Huang, X.-J., Chen, J., He, X.-M., Ji, Z.-Y., Bao, H., Yang, X., Li, P., Li, L., 2017. Novel mutations in CFAP44 and CFAP43 cause multiple morphological abnormalities of the sperm flagella (MMAF). Reprod Sci 1933719117749756. https://doi.org/10.1177/1933719117749756.

Spassky, N., Merkle, F.T., Flames, N., Tramontin, A.D., García-Verdugo, J.M., Alvarez-Buylla, A., 2005. Adult ependymal cells are postmitotic and are derived from radial glial cells during embryogenesis. Neuroscience 25, 10–18. https://doi.org/10.1523/JNEUROSCI.1108-04.2005.

Stannard, W., O'Callaghan, C., 2006. Ciliary function and the role of cilia in clearance. J. Aerosol Med. 19, 110–115. https://doi.org/10.1089/jam.2006.19.110.

Stauber, M., Weidemann, M., Dittrich Breiholz, O., Lobschat, K., Alten, L., Mai, M., Beckers, A., Kracht, M., Gossler, A., 2017. Identification of FOXJ1 effectors during ciliogenesis in the foetal respiratory epithelium and embryonic left-right organiser of the mouse. Dev. Biol. 423, 170–188. https://doi.org/10.1016/j.ydbio.2016.11.019.

Takeda, S., Narita, K., 2012. Structure and function of vertebrate cilia, towards a new taxonomy. Differentiation 83, S4–S11. https://doi.org/10.1016/j.diff.2011.11.002.

Tang, S., Wang, X., Li, W., Yang, X., Li, Z., Liu, W., Li, C., Zhu, Z., Wang, L., Wang, J., Zhang, L., Sun, X., Zhi, E., Wang, H., Li, H., Jin, L., Luo, Y., Wang, J., Yang, S., Zhang, F., 2017. Biallelic mutations in CFAP43 and CFAP44 cause male infertility with multiple morphological abnormalities of the sperm flagella. Am. J. Hum. Genet. 100, 854–864. https://doi.org/10.1016/j.ajhg.2017.04.012.

Urbanska, P., Joachimiak, E., Bazan, R., Fu, G., Poprzeczko, M., Fabczak, H., Nicastro, D., Wloga, D., 2018. Ciliary proteins Fap43 and Fap44 interact with each other and are essential for proper cilia and flagella beating. Cell. Mol. Life Sci. 100, 2008. https://doi.org/10.1007/s00018-018-2819-7.

Vizcaíno, J.A., Csordas, A., del-Toro, N., Dianes, J.A., Griss, J., Lavidas, I., Mayer, G., Perez-Riverol, Y., Reisinger, F., Ternent, T., Xu, Q.-W., Wang, R., Hermjakob, H., 2016. 2016 update of the PRIDE database and its related tools. Nucleic Acids Res. 44, D447–D456. https://doi.org/10.1093/nar/gkv1145.

Walentek, P., Quigley, I.K., 2017. What we can learn from a tadpole about ciliopathies and airway diseases: using systems biology in Xenopus to study cilia and mucociliary epithelia. Genesis 55, e23001. https://doi.org/10.1002/dvg.23001.

Wolf, E., Kim, P.S., Berger, B., 1997. MultiCoil: a program for predicting two- and three-stranded coiled coils. Protein Sci. 6, 1179–1189. https://doi.org/10.1002/pro.5560060606.

Yoshiba, S., Hamada, H., 2014. Roles of cilia, fluid flow, and Ca2+ signaling in breaking of left-right symmetry. Trends Genet. 30, 10–17. https://doi.org/10.1016/j.tig.2013.09.001.

You, Y., Brody, S.L., 2013. Culture and differentiation of mouse tracheal epithelial cells. Methods Mol. Biol. 945, 123–143. https://doi.org/10.1007/978-1-62703-125-7_9.

Zein, El, L., Ait-Lounis, A., Morle, L., Thomas, J., Chhin, B., Spassky, N., Reith, W., Durand, B., 2009. RFX3 governs growth and beating efficiency of motile cilia in mouse and controls the expression of genes involved in human ciliopathies. J. Cell Sci. 122, 3180–3189. https://doi.org/10.1242/jcs.048348.

The FOXJ1 target *Cfap206* is required for sperm motility, mucociliary clearance of the airways and brain development

The FOXJ1 target *Cfap206* is required for sperm motility, mucociliary clearance of the airways and brain development

Anja Beckers[1*], Christian Adis[1§*], Karin Schuster-Gossler[1], Lena Tveriakhina[1], Tim Ott[2], Franziska Fuhl[2], Jan Hegermann[3], Karsten Boldt[4], Katrin Serth[1], Ev Rachev[1], Leonie Alten[1§§], Elisabeth Kremmer[5#], Marius Ueffing[4], Martin Blum[2&], and Achim Gossler[1&].

[1] Institute for Molecular Biology, OE5250, Hannover Medical School, Carl-Neuberg-Str. 1, 30625 Hannover, Germany

[2] Institute of Zoology, University of Hohenheim, Garbenstraße 30, 70593 Stuttgart, Germany

[3] Institute of Functional and Applied Anatomy, OE8840, Hannover Medical School, Carl-Neuberg-Str. 1, 30625 Hannover, Germany

[4] Institute of Ophthalmic Research, Center for Ophthalmology, University of Tübingen, Röntgenweg 11, 72076 Tübingen, Germany

[5] Institute of Molecular Immunology, Helmholtz Zentrum München, German Research Center for Environmental Health (GmbH), Core Facility Monoclonal Antibodies, Marchioninistr. 25, 81377 München, Germany

[§] present address: Mediagnost Gesellschaft für Forschung und Herstellung von Diagnostika GmbH, Aspenhaustr. 25, 72770 Reutlingen, Germany

[§§] present address: Twist Bioscience, 681 Gateway Blvd South, South San Francisco, CA 94080

[#] present address: Department of Biology II, Ludwig-Maximilians University, Großhaderner Straße 2, 82152 Martinsried, Germany

* these authors contributed equally to this work

[&] corresponding authors

Martin Blum: (martin.blum@uni-hohenheim.de)

Achim Gossler: (gossler.achim@mh-hannover.de)

Keywords: motile cilia, hydrocephalus, male infertility, mucus accumulation, radial spoke defect, ciliary beat frequency

Running title: Ciliary functions of CFAP206

Summary Statement

The evolutionary conserved CFAP206 modulates ciliary beat frequency in multiciliated cells in *Xenopus* and mouse, and is required for radial spoke arrangement in mouse sperm flagella.

ABSTRACT

Cilia are complex cellular protrusions consisting of hundreds of proteins. Defects in ciliary structure and function, many of which have not been characterised molecularly, cause ciliopathies, a heterogeneous group of human syndromes. Here we report on the FOXJ1 target gene *Cfap206,* orthologues of which so far have only been studied in *Chlamydomonas* and *Tetrahymena*. In mouse and *Xenopus*, *Cfap206* was co-expressed with and dependent on *Foxj1*. CFAP206 protein localised to the basal body and to the axoneme of motile cilia. In *Xenopus* crispant larvae ciliary beat frequency of skin multiciliated cells was enhanced and bead transport across the epidermal mucociliary epithelium was reduced. Likewise, *Cfap206* knockout mice revealed ciliary phenotypes. Electron tomography of immotile knockout mouse sperm flagella indicated a role in radial spokes formation reminiscent of FAP206 function in *Tetrahymena*. Male infertility, hydrocephalus and impaired mucociliary clearance of the airways in the absence of laterality defects in *Cfap206* mutant mice suggests that *Cfap206* may represent a candidate for the subgroup of human primary ciliary dyskinesia caused by radial spoke defects.

INTRODUCTION

Cilia are projections found on the surface of many eukaryotic cells. They are essential for development and adult tissue homeostasis. Cilia can be non-motile (or sensory) or motile and cells can carry a single (motile or immotile) cilium or up to several hundred motile ones (Takeda and Narita, 2012). The ciliary core, the axoneme, consists of nine peripheral microtubular doublets and may or may not possess a central pair of single microtubules. Cilia consist of hundreds of proteins, many of which are common to non-motile and motile cilia (Arnaiz et al., 2009; Gherman et al., 2006; Inglis et al., 2006). Non-motile cilia often sense environmental cues, whereas motile cilia move extracellular fluids or mediate cell motility. In early fish, amphibian and mammalian embryos, the rotation of single motile cilia of left-right organizer cells (LRO) generates a leftward fluid flow in the extracellular space. The resulting left-asymmetric gene expression establishes left-right asymmetry and drives asymmetric morphogenesis and placement of visceral organs (Blum and Ott, 2018; Hirokawa et al., 2006). Wave-like beating of cilia on airway epithelial multiciliated cells (MCCs) is essential for airway clearance throughout postnatal life (Jain et al., 2010; Stannard and O'Callaghan, 2006). MCCs on ependymal cells lining the brain ventricles are responsible for cerebrospinal fluid movement (Banizs et al., 2005; Jacquet et al., 2009; Lee, 2013; Spassky et al., 2005). Motile cilia in the fallopian tubes contribute to movement of egg and zygote (Lyons et al., 2006), and the sperm flagellum is essential for its motility (Afzelius and Eliasson, 1983). The central pair and its accessory structures, namely radial spokes that connect the central pair to the outer microtubule doublets, are critical for the planar beating pattern of 9+2 cilia (Shinohara et al.,

2015) as well as regulation of dynein motor activity and microtubule sliding (Lindemann and Lesich, 2010; Satir et al., 2014).

The evolutionary conserved transcription factor FOXJ1 plays a central role in motile ciliogenesis (Choksi et al., 2014). Loss of FOXJ1 leads to non-functional rotating cilia in the LRO of the mouse, the ventral node (Alten et al., 2012), and complete absence of motile cilia on multiciliated cells (MCCs), such as airway epithelial cells or brain ependyma (Brody et al., 2000; Chen et al., 1998). Defects in motile ciliary structure and/or function can lead to primary ciliary dyskinesia (PCD, OMIM 244400), a syndrome which affects about 1/10 000 – 1/15 000 humans (Lucas et al., 2019). PCD is a heterogeneous disorder; patients suffer from recurrent infections of the airways, male sterility, laterality defects in 50% of cases and – more rarely – hydrocephalus (Praveen et al., 2015). Nonsense or frameshift mutations in FOXJ1 that cause an autosomal dominant form of PCD have been identified (Wallmeier et al., 2019), and dysfunction of direct or indirect FOXJ1 targets are implicated in the development of numerous human PCD cases (Mukherjee et al., 2019). In microarray screens we identified additional cilia associated target genes of FOXJ1 (Stauber et al., 2017). We have started to evaluate selected evolutionary conserved candidates by descriptive and loss-of-function analyses in two vertebrate model organisms, the frog *Xenopus laevis* and the mouse. All of these candidates were co-expressed with *Foxj1* throughout embryonic development in mouse and frog, including the LRO (mouse and frog), MCCs of the ependyma (mouse and frog), airways (mouse) and larval skin (frog) as well as sperm cells (mouse). These genes were found to have distinct context- and species-specific functions in motile cilia (Beckers et al., 2018; Weidemann et al., 2016).

Here, we report on the analysis of *Cfap206* as an additional evolutionary conserved FOXJ1 target gene that so far has only been analysed in single-celled eukaryotes. FAP206, the orthologue of the green alga *Chlamydomonas*, is a potential component of the nexin-dynein regulatory complex (Lin et al., 2011) and interacts with radial spoke protein 3 (RSP3) (Gupta et al., 2012). FAP206 of the ciliate *Tetrahymena* is required for anchoring radial spoke 2 (RS2) to microtubule doublets and for generating the waveform of ciliary movement (Vasudevan et al., 2015). We show that the vertebrate homolog CFAP206 localises to the basal body/centrosome and to cilia, and its expression correlates with and depends on *Foxj1* expression. Genome editing in *Xenopus* resulted in moderate ciliary defects during larval development, namely slightly increased ciliary beat frequency of epidermal MCCs and slightly impaired bead transport across the skin epithelium. Knockout mice postnatally developed hydrocephalus, revealed impaired mucociliary clearance of the airways, and were characterised by male infertility. As in *Xenopus*, CFAP206 loss affected beat frequency of cilia on

105 tracheal MCCs, while sperm were largely immotile. Electron tomographic analysis revealed that
106 CFAP206 was needed to establish the repetitive pattern of RS1, 2, and 3 in the sperm flagellum,
107 reminiscent of the function described in *Tetrahymena*. Immotile sperm, impaired mucociliary
108 clearance of the airways and hydrocephalus are hallmarks of PCD. Our analyses of *Cfap206* as a
109 thus far uncharacterised *Foxj1* target therefore indicates that this gene may qualify as a new PCD
110 candidate gene worth studying in human PCD cohorts.

4

111 **RESULTS**

112 ***Cfap206* is co-expressed with and dependent on *Foxj1* in mouse and frog**

113 The mouse *Cfap206* gene

114 (http://www.ensembl.org/Mus_musculus/Gene/Summary?db=core;g=ENSMUSG00000028294)

115 gives rise to two transcripts by differential splicing encoding proteins of 622 and 504 amino acids

116 (aa; Fig. 1A). The shorter protein (CFAP206 S) lacks the C-terminal portion and is characterised by

117 6 unique amino acids at its C-terminus, while the remaining protein is identical to the long variant

118 (CFAP206 L). CFAP206 is an evolutionary conserved protein (Table S1). It lacks known motifs or

119 domains except for a 280aa unique domain of unknown function with conserved motifs GFC and

120 GIL. Expression analysis of mRNAs by RT-PCR demonstrated that both variants were co-

121 expressed in adult tissues (Fig. 1B). This pattern coincided with *Foxj1*, supporting the identification

122 of *Cfap206* as a target gene (Fig. 1B). *In situ* hybridisation of adult tissue sections using a probe

123 detecting both transcripts (Fig. 1A) revealed mRNA expression in cells carrying motile cilia of the

124 male and female reproductive tract (sperm and oviduct; Fig. 1Ca,a',b,b'), the airways (lung and

125 nasal cavity; Fig. 1Cc,c',d,d') as well as brain ependyma and choroid plexus (CP; Fig. 1Ce,e').

126 During embryogenesis (E17.5), mRNA was found in airway epithelia (Fig. 1Da-c,a'-c') and brain

127 ependymal tissues, i.e. correlated with MCCs (Fig. 1Dd,d'). Early in development, *Cfap206* mRNA

128 was confined to the LRO (ventral node) of 8-day embryos (E8.0; Fig. 1Ea). Expression in a number

129 of cell types carrying non-motile cilia was also detected (Fig. S1). The dependence of *Cfap206*

130 expression on the activity of the transcription factor FOXJ1 was analysed in *Foxj1* knockout mice

131 (*Foxj1*$^{-/-}$). *Cfap206* transcripts were severely downregulated or nearly absent in *Foxj1* mutants (Fig.

132 1E), corroborating that *Cfap206* acts downstream of FOXJ1.

133

134 During *Xenopus* embryogenesis, *cfap206* mRNA transcription paralleled that of *foxj1* as well, with

135 few exceptions. Prominent *cfap206* signals were seen in the *Xenopus* LRO i.e. gastrocoel roof plate,

136 the floor plate of the neural tube (FP), MCCs of the larval skin, the nephrostomes, the branchial

137 chambers (BC) and the stomach (Fig. 2Af,g,h',h''), i.e. in cells and tissues that harbour motile cilia.

138 Expression of *foxj1* transcripts were detected in the same tissues (Fig. 2Ab,c,d,d',d'',d''') except for

139 the LRO (Fig. 2Ab'; staining in b reflects expression in the FP). *Foxj1* signals, however, were

140 present in the LRO precursor tissue of the superficial mesoderm (SM; Fig. 2Aa), where no *cfap206*

141 signals were found (Fig. 2Ae). In the brain, *foxj1* and *cfap206* were expressed in the zona limitans

142 intrathalamica (ZLI), in the sub-commissural organ (SCO) and in the FP (Fig. 2Ad''',h'''), where

143 *foxj1* signals were much stronger than that of *cfap206*. Ectopic expression of *foxj1* on one side of

144 the larva, following unilateral injection of synthetic mRNA at the 4-cell stage, resulted in strong

145 induction of ectopic *cfap206* transcription on the injected side (asterisk; Fig. 2B). The dependence

of *cfap206* transcription on *foxj1* was analysed in specimens that were genome-edited at the *foxj1* gene locus by CRIPSR/Cas9 (Rachev et al., 2020). Signal intensities were greatly reduced in crispants (Fig. 2C), corroborating data in the mouse. Together, these experiments in mouse and frog demonstrate that FOXJ1 is the decisive transcription factor for *cfap206* activation in cells carrying motile cilia during embryonic development and likely for its expression in adult tissues as well.

CFAP206 localises to the ciliary axoneme and basal body

To study CFAP206 localisation we generated polyclonal antibodies in rabbits and monoclonal antibodies in rats. One polyclonal antibody was directed against a peptide (pepI: aa194-207; encoded by exon 6; green box Fig. 3A) present in both protein variants, a second one was specific for the long CFAP206 protein (pepII: aa576-589; encoded by exon 13; orange box Fig. 3A). Both polyclonal antibodies detected Flag- or GFP-tagged CFAP206 over-expressed in CHO cells (Fig. 3A). The monoclonal antibodies were directed against a peptide largely overlapping with pepII (ORF2: aa574-586; cyan box Fig. 3A) and therefore also specific for the long CFAP206 protein variant. Endogenous CFAP206 protein was detected in Western blots of testis lysates (Fig. 3A) as well as in cell lines carrying non-motile cilia (Fig. S1C). Since the α-pepI antibodies gave rise to high background in immunofluorescence staining, the subcellular localisation of CFAP206 was assessed using the long form-specific α-pepII antibody on sections of the nasal respiratory epithelium and adult mouse testis (Fig. 3B). In motile cilia of the adult nasal respiratory epithelium, CFAP206 staining largely overlapped with acetylated-α-tubulin (ac-TUB). Signals were also detected proximally to ac-TUB (arrowheads in Fig. 3Bd,d'), reflecting a potential localisation at basal bodies, which was clearly observed in mIMCD3 cells (Fig. S1Da-d). No clear overlap of CFAP206 staining with ac-TUB was observed at the distal tip of cilia (arrows in Fig. 3Bd,d'), suggesting that CFAP206 was present throughout the axoneme except for the tip region. In spermatozoa CFAP206 was co-detected with ac-TUB in the flagella (Fig. 3Be-g). Expression in differentiating spermatids was found from the earliest stages of spermiogenesis onwards (Fig. S2).

In *Xenopus*, the polyclonal rabbit antibodies (pepI and pepII) against mouse CFAP206 did not give rise to any staining (not shown). In order to assess ciliary localisation in an indirect manner, fusion proteins were expressed by targeted injection of mRNAs into the epidermal lineage at the 2-4 cell stage. A GFP-fusion protein with murine CFAP206 was used (GFP-CFAP206), which – when injected at high levels – labelled defined spherical structures throughout the cell, resembling previously described liquid-like organelles (not shown; Huizar et al., 2018) (Fig.3C). GFP-CFAP206 partially overlapped with RFP-tagged centrin4 (Cetn4-RFP) (Cetn4; Zhang and Mitchell, 2016) at basal bodies of epidermal MCCs (Fig. 3Ca). The orthogonal projection depicted in Fig.

3Ca' revealed a defined succession of domains, with proximal (i.e. closest to the axoneme) centrin4-staining, followed by a small zone of centrin4-CFAP206 overlap and a distal CFAP206 domain. Basal body localisation was confirmed by co-staining of GFP-CFAP206 with the basal foot marker tubulin γ1 (Tubg1; Fig. 3Cb). GFP-CFAP206 partially overlapped with Tubg1, both in the plane parallel to the cell surface (Fig. 3Cb') as well as in an orthogonal projection (Fig. 3Cb''), where GFP-CFAP206 extended towards the distal end of the basal body, at the level of the sub-apical actin network (Fig. 3Cb''). The GFP-CFAP206 domain, therefore, appears below the basal body in relationship to both centrin4 and Tubg1, potentially localising to the rootlet or at the junction between the basal body and the rootlet. GFP-CFAP206 was also expressed throughout the axoneme, though at a lower level, as demonstrated by co-staining with an antibody against acetylated α-tubulin (ac. Tuba4a; Fig. 3Cc,c',c'', d).

Functional analysis of *cfap206* during embryonic development of the frog *Xenopus*

The use of morpholino oligomers (MOs) to interfere with *cfap206* mRNA translation (TBMO) or splicing (SBMO) yielded variable results. Occasionally, hydrocephalus and MCC motility defects were observed, which were not consistently encountered, nor could they be rescued by co-injection of full-length murine *Cfap206* not targeted by the MOs (wild type and GFP-fusion constructs; not shown). We therefore turned to genome editing and designed two sgRNAs targeting exon 2 and exon 5. Genome editing was confirmed via direct sequencing of PCR products with pooled DNAs from 10 F0 crispants (Fig. S3A,B). Crispant specimens were analysed for laterality defects, and nephrostome and ependymal cilia function by assessing organ situs, formation of kidney cysts and development of externally visible hydrocephalus in stage 45 tadpoles. No deviations from uninjected wild type control specimens were observed (Fig. S4A-D).

To address potential changes in ciliary beating of *cfap206* crispants, motility of epidermal MCCs was analysed in high-speed time-lapse videos recorded from wild type and crispant larvae at stage 32 (Movie 1). Ciliary beat frequencies were calculated as previously reported (Rachev et al., 2020) and found to be significantly elevated, from 22.5 Hz in wild type to 24.5 Hz in sgRNA1 crispants and 26.5 Hz in sgRNA2 crispants (Fig. 4Aa, Table S3). Representative kymographs illustrate these differences (Fig. 4Ab). In order to investigate whether the function of epidermal MCCs was altered in crispants, fluorescent beads were added to stage 32 larvae and bead transport was assessed in time-lapse movies (Movie 2), as described (Rachev et al., 2020). In comparison to wild type specimens, bead transport was significantly reduced, from 550 µm/s in wild type to 460 µm/s in sgRNA1 crispants and 410 µm/s in sgRNA2 crispants (Fig. 4Ba, Table S2). In summary, ciliary phenotypes during embryonic frog development up to metamorphosis were restricted to the

mucociliary epithelium of the larval skin, where a slight increase in ciliary beat frequency resulted in a significant reduction of cilia-mediated bead transport.

Cfap206 knockout mice suffer from hydrocephalus, defective mucociliary clearance of the airways and male infertility

To analyse the function of CFAP206 in mice, we generated a conditional allele by flanking exon 4 by loxP sites (Fig. 5A). Deletion of exon 4 by Cre-mediated site-specific recombination leads to a frame shift after aa 64, resulting in a stop codon 30 bp downstream in exon 5, which should prevent translation of a functional protein. To delete CFAP206 in all tissues we excised exon 4 (*Cfap206*$^{\Delta ex4}$) in the female germ line using ZP3:Cre mice (de Vries et al., 2000). Homozygous *Cfap206*$^{\Delta ex4}$ mice were born at Mendelian ratio (wild type 147, het 306, hom 118; X^2=5.89, p=0.0526) and initially showed no obvious gross abnormalities. Western blot analyses with polyclonal antibodies α-pepI and α-pepII did not reveal any CFAP206 specific signal in *Cfap206*$^{\Delta ex4/\Delta ex4}$ testis lysates (arrows in Fig. 5B), demonstrating that both CFAP206 protein variants were present in wild type and deleted in *Cfap206*$^{\Delta ex4/\Delta ex4}$ testes. Likewise, the α-pepII antibody did not detect CFAP206 protein in sections of the mutant testis and the respiratory epithelium (Fig. 5Ci,l). These data indicate that deletion of exon 4 effectively abolished translation of CFAP206 protein, i.e. that *Cfap206*$^{\Delta ex4}$ very likely represented a bona fide null allele deleting both protein variants. Therefore, the description of CFAP206 function below refers to the function of both protein variants.

Beginning 2-3 weeks after birth, 79 % (118/150) of homozygous *Cfap206*$^{\Delta ex4}$ mice developed externally visible enlarged cranial vaults suggesting ventricular dilatation and hydrocephalus (Fig. 6Ab). Dissected brains of *Cfap206*$^{\Delta ex4}$ mutants showed severely dilated and fused lateral ventricles (Fig. 6Ad). Dilated ventricles were already observed in homozygous mutants without external signs of hydrocephalus on postnatal day P1 (n=3/3) and P6 (n=4/4) (Fig. 6B). Hematoxylin-Eosin (HE) staining of mid-sagittal brain sections of P6 mutant brains revealed stenotic or closed sylvian aqueducts, which connect the 3rd to the 4th ventricle (Fig. 6C). In high-speed microscopy of P7 lateral ventricle explants we did not detect a reduction in ependymal cilia generated flow (CGF, Fig. 6D; Movie 3; Table S5). The stenotic or closed sylvian aqueduct therefore appears to develop despite the establishment of postnatal flow. We further analysed whether CFAP206 might be important for the function of motile cilia in other contexts. In PAS stainings of nasal cavities we noticed mucus accumulation in mutants at different ages (3 weeks, n=2/3; 2 months n=2/2 and 8/9 months n=3/4; Fig. 6E). Isolated mTECs from 3/4 months wild type and *Cfap206*$^{\Delta ex4}$ mutants did

not show obvious differences in cilia presence and length (Fig. 5D, Table S4). However, high-speed video analysis of ciliary beat frequency (CBF) of tracheal explant MCCs from 10 weeks up to 3 month old animals exhibited a significant increase in CBF from an average of 12.6 Hz in wild type to about 17.3 Hz in *Cfap206*$^{\Delta ex4}$ mutants (Fig. 6Fa,b; Movie 4; Fig. S11; Table S6). The analysis of bead velocity, however, revealed no significant alterations of CGF in mutants compared to wild type in this assay (Fig. 6Fc; Movie 5; Fig. S11; Table S7), and changes of the waveform could not be assessed.

No defects in the establishment of the left-right asymmetry were observed in *Cfap206*$^{\Delta ex4/\Delta ex4}$ mutant animals (n=150), although *Cfap206* expression was prominent in the ventral node (Fig. 1Ea). This finding indicated that CFAP206 was dispensable for the rotational movement of cilia at the LRO. Homozygous females that did not develop hydrocephalus were fertile and raised litters normally. In contrast, homozygous males (without hydrocephalus; n=5) did not give rise to offspring even after prolonged matings to wild type females. Analyses of HE-stained testis and epididymis sections showed no obvious morphological differences. Structure of seminiferous tubules and lumina containing sperm were unaltered in mutants (Fig. 7A). Sperm quality of *Cfap206*$^{\Delta ex4}$ mutants was addressed by computer-assisted sperm analysis (CASA). Sperm cell concentration of 2-3 months old mutants was similar to wild type (Fig. 7Ba; Table S8). However, the motility of mutant sperm cells was significantly reduced compared to wild type (Fig. 7Bb; Table S8). This defect was also observed by video microscopy of isolated sperm (Movie 6). Mutant sperm were unable to move effectively; motion appeared rolling or tumbling, with mutant sperm cells not moving across greater distances. In IVF (*in vitro* fertilisation) experiments, 57.8±2.8% of eggs (n=656/1132; 3 experiments; Table S9) in contact with wild type sperm initiated embryonic development. In contrast, hardly any (0.7±0.7%; n=11/1657; 3 experiments; Table S9) eggs incubated with *Cfap206*$^{\Delta ex4/\Delta ex4}$ sperm developed into blastocysts (Fig. 7Bc; Table S9). *Cfap206*$^{\Delta ex4/\Delta ex4}$ sperm did not efficiently move towards and attach to the eggs (Fig. 7Bd,e; Movie 7), indicating that even when brought into close proximity, sperm lacking CFAP206 were unable to effectively fertilise wild type eggs.

Sperm isolated from cauda epididymis had long flagella containing microtubules, as indicated by staining for ac-TUB (Fig. 7Cg'-i',l'). The size and shape of nuclei (DAPI staining) and acrosomes (stained by PNA lectin) were indistinguishable from wild type sperm (Fig. 7Cg'-l'). Staining of the fibrous sheath (by AKAP3), mitochondria (by COXIV) and annulus (by SEPTIN7) revealed the presence of distinct mid- and principal pieces (Fig. 7Ch'-l'). However, only 55% (626/1170) of mutant sperm had an extended flagellum, compared to 85.8% (1102/1274) of wild type sperm.

40.5% (496/1170) of mutant flagella displayed a sharp bent (wild type 12.5%) and 4.6% (48/1170) showed coiled flagella (wild type 1.6%) (Fig. S5A; Table S10). Structural abnormalities were not detected by immunofluorescence staining using common markers. However, transmission electron microscopy of epididymis sections revealed highly abnormal axonemal structures. Circular (Fig. 8Ad) and bent (Fig. 8Ae) flagella were observed, which most likely represented spermatozoa shown in Fig. 7Cg,g' and k,k', respectively. We rarely observed normal microtubule doublets (green arrows in inset of Fig. 8Af). Most flagellar cross sections contained variable numbers of irregularly arranged single microtubules at different flagellar levels (Fig. 8Af,f',g,h). Groups of axonemal profiles (white asterisks Fig. 8Af) that were surrounded by a common plasma membrane (dark blue arrows in Fig. 8Af') were also observed. Therefore, coiled flagella found in sperm isolated from the cauda epididymis, at least in part, reflected bundles of axonemes within a common plasma membrane rather than folded or clustered flagella. The vesicular material next to the axonemal profiles (red asterisks in Fig. 8Ad,e,f') were indicative of Golgi remnants, which might explain the structure detected in coiled flagella using the acrosomal marker PNA lectin (arrowhead in Fig. 7Cg'). Electron tomography on cryo-conserved sperm flagella from cauda epididymides revealed defects in the repetitive pattern of radial spokes (RS; Fig. 8B, Fig. S5). In wild type sperm, RS1, 2, and 3 were arranged in 96 nm repeats (Fig. 8Ba, Fig. S5B). Mutants displayed one RS per 96 nm repeat (Fig. 8Bc, Fig. S5B) and absent or incomplete RS in-between, indicating that CFAP206 was needed for the establishment of radial spokes in mammalian sperm flagella.

304 **DISCUSSION**

305 We identified *Cfap206* in a screen for genes that act downstream of FOXJ1. Consistent with its
306 direct or indirect regulation by FOXJ1, *Cfap206* expression correlated very well with expression of
307 *Foxj1*, both in *Xenopus* and mouse. Ectopic *foxj1* expression in frog embryos induced *cfap206*
308 transcription, and loss of FOXJ1 in mouse and frog embryos led to severe downregulation of
309 *Cfap206* mRNA expression. Here we show that the evolutionary conserved CFAP206 protein is
310 essential for sperm motility in mice and modulates ciliary beat frequency of MCCs both in the
311 *Xenopus* larva and mouse trachea. Ciliary defects during embryogenesis in *Xenopus* were restricted
312 to the mucociliary epithelium of the larval skin, which was unexpected given the co-expression with
313 *foxj1* from the earliest developmental stages onwards (Fig. 2). Several possible mechanisms could
314 underlie these differences. Phenotypes may only become evident at later stages, during
315 metamorphosis or in adult frogs. The observed mouse defects revealed themselves postnatally, in
316 line with this reasoning. The long generation time and legal restriction to raise adult frogs prevented
317 us from analysing this possibility. As another option, in a laboratory setting lacking environmental
318 challenges such as poor water quality or the presence of pathogens and pollutants, *Cfap206* function
319 may not reveal itself, particularly in the mucociliary epithelium of the larval skin, which serves as a
320 first line of defence in much the same way as the mouse airway epithelium (Dubaissi and
321 Papalopulu, 2011; Hayes et al., 2007; Walentek and Quigley, 2017). Loss of *cfap206* gene function
322 may also be compensated for by upregulation of related genes (El-Brolosy et al., 2019; Rossi et al.,
323 2015). Ciliary phenotypes in morphants, including cysts and hydrocephalus, seem to support such
324 reasoning, however we were unable to successfully rescue these phenotypes and prove MO-
325 specificity, which is why we did not include these data sets into our analysis. The maintenance of
326 *cfap206* transcripts in crispant specimens (not shown) also argues against this possibility, as
327 nonsense-mediated mRNA decay has been shown in several cases to be a pre-requisite for
328 compensation in zebrafish (El-Brolosy et al., 2019), which might be a cell type-specific
329 phenomenon in mice (Hall et al., 2013). Short of a biochemical understanding of Cfap206 function,
330 we cannot discriminate between these and other possible explanations at this time.
331
332 In mouse, *Cfap206* gives rise to two transcripts that were detected in all analysed tissues and cell
333 lines. Whether both transcripts (and the resulting protein variants) are present in the same cell
334 remains to be determined. As CFAP206 L was detected in apparently all cilia of respiratory MCCs
335 (e.g. Fig. 3B), and both transcripts were present in this tissue, it is reasonable to assume that both
336 proteins co-exist in cells carrying motile cilia, the functional significance of which is unknown thus
337 far. CFAP206 L is more similar in length to FAP206 from *Tetrahymena* (622 vs 635 aa), which
338 might indicate that this protein is the fully functional variant. To analyse whether CFAP206 S is

sufficient to substitute for CFAP206 L will require the generation of a mutant allele that specifically removes CFAP206 L. Notwithstanding potential functional differences of these two protein variants, our null allele should delete all CFAP206 functions, because both protein variants were effectively eliminated.

In *Tetrahymena* FAP206 acts as a microtubule-docking adapter for RS2 (Vasudevan et al., 2015). The knock-out of FAP206 in *Tetrahymena* resulted in the loss of RS2, in some cases absence of RS3 as well, leading to an abnormal flagellar waveform and a reduction of the swim rate to 30% (Vasudevan et al., 2015). This function appears to be conserved in mouse sperm cells, as one or two RSs were missing in mutants (Fig. 8B, Fig. S5B,C). The resolution of our tomography does not allow to unequivocally identify the consistently present radial spoke as RS1. However, given the specific function as an adapter for RS2 in *Tetrahymena* it seems reasonable to assume that the RS consistently observed at 96 nm distance in mutant mouse sperm is RS1. A RS-related function of CFAP206 is also supported by its absence from the ciliary tip that apparently lacks radial spokes (reviewed in Osinka et al., 2019; Reynolds et al., 2018; Soares et al., 2019) and would be consistent with the lack of laterality defects in mouse and frog, as motile cilia at the LRO lack the central pair and RSs and show a rotational movement (Nonaka et al., 1998). The absence of LR defects is also a characteristic of PCD patients with defects in radial spokes and the central pair (Edelbusch et al., 2017; Lucas et al., 2019).

Loss of RS2 in *Tetrahymena* FAP206 mutants caused compressed ciliary cross sections but did not disrupt the central pair or outer microtubule doublets (Vasudevan et al., 2015). Disruption of RS assembly in mouse ependymal cells by depletion of RSPH9 abolished the central pair but left the outer doublets largely intact (Zhu et al., 2019). RS deficiency in *Chlamydomonas* resulted in a lateral shift of the central pair, without impact on the outer doublets (Sivadas et al., 2012). This contrasts with defective microtubular doublets that we frequently observed in mouse sperm flagella, suggesting that CFAP206 has additional microtubule-stabilising functions in the specialised cilium of mammalian sperm. The identification of these functions should be aided by the identification of CFAP206-interacting proteins in sperm cells. Towards this aim we identified potential interaction partners by immunoprecipitation of CFAP206 from adult mouse testes and subsequent mass spectrometry. These analyses led to a number of promising candidate proteins (Table S11) that - following validation - should provide further insights into CFAP206 function.

In contrast to the largely immotile sperm cell flagella, cilia on multiciliated tracheal cells were motile and even showed an enhanced beating frequency. While we cannot exclude subtle deviations

374 of the ciliary beating patterns, the motility of these cilia suggests that they don't have major
375 structural defects. In line with this notion, PCD patients with defects in RS function show very
376 subtle ciliary beating abnormalities, and cross-sections of respiratory cilia can reveal normal
377 ultrastructure (Burgoyne et al., 2014; Castleman et al., 2009; e.g. Frommer et al., 2015; Knowles et
378 al., 2014; Ziętkiewicz et al., 2012). The increased beating frequency of *Cfap206* mutant cilia was
379 accompanied by a reduction of the speed of cilia-generated flow to about 80% in the frog larval skin
380 (Movies 1, 2 and Fig. 4), but had no apparent effect on the speed of cilia-generated flow in mouse
381 tracheal explants (Fig. 6F). This differs from *Tll1* (Ikegami et al., 2010) and *Cfap43* mutants
382 (Rachev et al., 2020), in which an increase in beating frequency was associated with reduced cilia
383 generated flow. While loss of CFAP206 clearly affects ciliary beating in respiratory epithelium it
384 remains to be seen how this relates to mucus accumulation. It appears plausible, however, that
385 mucus accumulation is causatively linked to the altered ciliary beat frequency. Altered frequencies
386 may result in subtle alterations of the ciliary wave form and/or changes of beating asymmetry,
387 which might reduce efficient flow in the native lung and lead to mucus accumulation over time.
388
389 Similar to flow generated by MCCs of the trachea, ependymal flow in explants of postnatal lateral
390 ventricles (P7) was apparently unaltered, although enlarged ventricles were present accompanied by
391 obstruction of the aqueduct (Fig. 6C). It is unclear whether apparently normal flow is maintained in
392 older animals (which could not be analysed due to restrictions by animal welfare regulations).
393 Aqueduct obstruction, maintenance of flow generated by ependymal cells of the lateral walls of the
394 lateral ventricle and build-up of pressure might all contribute to the highly penetrant progression of
395 ventricle enlargement after P14. The basis for the development of hydrocephalus in *Cfap206*
396 mutants already on P1, prior to the presence of motile cilia on the lateral ventricular walls (Banizs
397 et al., 2005) and the onset of postnatal flow, is less clear. It implies that CFAP206 function is
398 required early-on, already during embryonic development. Consistent with this notion *Cfap206* was
399 detected already at E16.5 in the developing brain, although at low levels (Fig. S6). Analyses of
400 *Ccdc39* mutant mice revealed that ependymal MCCs with motile cilia are present on the ventro-
401 medial wall of the lateral ventricle around P1. Functional impairment of these motile cilia led to
402 enlarged ventricles shortly after birth (Abdelhamed et al., 2018), prior to the emergence of motile
403 cilia on the lateral ventricular walls (Banizs et al., 2005) and the onset of postnatal flow. Loss of
404 CFAP206 might therefore impact on early flow and lead to early aqueduct obstruction, which
405 blocks drainage of cerebrospinal fluid causing subsequent progressive lateral ventricle enlargement.
406 A requirement of ependymal flow to keep the aqueduct postnatally open has been established in
407 *Mdnah5* mutant mice. These lacked directed ependymal flow at lateral ventricles and developed

hydrocephalus beginning at P6, with subsequent stenosis of the aqueduct at P12, which was attributed to the absence of postnatal ependymal flow (Ibañez-Tallon et al., 2004).

In conclusion, our descriptive and functional analysis of *Cfap206* in mouse and *Xenopus* demonstrated that this highly conserved ciliary gene functions in defined ciliary contexts, predominantly at post-embryonic stages in both species. Male sterility caused by severe flagellar malformations in mice suggests that mutations of CFAP206 may also underlie male infertility in humans. Mutant alleles might lead to milder forms of PCD, without clear ultrastructure cilia defects and only subtle changes of ciliary movement, which might complicate diagnosis of patients.

418 **MATERIALS AND METHODS**

419 *Ethics statement and husbandry of mice and frogs:*

420 Mice and *Xenopus laevis* were handled in accordance with the German laws and regulations
421 (Tierschutzgesetz). All procedures were approved by the ethics committee of Lower Saxony for
422 care and use of laboratory animals LAVES and by the Regional Council Stuttgart, Germany
423 (A379/12 Zo, 'Molekulare Embryologie', V340/17 ZO and V349/18 ZO, '*Xenopus* Embryonen in
424 der Forschung'). *Xenopus* embryos obtained by *in vitro* fertilisation were maintained in 0.1x
425 modified Barth medium (Sive et al., 2000), and staged according to (Nieuwkoop and Faber, 1994).
426 Mice were housed in the animal facility of Hannover Medical School (ZTL) as approved by the
427 responsible Veterinary Officer of the City of Hannover, Germany. Animal welfare was supervised
428 and approved by the Institutional Animal Welfare Officer.
429
430 *Multiple sequence alignment of CFAP206 proteins:*
431 Sequences were aligned using ClustalW (v1.83; multiple sequence alignment; Pairwise Alignment
432 Mode: Slow; Pairwise Alignment Parameters: Open Gap Penalty = 10.0, Extend Gap Penalty = 0.1,
433 Similarity Matrix: gonnet; Multiple Alignment Parameters: Open Gap Penalty = 10.0, Extend Gap
434 Penalty = 0.2, Delay Divergent = 30%, Gap Distance = 4; Similarity Matrix: gonnet).
435
436 **Mouse methods**
437 *Generation of* Cfap206$^{\Delta ex4}$ *mice:*
438 *Cfap206*^{loxP} mice were generated by Cyagen (Cyagen Biosciences, 2255 Martin Ave, Ste E, Santa
439 Clara California 95050, USA). The positive selection marker (neo cassette) was flanked by FRT
440 sites and removed by FLP-mediated recombination. Germ line deletion of exon 4 was achieved by
441 crossing of *Cfap206*^{loxP}; ZP3:Cre (de Vries et al., 2000) double heterozygous females to wild type
442 males. The floxed allele was originally generated on the C57BL/6 background. Breeding to FLPe
443 and ZP3:Cre mice generated a mixed genetic background (predominantly 129Sv/CD1), on which
444 the strain was maintained. The phenotype of *Cfap206*$^{\Delta ex4}$ mice was analysed on this mixed genetic
445 background. *Foxj1*$^{-/-}$ mutant mice (*Foxj1*^{lacZ}) were described previously (Brody et al., 2000), as was
446 FLPe mice (Rodríguez et al., 2000).
447
448 *Genotyping of mice:*
449 *Cfap206* mutant and wild type mice were genotyped by PCR with allele-specific primer pairs:
450 Cfap206-loxP-F1: 5'-ATCACGGAGTCAGGGCTAAGTTG-3', Cfap206-loxP-R1:
451 5'-GGCAAGCAGTCTACCAACTGAGG-3', 238 bp wild type, and 299 bp *Cfap206*^{loxP} product.
452 Cfap206-loxP-F1: 5'-ATCACGGAGTCAGGGCTAAGTTG-3', Cfap206-R1:

5'-CCAACCAGCCCATACTATTC-3', 246 bp *Cfap206*$^{\Delta ex4}$ and 1225 bp wild type.

Reverse transcription (RT-) PCR from total RNA:

Total RNA was isolated from dissected mouse tissues using TriReagent (Zymo Research). cDNA was synthesised using SuperScriptII Reverse Transcriptase (Invitrogen), according to the manufacturer's instructions. PCR was performed using primer pairs: Cfap206_Ex8for: 5'-TCCCAAGTCTTCCCCATCTTCG-3', Cfap206_Ex12rev: 5'-TGTGTGTATCTGTCTGTGTGCCG-3' specific for the *Cfap206* mRNA encoding the long protein, 619 bp product (shown in Fig. 1B); Cfap206_RTex9for: 5'-CGATGGCGTCGTCGTGAAAAG-3', Cfap206_RTex13rev: 5'-CCCACGAAGGCCAGCTATGAA-3' specific for the *Cfap206* mRNA encoding the long protein, 697 bp product (shown in Fig. S1B); Cfap206_Ex8for: 5'-AAAATCTAAGACGGCGGTCCC-3', Cfap206_Ex11rev: 5'-AGTCAGGAGTTACAAACCCAGGTG-3' specific for the *Cfap206* mRNA, encoding the short protein, 619 bp product (shown in Fig. 1B and S1B). Hprt_RT_for_ex7: 5'-GCTGGTGAAAAGGACCTCT-3', Hprt_RT_rev_ex9: 5'-CACAGGACTAGAACACCTGC-3' specific for the *Hprt* mRNA, 248 bp product. Foxj1_RT_for_ex2: 5'-CTTCTGCTACTTCCGCCATGC-3', Foxj1_RT_rev_ex3: 5'-TCCTCCTGGGTCAGCAGTAAGG-3' specific for the *Foxj1* mRNA, 432 bp product.

Tissue collection, embedding, sectioning:

Mice were killed by cervical dislocation and dissected tissues were fixed at 4°C in 4% PFA or 100% methanol overnight. If necessary, materials were decalcified in 0.5 M EDTA for several days up to two weeks, with EDTA changes every other day. Subsequently, the tissues were dehydrated and embedded in paraffin according to standard procedures. Embedded tissues were sectioned at 5 or 10 μm. Sperm cells were isolated as described (Rachev et al., 2020).

Histological methods:

Histological staining was performed on 10 μm sections of PFA fixed and paraffin-embedded tissues. HE staining was performed according to standard procedures. Periodic Acid-Schiff (PAS) staining was carried out using the Sigma Aldrich PAS staining kit (395B).

Section and whole-mount in situ *hybridisation (SISH and WISH):*

SISH was performed on 10 μm paraffin sections of formaldehyde fixed tissues that were dewaxed, hydrated, digested with Proteinase K, fixed with formaldehyde and hybridised over night at 70°C (Moorman et al., 2001). The DIG-labelled RNA probe was synthesised from *Cfap206* cDNA (Fantom clone accession number AK005650, coordinates ZX00119D08), using the Roche DIG

RNA labelling system. WISH was carried out using standard procedures as described (Stauber et al., 2017). SISH and WISH results were documented with a Leica DM5000B microscope with Leica Firecam software.

Isolation and processing of sperm cells for video microscopy or immunofluorescence staining:

For isolation of sperm cells, cauda epididymis was collected and cut into 2-3 mm pieces that were transferred into HTF medium (101.65 mM NaCl, 4.7 mM KCl, 199.5 µM $MgSO_4$, 370.5 µM KH_2PO_4, 25 mM $NaHCO_3$, 2.7 mM $CaCl_2$, 2.8 mM glucose, 0.33 mM sodium pyruvate, 18.3 mM sodium lactate, Pen/Strep, 0.0002% phenol red, 4 mg/ml BSA). The dissected epididymis was agitated for 15 min at 600 rpm. For video microscopy, sperm was incubated in HTF containing 0.5% methyl-cellulose for 1 h before documentation. PBS containing sperm was spread on glass slides and dried before further processing.

Computer assisted sperm analysis (CASA):

Sperm cells were isolated from the cauda epididymis in 150 µl HTF medium and capacitated for 90 min at 37°C. Aliquots of 3 µl sperm suspension were analysed in a Leja Standard Count 4 Chamber Slide using an Olympus CX41 (Zuber Optik) and the QualiSperm software (Biophos optimised for human sperm), that measures motility rates and concentration of sperm. Statistical analysis was performed with Prism (GraphPad) using two-tailed t-test.

In vitro *fertilisation (IVF):*

Sperm cells isolated from the cauda epididymis were capacitated for 2 h at 37°C and 5% CO_2 and 5% O_2 in HTF medium. Eggs were isolated from wild type females, incubated in HTF in groups of 40 with sperm for 6 h at 37°C under oil, washed in HTF and after 24 h transferred to KSOM medium. Development of embryos was tracked until day 7.5 after IVF. Statistical analysis was performed with Prism (GraphPad) using two-tailed t-test.

Cell culture:

CHO, mIMCD3 and L-cells were maintained in DMEM/F12 (Gibco) containing 10% FCS, Pen/Strep, and 2 mM Glutamax. Transfections of CHO cells were performed using Perfectin (Genlantis) according to manufacturer's instructions.

Generation of CFAP206 specific antibody:

Rabbit polyclonal antibodies detecting CFAP206 were produced by immunisation of rabbits with mouse CFAP206 peptide IRLFNRDSGKGGEG, (pepI; aa194-207) and KEASTQSKREGSSR

(pepII; aa576-589). The antibodies were generated by Biogenes (Berlin, Germany). Peptides were selected regarding: hydrophilicity (according to Kyte-Doolittle); surface probability (according to Emini); chain flexibility (according to Karplus-Schulz); secondary structure (according to Chou-Fasman); antigenicity index (according to Jameson-Wolf). CFAP206 antibodies were purified using the respective CFAP206 polypeptide and SulfoLink coupling resin (Thermo Fisher Scientific, San Jose, CA, USA). Purification was performed according to the manufacturer's instructions. Monoclonal antibodies (mAbs) against mouse CFAP206 epitope PLKEASTQSKREG (ORF2; aa574-586) were generated as described (Rachev et al., 2020). mAbs that reacted specifically with CFAP206 were analysed on Western blots. In this study, α-ORF2-2A7 (rat IgG2a) 1:1, and α-ORF2-4F5 (rat IgG2c) 1:1 were used.

Immunofluorescence staining:

Paraffin sections were deparaffinised, rehydrated and antigens were unmasked by boiling for 20 min in 10 mM Tris-HCl pH 9.5, 1 mM EDTA. Dried sperm were washed in PBS. To block unspecific binding, 5% FCS in PBS was used. Primary antibodies were incubated overnight at 4°C, secondary antibodies for 1 h at room temperature. Antibodies were diluted in blocking solution. The following primary antibodies were used: α-acetylated α-tubulin (ac-TUB) *Clone 6-11B-1*; (axoneme; Sigma Aldrich T6793) 1:1 000, α-gamma-Tubulin (γ-TUB) Clone GTU-88; (basal body; Sigma Aldrich, T5326) 1:4 000, α-CFAP206 (pepII) testis 1:50; nasal cavity and lung 1:10; α-AKAP3 (fibrous sheath; Proteintech 13907-1-AP) 1:200; α-COXIV (mitochondria; Abcam ab202554) 1:200; α-SEPTIN7 (annulus; IBL international #18991) 1:200. The following secondary antibodies were used: α-mouse-Alexa555 (Invitrogen A21424) 1:500; α-rabbit-Alexa555 (1:1 000, Invitrogen A21429); α-mouse-Alexa488 (1:1 000, Invitrogen A11029); α-rabbit-Alexa488 (Invitrogen A11034) 1:500. DAPI (0.5 µg/ml, Applichem) and PNA-lectin-Alexa488 (1:250-500, Invitrogen L-21409) were incubated together with secondary antibodies.

Image processing:

All images were processed and analysed using Fiji (ImageJ). Brightness and contrast were adjusted with Fiji and in immunofluorescence staining the red channels (Alexa555 detection) were changed to magenta to make images accessible to colour vision impaired readers.

Isolation of mouse tracheal epithelial cells (mTECs):

mTECs were isolated by tracheal brushings as described (Rachev et al., 2020).

Ex vivo *imaging of mouse tracheal multiciliated cells; flow tracking and beat frequency analysis:*

Tracheas of 10 weeks to 3 months old wild type and *Cfap206*$^{\Delta ex4/\Delta ex4}$ mice were dissected and analysed as described (Rachev et al., 2020); used method is based on (Francis and Lo, 2013).

Determination of ciliary flow in lateral ventricles:

Explanted P7 mouse brains were analysed as described (Rachev et al., 2020).

Transmission electron microscopy (TEM):

Caudae epididymides were dissected from 3 months old wild type and *Cfap206*$^{\Delta ex4/\Delta ex4}$ litter mates, fixed, embedded and analysed as described (Rudat et al., 2014).

Electron tomography:

Epididymides of wild type and *Cfap206*$^{\Delta ex4/\Delta ex4}$ males were freshly prepared and high pressure frozen as described (Guzman et al., 2014). Sections (300 nm) were imaged in a Tecnai 20 operated at 200 kV. Two tilt series with 90° rotations were recorded from -60° to +60° with an increment of 1°. Tomograms were generated using imod (Kremer et al., 1996), using 10 nm gold beads as fiducials, applied to both sides of the sections. The final tomogram was displayed in the slicer window with a section plane parallel to the central pair of microtubules.

Immunoprecipitations for mass spectrometry:

CFAP206 was immunoprecipitated from mouse testis (excluding epididymis) using the Pierce crosslink IP kit (Thermo Scientific) with α-pepII antibody. IP was performed according to the manufacturer's instructions with some modifications. Lysebuffer (150 mM NaCl; 50 mM Tris-HCl, pH 7,4; 0,55% Nonidet P40; 1x Halt Prot/Phos Inhibitor Mix) and Washbuffer (150 mM NaCl; 50 mM Tris-HCl, pH 7,4; 0,12% Nonidet P40; 1x Halt Prot/Phos Inhibitor Mix) were optimised for α-CFAP206-pepII. And for elution 60 µL Neutralisationbuffer (1 M Tris-HCl, pH 8) was added per reaction tube, and elution was done 3 times using 200 µL Elutionbuffer (200 mM Glycin, pH 2.5). For mass spectrometry analysis 10 independent wild type, and 10 independent *Cfap206*$^{\Delta ex4/\Delta ex4}$ IPs (technical replicates) were used, collected from 3 different animals (biological replicates), respectively.

Mass spectrometry:

Eluates were precipitated with chloroform and methanol followed by trypsin digestion as described before (Gloeckner et al., 2009). C-MS/MS analysis was performed on Ultimate3000 nanoRSLC systems (Thermo Scientific) coupled to an Orbitrap Fusion Tribrid mass spectrometer (Thermo Scientific) by a nano spray ion source. Tryptic peptide mixtures were injected automatically and

loaded at a flow rate of 30 µl/min in 0.1% trifluoroacetic acid in HPLC-grade water onto a nano trap column (300 µm i.d. × 5 mm Pre collumn, packed with Acclaim PepMap100 C18, 5 µm, 100 Å; Thermo Scientific). After 3 minutes, peptides were eluted and separated on the analytical column (75 µm i.d. × 25 cm, Acclaim PepMap RSLC C18, 2 µm, 100 Å; Thermo Scientific) by a linear gradient from 2% to 30% of buffer B (80% acetonitrile and 0.08% formic acid in HPLC-grade water) in buffer A (2% acetonitrile and 0.1% formic acid in HPLC-grade water) at a flow rate of 300 nl/min over 117 minutes. Remaining peptides were eluted by a short gradient from 30% to 95% buffer B in 5 minutes. Analysis of the eluted peptides was done on an LTQ Fusion mass spectrometer. From the high resolution MS pre-scan with a mass range of 335 to 1500, the most intense peptide ions were selected for fragment analysis in the orbitrap depending by using a high speed method if they were at least doubly charged. The normalized collision energy for HCD was set to a value of 27 and the resulting fragments were detected with a resolution of 120,000. The lock mass option was activated; the background signal with a mass of 445.12003 was used as lock mass (Olsen et al., 2005). Every ion selected for fragmentation was excluded for 20 seconds by dynamic exclusion. MS/MS data were analysed using the MaxQuant software (version 1.6.1.0) (Cox and Mann, 2008; Cox et al., 2009). As a digesting enzyme, Trypsin/P was selected with maximal 2 missed cleavages. Cysteine carbamidomethylation was set for fixed modifications, and oxidation of methionine and N-terminal acetylation were specified as variable modifications. The data were analysed by label-free quantification with the minimum ratio count of 3. The first search peptide tolerance was set to 20, the main search peptide tolerance to 4.5 ppm and the re-quantify option was selected. For peptide and protein identification the mouse subset of the SwissProt database (release 2014_04) was used and contaminants were detected using the MaxQuant contaminant search. A minimum peptide number of 2 and a minimum length of 7 amino acids was tolerated. Unique and razor peptides were used for quantification. The match between run option was enabled with a match time window of 0.7 min and an alignment time window of 20 min. For each genotype 8 technical replicates derived from 3 wild type and 3 mutant males were analysed. The statistical analysis including ratio, t-test and significance A calculation was done using the Perseus software (version 1.5.5.3; Tyanova et al., 2016). The full mass spectrometry proteomics data have been deposited to the ProteomeXchange Consortium via the PRIDE (Vizcaíno et al., 2016) partner repository with the dataset identifier PXD018554.

***Xenopus* methods**

Microinjections

627 *Xenopus laevis* embryos were injected at the 4-cell stage into defined lineages to target neural
628 (hydrocephalus), axial mesodermal (laterality), paraxial mesodermal (kidney) or epidermal cells.
629 Drop size was calibrated to 4 nl per injection. *Alexa Fluor* 488 dextran was added as lineage tracer
630 (MW 70 000 or 10 000, 0.5–1 µg/µl; Thermo Fisher Scientific).
631
632 *WMISH*:
633 *In situ* hybridisations were performed using standard procedures. Histological sections (30 µm)
634 were prepared following embedding of embryos in a gelatine-albumin mix using a vibratome
635 (Leica).
636
637 *Statistical analysis of* Xenopus *phenotypes:*
638 FIJI was used for all measurements. Chi square analysis was performed to calculate significances
639 of occurrence of organ situs defects and kidney cyst.
640
641 *CRISPR/Cas9 mediated genome editing:*
642 The CRISPRscan algorithm was used to design single guide RNAs (sgRNAs; Moreno-Mateos et
643 al., 2015). sgRNAs targeting exon 2 and 5 were transcribed using the MEGAshortscript T7 Kit
644 (Invitrogen) from synthetic DNA oligomers. sgRNAs were purified using the MEGAclear
645 Transcription Clean-Up Kit (Invitrogen). Embryos were injected at the 1-cell stage with 1 ng
646 Cas9 (PNA Bio) and 300 pg sgRNA. Following injections, embryos were cultivated at room
647 temperature. To confirm genome editing, direct sequencing of PCR products was applied. DNAs
648 from pools of 10 stage 45 embryos were isolated and gene-specific primers were used to amplify
649 targeted *cfap206* sequences. Genome editing efficiency was calculated using Synthego ICE
650 (https://tools.synthego.com/#/).
651
652 *High-speed video microscopy of larval epidermal cilia*:
653 Control or crispant stage 32 embryos were analysed for epidermal ciliary beating patterns.
654 Specimens were placed into a rectangular chamber constructed from duct tape which was mounted
655 on a slide. Ciliary beating was recorded for 1 sec at the ventral-most aspect of the embryo using
656 high-speed Hamamatsu video camera Orca flash 4.0 at 800 fps (frames per second). For analysis of
657 ciliary flow, fluorescent beads of 1 µm diameter (Invitrogen FluoSpheres; 1:2 000) were added to
658 the culture medium. Embryos were imaged using a Zeiss Axiocam HSm camera at 175 fps.
659 Evaluation of CBF and ciliary flow was as described above in the respective mouse section.
660
661

ACKNOWLEDGEMENTS

We thank S. Brody (Washington University, St. Louis) for *Foxj1* mutant mice, M. Menon and M. Gaestel (Institute for Physiological Chemistry, MHH, Hannover, Germany) for α–SEPTIN7 antibody; D. Conrad, C. Schippert and P. Hillemanns (Department of Gynaecology and Obstetrics, MHH, Hannover, Germany) for the access to the CASA instrument and their help, R. Bauerfeind for helping monitoring tracheal cilia. We thank A. Heiser for his assistance in mice care and genotyping. This work was financially supported by the DFG (GO 449/14-1 and BL285/14-1) and by the DFG Cluster of Excellence "REBIRTH" to AG. TO was supported by a Ph.D. fellowship from the Landesgraduiertenförderung Baden-Württemberg.

AUTHOR CONTRIBUTIONS

Conceptualisation: MB, AB, AG, TO, LT. Methodology: AB, LT, KSG, JH, KB, TO. Reagents: EK. Formal analysis: AB, CA, KSG, LT, TO, FF, JH, KB, KS, ER, MB, AG. Investigation: AB, CA, KSG, LT, TO, FF, JH, KB, KS, ER, LA. Writing - original draft: MB, AG, AB, LT. Writing - review & editing: all authors. Supervision: MB, AG, MU. Project administration: MB, AG. Funding acquisition: MB, AG, MU.

678 REFERENCES

679

680 **Abdelhamed, Z., Vuong, S. M., Hill, L., Shula, C., Timms, A., Beier, D., Campbell, K.,**
681 **Mangano, F. T., Stottmann, R. W. and Goto, J.** (2018). A mutation in Ccdc39 causes
682 neonatal hydrocephalus with abnormal motile cilia development in mice. *Development* **145**,
683 dev154500.

684 **Afzelius, B. A. and Eliasson, R.** (1983). Male and female infertility problems in the immotile-cilia
685 syndrome. *Eur J Respir Dis Suppl* **127**, 144–147.

686 **Alten, L., Schuster-Gossler, K., Beckers, A., Groos, S., Ulmer, B., Hegermann, J., Ochs, M.**
687 **and Gossler, A.** (2012). Differential regulation of node formation, nodal ciliogenesis and cilia
688 positioning by Noto and Foxj1. *Development* **139**, 1276–1284.

689 **Arnaiz, O., Malinowska, A., Klotz, C., Sperling, L., Dadlez, M., Koll, F. and Cohen, J.** (2009).
690 Cildb: a knowledgebase for centrosomes and cilia. *Database (Oxford)* **2009**, bap022–bap022.

691 **Banizs, B., Pike, M. M., Millican, C. L., Ferguson, W. B., Komlosi, P., Sheetz, J., Bell, P. D.,**
692 **Schwiebert, E. M. and Yoder, B. K.** (2005). Dysfunctional cilia lead to altered ependyma and
693 choroid plexus function, and result in the formation of hydrocephalus. *Development* **132**, 5329–
694 5339.

695 **Beckers, A., Ott, T., Schuster-Gossler, K., Boldt, K., Alten, L., Ueffing, M., Blum, M. and**
696 **Gossler, A.** (2018). The evolutionary conserved FOXJ1 target gene Fam183b is essential for
697 motile cilia in Xenopus but dispensable for ciliary function in mice. *Sci Rep* **8**, 14678.

698 **Blum, M. and Ott, T.** (2018). Animal left–right asymmetry. *Curr Biol* **28**, R301–R304.

699 **Brody, S. L., Yan, X. H., Wuerffel, M. K., Song, S. K. and Shapiro, S. D.** (2000). Ciliogenesis
700 and left-right axis defects in forkhead factor HFH-4-null mice. *Am J Respir Cell Mol Biol* **23**,
701 45–51.

702 **Burgoyne, T., Lewis, A., Dewar, A., Luther, P., Hogg, C., Shoemark, A. and Dixon, M.** (2014).
703 Characterizing the ultrastructure of primary ciliary dyskinesia transposition defect using
704 electron tomography. *Cytoskeleton (Hoboken)* **71**, 294–301.

705 **Castleman, V. H., Romio, L., Chodhari, R., Hirst, R. A., de Castro, S. C. P., Parker, K. A.,**
706 **Ybot-Gonzalez, P., Emes, R. D., Wilson, S. W., Wallis, C., et al.** (2009). Mutations in radial
707 spoke head protein genes RSPH9 and RSPH4A cause primary ciliary dyskinesia with central-
708 microtubular-pair abnormalities. *Am. J. Hum. Genet.* **84**, 197–209.

709 **Chen, J., Knowles, H. J., Hebert, J. L. and Hackett, B. P.** (1998). Mutation of the mouse
710 hepatocyte nuclear factor/forkhead homologue 4 gene results in an absence of cilia and random
711 left-right asymmetry. *J. Clin. Invest.* **102**, 1077–1082.

712 **Choksi, S. P., Lauter, G., Swoboda, P. and Roy, S.** (2014). Switching on cilia: transcriptional
713 networks regulating ciliogenesis. *Development* **141**, 1427–1441.

714 **Cox, J. and Mann, M.** (2008). MaxQuant enables high peptide identification rates, individualized
715 p.p.b.-range mass accuracies and proteome-wide protein quantification. *Nat Biotechnol* **26**,
716 1367–1372.

Cox, J., Matic, I., Hilger, M., Nagaraj, N., Selbach, M., Olsen, J. V. and Mann, M. (2009). A practical guide to the MaxQuant computational platform for SILAC-based quantitative proteomics. *Nature Protocols* **4**, 698–705.

de Vries, W. N., Binns, L. T., Fancher, K. S., Dean, J., Moore, R., Kemler, R. and Knowles, B. B. (2000). Expression of Cre recombinase in mouse oocytes: a means to study maternal effect genes. *Genesis* **26**, 110–112.

Dubaissi, E. and Papalopulu, N. (2011). Embryonic frog epidermis: a model for the study of cell-cell interactions in the development of mucociliary disease. *Disease Models & Mechanisms* **4**, 179–192.

Edelbusch, C., Cindrić, S., Dougherty, G. W., Loges, N. T., Olbrich, H., Rivlin, J., Wallmeier, J., Pennekamp, P., Amirav, I. and Omran, H. (2017). Mutation of serine/threonine protein kinase 36 (STK36) causes primary ciliary dyskinesia with a central pair defect. *Hum. Mutat.* **38**, 964–969.

El-Brolosy, M. A., Kontarakis, Z., Rossi, A., Kuenne, C., nther, S. G. X., Fukuda, N., Kikhi, K., Boezio, G. L. M., Takacs, C. M., Lai, S.-L., et al. (2019). Genetic compensation triggered by mutant mRNA degradation. *Nature* 1–26.

Francis, R. and Lo, C. (2013). Ex vivo method for high resolution imaging of cilia motility in rodent airway epithelia. *J Vis Exp* e50343.

Frommer, A., Hjeij, R., Loges, N. T., Edelbusch, C., Jahnke, C., Raidt, J., Werner, C., Wallmeier, J., Große-Onnebrink, J., Olbrich, H., et al. (2015). Immunofluorescence Analysis and Diagnosis of Primary Ciliary Dyskinesia with Radial Spoke Defects. *Am J Respir Cell Mol Biol* **53**, 150319114504004–573.

Gherman, A., Davis, E. E. and Katsanis, N. (2006). The ciliary proteome database: an integrated community resource for the genetic and functional dissection of cilia. *Nat Genet* **38**, 961–962.

Gloeckner, C. J., Boldt, K. and Ueffing, M. (2009). Strep/FLAG tandem affinity purification (SF-TAP) to study protein interactions. *Curr Protoc Protein Sci* **Chapter 19**, Unit19.20.

Gupta, A., Diener, D. R., Sivadas, P., Rosenbaum, J. L. and Yang, P. (2012). The versatile molecular complex component LC8 promotes several distinct steps of flagellar assembly. *The Journal of Cell Biology* **198**, 115–126.

Guzman, R. E., Alekov, A. K., Filippov, M., Hegermann, J. and Fahlke, C. (2014). Involvement of ClC-3 chloride/proton exchangers in controlling glutamatergic synaptic strength in cultured hippocampal neurons. *Front Cell Neurosci* **8**, 143.

Hall, E. A., Keighren, M., Ford, M. J., Davey, T., Jarman, A. P., Smith, L. B., Jackson, I. J. and Mill, P. (2013). Acute versus chronic loss of mammalian Azi1/Cep131 results in distinct ciliary phenotypes. *PLoS Genet* **9**, e1003928.

Hayes, J. M., Kim, S. K., Abitua, P. B., Park, T. J., Herrington, E. R., Kitayama, A., Grow, M. W., Ueno, N. and Wallingford, J. B. (2007). Identification of novel ciliogenesis factors using a new in vivo model for mucociliary epithelial development. *Dev Biol* **312**, 115–130.

Hirokawa, N., Tanaka, Y., Okada, Y. and Takeda, S. (2006). Nodal Flow and the Generation of Left-Right Asymmetry. *Cell* **125**, 33–45.

757 **Huizar, R. L., Lee, C., Boulgakov, A. A., Horani, A., Tu, F., Marcotte, E. M., Brody, S. L. and**
758 **Wallingford, J. B.** (2018). A liquid-like organelle at the root of motile ciliopathy. *Elife* 7,
759 4154.

760 **Ibañez-Tallon, I., Pagenstecher, A., Fliegauf, M., Olbrich, H., Kispert, A., Ketelsen, U.-P.,**
761 **North, A., Heintz, N. and Omran, H.** (2004). Dysfunction of axonemal dynein heavy chain
762 Mdnah5 inhibits ependymal flow and reveals a novel mechanism for hydrocephalus formation.
763 *Human Molecular Genetics* **13**, 2133–2141.

764 **Ikegami, K., Sato, S., Nakamura, K., Ostrowski, L. E. and Setou, M.** (2010). Tubulin
765 polyglutamylation is essential for airway ciliary function through the regulation of beating
766 asymmetry. *Proc. Natl. Acad. Sci. U.S.A.* **107**, 10490–10495.

767 **Inglis, P. N., Boroevich, K. A. and Leroux, M. R.** (2006). Piecing together a ciliome. *Trends*
768 *Genet.* **22**, 491–500.

769 **Jacquet, B. V., Salinas-Mondragon, R., Liang, H., Therit, B., Buie, J. D., Dykstra, M.,**
770 **Campbell, K., Ostrowski, L. E., Brody, S. L. and Ghashghaei, H. T.** (2009). FoxJ1-
771 dependent gene expression is required for differentiation of radial glia into ependymal cells and
772 a subset of astrocytes in the postnatal brain. *Development* **136**, 4021–4031.

773 **Jain, R., Pan, J., Driscoll, J. A., Wisner, J. W., Huang, T., Gunsten, S. P., You, Y. and Brody,**
774 **S. L.** (2010). Temporal relationship between primary and motile ciliogenesis in airway
775 epithelial cells. *Am J Respir Cell Mol Biol* **43**, 731–739.

776 **Knowles, M. R., Ostrowski, L. E., Leigh, M. W., Sears, P. R., Davis, S. D., Wolf, W. E.,**
777 **Hazucha, M. J., Carson, J. L., Olivier, K. N., Sagel, S. D., et al.** (2014). Mutations in RSPH1
778 cause primary ciliary dyskinesia with a unique clinical and ciliary phenotype. *Am J Respir Crit*
779 *Care Med* **189**, 707–717.

780 **Kremer, J. R., Mastronarde, D. N. and McIntosh, J. R.** (1996). Computer visualization of three-
781 dimensional image data using IMOD. *Journal of Structural Biology* **116**, 71–76.

782 **Lee, L.** (2013). Riding the wave of ependymal cilia: genetic susceptibility to hydrocephalus in
783 primary ciliary dyskinesia. *J. Neurosci. Res.* **91**, 1117–1132.

784 **Lin, J., Tritschler, D., Song, K., Barber, C. F., Cobb, J. S., Porter, M. E. and Nicastro, D.**
785 (2011). Building blocks of the nexin-dynein regulatory complex in Chlamydomonas flagella.
786 *Journal of Biological Chemistry* **286**, 29175–29191.

787 **Lindemann, C. B. and Lesich, K. A.** (2010). Flagellar and ciliary beating: the proven and the
788 possible. *J Cell Sci* **123**, 519–528.

789 **Lucas, J. S., Davis, S. D., Omran, H. and Shoemark, A.** (2019). Primary ciliary dyskinesia in the
790 genomics age. *Lancet Respir Med.*

791 **Lyons, R. A., Saridogan, E. and Djahanbakhch, O.** (2006). The reproductive significance of
792 human Fallopian tube cilia. *Hum. Reprod. Update* **12**, 363–372.

793 **Moorman, A. F., Houweling, A. C., de Boer, P. A. and Christoffels, V. M.** (2001). Sensitive
794 nonradioactive detection of mRNA in tissue sections: novel application of the whole-mount in
795 situ hybridization protocol. *J. Histochem. Cytochem.* **49**, 1–8.

796 **Moreno-Mateos, M. A., Vejnar, C. E., Beaudoin, J.-D., Fernandez, J. P., Mis, E. K., Khokha,**
797 **M. K. and Giraldez, A. J.** (2015). CRISPRscan: designing highly efficient sgRNAs for
798 CRISPR-Cas9 targeting in vivo. *Nat Meth* **12**, 982–988.

799 **Mukherjee, I., Roy, S. and Chakrabarti, S.** (2019). Identification of Important Effector Proteins
800 in the FOXJ1 Transcriptional Network Associated With Ciliogenesis and Ciliary Function.
801 *Front Genet* **10**, 23.

802 **Nieuwkoop, P. D. and Faber, J.** (1994). *Normal table of Xenopus laevis (Daudin) : a systematical*
803 *and chronological survey of the development from the fertilized egg till the end of*
804 *metamorphosis*. New York: Garland Publishing Inc.

805 **Nonaka, S., Tanaka, Y., Okada, Y., Takeda, S., Harada, A., Kanai, Y., Kido, M. and**
806 **Hirokawa, N.** (1998). Randomization of left-right asymmetry due to loss of nodal cilia
807 generating leftward flow of extraembryonic fluid in mice lacking KIF3B motor protein. *Cell* **95**,
808 829–837.

809 **Olsen, J. V., de Godoy, L. M. F., Li, G., Macek, B., Mortensen, P., Pesch, R., Makarov, A.,**
810 **Lange, O., Horning, S. and Mann, M.** (2005). Parts per million mass accuracy on an Orbitrap
811 mass spectrometer via lock mass injection into a C-trap. *Mol. Cell Proteomics* **4**, 2010–2021.

812 **Osinka, A., Poprzeczko, M., Zielinska, M. M., Fabczak, H., Joachimiak, E. and Wloga, D.**
813 (2019). Ciliary Proteins: Filling the Gaps. Recent Advances in Deciphering the Protein
814 Composition of Motile Ciliary Complexes. *Cells* **8**.

815 **Praveen, K., Davis, E. E. and Katsanis, N.** (2015). Unique among ciliopathies: primary ciliary
816 dyskinesia, a motile cilia disorder. *F1000Prime Rep* **7**, 36.

817 **Rachev, E., Schuster-Gossler, K., Fuhl, F., Ott, T., Tveriakhina, L., Beckers, A., Hegermann,**
818 **J., Boldt, K., Mai, M., Kremmer, E., et al.** (2020). CFAP43 modulates ciliary beating in
819 mouse and Xenopus. *Dev Biol* **459**, 109–125.

820 **Reynolds, M. J., Phetruen, T., Fisher, R. L., Chen, K., Pentecost, B. T., Gomez, G., Ounjai, P.**
821 **and Sui, H.** (2018). The Developmental Process of the Growing Motile Ciliary Tip Region. *Sci*
822 *Rep* **8**, 7977–10.

823 **Rodríguez, C. I., Buchholz, F., Galloway, J., Sequerra, R., Kasper, J., Ayala, R., Stewart, A.**
824 **F. and Dymecki, S. M.** (2000). High-efficiency deleter mice show that FLPe is an alternative
825 to Cre-loxP. *Nat Genet* **25**, 139–140.

826 **Rossi, A., Kontarakis, Z., Gerri, C., Nolte, H., Hölper, S., Krüger, M. and Stainier, D. Y. R.**
827 (2015). Genetic compensation induced by deleterious mutations but not gene knockdowns.
828 *Nature* **524**, 230–233.

829 **Rudat, C., Grieskamp, T., Röhr, C., Airik, R., Wrede, C., Hegermann, J., Herrmann, B. G.,**
830 **Schuster-Gossler, K. and Kispert, A.** (2014). Upk3b is dispensable for development and
831 integrity of urothelium and mesothelium. *PLoS ONE* **9**, e112112.

832 **Satir, P., Heuser, T. and Sale, W. S.** (2014). A Structural Basis for How Motile Cilia Beat.
833 *Bioscience* **64**, 1073–1083.

834 **Shinohara, K., Chen, D., Nishida, T., Misaki, K., Yonemura, S. and Hamada, H.** (2015).
835 Absence of Radial Spokes in Mouse Node Cilia Is Required for Rotational Movement but
836 Confers Ultrastructural Instability as a Trade-Off. *Dev Cell* **35**, 236–246.

Sivadas, P., Dienes, J. M., St Maurice, M., Meek, W. D. and Yang, P. (2012). A flagellar A-kinase anchoring protein with two amphipathic helices forms a structural scaffold in the radial spoke complex. *The Journal of Cell Biology* **199**, 639–651.

Sive, H. L., Grainger, H. M. and Harland, R. M. (2000). *Early Development of Xenopus Laevis: A Laboratory Manual*. Cold Spring Harbor: Cold Spring Harbor Laboratory Press.

Soares, H., Carmona, B., Nolasco, S., Viseu Melo, L. and Gonçalves, J. (2019). Cilia Distal Domain: Diversity in Evolutionarily Conserved Structures. *Cells* **8**.

Spassky, N., Merkle, F. T., Flames, N., Tramontin, A. D., García-Verdugo, J. M. and Alvarez-Buylla, A. (2005). Adult ependymal cells are postmitotic and are derived from radial glial cells during embryogenesis. *Neurosci* **25**, 10–18.

Stannard, W. and O'Callaghan, C. (2006). Ciliary function and the role of cilia in clearance. *J Aerosol Med* **19**, 110–115.

Stauber, M., Weidemann, M., Dittrich Breiholz, O., Lobschat, K., Alten, L., Mai, M., Beckers, A., Kracht, M. and Gossler, A. (2017). Identification of FOXJ1 effectors during ciliogenesis in the foetal respiratory epithelium and embryonic left-right organiser of the mouse. *Dev Biol* **423**, 170–188.

Takeda, S. and Narita, K. (2012). Structure and function of vertebrate cilia, towards a new taxonomy. *Differentiation* **83**, S4–11.

Tyanova, S., Temu, T., Sinitcyn, P., Carlson, A., Hein, M. Y., Geiger, T., Mann, M. and Cox, J. (2016). The Perseus computational platform for comprehensive analysis of (prote)omics data. *Nat Meth* **13**, 731–740.

Vasudevan, K. K., Song, K., Alford, L. M., Sale, W. S., Dymek, E. E., Smith, E. F., Hennessey, T., Joachimiak, E., Urbanska, P., Wloga, D., et al. (2015). FAP206 is a microtubule-docking adapter for ciliary radial spoke 2 and dynein c. *Mol. Biol. Cell* **26**, 696–710.

Vizcaíno, J. A., Csordas, A., del-Toro, N., Dianes, J. A., Griss, J., Lavidas, I., Mayer, G., Perez-Riverol, Y., Reisinger, F., Ternent, T., et al. (2016). 2016 update of the PRIDE database and its related tools. *Nuc Acids Res* **44**, D447–56.

Walentek, P. and Quigley, I. K. (2017). What we can learn from a tadpole about ciliopathies and airway diseases: Using systems biology in Xenopus to study cilia and mucociliary epithelia. *Genesis* **55**, e23001.

Wallmeier, J., Frank, D., Shoemark, A., Nöthe-Menchen, T., Cindrić, S., Olbrich, H., Loges, N. T., Aprea, I., Dougherty, G. W., Pennekamp, P., et al. (2019). De Novo Mutations in FOXJ1 Result in a Motile Ciliopathy with Hydrocephalus and Randomization of Left/Right Body Asymmetry. *Am. J. Hum. Genet.* **105**, 1030–1039.

Weidemann, M., Schuster-Gossler, K., Stauber, M., Wrede, C., Hegermann, J., Ott, T., Boldt, K., Beyer, T., Serth, K., Kremmer, E., et al. (2016). CFAP157 is a murine downstream effector of FOXJ1 that is specifically required for flagellum morphogenesis and sperm motility. *Development* **143**, 4736–4748.

Zhang, S. and Mitchell, B. J. (2016). Basal bodies in Xenopus. *Cilia* 1–6.

876 **Zhu, L., Liu, H., Chen, Y., Yan, X. and Zhu, X.** (2019). Rsph9 is critical for ciliary radial spoke
877 assembly and central pair microtubule stability. *Biol. Cell* **111**, 29–38.

878 **Ziętkiewicz, E., Bukowy-Bieryłło, Z., Voelkel, K., Klimek, B., Dmeńska, H., Pogorzelski, A.,**
879 **Sulikowska-Rowińska, A., Rutkiewicz, E. and Witt, M.** (2012). Mutations in radial spoke
880 head genes and ultrastructural cilia defects in East-European cohort of primary ciliary
881 dyskinesia patients. *PLoS ONE* 7, e33667

882 **FIGURE LEGENDS**

883

884 **Fig. 1. Structure of the mouse *Cfap206* and *Cfap206* expression.**

885 **(A)** Schematic depiction of the *Cfap206* genomic structure, transcripts and resulting proteins. The
886 *Cfap206* gene consists of 13 exons (middle row) that give rise to two transcripts: a short form
887 (*Cfap206 S*; upper row) and a long form (*Cfap206 L*; lower row), generated by the differential
888 usage of a splice donor site in exon 11. Grey boxes indicate ORFs, white boxes 5'- and 3'-UTR,
889 respectively. PCR *Cfap206 S* and PCR *Cfap206 L* indicate the position of primers and PCR
890 products used to distinguish between both transcripts. Blue box marks the region used to generate
891 the *in situ* hybridisation probe, which detected both transcript. **(B)** Correlation of *Cfap206 S,*
892 *Cfap206 L* and *Foxj1* expression in adult tissues assessed by RT-PCR. *Hprt* was used as quality
893 control. The full-size agarose gel is shown in Fig. S7. **(C)** Expression of *Cfap206* in adult tissues
894 detected by SISH. Boxed areas in (a-e) indicate the regions shown at higher magnification in (a'-
895 e'). Arrowheads point to regions of expression. CP: choroid plexus. **(D)** Expression of *Cfap206* in
896 tissues developing or carrying motile cilia at E17.5 detected by SISH. Boxed areas in (a-d) indicate
897 the regions shown at higher magnification in (a'-d'). **(E)** Dependence of *Cfap206* expression on
898 FOXJ1. WISH (a,d) and SISH (b,c,e,f) on wild type (a-c) and *Foxj1* mutant (d-f) E8.0 embryos
899 (a,d) and E17.5 nasal cavities (b,e) and lungs (c,f). Red boxes in (b,c,e,f) indicate regions enlarged
900 in (b',c',e',f'). Note that *Cfap206* expression was reduced or nearly absent in the mouse left-right
901 organiser (LRO), the respiratory epithelium and bronchi of *Foxj1* mutants (red arrowheads in
902 d,e',f'). Scale bars: C,D = 500 μm; Eb,c,e,f = 200 μm.

903

904 **Fig. 2. *cfap206* is co-expressed with and dependent on *foxj1* in *Xenopus laevis*.**

905 **(A)** Analysis of *foxj1* and *cfap206* mRNA expression in staged embryos using antisense RNA
906 probes. (a,e) In gastrula stage 10 embryos, *foxj1* transcripts were present in the LRO precursor, the
907 superficial mesoderm (SM; a), while *cfap206* was not detected by *in situ* hybridisation (e).
908 Histological sections (b',f'; planes of sections indicated by red dashed lines in b,f) of stage 19
909 dorsal explants (b,f) revealed overlapping expression of *foxj1* (b,b') and *cfap206* (f,f') in the floor
910 plate (FP), while in the gastrocoel roof plate (area of LRO; outlined by dashed lines in b,f), only
911 *cfap206* transcripts were detected. Staining in (b) reflects expression in the floorplate above the
912 LRO. (e,g) In stage 29 larvae, both genes were co-expressed in the nephrostomes (white
913 arrowheads) and MCCs. (d,h) In the head of stage 45 tadpoles, strong neural expression of *foxj1*
914 was seen in the sub-commissural organ (SCO), zona limitans intrathalamica (ZLI) and FP (d'''').
915 Transcripts of *cfap206* were detected in the same tissues, however at reduced levels (h'''). Non-
916 neural expression was found in the stomach (stom.; d',h') and in dorsal cells lining the branchial

chamber (BC; d'',h''). **(B,C)** *Cfap206* is a *foxj1* target gene. (B) Strong *cfap206* induction in embryos unilaterally injected with *foxj1* mRNA. *, injected side. (C) Reduction of *cfap206* expression in stage 24 *foxj1* F0 crispant embryos (b,b'), as compared to wild type (a,a'). Boxed areas in (a,b) indicate the regions shown at higher magnification in (a',b'). Scale bars: 100 µm.

Fig. 3. Subcellular localisation of CFAP206 protein to the axoneme and basal bodies.
(A) Schematic depiction of short (CFAP206 S; upper row) and long (CFAP206 L; lower row) CFAP206 protein. Coloured boxes indicate position of peptides (green pepI; orange pepII; cyan ORF2) used to generate antibodies. Detection of tagged CFAP206 overexpressed in CHO cells and of endogenous CFAP206 protein in lysates of mouse testis with the different antibodies. The full-size Western blots are shown in Fig. S9. **(B)** Localisation of endogenous CFAP206 (α-pepII) to cilia on respiratory epithelial cells (a-d) and flagella of spermatozoa (e-g). Boxed areas in a-d indicate the region shown in (a'-d'). White dashed boxes in (a-d) indicate regions shown enlarged in (a'-d'). Arrowheads in d and d' point to localisation of CFAP206 non-overlapping with acetylated α-tubulin (ac-TUB). Arrows highlight ciliary tips, which lack CFAP206. **(C)** Subcellular localisation of murine GFP-CFAP206 in *Xenopus* skin MCCs. (a) Co-staining with the basal body marker Centrin4-RFP (Cetn4-RFP; a). Orthogonal projection shown in (a') demonstrated partial overlap at the basal body. (b) Co-staining with phalloidin to highlight F-actin and the basal foot marker Tubulin gamma-1 (Tubg1) confirmed basal body staining (b') and partial overlap at the basal foot (b''). (c) Axonemal staining, as shown by co-staining with an antibody against acetylated alpha-tubulin (ac-Tuba4a). (d) Cartoon of GFP-CFAP206 localisation at the *Xenopus* cilium. Scale bars: B = 10 µm, C = 1 µm.

Fig. 4. Ciliary defects in MCCs of *Xenopus cfap206* crispants.
(A) Enhanced ciliary beat frequency (CBF) in crispants. (a) Statistical evaluation of CBF in wild type and *cfap206* crispants. Results from 3 independent experiments with 15 embryos each and 5 analysed MCCs per embryo. Raw data are shown in Table S3. (b) Kymographs of ciliary motility of single MCCs, generated from control wild type, sgRNA1- and sgRNA2-injected specimens. **(B)** Reduced bead transport in *cfap206* crispant skin mucociliary epithelia. (a) Velocities of bead transport in wild type, sgRNA1- and sgRNA2-injected specimens. Results from 3 independent experiments with 8 analysed specimens each. Raw data are shown in Table S2. (b) Maximum intensity projections of single control wild type, sgRNA1- and sgRNA2-injected embryos. *, $p<0.05$; ***, $p<0.001$.

Fig. 5. Generation and characterisation of a *Cfap206* null mouse.

952 **(A)** Schematic drawing depicting the structure of the targeted locus, the locus after FLP mediated
953 removal of the neo cassette (*Cfap206*^{loxP}), and following Cre mediated excision of exon 4
954 (*Cfap206*$^{\Delta ex4}$). **(B)** Western blot analysis of testis lysates of wild type and *Cfap206*$^{\Delta ex4/\Delta ex4}$ mice with
955 α-pepI and α-pepII antibodies demonstrated absence of both CFAP206 protein variants in mutant
956 tissue. Arrows indicate the expected sizes of the CFAP206 proteins. The full-size Western blots are
957 shown in Fig. S10. **(C)** Indirect immunofluorescence staining of wild type (a-f) and *Cfap206*$^{\Delta ex4/\Delta ex4}$
958 (g-l) testis (a-c,g-i) and respiratory epithelium (d-f,j-l) sections for CFAP206, indicating loss of
959 staining in mutant tissues. **(D)** Analysis of cilia length in mouse tracheal epithelial cells (mTECs)
960 isolated from wild type and *Cfap206*$^{\Delta ex4/\Delta ex4}$ mutants revealed no change in ciliary length upon
961 CFAP206 loss. Each dot represents the average cilia length of one specimen analysed (n=3). Graph
962 in D displays respective values with mean and s.d. Raw data are shown in Table S4. Scale bars: C =
963 10 µm; D = 5 µm.
964
965 **Fig. 6. Enlarged ventricles and mucus accumulation in *Cfap206*$^{\Delta ex4/\Delta ex4}$.**
966 **(A)** External views (a,b) and HE stained coronal sections (c,d) of wild type (a,c) and
967 *Cfap206*$^{\Delta ex4/\Delta ex4}$ (b,d) heads revealed doomed skull and expanded and fused ventricles of
968 *Cfap206*$^{\Delta ex4/\Delta ex4}$ mutants. **(B)** HE stained coronal sections of wild type (a,b) and *Cfap206*$^{\Delta ex4/\Delta ex4}$
969 mutant (c,d) brains demonstrated the presence of enlarged ventricles on postnatal day 1 (P1). Boxed
970 areas in (a-d) indicate the regions shown at higher magnification in (a'-d'). **(C)** (a) Schematic
971 representation of a P6 brain. Red line indicates plane of section. The mid-sagittal sections of
972 heterozygous *Cfap206*$^{\Delta ex4}$ (representing wild type condition; b) and homozygous *Cfap206*$^{\Delta ex4}$
973 mutants (c,d) were HE-stained to visualise the aqueduct (AQ). Homozygous mutants showed
974 stenotic (black arrowhead in c) or obstructed aqueducts (red arrowhead in d). **(D)** Cilia generated
975 ventricular flow at P7 was comparable in wild type and *Cfap206*$^{\Delta ex4/\Delta ex4}$ littermates. Each dot
976 represents the average speed of all tracked particles of each individual (wild type n=8 and
977 *Cfap206*$^{\Delta ex4/\Delta ex4}$ n=12). Numerical values used to generate the dot plot are shown in Table S5. **(E)**
978 Coronal sections of wild type (a-c) and *Cfap206*$^{\Delta ex4/\Delta ex4}$ mutant (d-f) nasal cavities demonstrating
979 progressive mucus accumulation in mutants. Boxed areas in (a-f) indicate regions shown at higher
980 magnification in (a'-f'). **(F)** Kymographs and derived CBF. (a) Representative kymographs (upper
981 panels) and plotted values (lower panels) of wild type (violet) and *Cfap206*$^{\Delta ex4/\Delta ex4}$ (green) tracheal
982 cilia motility (t = 1 s) depict CBF. (b) CBF of cilia of *Cfap206*$^{\Delta ex4/\Delta ex4}$ tracheas was enhanced
983 compared to wild type. Each dot represents the average CBF of one specimen analysed (wild type
984 n=4 and *Cfap206*$^{\Delta ex4/\Delta ex4}$ n=3). Additional details of CBF measurements are shown in Fig. S11. Raw

985 data are shown in Table S6. (c) Cilia generated flow (CGF) was unchanged in *Cfap206*$^{\Delta ex4/\Delta ex4}$
986 trachea explants compared to wild type. Raw data are shown in Table S7.
987 Graphs in D and F display respective values with mean and s.d. Scale bars: Ac,d and B = 500 µm;
988 C,E = 1 mm.
989
990 **Fig. 7. Non-functional spermatozoa of *Cfap206*$^{\Delta ex4/\Delta ex4}$ mutant males.**
991 **(A)** HE stained sections of wild type (a,b) and *Cfap206*$^{\Delta ex4/\Delta ex4}$ mutant (c,d) testes (a,c) and
992 epididymides (b,d). **(B)** CASA analysis and results of IVF showing normal sperm concentration in
993 *Cfap206*$^{\Delta ex4/\Delta ex4}$ mutants (a), reduced *Cfap206*$^{\Delta ex4/\Delta ex4}$ sperm motility (b), inability of
994 *Cfap206*$^{\Delta ex4/\Delta ex4}$ sperm to support early development after IVF (c) and reduced attachment to the
995 zona pellucida *in vitro* (e). (d) wild type egg with wild type sperm cells. (e) wild type egg with
996 *Cfap206*$^{\Delta ex4/\Delta ex4}$ sperm. Raw data concerning CASA analysis (a,b) are shown in Table S8 and
997 concerning IVF (c) are shown in Table S9. **(C)** Bright field (a-l) and fluorescence (a'-l') images of
998 wild type (a,a'-f,f') and *Cfap206*$^{\Delta ex4/\Delta ex4}$ (g,g'-l,l') sperm cells isolated from the cauda epididymis.
999 The following dyes and antibodies were used to visualise organelles and subcellular compartments:
1000 DAPI (nuclei; a'-l'; blue); α-ac-TUB (axonemes; a'-c',g'-i'; magenta); PNA-lectin (acrosomes;
1001 b',d',h',j'; green); α-AKAP3 (fibrous sheath; b',h'; green); α-SEPT7 (annuli; c',e',i',k'; green); α-
1002 COXIV (mitochondria; d'-f',j'-l'; magenta). Arrowhead in g' highlights a coiled flagellum with
1003 PNA stained material, arrows in (c',e',i',k') to annuli. Graphs in B display respective values with
1004 mean and s.d. Scale bars: A = 100 µm; C = 10 µm.
1005
1006 **Fig. 8. Electron microscopic analysis of wild type and *Cfap206*$^{\Delta ex4/\Delta ex4}$ mutant sperm.**
1007 **(A)** TEM analysis of wild type (a-c) and *Cfap206*$^{\Delta ex4/\Delta ex4}$ (d-h) epididymis sperm. (a-c) Overviews
1008 of wild type sections; red stars, sperm heads; blue arrow, fibrous sheath; yellow star, mitochondria;
1009 green star, ODFs. Longitudinal section through *Cfap206*$^{\Delta ex4/\Delta ex4}$ circular (d) or bent (e) axonemes
1010 surrounding vesicular material (red asterisks). (f) Groups of axonemes (marked with white
1011 asterisks) surrounded by a single plasma membrane (dark blue arrows in f', magnified region of the
1012 black stippled inset) and axonemal profiles with apparently normal microtubule doublets (green
1013 arrows in white stippled inset). In (f") vesicular structures (red asterisks) and multiple axonemal
1014 profiles from the midpiece and principle piece region (indicated by the presence of mitochondria
1015 (yellow stars) and fibrous sheath (light blue arrows)) with disorganized microtubules and ODFs
1016 (green stars) surrounded by a single plasma membrane (dark blue arrows). (g) Axonemal profile of
1017 the midpiece region showing few irregular single microtubules (red arrow) and ODFs (green stars).
1018 (h) Axonemal profiles of principal pieces with disorganized ODFs (green stars) and microtubules

surrounded by fibrous sheaths (light blue arrows). **(B)** Electron tomography revealed radial spokes (red arrowheads) between the inner central pair of microtubules and the outer microtubules (anchored at the A-tubule) in wild type (a). Radial spokes (red arrowheads, RS1-3) appeared in a repetitive pattern, interrupted by electron lucent gaps repeating every 96 nm. In *Cfap206*$^{\Delta ex4/\Delta ex4}$ mutant sperm tails (c) the radial spokes were rather irregular and/or incomplete (unfilled red arrowheads) and missing. (b) and (d) show cross sections of the wild type and *Cfap206*$^{\Delta ex4/\Delta ex4}$ tomograms shown in (a) and (c), respectively. Green stars indicate ODFs. Further details of the tomography and section planes are shown in Fig. S5B,C. Scale bars: Aa,d – 2 µm, b,e,f – 1 µm; c,g,h = 500 nm; B = 100 nm.

33

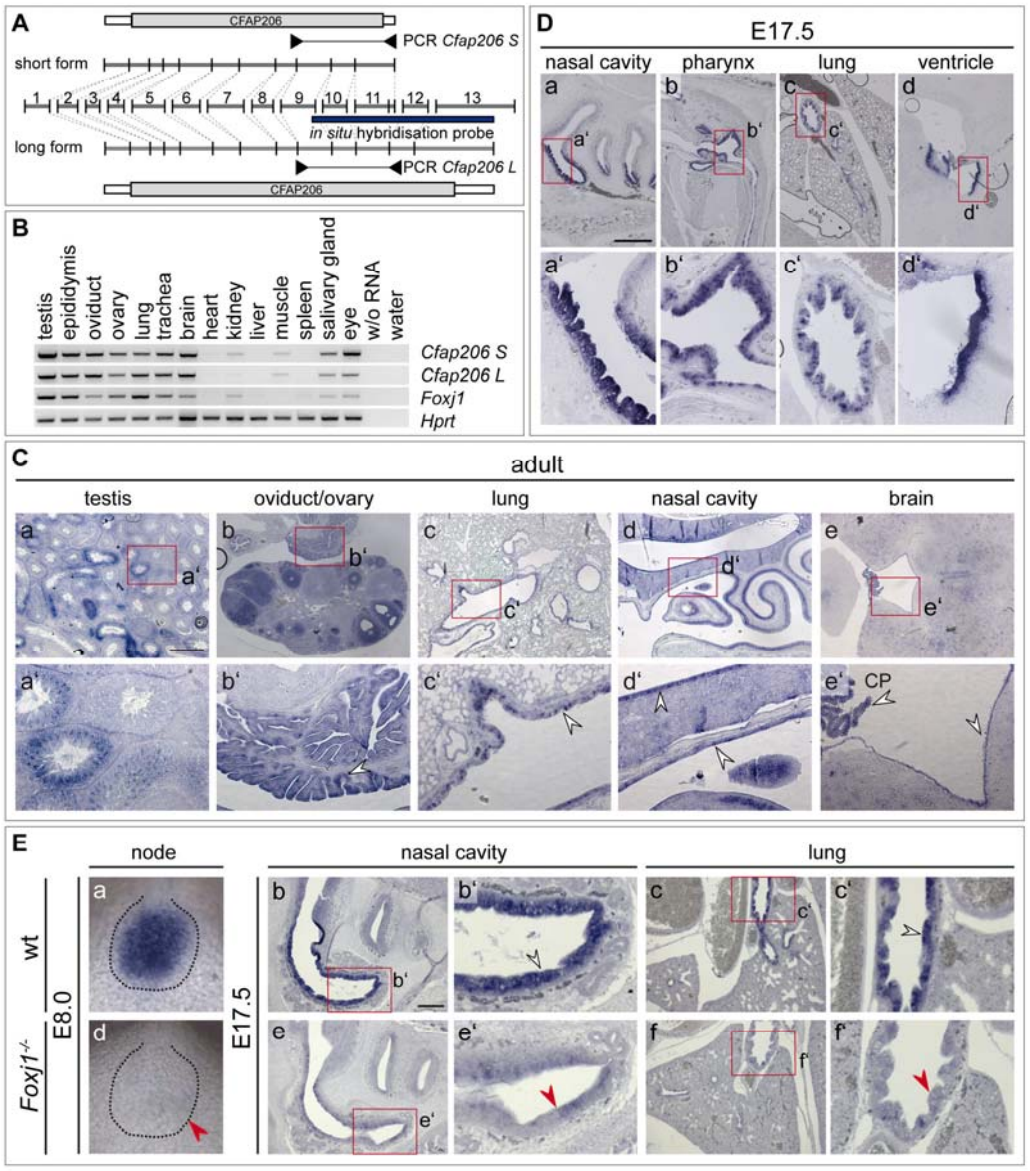
A
CFAP206
PCR Cfap206 S
short form
1 2 3 4 5 6 7 8 9 10 11 12 13
in situ hybridisation probe
long form
PCR Cfap206 L
CFAP206
B
testis
epididymis
oviduct
ovary
lung
trachea
brain
heart
kidney
liver
muscle
spleen
salivary gland
eye
w/o RNA
water
Cfap206 S
Cfap206 L
Foxj1
Hprt
D
E17.5
nasal cavity
pharynx
lung
ventricle
C
adult
testis
oviduct/ovary
lung
nasal cavity
brain
CP
E
node
nasal cavity
lung
wt
Foxj1-/-
E8.0
E17.5

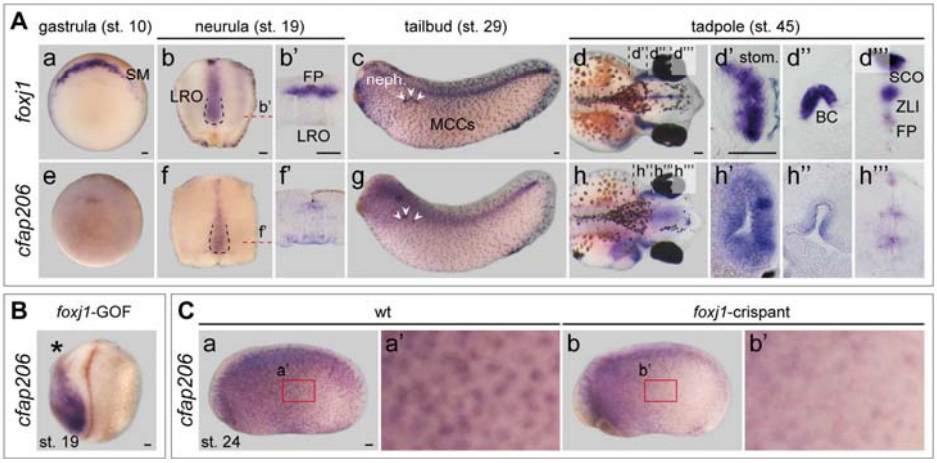
A
gastrula (st. 10)
neurula (st. 19)
tailbud (st. 29)
tadpole (st. 45)
foxj1
cfap206
SM
LRO
FP
nephr.
MCCs
stom.
BC
SCO
ZLI
B
foxj1-GOF
st. 19
C
wt
foxj1-crispant
st. 24

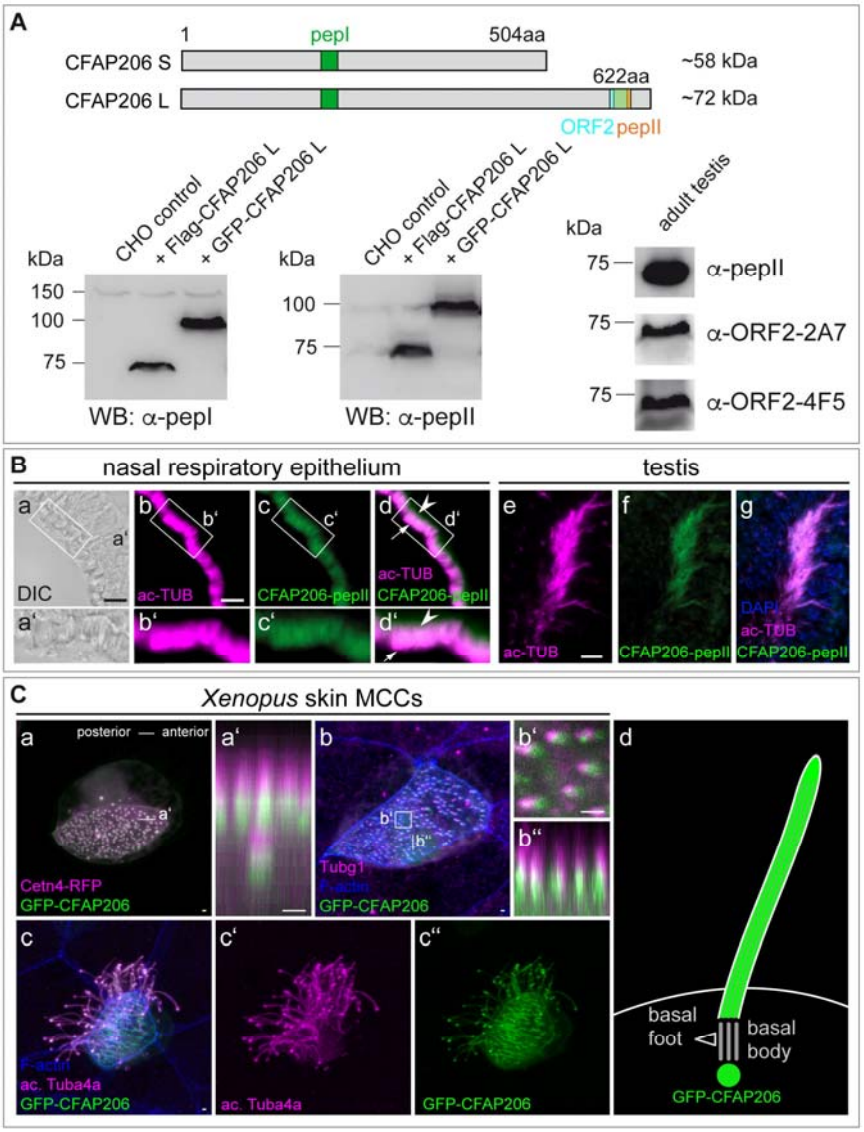
A
1
pepI
504aa
CFAP206 S
~58 kDa
622aa
CFAP206 L
~72 kDa
ORF2 pepII
CHO control
+ Flag-CFAP206 L
+ GFP-CFAP206 L
kDa
150
100
75
WB: α-pepI
WB: α-pepII
adult testis
α-pepII
α-ORF2-2A7
α-ORF2-4F5
B
nasal respiratory epithelium
testis
DIC
ac-TUB
CFAP206-pepII
DAPI
C
Xenopus skin MCCs
posterior — anterior
Cetn4-RFP
GFP-CFAP206
Tubg1
F-actin
ac. Tuba4a
basal foot
basal body

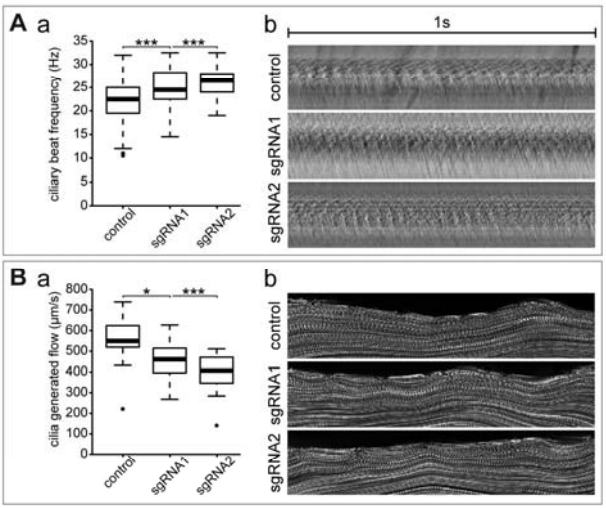
A a
ciliary beat frequency (Hz)
***
***
control
sgRNA1
sgRNA2
b
1s
control
sgRNA1
sgRNA2
B a
cilia generated flow (µm/s)
*
***
control
sgRNA1
sgRNA2
b
control
sgRNA1
sgRNA2

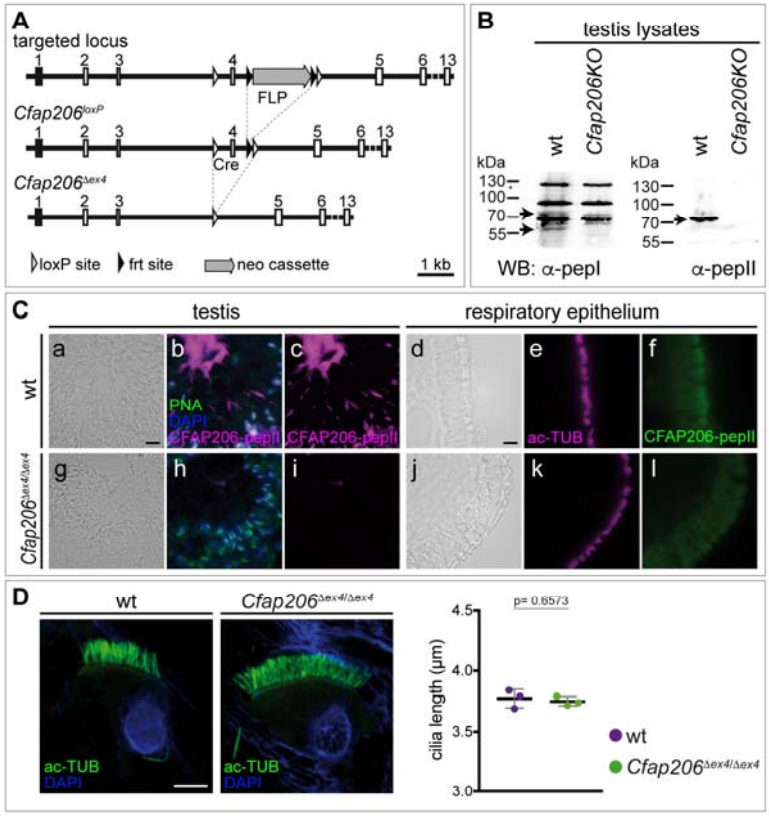
A
targeted locus
FLP
Cre
loxP site
frt site
neo cassette
1 kb
B
testis lysates
wt
Cfap206KO
kDa
WB: α-pepI
α-pepII
C
testis
respiratory epithelium
PNA
DAPI
CFAP206-pepII
ac-TUB
D
wt
ac-TUB
DAPI
p= 0.6573
cilia length (µm)

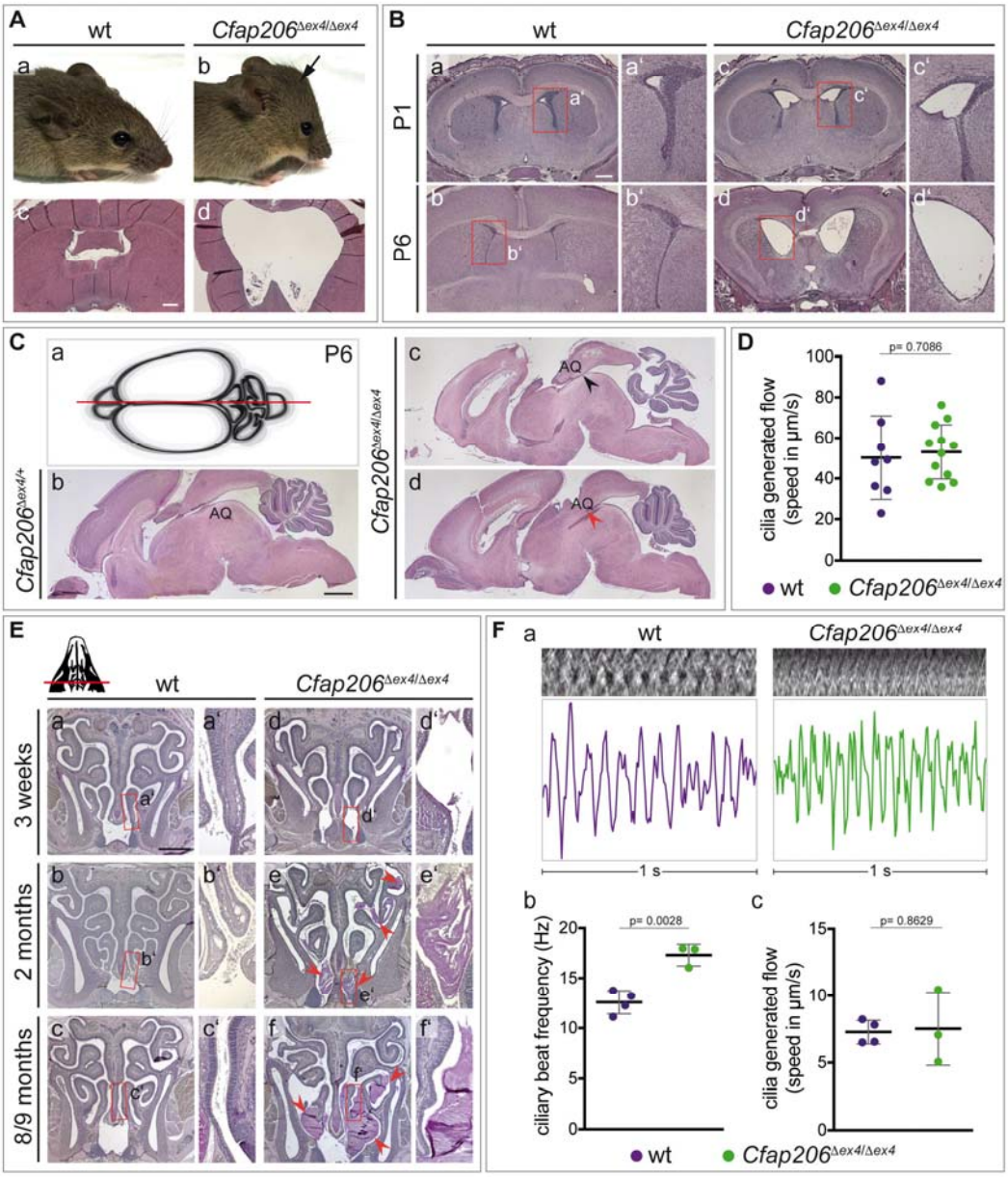
A
wt
Cfap206Δex4/Δex4
B
wt
Cfap206Δex4/Δex4
P1
P6
C
P6
Cfap206Δex4/+
Cfap206Δex4/Δex4
AQ
D
p= 0.7086
cilia generated flow (speed in µm/s)
wt
Cfap206Δex4/Δex4
E
wt
Cfap206Δex4/Δex4
3 weeks
2 months
8/9 months
F
wt
Cfap206Δex4/Δex4
1 s
ciliary beat frequency (Hz)
p= 0.0028
p= 0.8629
cilia generated flow (speed in µm/s)

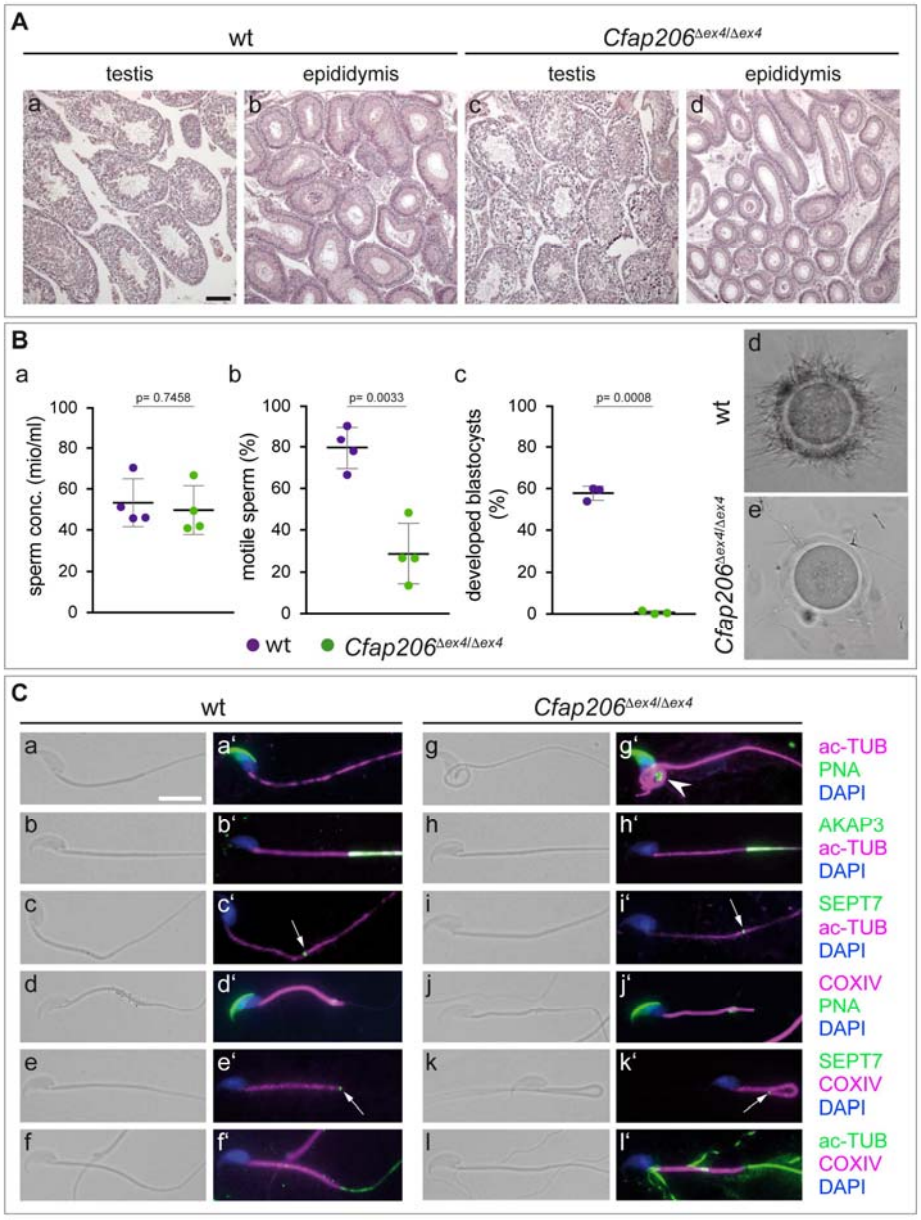
A
wt
Cfap206Δex4/Δex4
testis
epididymis
testis
epididymis
a
b
c
d
B
a
b
c
p= 0.7458
p= 0.0033
p= 0.0008
sperm conc. (mio/ml)
motile sperm (%)
developed blastocysts (%)
100
80
60
40
20
0
wt
Cfap206Δex4/Δex4
d
e
wt
Cfap206Δex4/Δex4
C
wt
Cfap206Δex4/Δex4
ac-TUB
PNA
DAPI
AKAP3
ac-TUB
DAPI
SEPT7
ac-TUB
DAPI
COXIV
PNA
DAPI
SEPT7
COXIV
DAPI
ac-TUB
COXIV
DAPI

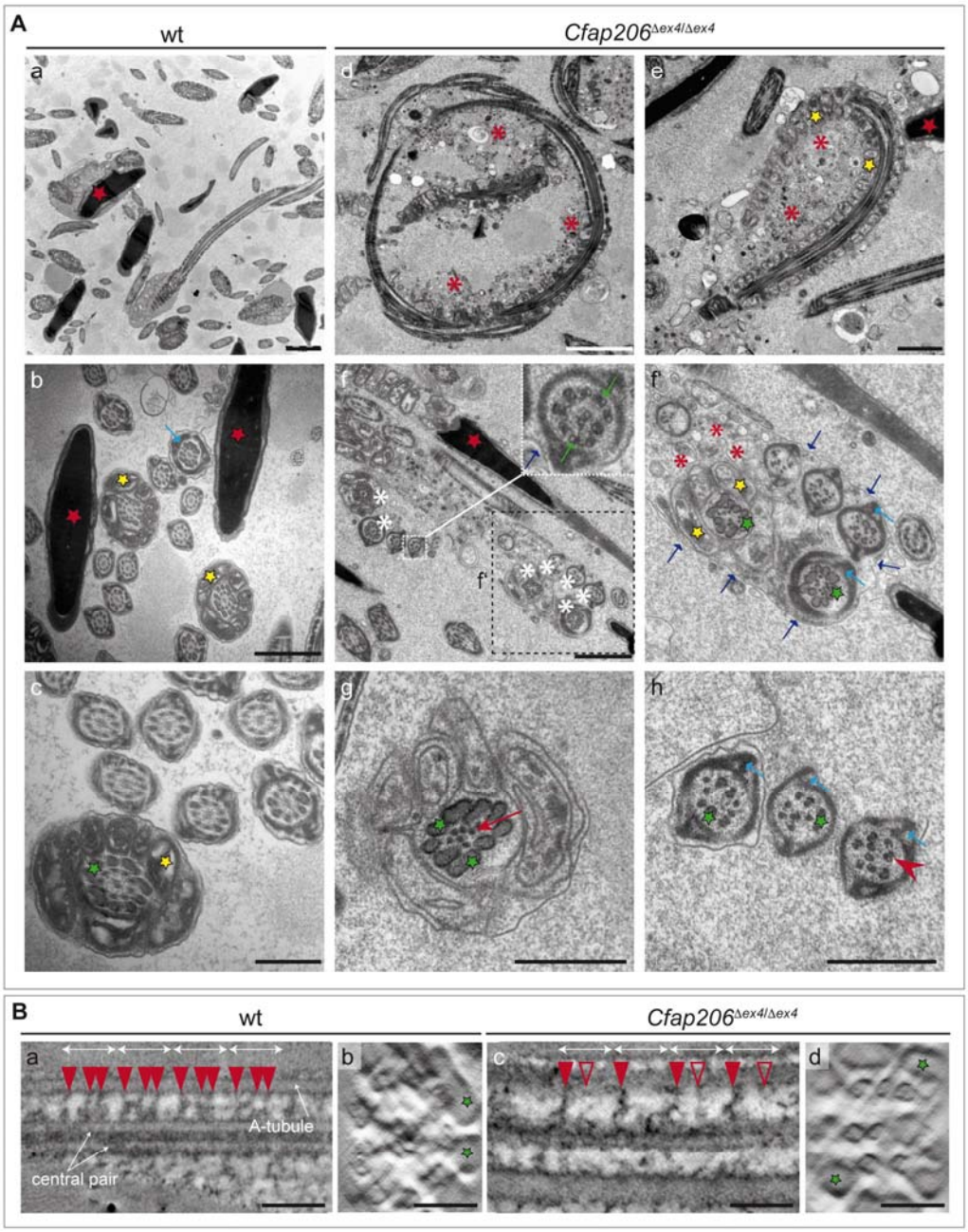
A
wt
Cfap206Δex4/Δex4
a
d
e
b
f
f'
f'
c
g
h
B
wt
Cfap206Δex4/Δex4
a
b
c
d
A-tubule
central pair

Original research chapter II:

PCD independent laterality defects

A Conserved Role of the Unconventional Myosin 1d in Laterality Determination

Report

Current Biology

A Conserved Role of the Unconventional Myosin 1d in Laterality Determination

Graphical Abstract

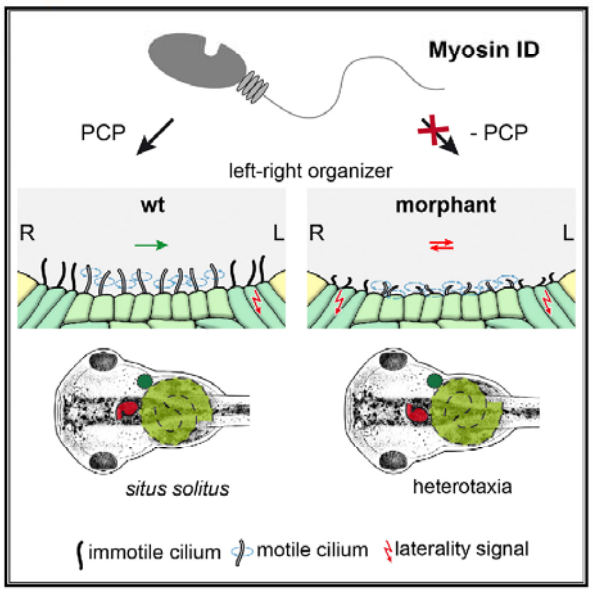

Authors

Melanie Tingler, Sabrina Kurz, Markus Maerker, ..., Janine M. LeBlanc-Straceski, Stéphane Noselli, Martin Blum

Correspondence

martin.blum@uni-hohenheim.de

In Brief

Tingler et al. show that myosin 1D is required for laterality in the frog *Xenopus*, namely for left-asymmetric gene expression and leftward flow. Myosin 1D acts through the planar cell polarity pathway, a key feature of asymmetric gonad and gut morphogenesis in *Drosophila*, suggesting a common evolutionary origin of arthropod and chordate laterality.

Highlights

- The unconventional myosin 1D is required for vertebrate left-right asymmetry
- Loss of *myo1d* causes aberrant leftward flow and laterality defects in *Xenopus*
- The function of myosin1D is mediated through the planar cell polarity pathway
- Myosin 1D links laterality in arthropods and chordates

Tingler et al., 2018, Current Biology *28*, 810–816
March 5, 2018
https://doi.org/10.1016/j.cub.2018.01.075

CellPress

Current Biology
Report

A Conserved Role of the Unconventional Myosin 1d in Laterality Determination

Melanie Tingler,[1,4] Sabrina Kurz,[1,4] Markus Maerker,[1,4] Tim Ott,[1,4] Franziska Fuhl,[1,4] Axel Schweickert,[1] Janine M. LeBlanc-Straceski,[2] Stéphane Noselli,[3] and Martin Blum[1,5,*]
[1]University of Hohenheim, Institute of Zoology, Garbenstrasse 30, 70593 Stuttgart, Germany
[2]Department of Biology, Merrimack College, 315 Turnpike Street, North Andover, MA 01845, USA
[3]Université Côte d'Azur, CNRS, INSERM, Institut de Biologie Valrose, Parc Valrose, 06108 Nice, France
[4]These authors contributed equally
[5]Lead Contact
*Correspondence: martin.blum@uni-hohenheim.de
https://doi.org/10.1016/j.cub.2018.01.075

SUMMARY

Anatomical and functional asymmetries are widespread in the animal kingdom [1, 2]. In vertebrates, many visceral organs are asymmetrically placed [3]. In snails, shells and inner organs coil asymmetrically, and in *Drosophila*, genitalia and hindgut undergo a chiral rotation during development. The evolutionary origin of these asymmetries remains an open question [1]. Nodal signaling is widely used [4], and many, but not all, vertebrates use cilia for symmetry breaking [5]. In *Drosophila*, which lacks both cilia and Nodal, the unconventional *myosin ID* (*myo1d*) gene controls dextral rotation of chiral organs [6, 7]. Here, we studied the role of *myo1d* in left-right (LR) axis formation in *Xenopus*. Morpholino oligomer-mediated *myo1d* downregulation affected organ placement in >50% of morphant tadpoles. Induction of the left-asymmetric Nodal cascade was aberrant in >70% of cases. Expression of the flow-target gene *dand5* was compromised, as was flow itself, due to shorter, fewer, and non-polarized cilia at the LR organizer. Additional phenotypes pinpointed Wnt/planar cell polarity signaling and suggested that *myo1d*, like in *Drosophila* [8], acted in the context of the planar cell polarity pathway. Indeed, convergent extension of gastrula explant cultures was inhibited in *myo1d* morphants, and the *ATF2* reporter gene for non-canonical Wnt signaling was downregulated. Finally, genetic interference experiments demonstrated a functional interaction between the core planar cell polarity signaling gene *vangl2* and *myo1d* in LR axis formation. Thus, our data identified *myo1d* as a common denominator of arthropod and chordate asymmetry, in agreement with a monophyletic origin of animal asymmetry.

RESULTS AND DISCUSSION

The Unconventional *myosinID* Gene Is Required for LR Axis Formation in *Xenopus laevis*

We have previously shown that maternal and zygotic Myo1d is present in the *Xenopus* egg cell and throughout the first 3 days of embryogenesis [9], i.e., before, during, and after left-right (LR) symmetry breaking [5]. Zygotic mRNA expression was predominantly found in presomitic mesoderm and somites [9], tissues related to the *Xenopus* LR organizer (LRO) [5]. To assess a possible function of *myo1d* in *Xenopus* LR axis formation, an antisense morpholino oligomer (MO) was designed that targeted sequences overlapping the translational start site (AUG-MO). AUG-MO was injected at the 4-cell stage and targeted toward the LRO. Specimens were cultivated until they reached stages 24, 32, or 45 to investigate *nodal1* or *pitx2* expression and organ situs, respectively. Organ placement, as assessed by heart and gut looping as well as positioning of the gall bladder (Figure 1A), was significantly disturbed in specimens injected with AUG-MO (Figures 1B–1D). Likewise, left-asymmetric expression of *nodal1* and *pitx2* were disturbed in >70% of AUG-MO-injected morphants, with bilateral expression in the left and right lateral plate mesoderm (LPM) representing the most commonly observed defective pattern (Figures 1E and 1F; Figures S1A–S1H). Remarkably, AUG-MO caused phenotypes at very low doses (0.2 pmol or 3.3 ng per embryo). Furthermore, a scrambled mismatch MO (MM-MO) did not affect the laterality of injected embryos (Figures 1E and 1F). In addition, Myo1d protein was downregulated in morphant embryos, as shown by western blot analysis (Figure S1I). A full-length *myo1d* expression construct [10] that was not targeted by AUG-MO partially rescued left-asymmetric *nodal1* expression in the LPM (Figure 1E). Together, these experiments argue for MO specificity. Bilateral *nodal1/pitx2* expression, observed in the majority of LR-altered *myo1d* morphants (75%; *cf.* Figures 1E and 1F), also occurs when the midline barrier function is disturbed [11], i.e., when Nodal1 protein crosses from the left to the right side. However, the midline in *myo1d* morphants was normal, as shown by the wild-type expression pattern of the midline barrier gene *lefty1* (Figures S1J and S1K).

To confirm the MO-derived LR phenotypes, we created CRISPR/Cas9 F0 mutants in *Xenopus laevis*. Two guide RNAs were designed, targeting subdomains of the ATP-binding site

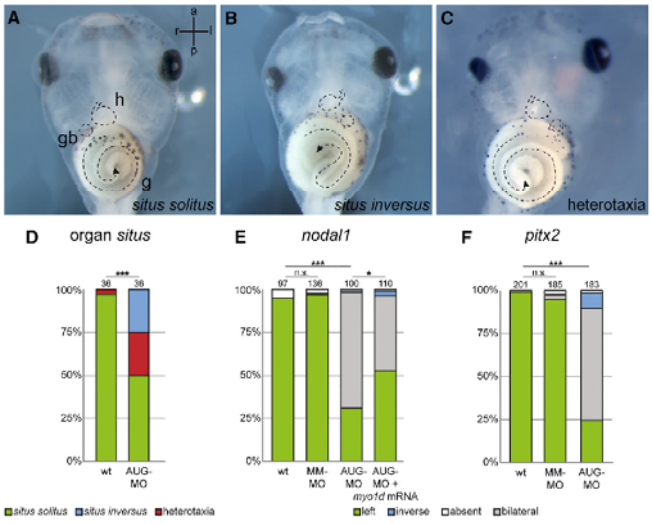

Figure 1. *myo1d* Is Required for LR Axis Formation in *Xenopus laevis*

(A–D) Organ situs in wild-type (A) and *myo1d* morphant tadpoles displaying situs inversus (B) and heterotaxia (C) at stage 45. g, gut; gb, gall bladder, h, heart.

(D) Quantification of organ situs analysis.

(E and F) Quantification of *nodal1* (E) and *pitx2* (F) expression patterns in wildtype embryos and specimens injected with MM-MO, AUG-MO or co-injected with AUG-MO and rescue mRNA. Numbers represent analyzed specimens, which were derived from 3 (D and E) and 5 (F) independent experiments.

See also Figure S1.

(Figure 2A), which were separately co-injected together with Cas9 protein into 1-cell-stage embryos [12]. Both resulted in identical ranges of phenotypes (Figures 2B and 2C): at least half the embryos were severely malformed, with gastrulation and blastopore closure defects, preventing the analysis of marker gene expression. Importantly, these phenotypes were encountered upon the injection of high doses of AUG-MO as well (data not shown). The remaining injected F0 specimens were evaluated for *pitx2* expression. About 60% lacked asymmetry and showed absent or bilateral *pitx2* expression (Figure 2D); remarkably, these embryos were also stunted, i.e., revealed a convergence extension phenotype (Figure 2C). The remaining specimens appeared normal and displayed left-asymmetric *pitx2* expression (Figures 2C and 2D). F0 *myo1d* mutants thus closely resembled *myo1d* morphants, as in both cases asymmetric marker gene expression was lost. Differences were recorded, however, namely that in morphants, Nodal cascade gene expression was bilateral in the vast majority of cases, while it was absent or bilateral in mutants. Although we lack a conclusive explanation at this time, beyond realizing that gene knockdowns differ from mosaic F0 mutants, genome editing provided additional proof of MO specificity, as in both cases the same quality of LR defect was observed, i.e., loss of asymmetry. In summary, these experiments demonstrated a role for *myo1d* in LR axis formation in *Xenopus*.

myo1d Is Required for LRO Morphogenesis and Leftward Flow

Induction of the left-asymmetric Nodal cascade in the LPM of the 2-day embryo is preceded by several well-defined morphogenetic and molecular steps, beginning with the specification of the LRO precursor, the so-called superficial mesoderm (SM), which forms caudal to the Spemann organizer at mid-gastrula stages [5, 13] (Figure S2A). The SM was not affected in *myo1d* morphants, as demonstrated by the expression of marker genes *foxj1* and *wnt11b* [14] (Figures S2B–S2E). The LRO in the frog is represented by the transient ciliated epithelium of the gastrocoel roof plate (GRP), which forms at the dorsal-posterior end of the primitive gut when SM cells involute during gastrulation [13, 15] (Figure S2A). We investigated whether the GRP had correctly formed in *myo1d* morphants using a Tektin isoform marker gene; *tekt2* expression was unaffected (Figures S2F and S2G), indicating that a GRP had formed. LRO function of the GRP arises when cilia develop and polarize in the central region of the GRP. As they become motile, they produce a leftward flow of extracellular fluids [16], which, presumably, is sensed by peripheral GRP cells harboring non-polarized and immotile cilia [1, 5].

To assess GRP morphogenesis, dorsal explants were prepared and analyzed for cilia by immunofluorescence (IF) using an antibody against acetylated alpha-tubulin. Figures 3A–3E show that, although cilia were present in morphant GRPs, ciliation was markedly altered. Cilia were significantly shorter, showed reduced polarization to the posterior pole of cells (a prerequisite of leftward flow), and were reduced in number (Figures 3F–3H). To determine if the flow itself was compromised, the transport of fluorescent microbeads was assessed using high-speed videography [16]. Time-lapse movies of GRPs show that flow was indeed disordered in *myo1d* morphants compared to wild-type specimens (Movie S1). Evaluation of flow parameters confirmed this disruption, with significantly reduced flow velocity and directionality in *myo1d* morphant specimens (Figures 3I and 3J). Importantly, some individual beads showed inverted movement, i.e., from left to right (Movie S1), in agreement with the observed predominant bilateral induction of asymmetric LPM marker genes (*cf.* Figures 1E and 1F). Leftward flow induces asymmetric LPM gene expression by downregulating the Nodal repressor *dand5* in lateral GRP cells (i.e., the purported flow sensor cells), where this gene is co-expressed with *nodal1* [17]. Expression of both genes was analyzed in dorsal explants isolated at post-flow stages (stage 19). Figures 3K–3O show that *nodal1* was unaffected in morphants, while *dand5* asymmetries were lost due to bilateral downregulation of mRNA expression. Expression of the

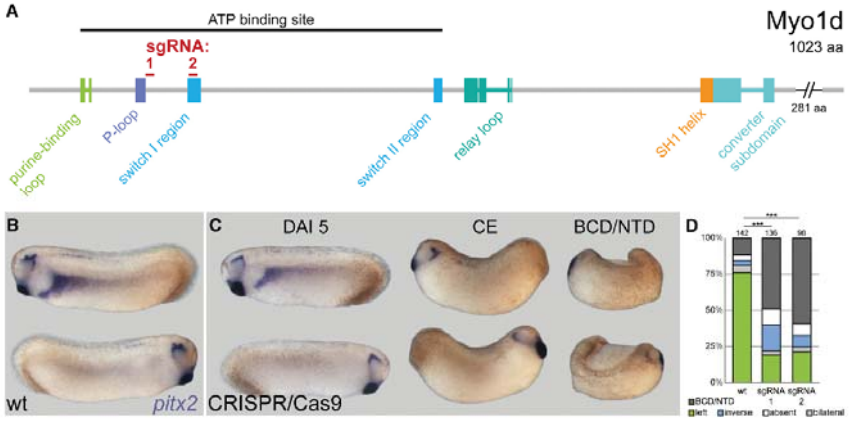

Figure 2. Laterality Defects in Genome-Edited F0 *myo1d* Mutant Tadpoles

(A) Schematic depicting Myo1d protein structure (sgRNA sites indicated).

(B and C) Appearance and *pitx2* gene expression in WT (B) and F0 *myo1d* mutant (C) tadpoles.

(D) Compilation of *pitx2* expression patterns. BCD, blastopore closure defect; NTD, neural tube closure defect. Note that mutant embryos with WT appearance showed WT *pitx2* expression in the left LPM, while stunted specimens with a convergent extension (CE) phenotype lacked expression or displayed mRNA expression on both sides.

transforming growth factor β (TGF-β) gene *gdf3*, the functional frog homolog of the Nodal agonist *Gdf1* in mouse, was unaltered in morphants (Figures S2H and S2I). In summary, these results demonstrated that *myo1d* was required for GRP morphogenesis and leftward flow and that downregulation of this conserved unconventional myosin resulted in a loss of molecular asymmetries and, consequently, a high frequency of heterotaxia (*situs ambiguus*) and *situs inversus* in morphant tadpoles (Figure 1).

PCP Defects in *myo1d* Morphant Frog Embryos

In *Drosophila*, *myo1d* interacts with both the global (Dachsous/Fat) and core (Frizzled/Wnt) PCP pathways to control chiral morphogenesis of the adult hindgut [8]. In the course of analyzing *myo1d* morphant *Xenopus* embryos, we noted a number of LR-unrelated developmental defects that have been linked to altered PCP signaling. First, the apical surface of GRP cells appeared enlarged in morphants as compared to wild-type (WT), suggesting a defect in apical constriction of involuting SM cells (*cf.* Figures 2A–2E). Apical constriction during gastrulation and neural tube closure is under the control of PCP [18]. Quantification of 25 cells each from 15 WT and 15 morphant embryos revealed that, on average, the cell surface in *myo1d* morphants was increased by 25% (Figure 4A). Second, neural tube closure was delayed in morphant embryos, i.e., the neural tube was still open at stage 18 when it had just closed in wild-type specimens (Figure 4B; Figures S3A and S3B; Movie S2). Delayed neural tube closure has been reported in the frog upon knockdown of *dishevveled2* (*dsh2*) and characterized as a convergent-extension (CE) defect that fails to narrow the midline [19]. In mouse embryos lacking one or both copies of the core PCP gene *vangl2*, the same phenotype was described [20]. Third, the ciliation of multi-ciliated cells (MCCs) in the larval skin of *myo1d* morphants was delayed. Ciliation of MCCs was much reduced on the morphant side of unilaterally injected stage 24 embryos, compared to the uninjected contralateral side (Figure S3C). No differences were recorded at stage 32, i.e., this phenotype represented a transient delay in MCC differentiation and apical intercalation (data not shown). MCC function was directly assessed by tracking fluorescent microbeads added to tadpoles. Figure 4C and Movies S3 and S4 demonstrate that defects observed at stage 24 were no longer present at stage 32 (data not shown). Such a transient delay in cilia extension of MCCs has previously been described upon *Foxn4* loss of function in *Xenopus* [21], and radial cell intercalation of MCC has been linked to PCP proteins Vangl2, Prickle3, and Disheveled [22]. Finally, the stunted appearance of F0 mutants with disturbed *pitx2* expression was reminiscent of a CE phenotype as well (*cf.* Figure 2C). Together, this evidence hinted at a more general role of *myo1d* in PCP signaling and CE.

To investigate *myo1d* function in the context of a well-established CE-Wnt/PCP assay, we employed Keller open-face explants [23]. Dorsal marginal zone tissue was isolated at stage 10–10.5 from WT and *myo1d* morphant embryos, and it was scored for CE when un-manipulated siblings reached stage 22 (Figure 4C). CE was classified into three categories, with class 0 representing explants without elongation, class 1 containing elongated specimens, and class 2 explants being those that were elongated and displayed a constriction (Figure 4C). While more than 90% of WT explants elongated, with the relative majority of specimens falling into class 2 (23/54, 43%), CE was severely compromised in *myo1d* morphants, with significantly reduced class 2 extensions (6/44), the relative majority of specimens elongating without constriction, and about 25% not

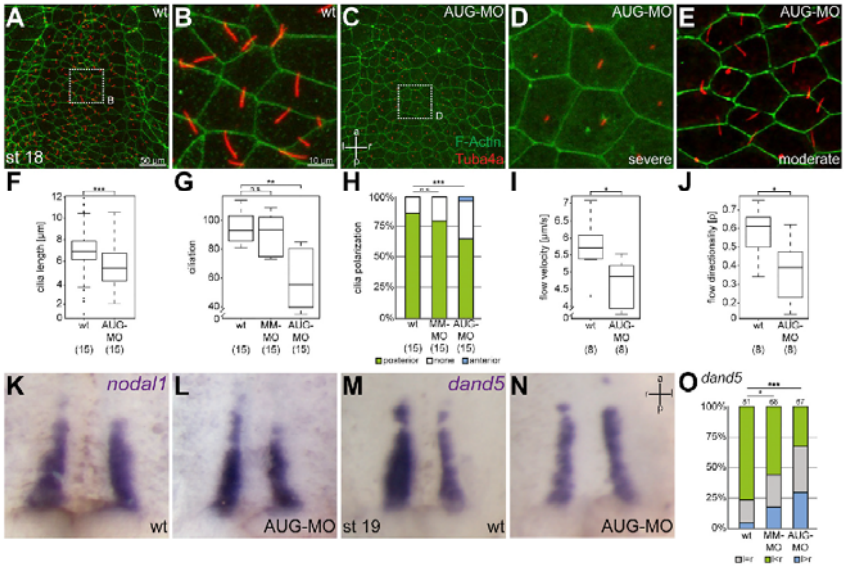

Figure 3. *myo1d* Is Required for GRP Morphogenesis and Leftward Flow

(A–E) GRP ciliation. Dorsal explants were prepared and analyzed for the presence and polarization of cilia by immunofluorescence using an antibody against acetylated alpha-tubulin. Counterstaining of actin using Phalloidin highlighted cell boundaries.

(A) Wild-type (blow-up shown in B).

(C) *myo1d* morphant.

(D and E) Blowups of severe phenotype shown in (D) and of moderate phenotype shown in (E).

(F–J) Quantification of cilia lengths (F), ciliation rate (G), cilia polarization (H), flow velocity (I), and flow directionality (J).

(K and L) Wild-type expression of *nodal1* in control (K) and *myo1d* morphant (L) stage 19 embryo.

(M–O) Asymmetrical *dand5* expression in lateral GRP cells of wild-type control embryo (M) was lost in *myo1d* morphant specimen (N).

(O) Quantification of *dand5* expression patterns.

(K)–(N) are shown at the same magnification.

Numbers represent analyzed specimens, which were derived from 3 (A–H), 2 (I and J), and 5 (K–O) independent experiments. For the assessment of cilia polarization, 15 cilia were analyzed per explant, for cilia lengths 30 cilia per GRP, and the ciliation rate was determined upon evaluating the entire GRP. See also Figure S2 and Movie S1.

elongating at all (class 1, 24/44, 61%; Figure 4C). Finally, an *ATF2*-based luciferase reporter was analyzed to monitor non-canonical Wnt signaling in *Xenopus* [24]. The reporter gene, alone or in combination with different concentrations of *myo1d* AUG-MO, was injected into the neural lineage at the 4-cell stage, neural plate explants were prepared at stage 14/15, and luciferase activity was recorded (Figure S3D). Compared to WT specimens, the reporter gene activity was dose-dependently downregulated in morphants (Figure S3D). In summary, these analyses of LR-unrelated phenotypes demonstrated that *myo1d* acted on non-canonical Wnt/PCP signaling and CE in the broader sense.

Functional Interaction between the Core PCP Signaling Gene *vangl2* and *myo1d* in LR Axis Formation in *Xenopus*

Finally, we asked whether PCP signaling and *myo1d* interacted during LR axis specification. Knockdown of the core PCP gene *vangl2* in *Xenopus* has been shown to disrupt cilia polarization and LPM *nodal1* expression [25]. For gene knockdown of *vangl2*, a combination of two previously characterized antisense MOs was injected [26]. To analyze the potential genetic interaction of *vangl2* and *myo1d*, MO doses were reduced such that individual knockdowns resulted in greatly attenuated phenotypes. When MOs were co-injected, LR phenotypes were observed, as documented for the expression of LPM *pitx2* (Figure 4D). These experiments unequivocally showed that *myo1d* was required for PCP-dependent determination of the LR axis in *Xenopus* in much the same way as in the fruit fly *Drosophila* [8]. A possible role of *myo1d* has been previously addressed by overexpression of a full-length expression construct [10]. Injections of high amounts of synthetic *myo1d* mRNAs (≥5 ng) resulted in 15% of specimens with heterotaxia, but the mechanism of action was not addressed in this study [10]. We were not able to reproduce this result; it is a hallmark of non-canonical Wnt signaling and PCP, however, that both gain- and loss-of-function manipulations result in qualitatively similar phenotypes [27].

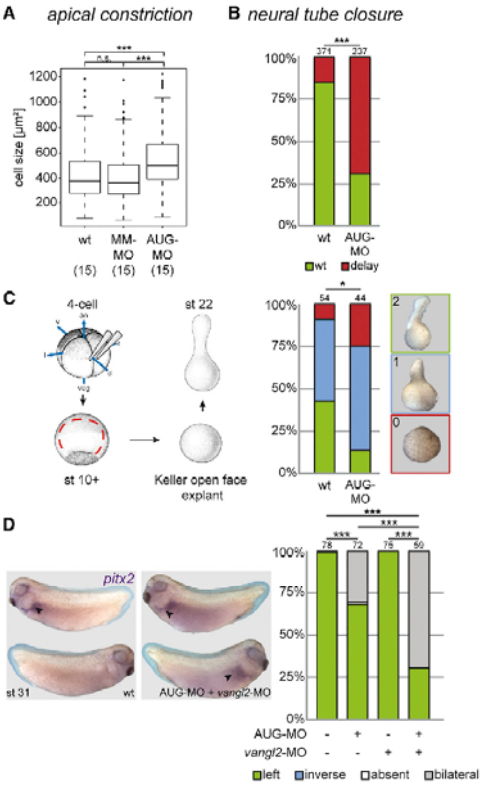

Figure 4. Functional Interaction between *myo1d* and PCP

(A and B) Morphant specimens displayed enhanced apical surfaces of GRP cells at stage 18 (A) and delayed neural tube closure at stage 18 (B).

(C) Convergent extension defects in Keller open-face explants of *myo1d* morphants at stage 22.

(D) Co-injection of *myo1d* AUG-MO with two antisense MOs directed against *vangl2* (at sub-phenotypic doses each) disrupted LR axis formation, as determined by expression of *pitx2* in the LPM. Numbers represent analyzed specimens, which were derived from 3 independent experiments for apical constriction defects of GRP cells, 7 experiments for neural tube closure delay, and 4 experiments for *myo1d* and *vangl2* interaction during LR axis formation. To determine the cell surface area, 25 cells from a central part of the GRP were analyzed in each case.

See also Figure S3 and Movies S2, S3, and S4.

The evolutionary origin of animal asymmetries has been controversially discussed in recent years [1, 28–30]. While morphological and functional asymmetries have been described in most phyla [1], there is no single common mechanism that accounts for asymmetric development. The Nodal cascade genes *nodal*, *lefty*, and *pitx2* are present and required for asymmetric development in lophotrochozoans (such as snails) and deuterostomes (sea urchins, uro- and cephalochordates as well as vertebrates), but they have not been described in ecdysozoans [1]. Cilia-driven leftward fluid flow at the LR organizer is a hallmark of some, but not all, chordates [1], and *Drosophila* as the sole ecdysozoan species studied in depth lacks Nodal and cilia but uses Myo1d, PCP, and the Hox gene *Abd-B* [7, 8] to achieve laterality. This diversity has been taken as evidence of multiple independent evolutionary pathways to establish LR asymmetry [31, 32].

Our finding of a role of *myo1d* in *Xenopus* LR development represents the first demonstration of a common denominator of ecdysozoan and deuterostome/chordate asymmetries. Interestingly, actomyosin-dependent asymmetric heart morphogenesis has recently been shown to depend on a right-sided instructive pathway that involves BMP signaling and, as a target, the homeobox gene *prrx1* [33]. It has been proposed that this BMP-Prrx1-actomyosin pathway is suggestive of a conserved role in laterality determination during bilaterian evolution [33], a notion that is fully supported by our data. Future studies will address the question of whether or not *myo1d* is involved in this pathway. Additionally, we uncovered a conserved link between PCP and *myo1d* in establishing LR asymmetry in flies and frogs. Interestingly, these results can be further generalized, as LR defects were also encountered in morphant and mutant CRISPR/Cas9 zebrafish embryos (S.N. and Max Furthauer, personal communication). Defects in zebrafish included shorter and mispolarized cilia, LRO morphogenetic defects, and aberrant leftward flow, resulting in absent Nodal cascade gene induction and organ situs distortions, and, most significantly, a genetic interaction with *vangl2* as well (S.N. and Max Furthauer, personal communication).

In conclusion, our data are consistent with a monophyletic origin of animal organ asymmetries. It may be beneficial to investigate other mechanisms of invertebrate asymmetries in vertebrate model organisms in the future (for which the frog *Xenopus* is particularly well suited [34]), such as the role of Hox genes, which may be involved in placing the LRO at the correct anterior-posterior position during development.

STAR★METHODS

Detailed methods are provided in the online version of this paper and include the following:

- KEY RESOURCES TABLE
- CONTACT FOR REAGENT AND RESOURCE SHARING
- EXPERIMENTAL MODEL AND SUBJECT DETAIL
- METHOD DETAILS
  - Plasmid construction
  - Immunfluorescence staining
  - Flow-analysis
  - Luciferase Assay
  - CRISPR/Cas9 mediated genome editing
  - Monoclonal Antibody Preparation
  - Western blot analysis
- QUANTIFICATION AND STATISTICAL ANALYSIS
  - Statistical analysis

SUPPLEMENTAL INFORMATION

Supplemental Information includes three figures and four movies and can be found with this article online at https://doi.org/10.1016/j.cub.2018.01.075.

ACKNOWLEDGMENTS

We are grateful to Michael Levin for sharing a full-length *myo1d* expression construct and to Susanne Bogusch, whose expert help was instrumental to cloning the rescue vector. Work in the Blum lab has been supported by DFG grants BL-285/9 and BL-285/10. S.K. and T.O. have been recipients of fellowships from the Landesgraduiertenförderung Baden-Württemberg. S.K. was also funded by the Federal Ministry of Education and Research (01PL11003), project Humboldt reloaded. J.M.L.-S. gratefully acknowledges several students in her 1998–2015 Molecular Biology and Biotechnology and Directed Research courses, especially G. Angelini, K. Ganser, S. Saldi, N. McIver, and B. Sickler; the Merrimack College Faculty Development Grant Program; Murray Fellowship; Yassini Award; NSF-RUI 0077516; and B. Bement, A. Sokac, S. Sokol, and members of his laboratory. Work in the Noselli lab was supported by grants from ANR (DRO-ASY ANR-13-BSV2-006, DroZeMyo, and LABEX SIGNALIFE ANR-11-LABX-0028-01).

AUTHOR CONTRIBUTIONS

M.B., M.T., A.S., and S.N. designed experiments. M.T., S.K., M.M., F.F., and J.M.L.-S. conducted experiments, with T.O. performing the CRISPR/Cas9 genome editing. M.B. wrote the manuscript with help from M.T., A.S., S.N., and J.M.L.-S.

DECLARATION OF INTERESTS

The authors declare no competing interests.

Received: October 19, 2017
Revised: January 1, 2018
Accepted: January 24, 2018
Published: February 22, 2018

REFERENCES

1. Blum, M., Feistel, K., Thumberger, T., and Schweickert, A. (2014a). The evolution and conservation of left-right patterning mechanisms. Development *141*, 1603–1613.
2. Coutelis, J.B., González-Morales, N., Géminard, C., and Noselli, S. (2014). Diversity and convergence in the mechanisms establishing L/R asymmetry in metazoa. EMBO Rep. *15*, 926–937.
3. Grimes, D.T., and Burdine, R.D. (2017). Left-Right Patterning: Breaking Symmetry to Asymmetric Morphogenesis. Trends Genet. *33*, 616–628.
4. Shiratori, H., and Hamada, H. (2014). TGFβ signaling in establishing left-right asymmetry. Semin. Cell Dev. Biol. *32*, 80–84.
5. Blum, M., Schweickert, A., Vick, P., Wright, C.V.E., and Danilchik, M.V. (2014b). Symmetry breakage in the vertebrate embryo: when does it happen and how does it work? Dev. Biol. *393*, 109–123.
6. Hozumi, S., Maeda, R., Taniguchi, K., Kanai, M., Shirakabe, S., Sasamura, T., Spéder, P., Noselli, S., Aigaki, T., Murakami, R., and Matsuno, K. (2006). An unconventional myosin in Drosophila reverses the default handedness in visceral organs. Nature *440*, 798–802.
7. Spéder, P., Adám, G., and Noselli, S. (2006). Type ID unconventional myosin controls left-right asymmetry in Drosophila. Nature *440*, 803–807.
8. González-Morales, N., Géminard, C., Lebreton, G., Cerezo, D., Coutelis, J.-B., and Noselli, S. (2015). The Atypical Cadherin Dachsous Controls Left-Right Asymmetry in Drosophila. Dev. Cell *33*, 675–689.
9. LeBlanc-Straceski, J.M., Sokac, A., Bement, W., Sobrado, P., and Lemoine, L. (2009). Developmental expression of Xenopus myosin 1d and identification of a myo1d tail homology that overlaps TH1. Dev. Growth Differ. *51*, 443–451.
10. McDowell, G.S., Lemire, J.M., Paré, J.-F., Cammarata, G., Lowery, L.A., and Levin, M. (2016). Conserved roles for cytoskeletal components in determining laterality. Integr. Biol. *8*, 267–286.
11. Meno, C., Shimono, A., Saijoh, Y., Yashiro, K., Mochida, K., Ohishi, S., Noji, S., Kondoh, H., and Hamada, H. (1998). lefty-1 is required for left-right determination as a regulator of lefty-2 and nodal. Cell *94*, 287–297.
12. Nakayama, T., Blitz, I.L., Fish, M.B., Odeleye, A.O., Manohar, S., Cho, K.W.Y., and Grainger, R.M. (2014). Cas9-based genome editing in Xenopus tropicalis. Methods Enzymol. *546*, 355–375.
13. Shook, D.R., Majer, C., and Keller, R. (2004). Pattern and morphogenesis of presumptive superficial mesoderm in two closely related species, Xenopus laevis and Xenopus tropicalis. Dev. Biol. *270*, 163–185.
14. Walentek, P., Schneider, I., Schweickert, A., and Blum, M. (2013). Wnt11b is involved in cilia-mediated symmetry breakage during Xenopus left-right development. PLoS ONE *8*, e73646.
15. Blum, M., Andre, P., Muders, K., Schweickert, A., Fischer, A., Bitzer, E., Bogusch, S., Beyer, T., van Straaten, H.W.M., and Viebahn, C. (2007). Ciliation and gene expression distinguish between node and posterior notochord in the mammalian embryo. Differentiation *75*, 133–146.
16. Schweickert, A., Weber, T., Beyer, T., Vick, P., Bogusch, S., Feistel, K., and Blum, M. (2007). Cilia-driven leftward flow determines laterality in Xenopus. Curr. Biol. *17*, 60–66.
17. Schweickert, A., Vick, P., Getwan, M., Weber, T., Schneider, I., Eberhardt, M., Beyer, T., Pachur, A., and Blum, M. (2010). The nodal inhibitor Coco is a critical target of leftward flow in Xenopus. Curr. Biol. *20*, 738–743.
18. Ossipova, O., Chuykin, I., Chu, C.-W., and Sokol, S.Y. (2015b). Vangl2 cooperates with Rab11 and Myosin V to regulate apical constriction during vertebrate gastrulation. Development *142*, 99–107.
19. Wallingford, J.B., and Harland, R.M. (2002). Neural tube closure requires Dishevelled-dependent convergent extension of the midline. Development *129*, 5815–5825.
20. Ybot-Gonzalez, P., Savery, D., Gerrelli, D., Signore, M., Mitchell, C.E., Faux, C.H., Greene, N.D.E., and Copp, A.J. (2007). Convergent extension, planar-cell-polarity signalling and initiation of mouse neural tube closure. Development *134*, 789–799.
21. Campbell, E.P., Quigley, I.K., and Kintner, C. (2016). Foxn4 promotes gene expression required for the formation of multiple motile cilia. Development *143*, 4654–4664.
22. Ossipova, O., Chu, C.-W., Fillatre, J., Brott, B.K., Itoh, K., and Sokol, S.Y. (2015a). The involvement of PCP proteins in radial cell intercalations during Xenopus embryonic development. Dev. Biol. *408*, 316–327.
23. Sive, H.L., Grainger, R.M., and Harland, R.M. (2007). Xenopus laevis Keller Explants. CSH Protoc. *2007*, pdb.prot4749.
24. Ohkawara, B., and Niehrs, C. (2011). An ATF2-based luciferase reporter to monitor non-canonical Wnt signaling in Xenopus embryos. Dev. Dyn. *240*, 188–194.
25. Antic, D., Stubbs, J.L., Suyama, K., Kintner, C., Scott, M.P., and Axelrod, J.D. (2010). Planar cell polarity enables posterior localization of nodal cilia and left-right axis determination during mouse and Xenopus embryogenesis. PLoS ONE *5*, e8999.
26. Prager, A., Hagenlocher, C., Ott, T., Schambony, A., and Feistel, K. (2017). hmmr mediates anterior neural tube closure and morphogenesis in the frog Xenopus. Dev. Biol. *430*, 188–201.
27. Wang, Y., and Nathans, J. (2007). Tissue/planar cell polarity in vertebrates: new insights and new questions. Development *134*, 647–658.
28. Boorman, C.J., and Shimeld, S.M. (2002). The evolution of left-right asymmetry in chordates. BioEssays *24*, 1004–1011.
29. Thompson, H., Shaw, M.K., Dawe, H.R., and Shimeld, S.M. (2012). The formation and positioning of cilia in Ciona intestinalis embryos in relation to the generation and evolution of chordate left-right asymmetry. Dev. Biol. *364*, 214–223.
30. Nakamura, T., and Hamada, H. (2012). Left-right patterning: conserved and divergent mechanisms. Development *139*, 3257–3262.

31. Okumura, T., Utsuno, H., Kuroda, J., Gittenberger, E., Asami, T., and Matsuno, K. (2008). The development and evolution of left-right asymmetry in invertebrates: lessons from Drosophila and snails. Dev. Dyn. *237*, 3497–3515.

32. Vandenberg, L.N., and Levin, M. (2013). A unified model for left-right asymmetry? Comparison and synthesis of molecular models of embryonic laterality. Dev. Biol. *379*, 1–15.

33. Ocaña, O.H., Coskun, H., Minguillón, C., Murawala, P., Tanaka, E.M., Galcerán, J., Muñoz-Chápuli, R., and Nieto, M.A. (2017). A right-handed signalling pathway drives heart looping in vertebrates. Nature *549*, 86–90.

34. Duncan, A.R., and Khokha, M.K. (2016). Xenopus as a model organism for birth defects-Congenital heart disease and heterotaxy. Semin. Cell Dev. Biol. *51*, 73–79.

STAR★METHODS

KEY RESOURCES TABLE

REAGENT or RESOURCE	SOURCE	IDENTIFIER
Antibodies		
Mouse monoclonal anti acetylated α tubulin	Sigma	T6793
Anti-mouse IgG (whole molecule) F(ab')2 fragment-Cy3	Sigma	C2181
Anti-mouse IgG (H+L), CF 405S	Sigma	SAB4600023
Alexa Fluor 488 Phalloidin	Invitrogen	A12379
Alexa Fluor 555 Phalloidin	Invitrogen	A34055
Chemicals, Peptides, and Recombinant Proteins		
Pfu DNA Polymerase	Promega	M7745
Cas9 with NLS	PNA BIO	CP01-50
FluoSpheres Carboxylate-Modified Microspheres, 0.5 μm, yellow-green fluorescent (505/515)	Invitrogen	F8813
Human chorionic gonadotropin (hCG)	Sigma	C0809-1VL
PureProteome NHS Flexibind Magnetic Beads	Milipore	LSKMAGA02
Laemmli sample buffer 2x	Sigma	S3401
Critical Commercial Assays		
MEGAshortscript T7 Transcription Kit	Thermo Fisher Scientific	AM1354
MEGAclear Transcription Clean-Up Kit	Thermo Fisher Scientific	AM1908
innuPREP DOUBLEpure Kit	Analytik Jena	845-KS-5050050
Ni-NTA affinity purification column	QIAGEN	N/A
EDTA-free Protease Inhibitor Cocktail	Roche	00000011873580001
Dual-Luciferase® Reporter Assay System	Promega	E1910
Experimental Models: Cell Lines		
BL21 Star One Shot cells	Invitrogen	C602003
Experimental Models: Organisms/Strains		
Xenopus laevis (female, male)	Nasco	https://www.enasco.com/xenopus/
Oligonucleotides		
sgRNA-RO: AAAAGCACCGACTCGGTGCCACTTTTTCAAGT TGATAACGGACTAGCCTTATTTTAACTTGCTATTTCTAGCT CTAAAAC	Merck	N/A
T7:sgRNA 1-FO: GCAGCTAATACGACTCACTATAGGTACT GCATGATGTACTTACGTTTTAGAGCTAGAAATAGCAAG	Merck	N/A
T7:sgRNA 2-FO: GCAGCTAATACGACTCACTATAGGGTT GTCGTTACGATTCGTCTGTTTTAGAGCTAGAAATAGCAAG	Merck	N/A
myo1d forward primer [5′ ATCCATGGCGGAACAAAGAGG GGCTGC 3′]	Sigma	N/A
myo1d reverse primer [5′ ATTCTAGATTAATTGGCTGGAAC ACTGAG 3′]	Sigma	N/A
Software and Algorithms		
Adobe Suite CS6: Photoshop and Illustrator	Adobe	N/A
ImageJ/Fiji	N/A	https://fiji.sc/
AxioVision 4.6	Zeiss	N/A
Zen 2012 Blue edition	Zeiss	https://www.zeiss.com
Statistical R-Gui	N/A	https://www.r-project.org/
RStudio	N/A	https://www.rstudio.com/

(*Continued on next page*)

CellPress

Continued

REAGENT or RESOURCE	SOURCE	IDENTIFIER
Other		
pET100/D-TOPO vector	Invitrogen	N/A
myo1d AUG-MO [5′ TGCAGCCCCTCTTGTTCCGCCATGT 3′]	GeneTools	N/A
myo1d mismatch-MO [5′ TGGACCCCGTCTTCTTCCCC CATGT 3′]	GeneTools	N/A
Axioplan2 imaging microscope	Zeiss	N/A
Zeiss LSM 700	Zeiss	N/A
GloMax® Explorer System	Promega	N/A
AxioCam HSm video camera	Zeiss	N/A
Xenbase	N/A	https://xenbase.org
PubMed	N/A	https://www.ncbi.nlm.nih.gov/pubmed/

CONTACT FOR REAGENT AND RESOURCE SHARING

Further information and requests for resources and reagents should be directed to and will be fulfilled by the Lead Contact, Martin Blum (martin.blum@uni-hohenheim.de).

EXPERIMENTAL MODEL AND SUBJECT DETAIL

For *in vivo* studies, *Xenopus laevis* was used as model organism. Frogs were obtained from Nasco (901 Janesville Avenue PO Box 901 Fort Atkinson). Handling, care and experimental manipulations of animals was approved by the Regional Government Stuttgart, Germany (Vorhaben A379/12 ZO "Molekulare Embryologie"), according to German regulations and laws (§6, article 1, sentence 2, nr. 4 of the animal protection act). Animals were kept at the appropriate condition (pH=7.7, 20°C) at a 12 h light cycle in the animal facility of the Institute of Zoology of the University of Hohenheim. Female frogs (4-20 years old) were stimulated with 25-75 units of human chorionic gonadotropin (hCG; Sigma), depending on weight and age, that was injected subcutaneously one week prior to oviposition. On the day prior to ovulation, female frogs were injected with 300-700 units of hCG. Eggs were collected into a petri dish by careful squeezing of the females, followed by *in vitro* fertilization. Sperm of male frogs was gained by dissecting of testes that were stored at 4°C in 1x MBSH (Modified Barth's Saline with HEPES).

METHOD DETAILS

Plasmid construction

The *myo1d*-CS2+ construct was a gift of Dr. Michael Levin (Tufts University). For generation of a rescue construct, *myo1d* was cloned into the CS2+ myc-tag vector that contained 5 myc sequences at the N terminus. The following primers were used for cloning:

myo1d forward primer: 5′ ATCCATGGCGGAACAAAGAGGGGCTGC 3′
myo1d reverse primer: 5′ ATTCTAGATTAATTGGCTGGAACACTGAG 3′

For *in vitro* synthesis of mRNA using the Ambion sp6 message kit, the plasmid was linearized with NotI.

Immunfluorescence staining

For immunofluorescence staining, embryos were fixed in 4% PFA for 1h at RT on a rocking platform, followed by 2 washes in calcium- and magnesium-free PBS (PBS$^-$) for 15 min each. For staining of GRP explants, embryos were dissected using a scalpel into anterior and posterior halves. Posterior halves (GRP explants) were collected and transferred to a 24 well plate and washed twice for 15 min in PBST. GRP-explants and whole embryos were blocked for 2h at RT in CAS-Block diluted 1:10 in PBST. The blocking reagent was replaced by antibody solution (anti acetylated tubulin antibody, diluted 1:700 in CAS-Block) and incubated overnight at 4°C. In the morning, the antibody solution was removed and explants/embryos were washed twice for 15 min in PBS$^-$. Finally, the secondary antibody (diluted 1:1000 in CAS-Block) was added together with Phalloidin (1:200) and incubated for a minimum of 3h at RT. Before photo documentation, embryos or explants were shortly washed in PBS$^-$ and transferred onto a microscope slide.

Flow-analysis

For analysis of leftward flow, dorsal posterior GRP-explants were dissected from stage 16/17 embryos in 1x MBSH [16]. GRP-explants were placed in a Petri dish containing fluorescent microbeads (diameter 0.5 μm; diluted 1:2500 in 1xMBSH) and incubated for a few seconds. Explants were transferred to a microscope slide which was prepared with Vaseline to create a small chamber

that contained fluorescent microbead solution; a coverslip was carefully pressed on to seal the chamber. Time lapse movies of leftward flow were recorded using an AxioCam HSm video camera (Zeiss) at 2 frames per second for 1 min using an Axioplan2 imaging microscope (Zeiss). For flow analysis, two open-source programs, ImageJ and statistical-R, were used. Using the Particle-Tracker plug-in from ImageJ, leftward flow was analyzed and particle movement was measured. Directionality and velocity of fluorescent microbeads were calculated using statistical-R.

Luciferase Assay

Luciferase reporter assays were carried out using the Promega Dual-Luciferase® Reporter Assay System. Embryos were injected at the 4-cell stage with AUG-MO, ATF2-luciferase DNA and Renilla DNA into the dorsal animal blastomeres, and neural tissue was dissected at stage 14/15 (*cf.* Figure S3D for a schematic depiction of the procedure [24];). Neural tissue was transferred into a 1.5 mL Eppendorf tube and the 0.1xMBSH buffer was removed, leaving the tissue moistened. The tissue was lysed and homogenized in 100 µl 1x passive lysis-buffer by pipetting the suspension up and down, followed by a 15 min incubation at RT. The lysate was centrifuged for 2 minutes at 14 000 rpm and the upper phase was transferred into a new tube. The lysate was re-centrifuged and two 25 µl aliquots (technical duplicates) were transferred into a 96well plate. 75 µl 1x Luciferase assay substrate was added through the GloMax® Explorer System and the luminescence was measured. This step was repeated with 75 µl 1x Stop and Glow reagents. To calculate the relative luciferase units (RLU in [%]) the ratio between luciferase and Renilla values was calculated and correlated to the wt control, which we set to 100%.

CRISPR/Cas9 mediated genome editing

sgRNA templates (under T7 promoter control) were generated using Pfu polymerase-mediated primer extension following *in vitro* synthesis (4 h) of the sgRNAs [12]. Prior to use, sgRNAs were denatured at 70°C for 2 min and immediately chilled on ice. Cas9 protein and sgRNAs were mixed and incubated at 37°C for 5 min to allow RNP formation. Zygotes were dejellied 20 min post fertilization and immediately injected with 8 nL of RNP mix. Injected embryos were cultivated for 12 h at 25°C to enhance cutting efficiency, followed by transfer to ambient temperature (20°C) until stage 28 was reached, when specimens were fixed for phenotype analysis.

Monoclonal Antibody Preparation

A monoclonal antibody, Mab4E12, was raised against the tail polypeptide NARNSNQFVSRSNE (aa834-847) of the *Xenopus laevis* myosin 1d L homolog (GenBank Accession Number AF540952.1) by AbPro, Woburn, MA, USA. A 828 bp tail region that included amino acids R729-N1007 was amplified by PCR from a cDNA clone optimized for expression in *E. coli* (GenScrpt), pXlMyo1d-opt, using the primers (Forward: CACCGCCGTTATAAAGTTAAAAGT; Reverse: TTATTAGTTTGCCGGAACAGACAG), and cloned into the pET100/D-TOPO vector (Invitrogen) to create pXlMyo1d-optTail2D. BL21 Star One Shot cells (Invitrogen) were transformed with this vector and expression of the 35 kDa fusion protein consisting of the myo1d tail and N terminus 6X His-tag was induced with IPTG. Cells were harvested after 1.5 hr of induction and the fusion protein was affinity purified using Ni-NTA affinity purification column from a cleared lysate under denaturing conditions (QIAGEN). The affinity purified tail polypeptide was cross-linked to PureProteome NHS Flexibind Magnetic Beads (Milipore), and Mab4E12 was purified following the manufacturer's instructions.

Western blot analysis

Embryos were injected at the 1-4 cell stage with 1 ng of MO and cultivated until stage 28. The antisense morpholino, AUG-MO, [5′ TGCAGCCCCTCTTGTTCCGCCATGT 3′] overlapped the start codon (underlined) of *myo1d*. The control mismatch morpholino MM-MO, [5′ TG**G**A**C**CCC**G**TCTT**C**TTCC**C**CCATGT 3′] was identical to the AUG-MO except for the five C/G mismatches (underlined and indicated by bold lettering). Embryo lysates were made by homogenizing 1 embryo in 20 µl of 4°C lysis buffer (50 mM Tris pH 8.0, 150 mMNaCl, 0.5% NP40 0.5 ml, 0.5% Triton X-100 0.5 ml, 1 mM EGTA) plus cOmplete, Mini, EDTA-free Protease Inhibitor Cocktail (Roche) and centrifuging at 13.000 x g for 10 min to remove cellular debris followed immediately by mixing the supernatant 1:1 with 2x Laemmli SDS sample buffer (SIGMA). Embryo lysates in Laemmli sample buffer were boiled for 5 min, snap cooled on ice, and spun to remove debris before loading onto gels. Bio-Rad Precision Plus Kaleidoscope markers and half-embryo equivalents were loaded per lane on Bio-Rad 4%–20% polyacrylamide precast gels at 100 V. Western blots were prepared using the Trans-Blot SD. Semi-Dry Transfer Cell at 15 V for 45 min. Blots were air-dried, blocked in 5% non-fat dry milk in TBS, rinsed and incubated in the affinity purified 4E12 monoclonal antibody at a concentration of 5 µg in 10 mL TBS overnight at 4°C. Blots were washed in TBS, re-blocked in 10% non-fat dry milk in TBS, rinsed and incubated with goat anti-mouse horseradish peroxidase (HRP) conjugated anti-mouse IgG (Jackson Labs) at 1:10.000 dilution for 1 hr at RT. After rinsing with TBS, chemiluminescent detection was performed using a peroxide-luminol/enhancer solution (Pierce) and GeneSnap image acquisition software on a SynGene gel documentation system.

QUANTIFICATION AND STATISTICAL ANALYSIS

Statistical analysis

Statistical calculations of marker gene expression patterns and cilia distribution were performed using Pearson's chi-square test (Bonferroni corrected) in statistical R. For statistical calculation of ciliation, cilia length, cell size, flow velocity and directionality Wilcoxon-Match-Pair test was used (RStudio).

Situs inversus and heterotaxy: the novel peptidase *tout de travers* (*TDT*) drives laterality development

Abstract

Abnormal organ chirality and/or placement occurs with an incidence of roughly 2 per 10 000 live births in humans. These so-called laterality defects are associated with severe health conditions that can already lead to intrauterine death. The group of Bruno Reversade identified loss-of-function mutations in a previously unannotated gene, which they termed *tout-de-travers* (*TDT*), in a cohort of patients with laterality defects. *TDT* encodes a conserved metzincin peptidase that is lost in deuterostomes without a fluid flow generating left-right organizer (LRO). This study confirms the laterality determining nature of *TDT* as *Xenopus* embryos phenocopied the human patients if the orthologues gene was depleted. Subsequent analysis revealed that Tdt acts downstream of the symmetry breaking leftward fluid flow and is required for the induction of the unilateral Nodal signaling cascade, which is instructive for the asymmetric organogenesis.

Introduction

Human laterality defects are rare occurring conditions in which the normal arrangement of the thoracoabdominal organs along the left-right axis, called *situs solitus* (SS), is disturbed. The International Working Group for Mapping and Coding of Nomenclatures for Paediatric and Congenital Heart Disease proposed a clinical definition that distinguishes two subcategories, namely *situs inversus* (SI) and heterotaxy (Jacobs et al., 2007). SI describes a complete mirror-imaged organ orientation relative to SS, which by itself is often but not necessarily associated with health constraints. Other *situs* variations are collectively referred to as heterotaxy and present severe disease states. However, there is disagreement in the field over the plausibility to separate SI from the category heterotaxy as the Greek-derived word heterotaxy translates literally as 'other arrangement' (Peeters and Devriendt, 2006). Differences in the definition and methodology make it difficult to compare epidemiological studies of laterality defects directly. A retrospective 12 years spanning, from 2002 to 2014, population-based study of live-born infants diagnosed with syndromic and non-syndromic laterality defects from Southern Nevada calculated a combined prevalence of 1.9 per 10 000 live births (Evans et al., 2015). The prevalence for heterotaxy was 1.3 per 10 000 live births versus 0.6 per 10 000 for SI (Evans et al., 2015). Severe forms of congenital heart disease, which require surgical intervention, are frequent comorbidities of *situs* anomalies and had a penetrance of more than 50 % (Evans et al., 2015).

The diverse group of syndromic laterality defects include various ciliopathies like polycystic kidney disease, Bardet-Biedl syndrome and most prominently primary ciliary dyskinesia (PCD) (Deng et al., 2014). An involvement of cilia in the process of laterality determination was first proposed by Björn Afzelius, who described 'a human syndrome caused by immotile cilia' that can lead to a complete Kartagener's triad of chronic

sinusitis, bronchiectasis and SI (Afzelius, 1977; Kartagener, 1933). This syndrome was later termed PCD (Sleigh, 1981) for which a large scale European survey concluded a prevalence of diagnosed cases in 5 to 14 year olds ranging from 1 to 2 per 10 000 (Kuehni et al., 2010). Laterality defects occur in affected individuals as predicted by Björn Afzelius in an almost random manner with a prevalence of 6.3 % for heterotaxy, 47.7 % for SI and 46.0 % for SS (Kennedy et al., 2007). Since then, a central and ancestral role of cilia during deuterostome symmetry breakage was proposed and systematically unraveled in vertebrate model systems.

The specification of the vertebrate left-right axis, in its most reduced form, relies on the action of a ciliated epithelium, called left-right organizer (LRO), which arises in the early embryo at the posterior notochord and varies species-dependent in shape. LRO precursor cells are collectively specified by the transcription factor and master regulator of motile cilia Forkhead box J1 (Foxj1) (Stubbs et al., 2008). However, the mature LRO is composed of two distinct types of monociliated cells (McGrath et al., 2003). Lateral LRO cells project non-polarized (Schweickert et al., 2007), immotile sensory cilia (Yoshiba et al., 2012) and express a defined set of morphogenes namely an orthologue of the transforming growth factor beta (TGF-β) superfamily member *nodal homolog 1* (*nodal1*) (Collignon et al., 1996; Lowe et al., 1996) as well as its inhibitor *DAN domain BMP antagonist family member 5* (*dand5*) (Pearce et al., 1999). Cilia of the central LRO cells are motile, posteriorly polarized (Okada et al., 2005) by the planar cell polarity pathway (Hashimoto et al., 2010) and rotate in a counterclockwise fashion, thereby generating a transient leftward fluid flow over the LRO epithelium (Nonaka et al., 1998). This fluid flow represents the symmetry-breaking stimulus (Schweickert et al., 2007), which is believed to be sensed by the sensory cilia of the lateral LRO cells (Yoshiba et al., 2012). Flow sensing most likely

involves a heteromeric ciliary sensor complex consisting of the multi-pass transmembrane proteins Polycystin 1 like 1, transient receptor potential channel interacting (Pkd1l1) (Field et al., 2011; Kamura et al., 2011) and Polycystin 2, transient receptor potential cation channel (Pkd2) (Yoshiba et al., 2012), that form a cation-permeable channel. Although the precise nature of the Pkd1l1-Pkd2 sensor complex activation and action remains enigmatic, *dand5* gets posttranscriptionally downregulated (Nakamura et al., 2012) in the left-sided sensor cells, as a response (Yoshiba et al., 2012). *dand5* downregulation was recently shown to be BicC family RNA binding protein 1 (Bicc1) dependent (Minegishi et al., 2020) and leads ultimately to the release of Nodal1 on the left side of the LRO. This release of repression mode for unilateral Nodal1 activation consecutively allows its long-range transfer through the extracellular matrix to the left lateral plate mesoderm (LPM) (Oki et al., 2007). There, Nodal1 initiates the so-called Nodal signaling cascade, which involves its self-induction (Levin et al., 1995; Saijoh et al., 2000), activation of its feedback-inhibitor and TGF-β superfamily member *left-right determination factor* (*lefty*) (Meno et al., 1996; Saijoh et al., 2000) as well as a specific isoform of the transcription factor *paired like homeodomain 2* (*pitx2*) (Ryan et al., 1998; Schweickert et al., 2000). Lefty limits Nodal signaling spatio-temporally, whereas Pitx2 mediates and orchestrates the asymmetric organogenesis.

Epidemiological data for cilia independent genetic laterality defects are missing but analysis of the underlying genes holds great potential to deepen our current understanding of vertebrate laterality determination and to reveal previously unknown processes.

Bruno Reversade's group identified one such factor, a formerly unannotated gene encoding a highly conserved peptidase, which was found to be mutated in 14

consanguineous families with non-syndromic laterality defects. They termed this overlooked human gene *tout-de-travers* (*TDT*), French for ‘everything inverted’. According to the MEROPS classification system for peptidases, TDT belongs in the subclan of metzincins MA(M) to the M8 family that encompasses GP63, also known as leishmanolysin, and its homologues (Rawlings et al., 2018). MA(M) subclan members are unified by the presence of the non-exclusive MA clan feature, a HEXXH motif, in combination with a methionine-turn (Met-turn) (Bode et al., 1993; Rawlings et al., 2018). The Glutamic acid of the HEXXH motif exerts catalytic function whereas the two histidins together with a more C-terminal histidine, glutamic or aspartic acid serve as Zn^{2+} ligands (Matthews et al., 1972; Rawlings et al., 2018). The Met-turn is a structural element in direct C-terminal proximity to the HEXXH motif (Bode et al., 1993).

GP63, the prototype M8 family peptidase, was identified as the major surface protein of *Leishmania* promastigotes (Lepay et al., 1983), the infective stage of this dimorphic protozoan parasite that causes leishmaniasis (Sunter and Gull, 2017). Flagellate promastigotes can be transmitted by sandflies to humans, where they invade phagocytic cells, typically macrophages, develop into aflagellate amastigotes, multiply by binary fission, break down their host cell and get phagocytosed again (Sunter and Gull, 2017). The *Leishmania* life cycle is closed with ingestion of infected cells by sandflies, allowing the amastigotes to develop into promastigotes in the digestive tract followed by two additional replication events, separated by the migration to the proboscis (Sunter and Gull, 2017). Virulence of *Leishmania* centrally depends on GP63, since it facilitates tissue invasion by degrading extra cellular matrix proteins (Mcgwire et al., 2003), protects from complement mediated lysis (Brittingham et al., 1995), enhances phagocytic uptake (Mosser and Edelson, 1985) and modulates massively the host cell physiology (Isnard et al., 2012). GP63 is synthesized as

preproprotein and appears to be membrane-bound, via either a glycosylphosphatidylinositol (GPI) anchor (Etges et al., 1986) or a potential transmembrane domain (Ramamoorthy et al., 1992). Additionally, GP63 can be directly secreted into the extracellular environment of the parasite (McGwire et al., 2002) or is released on exosomes (Marshall et al., 2018).

Homologues of *GP63* exist in all three domains of life and a duplication event at the base of Deuterostomia generated *leishmanolysin like peptidase* (*LMLN*) and *TDT*, meanwhile annotated as *leishmanolysin like peptidase 2* (*LMLN2*) in the human genome.

Vertebrate LMLN and the *Drosophila* homologue Invadolysin were studied in some detail. Localization-wise, metazoan LMLN, which generally seems not to be GPI-anchored, was found at the leading edge of migrating cells, at the surface of lipid droplets, to be directly secreted or released on vesicles. Functionally, LMLN was described to be involved in cell migration, mitotic progression (McHugh et al., 2004), normal mitochondria physiology and lipid storage (Cara et al., 2013).

Contrary to that, LMLN2/TDT function has never been assessed before. Therefore, this collaborative study was destined to dissect the role of TDT during laterality determination in the African clawed frog *Xenopus laevis* in parallel with the Reversade group who utilize the zebrafish *Danio rerio* for the same purpose.

Results

In silico identification and analysis of *Xenopus tdt* on DNA and protein level

In search of *Xenopus tdt*, a Translated Basic Local Alignment Search Tool Nucleotide (TBLASTN) query, with the 733 long amino acid sequence of human TDT, identified two cDNAs. By sequence similarity, the records with the accession numbers XM_018235608 and XM_018259585 were attributed to encode for the 667 amino acids long Lmln and for the 720 amino acids long Tdt, respectively. Both cDNA entries based on gene models, which were predicted by Gnomon, the National Center for Biotechnology Information (NCBI) eukaryotic gene prediction tool. The identity of *Xenopus tdt* was further confirmed, as the gene arrangement between the corresponding loci on the human chromosome 14 and chromosome 1L of *Xenopus*, was found to be largely conserved.

Further, the MEROPS database entry MER0180031 for human TDT allowed the annotation of the catalytic site (CS) residues and of the conserved Met-turn methionine, for the provisional *Xenopus* Tdt (Figure 1A). Analysis of the Tdt amino acid sequence via SignalP-5.0, PredGPI and TMHMM predicted a N-terminal signal peptide (SP), absence of an GPI-anchor and a C-terminal transmembrane domain (TM), respectively.

tdt is alternatively spliced and expressed in LRO precursor cells

In order to gain an entry point for *in vivo* experiments that could shed light on the physiological function of TDT in the context of laterality determination, a spatiotemporal

expression analysis of *Xenopus tdt* mRNA was required. Primers were designed to amplify full-length (FL) *tdt*, for cloning and subsequent synthetization of an antisense RNA *in situ* hybridization (ISH) probe. RT-PCR was performed on cDNAs from representative stages, covering the first week of *Xenopus* development.

The cloning process disclosed alternative splicing of the 15 *tdt* exons (Figure 1A). In total, 12 distinct transcript variants (*v1–12*) were identified, including the FL isoform (*v1*), from 39 positive samples. Interestingly, exons 3–8 and exon 11 used alternative splice donor or acceptor sites, varying only between plus or minus one or two bases. Usage of these alternative splice sites either destroyed the normal reading frame (*v2–4* & *v8–11*) or preserved it (*v6* & *v7*). Single or multiple exon skipping events occurred in nine variants (*v4–12*), whereas intron retention was only seen in one transcript (*v7*). Of note, the CS, encoded by exons 6–8, is only present in four isoforms (*v1*, *v3*, *v6* & *v7*).

The whole mount RNA ISH with a *tdt* antisense probe (Figure 1B) detected weak expression in the animal hemisphere during cleavage stages. Strong zygotic *tdt* expression started during gastrulation between stage 10.5 and 11 in cells of the involuting marginal zone (IMZ), along a dorsoventral gradient with strongest expression on the dorsal side. Dorsal IMZ cells include the LRO precursors, which are internalized during gastrulation with the endo- and mesodermal cell mass. *tdt* expression remained during gastrulation in the blastoporal field. Early neurulae of stage 14 showed strong *tdt* expression in cells of the circumblastoporal collar (CBC), a structure that all cells pass as they enter the LRO. Cellular transition from the CBC into the LRO is accompanied by a damped *tdt* signal. Another strong *tdt* expression domain was temporarily established in the ventral blood islands (VBI) of early tailbud stages, which peaked around stage 27. Additionally, these embryos showed weak *tdt*

staining throughout the anterior region, limited to non-endodermal tissues in more posterior regions.

Taken together, transcripts in the LRO and in its precursor cells point to a conserved function of *tdt* during laterality determination.

Tdt localizes to vesicular structures

Presence of an N-terminal signal peptide as well as a C-terminal transmembrane domain, indicated that Tdt may localizes to the plasma membrane, a finding also predicted by DeepLoc-1.0. Evaluation of the subcellular Tdt localization failed with two custom made antibodies, which were provided by the Reversade group (not shown). Hence, FL *tdt* was subcloned in an expression vector, with both an N-terminal HA tag inserted behind the cleavage site of the SP and an Myc tag at the C-terminus. This bivalent tagging approach allowed visualization of the subcellular localization of Tdt and identification of potential protein cleavage events. The DNA construct was introduced into the *Xenopus* LRO lineage and the tagged Tdt was detected via immunofluorescence with antibodies directed against the HA and Myc epitopes (Figure 1C). In relation to the cell borders, marked by phalloidin based F-actin fluorescence staining, Tdt appeared not to be membrane bound, but to localize to vesicular structures with an apical enrichment in LRO cells. Tdt foci just above the apical F-actin may indicated vesicular release. Unequivocal cleavage of Tdt was not observed, although an offset between the N- and C-terminal signals was constantly seen.

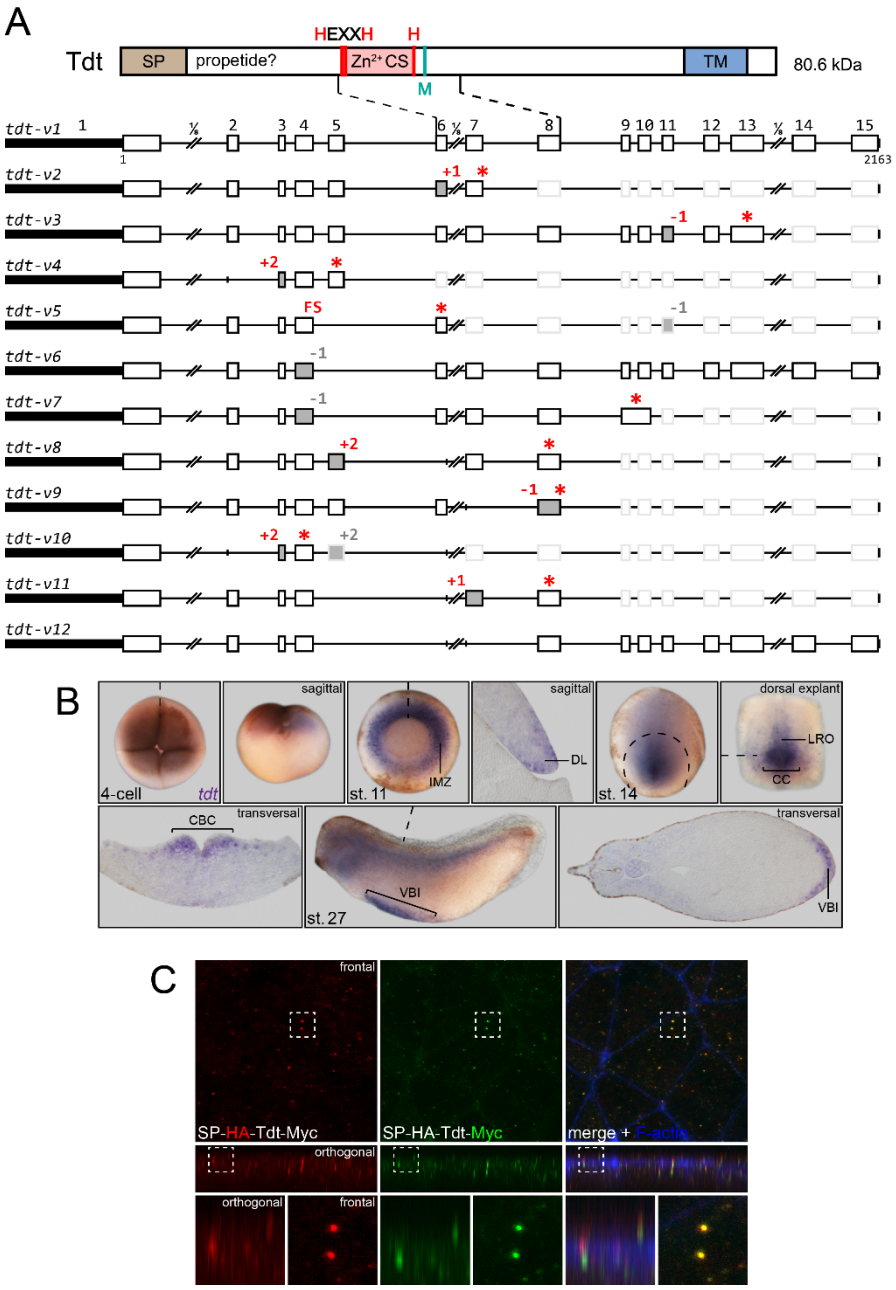

Figure 1: Tdt transcripts of the Metzinkin Tdt are LRO associated

(A) The predicted Tdt domain structure is altered due to alternative splicing and indicates localization of the FL protein to the plasma membrane. (B) Pronounced *tdt* expression started during gastrulation and was associated with LRO precursor cells in the IMZ. These cells translocate over the dorsal lip (DL) into the archenteron roof. Early neurulae limit most *tdt* expression to the CBC, which fades into the definitive LRO. (C) Misexpression of a double-tagged FL Tdt in LRO cells showed apically enriched vesicular localization of the protein.

Depletion of Tdt leads to laterality defects

To test if Tdt function is causally linked to laterality determination in *Xenopus*, Tdt was depleted using a splice blocking Morpholino oligomere (SBMO), targeting the splice donor site of *tdt* exon 1. The *tdt* SBMO was bilaterally injected against the standard control Morpolino oligomere (SCMO) into the LRO lineage of 4-cell embryos. Splice blocking of *tdt*, resulting in mRNA decay, was confirmed in pooled stage 14 embryos via RT-PCR, with intron 1 spanning primers (Figure 2A).

The *tdt* loss-of-function (LOF) phenotype was evaluated in tadpole embryos of stage 45, based on heart, gallbladder and intestine orientation (Figure 2B). *tdt* morphant embryos phenocopied, with high penetrance, the *situs* defects seen in humans harboring deleterious *TDT* variants, thereby confirming an involvement of TDT during laterality development.

However, heterologous rescue experiments failed with human or zebrafish wild type (WT) *TDT*. Likewise, bilateral misexpression of either the WT or catalytic dead (CD) mutant constructs did not induce laterality defects in a significant manner (not shown).

Therefore, the Clustered Regularly Interspaced Short Palindromic Repeats (CRISPR)/CRISPR-associated protein 9 (Cas9) system was utilized to verify the LOF phenotype by disrupting *tdt* on genome level. A Cas9 RNP (CRNP), made with a single guide RNA (sgRNA) targeting the splice acceptor site of *tdt* exon 4, was injected at the 1-cell stage. Mutagenesis of the *tdt* locus was confirmed via direct sequencing of PCR products, from genomic DNA of pooled stage 45 embryos, and subsequent Inference of CRISPR Edits (ICE) v2 analysis (Figure 2C). DNA species with deletions of the splice site along with the proximal part of *tdt* exon 4, dominated in *tdt* crispants.

Like *tdt* morphants, the crispants showed highly penetrant laterality defects at stage 45, which validated the previous results (Figure 2D). Moreover, unilateral injections of the *tdt* CRNP into dorsal blastomeres at the 4-cell stage, revealed a strict left sided requirement for Tdt during symmetry breakage (Figure 2E).

Tdt acts upstream of the Nodal signaling cascade

Tracing down the cause for the *tdt* LOF phenotype started with an expression analysis via RNA ISH of the most upstream asymmetrically expressed gene *pitx2* (Figure 2F). In most cases, *tdt* crispants failed to induce left-sided *pitx2* expression in the LPM. Absence of *pitx2* is usually accompanied and a result of impaired Nodal signaling. Consistent with this assumption, as judged by a *nodal1* RNA ISH, left-sided activation of *nodal1* in the LPM was perturbed in *tdt* crispants (Figure 2G). Compromised induction of the unilateral Nodal signaling cascade can be the result of a disturbed LRO, which may fails to generate or interpret the leftward fluid flow. A Tdt function, situated in such a way, would be in line with its early LRO associated expression pattern.

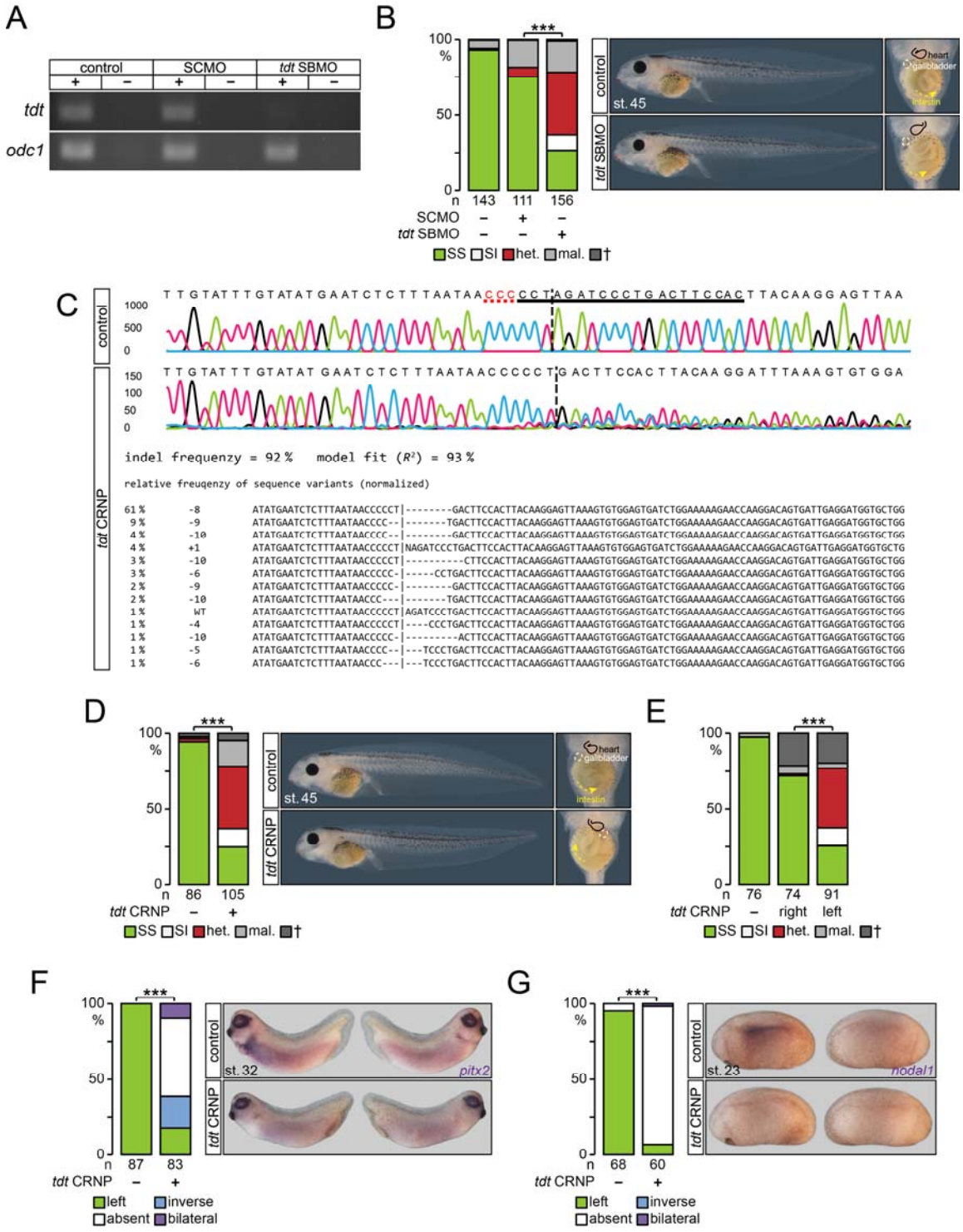

Figure 2: Tdt is required for laterality development in *Xenopus* upstream of the Nodal signaling cascade

(A) Introduction of *tdt* SBMO depleted *tdt* transcripts. (B) *tdt* morphants show SI and heterotaxia, thereby recapitulating the human laterality phenotype. (C) *tdt* genome editing was effectively deleted the splice acceptor site and the proximal part of exon 4. (D) *tdt* crispants phenocopy the *tdt* morphants and (E) unilateral *tdt* depletion revealed that Tdt is only required on the left side. (F) *pitx2* and (G) *nodal1* expression analysis of *tdt* crispants showed absence of the Nodal signaling cascade.

Normal LRO development is Tdt dependent

A potential *tdt* LOF effect on LRO morphology was assessed via negative labeling of stage 17 LRO cells with a RNA ISH for the pan-endodermal marker *SRY-box 17 alpha* (*sox17a*) in combination with a Hoechst fluorescence staining of DNA to visualize cell nuclei. Overall, *tdt* crispants displayed smaller LROs, using the most peripheral *sox17a* negative nuclei as reference points for size measurements (Figure 3A). Additionally, counting of all *sox17a* negative LRO nuclei, from the most anterior sensor cell to the most posterior CBC cell, showed that Tdt depleted embryos possess less LRO nuclei, hence less LRO cells (Figure 3B).

Cell size, cilia length as well as posterior cilia polarization are cellular parameters, which are critical for the central LRO cells to produce a robust and directed leftward fluid flow. These parameters were analyzed in a quadratic 100k µm² area of stage 17 LROs by an immunofluorescence for acetylated Tubulin alpha 4b (Tuba4b) along with a fluorescent phalloidin F-actin staining to label cilia and cell borders, respectively (Figure 3C). However, non of the three parameters were significantly altered in *tdt* crispants.

Accordingly, a semi-automated *in silico* analysis of the leftward fluid flow, monitored between stage 16 and 18 via fluorescent microspheres, showed no alterations of flow directionality and only a mild reduction of the median flow speed in *tdt* crispants (Figure 3D). As flow speed was still in WT range, leftward fluid flow was interpreted to be mechanistically sufficient for symmetry breakage in these embryos.

Lateral LRO cells perceive, process and implement the information from the leftward fluid flow. Therefore, these LRO cells were analyzed, post-flow at stage 19, by a RNA ISH for altered expression of their morphogenetic effectors *nodal1* (Figure 3E) and

dand5 (Figure 3F) after *tdt* LOF. Both genes were detectably expressed in *tdt* crispants, but an *in silico* quantification of the domain sizes via brightness thresholding revealed a marked reduction in each case. Remarkably, this reduction is also reflected by an overall less space-consuming LRO sensor cell population (Figure 3C).

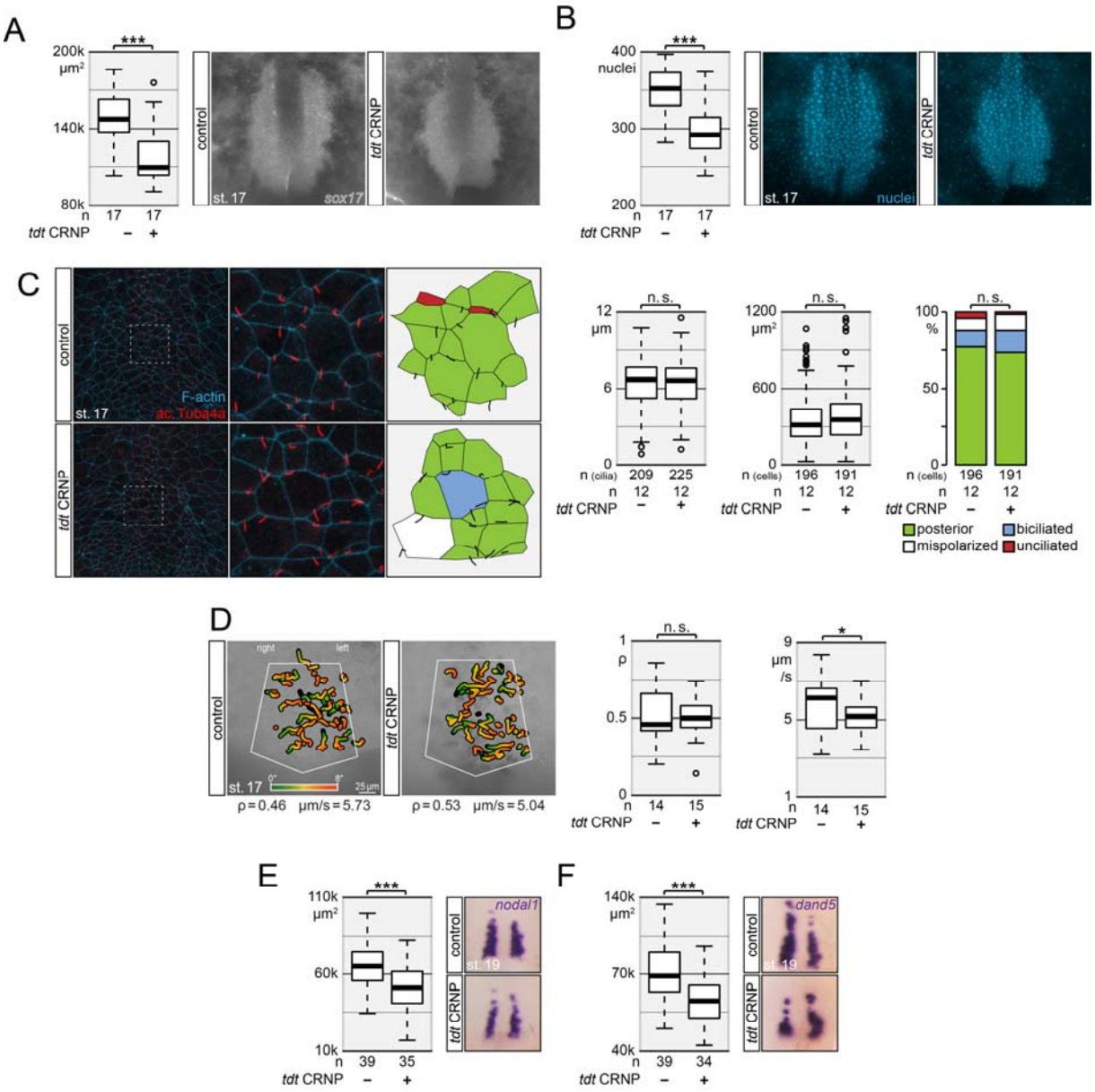

Figure 3: LRO sensor cell are disturbed in *tdt* depleted embryos

(A) LRO size as well as (B) LRO nuclei count was reduced in tdt genome edited embryos but (C) the flow determining cellular parameters, namely, cilia length, cell size and cilia polarization, were not affected. (D) Leftward fluid flow speed but not directionality was mildly affected but still occurred in WT range. (E) *nodal1* and (F) *dand5* mRNA expression was damped in the LRO sensor cells of *tdt* crispants.

Tdt is required for flow sensing upstream of Pkd2

Since *dand5* downregulation on mRNA level is a direct readout of the leftward fluid flow and a crucial event for the left-sided release of Nodal1, flow response was evaluated by size comparison of the left versus right *dand5* domain in the same embryos as analyzed before (Figure 4A). Interestingly, *tdt* crispants failed to attenuate *dand5* in the left lateral LRO cells, thus failed to respond to the leftward fluid flow.

Disturbed *dand5* repression could explain the absence of the Nodal signaling cascade, if all downstream events regarding Nodal1, namely expression, secretion, transfer to the LPM and perception, would be independent of Tdt. In this case, artificial removal of the remaining Dand5 should be competent to rescue the Tdt LOF phenotype. Indeed, *pitx2* expression was restored in the left LPM by targeting a translation blocking Morpholino oligomere (TBMO) directed against *dand5* to the left side of the LRO in 4-cell *tdt* crispants (Figure 4B).

The information mediated by the leftward fluid flow is still of unknown nature. In contrast, requirement of a sensor complex consisting of Pkd1l1 and Pkd2 that form a cation-permeable channel, which may selectively allows Ca^{2+} to enter the cilium of a sensor cells, is well proven. To test if Tdt acts up- or downstream of the sensor complex, a pharmacological bypassing or activation approach of Pkd2 was pursued. A2318, a ionophore for bivalent cations, and triptolide, a Pkd2 agonist, were injected in a wide range of doses into the archenteron of stage 16 embryos. Curiously, only triptolide was able to induce *situs* defects, as expected for a scenario of bilateral sensor bypassing or activation (not shown). In a preliminary experiment (Figure 4C) triptolide moderately activated *pitx2* in a bilateral fashion. However, if injected into the archenteron of *tdt* crispants, triptolide induced in the majority of embryos bilateral *pitx2*. This indicates that Tdt acts upstream of Pkd2.

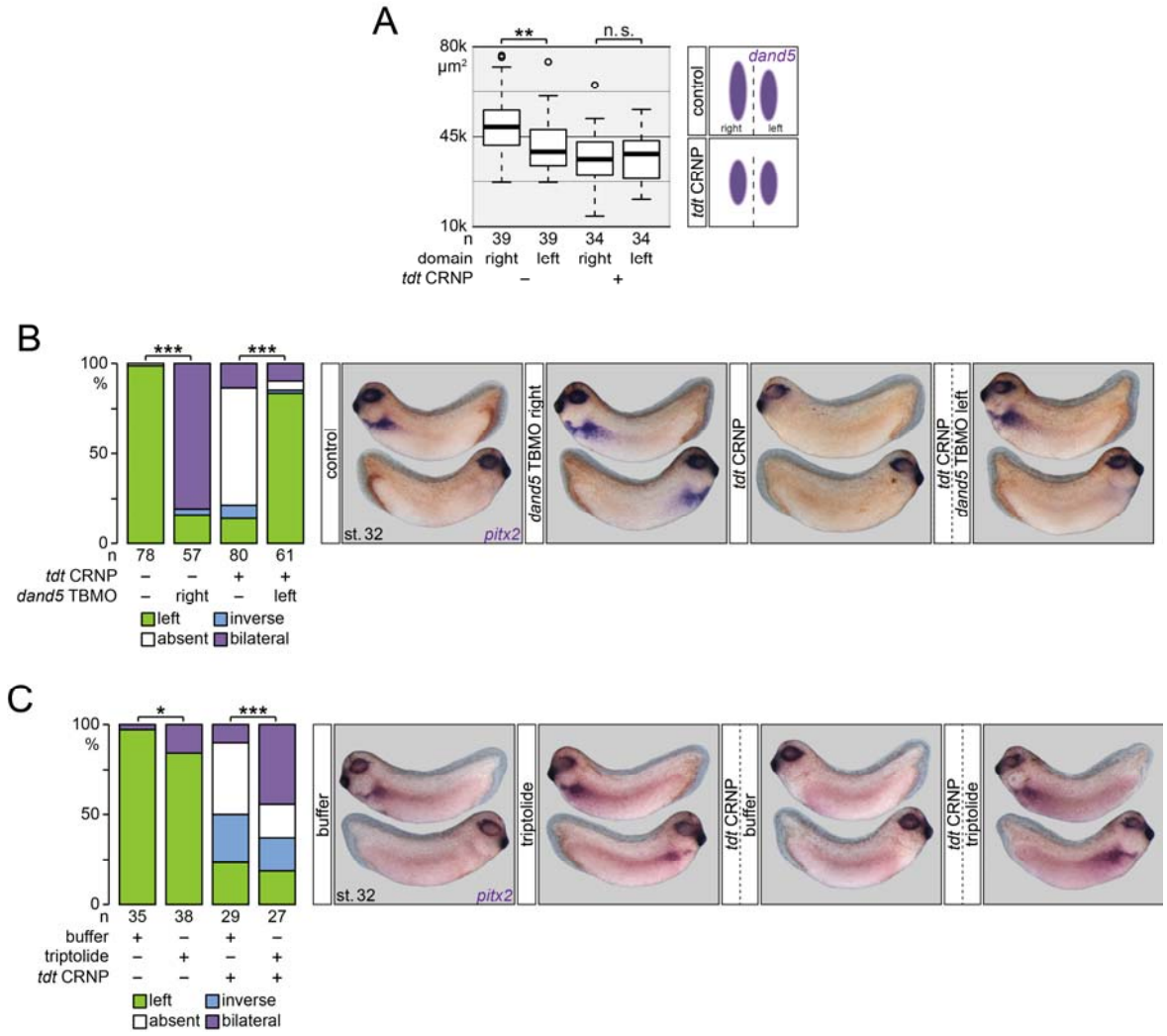

Figure 4: *tdt* is required for interpretation of the leftward fluid flow

(A) Evaluation of the left versus right *dand5* domain showed absence of flow dependent downregulation on the left side. (B) *dand5* TBMO injected to the left side of *tdt* crispants rescued the Nodal signaling cascade. (C) Pharmacological activation of the sensor complex component Pkd2 with triptolide, injected into the archenteron cavity, was able to induce the Nodal signaling cascade in absence of Tdt.

Discussion

The inner, left-right asymmetric body plan of an otherwise symmetric organism is an ancestral trait that is not exclusive to vertebrates. Asymmetric gene expression is key for the development of structural and/or functional chiral organs. Further, it allows a defined asymmetric organ arrangement, which perfectly compartmentalizes the space of the body cavity. Consequently, organisms with a higher level of complexity evolved. However, if laterality development is disturbed in humans, life threatening health conditions or even intrauterine death occur, especially if the heart function is compromised (Fesslova et al., 2019). Forward genetic studies already identified a variety of human laterality disease genes and variants.

TDT, the novel peptidase of the metzincin subclan, is one such factor that was found to be mutated in a cohort of patients with SI and heterotaxia. The Reversade group not only identified this gene but also noticed that functional orthologues are specifically missing in the genomes of sauropsids and cetartiodactyls. Organisms of these two taxons have in common that they apparently overcame the deuterostome fluid flow related mode of symmetry breakage (Chang et al., 2014; Kajikawa et al., 2020). This is in line with the results of this study, showing Tdt function in context of *Xenopus* leftward fluid flow. Like Dynein, axonemal, heavy chain 9 (Dnah9), which drives LRO cilia movement and thereby produces the leftward fluid flow (Vick et al., 2009), Tdt is only required on the left side of the LRO. More specifically, as the fluid flow was unaffected in the Tdt LOF, normal Tdt function is considered to be relevant in a hub situated downstream of flow at the level of normal LRO sensor cell physiology. This rather unsharp hierarchical placement of Tdt is due to the findings that it impacts on both LRO sensor cell development and action. Identification of *in vivo* Tdt substrates as well as a functional analysis of the *tdt* splice variants will be insightful. Currently,

three distinct but not mutual exclusive scenarios for Tdt action in the process of laterality determination are plausible and discussed below.

In the first scenario, Tdt is needed to establish and/or retain a population of LRO sensor cells with apical contact to the archenteron cavity, a prerequisite to perceive the information of the leftward fluid flow. This scenario is based on the marked reduction of the sensor cell domain and absence of the flow-dependent *dand5* regulation in *tdt* crispants. It is unclear but very likely that thresholds for the cell number and/or the special expansion of this cell population exist to grant robust flow responsiveness.

Fibroblast Growth Factor (FGF) signaling is the major positive regulator of the LRO sensor cells (Schneider et al., 2019) and interactions with peptidases, serving as competence factors, are described (Hou et al., 2007; Sohr et al., 2019). Additionally, the sensor cell precursors are sensitive to pharmacological inhibition of FGF signaling (Schneider et al., 2019) in a timeframe that closes as *tdt* expression starts during gastrulation. As inhibition of FGF signaling is capable to fully eliminate the LRO sensor cells, independently of apoptosis or attenuated proliferation (Schneider et al., 2019), it remains to be tested if Tdt acts as a downstream effector.

Alternatively, Tdt may regulates LRO sensor cell ingression, a process that has never been functionally analyzed but is known to be completed at the end of neurulation (Shook et al., 2004). Sensor cells ingress as bottle cells into the presumptive somites and draw as postulated by Shook and colleagues the lateral endodermal cells passively towards the midline (Shook et al., 2004). As *dand5* downregulation is only detectable in the anterior LRO sensor cells, premature ingression could spatio-temporally prevent sensing of the leftward fluid flow.

In the second scenario, Tdt regulates flow-dependently the sensor complex component Pkd1l1 to elevate or eliminate its inhibitory function on Pkd2. This setting is

hypothesized with respect to the loss of flow responsiveness in *tdt* crispants and the preliminary finding that the Nodal signaling cascade of these embryos can be rescued by the Pkd2 agonist triptolide. However, as the right side of these embryos respond to triptolide as well, one has to accept the bilateral induction as a causality of the omnilateral triptolide administration. Moreover, the relative low efficiency of triptolide to induce bilateral Nodal signaling in WT versus *tdt* crispant embryos indicates the presence of a Pkd2 inhibitor in the normal state. Consistently, an epistasis analysis in the mouse model revealed that *PKD1L1* acts as an upstream genetic repressor of *PKD2* in the context of laterality determination (Grimes et al., 2016). *PKD2* mutant mice fail to activate the Nodal signaling cascade, whereas *PKD1L1* mutants activate it bilaterally and the double mutants resemble the *PKD2* phenotype (Grimes et al., 2016). PKD1L1 co-localizes with PKD2 on sensory cilia and physical interaction is described (Grimes et al., 2016; Kamura et al., 2011), where Pkd1l1 may analogously to Polycystin 1, transient receptor potential channel interacting (PKD1) participates as pore-forming channel subunit in a heterotetramere with a PKD1L1/PKD2 stoichiometry of 1 to 3 (Su et al., 2018). Further, PKD1L1 responds to artificial flow-induced shear stress (Grimes et al., 2016) and proteolytic cleavage upon mechanical stimulus occurs in the related PKD1 (Chauvet et al., 2004). Therefore, Tdt may binds to the sensor complex via Pkd1l1, amplifies Pkd1l1 repressive capacity for Pkd2 and finally inactivates Pkd1l1 in response to flow via proteolytic cleavage.

In the third and last scenario, Tdt directly degrades Dand5 downstream of the leftward fluid flow to facilitate the unilateral Nodal signaling cascade. Considering the fatal outcome on organism level if correct symmetry breakage is disturbed (Fesslova et al., 2019), systemic robustness is needed. Therefore, it would be plausible if Dand5 is produced and released in excess to render abnormal Nodal signaling out, as recently

proposed by Martin Blum (personal communication). Within this conceptual framework, flow mediated Dand5 repression on mRNA level could be insufficient to subsequently allow an imminent release of Nodal1. Tdt dependent proteolysis of Dand5 in response to the leftward fluid flow could elegantly resolve this issue.

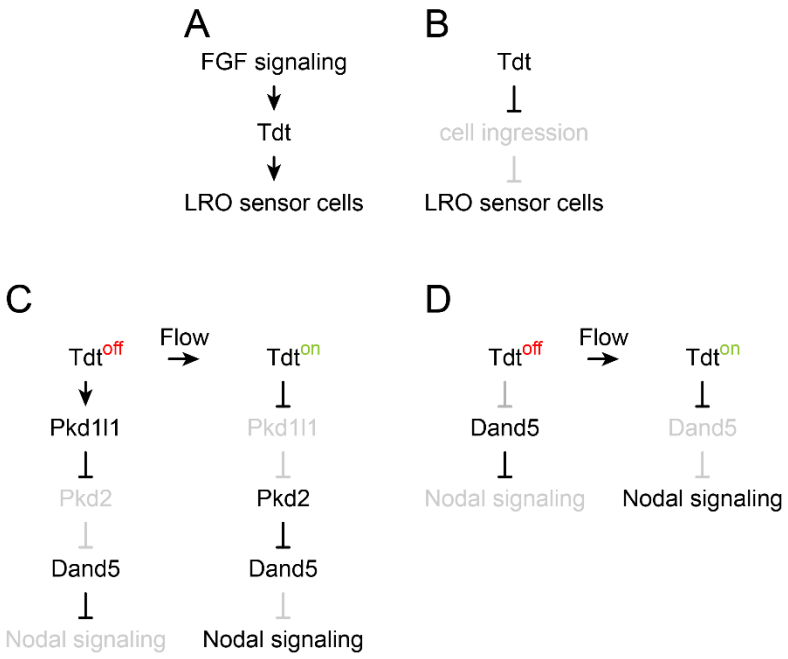

Figure 5: Proposed models for Tdt dependent laterality determination

(A) Tdt allows peptidase dependent FGF signaling to positively regulate the LRO sensor cell fate. (B) Premature ingression of the LRO sensor cells, which would ablate their sensory function, is prevented by Tdt. (C) In absence of flow, Tdt increases the potency of Pkd1l1 to repress Pkd2. Flow activated Tdt cleaves Pkd1l1, leading to a release of Pkd2 repression. Active Pkd2 inhibits Dand5 on mRNA level, which in turn leads to a release of Nodal1 repression and starts the Nodal signaling cascade. (D) Flow dependent activation of Tdt leads to direct degradation of Dand5 on protein level.

Especially the last two scenarios require a tightly controlled flow mediated activation of Tdt. The absence of any prominent phenotype upon heterologous misexpression of either human or zebrafish *TDT* in *Xenopus* embryos is fully in line with this assumption. It will be insightful to study if the cis-acting autocatalytic cysteine switch mechanism of GP63 activation (Macdonald et al., 1995) applies for Tdt as well and if it is triggered by the leftward fluid flow.

Material and Methods

Experimental animals

Adult *Xenopus laevis* frogs were purchased from Nasco and treated in accordance with the German Animal Welfare Act. *Xenopus* females were primed for spawning by injecting 50 units human chorionic gonadotropin (CG, Merck), approximately 3–6 days before embryos were needed. Ovulation was induced 12 hours after injecting further 300–600 units human CG. *Xenopus* males were sacrificed and testis were isolated to obtain sperms for subsequent *in vitro* fertilization of the oocytes.

Microinjections

Intracytoplasmic injections of 4 or 8 nl were performed at the 1- or 4-cell stage using the following reagents and doses: 2 pmol SCMO (Gene Tools, 5'-CCTCTTACCTCAGTTACAATTTATA-3'), 2 pmol *tdt* SBMO (Gene Tools, 5'-GAATGAAATGCTCACCTGAAAGTGT-3'), 0.75 pmol *dand5* TBMO (Gene Tools, 5'-TGGTGGCCTGGAACAGCAGCATGTC-3'), 200 pg *tdt* sgRNA (5'-GGGGAAGTCAGGGATCTAGG-3') plus 1 ng *Streptococcus pyogenes* Cas9 with NLS (PNA Bio), 200-800 pg mRNA encoding C-terminal PC tagged human WT or catalytic dead TDT, 200-800 pg mRNA encoding untagged zebrafish WT or catalytic dead Tdt as well as 16 pg pCS2+ harboring the coding sequence for *Xenopus* Tdt with both an N-terminal HA tag located behind the SP and a C-terminal Myc tag. Archenteron injections of stage 16 neurulae introduced buffer, x µmol A2318 (Merck) or x µmol triptolide (Selleck Chemicals) in volumes of 10 nl. *tdt* sgRNA design utilized CRISPRscan and the corresponding DNA templates were created in an oligo extension reaction with Pfu DNA polymerase (Promega). DNA templates were cleaned

with the GeneJET Gel Extraction and DNA Cleanup Micro Kit (Thermo Fisher Scientific). The T7 MEGAshortscript Kit (Thermo Fisher Scientific) in combination with the MEGAclear Transcription Clean-Up Kit (Thermo Fisher Scientific) were used for *tdt* sgRNA synthesis and purification. All mRNAs were transcribed with the SP6 mMESSAGE mMACHINE Kit (Thermo Fisher Scientific) and cleaned-up with the GeneJET RNA Purification Kit (Thermo Fisher Scientific).

LOF verification

Splice blocking of *tdt* was checked with the following primers: *tdt* exon 1 forward primer (5'-ATGACTGTTTCTTTCAGCA-3'), *tdt* exon 2 reverse primer (5'-GGTGCTCTCCAGACTGAGCGGC-3', *odc1* exon 5 forward primer (5'-GCCATTGTGAAGACTCTCTCCATTC-3') and *odc1* exon 6 reverse primer (5'-TTCGGGTGATTCCTTGCCAC-3'). *tdt* genome editing was verified with the primers: *tdt* exon 3/intron 3 5'-AAAGTGTTTGGACGTCACAGT-3' and *tdt* exon 4/intron 4 5'-TCACCTGAGCTGCACATTTCT-3'.

RNA ISH and fluorescence staining

Embryos were fixed over night in MEMFA (100 mM MOPS, 2 mM EGTA, 1 mM MgSO4, 3.7 % formaldehyde) and processed following standard procedures. All antisense RNA ISH probes were synthesized using SP6 or T7 RNA polymerases (Promega) in combination with DIG RNA Labeling Mix (Roche). Probes were detected by alkaline phosphatase (AP) conjugated anti-DIG Fab fragments (Roche). BM-Purple (Roche) was used as AP substrate. For immunofluorescence stainings the following primary antibodies were used: anti-acetylated Tuba4b (Merck, clone 6-11B-1, 1 : 800),

anti-HA tag (Roche, clone 3F10, 1 : 500), anti-Myc tag (Merck, clone 9E10, 1 : 500), anti-TDT (Reversade group, polyclonal antibody raised in rabbits against CWKKENGFPAGVDNPHGEI, various dilutions) and anti-Tdt (Reversade group, polyclonal antibody raised in rabbits against CWIEDNARSGMNEGGGEI, various dilutions). Alexa Fluor coupled secondary antibodies (Thermo Fisher Scientific, 1 : 500) were applied for primary antibodies detection. F-actin and DNA were directly visualized via Alexa Fluor phalloidin conjugates (Thermo Fisher Scientific, 1 : 100) and Hoechst 33342 (Thermo Fisher Scientific, 1 : 1 000), respectively.

LRO Analysis

LRO size, LRO nuclei number as well as the cellular parameters of the central LRO were all assessed in ImageJ. The leftward fluid flow was monitored on dorsal explants in a 30 seconds time window using 0.5 µm yellow-green FluoSpheres (Thermo Fisher Scientific, 1 : 2 500). Quantification of flow speed and directionality utilized the ImageJ plugin Particle Tracker and a custom made script written in R, as previously described. Size measurement of the *nodal1* and *dand5* expression domains was accomplished via the Color Threshold tool of ImageJ, which allowed to select the area of the domains based on a brightness threshold.

Statistics

Probability values were calculated for ordinal data with the two-tailed Fisher's exact test and for metric data with the two-tailed Wilcoxon signed-rank test. Significance levels were defined as follows: $p \geq 0.05$ is not significant, $p < 0.05$ is *, $p < 0.01$ is ** and $p < 0.001$ is ***.

References

Adzhubei, I. A. et al., 2010: A method and server for predicting damaging missense mutations. Nat. Methods: 7, 248–249.

Afzelius, B. A., 1977: A human syndrome caused by immotile cilia. Obstet. Gynecol. Surv.: 32, 49–50.

Afzelius, B. A. & Eliasson, R., 1983: Male and female infertility problems in the immotile-cilia syndrome. Eur. J. Respir. Dis. Suppl.: 127, 144–147.

Allen, B. G. & Weeks, D. L., 2005: Transgenic Xenopus laevis embryos can be generated using φC31 integrase. Nat. Methods: 2, 975–979.

Anzalone, A. V. et al., 2019: Search-and-replace genome editing without double-strand breaks or donor DNA. Nature: 576, 49–157.

Aslan, Y. et al., 2017: High-efficiency non-mosaic CRISPRmediated knock-in and indel mutation in F0 Xenopus. Development: 144, 2852–2858.

Assmann, V. et al., 1999: The intracellular hyaluronan receptor RHAMM/IHABP interacts with microtubules and actin filaments. J. Cell Sci.: 112, 3943–3954.

Barkovich, A. J. & Quint, D. J., 1993: Middle interhemispheric fusion: An unusual variant of holoprosencephaly. Am. J. Neuroradiol.: 14, 431–440.

Bendig, M. M., 1981: Persistence and expression of histone genes injected into Xenopus eggs in early development. Nature: 292, 65–67.

Birnstiel, M. L. et al., 1966: Localization of the ribosomal DNA complements in the nucleolar organizer region of Xenopus laevis. Natl. Cancer Inst. Monogr.: 23, 431–447.

Blitz, I. L. et al., 2013: Biallelic genome modification in F0 Xenopus tropicalis embryos using the CRISPR/Cas system. Genesis: 51, 827–834.

Bode, W. et al., 1993: Astacins, serralysins, snake venom and matrix metalloproteinases exhibit identical zinc-binding environments (HEXXHXXGXXH and Met-turn) and topologies and should be grouped into a common family, the “metzincins.” FEBS Lett.: 331, 134–140.

Brittingham, A. et al., 1995: Role of the Leishmania surface protease gp63 in complement fixation, cell adhesion, and resistance to complement-mediated lysis. Parasitol. Today: 11, 445–446.

Butts, T. et al., 2014: Transit amplification in the amniote cerebellum evolved via a heterochronic shift in NeuroD1 expression. Development: 141, 2791–2795.

Campbell, E. P. et al., 2016: Foxn4 promotes gene expression required for the formation of multiple motile cilia. Development: 143, 4654–4664.

Di Cara, F. et al., 2013: Invadolysin, a conserved lipid-droplet-associated metalloproteinase, is required for mitochondrial function in Drosophila. J. Cell Sci.: 126, 4769–4781.

Chang, C. F. et al., 2014: The cellular and molecular etiology of the craniofacial defects in the avian ciliopathic mutant talpid2. Development: 141, 3003–3012.

Chauvet, V. et al., 2004: Mechanical stimuli induce cleavage and nuclear translocation of the polycystin-1 C terminus. J. Clin. Invest.: 114, 1433–1443.

Chen, J. et al., 1998: Mutation of the mouse hepatocyte nuclear factor/forkhead homologue 4 gene results in an absence of cilia and random left-right asymmetry. J. Clin. Invest.: 102, 1077–1082.

Choksi, S. P. et al., 2014: Systematic discovery of novel ciliary genes through functional genomics in the zebrafish. Development: 141, 3410–3419.

Collignon, J. et al., 1996: Relationship between asymmetric nodal expression and the direction of embryonic turning. Nature: 381, 155–158.

Cong, L. et al., 2013: Multiplex genome engineering using CRISPR/Cas systems. Science: 339, 819–823.

Davidson, L. A. & Keller, R. E., 1999: Neural tube closure in Xenopus laevis involves medial migration, directed protrusive activity, cell intercalation and convergent extension. Development: 126, 4547–4556.

Deng, H. et al., 2014: Genetic basis of human left-right asymmetry disorders. Expert Rev. Mol. Med.: 16, 1–24.

Engelke, D. R. et al., 1980: Specific interaction of a purified transcription factor with an internal control region of 5S RNA genes. Cell: 19, 717–728.

Etges, R. et al., 1986: The major surface protein of Leishmania promastigotes is anchored in the membrane by a myristic acid-labeled phospholipid. EMBO J.: 5, 597–601.

Evans, W. N. et al., 2015: Heterotaxy in Southern Nevada: Prenatal Detection and Epidemiology. Pediatr. Cardiol.: 36, 930–934.

Fernandes, M. & Hébert, J.M., 2008: The ups and downs of holoprosencephaly: dorsal versus ventral patterning forces. Clin. Genet.: 73, 413–423.

Fesslova, V. et al., 2019: Characteristics and outcomes of fetuses with laterality defects are the current outcomes better? A single center study. J. Matern. Neonatal Med.

Field, S. et al., 2011: Pkd1l1 establishes left-right asymmetry and physically interacts with Pkd2. Development: 138, 1131–1142.

Fish, M. B. et al., 2012: Simple, fast, tissue-specific bacterial artificial chromosome transgenesis in Xenopus. Genesis: 50, 307–315.

Fong, C. P. et al., 2006: I-SceI meganuclease-mediated transgenesis in Xenopus. Dev. Dyn.: 235, 247–252.

Francis, R. & Lo, C., 2013: Ex vivo method for high resolution imaging of cilia motility in rodent airway epithelia. J. Vis. Exp.: 78, 50343

Grainger, R. M., 2012: Xenopus tropicalis as a Model Organism for Genetics and Genomics: Past, Present, and Future. Methods Mol. Biol.: 917, 3–15.

Grimes, D. T. et al., 2016: Genetic Analysis Reveals a Hierarchy of Interactions between Polycystin-Encoding Genes and Genes Controlling Cilia Function during Left-Right Determination. PLoS Genet.: 12, e1006070.

Gros, J. et al., 2009: Cell movements at Hensen's node establish left/right asymmetric gene expression in the chick. Science: 324, 941–944.

Gurdon, J. B., 1962: The developmental capacity of nuclei taken from intestinal epithelium cells of feeding tadpoles. J. Embryol. Exp. Morphol.: 10, 622–640.

Gurdon, J. B. & Hopwood N., 2000: The introduction of Xenopus laevis into developmental biology: of empire, pregnancy testing and ribosomal genes. Int. J. Dev. Biol.: 44, 43–50.

Hashimoto, M. et al., 2010: Planar polarization of node cells determines the rotational axis of node cilia. Nat. Cell Biol.: 12, 170–176.

Heasman, J. et al., 2000: β-catenin signaling activity dissected in the early Xenopus embryo: A novel antisense approach. Dev. Biol.: 222, 124–134.

Hellsten, U. et al., 2010: The genome of the Western clawed frog Xenopus tropicalis. Science: 328, 633–636.

Hogben, B. Y. L. et al., 1931: Studies On The Pituitary: VIII. The Relation Of The Pituitary Gland To Calcium Metabolism And Ovarian Function In Xenopus. J. Exp. Biol.: 8, 345–354.

Hou, S. et al., 2007: The Secreted Serine Protease xHtrA1 Stimulates Long-Range FGF Signaling in the Early Xenopus Embryo. Dev. Cell: 13, 226–241.

Ioannidis, N. M. et al., 2016: REVEL: An Ensemble Method for Predicting the Pathogenicity of Rare Missense Variants. Am. J. Hum. Genet.: 99, 877–885.

Isnard, A. et al., 2012: Impact of Leishmania metalloprotease GP63 on macrophage signaling. Front. Cell. Infect. Microbiol.: 2, 72.

Jacobs, J. P. et al., 2007: The nomenclature, definition and classification of cardiac structures in the setting of heterotaxy. Cardiol. Young: 17, 1–28.

Kajikawa, E. et al., 2020: Nodal paralogues underlie distinct mechanisms for visceral left–right asymmetry in reptiles and mammals. Nat. Ecol. Evol.: 4, 261–269.

Kamura, K. et al., 2011: Pkd1l1 complexes with Pkd2 on motile cilia and functions to establish the left-right axis. Development: 138, 1121–1129.

Kartagener, M., 1933: Zur Pathogenese der Bronchiektasien. Beitr. Klin. Tuberk. Spezif. Tuberkuloseforsch.: 83, 489–501.

Kennedy, M. P. et al., 2007. Congenital heart disease and other heterotaxic defects in a large cohort of patients with primary ciliary dyskinesia. Circulation: 115, 2814–2821.

Krieg, P. A. & Melton, D. A., 1984: Functional messenger RNAs are produced by SP6 in vitro transcription of cloned cDNAs. Nucleic Acids Res.: 12, 7057–7070.

Kroll, K. L. & Amaya, E., 1996: Transgenic Xenopus embryos from sperm nuclear transplantations reveal FGF signaling requirements during gastrulation. Development: 122, 3173–3183.

Kuehni, C. E. et al., 2010: Factors influencing age at diagnosis of primary ciliary dyskinesia in European children. Eur. Respir. J.: 36, 1248–1258.

Lebreton, G. et al., 2018: Molecular to organismal chirality is induced by the conserved myosin 1D. Science: 362, 949–952.

Lepay, D. A. et al., 1983: Surface antigens of Leishmania Donovani promastigotes. J. Exp. Med.: 157, 1562–1572.

Levin, M. et al., 1995: A molecular pathway determining left-right asymmetry in chick embryogenesis. Cell: 82, 803–814.

Lowe, L. A. et al., 1996: Conserved left-right asymmetry of nodal expression and alterations in murine situs inversus. Nature: 381, 158–161.

Lucas, J. S. et al., 2020: Primary ciliary dyskinesia in the genomics age. Lancet Respir. Med.: 8, 202–216.

Macdonald, M. H. et al., 1995: Analysis of the active site and activation mechanism of the Leishmania. Biochim. Biophys. Acta: 1253, 199–207.

Mali, P. et al., 2013: RNA-guided human genome engineering via Cas9. Science: 339, 823–826.

Marquez, J. et al., 2020: Disrupted ER membrane protein complex-mediated topogenesis drives congenital neural crest defects. J. Clin. Invest.: 1253, 199–207.

Marshall, S. et al., 2018: Extracellular release of virulence factor major surface protease via exosomes in Leishmania infantum promastigotes. Parasites and Vectors: 11, 1–10.

Matthews, B. W. et al., 1972: Structure of thermolysin. Nat. New Biol.: 238, 41–43.

McGrath, J. et al., 2003: Two populations of node monocilia initiate left-right asymmetry in the mouse. Cell: 114, 61–73.

McGwire, B. S. et al., 2003: Migration through the Extracellular Matrix by the Parasitic Protozoan. Infect. Immun.: 71, 1008–1010.

McGwire, B. S. et al., 2002: Extracellular release of the glycosylphosphatidylinositol (GPI)-linked Leishmania surface metalloprotease, gp63, is independent of GPI phospholipolysis. Implications for parasite virulence. J. Biol. Chem.: 277, 8802–8809.

McHugh, B. et al., 2004: Invadolysin: A novel, conserved metalloprotease links mitotic structural rearrangements with cell migration. J. Cell Biol.: 167, 673–686.

Meno, C. et al., 1996: Left-right asymmetric expression of the TGFβ-family member lefty in mouse embryos. Nature: 381, 151–155.

Minegishi, K. et al., 2020: Fluid flow-induced left-right asymmetric decay of Dand5 mRNA in the mouse embryo requires Bicc1-Ccr4 RNA degradation complex. bioRxiv: 931477.

Mitchell, D. R., 2017: Evolution of cilia. Cold Spring Harb. Perspect. Biol.: 9, a028290.

Moody, S. A., 1987: Fates of the blastomeres of the 32-cell-stage Xenopus embryo. Dev. Biol.: 122, 300–319.

Moreno-Mateos, M. A. et al., 2017: CRISPRCpf1 mediates efficient homology-directed repair and temperature-controlled genome editing. Nat. Commun.: 8, 1–9.

Morimoto, Y. et al., 2019: Nonsense mutation in CFAP43 causes normal-pressure hydrocephalus with ciliary abnormalities. Neurology: 92, E2364–E2374.

Mosser, D. M. & Edelson, P.J., 1985: The mouse macrophage receptor for C3bi (CR3) is a major mechanism in the phagocytosis of Leishmania promastigotes. J. Immunol.: 135, 2785–2789.

Moulton, J. D., 2016: Guide for Morpholino Users: Toward Therapeutics. J. Drug Discov. Dev. Deliv.: 3, 1023.

Murray, A. W. & Kirschner, M. W., 1989: Cyclin synthesis drives the early embryonic cell cycle. Nature: 339, 275–280.

Naganathan, S. R. et al., 2014: Active torque generation by the actomyosin cell cortex drives left-right symmetry breaking. eLife: 3, e04165.

Nakamura, T. et al., 2012: Fluid flow and interlinked feedback loops establish left-right asymmetric decay of Cerl2 mRNA. Nat. Commun.: 3, 1313–1322.

Nakayama, T. et al., 2013: Simple and efficient CRISPR/Cas9-mediated targeted mutagenesis in Xenopus tropicalis. Genesis: 51, 835–843.

Nguengang Wakap, S. et al., 2019: Estimating cumulative point prevalence of rare diseases: analysis of the Orphanet database. Eur. J. Hum. Genet.: 28, 165–173.

Niehrs, C., & Pollet, N., 1999: Synexpression groups in eukaryotes. Nature: 402, 483–487.

Niroula, A., & Vihinen, M., 2016: Variation Interpretation Predictors: Principles, Types, Performance, and Choice. Hum. Mutat.: 37, 579–597.

Niroula, A. & Vihinen, M., 2019: How good are pathogenicity predictors in detecting benign variants? PLoS Comput. Biol.: 15, 1–17.

Nonaka, S. et al., 1998: Randomization of left-right asymmetry due to loss of nodal cilia generating leftward flow of extraembryonic fluid in mice lacking KIF3B motor protein. Cell: 95, 829–837.

Okada, Y. et al., 1999: Abnormal nodal flow precedes situs inversus in iv and inv mice. Mol. Cell: 4, 459–468.

Oki, S. et al., 2007: Sulfated glycosaminoglycans are necessary for Nodal signal transmission from the node to the left lateral plate in the mouse embryo. Development: 134, 3893–3904.

Pearce, J. J. H. et al., 1999: A mouse cerberus/Dan-related gene family. Dev. Biol.: 209, 98–110.

Peeters, H. & Devriendt, K., 2006: Human laterality disorders. Eur. J. Med. Genet.: 49, 349–362.

Pimpale, L. et al., 2019: Cell lineage-dependent chiral actomyosin flows drive cellular rearrangements in early development. bioRxiv: 842922.

Quigley, I. K. & Kintner, C., 2017: Rfx2 stabilizes Foxj1 binding at chromatin loops to enable multiciliated cell gene expression. PLoS Genet.: 13, e1006538.

Ramamoorthy, R. et al., 1992: Three distinct RNAs for the surface protease gp63 are differentially expressed during development of Leishmania donovani chagasi promastigotes to an infectious form. J. Biol. Chem.: 267, 1888–1895.

Rawlings, N. D. et al., 2018: The MEROPS database of proteolytic enzymes, their substrates and inhibitors in 2017 and a comparison with peptidases in the PANTHER database. Nucleic Acids Res.: 46, D624–D632.

Rentzsch, P. et al., 2019: CADD: Predicting the deleteriousness of variants throughout the human genome. Nucleic Acids Res.: 47, D886–D894.

Di Resta, C. et al., 2018: Next-generation sequencing approach for the diagnosis of human diseases: Open challenges and new opportunities. Electron. J. Int. Fed. Clin. Chem. Lab. Med.: 29, 4–14.

Richards, S. et al., 2015: Standards and guidelines for the interpretation of sequence variants: a joint consensus recommendation of the American College of Medical Genetics and Genomics and the Association for Molecular Pathology. Genet. Med.: 17, 405–424.

De Robertis, E. M., 2008: Evo-Devo: Variations on Ancestral Themes. Cell: 132, 185–195.

Ryan, A. K. et al., 1998: Pitx2 determines left-right asymmetry of internal organs in vertebrates. Nature: 394, 545–551.

Saijoh, Y. et al., 2000: Left-right asymmetric expression of lefty2 and nodal is induced by a signaling pathway that includes the transcription factor FAST2. Mol. Cell: 5, 35–47.

Schneider, I. et al., 2019: A dual function of FGF signaling in Xenopus left-right axis formation. Development: 146, dev173575.

Schwarze, K. et al., 2018: Are whole-exome and whole-genome sequencing approaches cost-effective? A systematic review of the literature. Genet. Med.: 20, 1122–1130.

Schweickert, A. et al., 2007: Cilia-driven leftward flow determines laterality in Xenopus. Curr. Biol.: 17, 60–66.

Schweickert, A. et al., 2000: Pitx2 isoforms: Involvement of Pitx2c but not Pitx2a or Pitx2b in vertebrate left-right asymmetry. Mech. Dev.: 90, 41–51.

Session, A. M. et al., 2016: Genome evolution in the allotetraploid frog Xenopus laevis. Nature: 538, 336–343.

Shapiro, H. A. & Zwarenstein, H., 1934: A rapid test for pregnancy on Xenopus lævis. Nature: 133, 762.

Shi, Z. et al., 2015: Heritable CRISPR/Cas9-mediated targeted integration in Xenopus tropicalis. FASEB J.: 29, 4914–4923.

Shi, Z. et al., 2019: Modeling human point mutation diseases in Xenopus tropicalis with a modified CRISPR/Cas9 system. FASEB J.: 33, 6962–6968.

Shibazaki, Y. et al., 2004: Body handedness is directed by genetically determined cytoskeletal dynamics in the early embryo. Curr. Biol.: 14, 1462–1467.

Shook, D. R. et al., 2004: Pattern and morphogenesis of presumptive superficial mesoderm in two closely related species, Xenopus laevis and Xenopus tropicalis. Dev. Biol.: 270, 163–185.

Sinzelle, L. et al., 2006: Generation of trangenic Xenopus laevis using the Sleeping Beauty transposon system. Transgenic Res.: 15, 751–760.

Sleigh, M. A., 1981: Primary Ciliary Dyskinisia. Lancet: 318, 476.

Sohr, A. et al., 2019: Drosophila FGF cleavage is required for efficient intracellular sorting and intercellular dispersal. J. Cell Biol.: 218, 1653–1669.

Spéder, P. et al., 2006: Type ID unconventional myosin controls left-right asymmetry in Drosophila. Nature: 440, 803–807.

Stauber, M. et al., 2017: Identification of FOXJ1 effectors during ciliogenesis in the foetal respiratory epithelium and embryonic left-right organiser of the mouse. Dev. Biol.: 423, 170–188.

Stubbs, J. L. et al., 2008: The forkhead protein Foxj1 specifies node-like cilia in Xenopus and zebrafish embryos. Nat. Genet.: 40, 1454–1460.

Su, Q. et al., 2018: Structure of the human PKD1-PKD2 complex. Science: 361, eaat9819.

Sunter, J. & Gull, K., 2017: Shape, form, function and Leishmania pathogenicity: from textbook descriptions to biological understanding. Open Biol.: 7, 170165.

Suzuki, K. I. T. et al., 2018: A simple knock-in system for Xenopus via microhomology mediated end joining repair. Methods Mol. Biol.: 1865, 91–103

Szenker-Ravi, E. et al., 2018: RSPO2 inhibition of RNF43 and ZNRF3 governs limb development independently of LGR4/5/6. Nature: 557, 564–569.

Tang, S. et al., 2017: Biallelic mutations in CFAP43 and CFAP44 cause male infertility with multiple morphological abnormalities of the sperm flagella. Am. J. Hum. Genet.: 100, 854–864.

Vaser, R. et al., 2016: SIFT missense predictions for genomes. Nat. Protoc.: 11, 1–9.

Vick, P. et al., 2009: Flow on the right side of the gastrocoel roof plate is dispensable for symmetry breakage in the frog Xenopus laevis. Dev. Biol.: 331, 281–291.

Wallmeier, J. et al., 2019: De Novo Mutations in FOXJ1 Result in a Motile Ciliopathy with Hydrocephalus and Randomization of Left/Right Body Asymmetry. Am. J. Hum. Genet.: 105, 1030–1039.

Wood, W. B., 1991: Evidence from reversal of handedness in C. elegans embryos for early cell interactions determining cell fates. Nature: 349, 536–538.

Yoshiba, S. et al., 2012: Cilia at the node of mouse embryos sense fluid flow for left-right determination via Pkd2. Science: 338, 226–231.

Yu, X. et al., 2008: Foxj1 transcription factors are master regulators of the motile ciliogenic program. Nat. Genet.: 40, 1445–1453.

Original research chapter III:

Neurodevelopmental disorders

hmmr mediates anterior neural tube closure and morphogenesis in the frog *Xenopus*

Developmental Biology 430 (2017) 188–201

Contents lists available at ScienceDirect

Developmental Biology

journal homepage: www.elsevier.com/locate/developmentalbiology

hmmr mediates anterior neural tube closure and morphogenesis in the frog *Xenopus*

Angela Prager[a,1], Cathrin Hagenlocher[a,1,2], Tim Ott[a], Alexandra Schambony[b], Kerstin Feistel[a,*]

[a] University of Hohenheim, Institute of Zoology, Garbenstr. 30, 70599 Stuttgart, Germany
[b] Friedrich-Alexander University Erlangen-Nuremberg, Developmental Biology, Biology Department, Staudtstr. 5, 91058 Erlangen, Germany

ARTICLE INFO

Keywords:
Xenopus laevis
Neural tube closure
Rhamm
hmmr
Radial intercalation
Convergent extension

ABSTRACT

Development of the central nervous system requires orchestration of morphogenetic processes which drive elevation and apposition of the neural folds and their fusion into a neural tube. The newly formed tube gives rise to the brain in anterior regions and continues to develop into the spinal cord posteriorly. Conspicuous differences between the anterior and posterior neural tube become visible already during neural tube closure (NTC). Planar cell polarity (PCP)-mediated convergent extension (CE) movements are restricted to the posterior neural plate, i.e. hindbrain and spinal cord, where they propagate neural fold apposition. The lack of CE in the anterior neural plate correlates with a much slower mode of neural fold apposition anteriorly. The morphogenetic processes driving anterior NTC have not been addressed in detail. Here, we report a novel role for the breast cancer susceptibility gene and microtubule (MT) binding protein Hmmr (Hyaluronan-mediated motility receptor, RHAMM) in anterior neurulation and forebrain development in *Xenopus laevis*. Loss of *hmmr* function resulted in a lack of telencephalic hemisphere separation, arising from defective roof plate formation, which in turn was caused by impaired neural tissue narrowing. *hmmr* regulated polarization of neural cells, a function which was dependent on the MT binding domains. *hmmr* cooperated with the core PCP component *vangl2* in regulating cell polarity and neural morphogenesis. Disrupted cell polarization and elongation in *hmmr* and *vangl2* morphants prevented radial intercalation (RI), a cell behavior essential for neural morphogenesis. Our results pinpoint a novel role of *hmmr* in anterior neural development and support the notion that RI is a major driving force for anterior neurulation and forebrain morphogenesis.

1. Introduction

Neurulation is the process in which a flat neural plate generates folds that elevate, converge medially and fuse in the midline, creating a closed neural tube. Rostrally, the neural tube will go on to differentiate into the future brain while the caudal part continues to develop into the spinal cord. The morphogenesis of neural tube closure (NTC) requires the concerted action of cell shape changes together with cell polarization, migration and intercalation (Wallingford, 2005). Along the anterior-posterior (AP) neural axis, conspicuous morphological as well as temporal differences concerning NTC are detectable. While neural folds at the spinal cord level are converging readily, anterior neural fold apposition is lagging behind. This implies that NTC is differentially regulated between cranial and caudal levels, which is corroborated by the fact that NTC defects occur at specific sites and with varying severity along the AP axis (Greene and Copp, 2014; Wallingford et al., 2013). The severe NTC defect craniorachischisis e. g. causes the entire caudal neural tube to remain open from hindbrain levels onwards, while anterior NTC appears to proceed normally (Copp et al., 1994).

Non-canonical Wnt signaling, specifically the planar cell polarity (PCP) pathway, is a major regulator of NTC (Ueno and Greene, 2003; Wallingford, 2005). Manipulations of PCP pathway components such as *dvl2* or *vangl2* induce craniorachischisis. PCP signaling governs neural plate convergence and extension (CE), i.e. narrowing of the neural plate along the mediolateral (ML) axis and its consequential elongation along the AP axis (Wallingford et al., 2002). This is brought about by the polarization and intercalation of neural cells along the ML axis (ML intercalation, MLI). MLI / CE has been described as a prerequisite for maximal neural fold apposition, required for neural fold fusion along the dorsal midline (Wallingford and Harland, 2002).

* Corresponding author.
E-mail addresses: angela.prager@uni-hohenheim.de (A. Prager), cathrin.hagenlocher@izi.uni-stuttgart.de (C. Hagenlocher), tim.ott@uni-hohenheim.de (T. Ott), alexandra.schambony@fau.de (A. Schambony), k.feistel@uni-hohenheim.de (K. Feistel).
[1] These authors contributed equally.
[2] Present address: University of Stuttgart, Institute of Cell Biology and Immunology, Allmandring 31, 70569 Stuttgart, Germany.

http://dx.doi.org/10.1016/j.ydbio.2017.07.020
Received 18 January 2017; Received in revised form 19 July 2017; Accepted 26 July 2017
Available online 01 August 2017
0012-1606/

However, PCP-mediated MLI / CE is restricted to the hindbrain and spinal cord level since neural plate cells at the forebrain level do not converge mediolaterally (Darken et al., 2002; Goto and Keller, 2002; Keller et al., 1992; Lindqvist et al., 2010; Wallingford and Harland, 2002). This lack of CE anteriorly entails that neural fold apposition at the forebrain level is delayed compared to the hindbrain and spinal cord regions. Thus, in the forebrain area, PCP-mediated MLI / CE is not required for neural fold apposition and NTC. The nature of the morphogenetic processes which govern NTC at the forebrain level and a potential requirement for PCP signaling has remained elusive.

The microtubule (MT) cytoskeleton is essential for PCP signaling in both invertebrates and vertebrates (Harumoto et al., 2010; Matis et al., 2014; Sepich et al., 2011; Shimada et al., 2006; Vladar et al., 2012). The polarized nature of MTs makes them an ideal substratum for asymmetrically occurring transport processes using MT-dependent motor proteins. Indeed, Frizzled- as well as Dishevelled-containing vesicles move asymmetrically along MTs during establishment of PCP (Matis et al., 2014; Shimada et al., 2006). Furthermore, an organized MT cytoskeleton is required for NTC (Cearns et al., 2016; Suzuki et al., 2010), as MT inhibition during neural plate stages prevents the final steps of NTC (Karfunkel, 1971). Drug treatments targeting MTs induce apicobasally (AB) polarized and elongated neural cells to lose their polarized shape and round up (Karfunkel, 1971). Interestingly, the loss of AB neural cell polarization appears to specifically affect anterior NTC (Kee et al., 2008). In addition, the core PCP protein Vangl2 has recently been found to be asymmetrically localized to the apical tip of AB polarized neural cells in *Xenopus* (Ossipova et al., 2015a).

Here, we studied the MT-associated protein (MAP) Hmmr during *Xenopus* embryonic development and serendipitously uncovered a novel role in anterior NTC and forebrain morphogenesis. *hmmr* (hyaluronan-mediated motility receptor; RHAMM) mediates AB polarization of epithelial as well as front-rear polarization of mesenchymal cells (Maxwell et al., 2011; Silverman-Gavrila et al., 2011) and influences cell motility and migration (Hall et al., 1994, 1995). In addition, *hmmr* is a breast cancer susceptibility gene (MIM # 600936; Pujana et al., 2007) and human *HMMR* is involved in epithelial-to-mesenchymal and mesenchymal-to-epithelial transitions (EMT and MET) in cancer cells (Jiang et al., 2010). In human and mouse, *hmmr* was originally proposed to be an extracellular receptor for the glycosaminoglycan hyaluronan (hence the name). Such a function, however, remains controversial (Hofmann et al., 1998), and there is growing evidence that also in mammalian species, Hmmr predominantly plays an intracellular role in the binding of spindle and interphase MTs (Assmann et al., 1999; Li et al., 2015; Maxwell et al., 2003). The *Xenopus* ortholog of *hmmr* was first identified as MAP150 in a screen for MAPs that function during spindle assembly in oocytes (Groen et al., 2004). *hmmr* binds to and bundles MTs and consequentially contributes to their nucleation (Groen et al., 2004).

Here, we demonstrate a novel and physiological *in vivo* function of *hmmr* in anterior NTC and tissue morphogenesis. *hmmr* was required for forebrain hemisphere separation and cooperated with the core PCP component *vangl2* in controlling cell polarization as well as anterior neural morphogenesis. We propose that *hmmr* and *vangl2* cooperate to mediate radial cell intercalation, i.e. a major driving force for anterior NTC and forebrain development.

2. Materials and methods

2.1. Animals

All animals were treated according to the German regulations and laws for care and handling of research animals, and experimental manipulations according to § 6, article 1, sentence 2, no. 4 of the Animal Protection Act were approved by the Regional Government Stuttgart, Germany (Vorhaben A 379/12 ZO "Molekulare Embryologie").

2.2. Cloning of expression constructs

Full length *hmmr* (*hmmr* FL) was derived by PCR, using the ORF of *Xenopus laevis hmmr*. L in pFASTBAC_XRHAMM (Groen et al., 2004) as a template, and subcloned into pCS2+ yielding pCS2+_*hmmr*. L for expression in *Xenopus*. *hmmr* deletion constructs were obtained by a standard PCR-based cloning approach using pCS2+_*hmmr*. L as a template and subcloned into pCS2+ or CS2+MT vector. The *hmmr* ΔN construct is missing amino acids (AA) 1–130 of the conserved N-terminus which includes the MT binding domains (Assmann et al., 1999; Maxwell et al., 2003). The *hmmr* ΔC construct lacks AAs 1036–1175 and the *hmmr* ΔN+C construct lacks both segments. The coding sequence of FL *vangl2*. S was amplified from *Xenopus laevis* cDNA and subcloned into pCS2+YFP yielding YFP-*vangl2*.

2.3. Microinjections

Xenopus laevis embryos were injected at the 4–8 cell stage as previously described (Hagenlocher et al., 2013). Drop size was calibrated to 4 nl per injection and dextran tetramethylrhodamine or dextran Alexa Fluor 488 (MW 70,000 or 10,000, respectively, 0.5–1 μg/μl, Thermo Fisher Scientific) were added as a lineage tracer. *hmmr* morpholino oligomer (MO) 1 (5′ GCTGGAGCCCGCGATGCTTTCTTTC 3′), *hmmr* MO 2 (5′ AGCCTTGGGAAATGACATTTTGGCT 3′) or control MO (standard control morpholino; all Gene Tools) were injected to a final amount of 0.75–1 pmol. A mixture of two MOs targeting both alloalleles of *Xenopus laevis vangl2*, *vangl2* MO 1 (5′ ACTGGGAATCATTGTCCATGTTTTC 3′) and *vangl2* MO 2 (5′ CCTGGGTCGAAGCCAAAACTGCGAC 3′) was injected to a final total amount of 0.8 pmol. mRNAs were synthesized using mMessage mMachine (Thermo Fisher Scientific) and titrated in gain-of-function experiments. Rescue experiments were performed by injecting the optimal effective dose of *hmmr* MO 1 or *vangl2* MOs in conjunction with mRNAs encoding either *hmmr* FL (100 pg = 25 ng/μl), *hmmr* ΔN (300 pg = 75 ng/μl), *hmmr* ΔN+C (200 pg = 50 ng/μl), *hmmr* ΔC (200 pg = 50 ng/μl) or *vangl2* (*YFP-vangl2*; 100 pg = 25 ng/μl). In all experiments care was taken to exclude all specimens that were not targeted correctly, i.e. in which fluorescence was not restricted to the neural plate or in which fluorescence could not be evaluated optimally at mid-neurula stages.

2.4. Immunofluorescence

Embryos were fixed in a solution of 4% PFA in PBS for 1 h at room temperature, washed and bisected transversally at the forebrain level before immunostaining using CAS-Block (Thermo Fisher Scientific) blocking reagent. The following primary antibodies were used: anti-Tuba4a (α-Tubulin, clone DM1A, mouse IgG1, 1: 500; Sigma), anti-acetylated Tuba4a (acetylated α-Tubulin, clone 6-11B-1, mouse IgG2b, 1: 700; Sigma), anti-Tubg1 (γ-Tubulin, clone GTU-88, mouse IgG1, 1: 1000; Sigma), anti-Hmmr (rabbit polyclonal, 1: 300; gift from A. Groen / T. Mitchison; Groen et al., 2004), and anti-Mapre1 (EB1, clone 5/EB1, mouse IgG1, 1: 100; BD Biosciences). Wherever possible, subtype-specific secondary antibodies were used (Thermo Fisher Scientific). DNA was stained with Hoechst 33342 (Thermo Fisher Scientific) to visualize nuclei. Imaging was performed on a Zeiss LSM710 confocal microscope.

2.5. Scanning electron microscopy

Embryos were fixed in a mixture of 4% PFA and 2.5% glutaraldehyde in Soerensen's buffer (0.1 M sodium phosphate buffer; pH 7.4) overnight at 4 °C. After multiple washing steps in Soerensen's buffer, embryos were bisected transversally at the forebrain level and postfixed in 2% OsO_4 (Sigma; 50:50 mix with 0.2 M Soerensen's buffer) for 1 h at room temperature. Specimens were then dehydrated in a graded

ethanol series, critical point dried in a EM CPD030 (Leica) using CO_2 as a drying agent, mounted and sputter coated with gold in a EM SCD005 (Leica). Imaging was performed at 10 kV on a Jeol SEM.

2.6. *Whole-mount* in situ *hybridization*

Embryos were fixed for 2 h in 1x MEMFA and further processed as previously published (Hagenlocher et al., 2013). For histological analysis, embryos were embedded in gelatin-albumin and sectioned at 30–40 µm on a vibratome (Leica).

2.7. *Video-documentation of neural development*

In vivo imaging of NTC was performed after *hmmr* MO / control MO injection from stage 13 onwards. Embryos were arranged on a grid (meshsize 1 mm) in an agarose-coated petri dish filled with 0.1x MBSH. Timelapse sequences were recorded at 0.125 frame per minute on a Zeiss stereomicroscope (SteREO Discovery. V12) with an AxioCam HRc (Zeiss) using AxioVision 4.8 (Zeiss).

2.8. *Measurements and statistics*

All measurements were performed in ImageJ (http://imagej.nih.gov/ij/; Abràmoff et al., 2004). *p*-values were calculated using the Mann-Whitney *U*-test in statistical R or Fisher's Exact test at http://www.physics.csbsju.edu/stats/contingency.html. Significance was scored as follows: $p \geq 0.05$: not significant; $p < 0.05$: *; $p < 0.01$: **; $p < 0.001$: ***. Where necessary due to multiple testing, significance levels were adjusted according to Bonferroni correction.

3. Results

3.1. Hmmr *is required for forebrain development*

During embryogenesis, *hmmr* is specifically expressed in the developing neural plate (Casini et al., 2010; Fig. 4A). To knock down Hmmr protein function, antisense morpholino oligomers (MO) were used. Two translation-blocking MOs were employed, one located entirely in the 5′-UTR (MO 1) and another one covering the translational start site (MO 2). Both targeted the L-alloallele, which is the only one present in the genome of the allotetraploid *Xenopus laevis*. As both MOs induced identical phenotypes (data not shown), MO 1 was used in most experiments. MOs were targeted to neural tissue by injection into the animal pole of dorsal animal blastomeres of 4–8 cell embryos.

Loss-of-function (LOF) phenotypes were most apparent in tadpoles at stage (st.) 45. Anterior craniofacial structures of morphant embryos were conspicuously dysmorphic as compared to control specimens (Fig. 1A, B). Heads were narrower, interocular distance was reduced, eyes were smaller and the optic stalk was often pigmented. Co-injection of a full length *hmmr* construct (*hmmr* FL) rescued the MO phenotype (Fig. 1C). The phenotype was especially obvious on microdissected forebrains (Fig. 1D-F). Compared to control brains (Fig. 1D), morphant forebrains were narrower and the olfactory bulbs were smaller (Fig. 1E). Again, *hmmr* FL co-injection rescued the forebrain malformations (Fig. 1F), demonstrating the specificity of the MO effects.

Forebrain malformations are frequently the result of patterning defects arising in the ventral aspects of the brain, caused by defects in cilia-based Shh signaling (Chung et al., 2012; Murdoch and Copp, 2010; Park et al., 2006). Because *Xenopus* Hmmr has been described as a MAP (Groen et al., 2004), we wondered whether it exerted its function through localization to cilia. However, we never detected the protein on cilia (not shown). Also, no differences in primary cilia lengths between control and *hmmr* MO-injected cells were found (Fig. S1A-D). In addition, both *shh* and *ptch1* expression were unaffected in morphant brain tissues (Fig. S1E, F). Also, separation of the eye field, which requires hedgehog-mediated suppression of *pax6* expression (Chiang et al., 1996; Macdonald et al., 1995), occurred normally in *hmmr* morphants (not shown). These results indicated that forebrain malformations in *hmmr* morphants were independent of primary cilia-based Shh signaling, excluding a ventral origin of the observed forebrain malformations.

To analyze whether the forebrain defect originated from dorsal malformations instead, presence of roof plate-derived structures was assessed in microdissected brains. In the telencephalon, the septum, which divides the hemispheres, develops from an invagination of the dorsal roof plate (Gupta and Sen, 2016; Puelles and Rubenstein, 2015). Transverse sections of control forebrains showed wildtype (WT) morphology: a septum separating the two telencephalic lobes, each lobe with a distinct ventricular lumen (Fig. 1G, J, K). In the majority of morphant brains, the telencephalon was narrowed and fused into a single central mass of cells with no discernible septum and no left and right ventricular lumen (Fig. 1H, J, K). This loss of hemisphere separation was rescued by co-injection of *hmmr* FL, which restored forebrain width, the telencephalic ventricles and the septal structure (Fig. 1I, J, K).

In the diencephalon, a prominent roof plate derivative is the epiphysis (pineal gland) anlage, which expresses the homeodomain transcription factor *not*. Before it marks the epiphysis anlage as a morphological entity, expression of *not* also identifies two epiphysis precursor cell populations in the anterior neural folds (Fig. 1L, L′, Aquilina-Beck et al., 2007; Dassow et al., 1993). In WT embryos, these cell populations converge medially along with the neural folds and fuse at the midline, establishing the roof plate at the level of the caudal diencephalon (Fig. 1M, M′) and thus give rise to the epiphysis anlage. In embryos injected bilaterally with *hmmr* MO, *not* expressing cells are specified, however fail to converge and fuse in the midline (Fig. 1N, N′). Thus, *hmmr* LOF does not influence specification of dorsal cell populations that give rise to the forebrain roof plate, but appears to impair their medially directed movement during NTC. Notably, a roof plate derivative at the hindbrain level, i.e. the rhombencephalic choroid plexus, was not affected by *hmmr* MO injection (data not shown), indicating that roof plate defects observed in *hmmr* morphants were indeed restricted to the forebrain.

3.2. Hmmr *and* vangl2 *interact in morphogenesis and closure of the anterior neural tube*

To monitor events during NTC, time lapse movies of neural fold convergence were recorded comparing control and morphant embryos (Movie 1). Care was taken that embryos were kept at the same temperature at all times, that eggs from the same clutch were used and that injections with control MO and *hmmr* MO were performed in parallel. A series of single frames from such a movie is presented in Fig. 2A. At st. 13, no differences in neurulation were apparent (Fig. 2A). In dorsal views of embryos around st. 15, neural folds of control specimens were more closely apposed than those of morphant embryos, however only in anterior regions (Fig. 2A). When controls had on average reached st. 19, neural folds in the spinal cord region were closely apposed both in controls and morphants, i.e. there was no difference in the distance between the folds (Fig. 2A). In contrast, the distance between the anterior neural folds was obviously different between controls and morphants (Fig. 2A). Measurements revealed that anterior neural folds of *hmmr* morphant embryos were approx. 5x further apart than those of controls (Fig. 2B). Anterior neural folds of morphants would eventually close with a temporal delay of about one to four hours, depending on clutch and incubation temperature. Thus, neural fold apposition and NTC in *hmmr* morphants was disturbed in anterior regions, but not further caudally at the spinal cord level.

Apical constriction (AC), i.e. reduction of the apical cell surface, is a major driving force for neural tube closure (Suzuki et al., 2012). In the

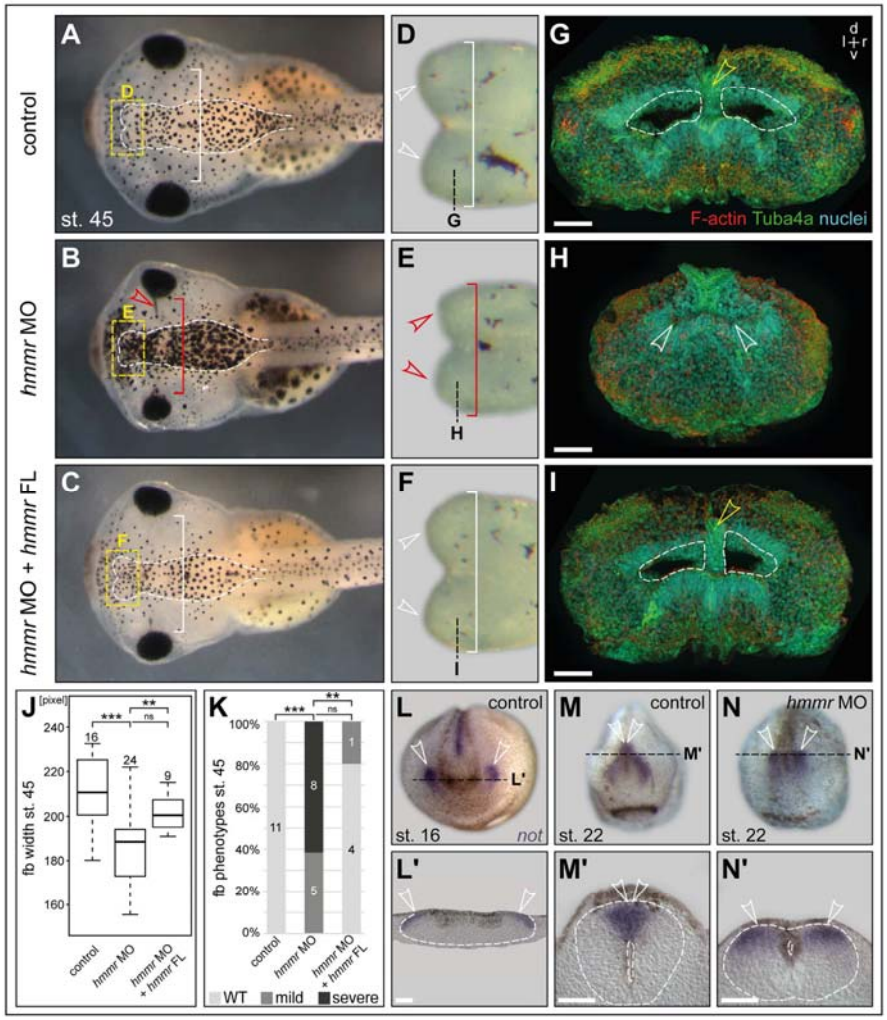

Fig. 1. Disruption of dorsal midline structures in *hmmr* morphants. (A-C) Dorsal (d) views of the head region of *Xenopus laevis* embryos at stage (st.) 45, rostral to the left. Control embryo (A) and embryos injected into both dorsal animal blastomeres at the eight cell stage with *hmmr* morpholino (MO; B) or *hmmr* MO together with full length (FL) *hmmr* (C). Brains outlined in white, white and red brackets indicate wildtype and reduced interocular distance, respectively. Arrowhead in (B) points to pigmented optic stalk. (D-F) Dorsal views of dissected forebrains (fb), brain area indicated by yellow boxes in (A-C); brackets indicate level of fb width measurement, arrowheads point to bilateral olfactory bulbs (OB). Note decrease in OB size and fb width in (E) and restoration of both in (F). (G-I) Fluorescently labeled nuclei and F-actin with immunofluorescence detecting α-tubulin (Tuba4a) reveal morphology of control (G) and treated (H, I) brains transversally bisected at level indicated in (D-F); scale bars: 50 μm. Ventricular lumina outlined in white, yellow arrowheads indicate septum separating hemispheres; note lack of midline separation and absence of lumina in morphant indicated by white arrowheads in (H). Restoration of ventricular lumina and septal structure (I). (J, K) Quantification and statistical analysis of fb width (J) as indicated in (D-F) and fb phenotypes (K). WT: normal lumina / septum, mild: lumina / septum reduced; severe: lumina / septum absent. Number of embryos indicated in each graph. (L-N) *not* expression in control (L, M) and morphant (N) neurula embryos after whole-mount *in situ* hybridization (anterior views). Arrowheads indicate medial convergence of bilateral *not*-expressing cell populations. (L′-N′) Transverse sections at the forebrain level as indicated in (L-N), neural tissue outlined in white. Note failure of medial convergence in morphant embryos (N, N′). Scale bars: 100 μm. l, left; r, right; v, ventral.

anterior neural plate of *Xenopus*, AC creates two lateral hinges in the superficial neuroectoderm along which the neural plate folds (Haigo et al., 2003). Loss of *hmmr* could potentially affect NTC by interfering with AC in superficial neural cells. However, morphologically, the anterior neural plate of *hmmr* morphants looks conspicuously different than that of embryos with perturbed AC (cf. Fig. 6 in Haigo et al., 2003). Analysis of cell surface areas in embryos injected unilaterally with *hmmr* MO revealed that morphant cells were equally capable of constricting apically as were control uninjected cells (Fig. S2). Specifically, lateral hinge points were not affected, demonstrating that the *hmmr* morphant phenotype did not arise from an impairment of AC in hinge point formation.

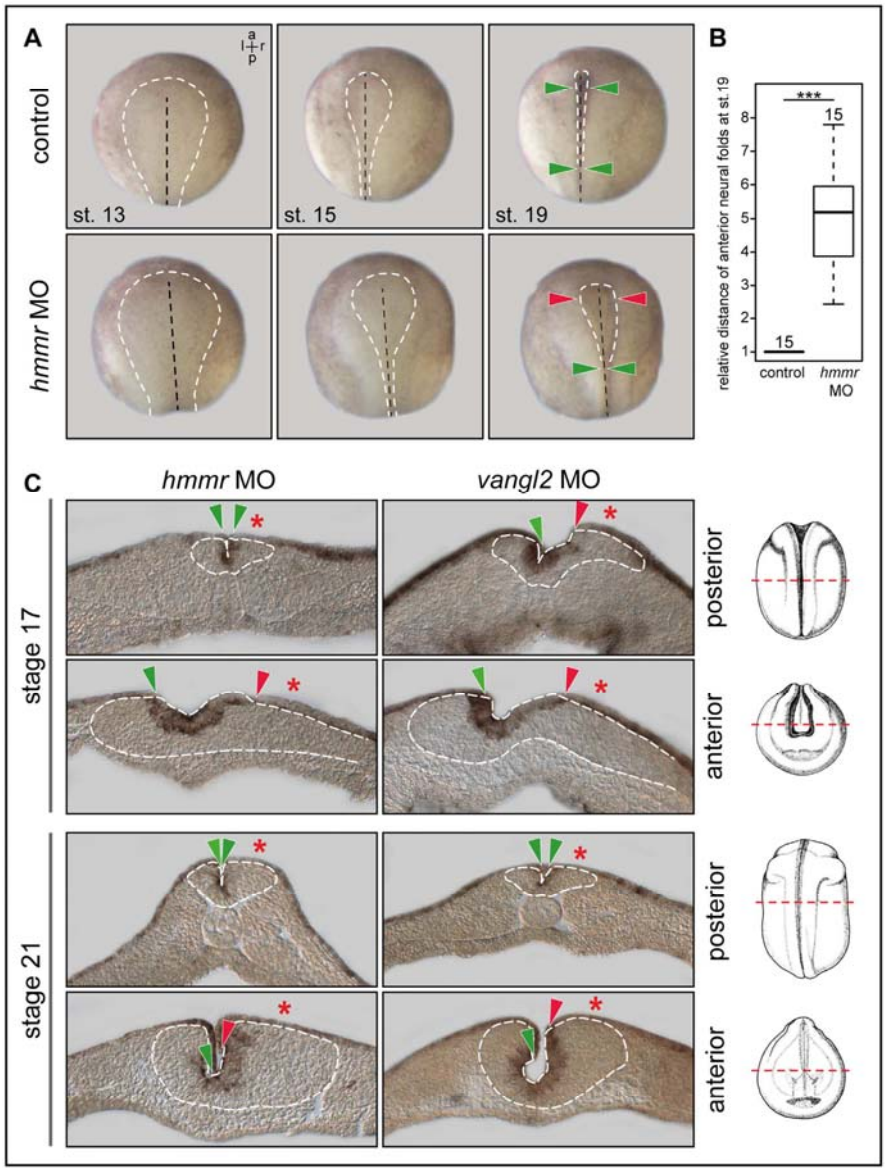

Fig. 2. Anterior neural tube closure defects in *hmmr* morphants. (A) Single frames from time-lapse movie during neurulation of embryos injected into both dorsal animal blastomeres with control morpholino (MO) or *hmmr* MO. Three different time points corresponding to control stages (st.) 13, 15 and 19 are shown in dorso-anterior views. Dashed white lines mark the border between superficial neural and non-neural ectoderm, dashed black lines indicate midline. Green arrowheads indicate wildtype distance of neural folds, red arrowheads indicate increased anterior neural fold distance in morphants. (B) Statistical analysis of anterior neural fold distance relative to control at st. 19. Number of embryos indicated above each plot. (C) Transverse histological sections of posterior or anterior neural tissue at st. 17 or 21 of embryos injected unilaterally into a single dorsal animal blastomere (injected side indicated by asterisk) with *hmmr* MO or *vangl2* MO. Borders of neural tissue are marked in white. Wildtype or aberrant neural fold convergence indicated by green or red arrowheads, respectively.

At the hindbrain / spinal cord level, neural fold apposition and NTC is governed by PCP-driven MLI / CE (Keller et al., 1992). Manipulation of core PCP proteins induces typical NTC defects, characterized by a failure to narrow and elongate the posterior neural plate (Darken et al., 2002; Wallingford and Harland, 2002). We reasoned that analysis of the differences between NTC defects in *hmmr* morphants and PCP

morphants should help to gain deeper insight into underlying morphogenetic mechanisms. Therefore, neural morphology of embryos injected unilaterally with *hmmr* MO or MOs targeting the core PCP component *vangl2* was compared on histological sections, using the uninjected side as an internal control (Fig. 2C). Two time points were chosen for analysis. At st. 17, which is prior to complete NTC, MLI / CE has brought the posterior neural folds into close apposition whereas the anterior neural folds are still further apart. Transverse sections through the posterior neural plate at st. 17 revealed that uninjected and injected neural folds were maximally apposed in *hmmr* morphants. In contrast, the injected neural fold of *vangl2* morphants gapped wide open, a typical CE defect of PCP morphants (Darken et al., 2002; Goto and Keller, 2002; Wallingford et al., 2002). Surprisingly, both morphants showed similar phenotypes in anterior regions as the injected neural fold did not converge properly towards the midline upon either treatment. Thus, *hmmr* morphants did not have classical CE defects but showed an anterior NTC delay which was similar between *hmmr* and *vangl2* morphants.

At st. 21, the epidermis has fused over the closed neural tube in WT embryos and remodeling of neural tissue leads to narrowing of the neural anlage (Davidson and Keller, 1999). Neural tube narrowing was conspicuously disturbed along the entire neural AP axis in either morphant (Fig. 2C). In addition, anterior NTC was impaired. This became visible by appearance of the epidermis which had fused over the posterior but not the anterior neural tube in *hmmr* morphants and in less severely affected *vangl2* morphants. The epidermis would eventually fuse over the anterior neural tube in all morphants, i.e. representing a closed neural tube defect which underlies conditions such as encephalocele (Gray et al., 2009; Wallingford et al., 2013). Interestingly, even severely affected *vangl2* morphants closed their anterior neural tube (not shown), which is in line with observations for PCP pathway manipulation in frog and mouse (Wallingford and Harland, 2002). The comparison between *hmmr* and *vangl2* phenotypes thus suggested that *hmmr* was not required for MLI / CE, but involved in a PCP-mediated morphogenetic behavior that specifically governs narrowing of the neural anlagen and has major impact for anterior NTC.

3.3. The N-terminal microtubule binding domains of hmmr are required for anterior neural tube morphogenesis

The failure of *hmmr* morphants to narrow the neural tube anteriorly suggested an underlying cytoskeletal defect. Since Hmmr is a MAP in *Xenopus* oocytes as well as in mouse and human somatic cells (Assmann et al., 1999; Groen et al., 2004; Maxwell et al., 2003; Tolg et al., 2010), we wanted to test whether or not MT binding of Hmmr was essential for neural morphogenesis. Therefore, deletion constructs were analyzed for their ability to rescue the failure of neural tissue narrowing upon co-injection with *hmmr* MO. The Hmmr amino terminus contains two conserved motifs that mediate MT binding (MT binding domains, MTBD 1 and 2; Fig. 3A) and their deletion has been shown to abolish MT binding of human and mouse proteins (Assmann et al., 1999; Maxwell et al., 2003).

Unilateral MO injections were performed such that the uninjected contralateral sides served as an internal control. Embryos at st. 21 were chosen for analysis, as in the WT both anterior and posterior neural folds are entirely closed at that time point. Neural morphogenesis at st. 21 is characterized by the beginning re-establishment of a central ventricular lumen and by narrowing of neural tissue (Davidson and Keller, 1999). Embryos were bisected at the forebrain level and hemisections were photodocumented under a stereomicroscope. In control embryos, both sides of the neural plate had fused in the midline to form a tube which was covered by epidermis (Fig. 3B). The width of each side was measured using the floor plate as a reference point for the midline. Since both sides were about equally wide in untreated specimens, the ratio between the two ranged around 1 in WT embryos (Fig. 3B, D). In unilateral *hmmr* morphants, the control side had narrowed towards the midline while the morphant side did not narrow properly and remained conspicuously wider than the control side (Fig. 3C). This shifted the ratio's mean to approx. 1.2, i. e. the morphant side was on average 20% wider than the control side (Fig. 3C, D). Unexpectedly, ectopic expression of *hmmr* FL dose-dependently interfered with neural tube narrowing as well (Fig. S3A), thus for rescue experiments, low doses were chosen which did not induce this gain-of-function (GOF) phenotype (100 pg = 25 ng/µl; Fig. S3A). Co-injection of low-dose *hmmr* FL brought the ratio back to 1.05 and thus significantly rescued the failure of neural tissue narrowing (Fig. 3D), providing additional proof of MO specificity.

A construct of *Xenopus* Hmmr lacking the MTBDs (AA 1–130 of the highly conserved N-terminus; ΔN; Fig. 3A) did not rescue the widened neural tissue of *hmmr* morphants (Fig. 3D). In line with this finding, there were no GOF effects observed when deletion constructs lacked the MTBDs (Fig. S3B). The C-terminus of Hmmr is also highly conserved between species and contains a bZIP motif required for centrosome localization (Chen et al., 2014; Maxwell et al., 2003).

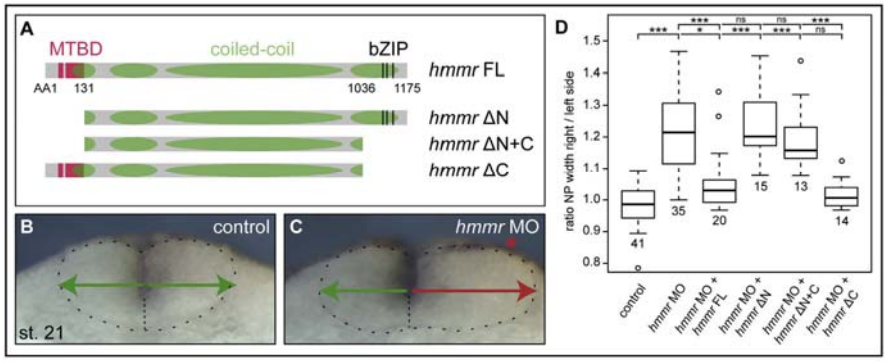

Fig. 3. Anterior neural tube morphogenesis requires the *hmmr* microtubule binding domains. (A) Schematic representation of *hmmr* full length (FL) and deletion (Δ) constructs lacking amino- (ΔN) or carboxy-terminal (ΔC) amino acids (AA) or both (ΔN+C). MTBD, microtubule binding domain. (B, C) Control embryo (B) and embryo injected unilaterally with *hmmr* morpholino (MO) into the right dorsal animal blastomere at the eight cell stage (st.; injected side marked by asterisk; C) and bisected transversally at the forebrain level at st. 21, views onto cut surfaces. Dashed black lines mark border of neural tissue and indicate the midline. Wildtype neural tissue width depicted by green arrow, widened neural tissue by red arrow. (D) Statistical analysis of neural tissue width upon injection of *hmmr* MO and deletion constructs. Note that presence of the MTBDs is required for rescue of tissue narrowing. Number of embryos indicated for each plot. ns, not significant.

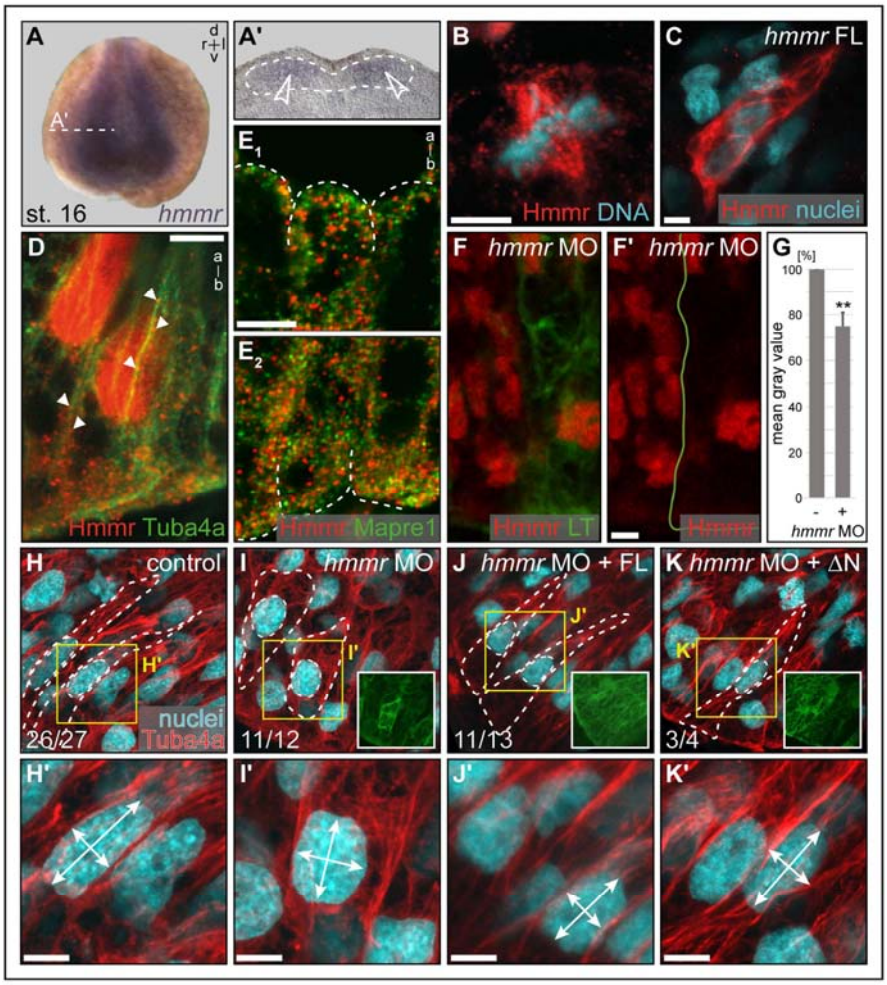

Fig. 4. Microtubule-localized Hmmr determines neural cell polarity. (A) *hmmr* gene expression in the stage (st.) 16 neural plate. Whole mount *in situ* hybridization (anterior view). (A′) Transversal histological section as indicated in (A). Arrowheads point to expression in deep neural cells, delineated in white. (B-E) Hmmr protein co-localizes with microtubules (MT) in st. 21 neural cells. (B) Endogenous Hmmr (red) localizes to spindle apparatus in mitotic cells in a dotted pattern. (C) Over-expressed full length Hmmr (*hmmr* FL; red) localizes with MTs in a pattern typical for over-expressed MAPs. (D) Endogenous Hmmr (red) localizes along MT fibers (arrowheads) and in basal (b) MT lattice detected by anti-Tuba4a antibody (green) as well as to nuclei. (E) Endogenous Hmmr (red) localizes close to MT plus ends apically (a; E_1) and basally (E_2) as visualized by co-staining for EB1 (Mapre1, green). (F, G) Reduction of Hmmr in *hmmr* MO-injected cells. Targeted cells identified by lineage tracer (LT) fluorescence (F); LT-positive field of cells indicated by green line in (F′). Quantification and statistical analysis of Hmmr fluorescence, n = eight embryos (G). (H-K, H′-K′) Loss of neural cell polarity in *hmmr* morphants is rescued by co-expression of FL mRNA. Comparison of cell shape (indicated with white dashed lines) and MT organization (Tuba4a, red) in wildtype (H, H′), morphant (I, I′), *hmmr* FL (J, J′) and *hmmr* ΔN (K, K′) rescued specimens; frequency of phenotypes indicated in each panel. Insets in (I-K) demonstrate LT fluorescence in respective area. Arrows in (H′-K′) indicate elongation / rounding of nuclei. Scale bars: 5 µm. d, dorsal; l, left; r, right, v, ventral.

Co-injection of *hmmr* MO with a C-terminal deletion construct lacking the last 139 AA (ΔC; Fig. 3A) re-established neural tissue narrowing with efficiencies similar to *hmmr* FL (Fig. 3D), demonstrating that the N-terminus, but not the C-terminus, plays a role in neural tube morphogenesis. Accordingly, a construct lacking both N- and C-terminus (ΔN+C; Fig. 3A) did not rescue the failure of neural tissue narrowing in morphant embryos (Fig. 3D). Together, these results suggested that MT binding via the conserved N-terminus mediated Hmmr function in NTC and neural morphogenesis.

3.4. Microtubule-localized Hmmr is required for neural cell polarization

Next we asked whether Hmmr was associated with MTs in *Xenopus* neural cells. Reinvestigation of the published expression pattern during neurulation (Casini et al., 2010) revealed that *hmmr* transcripts were enriched in the deep neural layer (Fig. 4A, A′), i.e. the very cells that are responsible for neural tissue narrowing (Davidson and Keller, 1999). These cells are characterized by AB cell elongation as well as AB

polarized MT arrays (Karfunkel, 1971). Using a *Xenopus*-specific antibody targeted against the C-terminus of Hmmr (Groen et al., 2004), the endogenous protein was detected on the mitotic spindle of dividing cells (Fig. 4B), matching spindle localization of Hmmr in cultured cells and in tissues of other organisms (Assmann et al., 1999; Maxwell et al., 2003). In elongated interphase cells of the neural tube, overexpressed Hmmr detected with the same anti-Hmmr antibody reflected the appearance of the MT cytoskeleton (Fig. 4C) while endogenous Hmmr was detected in small puncta which preferentially aligned along AB polarized MT bundles and within basal MT lattices (Fig. 4D). Nuclear Hmmr staining (Fig. 4D) has been previously described in cultured cells as well (Assmann et al., 1999; Maxwell et al., 2011), and was not assessed in the context of the present study. Hmmr puncta were enriched at the cell cortex apically (Fig. 4E_1) and basally (Fig. 4E_2). The MT plus end-binding protein Mapre1 (EB1) was detected in close vicinity to the punctate staining of Hmmr (Fig. 4$E_{1,2}$). Injection of *hmmr* MO in doses which were compatible with tissue integrity during neurulation significantly downregulated Hmmr in targeted cells by about 30% (Fig. 4F, G). Higher MO doses induced tissue disintegration, preventing protein analysis (not shown). Together with the GOF phenotypes (Fig. S3) this suggests that the embryo requires tight regulation of Hmmr levels to proceed through neurulation.

In order to relate the failure of neural tube narrowing in *hmmr* morphants to neural MT-based cytoarchitecture, cell shape and alignment of the MT cytoskeleton was analyzed in st. 21 *hmmr* morphants (Fig. 4H-K). In control embryos, cells in the deep neural layer were elongated along their AB (corresponding to the ventricular-pial) axis and often adopted a spindle-like appearance which was also reflected by an elliptical shape of the nucleus (Fig. 4H, H′). MTs appeared highly ordered and were predominantly arranged in linear arrays. Morphant cells, in contrast, were short and rounded with almost circular nuclei and MTs arranged in web-like structures (Fig. 4I, I′). Co-injection of *hmmr* MO and *hmmr* FL re-established cell and nuclear elongation, and restored MT cytoskeleton arrangements (Fig. 4J, J′). Interestingly, the ΔN construct, which failed to rescue neural plate narrowing, restored cell elongation and MT arrangement (Fig. 4K, K′), suggesting that narrowing and cell elongation are distinct processes which appear to be differentially mediated by subdomains of Hmmr. This also demonstrated that cell elongation alone was not sufficient for neural plate narrowing. In summary, these analyses strongly suggested that *Xenopus* Hmmr associates with MTs and influences MT cytoskeleton arrangement and cell polarization.

Despite the absence of posterior MLI / CE defects, aberrant tissue narrowing (Fig. 2C) indicated that cell morphology was affected also at the spinal cord level in *hmmr* morphants. Indeed, posterior neural tissue narrowing (Fig. S4A, A′, B) as well as cell elongation and MT polarization were impaired (Fig. S4C, D). The lack of posterior NTC defects despite these cytoarchitectural alterations suggests that an *hmmr*-dependent morphogenetic process mediates post-NTC tissue narrowing along the entire neural axis. However, while narrowing is not required for NTC at the hindbrain / spinal cord level, it is essential for timely NTC and neural morphogenesis specifically at the forebrain level.

3.5. hmmr *is required for radial intercalation concomitant with neural tube closure*

Narrowing of neural tissue accompanying NTC at the spinal cord level is brought about by a morphogenetic process termed radial intercalation (RI; Davidson and Keller, 1999). The failure of tissue narrowing both anteriorly and posteriorly suggests that *hmmr* could mediate RI along the entire neural axis. RI is defined as the intercalation of AB polarized cells along the AB axis of a stratified epithelium to result in fewer cell layers (Walck-Shannon and Hardin, 2014). Already during *Xenopus* gastrulation, RI movements occur in the dorsal non-involuting marginal zone (DNIMZ), where they are a prerequisite for tissue spreading driving epiboly (Keller, 1980). The anterior neuroectoderm (ANE) which gives rise to anterior brain regions, however, does not undergo RI during gastrulation (Keller, 1980). Since little is known about the morphogenesis of the ANE after gastrulation, we performed a detailed analysis of its cellular morphology between gastrulation and NTC, comparing the control and treated side of neural plates in embryos unilaterally injected with *hmmr* MO (Fig. 5). Immunolabeling of α-tubulin to visualize the MT cytoskeleton together with scanning electron microscopy (SEM; Fig. 5A-J) revealed distinct phases during ANE development. During early neurula stages (st. 13 / 14; Fig. 5A_1, B_1), cells of the deep layer elongated and proceeded to tilt their AB axis towards the midline (st. 15 / 16; Fig. 5C_1, D_1). Already during early neurula stages, cell elongation, assessed by calculating the height / width ratio of individual cells, differed significantly between control and injected side (Fig. 5A_2, B_2, K). Additionally, *hmmr* morphant cells were delayed in medialward tilting (Fig. 5C_2, D_2, L). During mid- to late neurulation (st. 17–19), control cells had elongated further and their progressive interdigitation created a dense meshwork in which individual cell layers could hardly be recognized (Fig. 5E_1, F_1). During these stages, morphant cells often failed to interdigitate, were more rounded and formed only loose cell-cell connections (Fig. 5E_2, F_2).

During elongation, tilting and interdigitation phases, *hmmr* MO injection did not change neural plate thickness, as the mean of the thickness ratio between both sides ranged around 1 (Fig. 5 M). This changed abruptly upon NTC, when the ratio's mean shifted to around 1.25, i.e. the injected side was now about 25% wider (thicker) than the control side (Fig. 5 M). The increase in the thickness ratio was reflected by cell rearrangements during this phase. Similar to what has been described for more caudal levels (Davidson and Keller, 1999), control cells started to intercalate radially around st. 20 in a ventral (floorplate) to dorsal (roofplate) fashion (Fig. 5G_1, I_1). In contrast, morphant cells did not undergo RI movements, which is in line with the emerging failure of narrowing (thinning) the neural plate (Fig. 5G_2, H_2, M). At st. 25, most of the narrow and AB elongated control cells spanned the entire neural tube wall (Fig. 5I_1, J_1) and were maximally tilted towards the midline (Fig. 5L). Thus, RI was complete on the control side, as supported by a drop in the layer index (see Keller, 1980) from approx. 5 at st. 15 to around 1 at st. 25, meaning that five cell layers had intercalated radially to give rise to a single-layered neural tube (Fig. 5N). Even though morphant cells were eventually tilted medially similar to control cells, they did not elongate further and failed to span the entire neural tube (Fig. 5I_2, J_2, K, L). The injected side was wider (thicker) and the layer index remained significantly higher (Fig. 5M, N), meaning that the morphant cell layers had not undergone complete RI. Together, this analysis showed that ANE cells successively underwent distinct morphological changes during neurulation, which culminated in RI to create a single-layered neural tube. The phenotype of morphant cells strongly suggests that *hmmr* became essential for RI in the ANE concomitant with neural tube closure.

3.6. hmmr *and* vangl2 *cooperate to control anterior neural morphogenesis and cell polarization*

The known connection between MTs and the PCP pathway together with the similar phenotypes in *hmmr* and *vangl2* morphants during anterior neurulation prompted us to ask whether *hmmr* and *vangl2* interact in anterior neural tube morphogenesis. We therefore tested a putative interaction using neural tissue narrowing (cf. Fig. 3) and cell elongation as well as MT arrangement (cf. Fig. 4H-K) as a read-out. While *hmmr* MO-injected neural tissue failed to narrow (Fig. 6A), co-injection of *vangl2* rescued the phenotype (Fig. 6A). At the cellular level, *vangl2* co-injection rescued cell elongation and re-established an AB polarized MT cytoskeleton (Fig. 4H, Fig. 6B). Interestingly, the reciprocal experiment yielded identical results. Upon *vangl2* LOF

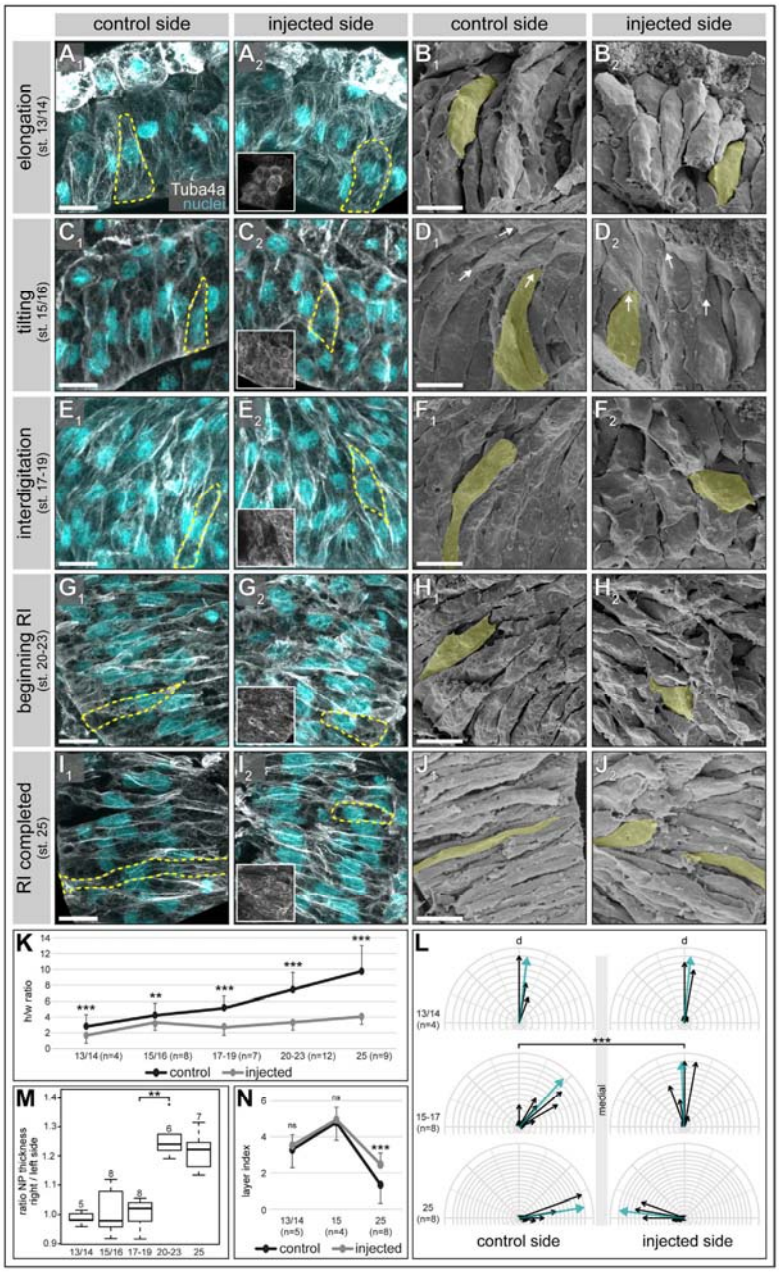

Fig. 5. *hmmr* impairs radial intercalation upon anterior neural tube closure. (A-J) Immunolabeling of α-tubulin (Tuba4a; A, C, E, G, I) and scanning electron microscopy (B, D, F, H, J) reveal progressive microtubule cytoskeleton polarization and cell morphology changes during neurulation in the anterior neuroectoderm (ANE) of embryos injected unilaterally with *hmmr* MO at the eight cell stage (st.). Dashed lines and color shading reveal cell shapes. Insets in (A_2, C_2, E_2, G_2, I_2) demonstrate lineage tracer fluorescence in the respective area. Scale bars: 20 µm. (K) Analysis of the height / width (h / w) ratio of deep ANE cells. Note progressive elongation in control vs. failure to elongate in morphant cells. (L) Tilting of ANE cells as measured by angular displacement of cell apices, indicated by arrows in (D_1, D_2). Note that cells are initially aligned along the dorsal (d) to ventral axis and

progressively tilt medially. Angles are binned in ten degree steps. Blue arrows indicate average angle of tilting, one concentric circle equals a frequency of one cell tilted in this direction. (M) ANE thickness as measured from apical side of superficial cells to basal side of adjacent deep cells; ratio between injected and control side reveals that loss of *hmmr* affects the ANE from st. 20 onwards. (N) Calculation of a layer index (Keller, 1980) shows failure of radial intercalation in morphant ANE. Note that layer analysis was impeded between st. 15 and 25 due to the complex interdigitation of individual cells. Numbers of specimens analyzed are indicated in each plot. Five cells were analyzed per specimen. ns, not significant.

neural tissue failed to narrow, neural cells were rounded and showed an aberrant MT cytoskeleton (Fig. 6A, C). Co-injection of *vangl2* MO and *hmmr* FL allowed for narrowing close to normal rates and rescued cell polarization as well as MT arrangement (Fig. 6A, D). To test whether the MTBDs of Hmmr were required for this process, the ΔN construct (cf. Fig. 3A) was injected together with *vangl2* MO. Despite a rescue towards cell elongation, the ΔN construct failed to re-establish neural tissue narrowing (Fig. 6A, E), which was similar to rescuing with the ΔN construct in *hmmr* morphants (Fig. 4K). In summary, these experiments demonstrated that *hmmr* and *vangl2* acted cooperatively in RI-mediated tissue narrowing as well as in cell and MT cytoskeleton polarization. While the former depended on the MTBDs of Hmmr, cell elongation did not require MT association.

4. Discussion

Thus far, *HMMR* has been primarily discussed in the context of tumor cell biology, in particular cell division and migration, i.e. MT-related processes. *In vivo* studies have been scarce; a knockout mouse is as yet not available. A mouse mutant in which the C-terminus was deleted shows defects in asymmetric cell divisions during male and female germ cell maturation (Li et al., 2015, 2016). The MT binding function has not been assessed *in vivo* in any system. Here, we describe an *in vivo* function of *hmmr* in *Xenopus* interphase cells, mediating morphogenetic movements which drive anterior neurulation and forebrain morphogenesis in cooperation with the PCP pathway.

4.1. hmmr *functions in forebrain roof plate formation*

hmmr morphant forebrains lacked a roof plate (and derived structures) as well as hemisphere separation, while ventral patterning and separation of the eye field was unaffected. This phenotype is reminiscent of a certain type of holoprosencephaly (HPE), known as the middle interhemispheric (MIH) HPE variant (Fernandes and Hébert, 2008). Classic HPE results from defects in the ventral forebrain, leading to severe craniofacial malformations such as cyclopia (Roessler and Muenke, 2010). In contrast, MIH HPE is characterized by a lack of forebrain hemisphere separation that results from dorsal forebrain defects, i.e. a defective roof plate (Fernandes and Hébert, 2008). Roof plate tissue is derived from lateral-most neural plate cells which move medially during NTC (Davidson and Keller, 1999; Schroeder, 1970; Fig. 7). In the mouse, telencephalic roof plate cells give rise to the septum that separates the brain hemispheres (Gupta and Sen, 2016; Puelles and Rubenstein, 2015), confirming our findings. Thus, an apparently mild neurulation phenotype which presents itself as a transient delay of NTC in the embryo may turn out as a dorsal brain defect which leads to severe malformations such as HPE in the adult.

4.2. hmmr *functions in radial intercalation*

Medial movement of lateral cells appears to be necessary for the entire neural tube, as neural tissue narrowing was impaired all along the AP axis in *hmmr* and *vangl2* morphants. Narrowing of neural tissue accompanying NTC as well as ventricular lumen formation is brought about by RI (Davidson and Keller, 1999) and we show here

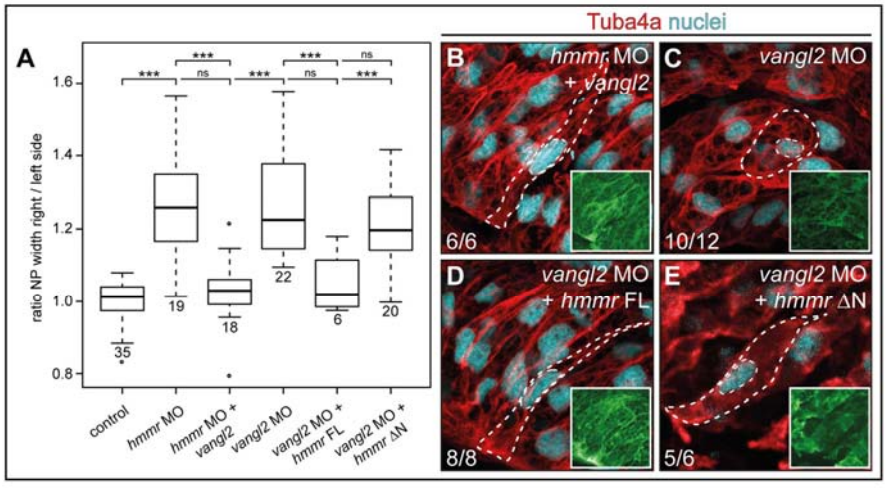

Fig. 6. *hmmr* and *vangl2* interact during anterior neural morphogenesis. Reciprocal rescue of anterior neural morphogenesis and cell polarity defects in *hmmr* and *vangl2* morphants. Embryos at the eight cell stage (st.) were injected into the right dorsal animal blastomere with morpholinos (MO) and mRNA as indicated and analyzed at st. 21. (A) Anterior neural morphogenesis. Statistical analysis of neural tissue width (cf. Fig. 3). ns, not significant; number of embryos analyzed indicated for each plot. Note that *hmmr* and *vangl2* interaction in mediating neural tissue narrowing requires the N-terminal microtubule (MT) binding domains of *hmmr*. (B-E) Neural cell polarity. Comparison of cell shape (indicated with white dashed lines) and MT organization (Tuba4a, red). Insets demonstrate lineage tracer fluorescence in the respective area. Frequency of phenotypes indicated in each panel. Note that despite the failure to rescue tissue narrowing (A), *hmmr* ΔN re-establishes cell polarization (E).

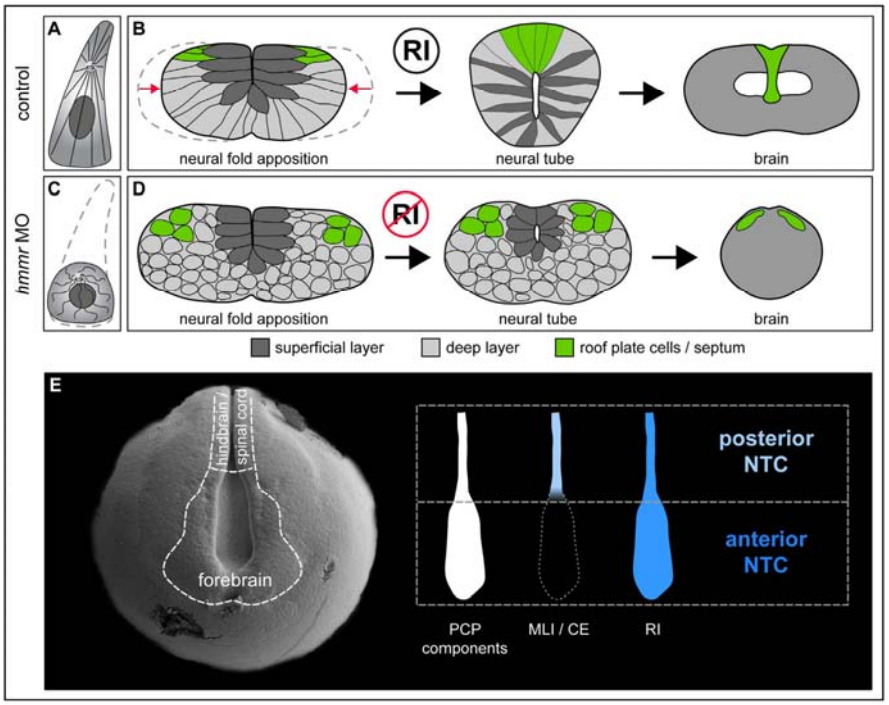

Fig. 7. Hypothetical model of *hmmr function* during anterior neural tube closure. (A) Elongated cell with polarized microtubule (MT) cytoskeleton in control embryo. (B) During neural fold apposition, cells of the superficial (dark gray) and deep (light gray) layer interdigitate, pulling lateral cells towards the midline (Davidson and Keller, 1999). Upon neural tube closure, cells finalize radial intercalation (RI) to form a unilayered epithelium which re-establishes a ventricular lumen. Far lateral cell populations (green) are directed towards the midline to establish the roof plate (Davidson and Keller, 1999). During further brain development, the roof plate invaginates forming e.g. the septum, which separates the telencephalic hemispheres. (C) Loss of *hmmr* disturbs cell elongation and MT polarization. (D) During neural tube closure, RI and, consequently, narrowing of neural tissue fails. After neural tube closure, lateral cell populations remain separated which prevents formation of a functional roof plate. (E) Conspicuous morphological differences are apparent in neural tube closure between forebrain and hindbrain / spinal cord regions. PCP components in general are required along the entire anterior-posterior neural axis (white). PCP proteins mediate RI along the entire neural axis (dark blue), while their function in mediolateral intercalation and convergent extension (MLI / CE) is restricted to the hindbrain and spinal cord level (light blue). Together, the two PCP protein-driven processes MLI / CE and RI bring about posterior neural tube closure and spinal cord morphogenesis. Anterior neural tube closure and forebrain morphogenesis is facilitated by PCP protein-driven RI alone.

that *hmmr* is required for RI of the ANE concomitant with NTC. Interestingly, the DNIMZ, which undergoes RI already during gastrulation stages (Keller, 1980), is also affected by loss of *hmmr* (our own unpublished observations). This suggests a general requirement of *hmmr* in RI movements and it will be interesting to test whether *hmmr* interacts with factors such as fibronectin, integrin or complement factor C3a, which mediate RI during gastrulation (Marsden and DeSimone, 2001; Szabó et al., 2016).

In WT embryos, neural cells with a polarized MT cytoskeleton are elongated along their AB axis (Fig. 7A). Superficial and deep layer cells intercalate radially to give rise to a single-layered neuroepithelium (Fig. 7B). Simultaneously, RI shifts lateral cells fated for the roof plate (such as those expressing *not*) medially, where the two populations merge. During further forebrain development, the roof plate invaginates and gives rise to the telencephalic septum (Fig. 7B). In *hmmr* morphants, neural cells lack a polarized MT cytoskeleton and are not elongated (Fig. 7C). These rounded cells are unable to intercalate radially and thus neural tissue remains multilayered. Cells fated for the roof plate remain lateral, the roof plate and septum do not form and hemisphere separation fails (Fig. 7D).

The AB polarization and elongation of neural cells thus appears to be essential for RI. PCP signaling interacts with pathways instructing AB cell polarity (Cha et al., 2011; Hatakeyama et al., 2014). In addition, similar to their role in MLI / CE, PCP proteins such as Vangl2 govern RI (Ossipova et al., 2015a). Vangl2 localizes to the apical tip of intercalating neural cells in *Xenopus*, reflecting and possibly influencing their AB polarity (Ossipova et al., 2015a). The failure of neural tissue to narrow in *hmmr* and *vangl2* morphants strongly suggests that these genes are required for PCP protein-mediated AB neural cell polarization and elongation, enabling RI during neural tissue narrowing.

Thus, PCP signaling components in general are required for morphogenesis along the entire neural tube (Fig. 7E). Importantly, however, they drive two distinct morphogenetic processes: while PCP-mediated MLI / CE is restricted to the hindbrain and spinal cord region, RI governed by PCP proteins is active along the entire neural axis (Fig. 7E). At the spinal cord / hindbrain level, where both cell movements overlap, neural folds appose rapidly. In anterior regions, in contrast, neural fold apposition relies on RI exclusively, which delays the process of NTC. These data therefore strongly suggest that RI is specifically important for anterior NTC.

4.3. hmmr and microtubule dynamics

How could one envision the contribution of *hmmr* to RI at the molecular level? In addition to the prerequisite for AB cell polarization and elongation, RI is a morphogenetic process driven by polarized protrusive activity which facilitates directional migration of cells (Davidson and Keller, 1999). *hmmr* is a MAP, and its interaction with the MT cytoskeleton could influence several processes leading to directional migration during RI. In *Xenopus* oocytes, Hmmr efficiently bundles MTs (Groen et al., 2004) and it has been suggested to act as a cross-linker between the MT and actin cytoskeleton (Assmann et al., 1999). Thus, Hmmr could contribute to the overall stability of cytoskeletal elements which should support cell elongation. Indeed, we find that an impairment in cell elongation is the earliest phenotype observable at the cell morphological level. Such a function of *hmmr* would likely be independent of the MTBD, since the ΔN construct which lacks the MTBD rescued cell elongation. On top of their elongated shape, radially intercalating cells within the *Xenopus* neural folds exhibit bilateral protrusions similar to mediolaterally intercalating cells during CE (Davidson and Keller, 1999). While the production of cell protrusions is an actin-based process, it is becoming increasingly clear that MTs regulate protrusion behavior by contacting cortical regions (reviewed in Etienne-Manneville, 2013). The spatially regulated formation of cell protrusions is essential for directed cell migration and the dynamic instability of polarized MTs plays an important role in this process (Etienne-Manneville, 2013; Jayachandran et al., 2016). Even slight perturbations in MT dynamic instability can induce a total halt of cell protrusion (Etienne-Manneville, 2013). This matches our observations that both *hmmr* GOF and LOF impaired neural tissue narrowing, implying that correct protein concentrations are essential. Along this line of reasoning it would imply that the N-terminus harboring the MTBDs is necessary for protrusion formation, enabling migratory behavior during RI. Thus, the MTBDs are dispensable for cell elongation but required for neural tissue narrowing, suggesting these are distinct processes regulated by distinct functional domains of Hmmr. These processes also appear to be separated temporally, as cell elongation defects already occur during emergence of the morphant phenotype around st. 15, while RI movements initiate and are impaired around st. 20. Thus, it is tempting to speculate that *hmmr* participates in neural morphogenesis by influencing the stability and / or dynamics of MTs.

4.4. The hmmr / vangl2 connection

How then is Vangl2 implicated in this process? As mentioned, PCP is intimately connected to MTs (Harumoto et al., 2010; Matis et al., 2014; Sepich et al., 2011; Shimada et al., 2006; Vladar et al., 2012). The reciprocal rescue between *hmmr* and *vangl2* suggests that the two function in parallel pathways to regulate a common target. In line with this reasoning, the small GTPase Rac1, i.e. an effector of PCP signaling, has been shown to act downstream of *vangl2* (Lindqvist et al., 2010). Rac1 stabilizes the MT cytoskeleton by initiating a multi-protein complex close to lamellipodia (Fukata et al., 2002; Watanabe et al., 2004). This complex captures MT plus ends at the cell cortex and could thus contribute to polarization of the MT cytoskeleton. *hmmr* has been shown to mediate Rac activation (Gouëffic et al., 2006), and thus, Rac1 is a good candidate for a common denominator of *hmmr* and *vangl2* function in cell polarization and RI. One could envision that *hmmr*, containing extensive coiled-coil domains, serves as a scaffold to assemble a protein complex which on the one hand enables Rac activation and on the other establishes proximity to MTs. In line with this reasoning, injection of a dominant-negative version of *rac1* phenocopies *hmmr* / *vangl2* loss of function in the ANE (our own preliminary observations).

In more general terms, the cooperation between *hmmr* and *vangl2* suggests that *hmmr* acts as a modifier of PCP-instructed polarization and intercalation processes. Vangl2 is present in the superficial as well as in the deep layer of the *Xenopus* neuroectoderm and influences both AP / AB polarity as well as MLI / CE and RI (Darken et al., 2002; Goto and Keller, 2002; Ossipova et al., 2015a, 2015b). It has been suggested that *vangl2* modifies CE (Park and Moon, 2002) and that high levels of *vangl2* in the head region prevent MLI / CE (Goto and Keller, 2002). Thus, the cumulative expression levels of *hmmr* and *vangl2* and / or their intracellular localization and activation in superficial vs. deep neuroectoderm might determine whether neural cells undergo MLI or RI. It will be interesting to test whether the same holds true for mammalian embryos, since *hmmr* is expressed during mouse NTC as well.

4.5. hmmr in embryonic development and cancer

What can be learned from this developmental study for the role of *hmmr* during tumor formation and metastasis? In most cancers, *HMMR* expression levels are elevated (Assmann et al., 2001; Maxwell et al., 2004 and references therein). During development, *hmmr* expression is conspicuously up-regulated in tissues which undergo MET, i.e. forming a single-layered epithelium from a mesenchymal arrangement of cells. In principle, the process of neural RI represents a MET as well, as mesenchymal cells from the deep neural layer intercalate to form a unilayered neural tube. This connection holds for other *hmmr* expression sites as well. *hmmr* is expressed in the mesenchyme of the pronephric anlage (Casini et al., 2010), which forms the pronephros by MET. Transcripts are also found in mesenchymal neural crest cells which integrate into their epithelial target tissues (Casini et al., 2010). *HMMR* expression is stimulated in processes requiring the epithelialization of mesenchymal cells such as glandular lumen formation of normal breast cell lines (Maxwell et al., 2011), wound repair (Tolg et al., 2014) and tail regeneration in *Xenopus* (Contreras et al., 2009). While *HMMR* is mostly up-regulated in tumors, decreased levels of *HMMR* have been correlated with an increased risk for breast cancer as well (Pujana et al., 2007). This is in line with our results showing that both up- and down-regulation of *hmmr* lead to defective RI, i.e. defective MET, in the context of a developing tissue. Inhibition of MET directs epithelializing cells towards a more mesenchymal morphology. Loss of polarization could also affect mature epithelia, leading to induction of EMT. Both inhibition of MET and induction of EMT would thus render cells more mesenchymal, possibly enhancing metastasizing abilities and contributing to tumor development.

In summary, our work has revealed a novel *in vivo* function of *hmmr* in anterior neural morphogenesis and NTC, that may have important implications for tissue integrity in the developing and adult human.

Funding sources

K.F. is indebted to the Baden-Württemberg Stiftung for the financial support of this research project by the Eliteprogramme for Postdocs and the support through a Margarete-von-Wrangell fellowship, funded by the European Social Fund and by the Ministry of Science, Research and the Arts in Baden-Württemberg. T.O. is supported by a fellowship for graduate students from the Landesgraduiertenförderung in Baden-Wuerttemberg. A.S. is funded by the German Research foundation (DFG), grant number SCHA965/6-2.

Acknowledgements

We are thankful for invaluable technical help by Anna Iwanska and Elisabeth Schuster. We thank Martin Blum for support and critical reading of the manuscript and members of the Institute of Zoology, especially Axel Schweickert, for advice and discussion. We thank Thomas Thumberger for discussion and comments during the work.

We acknowledge the generous gifts of Hmmr antibody and plasmid by Aaron Groen and Tim Mitchison.

Appendix A. Supporting information

Supplementary data associated with this article can be found in the online version at doi:10.1016/j.ydbio.2017.07.020.

References

Abràmoff, M.D., Magalhães, P.J., Ram, S.J., 2004. Image Processing with ImageJ, Biophotonics International. Laurin Publishing, Pittsfield, MA, USA.

Aquilina-Beck, A., Ilagan, K., Liu, Q., Liang, J.O., 2007. Nodal signaling is required for closure of the anterior neural tube in zebrafish. BMC Dev. Biol. 7, 126. http://dx.doi.org/10.1186/1471-213X-7-126.

Assmann, V., Jenkinson, D., Marshall, J.F., Hart, I.R., 1999. The intracellular hyaluronan receptor RHAMM/IHABP interacts with microtubules and actin filaments. J. Cell Sci. 112 (Pt 22), 3943–3954.

Assmann, V., Gillett, C.E., Poulsom, R., Ryder, K., Hart, I.R., Hanby, A.M., 2001. The pattern of expression of the microtubule-binding protein RHAMM/IHABP in mammary carcinoma suggests a role in the invasive behaviour of tumour cells. J. Pathol. 195, 191–196. http://dx.doi.org/10.1002/path.941.

Casini, P., Nardi, I., Ori, M., 2010. RHAMM mRNA expression in proliferating and migrating cells of the developing central nervous system. Gene Expr. Patterns 10, 93–97. http://dx.doi.org/10.1016/j.gep.2009.12.003.

Cearns, M.D., Escuin, S., Alexandre, P., Greene, N.D.E., Copp, A.J., 2016. Microtubules, polarity and vertebrate neural tube morphogenesis. J. Anat. 229, 63–74. http://dx.doi.org/10.1111/joa.12468.

Cha, S.-W., Tadjuidje, E., Wylie, C., Heasman, J., 2011. The roles of maternal Vangl2 and aPKC in Xenopus oocyte and embryo patterning. Development 138, 3989–4000. http://dx.doi.org/10.1242/dev.068866.

Chen, H., Mohan, P., Jiang, J., Nemirovsky, O., He, D., Fleisch, M.C., Niederacher, D., Pilarski, L.M., Lim, C.J., Maxwell, C.A., 2014. Spatial regulation of Aurora A activity during mitotic spindle assembly requires RHAMM to correctly localize TPX2. Cell Cycle 13, 2248–2261. http://dx.doi.org/10.4161/cc.29270.

Chiang, C., Litingtung, Y., Lee, E., Young, K.E., Corden, J.L., Westphal, H., Beachy, P.A., 1996. Cyclopia and defective axial patterning in mice lacking Sonic hedgehog gene function. Nature 383, 407–413. http://dx.doi.org/10.1038/383407a0.

Chung, M.-I., Peyrot, S.M., LeBoeuf, S., Park, T.J., McGary, K.L., Marcotte, E.M., Wallingford, J.B., 2012. RFX2 is broadly required for ciliogenesis during vertebrate development. Dev. Biol. 363, 155–165. http://dx.doi.org/10.1016/j.ydbio.2011.12.029.

Contreras, E.G., Gaete, M., Sánchez, N., Carrasco, H., Larrain, J., 2009. Early requirement of Hyaluronan for tail regeneration in Xenopus tadpoles. Development 136, 2987–2996. http://dx.doi.org/10.1242/dev.035501.

Copp, A.J., Checiu, I., Henson, J.N., 1994. Developmental basis of severe neural tube defects in the loop-tail (Lp) mutant mouse: use of microsatellite DNA markers to identify embryonic genotype. Dev. Biol. 165, 20–29. http://dx.doi.org/10.1006/dbio.1994.1230.

Darken, R.S., Scola, A.M., Rakeman, A.S., Das, G., Mlodzik, M., Wilson, P.A., 2002. The planar polarity gene strabismus regulates convergent extension movements in Xenopus. EMBO J. 21, 976–985. http://dx.doi.org/10.1093/emboj/21.5.976.

von Dassow, G., Schmidt, J.E., Kimelman, D., 1993. Induction of the Xenopus organizer: expression and regulation of Xnot, a novel FGF and activin-regulated homeo box gene. Genes Dev. 7, 355–366.

Davidson, L.A., Keller, R.E., 1999. Neural tube closure in Xenopus laevis involves medial migration, directed protrusive activity, cell intercalation and convergent extension. Development 126, 4547–4556.

Etienne-Manneville, S., 2013. Microtubules in cell migration. Annu Rev. Cell Dev. Biol. 29, 471–499. http://dx.doi.org/10.1146/annurev-cellbio-101011-155711.

Fernandes, M., Hébert, J.M., 2008. The ups and downs of holoprosencephaly: dorsal versus ventral patterning forces. Clin. Genet. 73, 413–423. http://dx.doi.org/10.1111/j.1399-0004.2008.00994.x.

Fukata, M., Watanabe, T., Noritake, J., Nakagawa, M., Yamaga, M., Kuroda, S., Matsuura, Y., Iwamatsu, A., Perez, F., Kaibuchi, K., 2002. Rac1 and Cdc42 capture microtubules through IQGAP1 and CLIP-170. Cell 109, 873–885.

Goto, T., Keller, R., 2002. The planar cell polarity gene strabismus regulates convergence and extension and neural fold closure in Xenopus. Dev. Biol. 247, 165–181. http://dx.doi.org/10.1006/dbio.2002.0673.

Gouëffic, Y., Guilluy, C., Guérin, P., Patra, P., Pacaud, P., Loirand, G., 2006. Hyaluronan induces vascular smooth muscle cell migration through RHAMM-mediated PI3K-dependent Rac activation. Cardiovasc. Res. 72, 339–348. http://dx.doi.org/10.1016/j.cardiores.2006.07.017.

Gray, R.S., Abitua, P.B., Wlodarczyk, B.J., Szabo-Rogers, H.L., Blanchard, O., Lee, I., Weiss, G.S., Liu, K.J., Marcotte, E.M., Wallingford, J.B., Finnell, R.H., 2009. The planar cell polarity effector Fuz is essential for targeted membrane trafficking, ciliogenesis and mouse embryonic development. Nat. Cell Biol. 11, 1225–1232. http://dx.doi.org/10.1038/ncb1966.

Greene, N.D.E., Copp, A.J., 2014. Neural tube defects. Annu. Rev. Neurosci. 37, 221–242. http://dx.doi.org/10.1146/annurev-neuro-062012-170354.

Groen, A.C., Cameron, L.A., Coughlin, M., Miyamoto, D.T., Mitchison, T.J., Ohi, R., 2004. XRHAMM functions in ran-dependent microtubule nucleation and pole formation during anastral spindle assembly. CURBIO 14, 1801–1811. http://dx.doi.org/10.1016/j.cub.2004.10.002.

Gupta, S., Sen, J., 2016. Roof plate mediated morphogenesis of the forebrain: new players join the game. Dev. Biol. 413, 145–152. http://dx.doi.org/10.1016/j.ydbio.2016.03.019.

Hagenlocher, C., Walentek, P., Mueller, C., Thumberger, T., Feistel, K., 2013. Ciliogenesis and cerebrospinal fluid flow in the developing Xenopus brain are regulated by foxj1. Cilia 2, 12. http://dx.doi.org/10.1186/2046-2530-2-12.

Haigo, S.L., Hildebrand, J.D., Harland, R.M., Wallingford, J.B., 2003. Shroom induces apical constriction and is required for hingepoint formation during neural tube closure. Curr. Biol. 13, 2125–2137.

Hall, C.L., Wang, C., Lange, L.A., Turley, E.A., 1994. Hyaluronan and the hyaluronan receptor RHAMM promote focal adhesion turnover and transient tyrosine kinase activity. J. Cell Biol. 126, 575–588.

Hall, C.L., Yang, B., Yang, X., Zhang, S., Turley, M., Samuel, S., Lange, L.A., Wang, C., Curpen, G.D., Savani, R.C., Greenberg, A.H., Turley, E.A., 1995. Overexpression of the hyaluronan receptor RHAMM is transforming and is also required for H-ras transformation. Cell 82, 19–26.

Harumoto, T., Ito, M., Shimada, Y., Kobayashi, T.J., Ueda, H.R., Lu, B., Uemura, T., 2010. Atypical cadherins Dachsous and Fat control dynamics of noncentrosomal microtubules in planar cell polarity. Dev. Cell 19, 389–401. http://dx.doi.org/10.1016/j.devcel.2010.08.004.

Hatakeyama, J., Wald, J.H., Printsev, I., Ho, H.Y.H., Carraway, K.L., 2014. Vangl1 and Vangl2: planar cell polarity components with a developing role in cancer. Endocr. Relat. Cancer 21, R345–R356. http://dx.doi.org/10.1530/ERC-14-0141.

Hofmann, M., Assmann, V., Fieber, C., Sleeman, J.P., Moll, J., Ponta, H., Hart, I.R., Herrlich, P., 1998. Problems with RHAMM: a new link between surface adhesion and oncogenesis? Cell 95, 591–592, (author reply 592–593).

Jayachandran, P., Olmo, V.N., Sanchez, S.P., McFarland, R.J., Vital, E., Werner, J.M., Hong, E., Sanchez-Alberola, N., Molodstov, A., Brewster, R.M., 2016. Microtubule-associated protein 1b is required for shaping the neural tube. Neural Dev. 11, 1. http://dx.doi.org/10.1186/s13064-015-0056-4.

Jiang, J., Casalegno-Garduno, R., Chen, H., Schmitt, A., Schmitt, M., Maxwell, C.A., 2010. Multifunctional proteins bridge mitosis with motility and cancer with inflammation and arthritis. Sci. World J. 10, 1244–1257. http://dx.doi.org/10.1100/tsw.2010.141.

Karfunkel, P., 1971. The role of microtubules and microfilaments in neurulation in Xenopus. Dev. Biol. 25, 30–56.

Kee, N., Wilson, N., De Vries, M., Bradford, D., Key, B., Cooper, H.M., 2008. Neogenin and RGMa control neural tube closure and neuroepithelial morphology by regulating cell polarity. J. Neurosci. 28, 12643–12653. http://dx.doi.org/10.1523/JNEUROSCI.4265-08.2008.

Keller, R., Shih, J., Sater, A., 1992. The cellular basis of the convergence and extension of the Xenopus neural plate. Dev. Dyn. 193, 199–217. http://dx.doi.org/10.1002/aja.1001930302.

Keller, R.E., 1980. The cellular basis of epiboly: an SEM study of deep-cell rearrangement during gastrulation in Xenopus laevis. J. Embryol. Exp. Morphol. 60, 201–234.

Li, H., Moll, J., Winkler, A., Frappart, L., Brunet, S., Hamann, J., Kroll, T., Verlhac, M.-H., Heuer, H., Herrlich, P., Ploubidou, A., 2015. RHAMM deficiency disrupts folliculogenesis resulting in female hypofertility. Biol. Open 4, 562–571. http://dx.doi.org/10.1242/bio.201410892.

Li, H., Frappart, L., Moll, J., Winkler, A., Kroll, T., Hamann, J., Kufferath, I., Groth, M., Taudien, S., Schiitte, M., Yaspo, M.-L., Heuer, H., Lange, B.M.H., Platzer, M., Zatloukal, K., Herrlich, P., Ploubidou, A., 2016. Impaired planar germ cell division in the testis, caused by dissociation of RHAMM from the spindle, results in hypofertility and seminoma. Cancer Res.. http://dx.doi.org/10.1158/0008-5472.CAN-16-0179, (0179.2016).

Lindqvist, M., Horn, Z., Bryja, V., Schulte, G., Papachristou, P., Ajima, R., Dyberg, C., Arenas, E., Yamaguchi, T.P., Lagercrantz, H., Ringstedt, T., 2010. Vang-like protein 2 and Rac1 interact to regulate adherens junctions. J. Cell Sci. 123, 472–483. http://dx.doi.org/10.1242/jcs.048074.

Macdonald, R., Barth, K.A., Xu, Q., Holder, N., Mikkola, I., Wilson, S.W., 1995. Midline signalling is required for Pax gene regulation and patterning of the eyes. Development 121, 3267–3278. http://dx.doi.org/10.1038/368208a0.

Marsden, M., DeSimone, D.W., 2001. Regulation of cell polarity, radial intercalation and epiboly in Xenopus: novel roles for integrin and fibronectin. Development 128, 3635–3647.

Matis, M., Russler-Germain, D.A., Hu, Q., Tomlin, C.J., Axelrod, J.D., 2014. Microtubules provide directional information for core PCP function. eLife 3, e02893. http://dx.doi.org/10.7554/eLife.02893.

Maxwell, C.A., Keats, J.J., Crainie, M., Sun, X., Yen, T., Shibuya, E., Hendzel, M., Chan, G., Pilarski, L.M., 2003. RHAMM is a centrosomal protein that interacts with dynein and maintains spindle pole stability. Mol. Biol. Cell 14, 2262–2276. http://dx.doi.org/10.1091/mbc.E02-07-0377.

Maxwell, C.A., Rasmussen, E., Zhan, F., Keats, J.J., Adamia, S., Strachan, E., Crainie, M., Walker, R., Belch, A.R., Pilarski, L.M., Barlogie, B., Shaughnessy, J., Reiman, T., 2004. RHAMM expression and isoform balance predict aggressive disease and poor survival in multiple myeloma. Blood 104, 1151–1158. http://dx.doi.org/10.1182/blood-2003-11-4079.

Maxwell, C.A., Benítez, J., Gómez-Baldó, L., Osorio, A., Bonifaci, N., Fernández-Ramires, R., Costes, S.V., Guinó, E., Chen, H., Evans, G.J.R., Mohan, P., Català, I., Petit, A., Aguilar, H., Villanueva, A., Aytes, A., Serra-Musach, J., Rennert, G., Lejbkowicz, F., Peterlongo, P., Manoukian, S., Peissel, B., Ripamonti, C.B., Bonanni, B., Viel, A., Allavena, A., Bernard, L., Radice, P., Friedman, E., Kaufman, B., Laitman, Y., Dubrovsky, M., Milgrom, R., Jakubowska, A., Cybulski, C., Gorski, B., Jaworska, K., Durda, K., Sukiennicki, G., Lubiński, J., Shugart, Y.Y., Domchek, S.M., Letrero, R., Weber, B.L., Hogervorst, F.B.L., Rookus, M.A., Collee, J.M., Devilee, P., Ligtenberg, M.J., Luijt, R.B.V.D., Aalfs, C.M., Waisfisz, Q., Wijnen, J., Roozendaal, C.E.P.V.,

HEBON, EMBRACE, Easton, D.F., Peock, S., Cook, M., Oliver, C., Frost, D., Harrington, P., Evans, D.G., Lalloo, F., Eeles, R., Izatt, L., Chu, C., Eccles, D., Douglas, F., Brewer, C., Nevanlinna, H., Heikkinen, T., Couch, F.J., Lindor, N.M., Wang, X., Godwin, A.K., Caligo, M.A., Lombardi, G., Loman, N., Karlsson, P., Ehrencrona, H., Wachenfeldt, A.V., SWE-BRCA, Barkardottir, R.B., Hamann, U., Rashid, M.U., Lasa, A., Caldés, T., Andrés, R., Schmitt, M., Assmann, V., Stevens, K., Offit, K., Curado, J., Tilgner, H., Guigó, R., Aiza, G., Brunet, J., Castellsagué, J., Martrat, G., Urruticoechea, A., Blanco, I., Tihomirova, L., Goldgar, D.E., Buys, S., John, E.M., Miron, A., Southey, M., Daly, M.B., BCFR, Schmutzler, R.K., Wappenschmidt, B., Meindl, A., Arnold, N., Deissler, H., Varon-Mateeva, R., Sutter, C., Niederacher, D., Imyamitov, E., Sinilnikova, O.M., Stoppa-Lyonnet, D., Mazoyer, S., Verny-Pierre, C., Castera, L., de Pauw, A., Bignon, Y.-J., Uhrhammer, N., Peyrat, J.-P., Vennin, P., Fert Ferrer, S., Collonge-Rame, M.-A., Mortemousque, I., GEMO Study Collaborators, Spurdle, A.B., Beesley, J., Chen, X., Healey, S., kConFab, Barcellos-Hoff, M.H., Vidal, M., Gruber, S.B., Lázaro, C., Capellá, G., McGuffog, L., Nathanson, K.L., Antoniou, A.C., Chenevix-Trench, G., Fleisch, M.C., Moreno, V., Pujana, M.A., 2011. Interplay between BRCA1 and RHAMM regulates epithelial apicobasal polarization and may influence risk of breast cancer. PLoS Biol. 9, e1001199. http://dx.doi.org/10.1371/journal.pbio.1001199.

Murdoch, J.N., Copp, A.J., 2010. The relationship between sonic Hedgehog signaling, cilia, and neural tube defects. Birth Defects Res. Part A: Clin. Mol. Teratol. 88, 633–652. http://dx.doi.org/10.1002/bdra.20686.

Ossipova, O., Chu, C.-W., Fillatre, J., Brott, B.K., Itoh, K., Sokol, S.Y., 2015a. The involvement of PCP proteins in radial cell intercalations during Xenopus embryonic development. Dev. Biol. 408, 316–327. http://dx.doi.org/10.1016/j.ydbio.2015.06.013.

Ossipova, O., Kim, K., Sokol, S.Y., 2015b. Planar polarization of Vangl2 in the vertebrate neural plate is controlled by Wnt and Myosin II signaling. Biol. Open 4, 722–730. http://dx.doi.org/10.1242/bio.201511676.

Park, M., Moon, R.T., 2002. The planar cell-polarity gene stbm regulates cell behaviour and cell fate in vertebrate embryos. Nat. Cell Biol. 4, 20–25. http://dx.doi.org/10.1038/ncb716.

Park, T.J., Haigo, S.L., Wallingford, J.B., 2006. Ciliogenesis defects in embryos lacking inturned or fuzzy function are associated with failure of planar cell polarity and Hedgehog signaling. Nat. Genet. 38, 303–311. http://dx.doi.org/10.1038/ng1753.

Puelles, L., Rubenstein, J.L.R., 2015. A new scenario of hypothalamic organization: rationale of new hypotheses introduced in the updated prosomeric model. Front. Neuroanat. 9, 27. http://dx.doi.org/10.3389/fnana.2015.00027.

Pujana, M.A., Han, J.-D.J., Starita, L.M., Stevens, K.N., Tewari, M., Ahn, J.S., Rennert, G., Moreno, V., Kirchhoff, T., Gold, B., Assmann, V., Elshamy, W.M., Rual, J.-F., Levine, D., Rozek, L.S., Gelman, R.S., Gunsalus, K.C., Greenberg, R.A., Sobhian, B., Bertin, N., Venkatesan, K., Ayivi-Guedehoussou, N., Solé, X., Hernández, P., Lázaro, C., Nathanson, K.L., Weber, B.L., Cusick, M.E., Hill, D.E., Offit, K., Livingston, D.M., Gruber, S.B., Parvin, J.D., Vidal, M., 2007. Network modeling links breast cancer susceptibility and centrosome dysfunction. Nat. Genet. 39, 1338–1349. http://dx.doi.org/10.1038/ng.2007.2.

Roessler, E., Muenke, M., 2010. The molecular genetics of holoprosencephaly. Am. J. Med. Genet. C Semin. Med. Genet. 154C, 52–61. http://dx.doi.org/10.1002/ajmg.c.30236.

Schroeder, T.E., 1970. Neurulation in Xenopus laevis. An analysis and model based upon light and electron microscopy. J. Embryol. Exp. Morphol. 23, 427–462.

Sepich, D.S., Usmani, M., Pawlicki, S., Solnica-Krezel, L., 2011. Wnt/PCP signaling controls intracellular position of MTOCs during gastrulation convergence and extension movements. Development 138, 543–552. http://dx.doi.org/10.1242/dev.053959.

Shimada, Y., Yonemura, S., Ohkura, H., Strutt, D., Uemura, T., 2006. Polarized transport of Frizzled along the planar microtubule arrays in Drosophila wing epithelium. Dev. Cell 10, 209–222. http://dx.doi.org/10.1016/j.devcel.2005.11.016.

Silverman-Gavrila, R., Silverman-Gavrila, L., Hou, G., Zhang, M., Charlton, M., Bendeck, M.P., 2011. Rear polarization of the microtubule-organizing center in neointimal smooth muscle cells depends on PKC. Am. J. Phys. Anthropol. 178, 895–910. http://dx.doi.org/10.1016/j.ajpath.2010.10.001.

Suzuki, M., Hara, Y., Takagi, C., Yamamoto, T.S., Ueno, N., 2010. MID1 and MID2 are required for Xenopus neural tube closure through the regulation of microtubule organization. Development 137, 2329–2339. http://dx.doi.org/10.1242/dev.048769.

Suzuki, M., Morita, H., Ueno, N., 2012. Molecular mechanisms of cell shape changes that contribute to vertebrate neural tube closure. Dev. Growth Differ. 54, 266–276. http://dx.doi.org/10.1111/j.1440-169X.2012.01346.x.

Szabó, A., Cobo, I., Omara, S., McLachlan, S., Keller, R., Mayor, R., 2016. The molecular basis of radial intercalation during tissue spreading in early development. Dev. Cell 37, 213–225. http://dx.doi.org/10.1016/j.devcel.2016.04.008.

Tolg, C., Hamilton, S.R., Morningstar, L., Zhang, J., Zhang, S., Esguerra, K.V., Telmer, P.G., Luyt, L.G., Harrison, R., McCarthy, J.B., Turley, E.A., 2010. RHAMM promotes interphase microtubule instability and mitotic spindle integrity through MEK1/ERK1/2 activity. J. Biol. Chem. 285, 26461–26474. http://dx.doi.org/10.1074/jbc.M110.121491.

Tolg, C., McCarthy, J.B., Yazdani, A., Turley, E.A., 2014. Hyaluronan and RHAMM in wound repair and the "cancerization" of stromal tissues. Biomed. Res. Int. 2014, 103923. http://dx.doi.org/10.1155/2014/103923.

Ueno, N., Greene, N.D.E., 2003. Planar cell polarity genes and neural tube closure. Birth Defects Res. C Embryo Today 69, 318–324. http://dx.doi.org/10.1002/bdrc.10029.

Vladar, E.K., Bayly, R.D., Sangoram, A.M., Scott, M.P., Axelrod, J.D., 2012. Microtubules enable the planar cell polarity of airway cilia. Curr. Biol. 22, 2203–2212. http://dx.doi.org/10.1016/j.cub.2012.09.046.

Walck-Shannon, E., Hardin, J., 2014. Cell intercalation from top to bottom. Nat. Rev. Mol. Cell Biol. 15, 34–48. http://dx.doi.org/10.1038/nrm3723.

Wallingford, J.B., 2005. Neural tube closure and neural tube defects: studies in animal models reveal known knowns and known unknowns. Am. J. Med. Genet. C Semin. Med. Genet. 135C, 59–68. http://dx.doi.org/10.1002/ajmg.c.30054.

Wallingford, J.B., Harland, R.M., 2002. Neural tube closure requires Dishevelled-dependent convergent extension of the midline. Development 129, 5815–5825.

Wallingford, J.B., Fraser, S.E., Harland, R.M., 2002. Convergent extension: the molecular control of polarized cell movement during embryonic development. Dev. Cell 2, 695–706.

Wallingford, J.B., Niswander, L.A., Shaw, G.M., Finnell, R.H., 2013. The continuing challenge of understanding, preventing, and treating neural tube defects. Science 339. http://dx.doi.org/10.1126/science.1222002.

Watanabe, T., Wang, S., Noritake, J., Sato, K., Fukata, M., Takefuji, M., Nakagawa, M., Izumi, N., Akiyama, T., Kaibuchi, K., 2004. Interaction with IQGAP1 links APC to Rac1, Cdc42, and actin filaments during cell polarization and migration. Dev. Cell 7, 871–883. http://dx.doi.org/10.1016/j.devcel.2004.10.017.

The Frog Xenopus as a Model to Study Joubert Syndrome: The Case of a Human Patient With Compound Heterozygous Variants in *PIBF1*

frontiers in Physiology

ORIGINAL RESEARCH
published: 25 February 2019
doi: 10.3389/fphys.2019.00134

The Frog *Xenopus* as a Model to Study Joubert Syndrome: The Case of a Human Patient With Compound Heterozygous Variants in *PIBF1*

Tim Ott[1], Lilian Kaufmann[2], Martin Granzow[2], Katrin Hinderhofer[2], Claus R. Bartram[2], Susanne Theiß[2], Angelika Seitz[3], Nagarajan Paramasivam[4,5], Angela Schulz[6], Ute Moog[2], Martin Blum[†] and Christina M. Evers[2†]*

[1] Institute of Zoology, University of Hohenheim, Stuttgart, Germany, [2] Institute of Human Genetics, Heidelberg University, Heidelberg, Germany, [3] Department of Neuroradiology, University Hospital Heidelberg, Heidelberg, Germany, [4] Medical Faculty Heidelberg, Heidelberg University, Heidelberg, Germany, [5] Division of Theoretical Bioinformatics, German Cancer Research Center (DKFZ), Heidelberg, Germany, [6] Genomics & Proteomics Core Facility, German Cancer Research Center (DKFZ), Heidelberg, Germany

OPEN ACCESS

Edited by:
Emily Sempou,
Yale University, United States

Reviewed by:
Mustafa Khokha,
Yale University, United States
Sally Ann Moody,
George Washington University, United States

***Correspondence:**
Christina M. Evers
christina.evers@med.uni-heidelberg.de

[†]*These authors have contributed equally to this work*

Specialty section:
This article was submitted to Embryonic and Developmental Physiology, a section of the journal Frontiers in Physiology

Received: *14 September 2018*
Accepted: *04 February 2019*
Published: *25 February 2019*

Citation:
Ott T, Kaufmann L, Granzow M, Hinderhofer K, Bartram CR, Theiß S, Seitz A, Paramasivam N, Schulz A, Moog U, Blum M and Evers CM (2019) The Frog Xenopus as a Model to Study Joubert Syndrome: The Case of a Human Patient With Compound Heterozygous Variants in PIBF1. Front. Physiol. 10:134. doi: 10.3389/fphys.2019.00134

Joubert syndrome (JS) is a congenital autosomal-recessive or—in rare cases–X-linked inherited disease. The diagnostic hallmark of the so-called molar tooth sign describes the morphological manifestation of the mid- and hind-brain in axial brain scans. Affected individuals show delayed development, intellectual disability, ataxia, hyperpnea, sleep apnea, abnormal eye, and tongue movements as well as hypotonia. At the cellular level, JS is associated with the compromised biogenesis of sensory cilia, which identifies JS as a member of the large group of ciliopathies. Here we report on the identification of novel compound heterozygous variants (p.Y503C and p.Q485*) in the centrosomal gene *PIBF1* in a patient with JS via trio whole exome sequencing. We have studied the underlying disease mechanism in the frog *Xenopus*, which offers fast assessment of cilia functions in a number of embryological contexts. Morpholino oligomer (MO) mediated knockdown of the orthologous *Xenopus pibf1* gene resulted in defective mucociliary clearance in the larval epidermis, due to reduced cilia numbers and motility on multiciliated cells. To functionally assess patient alleles, mutations were analyzed in the larval skin: the p.Q485* nonsense mutation resulted in a disturbed localization of PIBF1 to the ciliary base. This mutant failed to rescue the ciliation phenotype following knockdown of endogenous *pibf1*. In contrast, the missense variant p.Y503C resulted in attenuated rescue capacity compared to the wild type allele. Based on these results, we conclude that in the case of this patient, JS is the result of a pathogenic combination of an amorphic and a hypomorphic *PIBF1* allele. Our study underscores the versatility of the *Xenopus* model to study ciliopathies such as JS in a rapid and cost-effective manner, which should render this animal model attractive for future studies of human ciliopathies.

Keywords: PIBF1, Joubert syndrome, *Xenopus*, molar tooth sign, cilia, ciliopathy

INTRODUCTION

Joubert syndrome (JS, OMIM # 213300) comprises a group of autosomal recessive or X-linked inherited disorders with a distinct cerebellar and brainstem malformation recognizable on brain imaging, the "molar tooth sign." The typical brain malformation of JS patients gives their midbrain an appearance reminiscent of a molar or wisdom tooth on axial MRI (**Figures 1E–H**). The "molar tooth" appearance results from three anatomical abnormalities of brainstem and cerebellum: (a) an abnormally deep "interpeduncular fossa," (b) prominent, thickened, and elongated "superior cerebellar peduncles," and (c) absence or hypoplasia of the midline portion of the cerebellum, the "cerebellar vermis" (see **Figures 1E–H** for the "molar tooth sign" and **Figures 1I–L** showing the corresponding MRI of a healthy control individual) (Maria et al., 1997, 1999). Typical clinical symptoms of JS are hypotonia, global developmental delay, intellectual disability, abnormal breathing pattern, abnormal eye movements, and cerebellar ataxia. Additional features include retinal dystrophy, cystic kidney disease, liver fibrosis, polydactyly, cleft palate, and facial dysmorphism in some patients (for review see (Parisi and Glass, 1993)). The estimated birth prevalence of JS is 1:80,000–1:100,000 (Parisi and Glass, 1993), but this may represent an underestimate due to many undiagnosed cases. A higher prevalence is found in the French–Canadian population, with several founder variants noted (Badhwar et al., 2000; Srour et al., 2012a,b, 2015). Founder variants in different genes have also been identified in the Canadian Hutterite, the Ashkenazi Jewish, and the Dutch population (Edvardson et al., 2010; Valente et al., 2010; Huang et al., 2011; Shaheen et al., 2014; Kroes et al., 2016). To date, pathogenic variants in more than 30 genes are known to cause JS (for review see Parisi and Glass, 1993). The encoded proteins of all these genes localize either to the primary cilium, basal body and/or centrosome and play a role in the formation, morphology, and/or function of these organelles, rendering JS a member of the rapidly expanding family of ciliopathies (Parisi and Glass, 1993; Romani et al., 2013). Common features of many ciliopathies include brain malformation, renal disease, retinal dystrophy, and polydactyly. Pathogenic variants in genes that cause Joubert syndrome have also been identified in ciliopathies with clinical findings that overlap with JS, e.g., Meckel-Gruber syndrome (MKS), Jeune asphyxiating thoracic dystrophy (JATD), Bardet-Biedl syndrome (BBS), oral-facial-digital syndrome (OFD), and juvenile nephronophthisis. The severe end of the clinical spectrum is represented by the lethal disorder MKS (Barker et al., 2014). Most of the genes causative of MKS are also associated with JS, namely *CEP290, TMEM67, RPGRIP1L, CC2D2A, CEP41, MKS1, B9D1, B9D2, TMEM138, TMEM231, TCTN2, TCTN3, TMEM237, CPLANE1, CSPP1, CEP120, TMEM107,* and *TMEM216* (Parisi and Glass, 1993; Valente et al., 2010; Thomas et al., 2012; Romani et al., 2014; Bachmann-Gagescu et al., 2015; Knopp et al., 2015; Shaheen et al., 2015; Roosing et al., 2016; Slaats et al., 2016). In addition, several families with occurrence of JS and MKS in siblings have been reported (Brancati et al., 2009; Valente et al., 2010). Features of the skeletal ciliopathy JATD have been reported in several children with JS caused by mutations in *CSPP1* and *KIAA0586* (Tuz et al., 2014; Malicdan et al., 2015). Pathogenic variants in the three BBS genes *CEP290, MKS1*, and *NPHP1* have been shown to cause both BBS and JS (Leitch et al., 2008; Zaghloul and Katsanis, 2009; Knopp et al., 2015). Patients with oral-facial-digital syndrome (OFD) show features that overlap considerably with JS, as do several genes causative for OFD (Franco and Thauvin-Robinet, 2016). Patients with juvenile nephrophthisis can also show clinical overlap with JS: about 10% of individuals have extrarenal findings, including the molar tooth sign in some cases (Saunier et al., 2005). Conversely, nephronophthisis, can also be a renal manifestation in JS (Parisi and Glass, 1993). These examples illustrate the complex clinical and genetic background of JS and related ciliopathies. Preliminary genotype-phenotype correlation for some genes indicate that biallelic null alleles lead to MKS while at least one hypomorphic (e.g., missense) variant is associated with JS (Delous et al., 2007; Mougou-Zerelli et al., 2009; Tallila et al., 2009; Iannicelli et al., 2010; Romani et al., 2014). However, the molecular and cellular mechanisms that lead to a specific phenotype in patients with ciliopathies are not fully understood. Altered sonic hedgehog (SHH) signaling via defective cilia has been proposed to be the causative pathomechanism for the characteristic molar tooth sign in JS, but does not fully explain the mid-hindbrain phenotype (Spassky et al., 2008; Doherty, 2009).

Recently, mutations in *PIBF1* have been identified as a cause of JS, using a combination of a siRNA-based functional genomics screen and exome sequencing data (Wheway et al., 2015). A second publication reported a girl with a biallelic 36-bp insertion in *PIBF1* and clinical signs of JS (Hebbar et al., 2018). The patients presented with ataxia and developmental delay, ranging from mild to moderate. Imaging ranged from the classic molar tooth sign to moderate vermis hypoplasia with mildly thick superior cerebellar peduncles and characteristic superior cerebellar dysplasia (Wheway et al., 2015). In addition, thinning of corpus callosum, facial dysmorphism, hypotonia and enlarged cystic kidneys were observed in one patient (Hebbar et al., 2018). Polymicrogyria has not been described in association with *PIBF1* variants so far.

PIBF1, also known as *PIBF, CEP90, JBTS33*, and *C13orf24*, consists of 22 coding exons and is widely expressed in different human tissues, including the brain, kidney, and liver, with the highest expression in testis and thyroid (Fagerberg et al., 2014). *PIBF1* encodes the progesterone immunomodulatory binding factor 1 that is induced by the steroid hormone progesterone and overexpressed in highly proliferating cells (Lachmann et al., 2004; Cohen et al., 2016). The parent compound measures 90 kDa and is associated with the centrosome (Lachmann et al., 2004). A splice variant that is found in cytoplasm measures 34–36 kDa (Polgar et al., 2003; Lachmann et al., 2004). The protein regulates the immune system to maintain a normal pregnancy, may play a role in preterm labor and promotes the proliferation, migration, and invasion of astrozytoma/glioblastoma cells (Gonzalez-Arenas et al., 2014; Hudic et al., 2015, 2016; Gutierrez-Rodriguez et al., 2017). *PIBF1* encodes a centrosomal protein that may play an important role in ciliogenesis (Wheway et al., 2015). However, the precise molecular and cellular mechanisms that cause the

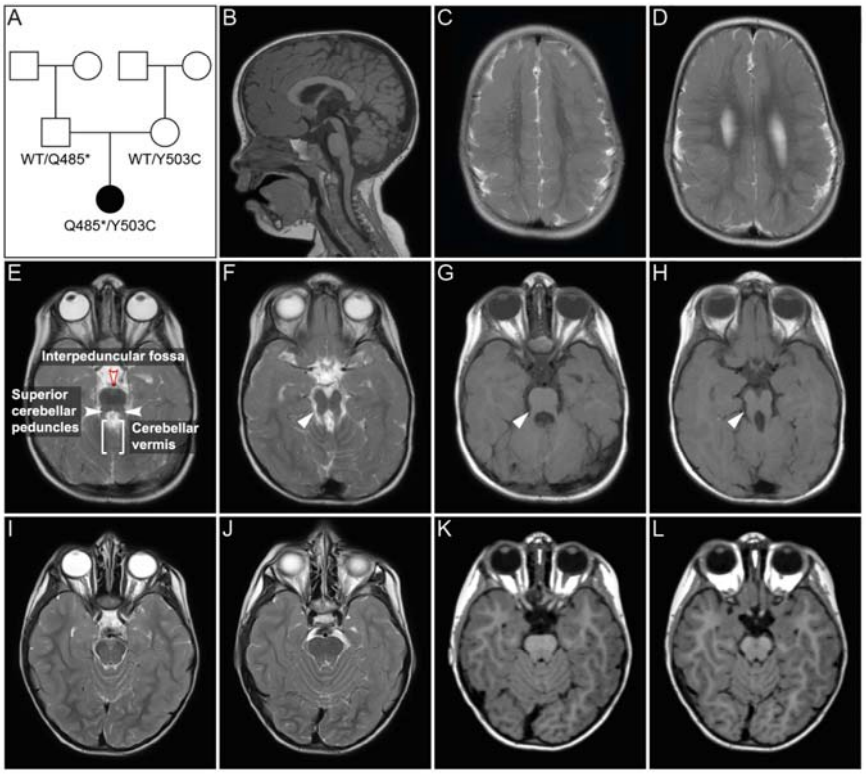

FIGURE 1 | Pedigree and MRI scans. **(A)** Pedigree of patient family. Black symbol, affected individual; White symbols, unaffected individuals. **(B–H)** MR imaging of the patient at age 2 years and 6 months. Sagittal **(B)** and axial **(C–H)** images showed polymicrogyria in the parietal and temporal region **(C,D)** and hypoplasia of vermis cerebellum **(B,E–H)**. Axial MR images of cerebellum and brainstem **(E–H)** showed a mild "molar tooth sign" (marked with white arrows in **F–H**) due to a deep interpeduncular fossa, prominent and elongated superior cerebellar peduncles and a hypoplastic cerebellar vermis. **(I–L)** Corresponding MR images of a healthy control individual.

complex JS phenotype in individuals with *PIBF1* mutations have not yet been elucidated.

Here, we report on novel *PIBF1* variants in a girl with JS. The variants were identified by whole-exome sequencing (WES) and functionally assessed in the *Xenopus* model. Our analyses demonstrate that both *PIBF1* alleles reflected loss of function variants. In general terms, the *Xenopus* model proves to be an excellent model to study the functional impact of rare genetic variants identified by diagnostic exome sequencing in patients with human ciliopathies.

MATERIALS AND METHODS

Participants

The patient and her parents were recruited and clinically phenotyped by the Outpatient Clinic of the Institute of Human Genetics, University Hospital Heidelberg, as part of the "Genome-wide genetic analysis of rare hereditary disorders" study. Written informed consent for participation in the study and publication of study results was obtained from both parents. The study was approved by the Ethics Committee of the Faculty of Medicine at the University of Heidelberg and adhered to the tenets of the Declaration of Helsinki. A summary of the study results and its clinical implications have been published elsewhere (Evers et al., 2017). Written informed consent for the publication of this case report and parental results was obtained from the patient's parents.

Case Report

The girl was the first child of non-consanguineous healthy parents from Germany. Her pedigree is shown in **Figure 1A**. She was born after 40 weeks of gestation with a birth weight

of 2,620 g (1st centile), length of 48 cm (3rd centile), and head circumference (OFC) of 34 cm (20th centile). Soon after birth, spastic tetraparesis, truncal hypotonia, and feeding difficulties were noted. At age 6 months, she developed abnormal eye movements. An electroencephalogram (EEG) was normal. The girl showed a severe failure to thrive and developmental delays. Routine pediatric investigations, including basic laboratory testing and metabolic screening, resulted in normal values with the exception of mildly elevated liver enzymes (GOT: 134U/l, GTP: 164 U/l, GGT: 493 U/l), which persisted during childhood. Regular abdominal ultrasound examinations were normal with no signs of hepatic fibrosis. Ophthalmological examination including fundoscopy at age 3 years showed no abnormalities. At her first visit to the Genetic Outpatient Department at age 4 years 2 month, she presented with global developmental delay, no speech, spastic tetraplegia and a submucosal cleft palate. Her height was 85 cm (<1st centile, −4.99 SDS), her weight 11.47 kg (<1st centile, −3.08 SDS) and her OFC 49.5 cm (8th centile, −1.43 SDS). At follow up examination at age 6 years 9 months, she had a height of 98.0 cm (<1st centile, −5.49 SDS), a weight of 13.6 kg (<1st centile, −4.30 SDS) and an OFC of 50 cm (2nd centile, −2.09 SDS). cMRI at age 6 months revealed bilateral polymicrogyria in the parietal and temporal areas. Follow up MRIs at age 23 months and 2 years and 6 months showed polymicrogyria, hypoplasia of vermis cerebelli, and a mild molar tooth sign (**Figures 1E–H**). Chromosomal analysis and molecular karyotyping (array analysis) gave normal results. Gene panel diagnostics for Joubert syndrome by next generation sequencing of 129 known and potentially ciliopathy genes showed no pathogenic mutation. The gene panel did not include *PIBF1*, which was not known to cause JS at the time of analysis. A single gene test by Sanger sequencing of *GPR5*, a gene associated with polymicrogyria, gave normal results.

Exome Sequencing

Genomic DNA was isolated from leukocytes of the patient and both parents by standard procedures (Miller et al., 1988). Whole exome sequencing (WES) and analysis of the sequence data of the patient and her parents was performed at the German Cancer Research Center (DKFZ) in Heidelberg, Germany, as described previously (Paramasivam et al., 2018). Variants with a minor allele frequency (MAF) >1% in the 1000 genome phase III and Exome Aggregation Consortium (ExAC) database (Lek et al., 2016) were considered common alleles and discarded, as were variants detected in 328 WES and 177 whole genome sequencing (WGS) local control samples with a frequency above 2%. Gene-based annotations from Gencode V19 were added using ANNOVAR (Wang et al., 2010). All single nucleotide variants (SNVs) and indels affecting protein sequences and variants within ±2 bases around the intron-exon junction were considered as functional. Variants were further assessed by the seven different variant effect prediction tools SIFT, PolyPhen2, LRT, MutationTaster, MutationAssessor, FATHMM, and PROVEAN from dbNSFP (Ng and Henikoff, 2003; Chun and Fay, 2009; Adzhubei et al., 2010; Schwarz et al., 2010; Reva et al., 2011; Choi et al., 2012; Liu et al., 2013; Shihab et al., 2013) and CADD scores (Kircher et al., 2014). Variants were classified according to standards and guidelines of the American College of Medical Genetics and Genomics (ACMG) (Richards et al., 2015). To confirm WES data by Sanger sequencing, exons 11 and 12 and adjacent intron boundaries of *PIBF1* (RefSeq NM_006346.2, ensemble transcript ENST00000326291.6) were sequenced using Big Dye Terminator V1.1 cycle sequencing kit and ABI 3130xl genetic analyzer. Primer sequences and PCR conditions are available upon request.

RT PCR, qPCR, and Sequencing

Total RNA from patients, parents, and control blood was extracted using the MasterPure RNA Purification Kit (Epicentre Biotechnologies). cDNA was synthesized using random hexamer primers and reverse transcriptase RT Maxima (Fermentas). qPCR was carried out using SybrGreen mix (Thermo Scientific). Expression levels using primer pairs for the three regions of *PIBF1* (exon 2–4, exon 10–12, exon 15–17) were normalized to *ADP-ribosylation factor 1 (ARF1)*. PCR products of patient, parents and control were sequenced by Sanger sequencing (GATC).

Western Blot Analysis of Overexpressed Protein

To analyze the expression of overexpressed PIBF1 variants, Hek293T cells were transfected in 6-well plates with 1 µg of the corresponding plasmids using Turbofect transfection reagent (Thermo Scientific. Cells were lysed 24 h post transfection and proteins were separated by 10% SDS-PAGE. For Western blot analysis, a rabbit anti-GFP antibody (1:1,000, Adgene) and a mouse anti-PIBF1 antibody (1:500, Biozol) were used.

Protein Structure Analysis

For analyzing putative protein domains, the following algorithms were used: NCBI conserved domain search (https://www.ncbi.nlm.nih.gov/Structure/cdd/wrpsb.cgi), InterProScan (https://www.ebi.ac.uk/interpro/search/sequence-search), WoLF PSORT (https://wolfpsort.hgc.jp), and epestfind (http://emboss.bioinformatics.nl/cgi-bin/emboss/epestfind).

Xenopus Injection Experiments

Adult *Xenopus laevis* frogs were obtained from Nasco (U.S.A.; https://www.enasco.com/c/Education-Supplies/Xenopus-Frogs). *Xenopus laevis* embryos were injected at the 4-cell stage into the ventral marginal zone to target the epidermal cell lineage (Moody, 2000). Translation blocking morpholino oligomere (TBMO; 5′-CCGGGACATCTTTACACTTTACATA-3′) was injected at 4 pmol per embryo. mRNAs of *EGFP* or *PIBF1* fusion constructs were injected at a dose of 0.4 pmol per embryo. Lineage tracer Fluorescein Dextran (FD, 10,000 MW, anionic, lysine fixable) was used at 50 ng per injection. Embryos were cultured until stage 30 and subsequently processed for analyses.

RNA *in situ* Hybridization and Immunofluorescence Staining

Xenopus embryos were fixed using 4% paraformaldehyde solution (for *in situ* hybridization and acetylated Tuba4a staining) or Dent's (for Pibf1 and Tjp1 staining). RNA *in*

situ hybridization was performed as described previously (Belo et al., 1997) using a full length digoxigenin labeled *pibf1* probe. The following reagents were used for immunofluorescence staining: anti-acetylated Tuba4a (T6793, Sigma; 1:800), anti-Pibf1 (SAB1401526, Sigma; 1:200), and anti-Tjp1 (21773-1-AP, Proteintech Europe; 1:400).

High-Speed Video-Microscopy

Capturing of ciliary beating required flat mounting of the specimens in a chamber constructed on a slide with tape and a cover slip. Only the most ventral cells allowed differential interference contrast microscopy of the ciliary tufts, which were recorded at 600 fps using a Hamamatsu X high speed video camera. Kymographs were generated using ImageJ (https://imagej.net/Generate_and_exploit_Kymographs).

RESULTS

The phenotypic features of the patient (cf. section Case Report), including developmental delay, hypotonia, polymicrogyria, vermian hypoplasia, and mild molar tooth sign (**Figure 1**), led to the clinical diagnosis of JS. The observed liver involvement with elevated GOT/GRP is also a typical finding of this ciliopathy. A cleft palate reported here is a rare finding in JS and demonstrates its clinical overlap with oral-facial-digital syndrome. The microcephaly of the patient is not part of the classical JS spectrum, but has been reported in a patient with a *PIBF1* missense mutation (Kodani et al., 2015).

Exome Sequencing

Exome sequencing variants were filtered as described above and only heterozygous *de novo* variants and variants being consistent with an autosomal recessive disease model were considered. Applying these filter criteria, 10 variants remained (**Table 1**). These were further assessed by *in silico* predicted effects on protein function, as described above (**Table 1**). Subsequently, a literature search was performed to gain further information about gene function and to determine if the gene had been previously associated with intellectual disability, neurological or developmental disorders in humans. This narrowed the candidate list to *PIBF1* variants c.1453C>T; p.(Q485*) and c.1508A>G; p.(Y503C). The variant c.1453C>T; p.(Q485*) was classified as pathogenic [class 5, according to ACMG criteria; (Richards et al., 2015)]. The variant c.1508A>G; p.(Y503C) was classified as variant of unknown significance [class 3, according to (Richards et al., 2015)].

Expression Analysis of *PIBF1* Variants in the Patient

cDNA fragments of three different regions of *PIBF1* (exons 2–4, 10–12, and 15–17) were amplified from the patient and both parents, showing a higher expression in the patient compared to mother, father, adult, and infant control (**Figure S1A**). Interestingly, the cDNA of exons 15–17, which are localized 3′ of the predicted premature stop codon of the variant p.(Q485*), showed a higher expression in the patient as well. However, whether both variants are transcribed in the patient was still unclear. Sequencing of the PCR product of the patient showed that both *PIBF1* variants could be detected in the patient (**Figure 2A**). The parents' cDNAs carried either the missense or the nonsense variant in heterozygous state (data not shown). This indicated that mRNA harboring the predicted pathogenic variant was not degraded by nonsense-mediated mRNA decay (NMD) and that both variants resulted in stable mRNAs. The enhanced transcription of both *PIBF1* variants in the patient could be a compensatory response to decreased PIBF1 protein levels due to protein instability of the mutants. The *PIBF1* nonsense variant p.(Q485*) was expected to result in the synthesis of a truncated protein lacking the C-terminal 273 amino acids. Expression

TABLE 1 | *De novo* and compound heterozygous variants and prediction of their functional effects.

Affected genes	RefSeq transcript and variant information*	Variant status	*in silico* parameters **: MT/MA/SIFT/PPH2(HDIV: HVAR)//FATMM/PROVEAN/LRT
ATXN1	ENST00000436367.1:exon7:c.G630T:p.Q210H	Heterozygous *de novo*	N/N/D/-:-/T/N/-
DSPP	ENST00000399271.1:exon5:c.2001_2003del:p.667_668del	Heterozygous *de novo*	Poly/-/-/-:-/-/-/-
EPS8L2	ENST00000318562.8:exon8:c.G616T:p.A206S	Heterozygous	DC/M/T/B:B/T/N/Del
EPS8L2	ENST00000318562.8:exon13:c.1071_1072insCTG:p.T357delinsTL	Heterozygous	Poly /-/-/-:-/-/-/-
OBSCN	ENST00000366707.4:exon52:c.A5292T:p.Q1764H	Heterozygous	N/N/T/D:P/T/N/N
OBSCN	ENST00000422127.1:exon94:c.20514_20515del:p.6838_6839del	Heterozygous	DC/-/-/-:-/-/-/-
PIBF1	ENST00000326291.6:exon11:c.C1453T:p.Q485X	Heterozygous	DC/-/-/-:-/-/-/-
PIBF1	ENST00000326291.6:exon12:c.A1508G:p.Y503C	Heterozygous	DC/M/D/D:D/T/D/Del
ZFHX3	ENST00000397992.5:exon9:c.C7543T:p.R2515C	Heterozygous	DC/N/T/D:B/D/N/Del
ZFHX3	ENST00000397992.5:exon8:c.G5535T:p.Q1845H	Heterozygous	DC/L/T/D:D/T//Del

*According to Ensembl database (http://www.ensembl.org).

**Obtained by prediction tools MutationTaster (MT) (Schwarz et al., 2010), MutationAssessor (MA) (Reva et al., 2011), SIFT (Ng and Henikoff, 2003), PolyPhen2 (PPH2) HDIV and PPH2 HVAR (Adzhubei et al., 2010), FATHMM (Shihab et al., 2013), PROVEAN (Choi et al., 2012) and LRT (Chun and Fay, 2009).

B, benign; D, damaging; DC, disease causing; Del, deleterious; L, predicted functional effect is low; M, predicted functional effect is medium, N, neutral; Poly, Polymorphism; ProbD, probably damaging; T, tolerated; PosD, possibly damaging.

analysis of wildtype (WT) and mutated EGFP-PIBF1 constructs using an anti GFP antibody showed expression of WT and both mutated proteins, the one with the missense and the one with the truncating variant at expected size (**Figure S1B**). This result indicated that both, missense and the nonsense variant, resulted in the synthesis of stable proteins with the nonsense variant being smaller than the WT and the missense, as expected. Analyses using an antibody against the full length PIBF1 protein could detect the WT and the missense variant, but not the truncated nonsense variant. However, the sensitivity of the antibody was far lower than that of the GFP antibody and it has not been tested on truncated PIBF1 proteins so far. Whether its epitope is in the lacking C-terminus has to be determined.

Protein Structure and Evolutionary Conservation of *Pibf1*

A comparison of PIBF1 protein sequences from various vertebrate species revealed a high degree of conservation (**Figure 2B**). The *Xenopus* sequence showed 69.5% identity (84.2% similarity) to human PIBF1, very close to the mouse (**Figure 2B**). Functional studies at the protein level have not been reported for PIBF1 so far. Applying the NCBI conserved domain search algorithm highlighted three possible SMC-related domains (structural maintenance of chromosomes; **Figure 2C**). Additional searches identified a putative PEST domain, two ER membrane retention signals including one R-4 motiv, two nuclear localization sequences (NLS), a peroxisomal targeting signal (PTS), and two leucine zipper sequences as well as 11 coiled-coil domains along the 757 amino acids (**Figure 2C**). The three known JS mutations as well as the two novel alleles reported here localize to the C-terminal half of the protein and within coil-coiled domain, while a 6th mutation, which caused microcephaly, was found at the N-terminus, again in a coiled-coil domain (**Figure 2C**).

The above *in silico* analyses thus showed that the two novel mutations are located in important regions of a highly conserved JS candidate gene. In order to prove that these alleles indeed were causative for JS in the patient, they needed to be functionally tested in a relevant vertebrate model organism, particularly because the variant p.(Y503C) did not fulfill the ACMG-criteria to be classified as pathogenic or likely pathogenic (Richards et al., 2015). We chose to apply the *Xenopus* model, because of its suitability for studying ciliopathies: speed, high-throughput, and low cost of analyses (Johnston et al., 2017; Blum and Ott, 2018).

Expression of *pibf1* in Ciliated Tissues During *Xenopus* Embryonic Development

As a prerequisite to functionally analyzing the putative JS alleles, we analyzed whether the endogenous *pibf1* mRNA was expressed in tissues related to cilia. Transcription of *pibf1* in embryos of defined developmental stages was analyzed using whole-mount *in situ* hybridization. Maternally deposited *pibf1* mRNA was present in the cytoplasm of the animal hemisphere in cleavage stage embryos (**Figure 3A**). At the onset of gastrulation, signals were found in future mesodermal tissues (**Figure 3B**; involuting marginal zone). From neurulation onwards, expression was found in the axial (notochord) and paraxial (somites) mesoderm (**Figures 3C,D**). Additionally, a dotted epidermal pattern was obvious which resembled the distribution of multiciliated cells (MCCs) in the larval skin and was maintained until the end of neurulation (**Figures 3C,D**). In the 2-day larva (stage 25, **Figure 3E**), mRNA transcripts were seen in the ciliated otic vesicle (**Figure 3E′**) as well as in the forming ciliated nephrostomes of the embryonic kidney. The latter staining intensified and was prominently visible in sections of stage 30 tadpoles (**Figures 3E,F′**). A persistent staining in the head region became more pronounced from stage 30 onwards (**Figures 3F–H**). Enrichment of *pibf1* transcripts in the head region as well as in the spinal cord was in agreement with the expected function of Pibf1 during neural development (**Figures 3E–G**). At these stages, the *pibf1* signal became less discrete, appeared more diffuse and was present at low levels in most tissues (**Figures 3E–G**). Histological sectioning revealed enrichment in the retina and inner nuclear cell layer (**Figure 3H′**). In summary, *pibf1* was expressed in many tissues harboring cilia, namely otic vesicle, nephrostomes, brain, retina, and possibly MCCs.

Pibf1 Protein Localization in Larval Skin MCCs

JS is associated with dysfunctional primary, i.e., immotile and sensory cilia. The unexpected mRNA expression in the larval skin hinted at localization in MCCs, which harbor hundreds of motile cilia. In order to investigate the possible expression of Pibf1 in MCCs, immunofluorescence staining using a monoclonal mouse PIBF1 antibody raised against the human protein was applied. This antibody detected hundreds of spots on individual cells dotted on the larval skin (**Figures 4A,A′**). Co-staining with the basal body marker (Cetn1; Park et al., 2008) unequivocally demonstrated that Pibf1 indeed localized to the base of individual cilia on MCCs, specifically to basal bodies, as Pibf1 and Cetn1 partially overlapped (**Figures 4A–C**). Therefore, Pibf1 seemed to be a *bona fide* component of all basal bodies in ciliated cells in *Xenopus*.

In order to ascertain whether or not the missense or nonsense mutations have impact on the localization of PIBF1 to basal bodies, we cloned fusion constructs in which the N-terminus of the human WT or mutant ORFs of *PIBF1* were linked to *EGFP*. Injection of the WT PIBF1 construct into the *Xenopus* epidermis recapitulated the endogenous distribution at the basal bodies of MCCs (**Figures 4D–F**), demonstrating that ectopic expression of a fusion protein did not interfere with correct localization of the protein. In many cases, aggregates of fusion protein were additionally found in targeted cells (**Figures 4D,G**). The missense construct fully phenocopied this localization (**Figures 4G–I**). In contrast, the signal of the nonsense variant was much attenuated at basal bodies and was additionally found in a non-localized manner throughout the cell (**Figures 4J–L**). Taken together, these analyses showed that (1) Pibf1 was unexpectedly expressed in motile cilia of the larval skin; (2) Pibf1 localized to basal bodies, in agreement with its centrosomal expression in other contexts (Kim and Rhee, 2011; Kim et al., 2012); (3) the nonsense allele

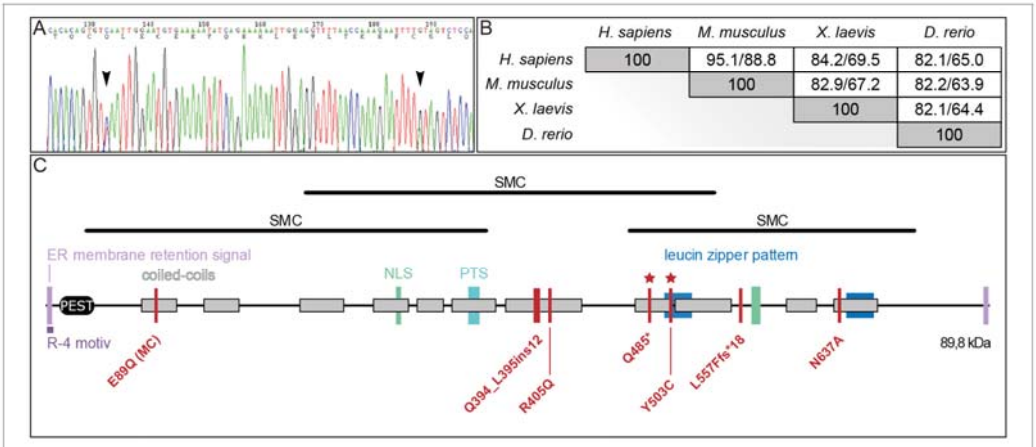

FIGURE 2 | PIBF1 protein conservation and domain structure. **(A)** Sanger sequencing of *PIBF1* from RT-PCR product of the patient mRNA extracted from blood. Black arrow heads indicate position of mutations. **(B)** Conservation of amino acid sequences between human, mouse, *Xenopus*, and zebrafish PIBF1. **(C)** Putative domain structure. JS and microcephaly (MC) mutations are indicated as red bars. For details see text. *Novel mutations identified in this study.

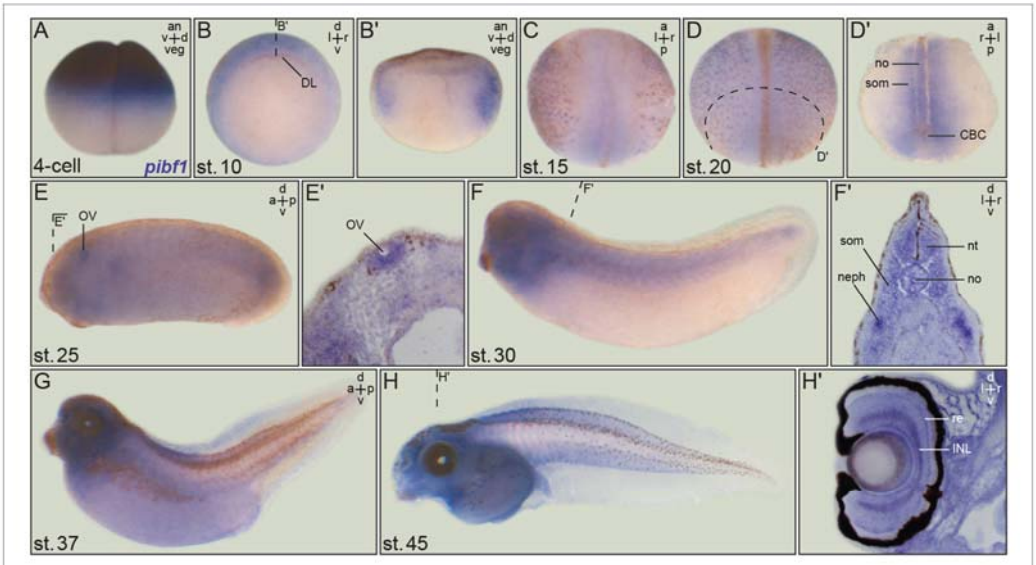

FIGURE 3 | Embryonic *pibf1* expression correlates with ciliated tissues. Embryos of defined stages were analyzed for *pibf1* mRNA by whole-mount *in situ* hybridization using a digoxigenin-labeled antisense probe. **(A)** Maternal transcripts in the animal hemisphere of the 4-cell embryo. **(B)** Expression in the involuting marginal zone tissue of the early gastrula embryo. **(C)** Staining of *pibf1* in the axial and paraxial mesoderm at early neurula stages. **(D)** *Pibf1* signals in skin MCCs and axial/paraxial mesoderm. **(E)** Expression in the otic vesicle at stage 25. **(F–H)** Expression pattern in tadpoles, including the head region, somites, and nephrostomes. Histological section of the eye **(H')** revealed signals in the retina as well as the inner nuclear cell layer. Planes of histological sections in **(B',D',E',F',H')** are indicated in the respective panels. an, animal; a, anterior; d, dorsal; DL, dorsal lip; INL, inner nuclear layer; l, left; neph, nephrostomes; no, notochord; nt, neural tube; ov, otic vesicle; p, posterior; r, right; re, retina; som, somite; v, ventral; veg, vegetal.

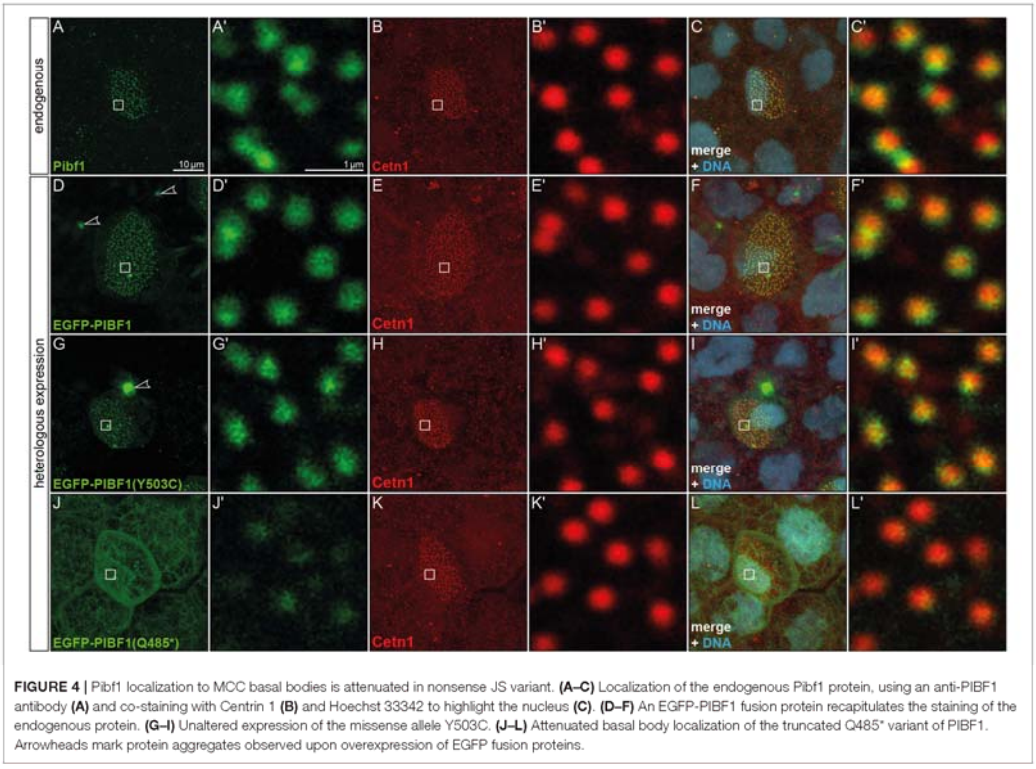

FIGURE 4 | Pibf1 localization to MCC basal bodies is attenuated in nonsense JS variant. **(A–C)** Localization of the endogenous Pibf1 protein, using an anti-PIBF1 antibody **(A)** and co-staining with Centrin 1 **(B)** and Hoechst 33342 to highlight the nucleus **(C)**. **(D–F)** An EGFP-PIBF1 fusion protein recapitulates the staining of the endogenous protein. **(G–I)** Unaltered expression of the missense allele Y503C. **(J–L)** Attenuated basal body localization of the truncated Q485* variant of PIBF1. Arrowheads mark protein aggregates observed upon overexpression of EGFP fusion proteins.

was much reduced in its localization to ciliary basal bodies, indicative of a ciliary function; (4) the missense allele appeared unaffected in its ciliary localization, raising questions as to the underlying mechanism of JS in the patient.

Functional Analysis of Wildtype and Mutant *PIBF1* Alleles in the *Xenopus* Larval Skin

Although JS is not related to motile cilia, the expression and localization of Pibf1 in basal bodies of MCCs afforded the opportunity of testing whether this protein played a role in motile cilia as well and whether the mutant alleles were affected in this function. Skin MCCs of *Xenopus* larvae function in much the same way as human airway epithelia, namely in mucociliary clearance as a first line of defense against pathogens (Dubaissi and Papalopulu, 2011; Walentek et al., 2014; Blum and Ott, 2018). MCC cilia beat in a coordinated manner to move mucus, produced by goblet cells, from anterior to posterior (head to tail), and to thereby remove environmental particles and pathogens caught by the mucus layer (Brooks and Wallingford, 2014). In order to assess a possible role of *pibf1* in this process, an antisense morpholino oligomer (MO) targeting the translational start site of the mRNA (translation blocking MO, TBMO) was designed. In retinal epithelial cells (RPE-1) and inner medullary collecting duct cells (IMCD3), loss of Pibf1 resulted in fewer or absent cilia (Kim et al., 2012; Wheway et al., 2015). We therefore analyzed the presence of MCC cilia in morphant larvae that were injected with TBMO into the skin lineage at the 4-cell stage. Successful gene knockdown was proven by immunofluorescence staining for Pibf1, which demonstrated the efficient depletion of the protein from MCCs of morphant specimens (**Figure 5**). Immunofluorescence staining of cilia in morphant specimens was performed by staining the ciliary axoneme with an antibody against acetylated tubulin (Tuba4a). This analysis clearly demonstrated markedly reduced numbers of cilia on morphant MCCs (**Figures 6A–E**). Functional consequences of reduced cilia numbers were assessed by high-speed video microscopy of larval skin at stage 30. **Movie S1** shows that coordinated ciliary beating was lost in morphants as compared to WT specimens. The loss of cilia was also apparent in kympgraphs from high-speed movies (**Figure 6L,M**). Ciliary tufts on WT and morphant MCCs were grouped into three classes, representing normal, mild, or strong reduction of cilia numbers. No unaffected ciliary tufts were retained in morphant MCCs, as displayed in **Figure 6M**.

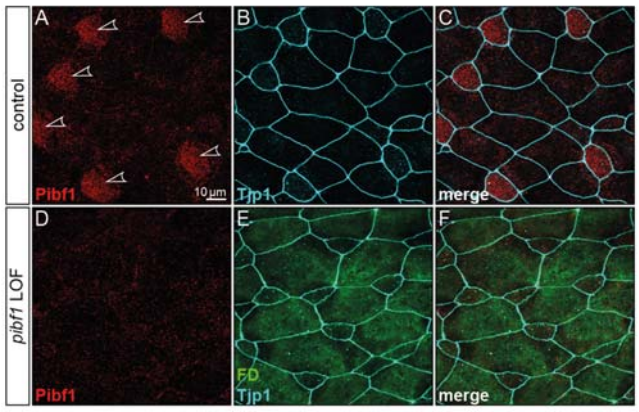

FIGURE 5 | Loss of Pibf1 protein in *pibf1* morphant *Xenopus* skin MCCs. Basal body staining of Pibf1 **(A–C)** was lost in TBMO injected specimen **(D–F)**. Tjp1 immunofluorescence was used to mark cell boundaries **(B,C,E,F)**. Fluorescent dextrane (green) was co-injected as lineage tracer to control targeting of injections **(E,F)**. Arrowheads highlight MCC cilia in WT embryo.

Next, we asked whether heterologous expression of a WT human *PIBF1* construct was able to rescue cilia numbers in morphants. To that end, TBMO and WT PIBF1 were co-injected into 4-cell embryos and targeted to the larval skin. As shown in **Figures 6E–G**, the WT human gene rescued cilia numbers in a highly significant manner. In a last set of experiments, we analyzed the rescue capacity of equimolar amounts of the two novel *Pibf1* alleles identified in our JS patient. While the nonsense mutant was unable to rescue the gene knockdown (**Figures 6E,H,I**), a residual and attenuated rescue capability was observed when the missense mutant allele was co-injected (**Figures 6E,J,K**). In summary, our functional analysis of mutant *Pibf1* alleles demonstrated a role of Pibf1 in motile cilia of larval skin MCCs in *Xenopus*, and identified both nonsense and missense allele as non-functional, in agreement with the manifested JS in the patient girl.

DISCUSSION

Mutant gene alleles identified in patient DNAs represent a valuable resource for studying protein function and are a prerequisite for the elucidation of pathomechanisms at the molecular level. A given mutation may not, however, reveal its pathogenicity at first glance. In the case of the compound heterozygous JS patient analyzed here, one of the mutations, the truncation variant p.Q485*, was highlighted as pathogenic according to ACMG criteria (Richards et al., 2015). Our analysis in ciliated *Xenopus* cells confirmed its predicted pathogenicity. The disturbed localization of this variant at basal bodies in combination with the inability to rescue the ciliation phenotype of Pibf1 deficient frog MCCs identifies it as an amorphic allele. Clinically even more important, our studies of the missense-variant p.Y503C indicated a pathogenic effect of this variant, too. A careful cell by cell analysis of mutant MCCs revealed that this mutant showed an about 50% rescue capacity, significantly below the >80% achieved with the WT allele (**Figure 6**). It should be noted, that this analysis was performed in a tissue that is not relevant in JS patients and on motile cilia, while JS is caused by defects of primary, immotile cilia. Therefore, in the context of a *bona fide* JS target tissues, the combination of these mutations may give rise to even more pronounced defects at high frequency. Recapitulating the patient gene setup in any animal model would be experimentally more challenging, require more time and be more expensive. The attenuated rescue ability, however, unequivocally demonstrates that the missense variant is hypomorphic in nature, leading to a re-classification of the allele from "unkown significant" to "likely pathogenic," according to ACMG criteria (Richards et al., 2015). The finding of a hypomorphic allele due to a missense mutation in combination with a null allele due to a truncating mutation is a typical finding in patients with JS and has been reported for a number of other causative genes (such as *RPGRIP1L*, *TMEM67*, *CCD2D2A*, and *TCTN3*), whereas biallelic null alleles in these genes are associated with a more severe phenotype (Delous et al., 2007; Mougou-Zerelli et al., 2009; Tallila et al., 2009; Iannicelli et al., 2010; Romani et al., 2014).

The precise role of PIBF1 in the context of ciliary biogenesis is not well-understood. All JS-associated mutations in *PIBF1* identified so far cluster in the C-terminal region of the protein [**Figure 2**; (Wheway et al., 2015; Hebbar et al., 2018)]. In contrast, a homozygous missense mutation that is linked to microcephaly is present within the N-terminus [**Figure 2**; (Kodani et al., 2015)]. The large structural maintenance of chromosomes (SMC) domains constitute almost 90% of the protein, suggesting that PIBF serves as a scaffolding factor which may dimerize with ciliary SMC proteins such as SMC1A or SMC3 (Khanna

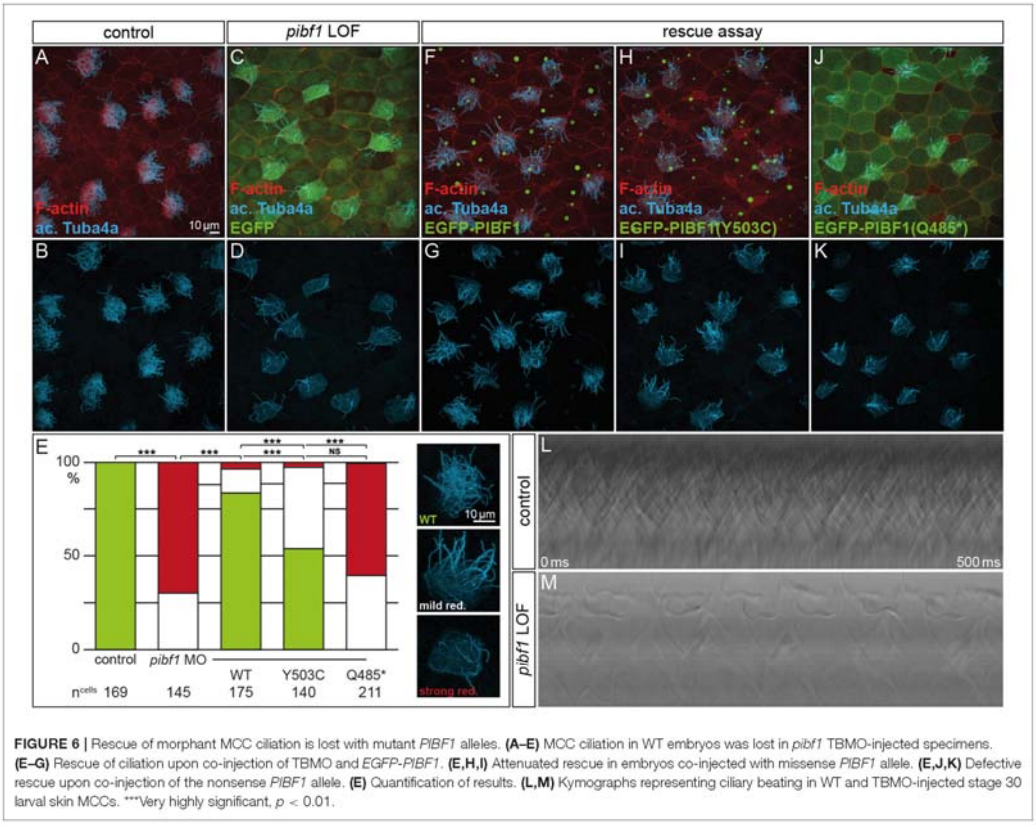

FIGURE 6 | Rescue of morphant MCC ciliation is lost with mutant *PIBF1* alleles. **(A–E)** MCC ciliation in WT embryos was lost in *pibf1* TBMO-injected specimens. **(E–G)** Rescue of ciliation upon co-injection of TBMO and *EGFP-PIBF1*. **(E,H,I)** Attenuated rescue in embryos co-injected with missense *PIBF1* allele. **(E,J,K)** Defective rescue upon co-injection of the nonsense *PIBF1* allele. **(E)** Quantification of results. **(L,M)** Kymographs representing ciliary beating in WT and TBMO-injected stage 30 larval skin MCCs. ***Very highly significant, $p < 0.01$.

et al., 2005). A search of the protein interaction database IntAct (https://www.ebi.ac.uk/intact/) revealed a number of SMC proteins that were shown to interact with PIBF1, for example CEP63 and PCM1 (Kim et al., 2012; Gupta et al., 2015; Yachie et al., 2016). As PCM1 is not relevant for cilia formation in multiciliated mouse tracheal epithelial cells, it is not a promising candidate to explain the loss of cilia in PIBF1 depleted MCCs (Vladar and Stearns, 2007). CEP63, in contrast, is required during the centriolar duplication cycle, acts in parallel with its paralog deup1 in basal body formation in MCCs and harbors an SMC related domain (Zhao et al., 2013). The reduced number of cilia on morphant MCCs may result from such a mechanism. *Xenopus* MCC offer themselves for in-depth analyses of potential interaction partners, which are beyond the scope of the present study.

The advent of high-throughput sequencing technology, in particular whole exome sequencing (WES), has led to a revolution of genetic diagnostics of rare diseases, e.g., developmental disorders. Before the era of WES many patients had undergone a long and frustrating "diagnostic odyssey" to obtain an accurate diagnosis. This has been widely overcome with the introduction of WES, which has emerged as an effective diagnostic tool leading to diagnostic rates of around 40% in patients with previously undiagnosed neurodevelopmental or pediatric neurologic disorders [for review see (Wright et al., 2018)]. A diagnosis is essential for an optimal clinical management of the particular patient, e.g., initiation of a specific therapy or surveillance program, and appropriate access to education, social care and patient support groups (Boycott et al., 2017). A molecular diagnosis is also important for the patients' parents and other family members, in particular for informed decision-making with regard to family planning, and possibly prenatal diagnosis (PD) or preimplantation genetic diagnosis (PGD). In the case reported here, a molecular diagnosis could not have been established without the *Xenopus* analysis of the *PIBF1* missense variant and the resulting re-classification as likely pathogenic. Important consequence for the parents, who previously had decided against further children for fear of another disabled child, was that they now opt for a further pregnancy with PD.

Furthermore, identifying the molecular genetic cause of a disease is essential for a better understanding of its pathogenesis and the development of novel treatment strategies. However, interpretation of high-throughput sequencing data can be difficult. WES also uncovers many rare variants of which the functional impact is not known. Thus, a molecular diagnosis may be missed. Furthermore, recent studies in the field of cancer genetics and prenatal diagnosis indicate that unambiguous genetic results such as the finding of unclassified variants can lead to false treatment decisions and dissatisfaction with genomic testing (Kurian et al., 2017; Desai et al., 2018). Therefore, animal models are needed to verify or discard candidate disease alleles. Because of its genetic closeness, the mouse has been the model of choice to assess human genetic diseases. However, analyses in mice are costly and slow; in addition, the mouse is not suited for high-throughput analysis and cannot possibly keep up with the pace at which candidate variants keep being identified by WES. Therefore, additional and complementing animal models need to be promoted. Among the non-mammalian models, the zebrafish is widely used, while *Xenopus* is less well-known among clinical scientists. The frog, however, offers unique advantages particularly when investigating ciliopathies (Blum and Ott, 2018). The developing embryo presents its ciliated skin for a total of 3 days and allows easy and straightforward observation (including video microscopy) and functional analyses. Manipulations can be performed in a unilateral fashion, such that the non-manipulated side serves as an internal control. Given the inter-individual variability of phenotypes, this represents a unique advantage of the *Xenopus* model. The present analysis demonstrates that a syndrome like JS, which is caused by defects of primary, immotile cilia, can be successfully dissected in the context of motile cilia, as the expression analysis revealed a pan-ciliary presence of *pibf1* mRNA. This is likely true for most ciliopathies of primary cilia. Other organs that are easily addressed in the *Xenopus* model include the kidney (Getwan and Lienkamp, 2017) and heart (Duncan and Khokha, 2016). It seems, therefore, warranted to promote *Xenopus* among clinical scientist as a complementing model to mouse and zebrafish, in order to allow for the most efficient assessment of disease alleles.

AUTHOR'S NOTE

The authors dedicate this paper to the memory of the late Herbert Steinbeißer, who has been an inspiration to all of us and who has brought this group of people together.

AUTHOR CONTRIBUTIONS

TO conceived *Xenopus* experiments together with MB, performed and evaluated all *Xenopus* experiments, and wrote the manuscript together with MB and CE. MB conceived and evaluated experiments and wrote the paper. LK and ST performed mRNA/cDNA analysis of the patient and parents and westernblots. LK wrote sections of the manuscript. WES study coordination was done by CB and UM. NP and ASc performed WES analysis. Bioinformatic WES data analysis was done by NP, ASc, and MG, further evaluation of WES data was done by CE and UM. KH performed confirmation of WES variants by Sanger-Sequencing. ASe performed MRI images and their interpretation. Genotype–Phenotype correlation was done by CE, MG, KH, LK, and UM. All authors contributed to manuscript revision, read and approved the submitted version.

SUPPLEMENTARY MATERIAL

The Supplementary Material for this article can be found online at: https://www.frontiersin.org/articles/10.3389/fphys.2019.00134/full#supplementary-material

Movie S1 | Uncoordinated beating of MCC cilia upon *pibf1* gene knockdown. Coordinated ciliary beating of MCC (left) was lost in *pibf1* morphant specimen (right). Note the reduced number of cilia on morphant cell. Time lapse movie was recorded at 600 fps and plays at 30 fps (0.05 × real time).

Figure S1 | Expression anlayses of PIBF1 variants. **(A)** Relative expression levels of *PIBF1* exons analyzed by qPCR from patient, parents' and control blood. Shown are the mean ± SD of three independent RT-PCRs and subsequent qPCRs. *ARF1* expression was used for normalization. **(B)** Western blot analyses of overexpressed EGFP-PIBF1 constructs in HEK293 cells, using anti-GFP and anti-PIBF1 antibodies, respectively.

REFERENCES

Adzhubei, I. A., Schmidt, S., Peshkin, L., Ramensky, V. E., Gerasimova, A., Bork, P., et al. (2010). A method and server for predicting damaging missense mutations. *Nat. Methods* 7, 248–249. doi: 10.1038/nmeth0410-248

Bachmann-Gagescu, R., Dempsey, J. C., Phelps, I. G., O'Roak, B. J., Knutzen, D. M., Rue, T. C., et al. (2015). Joubert syndrome: a model for untangling recessive disorders with extreme genetic heterogeneity. *J. Med. Genet.* 52, 514–522. doi: 10.1136/jmedgenet-2015-103087

Badhwar, A., Andermann, F., Valerio, R. M., and Andermann, E. (2000). Founder effect in Joubert Syndrome. *Ann. Neurol.* 48, 435–436.

Barker, A. R., Thomas, R., and Dawe, H. R. (2014). Meckel-Gruber syndrome and the role of primary cilia in kidney, skeleton, and central nervous system development. *Organogenesis* 10, 96–107. doi: 10.4161/org.27375

Belo, J. A., Bouwmeester, T., Leyns, L., Kertesz, N., Gallo, M., Follettie, M., et al. (1997). Cerberus-like is a secreted factor with neutralizing activity expressed in the anterior primitive endoderm of the mouse gastrula. *Mech. Dev.* 68, 45–57. doi: 10.1016/S0925-4773(97)00125-1

Blum, M., and Ott, T. (2018). Xenopus: an undervalued model organism to study and model human genetic disease. *Cells Tissues Organs.* doi: 10.1159/000490898. [Epub ahead of print].

Boycott, K. M., Rath, A., Chong, J. X., Hartley, T., Alkuraya, F. S., Baynam, G., et al. (2017). International cooperation to enable the diagnosis of all rare genetic diseases. *Am. J. Hum. Genet.* 100, 695–705. doi: 10.1016/j.ajhg.2017.04.003

Brancati, F., Iannicelli, M., Travaglini, L., Mazzotta, A., Bertini, E., Boltshauser, E., et al. (2009). MKS3/TMEM67 mutations are a major cause of COACH Syndrome, a Joubert Syndrome related disorder with liver involvement. *Hum. Mutat.* 30, E432–E442. doi: 10.1002/humu.20924

Brooks, E. R., and Wallingford, J. B. (2014). Multiciliated cells. *Curr. Biol.* 24, R973–R982. doi: 10.1016/j.cub.2014.08.047

Choi, Y., Sims, G. E., Murphy, S., Miller, J. R., and Chan, A. P. (2012). Predicting the functional effect of amino acid substitutions and indels. *PLoS ONE* 7:e46688. doi: 10.1371/journal.pone.0046688

Chun, S., and Fay, J. C. (2009). Identification of deleterious mutations within three human genomes. *Genome Res.* 19, 1553–1561. doi: 10.1101/gr.092619.109

Cohen, R. A., Check, J. H., and Dougherty, M. P. (2016). Evidence that exposure to progesterone alone is a sufficient stimulus to cause a precipitous rise in the immunomodulatory protein the progesterone induced blocking factor (PIBF). *J. Assist. Reprod. Genet.* 33, 221–229. doi: 10.1007/s10815-015-0619-7

Delous, M., Baala, L., Salomon, R., Laclef, C., Vierkotten, J., Tory, K., et al. (2007). The ciliary gene RPGRIP1L is mutated in cerebello-oculo-renal syndrome (Joubert syndrome type B) and Meckel syndrome. *Nat. Genet.* 39, 875–881. doi: 10.1038/ng2039

Desai, P., Haber, H., Bulafka, J., Russell, A., Clifton, R., Zachary, J., et al. (2018). Impacts of variants of uncertain significance on parental perceptions of children after prenatal chromosome microarray testing. *Prenat. Diagn.* 38, 740–747. doi: 10.1002/pd.5323

Doherty, D. (2009). Joubert syndrome: insights into brain development, cilium biology, and complex disease. *Semin. Pediatr. Neurol.* 16, 143–154. doi: 10.1016/j.spen.2009.06.002

Dubaissi, E., and Papalopulu, N. (2011). Embryonic frog epidermis: a model for the study of cell-cell interactions in the development of mucociliary disease. *Dis. Model. Mech.* 4, 179–192. doi: 10.1242/dmm.006494

Duncan, A. R., and Khokha, M. K. (2016). Xenopus as a model organism for birth defects-Congenital heart disease and heterotaxy. *Semin. Cell Dev. Biol.* 51, 73–79. doi: 10.1016/j.semcdb.2016.02.022

Edvardson, S., Shaag, A., Zenvirt, S., Erlich, Y., Hannon, G. J., Shanske, A. L., et al. (2010). Joubert syndrome 2 (JBTS2) in Ashkenazi Jews is associated with a TMEM216 mutation. *Am. J. Hum. Genet.* 86, 93–97. doi: 10.1016/j.ajhg.2009.12.007

Evers, C., Staufner, C., Granzow, M., Paramasivam, N., Hinderhofer, K., Kaufmann, L., et al. (2017). Impact of clinical exomes in neurodevelopmental and neurometabolic disorders. *Mol. Genet. Metab.* 121, 297–307. doi: 10.1016/j.ymgme.2017.06.014

Fagerberg, L., Hallstrom, B. M., Oksvold, P., Kampf, C., Djureinovic, D., Odeberg, J., et al. (2014). Analysis of the human tissue-specific expression by genome-wide integration of transcriptomics and antibody-based proteomics. *Mol. Cell. Proteomics* 13, 397–406. doi: 10.1074/mcp.M113.035600

Franco, B., and Thauvin-Robinet, C. (2016). Update on oral-facial-digital syndromes (OFDS). *Cilia* 5:12. doi: 10.1186/s13630-016-0034-4

Getwan, M., and Lienkamp, S. S. (2017). Toolbox in a tadpole: Xenopus for kidney research. *Cell Tissue Res.* 369, 143–157. doi: 10.1007/s00441-017-2611-2

Gonzalez-Arenas, A., Valadez-Cosmes, P., Jimenez-Arellano, C., Lopez-Sanchez, M., and Camacho-Arroyo, I. (2014). Progesterone-induced blocking factor is hormonally regulated in human astrocytoma cells, and increases their growth through the IL-4R/JAK1/STAT6 pathway. *J. Steroid Biochem. Mol. Biol.* 144(Pt B), 463–46470. doi: 10.1016/j.jsbmb.2014.09.007

Gupta, G. D., Coyaud, E., Goncalves, J., Mojarad, B. A., Liu, Y., Wu, Q., et al. (2015). A Dynamic protein interaction landscape of the human centrosome-cilium interface. *Cell* 163, 1484–1499. doi: 10.1016/j.cell.2015.10.065

Gutierrez-Rodriguez, A., Hansberg-Pastor, V., and Camacho-Arroyo, I. (2017). Proliferative and invasive effects of progesterone-induced blocking factor in human glioblastoma cells. *Biomed. Res. Int.* 2017:1295087. doi: 10.1155/2017/1295087

Hebbar, M., Kanthi, A., Shukla, A., Bielas, S., and Girisha, K. M. (2018). A biallelic 36-bp insertion in PIBF1 is associated with Joubert syndrome. *J. Hum. Genet.* 63, 935–939. doi: 10.1038/s10038-018-0462-7

Huang, L., Szymanska, K., Jensen, V. L., Janecke, A. R., Innes, A. M., Davis, E. E., et al. (2011). TMEM237 is mutated in individuals with a Joubert syndrome related disorder and expands the role of the TMEM family at the ciliary transition zone. *Am. J. Hum. Genet.* 89, 713–730. doi: 10.1016/j.ajhg.2011.11.005

Hudic, I., Stray-Pedersen, B., Szekeres-Bartho, J., Fatusic, Z., Dizdarevic-Hudic, L., Tomic, V., et al. (2015). Maternal serum progesterone-induced blocking factor (PIBF) in the prediction of preterm birth. *J. Reprod. Immunol.* 109, 36–40. doi: 10.1016/j.jri.2015.02.006

Hudic, I., Szekeres-Bartho, J., Stray-Pedersen, B., Fatusic, Z., Polgar, B., and Ecim-Zlojutro, V. (2016). Lower urinary and serum progesterone-induced blocking factor in women with preterm birth. *J. Reprod. Immunol.* 117, 66–69. doi: 10.1016/j.jri.2016.07.003

Iannicelli, M., Brancati, F., Mougou-Zerelli, S., Mazzotta, A., Thomas, S., Elkhartoufi, N., et al. (2010). Novel TMEM67 mutations and genotype-phenotype correlates in meckelin-related ciliopathies. *Hum. Mutat.* 31, E1319–E1331. doi: 10.1002/humu.21239

Johnston, J. J., Lee, C., Wentzensen, I. M., Parisi, M. A., Crenshaw, M. M., Sapp, J. C., et al. (2017). Compound heterozygous alterations in intraflagellar transport protein CILIAP1 in a child with a novel Joubert and oral-facial-digital overlap syndrome. *Cold Spring Harb. Mol. Case Stud.* 3:a001321. doi: 10.1101/mcs.a001321

Khanna, H., Hurd, T. W., Lillo, C., Shu, X., Parapuram, S. K., He, S., et al. (2005). RPGR-ORF15, which is mutated in retinitis pigmentosa, associates with SMC1, SMC3, and microtubule transport proteins. *J. Biol. Chem.* 280, 33580–33587. doi: 10.1074/jbc.M505827200

Kim, K., Lee, K., and Rhee, K. (2012). CEP90 is required for the assembly and centrosomal accumulation of centriolar satellites, which is essential for primary cilia formation. *PLoS ONE* 7:e48196. doi: 10.1371/journal.pone.0048196

Kim, K., and Rhee, K. (2011). The pericentriolar satellite protein CEP90 is crucial for integrity of the mitotic spindle pole. *J. Cell Sci.* 124(Pt 3), 338–347. doi: 10.1242/jcs.078329

Kircher, M., Witten, D. M., Jain, P., O'Roak, B. J., Cooper, G. M., and Shendure, J. (2014). A general framework for estimating the relative pathogenicity of human genetic variants. *Nat. Genet.* 46, 310–315. doi: 10.1038/ng.2892

Knopp, C., Rudnik-Schoneborn, S., Eggermann, T., Bergmann, C., Begemann, M., Schoner, K., et al. (2015). Syndromic ciliopathies: from single gene to multi gene analysis by SNP arrays and next generation sequencing. *Mol. Cell. Probes* 29, 299–307. doi: 10.1016/j.mcp.2015.05.008

Kodani, A., Yu, T. W., Johnson, J. R., Jayaraman, D., Johnson, T. L., Al-Gazali, L., et al. (2015). Centriolar satellites assemble centrosomal microcephaly proteins to recruit CDK2 and promote centriole duplication. *eLife* 4:7519. doi: 10.7554/eLife.07519

Kroes, H. Y., Monroe, G. R., van der Zwaag, B., Duran, K. J., de Kovel, C. G., van Roosmalen, M. J., et al. (2016). Joubert syndrome: genotyping a Northern European patient cohort. *Eur. J. Hum. Genet.* 24, 214–220. doi: 10.1038/ejhg.2015.84

Kurian, A. W., Li, Y., Hamilton, A. S., Ward, K. C., Hawley, S. T., Morrow, M., et al. (2017). Gaps in incorporating germline genetic testing into treatment decision making for early stage breast cancer. *J. Clin. Oncol.* 35, 2232–2239. doi: 10.1200/JCO.2016.71.6480

Lachmann, M., Gelbmann, D., Kalman, E., Polgar, B., Buschle, M., Von Gabain, A., et al. (2004). PIBF (progesterone induced blocking factor) is overexpressed in highly proliferating cells and associated with the centrosome. *Int. J. Cancer* 112, 51–60. doi: 10.1002/ijc.20326

Leitch, C. C., Zaghloul, N. A., Davis, E. E., Stoetzel, C., Diaz-Font, A., Rix, S., et al. (2008). Hypomorphic mutations in syndromic encephalocele genes are associated with Bardet-Biedl syndrome. *Nat. Genet.* 40, 443–448. doi: 10.1038/ng.97

Lek, M., Karczewski, K. J., Minikel, E. V., Samocha, K. E., Banks, E., Fennell, T., et al. (2016). Analysis of protein-coding genetic variation in 60,706 humans. *Nature* 536, 285–291. doi: 10.1038/nature19057

Liu, X., Jian, X., and Boerwinkle, E. (2013). dbNSFP v2.0: a database of human non-synonymous SNVs and their functional predictions and annotations. *Hum. Mutat.* 34, E2393–E2402. doi: 10.1002/humu.22376

Malicdan, M. C., Vilboux, T., Stephen, J., Maglic, D., Mian, L., Konzman, D., et al. (2015). Mutations in human homologue of chicken talpid3 gene (KIAA0586) cause a hybrid ciliopathy with overlapping features of Jeune and Joubert syndromes. *J. Med. Genet.* 52, 830–839. doi: 10.1136/jmedgenet-2015-103316

Maria, B. L., Hoang, K. B., Tusa, R. J., Mancuso, A. A., Hamed, L. M., Quisling, R. G., et al. (1997). "Joubert syndrome" revisited: key ocular motor signs with magnetic resonance imaging correlation. *J. Child Neurol.* 12, 423–430. doi: 10.1177/088307389701200703

Maria, B. L., Quisling, R. G., Rosainz, L. C., Yachnis, A. T., Gitten, J., Dede, D., et al. (1999). Molar tooth sign in Joubert syndrome: clinical, radiologic, and pathologic significance. *J. Child Neurol.* 14, 368–376. doi: 10.1177/088307389901400605

Miller, S. A., Dykes, D. D., and Polesky, H. F. (1988). A simple salting out procedure for extracting DNA from human nucleated cells. *Nucleic Acids Res.* 16:1215. doi: 10.1093/nar/16.3.1215

Moody, S. A. (2000). Cell lineage analysis in Xenopus embryos. *Methods Mol. Biol.* 135, 331–347. doi: 10.1385/1-59259-685-1:331

Mougou-Zerelli, S., Thomas, S., Szenker, E., Audollent, S., Elkhartoufi, N., Babarit, C., et al. (2009). CC2D2A mutations in Meckel and Joubert syndromes indicate a genotype-phenotype correlation. *Hum. Mutat.* 30, 1574–1582. doi: 10.1002/humu.21116

Ng, P. C., and Henikoff, S. (2003). SIFT: predicting amino acid changes that affect protein function. *Nucleic Acids Res.* 31, 3812–3814. doi: 10.1093/nar/gkg509

Paramasivam, N., Granzow, M., Evers, C., Hinderhofer, K., Wiemann, S., Bartram, C. R., et al. (2018). Identification and prioritization of causal variants of human genetic disorders from exome or whole genome sequencing data. *OBM Genet.* doi: 10.1101/209882. [Epub ahead of print].

Parisi, M., and Glass, I. (1993). "Joubert syndrome," in *GeneReviews®*, eds M. P. Adam, H. H. Ardinger, R. A. Pagon, S. E. Wallace, L. J. H. Bean, K. Stephens, and A. Amemiya (Seattle, WA).

Park, T. J., Mitchell, B. J., Abitua, P. B., Kintner, C., and Wallingford, J. B. (2008). Dishevelled controls apical docking and planar polarization of basal bodies in ciliated epithelial cells. *Nat. Genet.* 40, 871–879. doi: 10.1038/ng.104

Polgar, B., Kispal, G., Lachmann, M., Paar, C., Nagy, E., Csere, P., et al. (2003). Molecular cloning and immunologic characterization of a novel cDNA coding for progesterone-induced blocking factor. *J. Immunol.* 171, 5956–5963. doi: 10.4049/jimmunol.171.11.5956

Reva, B., Antipin, Y., and Sander, C. (2011). Predicting the functional impact of protein mutations: application to cancer genomics. *Nucleic Acids Res.* 39:e118. doi: 10.1093/nar/gkr407

Richards, S., Aziz, N., Bale, S., Bick, D., Das, S., Gastier-Foster, J., et al. (2015). Standards and guidelines for the interpretation of sequence variants: a joint consensus recommendation of the American College of Medical Genetics and Genomics and the Association for Molecular Pathology. *Genet. Med.* 17, 405–424. doi: 10.1038/gim.2015.30

Romani, M., Micalizzi, A., Kraoua, I., Dotti, M. T., Cavallin, M., Sztriha, L., et al. (2014). Mutations in B9D1 and MKS1 cause mild Joubert syndrome: expanding the genetic overlap with the lethal ciliopathy Meckel syndrome. *Orphanet J. Rare Dis.* 9:72. doi: 10.1186/1750-1172-9-72

Romani, M., Micalizzi, A., and Valente, E. M. (2013). Joubert syndrome: congenital cerebellar ataxia with the molar tooth. *Lancet Neurol.* 12, 894–905. doi: 10.1016/S1474-4422(13)70136-4

Roosing, S., Romani, M., Isrie, M., Rosti, R. O., Micalizzi, A., Musaev, D., et al. (2016). Mutations in CEP120 cause Joubert syndrome as well as complex ciliopathy phenotypes. *J. Med. Genet.* 53, 608–615. doi: 10.1136/jmedgenet-2016-103832

Saunier, S., Salomon, R., and Antignac, C. (2005). Nephronophthisis. *Curr. Opin. Genet. Dev.* 15, 324–331. doi: 10.1016/j.gde.2005.04.012

Schwarz, J. M., Rodelsperger, C., Schuelke, M., and Seelow, D. (2010). MutationTaster evaluates disease-causing potential of sequence alterations. *Nat. Methods* 7, 575–576. doi: 10.1038/nmeth0810-575

Shaheen, R., Almoisheer, A., Faqeih, E., Babay, Z., Monies, D., Tassan, N., et al. (2015). Identification of a novel MKS locus defined by TMEM107 mutation. *Hum. Mol. Genet.* 24, 5211–5218. doi: 10.1093/hmg/ddv242

Shaheen, R., Shamseldin, H. E., Loucks, C. M., Seidahmed, M. Z., Ansari, S., Ibrahim Khalil, M., et al. (2014). Mutations in CSPP1, encoding a core centrosomal protein, cause a range of ciliopathy phenotypes in humans. *Am. J. Hum. Genet.* 94, 73–79. doi: 10.1016/j.ajhg.2013.11.010

Shihab, H. A., Gough, J., Cooper, D. N., Stenson, P. D., Barker, G. L., Edwards, K. J., et al. (2013). Predicting the functional, molecular, and phenotypic consequences of amino acid substitutions using hidden Markov models. *Hum. Mutat.* 34, 57–65. doi: 10.1002/humu.22225

Slaats, G. G., Isabella, C. R., Kroes, H. Y., Dempsey, J. C., Gremmels, H., Monroe, G. R., et al. (2016). MKS1 regulates ciliary INPP5E levels in Joubert syndrome. *J. Med. Genet.* 53, 62–72. doi: 10.1136/jmedgenet-2015-103250

Spassky, N., Han, Y. G., Aguilar, A., Strehl, L., Besse, L., Laclef, C., et al. (2008). Primary cilia are required for cerebellar development and Shh-dependent expansion of progenitor pool. *Dev. Biol.* 317, 246–259. doi: 10.1016/j.ydbio.2008.02.026

Srour, M., Hamdan, F. F., McKnight, D., Davis, E., Mandel, H., Schwartzentruber, J., et al. (2015). Joubert syndrome in French Canadians and identification of mutations in CEP104. *Am. J. Hum. Genet.* 97, 744–753. doi: 10.1016/j.ajhg.2015.09.009

Srour, M., Hamdan, F. F., Schwartzentruber, J. A., Patry, L., Ospina, L. H., Shevell, M. I., et al. (2012a). Mutations in TMEM231 cause Joubert syndrome in French Canadians. *J. Med. Genet.* 49, 636–641. doi: 10.1136/jmedgenet-2012-101132

Srour, M., Schwartzentruber, J., Hamdan, F. F., Ospina, L. H., Patry, L., Labuda, D., et al. (2012b). Mutations in C5ORF42 cause Joubert syndrome in the French Canadian population. *Am. J. Hum. Genet.* 90, 693–700. doi: 10.1016/j.ajhg.2012.02.011

Tallila, J., Salonen, R., Kohlschmidt, N., Peltonen, L., and Kestila, M. (2009). Mutation spectrum of Meckel syndrome genes: one group of syndromes or several distinct groups? *Hum. Mutat.* 30, E813–E830. doi: 10.1002/humu.21057

Thomas, S., Legendre, M., Saunier, S., Bessieres, B., Alby, C., Bonniere, M., et al. (2012). TCTN3 mutations cause Mohr-Majewski syndrome. *Am. J. Hum. Genet.* 91, 372–378. doi: 10.1016/j.ajhg.2012.06.017

Tuz, K., Bachmann-Gagescu, R., O'Day, D. R., Hua, K., Isabella, C. R., Phelps, I. G., et al. (2014). Mutations in CSPP1 cause primary cilia abnormalities and Joubert syndrome with or without Jeune asphyxiating thoracic dystrophy. *Am. J. Hum. Genet.* 94, 62–72. doi: 10.1016/j.ajhg.2013.11.019

Valente, E. M., Logan, C. V., Mougou-Zerelli, S., Lee, J. H., Silhavy, J. L., Brancati, F., et al. (2010). Mutations in TMEM216 perturb ciliogenesis and cause Joubert, Meckel and related syndromes. *Nat. Genet.* 42, 619–625. doi: 10.1038/ng.594

Vladar, E. K., and Stearns, T. (2007). Molecular characterization of centriole assembly in ciliated epithelial cells. *J. Cell Biol.* 178, 31–42. doi: 10.1083/jcb.200703064

Walentek, P., Bogusch, S., Thumberger, T., Vick, P., Dubaissi, E., Beyer, T., et al. (2014). A novel serotonin-secreting cell type regulates ciliary motility in the mucociliary epidermis of Xenopus tadpoles. *Development* 141, 1526–1533. doi: 10.1242/dev.102343

Wang, K., Li, M., and Hakonarson, H. (2010). ANNOVAR: functional annotation of genetic variants from high-throughput sequencing data. *Nucleic Acids Res.* 38:e164. doi: 10.1093/nar/gkq603

Wheway, G., Schmidts, M., Mans, D. A., Szymanska, K., Nguyen, T. T., Racher, H., et al. (2015). An siRNA-based functional genomics screen for the identification of regulators of ciliogenesis and ciliopathy genes. *Nat. Cell Biol.* 17, 1074–1087. doi: 10.1038/ncb3201

Wright, C. F., McRae, J. F., Clayton, S., Gallone, G., Aitken, S., FitzGerald, T. W., et al. (2018). Making new genetic diagnoses with old data: iterative reanalysis and reporting from genome-wide data in 1,133 families with developmental disorders. *Genet. Med.* 20, 1216–1223. doi: 10.1038/gim.2017.246

Yachie, N., Petsalaki, E., Mellor, J. C., Weile, J., Jacob, Y., Verby, M., et al. (2016). Pooled-matrix protein interaction screens using Barcode Fusion Genetics. *Mol. Syst. Biol.* 12:863. doi: 10.15252/msb.20156660

Zaghloul, N. A., and Katsanis, N. (2009). Mechanistic insights into Bardet-Biedl syndrome, a model ciliopathy. *J. Clin. Invest.* 119, 428–437. doi: 10.1172/JCI37041

Zhao, H., Zhu, L., Zhu, Y., Cao, J., Li, S., Huang, Q., et al. (2013). The Cep63 paralogue Deup1 enables massive *de novo* centriole biogenesis for vertebrate multiciliogenesis. *Nat. Cell Biol.* 15, 1434–1444. doi: 10.1038/ncb2880

Conflict of Interest Statement: The authors declare that the research was conducted in the absence of any commercial or financial relationships that could be construed as a potential conflict of interest.

Review and hypothesis articles

Vertebrate Left-Right Asymmetry: What Can Nodal Cascade Gene Expression Pattern Tell Us?

Journal of Cardiovascular Development and Disease

MDPI

Review

Vertebrate Left-Right Asymmetry: What Can Nodal Cascade Gene Expression Patterns Tell Us?

Axel Schweickert, Tim Ott, Sabrina Kurz, Melanie Tingler, Markus Maerker, Franziska Fuhl and Martin Blum *

Institute of Zoology, University of Hohenheim, 70593 Stuttgart, Germany;
axel.schweickert@uni-hohenheim.de (A.S.); tim.ott@uni-hohenheim.de (T.O.);
sabrina.kurz@uni-hohenheim.de (S.K.); melanie.tingler@uni-hohenheim.de (M.T.);
markus.maerker@uni-hohenheim.de (M.M.); franziska.fuhl@uni-hohenheim.de (F.F.)
* Correspondence: martin.blum@uni-hohenheim.de; Tel.: +49-711-4592-2255

Received: 11 December 2017; Accepted: 25 December 2017; Published: 29 December 2017

Abstract: Laterality of inner organs is a wide-spread characteristic of vertebrates and beyond. It is ultimately controlled by the left-asymmetric activation of the Nodal signaling cascade in the lateral plate mesoderm of the neurula stage embryo, which results from a cilia-driven leftward flow of extracellular fluids at the left-right organizer. This scenario is widely accepted for laterality determination in wildtype specimens. Deviations from this norm come in different flavors. At the level of organ morphogenesis, laterality may be inverted (situs inversus) or non-concordant with respect to the main body axis (situs ambiguus or heterotaxia). At the level of Nodal cascade gene activation, expression may be inverted, bilaterally induced, or absent. In a given genetic situation, patterns may be randomized or predominantly lacking laterality (absence or bilateral activation). We propose that the distributions of patterns observed may be indicative of the underlying molecular defects, with randomizations being primarily caused by defects in the flow-generating ciliary set-up, and symmetrical patterns being the result of impaired flow sensing, on the left, the right, or both sides. This prediction, the reasoning of which is detailed in this review, pinpoints functions of genes whose role in laterality determination have remained obscure.

Keywords: left-right asymmetry; symmetry breaking; cilia; Nodal; leftward flow; left-right organizer; Nodal cascade; heterotaxia; situs ambiguus; situs inversus

1. Introduction

The development of the left-right body axis in an otherwise bilaterally symmetrical organism has drawn the attention of anatomists and developmental biologists alike at all times [1–3]. Asymmetric positioning and morphogenesis of many organs (*situs solitus*), including heart, lung, gut, liver, and stomach, is relevant to humans, as deviations from the norm impact on health or are even incompatible with life. A mirror-imaged organ placement (*situs inversus*), however, mostly lacks clinical relevance, in stark contrast to the misplacement of single organs (*situs ambiguus* or heterotaxia) or duplications of sided arrangements (left or right isomerism), which often cause embryonic lethality [4]. The molecular analysis of left-right (LR) development was initiated by the identification of left-asymmetrically expressed genes during neurula stages of chick, mouse, and frog embryos [5–7]. The TGFβ-type morphogene Nodal, its secreted feedback inhibitor Lefty, and the homeobox transcription factor Pitx2 are activated in a sided manner in the left lateral plate mesoderm (LPM) and make up the so-called Nodal cascade. Once activated, Nodal signaling directly induces its own transcription, resulting in the fast spreading of *nodal* mRNA expression in the LPM [8]. In addition, Nodal activates *lefty* and *pitx2* transcription. *Nodal* expression vanishes after a very short time, due to the feedback inhibition by Lefty, whereas left-sided *pitx2* expression

is maintained up to organ morphogenesis, which is initiated right after *Nodal* has disappeared from the LPM [9]. Several mutants affect this narrow timing, such as, for example, *dand5* in the mouse [10]. Loss-of-function experiments either targeting Nodal signaling or Pitx2 resulted in aberrant organ situs in all animal model systems analyzed, demonstrating the conserved requirement of the Nodal-Lefty-Pitx2 cassette for LR development [5,11]. The morphogen nodal, known to act as a long range signaling molecule, is further restricted by Lefty expression at the midline. Defective midline Lefty enables Nodal to diffuse to the right LPM and to activate a right-sided cascade, resulting in LR defects as well [12]. At an evolutionary scale, the Nodal cascade governs asymmetries in the entire deuterostome tree of life, from sea urchins to mammals [13,14].

Besides evolutionary implications, the presence of the Nodal cascade at the center of events leading up to asymmetric organ placement and morphogenesis has enabled the analysis of processes upstream and downstream [15,16]. A relatively strong correlation between organ situs and Nodal cascade induction has been observed in many mouse mutants, best exemplified by the classical LR mutant *inversus viscerum*, or *iv* [17–19]. Nodal cascade induction is completely randomized in *iv* mutant embryos, with equal 25% frequencies of wildtype, absent, bilateral and right-sided expression patterns each (Figure 1). The organs of homozygous *iv* mutants are either wt (*situs solitus*; SS), inverted (*situs inversus*; SI), or mirror images of the left or right body half (left or right isomerism) [17–19], although deviations from this predicted distribution were recorded as well [20]. *iv* specimens with isomerisms die *in utero*, while both SS and SI animals are born and vital. This correlation is less clear in other mutants, especially when aberrant organ situs is only encountered in a minority of cases. Compensation of germ line mutations is only beginning to be studied, let alone to be understood, but may contribute in cases when Nodal cascade expression patterns and organ situs correlate less well [21,22]. Lower vertebrates, i.e., fish and frog, for the most parts lack isomerisms at the organ level. Absent or bilateral expression of Nodal cascade genes therefore result in the same set of phenotypes, *situs solitus*, *situs inversus*, and *situs ambiguus* (heterotaxia). This observation suggests that gastrointestinal and heart primordia of lower vertebrates are able to undergo an intrinsic chiral morphogenesis, leading to asymmetric organ placement even when positional information by the Nodal cascade is lacking or present on both sides. Up to now, these differences of asymmetric organ morphogenesis between species have not been systematically addressed. When considering all cases, however, it seems safe to hypothesize that Nodal cascade gene expression patterns in the LPM are indicative of organ situs development. In the context of the present discussion, we shall therefore exclusively consider Nodal cascade patterns as indicators of upstream mechanisms. In the following, we will take what may be considered a somewhat unusual approach of a more theoretical look at concepts of flow generation, sensing and signal transfer. In some cases, this will result in over-simplifications that neglect the complexity of phenotypes encountered in mutants and morphants, for which we apologize, as we do to all colleagues whose work we could not cite due to space restrictions.

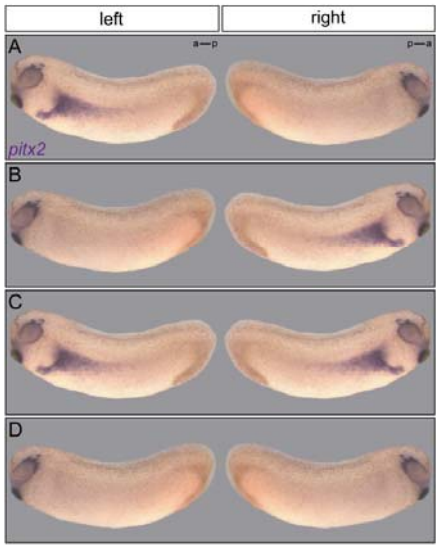

Figure 1. Expression patterns of Nodal cascade genes. Shown are *Pitx2* gene expression patterns in *Xenopus* tadpoles that can be wildtype (**A**), inverted (**B**), bilateral (**C**), or absent (**D**) on both sides, such as encountered in mutants and morphants of the dynein motor protein defective in *iv* mutant mice.

2. Cilia-Dependent Symmetry Breaking

While the mechanisms of asymmetric organ morphogenesis downstream of the Nodal cascade are only slowly beginning to be unraveled (cf. [16] for a recent review), upstream events have received much attention in the various model organisms and a great deal of knowledge has accumulated in recent years [15]. In a sense, the *iv* mutant again has paved the way: the identification of its target gene as an axonemal dynein motor has introduced cilia as a central player, with a multitude of ciliary mutants being involved in LR development and a great many of ciliopathies displaying LR defects as one of their characteristics [18]. In short, the situation as of today presents as follows (Figure 2): in the perfectly bilateral symmetrical neurula embryo, the ciliated left-right organizer (LRO) forms at the midline. Precursors arise during gastrulation and are patterned by the embryonic organizer (Figure 2). The LRO creates an extracellular fluid flow from the right to the left side. This leftward flow may or may not transport cargo, which should originate from within the LRO. The LRO harbors flow sensors at the margins on both sides, which react to flow and/or to the cargo when it gets delivered to the sensor. The sensor generates a signal that gets transmitted to the LPM, where it induces the Nodal cascade. Any disturbance of this sequence of events, which together rules symmetry breaking in the embryo, inevitably results in alterations of LPM Nodal cascade expression. However, the type of alteration observed does not necessarily pinpoint the underlying defects in symmetry breaking. For example, it is not easily reconciled that in a mutant such as *iv*, which renders cilia immotile one quarter of specimens develop without any LR defects, although left LPM Nodal in *iv* is not induced by the exactly same mechanism as in wildtype embryos [23,24]. Such cases have in the past led to the proposal that it is utterly impossible that cilia take center stage in symmetry breaking [25–27], and they continue to plague the field, as honestly nobody knows how left-asymmetric Nodal is induced in the absence of ciliary motility or in any of the other mutants that eventually show *situs solitus* in at least a proportion of homozygous specimens.

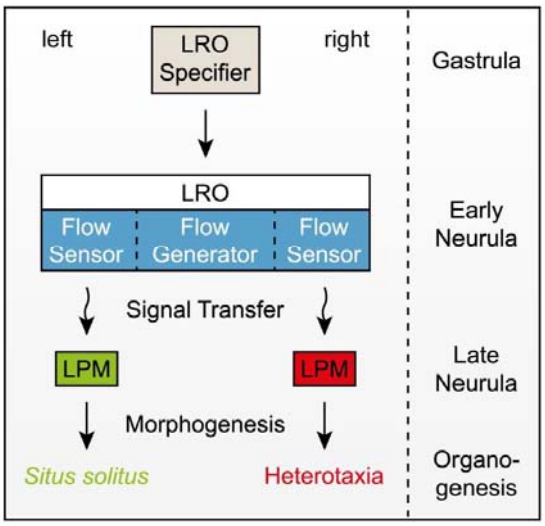

Figure 2. Schematic depiction of left-right (LR) axis specification in vertebrate embryos that use a ciliated left-right organizer (LRO) to break the bilateral symmetry of the early embryo. For a detailed discussion, see main text.

We propose that it is profitable to think about disturbances of distinct steps in the chain of events that account for symmetry breaking, and to predict what kind of alterations of Nodal cascade gene expression patterns should result. Some mutants will fall in one or another category, in some other cases combinations of defects may cause a specific pattern.

2.1. *LRO Specifier*

To start the discussion, we first like to consider global LRO specifiers, i.e., mutants in which an LRO does not form at all. So far, LRO precursors have only been identified in fish and frog with the dorsal forerunner cells and the superficial mesoderm, respectively [28,29]. From the timing and geometry of embryonic development, the generation of these LRO specifiers must be intimately linked to the function of the primary embryonic (or Spemann) organizer. LROs inevitably localize to the posterior end of the notochord, which develops from the organizer [30]. Interestingly, mechanical ablations of frog and fish LROs have not impacted on embryonic development beyond laterality determination, demonstrating that symmetry breaking is a distinct event [31–33]. Quite obviously, if no LRO is specified, then the Nodal cascade should not be induced, i.e., LPM gene expression should be absent. Several mutants are known in which LRO formation is distorted, but only one in which this ciliated epithelium does not form at all: *brachyury*. To no surprise, the LPM Nodal cascade is not induced, and this is true for mouse mutants [34–36] as well as frog morphants (SK and MB, unpublished. In zebrafish, although the LRO is missing (with flow generator and sensor being absent, see below), LPM *nodal* is induced (REF), which remains a mystery. Another prominent gene that affects LRO morphogenesis is *noto* [32,37]. In contrast to *brachyury*, LRO remnants form, for example, in zebrafish, where Kupffer's vesicle is present but much reduced in size [28]. In this case, the Nodal cascade is induced in a bilateral manner, i.e., both in the left and right LPM. Interestingly, LRO specifier genes are generally required for notochord formation, in agreement with the notion that LRO and notochord morphogenesis are intimately linked [30]. The exact pathway how these genes set up this

unique tissue during gastrulation has not been elucidated as yet, but mutants that abrogate LRO formation should always result in the absence of Nodal cascade gene induction.

2.2. Flow Generator

We next consider flow generators, i.e., cells that harbor motile cilia. These are found at the center of the LRO and may be present or absent and harbor cilia or not. If cilia are present, then they may be motile or immotile, of correct length, morphology, and posterior polarization, or not. As a result, leftward flow may proceed with normal speed and directionality or deviate from the norm. All of the deviations should result in altered LPM expression patterns. But what is to be expected in every single case? Mispolarized cilia should produce fluid flows that are directed to other dimensions than left-only. In such settings, the Nodal cascade might be induced on the right side. No case is known in which all cilia polarize in the wrong (anterior) direction and therefore invert the cascade, but several genes are known that result in a proportion of anteriorly polarized cilia. In such cases, which comprise some of the planar cell polarity genes, such as *vangl1/2* and *wnt11*, as well as the ion pump ATP4 [38–41], bilateral induction of the Nodal cascade has been reported (Table 1). Variations in cilia lengths cause altered flow dynamics and LR defects, as recently shown in zebrafish [42]. Deviations in speed of leftward flow have not systematically been studied, beyond reports of aberrant velocities in mutants, such as *inv* [23]. As flow is only required on the left side of the LRO [43], and a few cilia are sufficient to break symmetry [44], the vigor of flow may not be of too much relevance. However, the case is open; studies that assess physical flow parameters are few, and it may be profitable to re-investigate mutants that otherwise are hard to interpret. Absence and immobility of cilia have, however, been analyzed. Both should result in the absence of Nodal cascade induction, which is, however, not observed. Immotile cilia, such as in *iv* mutant embryos, cause randomized *nodal1* expression, which is counterintuitive, while mutants that lack cilia, such as *kif3a* [45] and *ift88* [46–48], display bilateral expression, which asks for a mechanistic explanation as well (and we shall come back to both scenarios below).

2.3. Flow Cargo

The question whether or not there is cargo that flow transports to the left has been controversially discussed in the field for more than a decade. Early evidence for the presence of so-called Nodal vesicular parcels, or NVPs [49,50], have not been followed up until recently, when the prevailing view that flow itself triggers the flow sensor [51,52] it has been challenged [53,54], but published novel evidence on this issue is still missing. For our hypothetical discussion, the presence, nature and mode of action of NVPs are irrelevant, though. If it were and cargo would be traveling along with leftward flow, this cargo could be present or absent, and it could reach the flow sensors in the presence or absence of leftward flow, for example by diffusion. This is when cases of randomized induction of the Nodal cascade become interesting. In the *iv* mutant, for example, cargo could be released at the LRO and reach the flow sensors on the left and right margin of the LRO in a stochastic manner. This scenario is still not totally satisfying, as the distribution of cases (25% each) asks for a mechanistic explanation. Taking some sort of cargo into account, however, helps the discussion. But, why should absence of cilia, such as in the *kif3a* or *ift88* mutants, be different and result in bilateral induction? In that case, one would need to argue that cargo release and the presence of cilia are coupled. There are several possible scenarios, such as, for example, cargo release from the tip of cilia (in form of exosomes). Care should be applied, however, as cilia mutants impact on very many signaling pathways, some of which may impact on LR patterning downstream of Nodal. Anyways, the cargo option in our opinion should be considered in cases of randomized Nodal expression patterns in the LPM, and the nearer future should tell whether NVPs exist beyond mouse, and when and how they act.

2.4. Flow Sensor

The flow sensor should be intimately linked to flow and cargo. In the absence of its trigger, the sensor should not be activated, i.e., Nodal should not be induced. In order to assure robust induction of the Nodal cascade on the left and not the right side of the LPM, the trigger must be locked in the absence of flow and/or cargo. The sensor could be present or absent, and it could be activated on the left, the right, on both or neither side. There should be an absolute correlation between sensor status (on/off) and Nodal cascade activation in the LPM at a slightly later stage. Conceptually, the sensor is the simplest player in the game, as it is this main gateway that should decide on laterality specification [15]. Experimental manipulations of the sensor should overrule all of the upstream events and should be autonomously capable of inducing the cascade on the side where it is touched off. Central to the sensor function is Nodal and its inhibitor Dand5 (formerly known as Coco in frog, charon in zebrafish, or cerl2 in mouse); both are co-expressed in the sensory cells at the LRO margin [55–60], or in neighboring cells in the case of zebrafish, where the transformation of the flat epithelium of primitive fish LRO, such as in the sturgeon [30], into the sphere of Kupffer's vesicle (KV) probably placed these cells just next to the KV. Experimental manipulations of both factors in these very cells underscore their central role: Nodal is strictly required on the left side of the LRO. Its presence in the sensor on the right is not required for left-sided LPM activation. Dand5, in contrast, has to be repressed on the left in order to de-repress Nodal action. When Dand5 disappears from the right sensor and Nodal is present, the cascade gets activated on both sides. Nodal and Dand5 are able to overrule a loss of the flow generator: flow-independent repression of Dand5 activates Nodal, as does the overexpression of Nodal itself. Dand5 depends on Nodal as the left determinant, as in the absence of Nodal in the sensor, Dand5 manipulations remain without consequences. Artificial flow can trigger the sensor in the absence of cilia or ciliary motility [51,61], demonstrating that flow is the natural activator of the sensor, but whether or not this artificial flow carries along cargo remains to be seen. Sensor manipulations are extremely efficient, at least in the frog *Xenopus*, where manipulations can be performed in a sided manner, and in the mouse, reaching efficiencies of close to one hundred percent [58], numbers that are never encountered with any other experimental or genetic manipulation. How flow sets off the sensor, i.e., represses Dand5, is a matter of intense research. Genes that fulfill characteristics, such as Nodal and Dand5, qualify for this process, i.e., flow sensing: they should be highly efficient in knockout or knockdown situations and they should act in a strictly sided manner. Screening the literature for factors complying with these criteria might uncover genes that are involved in sensor function; *pkd2* and *pkd1l1* are certainly good examples [62,63].

2.5. Signal Transfer

Finally, the signal that is generated in the sensor needs to transfer from the LRO to the LPM. The transfer system must be present on either side, otherwise bilateral induction of the cascade would not be possible. In its absence, Nodal should never get activated in the LPM. However, contrary to the sensor, it strictly depends on the upstream chain of events and cannot be activated in the absence of the signal. The conceptually most parsimonious scenario, namely that Nodal itself gets transferred, is fully compatible with the available experimental data. While *gdf1/gdf3*, which is expressed in the sensor and complex with Nodal, is required for de-repressed Nodal to transfer to the LPM [60,64], more specific transfer mutants are not known, indicating that the mechanism relies on available cell biological characteristics such as the extracellular matrix or coupling of cells by gap junctions [65–67]. Mutations in any such functions would likely impact on other processes as well, obscuring an LR-specific function. Contrary to all the other functions that are discussed above, transfer is likely permissive in nature and not instructive, which is why Nodal cascade expression patterns in our opinion do not reveal a lot in that context.

Table 1. Nodal cascade gene expression patterns in selected LR mutants.

Process	Gene/Treatment	Species	Mutant	Morphant	Nodal Cascade *	References
LRO specifier	*brachyury*	mouse	*T/T*		absent	[34,36]
			$T^{Wis/TWis}$		absent	
		fish	*ntl*		absent	[35]
		frog	*Xbra*	TBMO	absent	SK & MB (unpublished)
LRO flow	methyl cellulose	*Xenopus*			absent	[44,68]
		mouse			bilateral	
flow generator	*FOXJ1*	Zebrafish		TBMO	random	[69,70]
		mouse	$Foxj1^{neo/neo}$		random	
					absent, bilateral	
	KIF3A	mouse	-/-		bilateral	[45,61]
	RFX2	*Xenopus*		SBMO	absent, bilateral	[71,72]
		zebrafish		TBMO	absent	
cilia motility	*DNAH11*	mouse	$Dnah11^{iv/iv}$		random	[5,19,43]
	DNAH9	*Xenopus*		TBMO	absent	
	DNAH5	*Xenopus*		TBMO	absent	
	DYX1C1	zebrafish		TBMO	absent	
ciliapolarity	*VANGL1*	mouse	$Vangl1^{gt/gt}$		bilateral	[40,41]
	VANGL2		$Vangl2^{-/-}$		bilateral	
		Xenopus		TBMO	absent	
LRO sensor	*NODAL*	mouse			absent	[55]
		zebrafish		TBMO	random	[56–58]
		Xenopus		TBMO	absent	
	DAND5	mouse	-/-		random	[58–60]
		Xenopus		TBMO	bilateral	
		zebrafish		TBMO	bilateral	
	GDF1/GDF3	mouse	-/-		absent	[60]
		zebrafish		TBMO	absent	
		zebrafish	*mz-/-*		absent	
	PKD2	mouse	$Pkd2^{lacZ/lacZ}$		absent	[62]
		zebrafish		TBMO	bilateral	
		zebrafish		SBMO	absent	
	PKD1L1	mouse	$Pkd1l1^{rks/rks}$		absent	[63]
		medaka	abc^{mA12}		absent	

* Expression of *nodal*, *pitx2* and *lefty2* in the left lateral plate mesoderm.

2.6. Precautions

Besides the above-mentioned possibility of full or partial compensation of germline mutations [21], which might blur the function of a given gene when judged by the resulting LPM marker gene expression patterns, genes might act in more than one function, such as Nodal itself, which is required to set up the flow generator [73], in the sensor [74] and in the LPM [75,76]. Some ciliary genes certainly are required in the flow generator and the sensor as well, which has to be taken into account when analyzing the Nodal cascade. Despite these restrictions, we are convinced that a careful re-evaluation of LPM gene expression patterns might be beneficial to place factors in the progress of symmetry breaking, as does the assessment of novel factors that keep to be identified. Such analyses need of course be restricted to model organisms, in which a ciliated LRO has been demonstrated. In vertebrates, this excludes birds and reptiles, which likely have lost these mechanisms and have come up with an alternative strategy of left-asymmetric Nodal cascade induction (cf. [14] for a detailed discussion). Such a loss might even have happened in some mammalian groups, as indicated by the absence of a recently described novel LR determinant of unknown function, the matrix metalloproteinase Mmp21, in the cetartiodactyla, a systematic group of mammals that includes whales and even-toed ungulates [77]. That even-toed ungulates differ from other mammals has been previously suspected, as a ciliated LRO is absent in pig embryos [78].

3. Conclusions

In the more than 20 years that have passed since the first description of asymmetric gene expression in the left LPM of the chicken embryo [6], a great many of factors have been involved in the process of laterality determination. Despite all the progress, large gaps remain in our understanding of the molecular and cellular mechanisms that drive organ asymmetry. The majority of vertebrates use a cilia-dependent mode of symmetry breaking; in these cases, the assessment of Nodal cascade gene expression patterns in the LPM can tell us much about the underlying defects. We have argued here that randomized patterns are the result of defects in flow generation, while symmetric patterns arise from defective flow sensing. These different LPM patterns often are not discussed, or only very low cases numbers are reported when a new factor is presented in the literature; any deviation from the norm is taken as evidence for a general role in LR development. While this is correct, important information may be lost when the differences in efficacies and patterns are not pinpointed, evaluated, and weighed. The basic conceptual framework is there; we need to fill in the gaps. It should be profitable to discuss the options any result gives us, rather than concealing our uneasiness. The Nodal cascade has started the molecular analysis of LR analysis, and it remains at center stage now that we tackle the nature of flow generator and sensor.

Acknowledgments: Work in the Blum lab has been supported by DFG grants BL-285/9 and BL-285/10. S.K. and T.O. have been recipients of fellowships from the Landesgraduiertenförderung Baden-Württemberg. S.K. was also funded by the Federal Ministry of Education and Research (01PL11003), project Humboldt reloaded.

Author Contributions: A.S. had the idea for this review, which M.B. and A.S. wrote with the help of all authors. T.O. and S.K. assembled the Figures and M.T., M.M., F.F., S.K. and T.O. researched the data for the table.

Conflicts of Interest: The authors declare no conflict of interest.

References

1. Dareste, C. *Recherches sur la Production Artificielle des Monstruosités, ou Essais de Tératogénie Expérimentale*; C. Reinwald: Paris, France, 1891.
2. Fol, H.; Warynsky, S. Sur la production artificielle de l'inversion viscérale ou hétérotaxie chez des embryons de poulet. *CR Acad. Sci. Paris* **1883**, *96*, 1674–1676.
3. Tisler, M.; Schweickert, A.; Blum, M. Xenopus, an ideal model organism to study laterality in conjoined twins. *Genesis* **2017**, 55. [CrossRef] [PubMed]
4. Capdevila, J.; Vogan, K.J.; Tabin, C.J.; Izpisúa Belmonte, J.C. Mechanisms of left-right determination in vertebrates. *Cell* **2000**, *101*, 9–21. [CrossRef]
5. Campione, M.; Steinbeisser, H.; Schweickert, A.; Deissler, K.; van Bebber, F.; Lowe, L.A.; Nowotschin, S.; Viebahn, C.; Haffter, P.; Kuehn, M.R.; et al. The homeobox gene Pitx2: Mediator of asymmetric left-right signaling in vertebrate heart and gut looping. *Development* **1999**, *126*, 1225–1234. [PubMed]
6. Levin, M.; Johnson, R.L.; Sterna, C.D.; Kuehn, M.; Tabin, C. A molecular pathway determining left-right asymmetry in chick embryogenesis. *Cell* **1995**, *82*, 803–814. [CrossRef]
7. Nakamura, T.; Hamada, H. Left-right patterning: Conserved and divergent mechanisms. *Development* **2012**, *139*, 3257–3262. [CrossRef] [PubMed]
8. Nakamura, T.; Mine, N.; Nakaguchi, E.; Mochizuki, A.; Yamamoto, M.; Yashiro, K.; Meno, C.; Hamada, H. Generation of robust left-right asymmetry in the mouse embryo requires a self-enhancement and lateral-inhibition system. *Dev. Cell* **2006**, *11*, 495–504. [CrossRef] [PubMed]
9. Shiratori, H. Conserved regulation and role of Pitx2 in situs-specific morphogenesis of visceral organs. *Development* **2006**, *133*, 3015–3025. [CrossRef] [PubMed]
10. Inácio, J.M.; Marques, S.; Nakamura, T.; Shinohara, K.; Meno, C.; Hamada, H.; Belo, J.A. The dynamic right-to-left translocation of Cerl2 is involved in the regulation and termination of Nodal activity in the mouse node. *PLoS ONE* **2013**, *8*, e60406. [CrossRef] [PubMed]
11. Oki, S.; Kitajima, K.; Marques, S.; Belo, J.A.; Yokoyama, T.; Hamada, H.; Meno, C. Reversal of left-right asymmetry induced by aberrant Nodal signaling in the node of mouse embryos. *Development* **2009**, *136*, 3917–3925. [CrossRef] [PubMed]

12. Lohr, J.L.; Danos, M.C.; Groth, T.W.; Yost, H.J. Maintenance of asymmetric nodal expression in Xenopus laevis. *Dev. Genet.* **1998**, *23*, 194–202. [CrossRef]
13. Tisler, M.; Wetzel, F.; Mantino, S.; Kremnyov, S.; Thumberger, T.; Schweickert, A.; Blum, M.; Vick, P. Cilia are required for asymmetric nodal induction in the sea urchin embryo. *BMC Dev. Biol.* **2016**, *16*, 28. [CrossRef] [PubMed]
14. Blum, M.; Feistel, K.; Thumberger, T.; Schweickert, A. The evolution and conservation of left-right patterning mechanisms. *Development* **2014**, *141*, 1603–1613. [CrossRef] [PubMed]
15. Blum, M.; Schweickert, A.; Vick, P.; Wright, C.V.E.; Danilchik, M.V. Symmetry breakage in the vertebrate embryo: When does it happen and how does it work? *Dev. Biol.* **2014**, *393*, 109–123. [CrossRef] [PubMed]
16. Grimes, D.T.; Burdine, R.D. Left–Right Patterning: Breaking Symmetry to Asymmetric Morphogenesis. *Trends Genet.* **2017**, *33*, 616–628. [CrossRef] [PubMed]
17. Supp, D.M.; Brueckner, M.; Kuehn, M.R.; Witte, D.P.; Lowe, L.A.; McGrath, J.; Corrales, J.; Potter, S.S. Targeted deletion of the ATP binding domain of left-right dynein confirms its role in specifying development of left-right asymmetries. *Development* **1999**, *126*, 5495–5504. [PubMed]
18. Supp, D.M.; Witte, D.P.; Potter, S.S.; Brueckner, M. Mutation of an axonemal dynein affects left-right asymmetry in inversus viscerum mice. *Nature* **1997**, *389*, 963–966. [CrossRef] [PubMed]
19. Lowe, L.A.; Supp, D.M.; Sampath, K.; Yokoyama, T.; Wright, C.V.; Potter, S.S.; Overbeek, P.; Kuehn, M.R. Conserved left-right asymmetry of nodal expression and alterations in murine situs inversus. *Nature* **1996**, *381*, 158–161. [CrossRef] [PubMed]
20. Seo, J.W.; Brown, N.A.; Ho, S.Y.; Anderson, R.H. Abnormal laterality and congenital cardiac anomalies. Relations of visceral and cardiac morphologies in the iv/iv mouse. *Circulation* **1992**, *86*, 642–650. [CrossRef] [PubMed]
21. Rossi, A.; Kontarakis, Z.; Gerri, C.; Nolte, H.; Hölper, S.; Krüger, M.; Stainier, D.Y. Genetic compensation induced by deleterious mutations but not gene knockdowns. *Nature* **2015**, *524*, 230–233. [CrossRef] [PubMed]
22. Blum, M.; De Robertis, E.M.; Wallingford, J.B.; Niehrs, C. Morpholinos: Antisense and Sensibility. *Dev. Cell* **2015**, *35*, 145–149. [CrossRef] [PubMed]
23. Okada, Y.; Nonaka, S.; Tanaka, Y.; Saijoh, Y.; Hamada, H.; Hirokawa, N. Abnormal nodal flow precedes situs inversus in *iv* and *inv* mice. *Mol. Cell* **1999**, *4*, 459–468. [CrossRef]
24. Grimes, D.T.; Keynton, J.L.; Buenavista, M.T.; Jin, X.; Patel, S.H.; Kyosuke, S.; Vibert, J.; Williams, D.J.; Hamada, H.; Hussain, R.; et al. Genetic Analysis Reveals a Hierarchy of Interactions between Polycystin-Encoding Genes and Genes Controlling Cilia Function during Left-Right Determination. *PLoS Genet.* **2016**, *12*, e1006070. [CrossRef] [PubMed]
25. Vandenberg, L.N.; Levin, M. Consistent left-right asymmetry cannot be established by late organizers in Xenopus unless the late organizer is a conjoined twin. *Development* **2010**, *137*, 1095–1105. [CrossRef] [PubMed]
26. Vandenberg, L.N.; Levin, M. Far from solved: A perspective on what we know about early mechanisms of left-right asymmetry. *Dev. Dyn.* **2010**, *239*, 3131–3146. [CrossRef] [PubMed]
27. Vandenberg, L.N.; Levin, M. Perspectives and open problems in the early phases of left-right patterning. *Semin. Cell Dev. Biol.* **2009**, *20*, 456–463. [CrossRef] [PubMed]
28. Melby, A.E.; Warga, R.M.; Kimmel, C.B. Specification of cell fates at the dorsal margin of the zebrafish gastrula. *Development* **1996**, *122*, 2225–2237. [PubMed]
29. Shook, D.R.; Majer, C.; Keller, R. Pattern and morphogenesis of presumptive superficial mesoderm in two closely related species, *Xenopus laevis* and *Xenopus tropicalis*. *Dev. Biol.* **2004**, *270*, 163–185. [CrossRef] [PubMed]
30. Blum, M.; Andre, P.; Muders, K.; Schweickert, A.; Fischer, A.; Bitzer, E.; Bogusch, S.; Beyer, T.; van Straaten, H.W.; Viebahn, C. Ciliation and gene expression distinguish between node and posterior notochord in the mammalian embryo. *Differentiation* **2007**, *75*, 133–146. [CrossRef] [PubMed]
31. Bajoghli, B.; Aghaallaei, N.; Soroldoni, D.; Czerny, T. The roles of Groucho/Tle in left-right asymmetry and Kupffer's vesicle organogenesis. *Dev. Biol.* **2007**, *303*, 347–361. [CrossRef] [PubMed]
32. Essner, J.J.; Amack, J.D.; Nyholm, M.K.; Harris, E.B.; Yost, H.J. Kupffer's vesicle is a ciliated organ of asymmetry in the zebrafish embryo that initiates left-right development of the brain, heart and gut. *Development* **2005**, *132*, 1247–1260. [CrossRef] [PubMed]

33. Blum, M.; Beyer, T.; Weber, T.; Vick, P.; Andre, P.; Bitzer, E.; Schweickert, A. *Xenopus*, an ideal model system to study vertebrate left-right asymmetry. *Dev. Dyn.* **2009**, *238*, 1215–1225. [CrossRef] [PubMed]
34. King, T.; Beddington, R.S.; Brown, N.A. The role of the brachyury gene in heart development and left-right specification in the mouse. *Mech. Dev.* **1998**, *79*, 29–37. [CrossRef]
35. Amack, J.D.; Yost, H.J. The T box transcription factor no tail in ciliated cells controls zebrafish left-right asymmetry. *Curr. Biol.* **2004**, *14*, 685–690. [CrossRef] [PubMed]
36. Concepcion, D.; Papaioannou, V.E. Nature and extent of left/right axis defects in T^{Wis}/T^{Wis} mutant mouse embryos. *Dev. Dyn.* **2014**, *243*, 1046–1053. [CrossRef] [PubMed]
37. Beckers, A.; Alten, L.; Viebahn, C.; Andre, P.; Gossler, A. The mouse homeobox gene Noto regulates node morphogenesis, notochordal ciliogenesis, and left right patterning. *Proc. Natl. Acad. Sci. USA* **2007**, *104*, 15765–15770. [CrossRef] [PubMed]
38. Walentek, P.; Beyer, T.; Thumberger, T.; Schweickert, A.; Blum, M. ATP4a Is Required for Wnt-Dependent Foxj1 Expression and Leftward Flow in Xenopus Left-Right Development. *Cell Rep.* **2012**, *1*, 516–527. [CrossRef] [PubMed]
39. Walentek, P.; Schneider, I.; Schweickert, A.; Blum, M. Wnt11b is involved in cilia-mediated symmetry breakage during Xenopus left-right development. *PLoS ONE* **2013**, *8*, e73646. [CrossRef] [PubMed]
40. Song, H.; Hu, J.; Chen, W.; Elliott, G.; Andre, P.; Gao, B.; Yang, Y. Planar cell polarity breaks bilateral symmetry by controlling ciliary positioning. *Nature* **2010**, *466*, 378–382. [CrossRef] [PubMed]
41. Antic, D.; Stubbs, J.L.; Suyama, K.; Kintner, C.; Scott, M.P.; Axelrod, J.D. Planar cell polarity enables posterior localization of nodal cilia and left-right axis determination during mouse and *Xenopus* embryogenesis. *PLoS ONE* **2010**, *5*, e8999. [CrossRef] [PubMed]
42. Pintado, P.; Sampaio, P.; Tavares, B.; Montenegro-Johnson, T.D.; Smith, D.J.; Lopes, S.S. Dynamics of cilia length in left-right development. *R. Soc. Open Sci.* **2017**, *4*, 161102. [CrossRef] [PubMed]
43. Vick, P.; Schweickert, A.; Weber, T.; Eberhardt, M.; Mencl, S.; Shcherbakov, D.; Beyer, T.; Blum, M. Flow on the right side of the gastrocoel roof plate is dispensable for symmetry breakage in the frog *Xenopus laevis*. *Dev. Biol.* **2009**, *331*, 281–291. [CrossRef] [PubMed]
44. Kawasumi, A.; Takamatsu, A.; Yoshiba, S.; Botilde, Y.; Motoyama, N.; Reith, W.; Durand, B.; Shiratori, H.; Hamada, H. Two rotating cilia in the node cavity are sufficient to break left–right symmetry in the mouse embryo. *Nat. Commun.* **2011**, *3*, 622–628. [CrossRef]
45. Takeda, S.; Yonekawa, Y.; Tanaka, Y.; Okada, Y.; Nonaka, S.; Hirokawa, N. Left-right asymmetry and kinesin superfamily protein KIF3A: New insights in determination of laterality and mesoderm induction by kif3A$^{-/-}$ mice analysis. *J. Cell Biol.* **1999**, *145*, 825–836. [CrossRef] [PubMed]
46. Bisgrove, B.W.; Snarr, B.S.; Emrazian, A.; Yost, H.J. Polaris and Polycystin-2 in dorsal forerunner cells and Kupffer's vesicle are required for specification of the zebrafish left-right axis. *Dev. Biol.* **2005**, *287*, 274–288. [CrossRef] [PubMed]
47. Taulman, P.D.; Haycraft, C.J.; Balkovetz, D.F.; Yoder, B.K. Polaris, a protein involved in left-right axis patterning, localizes to basal bodies and cilia. *Mol. Biol. Cell* **2001**, *12*, 589–599. [CrossRef] [PubMed]
48. Yoder, B.K.; Tousson, A.; Millican, L.; Wu, J.H.; Bugg, C.E.; Schafer, J.A.; Balkovetz, D.F. Polaris, a protein disrupted in orpk mutant mice, is required for assembly of renal cilium. *Am. J. Physiol. Renal Physiol.* **2002**, *282*, F541–F552. [CrossRef] [PubMed]
49. Tanaka, Y.; Okada, Y.; Hirokawa, N. FGF-induced vesicular release of Sonic hedgehog and retinoic acid in leftward nodal flow is critical for left-right determination. *Nature* **2005**, *435*, 172–177. [CrossRef] [PubMed]
50. Hirokawa, N.; Tanaka, Y.; Okada, Y. Left-Right Determination: Involvement of Molecular Motor KIF3, Cilia, and Nodal Flow. *Cold Spring Harb. Perspect. Biol.* **2009**, *1*, a000802. [CrossRef] [PubMed]
51. Nonaka, S.; Shiratori, H.; Saijoh, Y.; Hamada, H. Determination of left-right patterning of the mouse embryo by artificial nodal flow. *Nature* **2002**, *418*, 96–99. [CrossRef] [PubMed]
52. Yuan, S.; Zhao, L.; Brueckner, M.; Sun, Z. Intraciliary calcium oscillations initiate vertebrate left-right asymmetry. *Curr. Biol.* **2015**, *25*, 556–567. [CrossRef] [PubMed]
53. Norris, D.P.; Jackson, P.K. Cell biology: Calcium contradictions in cilia. *Nature* **2016**, *531*, 582–583. [CrossRef] [PubMed]
54. Delling, M.; Indzhykulian, A.A.; Liu, X.; Li, Y.; Xie, T.; Corey, D.P.; Clapham, D.E. Primary cilia are not calcium-responsive mechanosensors. *Nature* **2016**, *531*, 656–660. [CrossRef] [PubMed]

55. Brennan, J.; Norris, D.P.; Robertson, E.J. Nodal activity in the node governs left-right asymmetry. *Genes Dev.* **2002**, *16*, 2339–2344. [CrossRef] [PubMed]
56. Sampath, K.; Robertson, E.J. Keeping a lid on nodal: Transcriptional and translational repression of nodal signalling. *Open Biol.* **2016**, *6*, 150200–150208. [CrossRef] [PubMed]
57. Toyoizumi, R.; Ogasawara, T.; Takeuchi, S.; Mogi, K. Xenopus nodal related-1 is indispensable only for left-right axis determination. *Int. J. Dev. Biol.* **2005**, *49*, 923–938. [CrossRef] [PubMed]
58. Schweickert, A.; Vick, P.; Getwan, M.; Weber, T.; Schneider, I.; Eberhardt, M.; Beyer, T.; Pachur, A.; Blum, M. The nodal inhibitor Coco is a critical target of leftward flow in Xenopus. *Curr. Biol.* **2010**, *20*, 738–743. [CrossRef] [PubMed]
59. Marques, S.; Borges, A.C.; Silva, A.C.; Freitas, S.; Cordenonsi, M.; Belo, J.A. The activity of the Nodal antagonist Cerl-2 in the mouse node is required for correct L/R body axis. *Genes Dev.* **2004**, *18*, 2342–2347. [CrossRef] [PubMed]
60. Vonica, A.; Brivanlou, A.H. The left-right axis is regulated by the interplay of Coco, Xnr1 and derrière in *Xenopus* embryos. *Dev. Biol.* **2007**, *303*, 281–294. [CrossRef] [PubMed]
61. Yoshiba, S.; Shiratori, H.; Kuo, I.Y.; Kawasumi, A.; Shinohara, K.; Nonaka, S.; Asai, Y.; Sasaki, G.; Belo, J.A.; Sasaki, H.; et al. Cilia at the node of mouse embryos sense fluid flow for left-right determination via Pkd2. *Science* **2012**, *338*, 226–231. [CrossRef] [PubMed]
62. Pennekamp, P.; Karcher, C.; Fischer, A.; Schweickert, A.; Skryabin, B.; Horst, J.; Blum, M.; Dworniczak, B. The ion channel polycystin-2 is required for left-right axis determination in mice. *Curr. Biol.* **2002**, *12*, 938–943. [CrossRef]
63. Field, S.; Riley, K.-L.; Grimes, D.T.; Hilton, H.; Simon, M.; Powles-Glover, N.; Siggers, P.; Bogani, D.; Greenfield, A.; Norris, D.P. Pkd1l1 establishes left-right asymmetry and physically interacts with Pkd2. *Development* **2011**, *138*, 1131–1142. [CrossRef] [PubMed]
64. Hanafusa, H.; Masuyama, N.; Kusakabe, M.; Shibuya, H.; Nishida, E. The TGF-β family member derrière is involved in regulation of the establishment of left-right asymmetry. *EMBO Rep.* **2000**, *1*, 32–39. [CrossRef] [PubMed]
65. Viotti, M.; Niu, L.; Shi, S.-H.; Hadjantonakis, A.-K. Role of the gut endoderm in relaying left-right patterning in mice. *PLoS Biol.* **2012**, *10*, e1001276. [CrossRef] [PubMed]
66. Bessodes, N.; Haillot, E.; Duboc, V.; Röttinger, E.; Lahaye, F.; Lepage, T. Reciprocal signaling between the ectoderm and a mesendodermal left-right organizer directs left-right determination in the sea urchin embryo. *PLoS Genet.* **2012**, *8*, e1003121. [CrossRef] [PubMed]
67. Beyer, T.; Thumberger, T.; Schweickert, A.; Blum, M. Connexin26-mediated transfer of laterality cues in Xenopus. *Biol. Open* **2012**, *1*, 473–481. [CrossRef] [PubMed]
68. Schweickert, A.; Weber, T.; Beyer, T.; Vick, P.; Bogusch, S.; Feistel, K.; Blum, M. Cilia-driven leftward flow determines laterality in *Xenopus*. *Curr. Biol.* **2007**, *17*, 60–66. [CrossRef] [PubMed]
69. Zhang, M.; Bolfing, M.F.; Knowles, H.J.; Karnes, H.; Hackett, B.P. Foxj1 regulates asymmetric gene expression during left-right axis patterning in mice. *Biochem. Biophys. Res. Commun.* **2004**, *324*, 1413–1420. [CrossRef] [PubMed]
70. Yu, X.; Ng, C.P.; Habacher, H.; Roy, S. Foxj1 transcription factors are master regulators of the motile ciliogenic program. *Nat. Genet.* **2008**, *40*, 1445–1453. [CrossRef] [PubMed]
71. Chung, M.I.; Peyrot, S.M.; LeBoeuf, S.; Park, T.J.; McGary, K.L.; Marcotte, E.M.; Wallingford, J.B. RFX2 is broadly required for ciliogenesis during vertebrate development. *Dev. Biol.* **2012**, *363*, 155–165. [CrossRef] [PubMed]
72. Bisgrove, B.W.; Makova, S.; Yost, H.J.; Brueckner, M. RFX2 is essential in the ciliated organ of asymmetry and an RFX2 transgene identifies a population of ciliated cells sufficient for fluid flow. *Dev. Biol.* **2012**, *363*, 166–178. [CrossRef] [PubMed]
73. Tözser, J.; Earwood, R.; Kato, A.; Brown, J.; Tanaka, K.; Didier, R.; Megraw, T.L.; Blum, M.; Kato, Y. TGF-β Signaling Regulates the Differentiation of Motile Cilia. *Cell Rep.* **2015**, *11*, 1000–1007. [CrossRef] [PubMed]
74. Norris, D.P.; Robertson, E.J. Asymmetric and node-specific nodal expression patterns are controlled by two distinct cis-acting regulatory elements. *Genes Dev.* **1999**, *13*, 1575–1588. [CrossRef] [PubMed]
75. Ohi, Y.; Wright, C.V.E. Anteriorward shifting of asymmetric *Xnr1* expression and contralateral communication in left-right specification in *Xenopus*. *Dev. Biol.* **2007**, *301*, 447–463. [CrossRef] [PubMed]

76. Marjoram, L.; Wright, C. Rapid differential transport of Nodal and Lefty on sulfated proteoglycan-rich extracellular matrix regulates left-right asymmetry in *Xenopus*. *Development* **2011**, *138*, 475–485. [CrossRef] [PubMed]
77. Guimier, A.; Gabriel, G.C.; Bajolle, F.; Tsang, M.; Liu, H.; Noll, A.; Schwartz, M.; El Malti, R.; Smith, L.D.; Klena, N.T.; et al. *MMP21* is mutated in human heterotaxy and is required for normal left-right asymmetry in vertebrates. *Nat. Genet.* **2015**, *47*, 1260–1263. [CrossRef] [PubMed]
78. Gros, J.; Feistel, K.; Viebahn, C.; Blum, M.; Tabin, C.J. Cell movements at Hensen's node establish left/right asymmetric gene expression in the chick. *Science* **2009**, *324*, 941–944. [CrossRef] [PubMed]

The Power of Strain: Organizing Left-Right Cilia

Developmental Cell
Previews

The Power of Strain: Organizing Left-Right Cilia

Martin Blum[1,*] and Tim Ott[1]
[1]Institute of Zoology, University of Hohenheim, Garbenstr. 30, 70599 Stuttgart, Germany
*Correspondence: martin.blum@uni-hohenheim.de
https://doi.org/10.1016/j.devcel.2018.04.015

Left-right organizers require motile and polarized cilia to break symmetry. In this issue of *Developmental Cell*, Chien et al. (2018) demonstrate that gastrulation-derived mechanical strain of the precursor tissue orients cilia and is required for cilia lengthening and motility.

Animal organ asymmetries are not an oddity of nature, but fulfill various purposes. A long gut, for example, gets stowed in an asymmetric and orderly manner and facilitates the efficient resorption of nutrients, whereas the four-chambered human heart allows separation of pulmonary and systemic circulation (reviewed in Blum and Ott, 2018). The early vertebrate embryo is symmetrical, though, and biased organ asymmetries need to be formed during development. Molecularly, asymmetric organ morphogenesis is under the control of the Nodal signaling cascade, which is activated on the left side of the early neurula embryo. Left-sided Nodal induction, in turn, depends on leftward fluid flow that is established at the left-right organizer (LRO), a transient ciliated epithelium at the roof of the primitive gut that forms during gastrulation (Figure 1). The LRO bears motile cilia, which are polarized to the posterior pole of the cell, such that clockwise rotational beating results in a flow of extracellular fluids from the right to the left side of the LRO. This flow is presumably sensed by lateral LRO cells, which bear unpolarized and immotile cilia and which process this signal to induce asymmetric Nodal at a distance (reviewed in Shinohara and Hamada, 2017). Cilia motility is dependent upon the expression of the forkhead transcription factor *foxj1* in the LRO precursor tissue, the so-called superficial mesoderm (SM), which localizes adjacent to the Spemann organizer of the gastrula embryo (Shook et al., 2004). Cilia polarization is ruled by the planar cell polarity (PCP) pathway (Shinohara and Hamada, 2017). From these data, a simple and highly plausible scenario emerges: namely, that the anterior-posterior (AP) axis of the embryo is used to align and polarize cilia for leftward fluid flow and symmetry breaking. How AP information is transferred to the LRO cilia, however, i.e., how the PCP vector is generated, has remained elusive, because globally acting morphogenetic signals have not been identified thus far. In this issue of *Developmental Cell*, Chris Kintner's lab, in collaboration with Ray Keller, uncover a novel mechanism that supersedes the need of global signaling cues. Using the frog *Xenopus* as a model, Chien et al. (2018) beautifully and convincingly demonstrate that mechanical strain of the LRO precursor tissue of the SM is necessary and sufficient for cilia lengthening, polarity and motility, and thus for the basic setup of directed flow generation at the LRO. Strain is naturally applied by the convergence and extension (CE) movements of SM cells as they involute into the primitive gut during gastrulation to give rise to the LRO (Figure 1).

In a previous joint paper, Kintner and Keller demonstrated that the polarity of multiciliated cells in the tadpole skin depends on mechanical strain that is exerted by the gastrulating mesoderm (Chien et al., 2015); the present study extends this analysis in an exciting way to the LRO. Re-evaluating Keller's fate map of superficial tissues (Keller, 1975) predicted that considerable strain is exerted on the superficial mesoderm during LRO formation, with an AP gradient of higher strain posteriorly and a medial-lateral (ML) gradient of high strain in the dorsal midline, tapering off toward both sides. Using assays they previously applied for their analysis of the skin, Chien et al. (2018) formally prove the existence of these gradients: early on (at stage 12 or late gastrula, when involution of the SM has just started), cells elongate along the AP axis, apical microtubules orient in the same direction, and—importantly—the core PCP components Frizzled and Vangl form stable complexes at the posterior and anterior membranes, respectively, i.e., orthogonal to the AP axis. At a later stage, when flow is in full swing (stage 18, early neurula), the earlier strain gradients correlate with both cilia length and polarization, with longer and more posteriorly localized cilia in the center, a remarkable finding that has gone unnoticed until now (Figure 1).

With the virtuoso skills of the experienced frog experimenters, the authors investigated the hypotheses that emerged from these descriptive findings, creating strain loss- and gain-of-function scenarios. To prevent CE and thus strain, the authors "glued" blastula explants that contained the presumptive LRO onto fibronectin-coated slides, with the short cilia that formed remaining in a central position. Explants that were able to extend grew cilia of normal length and polarity. To be able to apply strain ectopically, the authors developed a novel explant technique, which they called "LRO explants". This explant was made up of SM explanted together with the adhering deep cells, which caused the tissue to round up with the LRO on the outside. This round LRO explant, when left alone, grew short, immotile, and unpolarized cilia, and stable PCP complexes did not form. When LRO explants were partially sucked into a glass capillary, however, cilia elongated, polarized, and became motile. This response was rapid and occurred in just 3 hr, which is important, because the time window for symmetry breaking in the embryo is probably not much longer. Remarkably, strain level and duration both correlated in a linear way with cilia parameters length and polarization, in perfect agreement with the gradients seen in the embryo. Most significantly, cilia polarized in the direction of highest strain. Put another way,

Developmental Cell
Previews

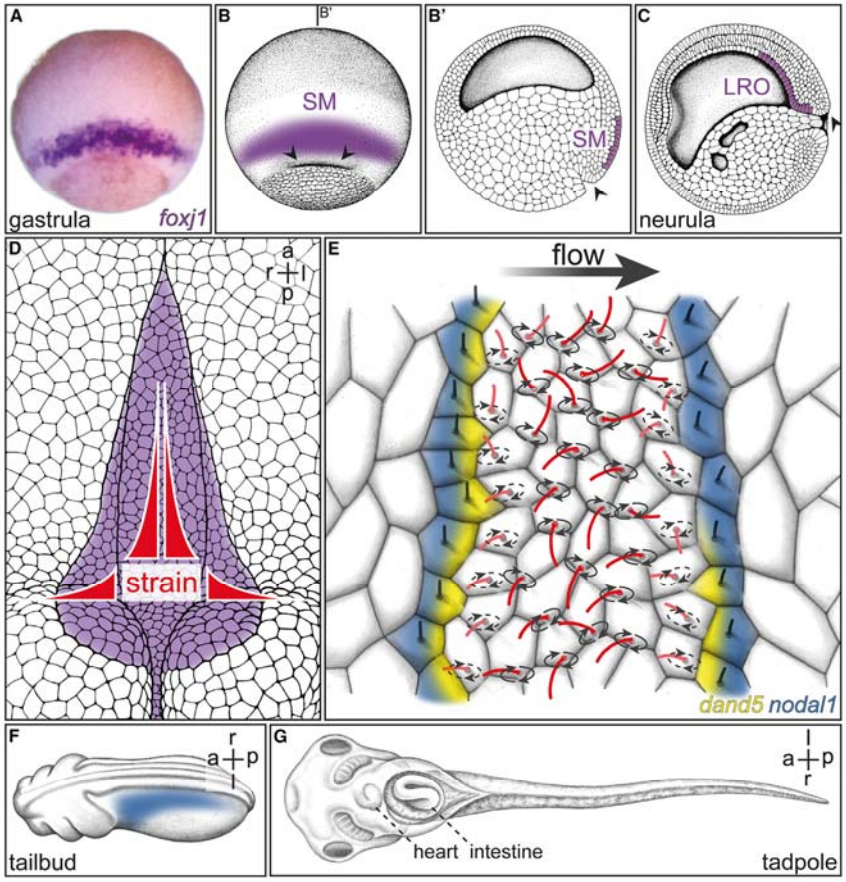

Figure 1. The Role of Mechanical Strain in *Xenopus* Left-Right Development

Foxj1 expression in the gastrula embryo (A) marks the superficial mesoderm (SM; B, B'), from which the left-right organizer (LRO; C) develops when the SM involutes during gastrulation. Convergent extension movements during involution exert graded mechanical strain (D), along which cilia lengthen, become motile, and polarize (E). The ensuing leftward flow is sensed by lateral LRO cells, which harbor immotile and non-polarized cilia that express *nodal1* (blue) and its inhibitor *dand5* (yellow). *Dand5* is inhibited by flow (E), resulting in Nodal cascade induction in the left lateral plate mesoderm (F) and asymmetric organ morphogenesis of the tadpole (G). Arrowheads, dorsal lip. A, anterior; l, left; r, right; p, posterior. Image provided by Jennifer Kreis.

strain generated the PCP vector, and in the embryo, the corresponding strain site would be the posterior pole. Apical microtubules oriented along the AP axis were biased such that a considerably higher fraction of plus ends was found pointing to the posterior pole of cells, perhaps reflecting vesicular trafficking of Frizzled, as the authors propose.

In a final set of experiments, Chien et al. (2018) looked into the specific role of *foxj1* in strain-mediated LRO morphogenesis and function. The graded *foxj1* expression in the SM of the blastula/early gastrula embryo indicated that the LRO precursor was pre-patterned before convergence extension. Indeed, more-lateral LRO explants responded less to strain, i.e., grew shorter and less-polarized cilia when sucked into the capillary, confirming a dorsal-ventral pre-pattern. In *foxj1* mutant embryos, core PCP components still localized as a response to strain, but cilia were not polarized and short. Nevertheless, *foxj1*, although it is required, is not sufficient to mediate the strain response. Ectodermal ciliated cells with induced ectopic *foxj1* expression did not respond to strain. Indeed, mesodermal pre-patterning was required for strain response, because when the authors co-injected *nodal2* along with *foxj1*, leading to mesodermal marker expression, the application of strain led to long and polarized ectopic cilia, reminiscent of the LRO. Mechanical strain exerted by

Developmental Cell
Previews

gastrulation CE movements thus acts on mesodermally pre-patterned LRO precursor cells to generate a planar axis and to lengthen and polarize motile cilia that break symmetry in a biased manner by leftward fluid flow.

One possible source of mesodermal pre-patterning might be buried in the different fates of the central and lateral LRO cells. The central LRO cells integrate into the notochord (which likely generates most of the strain), whereas the lateral LRO cells are somitic by nature. These lateral cells, besides harboring immotile and non-polarized cilia, also differ from notochordal cells by their co-expression of *nodal1* and its inhibitor *dand5*, an inhibition that becomes released as a result of flow (Blum et al., 2014). Perhaps strain is only required for cilia on notochordal cells in the process of flow generation, which can only be tested once factors that specify these different LRO fates become known.

What does this work tell us about how LROs work in general, beyond the frog? Primitive bony fish such as sturgeons gastrulate like frogs and have an identical LRO (Bolker, 1993). In mammals, the LRO and notochord are intimately linked as well, with notochord CE presenting a major source of strain (Balmer et al., 2016; Sulik et al., 1994). It may be beneficial to re-evaluate left-right defects in zebrafish and mouse notochord mutants against this background. Mechanical strain is thus likely a general determinant of LRO cilia function and flow, which is challenging or even impossible to test experimentally in other model organisms. The mechanism that the study by Chien et al. (2018) proposes is simple, elegant, and makes a lot of sense.

REFERENCES

Balmer, S., Nowotschin, S., and Hadjantonakis, A.-K. (2016). Notochord morphogenesis in mice: Current understanding & open questions. Dev. Dyn. *245*, 547–557.

Blum, M., and Ott, T. (2018). Animal left-right asymmetry. Curr. Biol. *28*, R301–R304.

Blum, M., Schweickert, A., Vick, P., Wright, C.V.E., and Danilchik, M.V. (2014). Symmetry breakage in the vertebrate embryo: when does it happen and how does it work? Dev. Biol. *393*, 109–123.

Bolker, J.A. (1993). The mechanism of gastrulation in the white sturgeon. J. Exp. Zool. *266*, 132–145.

Chien, Y.-H., Keller, R., Kintner, C., and Shook, D.R. (2015). Mechanical strain determines the axis of planar polarity in ciliated epithelia. Curr. Biol. *25*, 2774–2784.

Chien, Y.-H., Srinivasan, S., Keller, R., and Kintner, C. (2018). Mechanical strain determines cilia length, motility and planar position in the left-right organizer. Dev. Cell *45*, this issue, 316–330.

Keller, R.E. (1975). Vital dye mapping of the gastrula and neurula of Xenopus laevis. I. Prospective areas and morphogenetic movements of the superficial layer. Dev. Biol. *42*, 222–241.

Shinohara, K., and Hamada, H. (2017). Cilia in Left-Right Symmetry Breaking. Cold Spring Harb. Perspect. Biol. *9*, a028282.

Shook, D.R., Majer, C., and Keller, R. (2004). Pattern and morphogenesis of presumptive superficial mesoderm in two closely related species, Xenopus laevis and Xenopus tropicalis. Dev. Biol. *270*, 163–185.

Sulik, K., Dehart, D.B., Iangaki, T., Carson, J.L., Vrablic, T., Gesteland, K., and Schoenwolf, G.C. (1994). Morphogenesis of the murine node and notochordal plate. Dev. Dyn. *201*, 260–278.

Phosphorylation Leads the Way for Protein Aggregate Disassembly

Steven Boeynaems[1] and Aaron D. Gitler[1,*]
[1]Department of Genetics, Stanford University School of Medicine, Stanford, CA 94305, USA
*Correspondence: agitler@stanford.edu
https://doi.org/10.1016/j.devcel.2018.04.017

Protein aggregation can be beneficial, with important biological functions, but must be somehow controlled. In this issue of *Developmental Cell*, Carpenter et al. (2018) uncover how a solid-like supermolecular protein assembly that regulates yeast meiosis is disassembled through phosphorylation of a disordered prion-like domain to control the timing of meiotic progression.

Protein aggregation has historically been viewed as detrimental: these clumps of proteins are the pathological hallmark of many devastating human neurodegenerative diseases (Aguzzi and O'Connor, 2010). But seminal discoveries over the last two decades by the late Susan Lindquist and others have taught us that protein aggregation is not always a problem (Newby and Lindquist, 2013). Protein aggregates may even sometimes confer beneficial biological functions, and, in the case of fungal prions, evolution may have actually selected for aggregation-prone proteins. The aggregation-prone nature of fungal prions endows them with the ability to seed aggregation of their non-prion form, which can be transmitted from cell to cell in a heritable manner. Instead of causing diseases, the stable aggregates can confer beneficial phenotypes to the host yeast. At the molecular level, fungal prion proteins contain disordered protein domains, lacking stable secondary structure, that are enriched in uncharged polar amino acids (e.g., asparagine, glutamine, and tyrosine) and glycine (Alberti et al., 2009). Powerful algorithms built to detect these features have been turned loose to scour diverse

Animal left-right asymmetry

Current Biology
Magazine

and have at least two contact zones in South Africa, opening the door for studies on ecological speciation, that is, how divergent selection in different habitats may lead to the formation of new species.

Where can I learn more?

Dewsbury, D.A., and Dawson, W.W. (1979). African four-striped grass mouse (*Rhabdomys pumilio*), a diurnal-crepuscular muroid rodent, in the behavioral laboratory. Behav. Res. Meth. Instrument. *11*, 329–333.

Du Toit, N., Pillay, N., Ganem, G., and Relton, C. (2016). A conservation assessment of Rhabdomys spp. In The Red List of Mammals of South Africa, Swaziland and Lesotho, M. Child, L. Roxburgh, E. Do Linh San, D. Raimondo, and H. Davies-Mostert, eds. (South African National Biodiversity Institute and Endangered Wildlife Trust).

Hill, D.L., Pillay, N., and Schradin, C. (2015). Alternative reproductive tactics in female striped mice: heavier females are more likely to breed solitarily than communally. J. Anim. Ecol. *84*, 1497–1508.

Mallarino, R., Henegar, C., Mirasierra, M., Manceau, M., Schradin, C., Vallejo, M., Beronja, S., Barsh, G.S., and Hoekstra, H.E. (2016). Developmental mechanisms of stripe patterns in rodents. Nature *539*, 518–523.

Meynard, C.N., Pillay, N., Perrigault, M., Caminade, P., and Ganem, G. (2012). Evidence of environmental niche differentiation in the striped mouse (*Rhabdomys sp.*): inference from its current distribution in southern Africa. Ecol. Evol. *2*, 1008–1023.

Rambau, R.V., and Robinson, T.J. (2003). Molecular genetics of *Rhabdomys pumilio* subspecies boundaries: mtDNA phylogeography and karyotypic analysis by fluorescence in situ hybridization (FISH). Mol. Phyl. Evol. *28*, 564–575.

Rymer, T. L., Pillay, N., and Schradin, C. (2016). Resilience to droughts in mammals: A conceptual framework for estimating vulnerability of a single species. Q. Rev. Biol. *91*, 133–176.

Schradin, C., Lindholm, A.K., Johannesen, J., Schoepf, I., Yuen, C.-H., König, B., and Pillay, N. (2012). Social flexibility and social evolution in mammals: a case study of the African striped mouse (*Rhabdomys pumilio*). Mol. Ecol. *21*, 541–553.

Schradin, C. (2013). Intraspecific variation in social organization by genetic variation, developmental plasticity, social flexibility or entirely extrinsic factors. Philos. Trans. R. Soc. B. Apr 8; 368(1618), 20120346.

Schradin, C., Raynaud, J., Arrivé, M., and Blanc, S. (2014). Leptin levels in free ranging striped mice (*Rhabdomys pumilio*) increase when food decreases: the ecological leptin hypothesis. Gen. Comp. Endocrinol. *206*, 139–145.

[1]Department of Molecular Biology, Princeton University, Princeton, NJ 08540, USA. [2]School of Animal, Plant and Environmental Sciences, University of the Witwatersrand, South Africa. [3]Howard Hughes Medical Institute, Department of Organismic & Evolutionary Biology. Department of Molecular & Cellular Biology, Museum of Comparative Zoology, Harvard University, Cambridge, MA 02138, USA. [4]Université de Strasbourg, CNRS, IPHC UMR 7178, F-67000 Strasbourg, France.
*E-mail: carsten.schradin@iphc.cnrs.fr

Primer

Animal left–right asymmetry

Martin Blum* and Tim Ott

Symmetry is appealing, be it in architecture, art or facial expression, where symmetry is a key feature to finding someone attractive or not. Yet, asymmetries are widespread in nature, not as an erroneous deviation from the norm but as a way to adapt to the prevailing environmental conditions at a time. Asymmetries in many cases are actively selected for: they might well have increased the evolutionary fitness of a species. Even many single-celled organisms are built asymmetrically, such as the pear-shaped ciliate *Paramecium*, which may depend on its asymmetry to navigate towards the oxygen-richer surface of turbid waters, at least based on modeling. Everybody knows the lobster with its asymmetric pair of claws, the large crusher usually on the left and the smaller cutter on the right. Snail shells coil asymmetrically, as do the organs they house. Organ asymmetries are found throughout the animal kingdom, referring to asymmetric positioning, asymmetric morphology or both, with the vertebrate heart being an example for the latter. Functional asymmetries, such as that of the human brain with its localization of the language center in one hemisphere, add to the complexity of organ asymmetries and presumably played a decisive role for sociocultural evolution. The evolutionary origin of organ asymmetries may have been a longer than body length gut, which allows efficient retrieval of nutrients, and the need to stow a long gut in the body cavity in an orderly manner that ensures optimal functioning. Vertebrate organ asymmetries (*situs solitus*) are quite sophisticated: in humans, the apex of the asymmetrically built heart points to the left; the lung in turn, due to space restrictions, has fewer lobes on the left than on the right side (two versus three in humans), stomach and spleen are found on the left, the liver on the right, and small and large intestine coil in a chiral manner (Figure 1A). In very rare cases (1:10,000), the organ situs is inverted (*situs inversus*), while

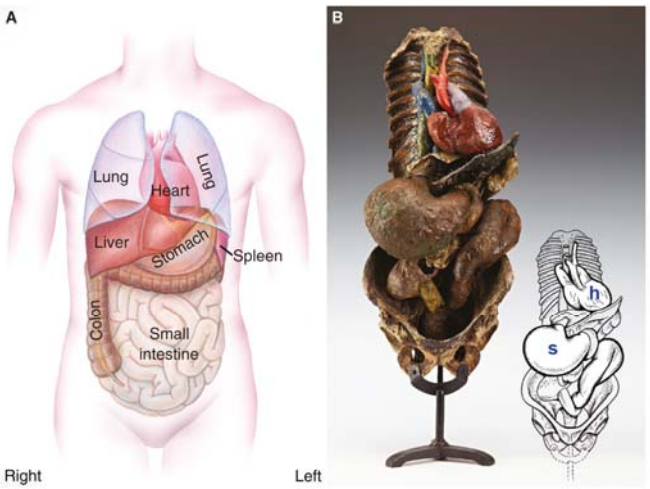

Figure 1. Human organ situs.
(A) Normal arrangement (*situs solitus*). (B) Historical preparation by Meckel the Elder of a human torso displaying heterotaxia, with normal position of the heart (h) and inverted stomach (s). From the Meckelsche Sammlungen of the Institute of Anatomy and Cell Biology, Martin-Luther University Halle-Wittenberg (Germany). Photograph by Janos Stekovics. Artwork by Bernd Schmid (University of Hohenheim).

CellPress

Current Biology
Magazine

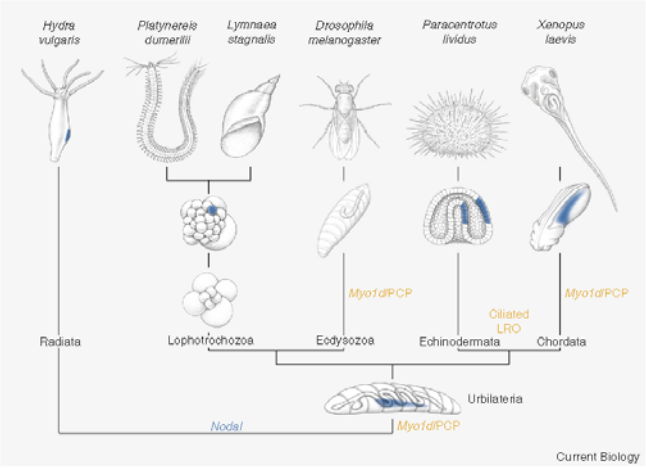

Figure 2. Animal asymmetry determinants.
Distribution of the known asymmetry determinants Nodal, Myosin 1d/PCP and cilia across the animal tree of life (depicted using the examples of the freshwater polyp *H. vulgaris*, the marine annelid worm *P. dumerilii*, the great pond snail *L. stagnalis*, the fruit fly *D. melanogaster*, the purple sea urchin *P. lividus* and the South African clawed frog *X. laevis*). In lophotrochozoans, spiral cleavage determines Nodal asymmetry, while ecdysozoans lack Nodal but depend on myo1d and PCP. Deuterostomes (echinoderms and chordates) use a ciliated left–right organizer for asymmetric Nodal induction, which in case of the frog depends on myo1d as well. We propose that urbilateria, the hypothetical common ancestor of proto- and deuterostomes, used Myo1d and asymmetric Nodal to position a long gut in the body cavity. Artwork by Bernd Schmid.

heterotaxia refers to another rare situation (about 1:1,000), in which subsets of organs show normal or aberrant positioning or morphology (Figure 1B). Individuals with *situs solitus* or *situs inversus* are healthy, whereas heterotaxia presents severe congenital malformations. Many human syndromes are known in which patients suffer from laterality defects, such as Katagener syndrome, in which the organ situs is inverted in one half of patients and males are sterile. Snail shells and vertebrate organs are examples of biased asymmetries with on average only one inversion in every 10,000 cases. Other asymmetries such as the coiling of the tails of piglets occur randomly with a 50:50 distribution. This primer exclusively deals with organ asymmetries in the animal kingdom, specifically with the mechanisms that ensure the development of biased asymmetries during embryogenesis.

Case studies: Nodal, cilia and Myosin

Nodal is an ancient gene that is present from radial symmetric animals, such as the freshwater polyp *Hydra* to vertebrates, including humans (Figure 2). It encodes a secreted growth factor which — besides other functions — is at the heart of asymmetry in many, and quite distantly related, phyla. Working in the chicken embryo, seminal work from Cliff Tabin and colleagues first demonstrated a left-asymmetric activity of Nodal in the early embryo, before the onset of organ morphogenesis, and the dependence of situs development on Nodal; their 1995 paper started the modern phase of asymmetry research. In short, Nodal is activated in the left lateral plate mesoderm of the early neurula embryo, where it induces its own transcription, that of its feedback inhibitor Lefty and the homeobox transcription factor Pitx2, which controls asymmetric placement and morphogenesis of organs during later development, long after Lefty has terminated Nodal activity. This basic plan is followed by all vertebrates, primitive chordates such as the lancelet *Amphioxus* or the tunicate *Halocynthia*, echinoderms such as sea urchins, protostomes like snails and even *Hydra*, where Nodal determines the asymmetric biradial bud formation during asexual reproduction that prevails when food is abundant (Figure 2). Quite remarkably, asymmetric Nodal induction occurs already during early cleavage in snails and the polychaete worm *Platynereis dumerilii* (Figure 2). Mollusks and annelids, and lophotrochozoans in general, undergo spiral cleavage divisions during early embryogenesis such that, starting with the third cell division, cells arrange in an asymmetric manner. Nodal asymmetry follows that of spiral cleavage, and asymmetric shell coiling in snails is dependent upon Nodal asymmetry. Lophotrochozoans comprise about one-third of phyla, suggesting that spiral cleavage and the resulting Nodal asymmetry are an ancient mechanism of symmetry breaking. Interestingly, *Platynereis* appears one hundred percent symmetrical, though Nodal asymmetry shows up in the same cell lineage as in snails, indicating that morphological asymmetries may get lost even against the background of molecular asymmetries. Also, Nodal is not present in ecdysozoans, such as nematode worms and insects like *Drosophila melanogaster* (Figure 2).

Deuterostomes, such as echinoderms and chordates, undergo symmetrical cleavage and activate the Nodal cascade only during early neurulation. In this setting, cilia take center stage. Ever since the identification of the Kartagener gene as an axonemal dynein motor in 1976, a role of cilia in vertebrate laterality determination was to be expected. In today's view, the archenteron, which is the primitive gut or remnants thereof, transiently harbors the ciliated epithelium of the left–right organizer during neurula stages. The left–right organizer is characterized by motile cilia at its center and immotile cilia at its lateral borders (Figure 3). The posterior orientation and tilt of motile cilia, together with their intrinsic clockwise rotation, give rise to a leftward fluid flow in the extracellular space that presumably is sensed by the lateral cilia at the left organizer margin. Subsequently, the Nodal cascade is activated at a distance in the left lateral plate mesoderm (Figure 2). A great many of cilia mutants and experimental manipulations of motile cilia in diverse

Current Biology
Magazine

vertebrate model organisms have underscored this general mechanism in fish, amphibians and mammals (including humans). Echinoderms rely on cilia for symmetry breaking and Nodal cascade activation as well, suggesting that Nodal and cilia represent the ancestral deuterostome mode of laterality determination. Left–right organizers are quite peculiar structures which form and disappear in passing; they derive from superficial cells, function as left–right organizers while embedded in the gut endoderm and — at least in the frog *Xenopus* but likely beyond — are destined to contribute to mesodermal tissues: notochord (medial flow generator) and somites (lateral flow sensor). They serve no other purpose than symmetry breaking and they may be needed as a flow-producing and -sensing tissue for no longer than two hours. In that sense, left–right organizers are truly unique. Unfortunately, this picture is too nice to be true in its entirety: birds (and likely reptiles too) as well as some mammals, such as pigs, have lost flow-generating cilia at the left–right organizer but maintained the Nodal-dependent mechanism of organ situs establishment; they thus resemble lophotrochozoans, an enigma that awaits clarification.

Last but not least there is the case of *Drosophila* as a representative of the ecdysozoans (Figure 2). Fruit flies lack Nodal and cilia but display very discrete organ asymmetries, namely a 360° embryonic genitalia rotation and asymmetric morphogenesis of the embryonic and adult hindgut. A *Drosophila* mutant defective in the untypical myosin motor protein myosin 1d (myo1d) shows a complete inversion of the wild-type situation. Myo1d interacts with the planar cell polarity (PCP) pathway that orients epithelial cells in a plane to cause genitalia rotation and asymmetric looping of the hindgut. The positioning of the left–right organizer in the hindgut in addition is dependent on the Hox gene *Abdominal-B*.

A common origin of animal asymmetry?

Comparing the three scenarios, they seem to share few commonalities at first glance, beyond the prominent role of Nodal. Evo-devo ogic has it that Nodal was lost in ecdysozoans, such as *Drosophila*, but does that need to mean that the three scenarios depicted above have evolved more or less independently? Spiral cleavage, which is the driving force of Nodal asymmetry in lophotrochozoans, depends on the asymmetric positioning of the spindle apparatus, which arises from the centrosome. The centrosome becomes a basal body when it docks to the apical membrane of an epithelial cell to organize a motile cilium, such as in the vertebrate left–right organizer. Leftward-directed fluid flow that develops there from the right to the left side, and which eventually breaks symmetry, develops due to the posterior polarization of cilia, which in turn is governed by the PCP pathway. The mechanism of asymmetric localization of the spindle in *Platynereis* as the model annelid worm is not fully understood, but PCP genes are transcriptionally induced exactly when the embryo undergoes spiral cleavage (in addition to mRNAs that are present in the egg). As mentioned, the PCP pathway is also instrumental for genitalia rotation and hindgut asymmetry in *Drosophila*. Very recently, it was reported that the *myo1d* gene is required for laterality determination in the frog *Xenopus* as well. Cilia polarization and leftward flow are disturbed in the absence of myo1d, resulting in aberrant Nodal cascade induction and organ situs. Remarkably, *myo1d* was shown to interact genetically with *vangl2*, one of the core PCP components, in *Xenopus* embryos. It should be interesting and rewarding to study *myo1d* in snails and annelid worms and to investigate a possible role in spiral cleavage. Myosin 1d may interact with the actin cytoskeleton as well, which is a well-established determinant of asymmetries in snails and nematodes. In *Caenorhabditis elegans*, a chiral cortical actomyosin flow is required for chirality of cleavage and symmetry breaking; it is an open question whether this intrinsic actin chirality plays a role in asymmetric spindle positioning in snails and annelid worms as well. Remarkably, the actin nucleator formin is associated with symmetry breaking in the pond snail.

Another putative commonality refers to where asymmetries arise during early embryogenesis. Both in *Drosophila* and the deuterostomes, left–right organizers are localized in the primitive gut or archenteron, although due to various adaptations the archenteron is not as easily recognized in bony fish and mammals as it is in primitive fish (sturgeon) and amphibians. Classical embryological literature, however, has recognized both the Kupffer's vesicle of bony fish and the node (or posterior notochord) of mammals as remnants of the archenteron. In snails and annelid worms, the fate of the so-called 2c-cell that first displays asymmetric Nodal activity is the right side of the stomodeum, which may be considered the anterior end of the embryonic gastro-intestinal tract. In *Drosophila*, the positioning of the left–right organizer in the larval gut is under the control of *Abd-B*. Vertebrate left–right organizers are precisely localized in neurula stage embryos as well, namely at the posterior end of the developing notochord. Whether or not Hox genes are involved in anterior–posterior positioning of vertebrate left–right organizers is an open question that needs to be experimentally tackled (which may be challenging, given that four paralogous genes exist in the *Abd-B* position of vertebrate Hox clusters). Animal asymmetries thus

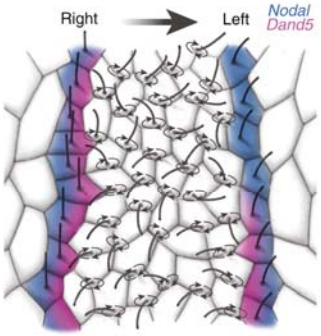

Figure 3. The vertebrate left–right organizer. Schematic of a vertebrate left–right organizer, as it appears for example in amphibians and mammals. The left–right organizer is embedded in the gut endoderm (large cells on either side). Central cells are characterized by flow-generating polarized cilia; flow is sensed by lateral cells harboring immotile and central cilia. Flow-sensing cells co-express Nodal (blue) and the Nodal-inhibitor Dand5 (magenta), which is downregulated through flow on the left side. Release of Nodal-repression results in asymmetric Nodal cascade gene activation in the left lateral plate mesoderm (not depicted). Artwork by Bernd Schmid.

CellPress

Current Biology
Magazine

may have originally evolved through Nodal-dependent and PCP-triggered asymmetric morphogenesis of the primitive gut. The 'urbilaterium', a hypothetical species at the base of all bilaterally symmetrical animal phyla, may have been characterized by an asymmetric, long and regionalized gut that arose during embryogenesis through a Nodal/PCP/Hox-dependent mechanism (Figure 2).

Cilia, however, with which the bulk of the left–right research and literature these days is concerned (due to a regrettable bias for vertebrate model organisms), most certainly were not involved in urbilaterian asymmetries. It is a fascinating question when and how cilia became co-opted into the pathway that leads to asymmetric Nodal induction. This co-option should have occurred at the base of the deuterostomes, as both sea urchins and vertebrates depend on cilia for symmetry breaking. Interestingly, there are signs for early cleavage asymmetries in vertebrates as well, not only with respect to the extrusion of polar bodies. The frog *Xenopus*, for example, displays a very discrete chirality of early cleavage divisions, which is dependent on the actin cytoskeleton and predictive for the organ situs that later develops in a cilia-dependent manner. This finding indicates that cilia evolved against the background of at least a cryptic form of chiral cleavage. Any disturbance of cilia structure or function at the left–right organizer, however, disrupts asymmetric development, suggesting that chiral cleavage in *Xenopus* represents an atavism. Yet, the question remains whether or not this atavism has become functional again when cilia were secondarily lost in birds such as chicken. Chicken embryos lack a recognizable ciliated left–right organizer; they manage to displace organizer Nodal to the left side, through chiral cell migration at Hensen's node, the mechanism of which, unfortunately, has not been worked out.

There is one particularly fascinating finding that may shed some first light on this phenomenon. The matrix metalloproteinase MMP21 was recently found to be involved in cilia-dependent symmetry breaking, when the molecular mechanism underlying a human mutation was investigated. Importantly, MMP21 is absent from the genome of birds and reptiles (sauropsida). Birds also lack this enigmatic entity of superficial cells that are fated to become mesoderm, from which ciliated vertebrate left–right organizers derive. What does the one have to do with the other? We don't know, experiments have not been reported so far. To top it off: MMP21 is also missing from the genome of cetartiodactyla, a monophyletic group that spans whales and even-toed ungulates. The pig as a representative of the latter lacks a ciliated left–right organizers but has an asymmetric node just like birds. Together, these loose ends may suggest that an ancestral cilia-based symmetry breaking mechanism disappeared secondarily due to gene loss(es), in parallel perhaps with reactivation of the atavistic chiral cleavage, at least during a narrow time window (gastrulation) in a discrete group of embryonic cells: Hensen's node, or the primary embryonic organizer. It remains to be seen whether MMP21 represents a singular gene loss or whether other genes disappeared in parallel.

The EvoDevo view spread out in a few facets above may provide some first hints as to the mechanisms underlying organ asymmetry across the animal kingdom. It is not too adventurous to propose that Nodal and PCP play pivotal roles in many phyla. Many fascinating questions remain: What is the spiral cleavage-dependent mechanism of asymmetric Nodal induction in annelids and snails? Is spiral cleavage controlled by PCP? Does myosin 1d play a role in this process as well? Do Hox-genes impact on laterality beyond *Drosophila* and what is their precise function? How come gene loss is related to a completely different mode of symmetry breaking in sauropsida and cetartiodactyla? What is the molecular basis of chiral cell migration in these species? Does it depend on PCP, myo1d or both? The short history of molecular asymmetry research since the mid-1990s has shown that a lot has been learned from comparative functional studies in diverse animal models. Hopefully, additional model organisms such as *Platynereis dumerilii* and the pig will be explored in the future, and established ones such as the chick followed up to tackle some of these questions. As of today, we would put our money on animal organ asymmetries having a monophyletic origin. We should stay alert for surprising conservations, novel factors and a variety of evolutionary adaptations.

FURTHER READING

Blum, M., Feistel, K., Thumberger, T., and Schweickert, A. (2014). The evolution and conservation of left-right patterning mechanisms. Development *141*, 1603–1613.

Chou, H.-C., Pruitt, M.M., Bastin, B.R., and Schneider, S.Q. (2016). A transcriptional blueprint for a spiral-cleaving embryo. BMC Genomics *17*, 552.

Coutelis, J.B., Gonzalez-Morales, N., Geminard, C., and Noselli, S. (2014). Diversity and convergence in the mechanisms establishing L/R asymmetry in metazoa. EMBO Rep. *15*, 926–937.

Danilchik, M.V., Brown, E.E., and Riegert, K. (2006). Intrinsic chiral properties of the Xenopus egg cortex: an early indicator of left-right asymmetry? Development *133*, 4517–4526.

Guimier, A., Gabriel, G.C., Bajolle, F., Tsang, M., Liu, H., Noll, A., Schwartz, M., Malti, El, R., Smith, L.D., Klena, N.T., *et al.* (2015). MMP21 is mutated in human heterotaxy and is required for normal left-right asymmetry in vertebrates. Nat. Genet. *47*, 1260–1263.

Hagen, ten, B., Kummel, F., Wittkowski, R., Takagi, D., Löwen, H., and Bechinger, C. (2014). Gravitaxis of asymmetric self-propelled colloidal particles. Nat. Commun. *5*, 4829.

Kuroda, R., Endo, B., Abe, M., and Shimizu, M. (2009). Chiral blastomere arrangement dictates zygotic left-right asymmetry pathway in snails. Nature *462*, 790–794.

Kuroda, R., Fujikura, K., Abe, M., Hosoiri, Y., Asakawa, S., Shimizu, M., Umeda, S., Ichikawa, F., and Takahashi, H. (2016). Diaphanous gene mutation affects spiral cleavage and chirality in snails. Sci. Rep. *6*, 34809.

Levin, M., Johnson, R.L., Sterna, C.D., Kuehn, M., and Tabin, C. (1995). A molecular pathway determining left-right asymmetry in chick embryogenesis. Cell *82*, 803–814.

Naganathan, S.R., Middelkoop, T.C., Fürthauer, S., and Grill, S.W. (2016). Actomyosin-driven left-right asymmetry: from molecular torques to chiral self organization. Curr. Opin. Cell Biol. *38*, 24–30.

Tingler, M., Kurz, S., Maerker, M., Ott, T., Fuhl, F., Schweickert, A., LeBlac-Straceski, J.M., Noselli, S., and Blum, M. (2018). A conserved role of the unconventional myosin 1d in laterality determination. Curr. Biol. *28*, 810–816.e3.

Tisler, M., Wetzel, F., Mantino, S., Kremnyov, S., Thumberger, T., Schweickert, A., Blum, M., and Vick, P. (2016). Cilia are required for asymmetric nodal induction in the sea urchin embryo. BMC Dev. Biol. *16*, 28.

Watanabe, H., Schmidt, H.A., Kuhn, A., Höger, S.K., Kocagöz, Y., Laumann-Lipp, N., Özbek, S., and Holstein, T.W. (2014). Nodal signalling determines biradial asymmetry in Hydra. 1–15.

Yoshiba, S., and Hamada, H. (2014). Roles of cilia, fluid flow, and Ca(2+) signaling in breaking of left-right symmetry. Trends Genet. *30*, 10–17.

University of Hohenheim, Institute of Zoology, Garbenstr. 30 70599 Stuttgart, Germany.
*E-mail: martin.blum@uni-hohenheim.de

Xenopus: An Undervalued Model Organism to Study and Model Human Genetic Disease

Developmental Biology / Review Article

Cells Tissues Organs

Cells Tissues Organs 2018;205:303–313
DOI: 10.1159/000490898

Accepted after revision: June 13, 2018
Published online: August 9, 2018

Xenopus: An Undervalued Model Organism to Study and Model Human Genetic Disease

Martin Blum Tim Ott

Institute of Zoology, University of Hohenheim, Stuttgart, Germany

Keywords

Xenopus · Disease modeling · Analysis of human disease alleles · Model organisms of human disease · Ciliopathy · Congenital heart disease · Cilia · Left-right asymmetry

Abstract

The function of normal and defective candidate genes for human genetic diseases, which are rapidly being identified in large numbers by human geneticists and the biomedical community at large, will be best studied in relevant and predictive model organisms that allow high-speed verification, analysis of underlying developmental, cellular and molecular mechanisms, and establishment of disease models to test therapeutic options. We describe and discuss the pros and cons of the frog *Xenopus*, which has been extensively used to uncover developmental mechanisms in the past, but which is being underutilized as a biomedical model. We argue that *Xenopus* complements the more commonly used mouse and zebrafish as a time- and cost-efficient animal model to study human disease alleles and mechanisms.

Introduction

Early researchers studying amphibian embryology collected specimens from the wild. They depended on environmental parameters they could not control, such as the weather in the spring when amphibians lay their eggs in ponds and puddles [Hamburger, 1988; Gurdon and Hopwood, 2000]. The frog *Xenopus* made its first appearance as an embryological laboratory animal in the early 1900s in the UK, when it first caught the attention of zoologists who found they could breed specimens in aquariums. Its call to fame happened in the 1940s and 1950s, when pregnancy testing was performed by injecting the urine of potentially pregnant women under the skin of female frogs: if gonadotropin was present, females reacted with egg-laying [Gurdon and Hopwood, 2000]. *Xeno-*

Abbreviations used in this paper

CHD	congenital heart disease
LRO	left-right organizer
MCCs	multiciliated cells
MO	morpholino oligomers
PCD	primary ciliary dyskinesia

KARGER

E-Mail karger@karger.com
www.karger.com/cto

Martin Blum
Institute of Zoology, University of Hohenheim
Garbenstrasse 30
DE–70599 Stuttgart (Germany)
E-Mail martin.blum@uni-hohenheim.de

Fig. 1. Development of *X. laevis* embryos from the fertilized egg to the 5-day-old tadpole. Developmental stages, times, and key time points for the differentiation of left-right asymmetry, kidney, brain ventricle, and skin cilia are indicated. Scale bar, 250 μm.

(Figure continued on next page.)

pus frogs in developmental biology research were introduced in the early 1950s; the most famous and celebrated experiment from this period no doubt was John Gurdon's demonstration of the pluripotency of the somatic nucleus [Gurdon et al., 1958]. Gurdon cloned the very first vertebrate by nuclear transfer into a denucleated fertilized zygote, an experiment acknowledged by a Nobel prize some 54 years later in 2012. In the last 3 decades of the 20th century, *Xenopus* was widely used in laboratories worldwide, and a great many fundamental cell biological and developmental concepts were derived from work with frog embryos, most importantly the molecular regulation of the cell cycle [reviewed in Philpott and Yew, 2008], the first identification of numerous key vertebrate developmental genes, including those expressed in Spemann's organizer [reviewed in De Robertis et al., 2000], and the fundamentals of many signaling pathways, most prominently Wnt and BMP signaling [reviewed in Cruciat and Niehrs, 2013; Bier and De Robertis, 2015]. As such, the value and versatility of *Xenopus* as a model organism for vertebrate developmental mechanisms has been proven and never debated.

However, when it comes to evaluating human disease alleles, most clinicians and human geneticists turn to the mouse and to zebrafish, which are considered the bona fide model organisms to study human disease mechanisms. Both were established from the start as genetic models, whereas *Xenopus* – and amphibians in general – excel as experimental models. However, with the development of the diploid *X. tropicalis* as a laboratory animal, the complete sequencing of the *X. laevis* and *X. tropicalis* genomes [Hellsten et al., 2010; Session et al., 2016], and the advent of genome editing, *Xenopus* has also become a member of the family of genetic model organisms. A number of transgenic lines are already available from the US and European resource centers (Xenbase.org; xenopusresource.org), and new ones can be generated fairly quickly [Aslan et al., 2017; Moreno-Mateos et al., 2017]. Candidate genes and alleles for human genetic disease are being identified at an enormous pace: analyses such as genome-wide association studies, GWAS, whole-exome sequencing, WES, and DNA and RNA sequencing from healthy and diseased tissues generate long lists of candidate genes and alleles that overwhelm biomedical researchers with the task of evaluating large data sets rapidly and at a manageable cost [MacArthur et al., 2014; Samocha et al., 2014; Getwan and Lienkamp, 2017]. The demand is for models to verify or discard candidate genes and to establish predictive models in which therapeutic options can be developed and tested.

Every model system, of course, has its benefits and its limitations. The mouse, for example, as a mammal has a very similar genome to that of humans and has an enormous tool box available for genetic manipulations. However, mouse models require costly investments in animal housing and maintenance, litter sizes are small with on average 8 offspring, only a fraction of which will carry the mutant allele, and the analysis of mutant mice is time consuming. Zebrafish produce large numbers of offspring, are less expensive to house, and have well-developed genetic approaches and many available mutant and reporter lines. However, the teleost genome duplication has led to the sub-functionalization of many biomedically relevant genes and a loss of synteny compared to mammals [Garcia de la Serrana et al., 2014]. The possibility to directly observe embryonic development and even perform live cell imaging has been extensively used with great success in zebrafish. However, this is not a unique feature of zebrafish; kidney development and neural crest cell migration, for example, have been directly imaged in live frog em-

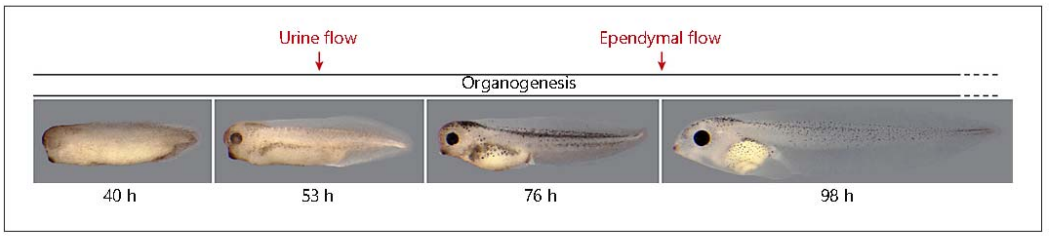

1

bryos at great temporal and spatial resolution [Lienkamp et al., 2010, 2012; Szabó et al., 2016; Getwan and Lienkamp, 2017]. Zebrafish also have certain organ-specific limitations. For example, they cannot model human syndromes that affect the limbs or digits, the lungs or the diaphragm, structures that are involved in many human congenital syndromes but are absent from fish. In addition, although the zebrafish heart has been an excellent model for studying regeneration, having just one atrium and one ventricle cannot fully model malformations of the human four-chambered heart. The frog *Xenopus*, as described below, has great potential to complement the more established mouse and zebrafish, and thus to greatly enhance the repertoire of predictive animal models of human disease. This review describes the many experimental attributes of *Xenopus* that enable detailed studies of candidate genes, with the intention of alerting clinical scientists and human geneticists of the potential of this established and still relevant, seminal animal model.

The African Frog, *Xenopus*

Two frog species are used in research these days, *X. laevis* (South African clawed frog), which has been utilized for decades, and *X. tropicalis* (Western clawed frog), which has only been introduced recently in many laboratories [Tandon et al., 2017]. *X. tropicalis* is a genetically diploid species that is raised at temperatures of 24–26 °C, whereas *X. laevis*, which prefers colder waters of 18 °C, is the product of a fertile hybridization of two species, i.e., contains a duplicated set of genes and chromosomes. Frogs as amphibians, of course, are distant from humans genetically, but they share a common tetrapod ancestry that is closer in evolutionary time than bony fish. The complete genome sequencing and careful annotation of both species reveal an astonishingly high degree of synteny with humans; even in the duplicated genome of *X. laevis*, because the two sets of chromosomes do not crossover, there has been less sub-functionalization of duplicated copies [Hellsten et al., 2010; Session et al., 2016; Harland and Gilchrist, 2017]. Close to 90% of human disease genes have homologs in both *Xenopus* species, and sequence conservation is generally high, a prerequisite for any predictive animal model. Many laboratories use both species in parallel, i.e., use *X. tropicalis* for genome editing and *X. laevis* for most other studies.

A central feature of this model, which has rendered it attractive in the past and shows great promise for future use, is the ease of gaining access to eggs and embryos: females lay large clutches of thousands of eggs and egg laying is inducible by hormone priming; researchers nowadays capitalize on the same principle that made the frog a system for pregnancy testing. Eggs can be fertilized by natural mating or artificially by the addition of sperm from testes, which in the case of *X. laevis* can be kept for days in the refrigerator without losing fertilization capacity. Eggs in addition are large, with diameters of 1.2 and 0.8 mm in *X. laevis* and *X. tropicalis*, respectively. This allows easy intracellular microinjections, either into the zygote or into defined blastomeres of early developmental stages, up to about the 64-cell stage, when cells become too small to be readily targeted. Furthermore, the lineage of individual cells is well known [Jacobson and Moody, 1984; Moody, 1987, 2000], i.e., injections can be very precisely targeted to tissues and organs at later developmental stages, up to the late tadpole stage, just before metamorphosis, which is reached after 5 days of development and in which organogenesis is basically completed (Fig. 1). Thus, precise manipulations can be performed during early cleavage stages in the first few hours of development, and consequences thereof be followed continuously for the next several days, throughout organ development. It is therefore possible to manipulate large numbers of embryos that develop very rapidly to the desired stages of organogenesis, making it possible to obtain

Cells Tissues Organs 2018;205:303–313
DOI: 10.1159/000490898

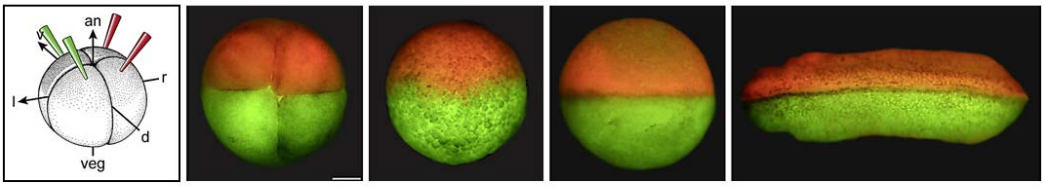

Fig. 2. Precise targeting of injections to the left and right side of the developing *Xenopus* embryo. A green and a red fluorescent dye were injected into left and right blastomeres at the 4-cell stage, respectively (scheme on left and photograph in second panel). This separation persists throughout development, as shown in a blastula stage embryo at the end of cleavage divisions, a neurula embryo, and a tadpole. This allows one-sided manipulations, i.e., the non-manipulated side can be used as an internal control. Scale bar, 250 μm.

results within a short time frame. Because the females will lay high quality eggs for many rounds per year, and housing is relatively inexpensive, animal costs are much lower particularly compared to mouse.

A unique feature that is not found in any other animal model used for the assessment of human genetic disease these days is the possibility of one-sided injections, meaning that only one side of the embryo is manipulated with the contralateral side serving as an internal control (Fig. 2). This attribute, which is a consequence of the first cleavage division separating the left and the right side of the embryo, is quite important when assessing the phenotypic consequences of experimental manipulations, because the variation in wild-type gene expression can sometimes be sizable across different clutches of embryos. The ability to manipulate a very large number of embryos per experiment and the possibility of selecting specimens for analysis based on the normal development on the control side adds a high level of rigor, statistical significance, and reproducibility to every study.

The large size of eggs and embryos, which distinguishes *Xenopus* frogs from both zebrafish and mouse, at least during the first third of embryonic development, offers one more unique advantage: enough material to perform proteomic analyses with a manageable number of specimens [Nagasawa et al., 2013; Amin et al., 2014; Wühr et al., 2014, 2015; Peshkin et al., 2015]. With the rapid advance of proteomics, this characteristic will certainly become more prominent in the near future and for example allow comparative interaction studies of wild-type and mutated proteins. A last feature deserves mentioning, as it comes unexpected to many who do not know the frog: there are stem cells and they can be easily differentiated to develop into defined tissues and organs (Fig. 3). These naive cells can be readily excised from the embryo at the end of cleavage divisions, before gastrulation and the specification of the germ layers begin. They reside at the animal pole, i.e., the pole pointing away from the gravity vector. Isolated so-called animal caps differentiate into undefined atypical ectoderm-like cells upon culture in a dish. However, the addition or injection of defined growth factors, transcription factors, or other inducers such as retinoic acid transforms these cells into all kinds of tissues, be it kidney, heart, or pancreas (Fig. 3) [reviewed in Asashima et al., 2009; Kurisaki et al., 2010; Hosoya et al., 2012]). In addition, morphogenetic movements can be studied, as explants may undergo what is called convergence extension [Keller et al., 2000; Keller, 2002], i.e., elongation due to the intercalation of cells (Fig. 3), a process that is under the control of non-canonical Wnt signaling, with relevance to many human diseases [reviewed in Xiao et al., 2017].

Intracellular microinjections are the single most important technique when using the frog model. The setup is fairly simple: a dissecting microscope fitted with a flexible light source and a device to hold and direct the injection needle. Hundreds of embryos can be injected on any given day. Most labs have a number of injection setups to allow the optimal use of egg clutches, which develop in synchrony and thus need to be injected during limited time windows of 30–45 min or so. Manipulations in many instances concern gene expression; antisense morpholino oligomers (MO), i.e., single-stranded nucleotide chains harboring a morpholino ring instead of ribose or deoxyribose, bind to mRNAs and interfere with translation, if they bind at the start AUG (translation-blocking MOs, or TBMOs), or with splicing, when they cover a splice donor or acceptor site (splice blocking, or SBMO) [Heasman, 2002]. The correct targeting to the tissue or organ of interest is usually monitored by co-injecting lineage tracers, for example fluorescent dextran or membrane-targeted GFP, that allow one to discard mistargeted specimens by

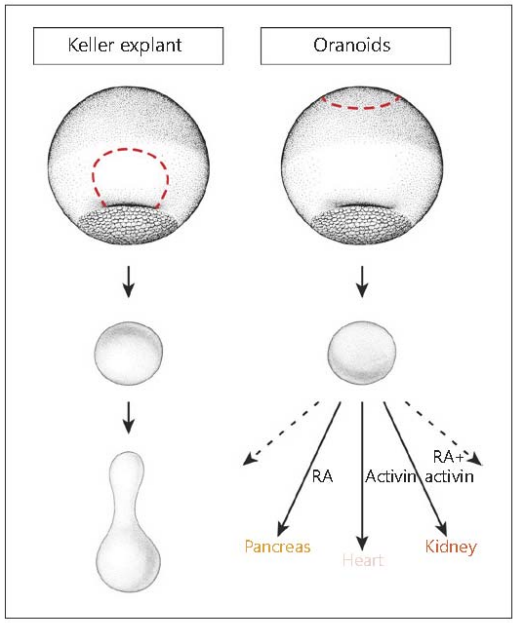

Fig. 3. Explant culture systems to study morphogenetic movements (convergent extension). Left: so-called Keller explants, which contain the Spemann organizer region and therefore elongate (extend and converge) in culture. In this system, non-canonical Wnt signaling can be studied and manipulated by injecting for example mRNAs into this region at the 4-cell stage and explanting at the beginning of gastrulation. Right: animal cap explants can be differentiated by injection or culture with inducers to become pancreas, heart, and kidney tissues, among other options available to the investigator [see Asashima et al., 2009].

just looking down the microscope. The specificity of MOs of course needs to be carefully controlled, as off-target effects cannot be excluded a priori, as with all manipulations that require interactions with specific nucleotide sequences, be it genomic or at the RNA level. Controls include the use of more than one MO, dose dependency, and rescue of phenotypes by co-injecting rescue mRNAs that are not targeted by the MO. The debate on specificities of gene and mRNA targeting is old and ongoing and should remind every researcher to remain critical and careful when interpreting a specific result [Eisen and Smith, 2008; Blum et al., 2015; Kok et al., 2015; Moulton, 2017; Gentsch et al., 2018]. In *Xenopus*, genome editing by the CRISPR/Cas9 technology is easily performed and can serve to validate the use of MOs, as well as being utilized as a valid genetic tool in its own rights [Garfinkel and Khokha, 2017; Naert et al., 2017; Tandon et al., 2017; Blitz, 2018; Naert and Vleminckx, 2018]. With respect to the analysis of candidate human disease genes and alleles, both techniques are successfully used (see below). The interaction of genes, however, which is of central importance when studying the molecular mechanisms underlying diseases, is studied with great ease by using MOs [Blum et al., 2015]: doses are selected for the two or three genes in question, which on their own do not result in any phenotypic alteration of development. Defects arising from their combined injections testify to genetic interactions, in much the same way as the analysis of compound heterozygotes in mouse and zebrafish (or invertebrate models such as *Drosophila*). Dosing of phenotypic effects in addition offers the advantage of circumventing early embryonic lethality and thus studying genes at developmental stages at which corresponding mutants are not available for analyses. Many human congenital syndromes are caused by a combination of heterozygous hypomorphic alleles, and thus better studied by reducing protein levels, compared to genetic null alleles. In addition, mutant human alleles can be easily expressed in *Xenopus* embryos, simply by microinjection of mutant mRNAs. In this way, disease alleles can be functionally assessed, either in wild-type embryos or in specimens in which the endogenous gene was knocked down by antisense MOs [Blum et al., 2015].

Suitability of *Xenopus* to Study Human Malformations and Disease

Over the past decade or so, the international *Xenopus* community has witnessed a change in focus, from studying primarily basic developmental and cell biological mechanisms to analyzing processes related to disease mechanisms in the wider sense. This may reflect policies of funding agencies such as in the USA, where translational research is more likely to receive funding than pure basic science, or just because of the biomedical task and because the frog has that potential to add knowledge in a substantial manner. It is beyond the scope of this review to give a full account of activities and successes. Examples of cases in which disease mechanisms have been elucidated by studies in *Xenopus* are detailed on the community website (http://www.xenbase.org/community/static/xenopus-whitepaper/2016/2016-XenopusWhitePaper-Final.pdf), which in addition provides a wealth of information for

Cells Tissues Organs 2018;205:303–313
DOI: 10.1159/000490898

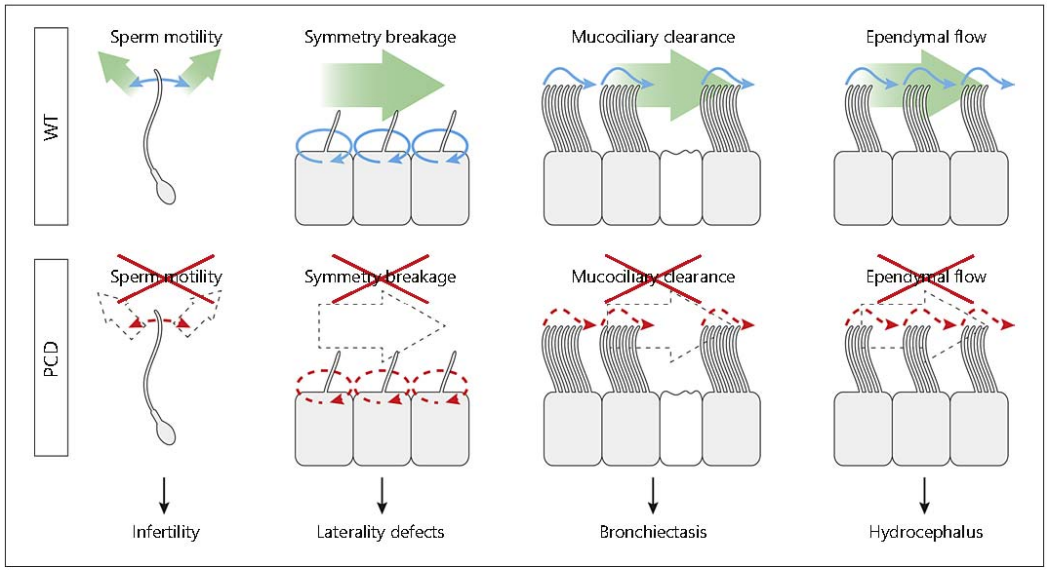

Fig. 4. Summary of PCD phenotypes. Except for sperm mobility, all others are easily studied in *Xenopus* embryos.

Xenopus researchers at large. It is worth citing a few examples, however, such as, among others, the work of Bruno Reversade at the Institute of Medical Biology in Singapore, who uses *Xenopus* alongside other model organisms, be it vertebrate or invertebrate, to unravel mechanisms of human diseases. Autosomal recessive cutis laxa, for example, a syndrome associated with – among others – lax and wrinkled skin, is caused by mutations in *PYCR1*, which encodes an enzyme involved in proline metabolism. Knockdown of the orthologous gene in *Xenopus* resulted in hypoplasia and wrinkles of the tadpole skin, i.e., was able to model the human disease [Reversade et al., 2009]. Mutations in the homeodomain transcription factor *IRX5* impair craniofacial development and germ cell migration in humans. When the *Xenopus* ortholog was knocked down, migration of progenitor cells in the branchial arches and gonads was disrupted, faithfully reproducing the human disease [Bonnard et al., 2012]. A last and spectacular example from the Reversade laboratory concerns mutations in *SMCHD1*, which encodes an epigenetic regulator. Patients suffer from an extremely rare syndrome in which the nose is completely absent. Biochemical studies in *Xenopus* embryos demonstrated that disease mutations resulted in gain-of-function alleles, a finding that would not have been possible by just pursuing loss-of-function approaches [Gordon et al., 2017]. Pediatricians Martina Brueckner and Mustafa Khokha at Yale have systematically identified genes and alleles in children suffering from congenital heart disease (CHD) [Fakhro et al., 2011; Boskovski et al., 2013; Endicott et al., 2015; del Viso et al., 2016; Griffin et al., 2018]. A series of high-profile publications has demonstrated that analyses of CHD candidate genes in *Xenopus* not only verified disease genes and mutations, but resulted in rather unexpected and spectacular findings, such as the identification of a protease that cleaves the Notch receptor in the process of specifying motile versus immotile cilia required for symmetry breaking and asymmetric heart morphogenesis [Boskovski et al., 2013]. Kidney disease is another very promising area in which *Xenopus* offers great potential, because the tadpole differentiates one fully functional nephron on either side, ideally suited to studying the various steps of kidney development from tubulogenesis to segmentation and active filtration, again in a one-sided manner with its internal control [Lienkamp et al., 2012; Hoff et al., 2013; Lienkamp, 2016]. Both these examples have recently been covered by excellent reviews, to which the interested reader is referred [Garfinkel and Khokha, 2017; Getwan and Lienkamp, 2017].

A large group of diverse genetic diseases that is particularly well qualified to be studied in *Xenopus* is represented by the so-called ciliopathies [Fliegauf et al., 2007; Mitchison and Valente, 2017]. Cilia protruding from the cell surface may act as antennas and harbor receptors for all sorts of extracellular signals (primary cilia), or they may be motile to propel the cell itself (such as the sperm cell) or the extracellular fluids surrounding the ciliated tissue [Marshall and Nonaka, 2006]. A great many diseases are caused by defective cilia of one kind or the other [Gerdes et al., 2009; Brown and Witman, 2014], with an estimated prevalence of up to one human patient in every 300–500 healthy individuals. These figures are preliminary, as cilia-relationships to diseases keep being discovered. In the following, we will focus on motile cilia, as this is an area of our own research and expertise. Human disorders resulting from cilia motility defects are summarized as primary ciliary dyskinesia (PCD) [Knowles et al., 2016; Bustamante-Marin and Ostrowski, 2017]. They mostly concern mucus clearance in the airways, where multiciliated cells (MCCs) beat in a coordinated manner to transport mucus, to which inhaled particles and pathogens adhere, upwards towards the pharynx (Fig. 4). To date, about 40 disease genes have been identified that explain some two-thirds of PCD in patients. It is expected that the so-far unexplained cases are caused by an additional large number of genes. Such disease candidate genes need to be assessed and *Xenopus* is an ideal model in which to do so [Walentek and Quigley, 2017].

Although aquatic and short of airways, the larval skin works the same way and fulfills the same function as the human airway: the epithelium harbors MCCs and cells that produce mucus [Dubaissi and Papalopulu, 2011; Brooks and Wallingford, 2014, 2015; Dubaissi et al., 2014; Walentek et al., 2014]. The skin serves as a first line of defense, i.e., pathogens adhering to the mucus are transported by coordinated ciliary movements that transport mucus along the specimen, from head to tail and off the tadpole (Fig. 4). Defective cilia render larvae susceptible to bacterial infections, a condition that is lethal during development [Dubaissi et al., 2014]. Skin MCCs can be easily visualized, histologically by staining the ciliary axonemes, and functionally by high-speed videography (Fig. 5; online suppl. movie 1; for all online suppl. material, see ww.karger.com/doi/10.1159/000490898). Motility can be easily manipulated as well, for example by knocking down *dnah9*, an axonemal dynein which is critically required for many motile cilia [Vick et al., 2009] (online suppl. movie 2). Ciliary defects such as those resulting from *dnah9* knockdown become immediately apparent in larvae, before muscles are fully functional. Larvae, laying on one side, move in a hovering motion across the agar-coated dish in which they are cultured due to the ciliary beating of their skin MCCs. By measuring the speed of the hovering movement on the control side and then flipping over the individual and doing the same measurement on the experimental side, one can detect cilia defects without elaborate and expensive equipment [Vick et al., 2009]. By simply observing the hovering behavior of the embryo, one can screen for which manipulations should be followed by more time-consuming and expensive additional experiments, such as histological assessment of ciliary parameters (number, length, orientation, and motility) or high-speed time-lapse videography to analyze the beat pattern directly. Motility should be rescued upon coinjection of a wild-type mRNA not targeted by the MO. Any allele of a gene that affects ciliary motility upon loss-of-function can be tested in the same setting, i.e., by co-injecting the allele in question along with a blocking MO. *Xenopus* is the only vertebrate model which allows fast and non-invasive in vivo assessment of human PCD disease alleles, avoiding artifacts that can arise from cultured cells such as air-liquid interphase cultures. A graded response may become visible by these types of analyses as well, such as for example alleles that do not result in complete paralysis of ciliary motion but in altered beat patterns or slower motilities.

PCD patients, depending on the genes mutated and the nature of the mutations, may suffer from immotile cilia at other sites and organs as well. For some of these, such as sperm immobility, which is frequently encountered in humans [Inaba and Mizuno, 2016], using the *Xenopus* microinjection approach is not recommended because the manipulation does not carry over to the next generation without using a transgenic approach (which are possible but would take months and extensive permits). However, defects that are readily studied with the fast and efficient *Xenopus* approaches include laterality defects and hydrocephalus [Blum et al., 2009; Hagenlocher et al., 2013; Blum and Ott, 2018b]. Both are prominent in PCD patients and are caused by cilia defects at the left-right organizer (LRO) and in the embryonic brain ventricles, respectively [Zariwala et al., 2007].

The LRO is the first tissue in the developing embryo in which motile cilia are required [Blum et al., 2014b; Shinohara and Hamada, 2017]. A monociliated epithelium forms during gastrulation and is positioned in the dorsal midline of the neurula embryo, in the posterior notochord ("node") of mice, in Kupffer's vesicle in zebrafish, and at the roof of the primitive gut or archenteron in frogs

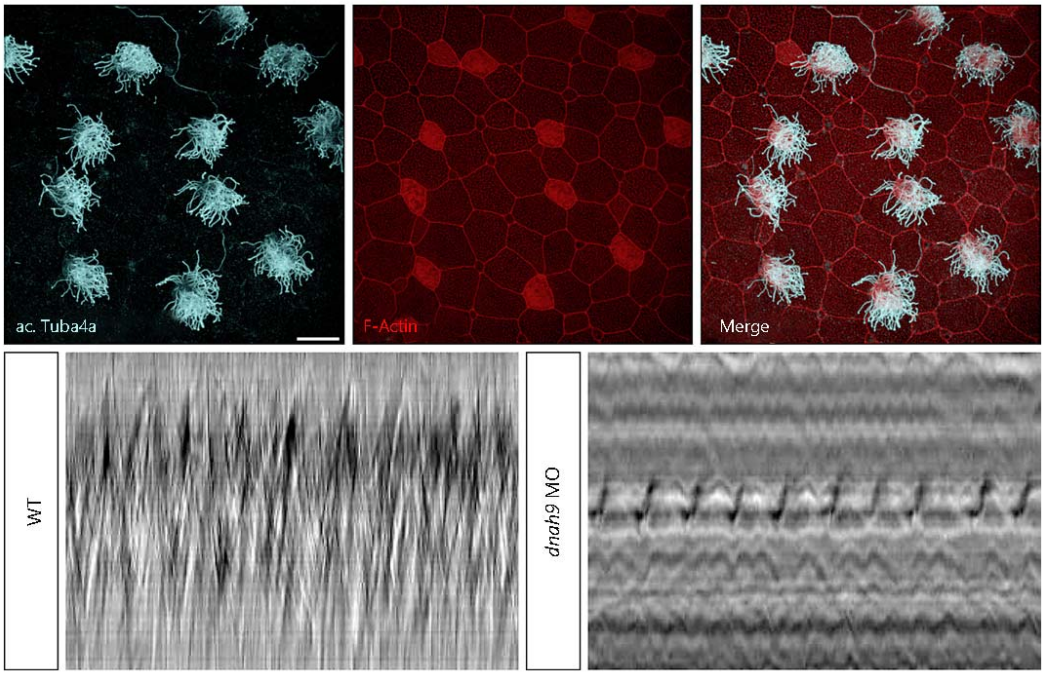

Fig. 5. The mucociliary epithelium of the larval skin. Top: immunofluorescence analysis of the larval epidermis, co-stained for cell boundaries (actin) with phalloidin and for cilia with an antibody directed against acetylated α-tubulin. Bottom: ciliary motility, as displayed by a horizontal kymograph of an epidermal ciliary tuft from a wild-type (left) or *dnah9* morphant embryo (right) to visualize ciliary beating over a 0.5-s time period. Scale bar, 25 µm.

[Blum et al., 2007]. Although LROs differ somewhat in their morphology, they are homologous structures and involve homologous genes for their function [Blum et al., 2014a]. In *Xenopus*, the sequence of events leading to asymmetric organ morphogenesis and placement in the tadpole are particularly well understood and accessible to manipulation and analysis at all stages, from the *foxj1*-dependent specification of the LRO precursor tissue to the leftward fluid flow at the LRO and to the left-asymmetric induction of the Nodal signaling cascade in the left lateral plate mesoderm, from which organ asymmetries ultimately result [Blum et al., 2014b]. Mutations in human PCD genes may or may not result in left-right defects; if they occur, they are readily detected along with other defects in the course of the same experiment: knockdown of the respective gene. This analysis will reveal another defect if present, namely hydrocephalus, i.e., expanded brain ventricles which – among other causes – may arise from defective brain MCCs (Fig. 4). Brain flow produced by these MCCs can be imaged in *Xenopus* tadpoles [Hagenlocher et al., 2013], and ciliary parameters, such as length and polarization, are equally accessible. Thus, except for sperm motility, the entire range of PCD defects is accessible for analysis in *Xenopus* tadpoles in a matter of days, once the tools for manipulation are available and have been tested for specificity.

Cilia function related to PCD in most cases (airways, LRO, brain) require oriented arrangement of cilia in order to produce a directed flow of extracellular fluids. Cilia orientation is governed by the planar cell polarity pathway, under the control of non-canonical Wnt signaling [Shinohara and Hamada, 2017]. The orientation of the PCP vector, however, is under biomechanical control, namely physical strain exerted by convergent extension

movement which shape the developing embryo during gastrulation [Shook et al., 2018]. This connection has only recently been made by studies in *Xenopus*. Chien et al. [2018] have explanted presumptive skin or LRO tissues and applied artificial strain to explants, i.e., they have sucked explants into glass capillaries to mimic gastrulation strain forces, which would not have been possible in any other vertebrate model [Chien et al., 2015; Blum and Ott, 2018a]. Their work beautifully and convincingly showed that strain is required for generation of the PCP vector, for cilia lengthening, and motility. These forces in all likelihood impact on ciliopathies such as PCD as well. No candidate gene has yet been assessed in that way, but such an analysis is easily performed in *Xenopus*.

We are in the process of analyzing a set of target genes of *foxj1*, which the Gossler laboratory in Hannover (Germany) has identified in mouse as PCD candidate genes [Weidemann et al., 2016; Stauber et al., 2017]. Interestingly, knock-down of some of these genes show clear cilia-related phenotypes in *Xenopus* even though genetically null mice are completely normal [unpubl. data from Achim Gossler, T.O. and M.B.]. These findings implicate genetic compensation by family members in null mutations, a phenomenon first described in zebrafish [Rossi et al., 2015] and commonly acknowledged in mice. This finding also underscores that for assessing human genetic disease mechanisms, more than one model organism should be used for the cautious interpretation of experimental data.

Conclusion and Perspectives

The frog *Xenopus* has contributed in a major way to our understanding of basic embryological and cell biological principles of development, from the pluripotency of the somatic cell nucleus to the elucidation of Spemann organizer and major signaling pathways. The experimental and molecular repertoire available to manipulate developmental interactions and developmentally relevant genes in a precise and controlled manner admits these species as full-fledged members of the small group of predictive animal models to study human disease mechanisms. We foresee that the frog will have a critically important role in biomedical research and encourage the clinical and genetic communities alike to utilize this model alongside the more common mouse and zebrafish. The challenges for fast and reliable assessment of candidate genes requires using all models in parallel and to carefully compare results. The frog community is ready to meet the demand and willing to collaborate and to contribute. The profit will be mutual for science and patients – this chance is not to be missed.

Disclosure Statement

We confirm that there are no conflicts of interest.

References

Amin, N.M., T.M. Greco, L.M. Kuchenbrod, M.M. Rigney, M.-I. Chung, J.B. Wallingford, I.M. Cristea, E.L. Conlon (2014) Proteomic profiling of cardiac tissue by isolation of nuclei tagged in specific cell types (INTACT). Development *141:* 962–973.

Asashima, M., Y. Ito, T. Chan, T. Michiue, M. Nakanishi, K. Suzuki, K. Hitachi, K. Okabayashi, A. Kondow, T. Ariizumi (2009) In vitro organogenesis from undifferentiated cells in *Xenopus*. Dev Dyn *238:* 1309–1320.

Aslan, Y., E. Tadjuidje, A.M. Zorn, S.-W. Cha (2017) High-efficiency non-mosaic CRISPR-mediated knock-in and indel mutation in F0 *Xenopus*. Development *144:* 2852–2858.

Bier, E., E.M. De Robertis (2015) Embryo development. BMP gradients: a paradigm for morphogen-mediated developmental patterning. Science *348:* aaa5838.

Blitz, I.L. (2018) Primordial germ cell transplantation for CRISPR/Cas9-based leapfrogging in *Xenopus*. J Vis Exp *132:* e56035.

Blum, M., P. Andre, K. Muders, A. Schweickert, A. Fischer, E. Bitzer, S. Bogusch, T. Beyer, H.W.M. van Straaten, C. Viebahn (2007) Ciliation and gene expression distinguish between node and posterior notochord in the mammalian embryo. Differentiation *75:* 133–146.

Blum, M., T. Beyer, T. Weber, P. Vick, P. Andre, E. Bitzer, A. Schweickert (2009) *Xenopus*, an ideal model system to study vertebrate left-right asymmetry. Dev Dyn *238:* 1215–1225.

Blum, M., E.M. De Robertis, J.B. Wallingford, C. Niehrs (2015) Morpholinos: antisense and sensibility. Dev Cell *35:* 145–149.

Blum, M., K. Feistel, T. Thumberger, A. Schweickert (2014a) The evolution and conservation of left-right patterning mechanisms. Development *141:* 1603–1613.

Blum, M., T. Ott (2018a) The power of strain: organizing left-right cilia. Dev Cell *45:* 277–279.

Blum, M., T. Ott (2018b) Animal left-right asymmetry. Curr Biol *28:* R301–R304.

Blum, M., A. Schweickert, P. Vick, C.V.E. Wright, M.V. Danilchik (2014b) Symmetry breakage in the vertebrate embryo: when does it happen and how does it work? Dev Biol *393:* 109–123.

Bonnard, C., A.C. Strobl, M. Shboul, H. Lee, B. Merriman, S.F. Nelson, O.H. Ababneh, E. Uz, T. Güran, H., Kayseriliet al. (2012) Mutations in IRX5 impair craniofacial development and germ cell migration via SDF1. Nat Genet *44:* 709–713.

Boskovski, M.T., S. Yuan, N.B. Pedersen, C.K. Goth, S. Makova, H. Clausen, M. Brueckner, M.K. Khokha (2013) The heterotaxy gene GALNT11 glycosylates Notch to orchestrate cilia type and laterality. Nature *504:* 456–459.

Brooks, E.R., J.B. Wallingford (2014) Multiciliated cells. Curr Biol *24:* R973–R982.

Brooks, E.R., J.B. Wallingford (2015) In vivo investigation of cilia structure and function using *Xenopus*. Methods Cell Biol *127:* 131–159.

Brown, J.M., G.B. Witman (2014) Cilia and diseases. Bioscience *64:* 1126–1137.

Bustamante-Marin, X.M., L.E. Ostrowski (2017) Cilia and mucociliary clearance. Cold Spring Harb Perspect Biol *9:* a028241.

Chien, Y.-H., R. Keller, C. Kintner, D.R. Shook (2015) Mechanical strain determines the axis of planar polarity in ciliated epithelia. Curr Biol *25:* 2774–2784.

Chien, Y.H., S. Srinivasan, R. Keller, C. Kintner (2018) Mechanical strain determines cilia length, motility and planar position in the left-right organizer. Dev Cell *45:* 316–330.

Cruciat, C.-M., C. Niehrs (2013) Secreted and transmembrane Wnt inhibitors and activators. Cold Spring Harb Perspect Biol *5:* a015081.

De Robertis, E.M., J. Larraín, M. Oelgeschläger, O. Wessely (2000) The establishment of Spemann's organizer and patterning of the vertebrate embryo. Nat Rev Genet *1:* 171–181.

del Viso, F., F. Huang, J. Myers, M. Chalfant, Y. Zhang, N. Reza, J. Bewersdorf, C.P. Lusk, M.K. Khokha (2016) Congenital heart disease genetics uncovers context-dependent organization and function of nucleoporins at cilia. Dev Cell *38:* 478–492.

Dubaissi, E., N. Papalopulu (2011) Embryonic frog epidermis: a model for the study of cell-cell interactions in the development of mucociliary disease. Dis Model Mech *4:* 179–192.

Dubaissi, E., K. Rousseau, R. Lea, X. Soto, S. Nardeosingh, A. Schweickert, E. Amaya, D.J. Thornton, N. Papalopulu (2014) A secretory cell type develops alongside multiciliated cells, ionocytes and goblet cells, and provides a protective, anti-infective function in the frog embryonic mucociliary epidermis. Development *141:* 1514–1525.

Eisen, J.S., J.C. Smith (2008) Controlling morpholino experiments: don't stop making antisense. Development *135:* 1735–1743.

Endicott, S.J., B. Basu, M. Khokha, M. Brueckner (2015) The NIMA-like kinase Nek2 is a key switch balancing cilia biogenesis and resorption in the development of left-right asymmetry. Development *142:* 4068–4079.

Fakhro, K.A., M. Choi, S.M. Ware, J.W. Belmont, J.A. Towbin, R.P. Lifton, M.K. Khokha, M. Brueckner (2011) Rare copy number variations in congenital heart disease patients identify unique genes in left-right patterning. Proc Natl Acad Sci USA *108:* 2915–2920.

Fliegauf, M., T. Benzing, H. Omran (2007) When cilia go bad: cilia defects and ciliopathies. Nat Rev Mol Cell Biol *8:* 880–893.

Garcia de la Serrana, D., E.A. Mareco, I.A. Johnston (2014) Systematic variation in the pattern of gene paralog retention between the teleost superorders Ostariophysi and Acanthopterygii. Genome Biol Evol *6:* 981–987.

Garfinkel, A.M., M.K. Khokha (2017) An interspecies heart-to-heart: Using *Xenopus* to uncover the genetic basis of congenital heart disease. Curr Pathobiol Rep *5:* 187–196.

Gentsch, G.E., T. Spruce, R.S. Monteiro, N.D.L. Owens, S.R. Martin, J.C. Smith (2018) Innate immune response and off-target Mis-splicing are common morpholino-induced side effects in *Xenopus*. Dev Cell *44:* 597–610.e10.

Gerdes, J.M., E.E. Davis, N. Katsanis (2009) The vertebrate primary cilium in development, homeostasis, and disease. Cell *137:* 32–45.

Getwan, M., S.S. Lienkamp (2017) Toolbox in a tadpole: *Xenopus* for kidney research. Cell Tissue Res *369:* 143–157.

Gordon, C.T., S. Xue, G. Yigit, H. Filali, K. Chen, N. Rosin, K.-I. Yoshiura, M. Oufadem, T.J. Beck, R. McGowanet al. (2017) De novo mutations in *SMCHD1* cause bosma arhinia microphthalmia syndrome and abrogate nasal development. Nat Genet *49:* 249–255.

Griffin, J.N., F. del Viso, A.R. Duncan, A. Robson, W. Hwang, S. Kulkarni, K.J. Liu, M.K. Khokha (2018) RAPGEF5 regulates nuclear translocation of β-catenin. Dev. Cell *44:* 248–260.e4.

Gurdon, J.B., T.R. Elsdale, M. Fischberg (1958) Sexually mature individuals of *Xenopus laevis* from the transplantation of single somatic nuclei. Nature *182:* 64–65.

Gurdon, J.B., N. Hopwood (2000) The introduction of *Xenopus laevis* into developmental biology: of empire, pregnancy testing and ribosomal genes. Int J Dev Biol *44:* 43–50.

Hagenlocher, C., P. Walentek, C. Müller, T. Thumberger, K. Feistel (2013) Ciliogenesis and cerebrospinal fluid flow in the developing *Xenopus* brain are regulated by foxj1. Cilia *2:* 12.

Hamburger, V. (1988) The Heritage of Experimental Embryology – Hans Spemann and the Organizer. New York, Oxford University Press.

Harland, R.M., M.J. Gilchrist (2017) Editorial: The *Xenopus laevis* genome. Dev Biol *426:* 139–142.

Heasman, J. (2002) Morpholino oligos: making sense of antisense? Dev Biol *243:* 209–214.

Hellsten, U., R.M. Harland, M.J. Gilchrist, D. Hendrix, J. Jurka, V. Kapitonov, I. Ovcharenko, N.H. Putnam, S. Shu, L. Taheret al. (2010) The genome of the Western clawed frog *Xenopus tropicalis*. Science *328:* 633–636.

Hoff, S., J. Halbritter, D. Epting, V. Frank, T.-M.T. Nguyen, J. van Reeuwijk, C. Boehlke, C. Schell, T. Yasunaga, M. Helmstädter et al. (2013) ANKS6 is a central component of a nephronophthisis module linking NEK8 to INVS and NPHP3. Nat Genet *45:* 951–956.

Hosoya, M., Y. Kunisada, A. Kurisaki, M. Asashima (2012) Induction of differentiation of undifferentiated cells into pancreatic beta cells in vertebrates. Int J Dev Biol *56:* 313–323.

Inaba, K., K. Mizuno (2016) Sperm dysfunction and ciliopathy. Reprod Med Biol *15:* 77–94.

Jacobson, M., S.A. Moody (1984) Quantitative lineage analysis of the frog's nervous system. I. Lineages of Rohon-Beard neurons and primary motoneurons. J Neurosci *4:* 1361–1369.

Keller, R. (2002) Shaping the vertebrate body plan by polarized embryonic cell movements. Science *298:* 1950–1954.

Keller, R., L. Davidson, A. Edlund, T. Elul, M. Ezin, D. Shook, P. Skoglund (2000) Mechanisms of convergence and extension by cell intercalation. Philos Trans R Soc Lond B Biol Sci *355:* 897–922.

Knowles, M.R., M. Zariwala, M. Leigh (2016) Primary ciliary dyskinesia. Clin Chest Med *37:* 449–461.

Kok, F.O., M. Shin, C.-W. Ni, A. Gupta, A.S. Grosse, A. van Impel, B.C. Kirchmaier, J. Peterson-Maduro, G. Kourkoulis, I. Male et al. (2015) Reverse genetic screening reveals poor correlation between morpholino-induced and mutant phenotypes in zebrafish. Dev Cell *32:* 97–108.

Kurisaki, A., Y. Ito, Y. Onuma, A. Intoh, M. Asashima (2010) In vitro organogenesis using multipotent cells. Hum Cell *23:* 1–14.

Lienkamp, S.S. (2016) Using *Xenopus* to study genetic kidney diseases. Semin Cell Dev Biol *51:* 117–124.

Lienkamp, S., A. Ganner, C. Boehlke, T. Schmidt, S.J. Arnold, T. Schäfer, D. Romaker, J. Schuler, S. Hoff, C. Powelske et al. (2010) Inversin relays Frizzled-8 signals to promote proximal pronephros development. Proc Natl Acad Sci USA *107:* 20388–20393.

Lienkamp, S.S., K. Liu, C.M. Karner, T.J. Carroll, O. Ronneberger, J.B. Wallingford, G Walz (2012) Vertebrate kidney tubules elongate using a planar cell polarity-dependent, rosette-based mechanism of convergent extension. Nat Genet *44:* 1382–1387.

MacArthur, D.G., T.A. Manolio, D.P. Dimmock, H.L. Rehm, J. Shendure, G.R. Abecasis, D.R. Adams, R.B. Altman, S.E. Antonarakis, E.A. Ashleyet al. (2014) Guidelines for investigating causality of sequence variants in human disease. Nature *508:* 469–476.

Marshall, W.F., S. Nonaka (2006) Cilia: tuning in to the cell's antenna. Curr Biol *16:* R604–R614.

Mitchison, H.M., E.M. Valente (2017) Motile and non-motile cilia in human pathology: from function to phenotypes. J Pathol *241:* 294–309.

Moody, S.A. (1987) Fates of the blastomeres of the 32-cell-stage *Xenopus* embryo. Dev Biol *122:* 300–319.

Moody, S.A. (2000) Cell lineage analysis in *Xenopus* embryos. Methods Mol Biol *135:* 331–347.

Moreno-Mateos, M.A., J.P. Fernandez, R. Rouet, C.E. Vejnar, M.A. Lane, E. Mis, M.K. Khokha, J.A. Doudna, A.J. Giraldez (2017) CRISPR-Cpf1 mediates efficient homology-directed repair and temperature-controlled genome editing. Nat Commun *8:* 2024.

Moulton, J.D. (2017) Making a morpholino experiment work: controls, favoring specificity, improving efficacy, storage, and dose. Methods Mol Biol *1565:* 17–29.

Naert, T., T. van Nieuwenhuysen, K. Vleminckx (2017) TALENs and CRISPR/Cas9 fuel genetically engineered clinically relevant *Xenopus tropicalis* tumor models. Genesis *55:* e23005.

Naert, T., K. Vleminckx (2018) CRISPR/Cas9-mediated knockout of Rb1 in *Xenopus tropicalis*. Methods Mol Biol *1726:* 177–193.

Nagasawa, K., Y. Tanizaki, T. Okui, A. Watarai, S. Ueda, T. Kato (2013) Significant modulation of the hepatic proteome induced by exposure to low temperature in *Xenopus laevis*. Biol Open *2:* 1057–1069.

Peshkin, L., M. Wühr, E. Pearl, W. Haas, R.M. Freeman Jr, J.C. Gerhart, A.M. Klein, M. Horb, S.P. Gygi, M.W. Kirschner (2015) On the relationship of protein and mRNA dynamics in vertebrate embryonic development. Dev Cell *35:* 383–394.

Philpott, A., P.R. Yew (2008) The *Xenopus* cell cycle: an overview. Mol Biotechnol *39:* 9–19.

Reversade, B., N. Escande-Beillard, A. Dimopoulou, B. Fischer, S.C. Chng, Y. Li, M. Shboul, P.-Y. Tham, H. Kayserili, L. Al-Gazali et al. (2009) Mutations in PYCR1 cause cutis laxa with progeroid features. Nat Genet *41:* 1016–1021.

Rossi, A., Z. Kontarakis, C. Gerri, H. Nolte, S. Hölper, M. Krüger, D.Y.R. Stainier (2015) Genetic compensation induced by deleterious mutations but not gene knockdowns. Nature *524:* 230–233.

Samocha, K.E., E.B. Robinson, S.J. Sanders, C. Stevens, A. Sabo, L.M. McGrath, J.A. Kosmicki, K. Rehnström, S. Mallick, A. Kirby et al. (2014) A framework for the interpretation of de novo mutation in human disease. Nat Genet *46:* 944–950.

Session, A.M., Y. Uno, T. Kwon, J.A. Chapman, A. Toyoda, S. Takahashi, A. Fukui, A. Hikosaka, A. Suzuki, M. Kondo et al. (2016) Genome evolution in the allotetraploid frog *Xenopus laevis*. Nature *538:* 336–343.

Shinohara, K., H. Hamada (2017) Cilia in left-right symmetry breaking. Cold Spring Harb Perspect Biol *9:* a028282.

Shook, D.R., E.M. Kasprowicz, L.A. Davidson, R. Keller (2018) Large, long range tensile forces drive convergence during *Xenopus* blastopore closure and body axis elongation. Elife *7:* 115.

Stauber, M., M. Weidemann, O. Dittrich-Breiholz, K. Lobschat, L. Alten, M. Mai, A. Beckers, M. Kracht, A. Gossler (2017) Identification of FOXJ1 effectors during ciliogenesis in the foetal respiratory epithelium and embryonic left-right organiser of the mouse. Dev Biol *423:* 170–188.

Szabó, A., M. Melchionda, G. Nastasi, M.L. Woods, S. Campo, R. Perris, R. Mayor (2016) In vivo confinement promotes collective migration of neural crest cells. J Cell Biol *213:* 543–555.

Tandon, P., F. Conlon, J.D. Furlow, M.E. Horb (2017) Expanding the genetic toolkit in *Xenopus*: approaches and opportunities for human disease modeling. Dev Biol *426:* 325–335.

Vick, P., A. Schweickert, T. Weber, M. Eberhardt, S. Mencl, D. Shcherbakov, T. Beyer, M. Blum (2009) Flow on the right side of the gastrocoel roof plate is dispensable for symmetry breakage in the frog *Xenopus laevis*. Dev Biol *331:* 281–291.

Walentek, P., S. Bogusch, T. Thumberger, P. Vick, E. Dubaissi, T. Beyer, M. Blum, A. Schweickert (2014) A novel serotonin-secreting cell type regulates ciliary motility in the mucociliary epidermis of *Xenopus* tadpoles. Development *141:* 1526–1533.

Walentek, P., I.K. Quigley (2017) What we can learn from a tadpole about ciliopathies and airway diseases: using systems biology in *Xenopus* to study cilia and mucociliary epithelia. Genesis *55:* e23001.

Weidemann, M., K. Schuster-Gossler, M. Stauber, C. Wrede, J. Hegermann, T. Ott, K. Boldt, T. Beyer, K. Serth, E. Kremmer et al. (2016) CFAP157 is a murine downstream effector of FOXJ1 that is specifically required for flagellum morphogenesis and sperm motility. Development *143:* 4736–4748.

Wühr, M., R.M. Freeman, M. Presler, M.E. Horb, L. Peshkin, S.P. Gygi, M.W. Kirschner (2014) Deep proteomics of the *Xenopus laevis* egg using an mRNA-derived reference database. Curr Biol *24:* 1467–1475.

Wühr, M., T. Güttler, L. Peshkin, G.C. McAlister, M. Sonnett, K. Ishihara, A.C. Groen, M. Presler, B.K. Erickson, T.J. Mitchison et al. (2015) The nuclear proteome of a vertebrate. Curr Biol *25:* 2663–2671.

Xiao, Q., Z. Chen, X. Jin, R. Mao, Z. Chen (2017) The many postures of noncanonical Wnt signaling in development and diseases. Biomed Pharmacother *93:* 359–369.

Zariwala, M.A., M.R. Knowles, H. Omran (2007) Genetic defects in ciliary structure and function. Annu Rev Physiol *69:* 423–450.

Mechanical strain, novel genes and evolutionary insights: news from the frog left-right organizer

Available online at www.sciencedirect.com

ScienceDirect

Current Opinion in Genetics & Development

Mechanical strain, novel genes and evolutionary insights: news from the frog left-right organizer

Martin Blum and Tim Ott

Animal asymmetries are widespread, from lobster claws to human handedness. Controlled by the left-sided Nodal signaling cascade, asymmetric morphogenesis and placement of vertebrate organs (heart, gut, etc.) are executed during embryogenesis. Fish, amphibians and mammals use a ciliated epithelium to break bilateral symmetry and induce the Nodal cascade. Cilia tilt and polarize to the posterior cell pole, such that clockwise rotation causes a leftward flow at the cell surface. Recent progress in *Xenopus* showed that mechanical strain drives cilia lengthening and polarization. Studying mutant alleles causing human organ situs defects and following novel EvoDevo approaches, new genes were discovered and functionally characterized in the frog, facilitated by a unique set of experimental tools.

Address
University of Hohenheim, Institute of Zoology, Garbenstraße 30, 70593 Stuttgart, Germany

Corresponding author: Blum, Martin (martin.blum@uni-hohenheim.de)

Current Opinion in Genetics and Development 2019, **56**:8–14

This review comes from a themed issue on **Molecular and genetic basis of disease**

Edited by **Philip W Ingham** and **Bruno Reversade**

For a complete overview see the Issue and the Editorial

Available online 8th June 2019

https://doi.org/10.1016/j.gde.2019.05.005

The frog offers unique opportunities for experimental embryologists

The generation of organ asymmetries, against the background of a bilaterally symmetrical body plan, has fascinated experimental embryologists ever since this discipline was born in the second half of the 19th century [1–5]. Besides the chick, amphibians have been the preferred study objects for their easy susceptibility to experimental manipulation. Today, the two species of the clawed frog *Xenopus*, *Xenopus laevis* and *Xenopus tropicalis* are the most commonly used amphibians [6,7]. The entire sequence of developmental events that led up to the asymmetric morphogenesis and placement of organs such as heart and gastrointestinal tract (GIT) have been described in great detail and are accessible to manipulations, both experimentally and genetically, facilitated by a powerful set of experimental tools [8]. This sequence includes (1) the specification of the precursor tissue of the ciliated left–right organizer (LRO) during gastrulation, (2) LRO morphogenesis at the roof of the forming primitive gut (gastrocoel roof plate, GRP), (3) symmetry breaking by cilia-driven leftward fluid flow, (4) transfer of the asymmetrical signal from the GRP to the left lateral plate mesoderm (LPM), (5) induction of the Nodal signaling cascade in the left LPM as well as (6) heart and GIT morphogenesis at early larval stages (Figure 1; cf. also an animated version of this scheme *link to authors' homepage will be provided*). Significant progress has been made over the course of the past two years by studying frog embryos at several of these stages. For instance, the asymmetric epithelial morphogenesis during curvature of the stomach and liver lobation has been linked to the Nodal cascade and specifically the transcription factor *Pitx2* [9,10]. This review, however, will be mainly concerned with the early events, particularly step 1, where first insights into signaling pathways that specify the unique LRO tissue emerged, and step 2, where for the first time the biomechanics of development have been linked to LRO morphogenesis, namely mechanical strain that accompanies the elongation of the post-gastrula embryo as determinant of cilia elongation and motility (Figure 2). Besides, studying human congenital heart disease (CHD) causing alleles in the frog has implicated novel genes in left-right (LR) development as have novel evolutionary approaches, and a century-old riddle, the observation of organ situs inversions in conjoined twins, was solved (Figure 3).

Specifying the LRO

A gene activity of utmost importance required in LRO precursor cells is that of the transcription factor *foxj1* (Figure 1) which induces motile ciliogenesis, one of the key features of flow-generating ciliated LRO cells [11,12]. The requirement of *foxj1* for LRO ciliogenesis, which previously rested on morpholino oligomer (MO) mediated gene knockdown, a technique lately discredited for off-target effects such as global mis-splicing and the induction of innate immune response [13], was recently confirmed by genome editing using CRISPR/Cas9 [14], a method becoming increasingly popular in the *Xenopus* community [15]. Because mostly pools of F0 individuals get analyzed, data from genome editing represent whole ranges of mutations and thus possess high validity, although the inherent heterogeneity and mosaicism may at times limit the ability to validate gene function in a specific fashion. *foxj1* expression marks the so-called superficial mesoderm (SM), from which the GRP, the frog LRO, develops following involution during late gastrulation [8] (Figure 1). Interestingly,

Figure 2

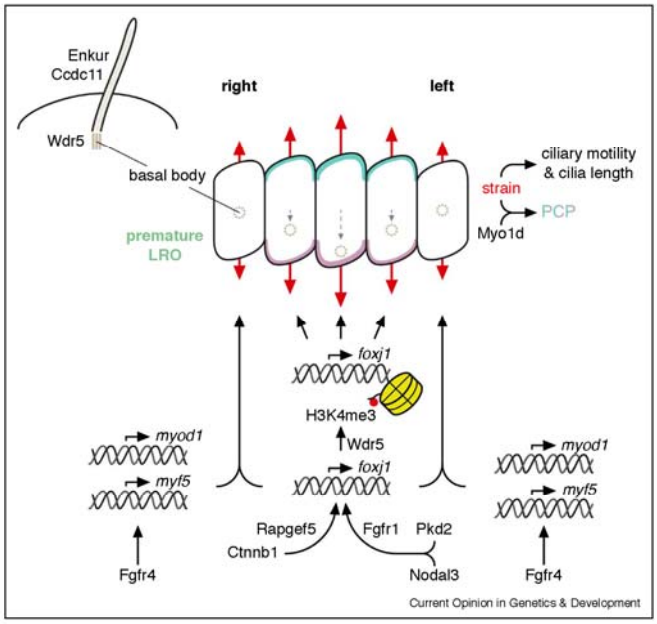

Novel insights into specification, morphogenesis and function of the frog LRO.
Induction of *foxj1* in central LRO precursor cells requires canonical Wnt signaling as well as signaling through Fgfr1. The latter is activated by the unconventional FGF ligand Nodal3, synergizing with Polycystin-2, whereas the former requires *rapgef5*, which presumably regulates nuclear import of ß-catenin (Ctnnb1). Lateral flow-sensing LRO cells depend on FGF signaling through receptor 4, which activates *myf5* and *myod1* in these cells that are fated to integrate into the somites. Accessibility of the *foxj1* promoter is regulated by methylation of histone H3 (H3K4me3); for assembly of the methyltransferase enzyme complex, Wdr5 constitutes a central scaffolding component. Mechanical strain (red arrows) exerted on the involuting LRO precursor causes PCP-dependent posterior polarization of LRO cilia, which become motile in a strain-dependent and *foxj1*-dependent manner. The *foxj1* gradient of gene expression (cf. Figure 1) is reflected by a medial-lateral gradient of cilia lengths and polarization. PCP is acted upon as well by the unconventional myosin Myo1d. Novel ciliary factors acting on cilia include Wdr5 (at the ciliary base) and Ccdc11 as well as Enkur (in the ciliary axoneme). These factors await detailed functional characterization.

with *foxj1* in *Xenopus* and mouse but only required in LR-unrelated tissues such as sperm cells in mouse and the embryonic kidney in *Xenopus* [21,22]. Additional *foxj1* target genes have shown a similar lack of LR phenotypes despite pronounced SM/LRO expression (A. Gossler, F. Fuhl, TO and MB, unpublished).

A new study of a well-known LR determinant in fish, amphibians and mammals, *pkd2* [23–26] has provided novel insights into how the SM is specified during gastrulation. The encoded transient receptor potential (TRP) cation channel Polycystin-2 is required early-on for *foxj1* induction in the SM [27•], independent of its later role in flow perception on immotile cilia of lateral LRO cells, as shown in mouse [28]. Using sided MO-mediated knockdown of *pkd2*, alone or in combination with other LR determinants such as *dand5*, Vick *et al.* demonstrated that Pkd2 synergizes with the atypical FGF ligand *nodal3.1* to induce *foxj1* and thus specify the LRO precursor SM [27•]. These experiments thus also implicated FGF signaling in *foxj1* induction. In another study [29], these authors found that FGF signaling indeed was required for SM specification, acting in parallel to FGF-mediated mesoderm induction. This notion was further supported by gene knockdown of *fgfr4* in *Xenopus*, which led to LR defects due to defective specification of the lateral LRO cells during early gastrulation [30]. Later, during LRO morphogenesis, the FGF/Ca^{2+}-branch was found to be involved in the specification of the flow sensing lateral LRO, a function related to FGF-mediated mesoderm morphogenesis. This second function, interestingly, again required input from *Pkd2* [27•,29].

Figure 3

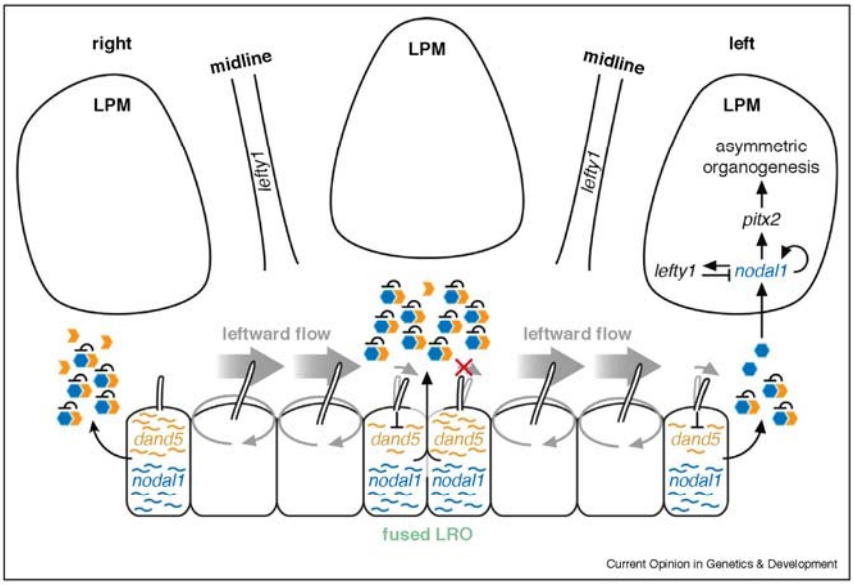

Organ situs determination in conjoined twins.
Experimentally created conjoined *Xenopus* embryos harbor a fused LRO in which the left margin of the right twin's LRO is fused to the right margin of the left one. Cilia-generated flow across the fused LRO represses *dand5* and induces asymmetric LRO Nodal signaling only in the left twin, while flow is insufficient to de-repress nodal1 in the fused central domain. As a result, the right twin lacks a biased asymmetric LRO signal and organ asymmetry develops in a random fashion.

The power of strain

The transformation of the SM into the LRO at the dorsal roof of the primitive gut (gastrocoel or archenteron) during late gastrulation is brought about by involution of the tissue, accompanied by expansion along the anterior–posterior (AP) axis [31]. The lengthening of the embryo, driven primarily by convergent-extension movements of the forming notochord, exert a mechanical strain on the developing GRP, which the Kintner and Keller labs determined in a collaborative effort [32••]. In a beautiful set of experiments that demonstrate the unique versatility of the frog embryo to experimentally manipulate development, they showed that strain was required and sufficient to lengthen and polarize the flow-generating motile cilia at the center of the GRP. Interestingly, lengths were found unequal across the GRP, following the *foxj1* mRNA gradient at the SM. Mechanical strain only acted in the presence of *foxj1*, once again demonstrating the eminent role of this gene for LR development. This work is of utmost importance for the understanding of cilia-mediated symmetry breaking, as it supersedes the up to then assumed requirement of a globally acting polarizing cue along the AP axis [32••,33] (Figure 2).

Novel players enter the game

Human genetics has proven a rich source for the identification of novel genes involved in laterality specification [34]. In contrast to studying a gene because of its expression in an LR pathway tissue during development, which may – as mentioned – be deceptive, any allele causing a laterality phenotype in humans has already proven its relevance. Ware and colleagues have analyzed copy number variants (CNVs) in >200 patients with heterotaxy, that is, disease-causing deviations from situs solitus mostly affecting the heart. Focusing on rare CNVs, they identified 165 genes in 35 CNVs. One patient carried a heterozygous deletion encompassing the platelet isoform of phosphofructosekinase (Pfkp) and the protease pitrilysin metallopeptidase 1 (Pitrm1). Knockdown of *pfkp* but not *pitrm1* resulted in tadpole heterotaxy. It should be interesting and rewarding to analyze in depth at what stage this enzyme which catalyzes the rate-limiting step of glycolysis interacts with the LR pathway, that is, which

stage is particularly energy-dependent. Perhaps ciliary motility qualifies as a candidate target.

With *wdr5*, the Khokha lab launched another novel CHD gene in the time period considered here, continuing on this most successful path [35]. This WD40 repeat-containing protein has been implicated in a number of cellular processes, most prominently as a core scaffolding component of histone methyltransferases [36]. The identification of a CHD/heterotaxy patient carrying a *de novo* mutation in *WDR5* at first glance just confirmed a role of epigenetic regulation in laterality determination, which had previously been inferred from a marked excess of *de novo* mutations in genes involved in production, removal and reading of histone 3 lysine 4 (H3K4) methylation, which together may account for up to 10% of severe CHD [37]. A report published in 2017 extended this notion to DNA methylation: both maintenance and *de novo DNA methyltransferases* were found to be required for LRO morphogenesis and function both in zebrafish and *Xenopus*, which — at least in zebrafish — was mediated through methylation of the *lefty2* enhancer and, perhaps, of *cadherin 1 type 1* (*cdh1*) [38]. The *WDR5* mutation found in the CDH patient, however, occurred in the very N-terminal region (K7Q), a protein domain thought not to be involved in H3K4 methyltransferase complex assembly. The study of Wdr5 function during LR axis formation in *Xenopus* now revealed a dual role of this multimodal protein [39•]: (1) a nuclear chromatin modifier function in LRO precursor cells, in which Wdr5 regulates the expression of *foxj1*, in agreement with the previous identification of the *FOXJ1* locus as a methylated locus targeted by WDR5; (2) an unexpected chromatin-independent function related to protein localization at the ciliary base, and it is this function that is affected in the WDR5 CHD patient. Tubulin association of WDR5 has previously been described for the spindle apparatus of mitotic cells as well as the midbody during cytokinesis [36]. It has been noted that histone and tubulin monomers both assemble into polymers that undergo specific post-translational modifications and that a tubulin code may regulate MT function in an analogous way to histone-code dependent regulation of gene function [40,41]. If the analysis of the patient's mutation were not offering enough excitement already, these parallels warrant a detailed analysis of ciliary WDR5 function.

The power of the *Xenopus* model to study human mutations was further demonstrated when a novel allele of the previously known LR determinant Ccdc11 [42,43] was assessed in the frog. Interestingly, gain-of-function of the wildtype and the truncated allele caused LR defects [44], though it is not clear with which pathway this overexpression intersects.

Evolutionary approaches

Taking a quite effective novel evolutionary approach, the group of Jeremy Reiter at UCSF compared the proteomes of cilia isolated from choanoflagellates, sea anemone and sea urchin embryos to reconstruct the evolutionary ancestry of cilia [45•]. Besides many known ones, they found hundreds of proteins that were not previously linked to cilia, and a good number of them to be conserved in vertebrates. One of these, the TRP channel-interacting protein Enkur, was found to be involved in LR axis formation and analyzed in some detail in *Xenopus* and mouse. Expressed in the LRO, gene loss-of-function caused aberrant Nodal cascade induction and organ situs defects. Interestingly, in a consanguineous family, patients with situs inversus and a homozygous *ENKUR* splice site mutation were identified, in which affected individuals lacked other hallmark ciliopathy phenotypes such as recurrent airway infections or male sterility. It remains to be seen whether ENKUR interacts with Polycystin-2 (or which other TRP channel it targets). Whether or not other candidate TRP-interacting proteins (golgin A2, protein kinase D1) that were identified in *Xenopus* play a role in LR pattering remains to be seen [46].

The fruit fly *Drosophila* shows organ asymmetries as well, including an asymmetric gut, but lacks a Nodal cascade and doesn't require cilia. Flies without a functional *Myo31DF* gene, which encodes an unconventional myosin motor protein, show situs inversion. Elegant work by the Noselli group showed that Myo31DF drives gliding of actin filaments in circular, counterclockwise paths *in vitro* and is able to cause chiral twisting *in vivo* [47]. Unexpectedly, the vertebrate orthologue *myo1d* is required in *Xenopus* for LR development as well, acting on planar cell polarity-mediated cilia orientation and leftward flow at the LRO [48•], a surprising finding confirmed by two studies in zebrafish [49,50]. The possibility that other *Drosophila* LR determinants such as Hox genes play a role in the vertebrates as well are fascinating and worth exploring.

Leftward flow determines organ situs defects in conjoined twins

One of the earliest results of experimental asymmetry research, the randomized organ situs in right conjoined twins, has remained unexplained for more than a century [7]. Originally described by Spemann and Falkenberg in ligature-induced amphibian conjoined twins [51], this condition mimics the situation in human cases, in which twins are joined at the chest and abdomen [7]. As twinning occurs during early embryogenesis, before the LRO has formed, this phenomenon has been taken as evidence for cilia and flow-independent symmetry breakage during early cleavage stages in amphibians and humans. Although several so-called early determinants, which should act upstream of flow, have in the meanwhile been linked to ciliary processes in the frog, new factors keep being proposed, such as for example the ion channel Hcn4, which was postulated to bypass LRO flow and the Nodal cascade to directly impact on organ situs based on an activity at the 2-cell stage [52]. While the case of Hcn4 awaits thorough analysis in the context of flow, the

riddle of the twins has been solved: the fused LRO in conjoined embryos produces a leftward flow just like in singleton embryos [53••]. In the right twin, however, flow is insufficient to repress the Nodal-inhibitor *dand5* in the fused middle domain, which is the left one of the right twin and at the same time the right one of the left twin (Figure 3). Therefore, only the left twin receives a wildtype left-asymmetric signal through flow, while *dand5* is not repressed and the Nodal cascade is not induced in the right one. Lacking an asymmetric signal, laterality develops in a random fashion (Figure 3). With this finding, cilia and flow emerged as the prime mode of symmetry breakage in the frog.

Conclusion and future directions

Undoubtably the biggest surprise in the past two years was the realization that mechanical strains are decisive in setting up a functional LRO. We expect that the same basic mechanism is at work in other vertebrates as well, as convergent-extension driven notochord formation is a chordate synapomorphy. This finding raises two eminent questions: why are lateral, flow-sensing LRO cells resistant to mechanical strain (perhaps due to their different fate as somite cells) [33]? Is cilia-independent symmetry breaking in birds, reptiles and perhaps some mammals also influenced by notochord formation and strain? We expect that the first question will be addressed in the frog very soon (and hope that labs working on chick will attend to question two). Evolutionary approaches should continue to yield novel insights as does the ongoing elucidation of human heterotaxia genes and alleles. Of particular interest should be factors that affect organ situs without impacting on ciliation and flow, as they will likely play roles in flow sensing, that is, relaying flow to Dand5 repression. We expect that the frog *Xenopus* will continue to be a major model organism in addressing these questions, given its unique set of manipulative tools, in combination with gene knockdown and genome editing techniques.

Conflict of interest statement

Nothing declared.

Acknowledgements

Work in the Blum lab has been supported by grants from the Deutsche Forschungsgemeinschaft (BL-285/9+10). T.O. has been a recipient of a fellowship of the Landesgraduiertenförderung Baden-Württemberg.

References and recommended reading

Papers of particular interest, published within the period of review, have been highlighted as:

- • of special interest
- •• of outstanding interest

1. Hamada H, Meno C, Watanabe D, Saijoh Y: **Establishment of vertebrate left-right asymmetry**. *Nat Rev Genet* 2002, **3**:103-113.
2. Blum M, Feistel K, Thumberger T, Schweickert A: **The evolution and conservation of left-right patterning mechanisms**. *Development* 2014, **141**:1603-1613.
3. Capdevila J, Vogan KJ, Tabin CJ, Izpisúa Belmonte JC: **Mechanisms of left-right determination in vertebrates**. *Cell* 2000, **101**:9-21.
4. McGrath J, Brueckner M: **Cilia are at the heart of vertebrate left-right asymmetry**. *Curr Opin Genet Dev* 2003, **13**:385-392.
5. Norris DP, Grimes DT: **Cilia discern left from right**. *Science* 2012, **338**:206-207.
6. Blum M, Beyer T, Weber T, Vick P, Andre P, Bitzer E, Schweickert A: **Xenopus, an ideal model system to study vertebrate left-right asymmetry**. *Dev Dyn* 2009, **238**:1215-1225.
7. Tisler M, Schweickert A, Blum M: **Xenopus, an ideal model organism to study laterality in conjoined twins**. *Genesis* 2017, **55**:e22993.
8. Blum M, Schweickert A, Vick P, Wright CVE, Danilchik MV: **Symmetry breakage in the vertebrate embryo: when does it happen and how does it work?** *Dev Biol* 2014, **393**:109-123.
9. Davis A, Amin NM, Johnson C, Bagley K, Ghashghaei HT, Nascone Yoder N: **Stomach curvature is generated by left-right asymmetric gut morphogenesis**. *Development* 2017, **144**:1477-1483.
10. Womble M, Amin NM, Nascone Yoder N: **The left-right asymmetry of liver lobation is generated by Pitx2c-mediated asymmetries in the hepatic diverticulum**. *Dev Biol* 2018, **439**:80-91.
11. Stubbs JL, Oishi I, Izpisúa-Belmonte JC, Kintner C: **The forkhead protein Foxj1 specifies node-like cilia in Xenopus and zebrafish embryos**. *Nat Genet* 2008, **40**:1454-1460.
12. Yu X, Ng CP, Habacher H, Roy S: **Foxj1 transcription factors are master regulators of the motile ciliogenic program**. *Nat Genet* 2008, **40**:1445-1453.
13. Gentsch GE, Spruce T, Monteiro RS, Owens NDL, Martin SR, Smith JC: **Innate immune response and off-target mis-splicing are common morpholino-induced side effects in Xenopus**. *Dev Cell* 2018, **44**:597-610.e10.
14. Campell EP, Quigley IK, Kintner C: **Foxn4 promotes gene expression required for the formation of multiple motile cilia**. *Development* 2016, **143**:4654-4664.
15. Tandon P, Conlon F, Furlow JD, Horb ME: **Expanding the genetic toolkit in Xenopus: approaches and opportunities for human disease modeling**. *Dev Biol* 2017, **426**:325-335.
16. Tingler M, Ott T, Tözser J, Kurz S, Getwan M, Tisler M, Schweickert A, Blum M: **Symmetry breakage in the frog Xenopus: role of Rab11 and the ventral-right blastomere**. *Genesis* 2014, **52**:588-599 http://dx.doi.org/10.1002/dvg.22766.
17. Walentek P, Schneider I, Schweickert A, Blum M: **Wnt11b is involved in cilia-mediated symmetry breakage during Xenopus left-right development**. *PLoS One* 2013, **8**:e73646.
18. Reller MD, Strickland MJ, Riehle-Colarusso T, Mahle WT, Correa A: **Prevalence of congenital heart defects in metropolitan Atlanta, 1998-2005**. *J Pediatr* 2008, **153**:807-813.
19. • Griffin JN, del Viso F, Duncan AR, Robson A, Hwang W, Kulkarni S, Liu KJ, Khokha MK: **RAPGEF5 regulates nuclear translocation of β-catenin**. *Dev Cell* 2018, **44**:248-260.e4.
This paper describes *Hapgef5* as a gene causing congenital heart disease when mutated in humans. Analysis in *Xenopus* suggests that *RAPGEF5* acts very early in the pathway, being involved in Wnt-dependent *foxj1* induction, specifically nuclear transport of ß-catenin.
20. Blum M, Ott T: **Xenopus: an undervalued model organism to study and model human genetic disease**. *Cells Tissues Organs* 2018, **205**:303-313 http://dx.doi.org/10.1159/000490898.
21. Weidemann M, Schuster-Gossler K, Stauber M, Wrede C, Hegermann J, Ott T, Boldt K, Beyer T, Serth K, Kremmer E *et al.*: **CFAP157 is a murine downstream effector of FOXJ1 that is specifically required for flagellum morphogenesis and sperm motility**. *Development* 2016, **143**:4736-4748.
22. Beckers A, Ott T, Schuster-Gossler K, Boldt K, Alten L, Ueffing M, Blum M, Gossler A: **The evolutionary conserved FOXJ1 target gene Fam183b is essential for motile cilia in Xenopus but dispensable for ciliary function in mice**. *Sci Rep* 2018, **8**:14678.

23. Pennekamp P, Karcher C, Fischer A, Schweickert A, Skryabin B, Horst J, Blum M, Dworniczak B: **The ion channel polycystin-2 is required for left-right axis determination in mice**. *Curr Biol* 2002, **12**:938-943.

24. McGrath J, Somlo S, Makova S, Tian X, Brueckner M: **Two populations of node monocilia initiate left-right asymmetry in the mouse**. *Cell* 2003, **114**:61-73.

25. Bisgrove BW, Snarr BS, Emrazian A, Yost HJ: **Polaris and Polycystin-2 in dorsal forerunner cells and Kupffer's vesicle are required for specification of the zebrafish left-right axis**. *Dev Biol* 2005, **287**:274-288.

26. Schweickert A, Weber T, Beyer T, Vick P, Bogusch S, Feistel K, Blum M: **Cilia-driven leftward flow determines laterality in Xenopus**. *Curr Biol* 2007, **17**:60-66.

27. • Vick P, Kreis J, Schneider I, Tingler M, Getwan M, Thumberger T, Beyer T, Schweickert A, Blum M: **An early function of polycystin-2 for left-right organizer induction in Xenopus**. *iScience* 2018, **2**:76-85.

Vick *et al.* describe a novel and early function of the cation channel Polycystin-2, namely the activation of foxj1 in the LRO precursor, in synergy with the FGF ligand nodal3.

28. Yoshiba S, Shiratori H, Kuo IY, Kawasumi A, Shinohara K, Nonaka S, Asai Y, Sasaki G, Belo JA, Sasaki H *et al.*: **Cilia at the node of mouse embryos sense fluid flow for left-right determination via Pkd2**. *Science* 2012, **338**:226-231.

29. Schneider I, Kreis J, Schweickert A, Blum M, Vick P: **A dual function of FGF signaling in Xenopusleft-right axis formation**. *Development* 2019, **146** http://dx.doi.org/10.1242/dev.173575.

30. Sempou E, Lakhani OA, Amalraj S, Khokha MK: **Candidate heterotaxy gene FGFR4 is essential for patterning of the left-right organizer in Xenopus**. *Front Physiol* 2018, **9**:1705.

31. Shook DR, Majer C, Keller R: **Pattern and morphogenesis of presumptive superficial mesoderm in two closely related species, *Xenopus laevis* and *Xenopus tropicalis***. *Dev Biol* 2004, **270**:163-185.

32. •• Chien YH, Srinivasan S, Keller R, Kintner C: **Mechanical strain determines cilia length, motility and planar position in the left-right organizer**. *Dev Cell* 2018, **45**:316-330.

This paper reports an elegant series of experiments, in which the authors– among others – employ mechanical strain of explanted LRO precursor tissue. They demonstrate that strain is required for cilia lengthening, polarization and motility in a *foxj1*-dependent manner. As strain derives from convergent-extension driven notochord formation, this mechanism likely is used by all chordates dependent on cilia-mediated symmetry breaking.

33. Blum M, Ott T: **The power of strain: organizing left-right cilia**. *Dev Cell* 2018, **45**:277-279.

34. Garfinkel AM, Khokha MK: **An interspecies heart-to-heart: using Xenopus to uncover the genetic basis of congenital heart disease**. *Curr Pathobiol Rep* 2017, **5**:187-196.

35. Fakhro KA, Choi M, Ware SM, Belmont JW, Towbin JA, Lifton RP, Khokha MK, Brueckner M: **Rare copy number variations in congenital heart disease patients identify unique genes in left-right patterning**. *Proc Natl Acad Sci U S A* 2011, **108**:2915-2920.

36. Guarnaccia AD, Tansey WP: **Moonlighting with WDR5: a cellular multitasker**. *J Clin Med* 2018, **7**:21 http://dx.doi.org/10.3390/jcm7020021.

37. Zaidi S, Choi M, Wakimoto H, Ma L, Jiang J, Overton JD, Romano-Adesman A, Bjornson RD, Breitbart RE, Brown KK *et al.*: **De novo mutations in histone-modifying genes in congenital heart disease**. *Nature* 2013, **498**:220-223.

38. Wang L, Liu Z, Lin H, Ma D, Tao Q, Liu F: **Epigenetic regulation of left–right asymmetry by DNA methylation**. *EMBO J* 2017 http://dx.doi.org/10.15252/embj.201796580.

39. • Kulkarni SS, Khokha MK: **WDR5 regulates left-right patterning via chromatin dependent and independent functions**. *Development* 2018, **145** dev.159889.

This paper shows that this highly conserved scaffolding protein, which is best known for its role in histone methyltransferase complexes, localizes to the base of cilia and impacts on LR asymmetry in a chromatin-independent manner.

40. Strahl BD, Allis CD: **The language of covalent histone modifications**. *Nature* 2000, **403**:41-45.

41. Gadadhar S, Bodakuntla S, Natarajan K, Janke C: **The tubulin code at a glance**. *J Cell Sci* 2017, **130**:1347-1353.

42. Silva E, Betleja E, John E, Spear P, Moresco JJ, Zhang S, Yates JR, Mitchell BJ, Mahjoub MR: **Ccdc11 is a novel centriolar satellite protein essential for ciliogenesis and establishment of left-right asymmetry**. *Mol Biol Cell* 2015 http://dx.doi.org/10.1091/mbc.E15-07-0474.

43. Narasimhan V, Hjeij R, Vij S, Loges NT, Wallmeier J, Koerner-Rettberg C, Werner C, Thamilselvam SK, Boey A, Choksi SP *et al.*: **Mutations in CCDC11, which encodes a coiled-coil containing ciliary protein, causes situs inversus due to dysmotility of monocilia in the left-right organizer**. *Hum Mutat* 2015, **36**:307-318.

44. Gur M, Cohen EB-T, Genin O, Fainsod A, Perles Z, Cinnamon Y: **Roles of the cilium-associated gene CCDC11 in left-right patterning and in laterality disorders in humans**. *Int J Dev Biol* 2017, **61**:267-276.

45. • Sigg MA, Menchen T, Lee C, Johnson J, Jungnickel MK, Choksi SP, Garcia G 3rd, Busengdal H, Dougherty GW, Pennekamp P *et al.*: **Evolutionary proteomics uncovers ancient associations of cilia with signaling pathways**. *Dev Cell* 2017, **43**:744-762.e11.

Through comparative evolutionary proteomic profiling of cilia from choanoflagellates, cnidarians and echinoderms, Reiter *et al.* identified novel ciliary genes, one of which, the TRP channel interacting protein ENKUR was shown to impair LR asymmetry in *Xenopus* and to cause situs inversus in humans, without other signs of ciliopathies.

46. Futel M, Le Bouffant R, Buisson I, Umbhauer M, Riou J-F: **Characterization of potential TRPP2 regulating proteins in early Xenopus embryos**. *J Cell Biochem* 2018, **119**:10338-10350.

47. Lebreton G, Geminard C, Lapraz F, Pyrpassopoulos S, Cerezo D, Spéder P, Ostap EM, Noselli S: **Molecular to organismal chirality is induced by the conserved myosin 1D**. *Science* 2018, **362**:949-952.

48. • Tingler M, Kurz S, Maerker M, Ott T, Fuhl F, Schweickert A, LeBlanc Straceski JM, Noselli S, Blum M: **A conserved role of the unconventional myosin 1d in laterality determination**. *Curr Biol* 2018, **28**:810-816.e3.

Myosin 1d drives organ asymmetry in *Drosophila* embryos which lack both cilia and a Nodal cascade. Unexpectedly, the frog ortholog impacts on cilia orientation at the LRO through the planar cell polarity pathway, a pathway involved in *Drosophila* as well, suggesting a common evolutionary origin of animal organ asymmetries.

49. Juan T, Géminard C, Coutelis J-B, Cerezo D, Polès S, Noselli S, Fürthauer M: **Myosin1D is an evolutionarily conserved regulator of animal left-right asymmetry**. *Nat Commun* 2018, **9**:1942.

50. Saydmohammed M, Yagi H, Calderon M, Clark MJ, Feinstein T, Sun M, Stolz DB, Watkins SC, Amack JD, Lo CW *et al.*: **Vertebrate myosin 1d regulates left-right organizer morphogenesis and laterality**. *Nat Commun* 2018, **9**:3381.

51. Spemann H, Falkenberg H: **Über asymmetrische Entwicklung und Situs inversus viscerum bei Zwillingen und Doppelbildungen**. *Archiv für Entwicklungsmechanik der Organismen* 1919, **45**:371-422.

52. Pai VP, Willocq V, Pitcairn EJ, Lemire JM, Paré J-F, Shi N-Q, McLaughlin KA, Levin M: **HCN4 ion channel function is required for early events that regulate anatomical left-right patterning in a nodal and lefty asymmetric gene expression-independent manner**. *Biol Open* 2017, **6**:1445-1457.

53. •• Tisler M, Thumberger T, Schneider I, Schweickert A, Blum M: **Leftward flow determines laterality in conjoined twins**. *Curr Biol* 2017, **27**:543-548.

Organ situs randomization in right conjoined twins has been known for more than a century. This paper demonstrates that equivalent situs defect in conjoined *Xenopus* tadpoles arises from an inability of flow to sufficiently repress dand5 in the central domain of the fused LRO, such that only the left twin receives a wildtype left-asymmetric flow signal. This finding supersedes the presumed requirements of earlier acting or maternal asymmetric determinants to account for twin situs defects.

Discussion

Biological and biomedical research ground on predictive *in vivo* model systems. In this collection of studies, the African clawed frog *Xenopus laevis* was utilized to analyze potential human disease genes and variants along with the associated developmental processes.

Principles of genetic disease modeling in *Xenopus*

Xenopus allows to model human genetic diseases and to assess candidate genes or variants in multiple ways. An idealized example is depicted below to generally discuss our and others' strategies, even if basic conditions vary. For this hypothetical case, an orthologue of the potential disease-causing candidate gene is present in the *Xenopus* genome. As *Xenopus* and humans share a high degree of sequence homology, nearly 80 % (Hellsten et al., 2010) of the currently known disease associated genes possess a *Xenopus* orthologue. This in principle enables the assessment of all related gene variants in *Xenopus*. For our case, we assume that the orthologue of the candidate gene is expressed during development and that expression occurs in a tissue that is linked with the presentation of the human disease. Furthermore, we assume that depletion of the *Xenopus* orthologue either phenocopies aspects of the human disease if caused by anti-, hypo- or amorphic variants, or results in a context-related phenotype in the case of hyper- and neomorphs (Figure 1A).

All these assumptions are based on a key concept of evolutionary developmental biology that an archetypal genetic tool-kit existed and was modified to evolve the various morphologies (De Robertis, 2008).

This scenario now allows to perform heterologous rescue experiments, in which the human wildtype as well as the potential disease-causing variant are separately co-injected along with the loss-of-function reagent. Whereas the wildtype variant should be competent to rescue the phenotype in *Xenopus*, a deleterious variant should not, display attenuated or increased rescue potential, thereby confirming or negotiating the *in silico* made predictions (Figure 1B).

In case the loss-of-function phenotype does not relate to the human phenotype at the level of the whole organism, one can refine the assessment by analyzing gene variants at the tissue, cellular or subcellular level. Alternatively, an unexpected phenotype can also be exploited to perform insightful rescue experiments. The same logic applies if a candidate gene in *Xenopus* is not or not exclusively expressed in the target tissue of the human disease, so that the non-target tissue can be utilized instead.

As an alternative to a fully executed rescue approach, can a plain loss-of-function study of a candidate gene already be telling, especially if the knowledge about the gene's function is limited (Figure 1A). Misexpression studies comparing wildtype with candidate variants can also be sufficient to reveal altered protein activities, if a phenotype manifests itself in one or the other variant (Figure 1C). This may also present a perspective to compare human gene variants without an orthologue in *Xenopus*.

Recreation of the precise genomic change via genome editing techniques, including DNA base editors or the novel prime editing method, is also feasible in *Xenopus*, but these emerging strategies can only be applied to highly conserved genes (Figure 1D).

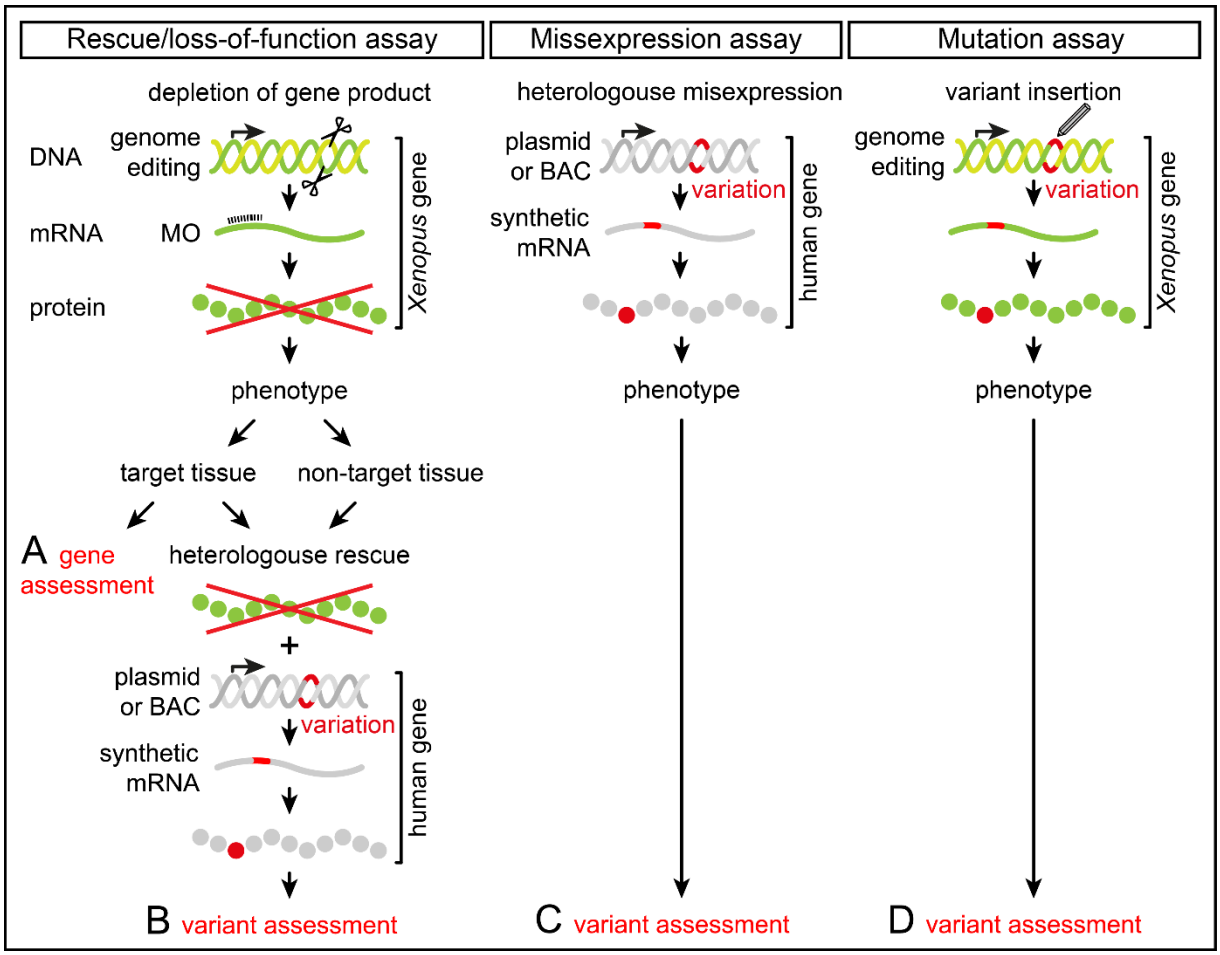

Figure 1: Strategies to investigate human disease genes and alleles in the frog *Xenopus*

(A) Gene loss-of-function phenotypes can be readily assessed following genome editing or MO-mediated knockdown in *Xenopus*. Phenotypes may resemble the human disease condition or occur in related embryonic contexts, verifying a given gene as disease-causing. (B) Introduction of the human wildtype allele should rescue the phenotype, while disease variants should reveal lack, attenuated or increased rescue capacities, which can be used to unravel disease mechanisms at the molecular level. (C) Misexpression of candidate human disease alleles in wildtype *Xenopus* embryos may reveal phenotypes, depending on the allele investigated. (C) Editing the homologous *Xenopus* gene to generate an allele corresponding to the human disease allows for disease modeling in a direct manner.

PCD: Foxj1 targets are trapped in synexpression

Our rational approach to identify and characterize potential PCD candidate genes in collaboration with the group of Achim Gossler based on a murine *Foxj1* target screen that they conducted (Stauber et al., 2017). FOXJ1 is a pioneer transcription factor and the master regulator of motile cilia (Chen et al., 1998; Stubbs et al., 2008; Yu et al.,

2008) that generally prefers binding to enhancer regions (Quigley and Kintner, 2017). Humans with deleterious heterozygous *FOXJ1* mutations display PCD with accompanying hydrocephalus, laterality defects, respiratory symptoms and infertility (Wallmeier et al., 2019). Conversely, the loss of *FOXJ1* in vertebrate model systems phenocopied the human PCD condition (Chen et al., 1998; Stubbs et al., 2008; Yu et al., 2008) and expression of known PCD genes was shown to be under Foxj1 control (Stubbs et al., 2008; Yu et al., 2008). All candidate genes, which encode most likely scaffolding proteins, were Foxj1 responsive, showed a strict *foxj1* related expression pattern and were found to localize to ciliary structures. However, major differences, within our collection, occurred in the loss of function scenarios. Male infertility, mucociliary clearance defects in combination with postnatal or early onset hydrocephalus were observed in *Cfap206* and *Cfap43* null mice, respectively. Genome edited *Xenopus* embryos recapitulated the mucociliary phenotype in each case. *Cfap157* knock out mice showed only isolated male infertility and *Xenopus cfap157* morphant embryos also lacked any externally visible phenotype. *Fam183b* mutant mice were not discernible different from their WT littermates, whereas *Xenopus fam183b* morphants displayed a defective mucociliary epithelium and renal cysts. Of note, cysts are a common phenotype of disturbed motile cilia in *Xenopus* as the ultrafiltrate transport is a cilia-driven process in the pronephros.

These phenotypic differences are also reflected by the variability that exists in the spectrum of PCD. Lucas and colleagues distinguished PCD genes, whether they affect laterality development or not (Lucas et al., 2020). Compromised inner or outer dynein arms cause PCD with laterality defects, whereas defects of the central apparatus, radial spokes, nexin links or the program for the generation of multiple cilia do not (Lucas et al., 2020). This phenomenon can be attributed to the specific biological task

that each protein or complex exerts, which is not necessarily relevant for all types of motile cilia, as they project from highly differentiated mono-, bi-, oligo- or multiciliated cells (Choksi et al., 2014). Interestingly, the last eukaryotic common ancestor most likely had two cilia in form of a gliding and a motile flagellum (Mitchell, 2017). This, in combination with our observation that the sperm flagellum was affected most severely and often, indicates that the sperm flagellum represents the ancestral cilium type. However, it is still puzzling that expression domains like in our collection the left-right organizer (LRO) exist in absence of an associated loss of function phenotype. Therefore, one can propose that such genes are trapped in a synexpression group (Niehrs and Pollet, 1999) and that there is no evolutionary pressure to uncouple relevant from *bona fide* irrelevant expression domains. Hence, this state was maintained although transcription factors like Forkhead box N4 (Foxn4) with Foxj1 overlapping target genes exist (Campell et al., 2016), which would theoretically allow for subfunctionalization.

In summary, we found and described novel PCD candidate genes with a broad motile cilia related expression pattern but with a limited functional scope. Importantly, the suitability of our approach was recently highlighted by two publications that described deleterious *CFAP43* variants in humans, which fall into the PCD spectrum (Morimoto et al., 2019; Tang et al., 2017).

PCD independent laterality defects: new evolutionary insights

We independently analyzed the *Xenopus* homologues of the potential human laterality disorder genes *MYO1D* and *TDT*, which encode an actin-based motor protein and a novel peptidase, respectively. *myo1d* was studied in collaboration with the group of

Stéphane Noselli, who discovered that the orthologues *Myo31DF* drives organ chirality in *Drosophila*. *tdt* was dissected in parallel with the group of Bruno Reversade, who utilized *Danio rerio* for the same purpose and initially identified *TDT* in patients with unassigned laterality defects. Depletion of either Myo1d or Tdt disturbed the normal organ orientation in *Xenopus* embryos, which confirmed their involvement in the context of laterality determination. Myo1d was attributed a central role in the PCP pathway, as the leftward fluid flow was disturbed in absence of Myo1d, due to mispolarized cilia, and because of its epistatic relation with the PCP core component VANGL planar cell polarity protein 2 (Vangl2). In contrast, Tdt was hierarchically placed upstream or at the level of the flow sensor, as *Xenopus* embryos without functional Tdt lost flow response but could be triggered with an agonist for the sensor complex component Polycystin 2, transient receptor potential cation channel (Pkd2). Collectively, these results not only complement the etiology of human laterality disease but also open a new perspective on how animal left-right asymmetry evolved.

As already touched, *Drosophila* employs actomyosin locally to establish a defined cell chirality in the primordia, which later translates to organ asymmetry (Lebreton et al., 2018; Spéder et al., 2006). Interestingly, the mollusc *Lymnaea stagnalis* and the nematode *Caenorhabditis elegans* also rely on actin to acquire laterality but already at the 4-cell stage (Naganathan et al., 2014; Shibazaki et al., 2004). This involves spindle twisting in the mollusc (Shibazaki et al., 2004) and spindle skewing (Wood, 1991) in the nematode, which were shown to depend on the actin nucleator Diaphanous related formin 2 (Dia2) (Davison et al., 2016) and cortical actomyosin flows (Naganathan et al., 2014; Pimpale et al., 2019), respectively. In the light of our Myo1d results, one can now propose that actin is the unifying root of laterality determination for protostomes and deuterostomes. In an ancestral setting, actin and Myo1d oriented spindles in a

way that imminently led to an asymmetric cell arrangement as seen in molluscs and nematodes. Drosophila lost this early and global type of left-right axis determination in adaption to its syncytial development, but retained an actomyosin driven mechanism that works later and locally. Deuterostomes also relocated symmetry breakage to later stages. Additionally, the interplay of actomyosin with spindles was modified to direct the ciliary-flow by orienting basal bodies, which share the centrosomal nature with spindles.

However, this switch in deuterostome development was accompanied by acquiring a fluid flow sensor module that includes Tdt. Along this line, sauropsids and cetartiodactyls, who independently overcame the ciliary-driven mode of laterality determination, consequently lost functional Tdt, as noticed by the Reversade group. Interestingly, chicken embryos display a chiral cell rearrangement in the region of the posterior notochord (Gros et al., 2009), where chordates usually generate the leftward fluid flow. As it was shown that this cell rearrangement is the crucial step during chicken symmetry breakage and depends on actomyosin (Gros et al., 2009), it appears that deuterostomes without a motile ciliated LRO may fall back to a more ancestral mode of laterality determination as seen in protostomes.

Neurodevelopmental disorders: HPE revisited and JS variants tested

In a collaborative study with the group of Kerstin Feistel, we dissected the potential HPE related phenotype of the microtubule binding protein Hmmr (Assmann et al., 1999). Indeed, close examination of Hmmr depleted *Xenopus* tadpoles revealed that they presented without telencephalic hemisphere separation. This phenotype resulted from a compromised roof plate, reminiscent of what is seen in the middle

interhemispheric variant of HPE (MIH) (Barkovich and Quint, 1993). By cooperatively regulating polarization of neural plate cells with Vangl2, Hmmr consecutively influences radial intercalation, neural fold apposition, roof plate formation and ultimately septum morphogenesis.

The discovery that primary morphological alterations, in contrast to specification defects, could cause MIH, challenges the current understanding of the MIH etiology (Fernandes and Hébert, 2008). These findings substantiate that human *HMMR* is a MIH candidate gene and should be screened for in unassigned MIH cases.

With respect to PIBF1, we worked together with the group of Christina Evers to test a novel missense as well as a nonsense variant of the centrosomal protein PIBF1, from a patient with JS, in a heterologous rescue assay. Generally, the cellular origin of JS was attributed to impaired ciliary biogenesis and/or function, defining it as a ciliopathy. As expected, *pibf1* was expressed in the target neural tissue during *Xenopus* development. However, we found a striking knock-down phenotype in the ciliated epidermis only 2 days after fertilization. We decided to use this non-target tissue, because the ciliated skin cells were readily accessible on the outside of the larva, as compared to the relative small cerebellum, which arises later in development (Butts et al., 2014). Pibf1 depleted *Xenopus* embryos disturbed epidermal ciliation, which could be restored by the human wildtype *PIBF1* but not by the patient-derived nonsense variant, while the missense variant yielded an attenuated rescue capacity. These results confirmed the classification of the nonsense variant as pathogenic and allowed the reclassification of the missense variant from unknown significant to likely pathogenic.

The ease and rapidity of our testing approach shows how well the *Xenopus* system is suited to not only study candidate disease genes and associated developmental

processes but also to characterize specific alleles from patients. Therefore *Xenopus* fulfills the current needs of the postgenomic era, in which more and more gene variants are identified by clinicians and wait to be functionally assessed in an predictive *in vivo* context.

Conclusion

The purpose of this work was to comprehensively study potential human disease genes and variants in *Xenopus* and to promote its capacity for disease modeling. Examples presented highlight the great potential of this cost-efficient aquatic model organism. Evaluation of potential disease-causing variants but also functional analysis of the underlying etiologies can be rapidly achieved in this system. *Xenopus* thus should be considered a complementing model organism to the more frequently used zebrafish and mouse.

References

Abdelhamed, Z. et al., 2018: A mutation in Ccdc39 causes neonatal hydrocephalus with abnormal motile cilia development in mice. Development: 145, dev154500.

Abdelkhalek, H. B. et al., 2004: The mouse homeobox gene Not is required for caudal notochord development and affected by the truncate mutation. Genes Dev.: 18, 1725–1736.

Abràmoff, M. D. et al., 2004: Image Processing with ImageJ. Biophotonics International: 11, 36–42.

Adzhubei, I. A. et al., 2010: A method and server for predicting damaging missense mutations. Nat. Methods: 7, 248–249.

Afzelius, B. A., 1959: Electron microscopy of the sperm tail; results obtained with a new fixative. J. Biophys. Biochem. Cytol.: 5, 269–278.

Afzelius, B. A., 1977: A human syndrome caused by immotile cilia. Obstet. Gynecol. Surv.: 32, 49–50.

Afzelius, B. A. & Eliasson, R., 1983: Male and female infertility problems in the immotile-cilia syndrome. Eur. J. Respir. Dis. Suppl.: 127, 144–147.

Ahmed, E. A. & de Rooij, D. G., 2009: Staging of mouse seminiferous tubule cross-sections. Methods Mol. Biol.: 558, 263–277.

Allen, B. G. & Weeks, D. L., 2005: Transgenic Xenopus laevis embryos can be generated using φC31 integrase. Nat. Methods: 2, 975–979.

Alten, L. et al., 2012: Differential regulation of node formation, nodal ciliogenesis and cilia positioning by Noto and Foxj1. Development: 139, 1276–1284.

Amack, J. D. & Yost, H. J., 2004: The T box transcription factor no tail in ciliated cells controls zebrafish left-right asymmetry. Curr. Biol.: 14, 685–690.

Amin, N. M. et al.: 2014: Proteomic profiling of cardiac tissue by isolation of nuclei tagged in specific cell types (INTACT). Development: 141, 962–973.

Andersen, J. S. et al., 2003: Proteomic characterization of the human centrosome by protein correlation profiling. Nature: 426, 570–574.

Antic, D. et al., 2010: Planar cell polarity enables posterior localization of nodal cilia and left-right axis determination during mouse and Xenopus embryogenesis. PLoS ONE: 5, e8999.

Anzalone, A. V. et al., 2019: Search-and-replace genome editing without double-strand breaks or donor DNA. Nature: 576, 49–157.

Arnaiz, O. et al., 2009: Cildb: a knowledgebase for centrosomes and cilia. Database: 2009, bap022.

Aquilina-Beck, A. et al., 2007: Nodal signaling is required for closure of the anterior neural tube in zebrafish. BMC Dev. Biol.: 7, 126.

Asashima, M. et al., 2009: In vitro organogenesis from undifferentiated cells in Xenopus. Dev. Dyn.: 238, 1309–1320.

Aslan, Y. et al., 2017: High-efficiency non-mosaic CRISPRmediated knock-in and indel mutation in F0 Xenopus. Development: 144, 2852–2858.

Assmann, V. et al., 1999: The intracellular hyaluronan receptor RHAMM/IHABP interacts with microtubules and actin filaments. J. Cell Sci.: 112, 3943–3954.

Assmann, V. et al., 2001: The pattern of expression of the microtubule-binding protein RHAMM/IHABP in mammary carcinoma suggests a role in the invasive behaviour of tumour cells. J. Pathol.: 195, 191–196.

Bachmann-Gagescu, R. et al., 2015: Joubert syndrome: a model for untangling recessive disorders with extreme genetic heterogeneity. J. Med. Genet.: 52, 514–522.

Badhwar, A. et al., 2000: Founder effect in Joubert Syndrome. Ann. Neurol.: 48, 435–436.

Bajoghli, B. et al., 2007: The roles of Groucho/Tle in left-right asymmetry and Kupffer's vesicle organogenesis. Dev. Biol.: 303, 347–361.

Balmer, S. et al., 2016: Notochord morphogenesis in mice: Current understanding & open questions. Dev. Dyn.: 245, 547–557.

Banizs, B. et al., 2005: Dysfunctional cilia lead to altered ependymal and choroid plexus function, and result in the formation of hydrocephalus. Development: 132, 5329–5339.

Barkovich, A. J. & Quint, D. J., 1993: Middle interhemispheric fusion: An unusual variant of holoprosencephaly. Am. J. Neuroradiol.: 14, 431–440.

Barker, A. R. et al., 2014: Meckel-Gruber syndrome and the role of primary cilia in kidney, skeleton, and central nervous system development. Organogenesis 10, 96–107.

Barriga, E. H. et al., 2015: Animal models for studying neural crest development: is the mouse different? Development 142: 1555–1560.

Beckers, A. et al., 2007: The mouse homeobox gene Noto regulates node morphogenesis, notochordal ciliogenesis, and left right patterning. Proc. Natl. Acad. Sci. USA: 104, 15765–15770.

Beckers, A. et al., 2018: The evolutionary conserved FOXJ1 target gene Fam183b is essential for motile cilia in Xenopus but dispensable for ciliary function in mice. Sci. Rep.: 8, 14678.

Belo, J. A. et al., 1997: Cerberus-like is a secreted factor with neutralizing activity expressed in the anterior primitive endoderm of the mouse gastrula. Mech. Dev. 68: 45–57.

Bendig, M. M., 1981: Persistence and expression of histone genes injected into Xenopus eggs in early development. Nature: 292, 65–67.

Berbari, N. F. et al., 2009: The Primary Cilium as a Complex Signaling Review Center. Curr. Biol.: 19, R526–R535.

Birnstiel, M. L. et al., 1966: Localization of the ribosomal DNA complements in the nucleolar organizer region of Xenopus laevis. Natl. Cancer Inst. Monogr.: 23, 431–447.

Bessodes, N. et al., 2012: Reciprocal signaling between the ectoderm and a mesendodermal left-right organizer directs left-right determination in the sea urchin embryo. PLoS Genet.: 8, e1003121.

Beyer, T. et al., 2012: Connexin26-mediated transfer of laterality cues in Xenopus. Biol. Open: 1, 473–481.

Beyer, T. et al., 2018: CRISPR/Cas9-mediated genomic editing of cluap1/IFT38 reveals a new role in actin arrangement. Mol. Cell. Proteom.: 17, 1285–1294.

Bier, E. & De Robertis, E. M., 2015: Embryo development. BMP gradients: a paradigm for morphogen-mediated developmental patterning. Science: 348, aaa5838.

Bisgrove, B. W. et al., 2005: Polaris and Polycystin-2 in dorsal forerunner cells and Kupffer's vesicle are required for specification of the zebrafish left-right axis. Dev. Biol.: 287, 274–288.

Bisgrove, B. W. et al., 2012: RFX2 is essential in the ciliated organ of asymmetry and an RFX2 transgene identifies a population of ciliated cells sufficient for fluid flow. Dev. Biol.: 363, 166–178.

Blitz, I. L. et al., 2013: Biallelic genome modification in F0 Xenopus tropicalis embryos using the CRISPR/Cas system. Genesis: 51, 827–834.

Blitz, I. L., 2018: Primordial germ cell transplantation for CRISPR/Cas9-based leapfrogging in Xenopus. J. Vis. Exp.: 132, e56035.

Blum, M. et al., 2007: Ciliation and gene expression distinguish between node and posterior notochord in the mammalian embryo. Differentiation: 75, 133–146.

Blum, M. et al., 2009: Xenopus, an ideal model system to study vertebrate left-right asymmetry. Dev. Dyn.: 238, 1215–1225.

Blum, M. et al., 2014: Symmetry breakage in the vertebrate embryo: when does it happen and how does it work? Dev. Biol.: 393, 109–123.

Blum, M. et al., 2014: The evolution and conservation of left-right patterning mechanisms. Development: 141, 1603–1613.

Blum, M. et al., 2015: Morpholinos: Antisense and Sensibility. Dev. Cell: 35, 145–149.

Blum, M. & Ott, T., 2018: Animal left–right asymmetry. Curr. Biol.: 28, R301–R304.

Blum, M. & Ott, T., 2018: Xenopus: an undervalued model organism to study and model human genetic disease. Cells Tissues Organs: 205, 303–313.

Blum, M. & Ott T., 2018: The power of strain: organizing left-right cilia. Dev. Cell: 45, 277-279.

Bode, W. et al., 1993: Astacins, serralysins, snake venom and matrix metalloproteinases exhibit identical zinc-binding environments (HEXXHXXGXXH and Met-turn) and topologies and should be grouped into a common family, the “metzincins.” FEBS Lett.: 331, 134–140.

de Boer, P. et al., 2015: A mutation study of sperm head shape and motility in the mouse: lessons for the clinic. Andrology: 3, 174–202.

Bolker, J. A., 1993: The mechanism of gastrulation in the white sturgeon. J. Exp. Zool.: 266, 132–145.

Boldt, K. et al., 2011: Disruption of intraflagellar protein transport in photoreceptor cilia causes Leber congenital amaurosis in humans and mice. J. Clin. Invest.: 121, 2169–2180.

Boldt, K. et al., 2016: An organelle-specific protein landscape identifies novel diseases and molecular mechanisms. Nat. Commun.: 7, 11491.

Bonnard, C. et al., 2012: Mutations in IRX5 impair craniofacial development and germ cell migration via SDF1. Nat. Genet.: 44, 709–713.

Boon, M. et al., 2014: MCIDAS mutations result in a mucociliary clearance disorder with reduced generation of multiple motile cilia. Nat. Commun.: 5, 1–8.

Boorman, C. J. & Shimeld, S. M., 2002: The evolution of left-right asymmetry in chordates. BioEssays: 24, 1004–1011.

Boskovski, M. T. et al., 2013: The heterotaxy gene GALNT11 glycosylates Notch to orchestrate cilia type and laterality. Nature: 504, 456–459.

Boycott, K. M. et al., 2017: International cooperation to enable the diagnosis of all rare genetic diseases. Am. J. Hum. Genet.: 100, 695–705.

Brancati, F. et al., 2009: MKS3/TMEM67 mutations are a major cause of COACH Syndrome, a Joubert Syndrome related disorder with liver involvement. Hum. Mutat.: 30, E432–E442.

Brennan, J. et al., 2002: Nodal activity in the node governs left-right asymmetry. Genes Dev.: 16, 2339–2344.

Brittingham, A. et al., 1995: Role of the Leishmania surface protease gp63 in complement fixation, cell adhesion, and resistance to complement-mediated lysis. Parasitol. Today: 11, 445–446.

Brody, S. L. et al., 2000: Ciliogenesis and left-right axis defects in forkhead factor HFH-4-null mice. Am. J. Respir. Cell Mol. Biol.: 23, 45–51.

Brooks, E. R. & Wallingford, J. B., 2014: Multiciliated cells. Curr. Biol.: 24, R973–R982.

Brooks, E. R. & Wallingford, J. B., 2015: In vivo investigation of cilia structure and function using Xenopus. Methods Cell Biol.: 127, 131–159.

Brown, J. M. & Witman, G. B., 2014: Cilia and diseases. Bioscience: 64, 1126–1137.

Buffone, M. G. et al., 2012: Heads or tails? Structural events and molecular mechanisms that promote mammalian sperm acrosomal exocytosis and motility. Mol. Reprod. Dev.: 79, 4–18.

Burgoyne, T. et al., 2014: Characterizing the ultrastructure of primary ciliary dyskinesia transposition defect using electron tomography. Cytoskeleton (Hoboken): 71, 294–301.

Bustamante-Marin, X. M. & Ostrowski, L. E., 2017: Cilia and mucociliary clearance. Cold Spring Harb. Perspect. Biol.: 9, a028241.

Butts, T. et al., 2014: Transit amplification in the amniote cerebellum evolved via a heterochronic shift in NeuroD1 expression. Development: 141, 2791–2795.

Campbell, E. P. et al., 2016: Foxn4 promotes gene expression required for the formation of multiple motile cilia. Development: 143, 4654–4664.

Campione, M. et al., 1999: The homeobox gene Pitx2: Mediator of asymmetric left-right signaling in vertebrate heart and gut looping. Development: 126, 1225–1234.

Di Cara, F. et al., 2013: Invadolysin, a conserved lipid-droplet-associated metalloproteinase, is required for mitochondrial function in Drosophila. J. Cell Sci.: 126, 4769–4781.

Capdevila, J. et al., 2000: Mechanisms of left-right determination in vertebrates. Cell: 101, 9–21.

Casini, P. et al., 2010: RHAMM mRNA expression in proliferating and migrating cells of the developing central nervous system. Gene Expr. Patterns: 10, 93–97.

Castleman, V. H. et al., 2009: Mutations in radial spoke head protein genes RSPH9 and RSPH4A cause primary ciliary dyskinesia with centralmicrotubular-pair abnormalities. Am. J. Hum. Genet.: 84, 197–209.

Cearns, M. D. et al., 2016: Microtubules, polarity and vertebrate neural tube morphogenesis. J. Anat. 229, 63–74.

Cha, S.-W. et al., 2011: The roles of maternal Vangl2 and aPKC in Xenopus oocyte and embryo patterning. Development: 138, 3989–4000.

Chang, C. F. et al., 2014: The cellular and molecular etiology of the craniofacial defects in the avian ciliopathic mutant talpid2. Development: 141, 3003–3012.

Chauvet, V. et al., 2004: Mechanical stimuli induce cleavage and nuclear translocation of the polycystin-1 C terminus. J. Clin. Invest.: 114, 1433–1443.

Chen, H. et al., 2014: Spatial regulation of Aurora A activity during mitotic spindle assembly requires RHAMM to correctly localize TPX2. Cell Cycle: 13, 2248–2261.

Chen, J. et al., 1998: Mutation of the mouse hepatocyte nuclear factor/forkhead homologue 4 gene results in an absence of cilia and random left-right asymmetry. J. Clin. Invest.: 102, 1077–1082.

Chiang, C., 1996: Cyclopia and defective axial patterning in mice lacking Sonic hedgehog gene function. Nature: 383, 407–413.

Chien, Y.-H. et al., 2015: Mechanical strain determines the axis of planar polarity in ciliated epithelia. Curr. Biol.: 25, 2774–2784.

Chien, Y.-H. et al., 2018: Mechanical strain determines cilia length, motility and planar position in the left-right organizer. Dev. Cell: 45, 316–330.

Choi, Y. et al., 2012: Predicting the functional effect of amino acid substitutions and indels. PLoS ONE: 7, e46688.

Choksi, S. P. et al., 2014: Systematic discovery of novel ciliary genes through functional genomics in the zebrafish. Development: 141, 3410–3419.

Choksi, S. P. et al., 2014: Switching on cilia: transcriptional networks regulating ciliogenesis. Development: 141, 1427–1441.

Chun, S. & Fay, J. C., 2009: Identification of deleterious mutations within three human genomes. Genome Res.: 19, 1553–1561.

Chung, M.-I. et al., 2012: RFX2 is broadly required for ciliogenesis during vertebrate development. Dev. Biol.: 363, 155–165.

Cohen, R. A. et al., 2016: Evidence that exposure to progesterone alone is a sufficient stimulus to cause a precipitous rise in the immunomodulatory protein the progesterone induced blocking factor (PIBF). J. Assist. Reprod. Genet.: 33, 221–229.

Collignon, J. et al., 1996: Relationship between asymmetric nodal expression and the direction of embryonic turning. Nature: 381, 155–158.

Concepcion, D. & Papaioannou, V. E., 2014: Nature and extent of left/right axis defects in TWis/TWis mutant mouse embryos. Dev. Dyn.: 243, 1046–1053.

Cong, L. et al., 2013: Multiplex genome engineering using CRISPR/Cas systems. Science: 339, 819–823.

The UniProt Consortium, 2019: UniProt: a worldwide hub of protein knowledge. Nucleic Acids Res.: 47, D506–D515.

Contreras, E. G. et al., 2009: Early requirement of Hyaluronan for tail regeneration in Xenopus tadpoles. Development: 136, 2987–2996.

Coutelis, J. B. et al., 2014: Diversity and convergence in the mechanisms establishing L/R asymmetry in metazoa. EMBO Rep.: 15, 926–937.

Coutton, C. et al., 2018: Mutations in CFAP43 and CFAP44 cause male infertility and flagellum defects in Trypanosoma and human. Nat. Commun.: 9, 686.

Cornwall, G. A., 2009: New insights into epididymal biology and function. Hum. Reprod. Update: 15, 213–227.

Cox, J. & Mann, M., 2008: MaxQuant enables high peptide identification rates, individualized p.p.b.-range mass accuracies and proteome-wide protein quantification. Nat. Biotechnol.: 26, 1367–1372.

Cox, J. et al., 2009: A practical guide to the MaxQuant computational platform for SILAC-based quantitative proteomics. Nat. Protocols: 4, 698–705.

Cruciat, C.-M. & Niehrs, C., 2013: Secreted and transmembrane Wnt inhibitors and activators. Cold Spring Harb. Perspect. Biol.: 5, a015081.

Cruz, C. et al., 2010: Foxj1 regulates floor plate cilia architecture and modifies the response of cells to sonic hedgehog signalling. Development: 137, 4271–4282.

Copp, A. J. et al., 1994: Developmental basis of severe neural tube defects in the loop-tail (Lp) mutant mouse: use of microsatellite DNA markers to identify embryonic genotype. Dev. Biol.: 165, 20–29.

Cummins, J. M. & Woodall, P. F., 1985: On mammalian sperm dimensions. J. Reprod. Fertil.: 75, 153–175.

Dareste, C., 1891: Recherches sur la Production Artificielle des Monstruosités, ou Essais de Tératogénie Expérimentale.

Darken, R. S. et al., 2002: The planar polarity gene strabismus regulates convergent extension movements in Xenopus. EMBO J.: 21, 976–985.

von Dassow, G. et al., 1993: Induction of the Xenopus organizer: expression and regulation of Xnot, a novel FGF and activin-regulated homeo box gene. Genes Dev.: 7, 355–366.

Daudin, F. M., 1802/03: Histoire naturelle des rainettes, des grenouilles et des crapauds.

Davidson, L. A. & Keller, R. E., 1999: Neural tube closure in Xenopus laevis involves medial migration, directed protrusive activity, cell intercalation and convergent extension. Development: 126, 4547–4556.

Davis, A. et al., 2017: Stomach curvature is generated by left-right asymmetric gut morphogenesis. Development: 144: 1477–1483.

Davison, A. et al., 2016: Formin is Associated with Left-Right Asymmetry in the Pond Snail and the Frog. Curr. Biol.: 26, 654–660.

Delling, M. et al., 2016: Primary cilia are not calcium-responsive mechanosensors. Nature: 531, 656–660.

Delous, M. et al., 2007: The ciliary gene RPGRIP1L is mutated in cerebello-oculo-renal syndrome (Joubert syndrome type B) and Meckel syndrome. Nat. Genet.: 39, 875–881.

Deng, H. et al., 2014: Genetic basis of human left-right asymmetry disorders. Expert Rev. Mol. Med.: 16, 1–24.

Desai, P. et al., 2018: Impacts of variants of uncertain significance on parental perceptions of children after prenatal chromosome microarray testing. Prenat. Diagn.: 38, 740–747.

Didon, L. et al., 2013: RFX3 modulation of FOXJ1 regulation of cilia genes in the human airway epithelium. Respir. Res.: 14, 70.

Doherty, D., 2009: Joubert syndrome: insights into brain development, cilium biology, and complex disease. Semin. Pediatr. Neurol.: 16, 143–154.

Drummond, I., 2009: Studying cilia in zebrafish. Methods Cell Biol.: 93, 197–217.

Dubaissi, E. & Papalopulu, N., 2011: Embryonic frog epidermis: a model for the study of cell-cell interactions in the development of mucociliary disease. Disease Models & Mechanisms: 4, 179–192.

Dubaissi, E. et al., 2014: A secretory cell type develops alongside multiciliated cells, ionocytes and goblet cells, and provides a protective, anti-infective function in the frog embryonic mucociliary epidermis. Development: 141, 1514–1525.

Duncan, A. R. & Khokha, M. K., 2016: Xenopus as a model organism for birth defects-Congenital heart disease and heterotaxy. Semin. Cell Dev. Biol.: 51, 73–79.

Eddy, E. M., 2006: The spermatozoon. Knobil and Neill's Physiology of Reproduction 3rd Edition. Academic Press.

Edelbusch, C. et al., 2017: Mutation of serine/threonine protein kinase 36 (STK36) causes primary ciliary dyskinesia with a central pair defect. Hum. Mutat.: 38, 964–969.

Edvardson, S. et al., 2010: Joubert syndrome 2 (JBTS2) in Ashkenazi Jews is associated with a TMEM216 mutation. Am. J. Hum. Genet.: 86, 93–97.

Eguether, T. et al., 2014: The deubiquitinating enzyme CYLD controls apical docking of basal bodies in ciliated epithelial cells. Nat. Commun.: 5, 4585.

Eisen, J. S. & Smith J. C., 2008: Controlling morpholino experiments: don't stop making antisense. Development: 135, 1735–1743.

El-Brolosy, M. A. et al., 2019: Genetic compensation triggered by mutant mRNA degradation. Nature: 568, 193–197.

El-Brolosy, M. A. & Stainier, D. Y. R., 2017: Genetic compensation: A phenomenon in search of mechanisms. PLoS Genet.: 13, e1006780.

Engelke, D. R. et al., 1980: Specific interaction of a purified transcription factor with an internal control region of 5S RNA genes. Cell: 19, 717–728.

Escalier, D., 2006: Knockout mouse models of sperm flagellum anomalies. Hum. Reprod. Update: 12, 449–461.

Essner, J. J. et al., 2005: Kupffer's vesicle is a ciliated organ of asymmetry in the zebrafish embryo that initiates left-right development of the brain, heart and gut. Development: 132, 1247–1260.

Etienne-Manneville, S., 2013: Microtubules in cell migration. Annu. Rev. Cell Dev. Biol.: 29, 471–499.

Etges, R. et al., 1986: The major surface protein of Leishmania promastigotes is anchored in the membrane by a myristic acid-labeled phospholipid. EMBO J.: 5, 597–601.

Evans, W. N. et al., 2015: Heterotaxy in Southern Nevada: Prenatal Detection and Epidemiology. Pediatr. Cardiol.: 36, 930–934.

Evers, C. et al., 2017: Impact of clinical exomes in neurodevelopmental and neurometabolic disorders. Mol. Genet. Metab.: 121, 297–307.

Fagerberg, L. et al., 2014: Analysis of the human tissue-specific expression by genomewide integration of transcriptomics and antibody-based proteomics. Mol. Cell. Proteomics: 13, 397–406.

Fakhro, K. A. et al., 2011: Rare copy number variations in congenital heart disease patients identify unique genes in left-right patterning. Proc. Natl. Acad. Sci. USA: 108, 2915–2920.

Fernandes, M. & Hébert, J.M., 2008: The ups and downs of holoprosencephaly: dorsal versus ventral patterning forces. Clin. Genet.: 73, 413–423.

Fesslova, V. et al., 2019: Characteristics and outcomes of fetuses with laterality defects are the current outcomes better? A single center study. J. Matern. Neonatal Med.

Field, S. et al., 2011: Pkd1l1 establishes left-right asymmetry and physically interacts with Pkd2. Development: 138, 1131–1142.

Fish, M. B. et al., 2012: Simple, fast, tissue-specific bacterial artificial chromosome transgenesis in Xenopus. Genesis: 50, 307–315.

Fléchon, J.-E., 2016: The acrosome of eutherian mammals. Cell Tissue Res.: 363, 147–157.

Fliegauf, M. et al., 2007: When cilia go bad: cilia defects and ciliopathies. Nat. Rev. Mol. Cell Biol.: 8, 880–893.

Fol, H. & Warynsky, S., 1883: Sur la production artificielle de l'inversion viscérale ou hétérotaxie chez des embryons de poulet.

Fong, C. P. et al., 2006: I-SceI meganuclease-mediated transgenesis in Xenopus. Dev. Dyn.: 235, 247–252.

Francis, R. & Lo, C., 2013: Ex vivo method for high resolution imaging of cilia motility in rodent airway epithelia. J. Vis. Exp.: 78, 50343

Franco, B. & Thauvin-Robinet, C., 2016: Update on oral-facial-digital syndromes (OFDS). Cilia: 5, 12.

Frommer, A. et al., 2015: Immunofluorescence Analysis and Diagnosis of Primary Ciliary Dyskinesia with Radial Spoke Defects. Am. J. Respir. Cell Mol. Biol.: 53, 563–573.

Fu, G. et al., 2018: The I1 dynein-associated tether and tether head complex is a conserved regulator of ciliary motility. Mol. Biol. Cell: 29, 1048–1059.

Fukata, M. et al., 2002: Rac1 and Cdc42 capture microtubules through IQGAP1 and CLIP-170. Cell: 109, 873–885.

Futel, M. et al., 2018: Characterization of potential TRPP2 regulating proteins in early Xenopus embryos. J. Cell. Biochem.: 119, 10338–10350.

Gadadhar, S. et al., 2017: The tubulin code at a glance. J. Cell Sci.: 130, 1347–1353.

Garcia de la Serrana, D. et al., 2014: Systematic variation in the pattern of gene paralog retention between the teleost superorders Ostariophysi and Acanthopterygii. Genome Biol. Evol.: 6, 981–987.

Garfinkel, A. M. & Khokha, M. K., 2017: An interspecies heart-to-heart: using Xenopus to uncover the genetic basis of congenital heart disease. Curr. Pathobiol. Rep.: 5, 187–196.

Gentsch, G. E. et al., 2018: Innate immune response and off-target mis-splicing are common morpholino-induced side effects in Xenopus. Dev. Cell: 44, 597–610.

Gerdes, J. M. et al., 2009: The vertebrate primary cilium in development, homeostasis, and disease. Cell: 137, 32–45.

Geremek, M. et al., 2011: Gene expression studies in cells from primary ciliary dyskinesia patients identify 208 potential ciliary genes. Hum. Genet.: 129, 283–293.

Geremek, M. et al., 2014: Ciliary genes are down-regulated in bronchial tissue of primary ciliary dyskinesia patients. PLoS ONE: 9, e88216.

Getwan, M. & Lienkamp, S. S., 2017: Toolbox in a tadpole: Xenopus for kidney research. Cell Tissue Res.: 369, 143–157.

Gherman, A. et al., 2006: The ciliary proteome database: an integrated community resource for the genetic and functional dissection of cilia. Nat. Genet.: 38, 961962.

Gloeckner, C. J. et al., 2007: A novel tandem affinity purification strategy for the efficient isolation and characterisation of native protein complexes. Proteomics: 7, 4228–4234.

Gloeckner, C. J. et al., 2009: Strep/FLAG tandem affinity purification (SFTAP) to study protein interactions. Curr. Protoc. Protein Sci.: 57, 19.20.1–19.20.19.

Gomperts, B. N. et al., 2004: Foxj1 regulates basal body anchoring to the cytoskeleton of ciliated pulmonary epithelial cells. J. Cell Sci.: 117, 1329–1337.

Gonzalez-Arenas, A. et al., 2014: Progesterone-induced blocking factor is hormonally regulated in human astrocytoma cells, and increases their growth through the IL-4R/JAK1/STAT6 pathway. J. Steroid Biochem. Mol. Biol.: 144, 463–470.

Gonzalez-Morales, N. et al., 2015: The Atypical Cadherin Dachsous Controls Left-Right Asymmetry in Drosophila. Dev. Cell: 33, 675–689.

Goto, T. & Keller, R., 2002. The planar cell polarity gene strabismus regulates convergence and extension and neural fold closure in Xenopus. Dev. Biol.: 247, 165–181.

Gouëffic, Y. et al., 2006: Hyaluronan induces vascular smooth muscle cell migration through RHAMM-mediated PI3Kdependent Rac activation. Cardiovasc. Res.: 72, 339–348.

Grainger, R. M., 2012: Xenopus tropicalis as a Model Organism for Genetics and Genomics: Past, Present, and Future. Methods Mol. Biol.: 917, 3–15.

Gray, R. S. et al., 2009: The planar cell polarity effector Fuz is essential for targeted membrane trafficking, ciliogenesis and mouse embryonic development. Nat. Cell Biol.: 11, 1225–1232.

Greene, N. D. E. & Copp, A. J., 2014: Neural tube defects. Annu. Rev. Neurosci.: 37, 221–242.

Griffin, J. N. et al., 2018: RAPGEF5 regulates nuclear translocation of b-catenin. Dev Cell: 44, 248–260.

Grimes, D. T. et al., 2016: Genetic Analysis Reveals a Hierarchy of Interactions between Polycystin-Encoding Genes and Genes Controlling Cilia Function during Left-Right Determination. PLoS Genet.: 12, e1006070.

Grimes, D. T. & Burdine, R. D., 2017: Left-Right Patterning: Breaking Symmetry to Asymmetric Morphogenesis. Trends Genet.: 33, 616–628.

Groen, A. C. et al., 2004: XRHAMM functions in ran-dependent microtubule nucleation and pole formation during anastral spindle assembly. Curr. Biol.: 14, 1801–1811.

Gros, J. et al., 2009: Cell movements at Hensen's node establish left/right asymmetric gene expression in the chick. Science: 324, 941–944.

Guarnaccia, A. D. & Tansey, W. P., 2018: Moonlighting with WDR5: a cellular multitasker. J. Clin. Med.: 7, 21.

Guimier, A. et al., 2015: MMP21 is mutated in human heterotaxy and is required for normal left-right asymmetry in vertebrates. Nat. Genet.: 47, 1260–1263.

Gupta, A. et al., 2012: The versatile molecular complex component LC8 promotes several distinct steps of flagellar assembly. J. Cell Biol.: 198, 115–126.

Gupta, G. D. et al., 2015: A Dynamic protein interaction landscape of the human centrosomecilium interface. Cell: 163, 1484–1499.

Gupta, S. & Sen, J., 2016: Roof plate mediated morphogenesis of the forebrain: new players join the game. Dev. Biol.: 413, 145–152.

Gur, M. et al., 2017: Roles of the cilium-associated gene CCDC11 in left-right patterning and in laterality disorders in humans. Int. J. Dev. Biol.: 61, 267–276.

Gurdon, J. B. et al., 1958: Sexually mature individuals of Xenopus laevis from the transplantation of single somatic nuclei. Nature: 182, 64–65.

Gurdon, J. B., 1962: The developmental capacity of nuclei taken from intestinal epithelium cells of feeding tadpoles. J. Embryol. Exp. Morphol.: 10, 622–640.

Gurdon, J. B. & Hopwood N., 2000: The introduction of Xenopus laevis into developmental biology: of empire, pregnancy testing and ribosomal genes. Int. J. Dev. Biol.: 44, 43–50.

Gutierrez-Rodriguez, A. et al., 2017: Proliferative and invasive effects of progesterone-induced blocking factor in human glioblastoma cells. Biomed. Res. Int.: 1295087.

Guzman, R. E. et al., 2014: Involvement of ClC-3 chloride/proton exchangers in controlling glutamatergic synaptic strength in cultured hippocampal neurons. Front. Cell. Neurosci.: 8, 143.

Hagenlocher, C. et al., 2013: Ciliogenesis and cerebrospinal fluid flow in the developing Xenopus brain are regulated by foxj1. Cilia: 2, 12.

Haigo, S. L. et al., 2003: Shroom induces apical constriction and is required for hingepoint formation during neural tube closure. Curr. Biol.: 13, 2125–2137.

Hall, E. A. et al., 2013: Acute versus chronic loss of mammalian Azi1/Cep131 results in distinct ciliary phenotypes. PLoS Genet.: 9, e1003928.

Hall, C. L. et al., 1994: Hyaluronan and the hyaluronan receptor RHAMM promote focal adhesion turnover and transient tyrosine kinase activity. J. Cell Biol.: 126, 575–588.

Hall, C. L. et al., 1995: Overexpression of the hyaluronan receptor RHAMM is transforming and is also required for H-ras transformation. Cell: 82, 19–26.

Hamburger, V., 1988: The Heritage of Experimental Embryology – Hans Spemann and the Organizer. Oxford University Press.

Hamada, H. et al., 2002: Establishment of vertebrate left-right asymmetry. Nat. Rev. Genet.: 3, 103–113.

Hanafusa, H. et al., 2000: The TGF-β family member derrière is involved in regulation of the establishment of left-right asymmetry. EMBO Rep.: 1, 32–39.

Harland, R. M. & Gilchrist, M. J., 2017: Editorial: The Xenopus laevis genome. Dev. Biol.: 426, 139–142.

Harumoto, T. et al., 2010: Atypical cadherins Dachsous and Fat control dynamics of noncentrosomal microtubules in planar cell polarity. Dev. Cell: 19, 389–401.

Hashimoto, M. et al., 2010: Planar polarization of node cells determines the rotational axis of node cilia. Nat. Cell Biol.: 12, 170–176.

Hatakeyama, J. et al., 2014: Vangl1 and Vangl2: planar cell polarity components with a developing role in cancer. Endocr. Relat. Cancer: 21, R345–R356.

Hayes, J. M. et al., 2007: Identification of novel ciliogenesis factors using a new in vivo model for mucociliary epithelial development. Dev. Biol.: 312, 115–130.

Hebbar, M. et al., 2018: A biallelic 36-bp insertion in PIBF1 is associated with Joubert syndrome. J. Hum. Genet.: 63, 935–939.

Hermo, L. et al., 2010: Surfing the wave, cycle, life history, and genes/proteins expressed by testicular germ cells. Part 3: developmental changes in spermatid flagellum and cytoplasmic droplet and interaction of sperm with the zona pellucida and egg plasma membrane. Microsc. Res. Tech. 73, 320–363.

Heasman, J. et al., 2000: β-catenin signaling activity dissected in the early Xenopus embryo: A novel antisense approach. Dev. Biol.: 222, 124–134.

Heasman, J., 2002: Morpholino oligos: making sense of antisense? Dev. Biol.: 243, 209–214.

Hellsten, U. et al., 2010: The genome of the Western clawed frog Xenopus tropicalis. Science: 328, 633–636.

Hirokawa, N. et al., 2006: Nodal Flow and the Generation of Left-Right Asymmetry. Cell: 125, 33–45.

Hirokawa, N. et al., 2009: Left-Right Determination: Involvement of Molecular Motor KIF3, Cilia, and Nodal Flow. Cold Spring Harb. Perspect. Biol.: 1, a000802.

Hirokawa, N. et al., 2012: KIF3 molecular motor and nodal flow. Curr. Opin. Cell Biol.: 24, 31–39.

Hoff, S. et al., 2013: ANKS6 is a central component of a nephronophthisis module linking NEK8 to INVS and NPHP3. Nat. Genet.: 45, 951–956.

Hofmann, M. et al., 1998: Problems with RHAMM: a new link between surface adhesion and oncogenesis? Cell: 95, 591–592.

Hogben, B. Y. L. et al., 1931: Studies On The Pituitary: VIII. The Relation Of The Pituitary Gland To Calcium Metabolism And Ovarian Function In Xenopus. J. Exp. Biol.: 8, 345–354.

Hoh, R. A. et al., 2012: Transcriptional program of ciliated epithelial cells reveals new cilium and centrosome components and links to human disease. PLoS ONE: 7, e52166.

Hoppeler-Lebel, A. et al., 2007: Centrosomal CAP350 protein stabilizes microtubules associated with the Golgi complex. J. Cell Sci.: 120, 3299–3308.

Hosoya, M. et al., 2012: Induction of differentiation of undifferentiated cells into pancreatic beta cells in vertebrates. Int. J. Dev. Biol.: 56, 313–323.

Hou, S. et al., 2007: The Secreted Serine Protease xHtrA1 Stimulates Long-Range FGF Signaling in the Early Xenopus Embryo. Dev. Cell: 13, 226–241.

Hozumi, S. et al., 2006: An unconventional myosin in Drosophila reverses the default handedness in visceral organs. Nature: 440, 798–802.

Huang, L. et al., 2011: TMEM237 is mutated in individuals with a Joubert syndrome related disorder and expands the role of the TMEM family at the ciliary transition zone. Am. J. Hum. Genet.: 89, 713–730.

Hudic, I. et al., 2015: Maternal serum progesterone-induced blocking factor (PIBF) in the prediction of preterm birth. J. Reprod. Immunol.: 109, 36–40.

Hudic, I., 2016: Lower urinary and serum progesterone-induced blocking factor in women with preterm birth. J. Reprod. Immunol.: 117, 66–69.

Huizar, R. L. et al., 2018: A liquid-like organelle at the root of motile ciliopathy. eLife: 7, 4154.

Ibañez-Tallon, I. et al., 2004: Dysfunction of axonemal dynein heavy chain Mdnah5 inhibits ependymal flow and reveals a novel mechanism for hydrocephalus formation. Hum. Mol. Genet.: 13, 2133–2141.

Iannicelli, M. et al., 2010: Novel TMEM67 mutations and genotype-phenotype correlates in meckelin-related ciliopathies. Hum. Mutat.: 31, E1319–E1331.

Ikegami, K. et al., 2010: Tubulin polyglutamylation is essential for airway ciliary function through the regulation of beating asymmetry. Proc. Natl. Acad. Sci. USA: 107, 10490–10495.

Inaba, K. & Mizuno, K., 2016: Sperm dysfunction and ciliopathy. Reprod. Med. Biol.: 15, 77–94.

Inácio, J. M. et al., 2013: The dynamic right-to-left translocation of Cerl2 is involved in the regulation and termination of Nodal activity in the mouse node. PLoS ONE: 8, e60406.

Inglis, P. N. et al., 2006: Piecing together a ciliome. Trends Genet.: 22, 491–500.

Ioannidis, N. M. et al., 2016: REVEL: An Ensemble Method for Predicting the Pathogenicity of Rare Missense Variants. Am. J. Hum. Genet.: 99, 877–885.

Irons, M. J. & Clermont, Y., 1982: Formation of the outer dense fibers during spermiogenesis in the rat. Anat. Rec.: 202, 463–471.

Irons, M. J. & Clermont, Y., 1982: Kinetics of fibrous sheath formation in the rat spermatid. Am. J. Anat.: 165, 121–130.

Isnard, A. et al., 2012: Impact of Leishmania metalloprotease GP63 on macrophage signaling. Front. Cell. Infect. Microbiol.: 2, 72.

Ivliev, A. E. et al., 2012: Exploring the transcriptome of ciliated cells using in silico dissection of human tissues. PLoS ONE: 7, e35618.

Jacobs, J. P. et al., 2007: The nomenclature, definition and classification of cardiac structures in the setting of heterotaxy. Cardiol. Young: 17, 1–28.

Jacobson, M. & Moody S. A., 1984: Quantitative lineage analysis of the frog's nervous system. I. Lineages of Rohon-Beard neurons and primary motoneurons. J. Neurosci.: 4, 1361–1369.

Jacquet, B. V. et al., 2009: FoxJ1-dependent gene expression is required for differentiation of radial glia into ependymal cells and a subset of astrocytes in the postnatal brain. Development: 136, 4021–4031.

Jain, R. et al., 2010: Temporal relationship between primary and motile ciliogenesis in airway epithelial cells. Am. J. Respir. Cell Mol. Biol.: 43, 731–739.

Jayachandran, P. et al., 2016: Microtubule-associated protein 1b is required for shaping the neural tube. Neural Dev.: 11, 1.

Jiang, J. et al., 2010: Multifunctional proteins bridge mitosis with motility and cancer with inflammation and arthritis. Sci. World J.: 10, 1244–1257.

Johnston, J. J. et al., 2017: Compound heterozygous alterations in intraflagellar transport protein CLUAP1 in a child with a novel Joubert and oral-facialdigital overlap syndrome. Cold Spring Harb. Mol. Case Stud.: 3, a001321.

Juan, T. et al., 2018: Myosin1D is an evolutionarily conserved regulator of animal left-right asymmetry. Nat. Commun.: 9, 1942.

Khanna, H. et al., 2005: RPGR-ORF15, which is mutated in retinitis pigmentosa, associates with SMC1, SMC3, and microtubule transport proteins. J. Biol. Chem.: 280, 33580–33587.

Kajikawa, E. et al., 2020: Nodal paralogues underlie distinct mechanisms for visceral left–right asymmetry in reptiles and mammals. Nat. Ecol. Evol.: 4, 261–269.

Kamura, K. et al., 2011: Pkd1l1 complexes with Pkd2 on motile cilia and functions to establish the left-right axis. Development: 138, 1121–1129.

Karfunkel, P., 1971: The role of microtubules and microfilaments in neurulation in Xenopus. Dev. Biol.: 25, 30–56.

Kartagener, M., 1933: Zur Pathogenese der Bronchiektasien. Beitr. Klin. Tuberk. Spezif. Tuberkuloseforsch.: 83, 489–501.

Kawai, J. & Hayashizaki, Y., 2003: DNA book. Genome Res.: 13, 1488–1495.

Kawasumi, A. et al., 2011: Two rotating cilia in the node cavity are sufficient to break left–right symmetry in the mouse embryo. Nat. Commun.: 3, 622–628.

Kee, N. et al., 2008: Neogenin and RGMa control neural tube closure and neuroepithelial morphology by regulating cell polarity. J. Neurosci.: 28, 12643–12653.

Kee, H. L. et al., 2012: A size-exclusion permeability barrier and nucleoporins characterize a ciliary pore complex that regulates transport into cilia. Nat. Cell Biol.: 14, 431–437.

Keller, R. E., 1975: Vital dye mapping of the gastrula and neurula of Xenopus laevis. I. Prospective areas and morphogenetic movements of the superficial layer. Dev. Biol.: 42, 222–241.

Keller, R. E., 1980: The cellular basis of epiboly: an SEM study of deep-cell rearrangement during gastrulation in Xenopus laevis. J. Embryol. Exp. Morphol.: 60, 201–234.

Keller, R. E. et al., 1992: The cellular basis of the convergence and extension of the Xenopus neural plate. Dev. Dyn.: 193, 199–217.

Keller, R., 2002: Shaping the vertebrate body plan by polarized embryonic cell movements. Science: 298, 1950–1954.

Keller, R. et al., 2000: Mechanisms of convergence and extension by cell intercalation. Philos. Trans. R. Soc. Lond. B Biol. Sci.: 355, 897–922.

Kennedy, M. P. et al., 2007. Congenital heart disease and other heterotaxic defects in a large cohort of patients with primary ciliary dyskinesia. Circulation: 115, 2814–2821.

Kim, K. et al., 2012: CEP90 is required for the assembly and centrosomal accumulation of centriolar satellites, which is essential for primary cilia formation. PLoS ONE: 7, e48196.

Kim, K. & Rhee, K., 2011: The pericentriolar satellite protein CEP90 is crucial for integrity of the mitotic spindle pole. J. Cell Sci.: 124, 338–347.

King, T. et al., 1998: The role of the brachyury gene in heart development and left-right specification in the mouse. Mech. Dev.: 79, 29–37.

Kircher, M. et al., 2014: A general framework for estimating the relative pathogenicity of human genetic variants. Nat. Genet.: 46, 310–315.

Kleene, K. C., 2005: Sexual selection, genetic conflict, selfish genes, and the atypical patterns of gene expression in spermatogenic cells. Dev. Biol.: 277, 16–26.

Knopp, C. et al., 2015: Syndromic ciliopathies: from single gene to multi gene analysis by SNP arrays and next generation sequencing. Mol. Cell. Probes: 29, 299–307.

Knowles, M. R. et al., 2014: Mutations in RSPH1 cause primary ciliary dyskinesia with a unique clinical and ciliary phenotype. Am. J. Respir. Crit. Care Med.: 189, 707–717.

Knowles, M. R. et al., 2016: Primary ciliary dyskinesia. Clin. Chest. Med.: 37, 449–461.

Kodani, A. et al., 2015: Centriolar satellites assemble centrosomal microcephaly proteins to recruit CDK2 and promote centriole duplication. eLife: 4, 7519.

Kok, F. O. et al., 2015: Reverse genetic screening reveals poor correlation between morpholino-induced and mutant phenotypes in zebrafish. Dev. Cell: 32, 97–108.

Kremer, J. R. et al., 1996: Computer visualization of three-dimensional image data using IMOD. Journal of Structural Biology: 116, 71–76.

Krieg, P. A. & Melton, D. A., 1984: Functional messenger RNAs are produced by SP6 in vitro transcription of cloned cDNAs. Nucleic Acids Res.: 12, 7057–7070.

Kroes, H. Y. et al., 2016: Joubert syndrome: genotyping a Northern European patient cohort. Eur. J. Hum. Genet.: 24, 214–220.

Kroll, K. L. & Amaya, E., 1996: Transgenic Xenopus embryos from sperm nuclear transplantations reveal FGF signaling requirements during gastrulation. Development: 122, 3173–3183.

Kuehni, C. E. et al., 2010: Factors influencing age at diagnosis of primary ciliary dyskinesia in European children. Eur. Respir. J.: 36, 1248–1258.

Kurian, A. W. et al., 2017: Gaps in incorporating germline genetic testing into treatment decision-making for early-stage breast cancer. J. Clin. Oncol.: 35, 2232–2239.

Kurisaki, A. et al., 2010: In vitro organogenesis using multipotent cells. Hum. Cell: 23, 1–14.

Kubo, T. et al., 2018. A microtubule-dynein tethering complex regulates the axonemal inner dynein f (I1). Mol. Biol. Cell: 19, 1003–1152.

Kulkarni, S. S. & Khokha, M. K., 2018: WDR5 regulates left-right patterning via chromatin dependent and independent functions. Development: 145, dev.159889.

Lachmann, M. et al., 2004: PIBF (progesterone induced blocking factor) is overexpressed in highly proliferating cells and associated with the centrosome. Int. J. Cancer: 112, 51–60.

Lebreton, G. et al., 2018: Molecular to organismal chirality is induced by the conserved myosin 1D. Science: 362, 949–952.

Le Clech, M., 2008: Role of CAP350 in centriolar tubule stability and centriole assembly. PLoS ONE: 3, e3855.

Lee, L., 2013: Riding the wave of ependymal cilia: genetic susceptibility to hydrocephalus in primary ciliary dyskinesia. J. Neurosci. Res.: 91, 1117–1132.

Leitch, C. C. et al., 2008: Hypomorphic mutations in syndromic encephalocele genes are associated with Bardet-Biedl syndrome. Nat. Genet.: 40, 443–448.

Lek, M. et al., 2016: Analysis of protein-coding genetic variation in 60,706 humans. Nature: 536, 285–291.

Lepay, D. A. et al., 1983: Surface antigens of Leishmania Donovani promastigotes. J. Exp. Med.: 157, 1562–1572.

Levin, M. et al., 1995: A molecular pathway determining left-right asymmetry in chick embryogenesis. Cell: 82, 803–814.

Li, H. et al., 2015: RHAMM deficiency disrupts folliculogenesis resulting in female hypofertility. Biol. Open: 4, 562–571.

Li, H. et al., 2016: Impaired planar germ cell division in the testis, caused by dissociation of RHAMM from the spindle, results in hypofertility and seminoma. Cancer Res.: 76, 6382–6395.

Li, W. et al., 2016: Alternative cleavage and polyadenylation in spermatogenesis connects chromatin regulation with post-transcriptional control. BMC Biol.: 14, 6.

Lienkamp, S. S. et al., 2010: Inversin relays Frizzled-8 signals to promote proximal pronephros development. Proc. Natl. Acad. Sci. USA: 107, 20388–20393.

Lienkamp, S. S. et al., 2012: Vertebrate kidney tubules elongate using a planar cell polarity-dependent, rosettebased mechanism of convergent extension. Nat. Genet.: 44, 1382–1387.

Lienkamp, S. S., 2016: Using Xenopus to study genetic kidney diseases. Semin. Cell Dev. Biol.: 51, 117–124.

Lin, J. et al., 2012: One of the nine doublet microtubules of eukaryotic flagella exhibits unique and partially conserved structures. PLoS One: 7, e46494.

Lindemann, C. B. & Lesich, K. A., 2010: Flagellar and ciliary beating: the proven and the possible. J. Cell Sci.: 123, 519–528.

Lindqvist, M. et al., 2010: Vang-like protein 2 and Rac1 interact to regulate adherens junctions. J. Cell Sci.: 123, 472–483.

Liu, X. et al., 2013: dbNSFP v2.0: a database of human nonsynonymous SNVs and their functional predictions and annotations. Hum. Mutat.: 34, E2393–E2402.

LeBlanc-Straceski, J. M. et al., 2009: Developmental expression of Xenopus myosin1d and identification of a myo1d tail homology that overlaps TH1. Dev. Growth Differ.: 51, 443–451.

Lindemann, C. B. et al., 1992: The flagellar beat of rat sperm is organized by the interaction of two functionally distinct populations of dynein bridges with a stable central axonemal partition. J. Cell Sci.: 102, 249–260.

Lohr, J. L. et al., 1998: Maintenance of asymmetric nodal expression in Xenopus laevis. Dev. Genet.: 23, 194–202.

Lowe, L. A. et al., 1996: Conserved left-right asymmetry of nodal expression and alterations in murine situs inversus. Nature: 381, 158–161.

Lucas, J. S. et al., 2020: Primary ciliary dyskinesia in the genomics age. Lancet Respir. Med.: 8, 202–216.

Lund, E. et al., 2011: Limiting ago protein restricts RNAi and microRNA biogenesis during early development in Xenopus laevis. Genes Dev.: 25, 1121–1131.

Lyons, R. A. et al., 2006: The reproductive significance of human Fallopian tube cilia. Hum. Reprod. Update: 12, 363–372.

MacArthur, D. G. et al., 2014: Guidelines for investigating causality of sequence variants in human disease. Nature: 508, 469–476.

Macdonald, R. et al., 1995: Midline signalling is required for Pax gene regulation and patterning of the eyes. Development: 121, 3267–3278.

Macdonald, M. H. et al., 1995: Analysis of the active site and activation mechanism of the Leishmania. Biochim. Biophys. Acta: 1253, 199–207.

Mali, P. et al., 2013: RNA-guided human genome engineering via Cas9. Science: 339, 823–826.

Malicdan, M. C. et al., 2015: Mutations in human homologue of chicken talpid3 gene (KIAA0586) cause a hybrid ciliopathy with overlapping features of Jeune and Joubert syndromes. J. Med. Genet.: 52, 830–839.

Marquez, J. et al., 2020: Disrupted ER membrane protein complex-mediated topogenesis drives congenital neural crest defects. J. Clin. Invest.: 1253, 199–207.

Maria, B. L. et al., 1997: “Joubert syndrome” revisited: key ocular motor signs with magnetic resonance imaging correlation. J. Child Neurol.: 12, 423–430.

Maria, B. L. et al., 1999: Molar tooth sign in Joubert syndrome: clinical, radiologic, and pathologic significance. J. Child Neurol.: 14, 368–376.

Marjoram, L. & Wright, C., 2011: Rapid differential transport of Nodal and Lefty on sulfated proteoglycan-rich extracellular matrix regulates left-right asymmetry in Xenopus. Development: 138, 475–485.

Marques, S. et al., 2004: The activity of the Nodal antagonist Cerl-2 in the mouse node is required for correct L/R body axis. Genes Dev.: 18, 2342–2347.

Marsden, M. & DeSimone, D. W., 2001: Regulation of cell polarity, radial intercalation and epiboly in Xenopus: novel roles for integrin and fibronectin. Development: 128, 3635–3647.

Marshall, S. et al., 2018: Extracellular release of virulence factor major surface protease via exosomes in Leishmania infantum promastigotes. Parasites and Vectors: 11, 1–10.

Marshall, W. F. & Nonaka, S., 2006: Cilia: tuning in to the cell’s antenna. Curr. Biol.: 16, R604–R614.

Matis, M. et al., 2014: Microtubules provide directional information for core PCP function. eLife: 3, e02893.

Matthews, B. W. et al., 1972: Structure of thermolysin. Nat. New Biol.: 238, 41–43.

Maxwell, C. A. et al., 2003: RHAMM is a centrosomal protein that interacts with dynein and maintains spindle pole stability. Mol. Biol. Cell: 14, 2262–2276.

Maxwell, C. A. et al., 2004: RHAMM expression and isoform balance predict aggressive disease and poor survival in multiple myeloma. Blood: 104, 1151–1158.

Maxwell, C. A. et al., 2011: Interplay between BRCA1 and RHAMM regulates epithelial apicobasal polarization and may influence risk of breast cancer. PLoS Biol.: 9, e1001199.

McGrath, J. et al., 2003: Two populations of node monocilia initiate left-right asymmetry in the mouse. Cell: 114, 61–73.

McGrath, J. & Brueckner M., 2003: Cilia are at the heart of vertebrate left-right asymmetry. Curr. Opin. Genet. Dev.: 13, 385–392.

McGwire, B. S. et al., 2003: Migration through the Extracellular Matrix by the Parasitic Protozoan. Infect. Immun.: 71, 1008–1010.

McGwire, B. S. et al., 2002: Extracellular release of the glycosylphosphatidylinositol (GPI)-linked Leishmania surface metalloprotease, gp63, is independent of GPI phospholipolysis. Implications for parasite virulence. J. Biol. Chem.: 277, 8802–8809.

McClintock, T. S. et al., 2008: Tissue expression patterns identify mouse cilia genes. Physiol. Genomics: 32, 198–206.

McDowell, G. S. et al., 2016: Conserved roles for cytoskeletal components in determining laterality. Integr. Biol.: 8, 267–286.

McHugh, B. et al., 2004: Invadolysin: A novel, conserved metalloprotease links mitotic structural rearrangements with cell migration. J. Cell Biol.: 167, 673–686.

Meno, C. et al., 1996: Left-right asymmetric expression of the TGFβ-family member lefty in mouse embryos. Nature: 381, 151–155.

Meistrich, M. L. & Hess, R. A., 2013: Assessment of spermatogenesis through staging of seminiferous tubules. Methods Mol. Biol.: 927, 299–307.

Melby, A. E. et al., 1996: Specification of cell fates at the dorsal margin of the zebrafish gastrula. Development: 122, 2225–2237.

Meno, C. et al., 1998: lefty-1 is required for left-right determination as a regulator of lefty-2 and nodal. Cell: 94, 287–297.

Miller, S. A. et al., 1988: A simple salting out procedure for extracting DNA from human nucleated cells. Nucleic Acids Res.: 16, 1215.

Minegishi, K. et al., 2020: Fluid flow-induced left-right asymmetric decay of Dand5 mRNA in the mouse embryo requires Bicc1-Ccr4 RNA degradation complex. bioRxiv: 931477.

Mitchell, D. R., 2017: Evolution of cilia. Cold Spring Harb. Perspect. Biol.: 9, a028290.

Mitchison, H. M. & Valente, E. M., 2017: Motile and non-motile cilia in human pathology: from function to phenotypes. J. Pathol.: 241, 294–309.

Mohr, K. & Koegl, M., 2012: High-throughput yeast two-hybrid screening of complex cDNA libraries. Methods Mol. Biol.: 812, 89–102.

Moody, S. A., 1987: Fates of the blastomeres of the 32-cell-stage Xenopus embryo. Dev. Biol.: 122, 300–319.

Moody, S. A., 2000: Cell lineage analysis in Xenopus embryos. Methods Mol. Biol.: 135, 331–347.

Moorman, A. F. et al., 2001: Sensitive nonradioactive detection of mRNA in tissue sections: novel application of the wholemount in situ hybridization protocol. J. Histochem. Cytochem.: 49, 1–8.

Moreno-Mateos, M. A. et al., 2015: CRISPRscan: designing highly efficient sgRNAs for CRISPR-Cas9 targeting in vivo. Nat. Methods: 12, 982–988.

Moreno-Mateos, M. A. et al., 2017: CRISPRCpf1 mediates efficient homology-directed repair and temperature-controlled genome editing. Nat. Commun.: 8, 1–9.

Morimoto, Y. et al., 2019: Nonsense mutation in CFAP43 causes normal-pressure hydrocephalus with ciliary abnormalities. Neurology: 92, E2364–E2374.

Mosser, D. M. & Edelson, P.J., 1985: The mouse macrophage receptor for C3bi (CR3) is a major mechanism in the phagocytosis of Leishmania promastigotes. J. Immunol.: 135, 2785–2789.

Mougou-Zerelli, S. et al., 2009: CC2D2A mutations in Meckel and Joubert syndromes

indicate a genotype-phenotype correlation. Hum. Mutat.: 30, 1574–1582.

Moulton, J. D., 2016: Guide for Morpholino Users: Toward Therapeutics. J. Drug Discov. Dev. Deliv.: 3, 1023.

Moulton, J. D., 2017: Making a morpholino experiment work: controls, favoring specificity, improving efficacy, storage, and dose. Methods Mol. Biol.: 1565, 17–29.

Mukherjee, I. et al., 2019: Identification of Important Effector Proteins in the FOXJ1 Transcriptional Network Associated With Ciliogenesis and Ciliary Function. Front. Genet.: 10, 23.

Murdoch, J. N. & Copp, A. J., 2010: The relationship between sonic Hedgehog signaling, cilia, and neural tube defects. Birth Defects Res. A Clin. Mol. Teratol.: 88, 633–652.

Murray, A. W. & Kirschner, M. W., 1989: Cyclin synthesis drives the early embryonic cell cycle. Nature: 339, 275–280.

Naert, T. et al., 2017: TALENs and CRISPR/Cas9 fuel genetically engineered clinically relevant Xenopus tropicalis tumor models. Genesis: 55, e23005.

Naert, T. & Vleminckx, K., 2018: CRISPR/Cas9-mediated knockout of Rb1 in Xenopus tropicalis. Methods Mol. Biol.: 1726, 177–193.

Naganathan, S. R. et al., 2014: Active torque generation by the actomyosin cell cortex drives left-right symmetry breaking. eLife: 3, e04165.

Nagasawa, K. et al., 2013: Significant modulation of the hepatic proteome induced by exposure to low temperature in Xenopus laevis. Biol Open: 2, 1057–1069.

Nakamura, T et al., 2006: Generation of robust left-right asymmetry in the mouse embryo requires a self-enhancement and lateral-inhibition system. Dev. Cell: 11, 495–504.

Nakamura, T. et al., 2012: Fluid flow and interlinked feedback loops establish left-right asymmetric decay of Cerl2 mRNA. Nat. Commun.: 3, 1313–1322.

Nakayama, T. et al., 2013: Simple and efficient CRISPR/Cas9-mediated targeted mutagenesis in Xenopus tropicalis. Genesis: 51, 835–843.

Nakamura, T. & Hamada, H., 2012: Left-right patterning: conserved and divergent mechanisms. Development: 139, 3257–3262.

Nakayama, T. et al., 2014: Cas9-based genome editing in Xenopus tropicalis. Methods Enzymol.: 546, 355–375.

Narasimhan, V. et al., 2015: Mutations in CCDC11, which encodes a coiled-coil containing ciliary protein, causes situs inversus due to dysmotility of monocilia in the left-right organizer. Hum. Mutat.: 36, 307–318.

Naz, R. K. et al., 2009: Gene knockouts that affect male fertility: novel targets for contraception. Front. Biosci.: 14, 3994–4007.

Newton, F. G. et al., 2012: Forkhead Transcription Factor Fd3F Cooperates with Rfx to Regulate a Gene Expression Program for Mechanosensory Cilia Specialization. Dev. Cell: 22, 1221–1233.

Ng, P. C. & Henikoff, S., 2003: SIFT: predicting amino acid changes that affect protein function. Nucleic Acids Res.: 31, 3812–3814.

Nguengang Wakap, S. et al., 2019: Estimating cumulative point prevalence of rare diseases: analysis of the Orphanet database. Eur. J. Hum. Genet.: 28, 165–173.

Niehrs, C., & Pollet, N., 1999: Synexpression groups in eukaryotes. Nature: 402, 483–487.

Nieuwkoop, P. D. & Faber, J., 1994: Normal table of Xenopus laevis (Daudin): a systematical and chronological survey of the development from the fertilized egg till the end of metamorphosis. Garland Publishing Inc.

Niroula, A., & Vihinen, M., 2016: Variation Interpretation Predictors: Principles, Types, Performance, and Choice. Hum. Mutat.: 37, 579–597.

Niroula, A. & Vihinen, M., 2019: How good are pathogenicity predictors in detecting benign variants? PLoS Comput. Biol.: 15, 1–17.

Nigg, E. A. & Raff, J. W., 2009: Centrioles, centrosomes, and cilia in health and disease. Cell: 139, 663–678.

Nonaka, S. et al., 1998: Randomization of left-right asymmetry due to loss of nodal cilia generating leftward flow of extraembryonic fluid in mice lacking KIF3B motor protein. Cell: 95, 829–837.

Nonaka, S. et al., 2002: Determination of left-right patterning of the mouse embryo by artificial nodal flow. Nature: 418, 96–99.

Norris, D. P. & Grimes, D. T., 2012: Cilia discern left from right. Science: 338, 206–207.

Norris, D. P. & Jackson, P. K., 2016: Cell biology: Calcium contradictions in cilia. Nature: 531, 582–583.

Norris, D. P. & Robertson, E. J., 1999: Asymmetric and node-specific nodal expression patterns are controlled by two distinct cis-acting regulatory elements. Genes Dev.: 13, 1575–1588.

O'Callaghan, C. A. et al., 1998: Production, crystallization, and preliminary X-ray analysis of the human MHC class Ib molecule HLA-E. Protein Sci.: 7, 1264–1266.

Ocana, O. H. et al., 2017: A right-handed signalling pathway drives heart looping in vertebrates. Nature: 549, 86–90.

Ohi, Y. & Wright, C. V. E., 2007: Anteriorward shifting of asymmetric Xnr1 expression and contralateral communication in left-right specification in Xenopus. Dev. Biol.: 301, 447–463.

Ohkawara, B. & Niehrs, C., 2011: An ATF2-based luciferase reporter to monitor non-canonical Wnt signaling in Xenopus embryos. Dev. Dyn.: 240, 188–194.

Okada, Y. et al., 1999: Abnormal nodal flow precedes situs inversus in iv and inv mice. Mol. Cell: 4, 459–468.

Okada, Y. et al., 2005: Mechanism of nodal flow: A conserved symmetry breaking event in left-right axis determination. Cell: 121, 633–644.

Oki, S. et al., 2007: Sulfated glycosaminoglycans are necessary for Nodal signal transmission from the node to the left lateral plate in the mouse embryo. Development: 134, 3893–3904.

Oki, S. et al., 2009: Reversal of left-right asymmetry induced by aberrant Nodal signaling in the node of mouse embryos. Development: 136, 3917–3925.

Okumura, T. et al., 2008: The development and evolution of left-right asymmetry in invertebrates: lessons from Drosophila and snails. Dev. Dyn.: 237, 3497–3515.

Olsen, J. V. et al., 2005: Parts per million mass accuracy on an Orbitrap mass spectrometer via lock mass injection into a C-trap. Mol. Cell Proteomics: 4, 2010–2021.

Osinka, A. et al., 2019: Ciliary Proteins: Filling the Gaps. Recent Advances in Deciphering the Protein Composition of Motile Ciliary Complexes. Cells: 8, 730.

Ossipova, O. et al., 2015: The involvement of PCP proteins in radial cell intercalations during Xenopus embryonic development. Dev. Biol.: 408, 316–327.

Ossipova, O. et al., 2015: Vangl2 cooperates with Rab11 and Myosin V to regulate apical constriction during vertebrate gastrulation. Development: 142, 99–107.

Ossipova, O. et al., 2015: Planar polarization of Vangl2 in the vertebrate neural plate is controlled by Wnt and Myosin II signaling. Biol. Open: 4, 722–730.

Pai, V. P. et al., 2017: HCN4 ion channel function is required for early events that regulate anatomical left-right patterning in a nodal and lefty asymmetric gene expression-independent manner. Biol. Open: 6, 1445–1457.

Paramasivam, N. et al., 2018: Identification and prioritization of causal variants of human genetic disorders from exome or whole genome sequencing data. OBM Genet.: 2.

Parisi, M. & Glass, I., 1993: Joubert syndrome. GeneReviews.

Park, M. & Moon, R. T., 2002: The planar cell-polarity gene stbm regulates cell behavior and cell fate in vertebrate embryos. Nat. Cell Biol.: 4, 20–25.

Park, T. J. et al., 2008: Dishevelled controls apical docking and planar polarization of basal bodies in ciliated epithelial cells. Nat. Genet.: 40, 871–879.

Park, T. J. et al., 2006: Ciliogenesis defects in embryos lacking inturned or fuzzy function are associated with failure of planar cell polarity and Hedgehog signaling. Nat. Genet.: 38, 303–311.

Patel, H. et al., 2005: Activity and subcellular compartmentalization of peroxisome proliferator-activated receptor alpha are altered by the centrosome-associated protein CAP350. J. Cell Sci.: 118,175–186.

Pearce, J. J. H. et al., 1999: A mouse cerberus/Dan-related gene family. Dev. Biol.: 209, 98–110.

Peeters, H. & Devriendt, K., 2006: Human laterality disorders. Eur. J. Med. Genet.: 49, 349–362.

Pimpale, L. et al., 2019: Cell lineage-dependent chiral actomyosin flows drive cellular rearrangements in early development. bioRxiv: 842922.

Pennekamp, P. et al., 2002: The ion channel polycystin-2 is required for left-right axis determination in mice. Curr. Biol.: 12, 938–943.

Pennekamp, P. et al., 2015: Situs inversus and ciliary abnormalities: 20 years later, what is the connection? Cilia: 4, 1.

Peshkin, L. et al., 2015: On the relationship of protein and mRNA dynamics in vertebrate embryonic development. Dev. Cell: 35, 383–394.

Philpott, A. & Yew, P. R., 2008: The Xenopus cell cycle: an overview. Mol. Biotechnol.: 39, 9–19.

Pintado, P. et al., 2017: Dynamics of cilia length in left-right development. R. Soc. Open Sci.: 4, 161102.

Prager, A. et al., 2017: hmmr mediates anterior neural tube closure and morphogenesis in the frog Xenopus. Dev. Biol.: 430, 188–201.

Praveen, K. et al., 2015: Unique among ciliopathies: primary ciliary dyskinesia, a motile cilia disorder. F1000Prime Rep.: 7, 36.

Polgar, B. et al., 2003: Molecular cloning and immunologic characterization of a novel cDNA coding for progesterone-induced blocking factor. J. Immunol.: 171, 5956–5963.

Puelles, L. & Rubenstein, J. L. R., 2015: A new scenario of hypothalamic organization: rationale of new hypotheses introduced in the updated prosomeric model. Front. Neuroanat.: 9, 27.

Pujana, M. A. et al., 2007: Network modeling links breast cancer susceptibility and centrosome dysfunction. Nat. Genet.: 39, 1338–1349.

Quigley, I. K. & Kintner, C., 2017: Rfx2 stabilizes Foxj1 binding at chromatin loops to enable multiciliated cell gene expression. PLoS Genet.: 13, e1006538.

Rachev, E. et al., 2020: CFAP43 modulates ciliary beating in mouse and Xenopus. Dev. Biol.: 459, 109–125.

Ramamoorthy, R. et al., 1992: Three distinct RNAs for the surface protease gp63 are differentially expressed during development of Leishmania donovani chagasi promastigotes to an infectious form. J. Biol. Chem.: 267, 1888–1895.

Rawlings, N. D. et al., 2018: The MEROPS database of proteolytic enzymes, their substrates and inhibitors in 2017 and a comparison with peptidases in the PANTHER database. Nucleic Acids Res.: 46, D624–D632.

Reller, M. D. et al., 2008: Prevalence of congenital heart defects in metropolitan Atlanta, 1998-2005. J. Pediatr.: 153, 807–813.

Rentzsch, P. et al., 2019: CADD: Predicting the deleteriousness of variants throughout the human genome. Nucleic Acids Res.: 47, D886–D894.

Di Resta, C. et al., 2018: Next-generation sequencing approach for the diagnosis of human diseases: Open challenges and new opportunities. Electron. J. Int. Fed. Clin. Chem. Lab. Med.: 29, 4–14.

Reva, B. et al., 2011: Predicting the functional impact of protein mutations: application to cancer genomics. Nucleic Acids Res.: 39, e118.

Reversade, B. et al., 2009: Mutations in PYCR1 cause cutis laxa with progeroid features. Nat. Genet.: 41, 1016–1021.

Reynolds, M. J. et al., 2018: The Developmental Process of the Growing Motile Ciliary Tip Region. Sci. Rep.: 8, 7977.

Richards, S. et al., 2015: Standards and guidelines for the interpretation of sequence variants: a joint consensus recommendation of the American College of Medical Genetics and Genomics and the Association for Molecular Pathology. Genet. Med.: 17, 405–424.

De Robertis, E. M. et al., 2000: The establishment of Spemann's organizer and patterning of the vertebrate embryo. Nat. Rev. Genet.: 1, 171–181.

De Robertis, E. M., 2008: Evo-Devo: Variations on Ancestral Themes. Cell: 132, 185–195.

Rodríguez, C. I. et al., 2000: High-efficiency deleter mice show that FLPe is an alternative to Cre-loxP. Nat. Genet.: 25, 139–140.

Roessler, E. & Muenke, M., 2010: The molecular genetics of holoprosencephaly. Am. J. Med. Genet. C Semin. Med. Genet.: 154C, 52–61.

Romani, M. et al., 2014: Mutations in B9D1 andMKS1 cause mild Joubert syndrome: expanding the genetic overlap with the lethal ciliopathy Meckel syndrome. Orphanet J. Rare Dis.: 9, 72.

Romani, M. et al., 2013: Joubert syndrome: congenital cerebellar ataxia with the molar tooth. Lancet Neurol.: 12, 894–905.

Roosing, S. et al., 2016: Mutations in CEP120 cause Joubert syndrome as well as complex ciliopathy phenotypes. J. Med. Genet.: 53, 608–615.

Rossi, A. et al., 2015: Genetic compensation induced by deleterious mutations but not gene knockdowns. Nature: 524, 230–233.

Rudat, C. et al., 2014: Upk3b is dispensable for development and integrity of urothelium and mesothelium. PLoS One: 9, e112112.

Ryan, A. K. et al., 1998: Pitx2 determines left-right asymmetry of internal organs in vertebrates. Nature: 394, 545–551.

Saijoh, Y. et al., 2000: Left-right asymmetric expression of lefty2 and nodal is induced by a signaling pathway that includes the transcription factor FAST2. Mol. Cell: 5, 35–47.

Sakai, Y. et al., 1986: Immunocytochemical study on fibrous sheath formation in mouse spermiogenesis using a monoclonal antibody. Anat. Rec.: 215, 119–126.

Samocha, K. E. et al., 2014: A framework for the interpretation of de novo mutation in human disease. Nat. Genet.: 46, 944–950.

Sampath, K. & Robertson E. J., 2016: Keeping a lid on nodal: Transcriptional and translational repression of nodal signalling. Open Biol.: 6, 150200–150208.

Santos, N. & Reiter, J. F., 2008: Building it up and taking it down: the regulation of vertebrate ciliogenesis. Dev. Dyn.: 237, 1972–1981.

Satir, P. et al., 2014: A Structural Basis for How Motile Cilia Beat. Bioscience: 64, 1073–1083.

Saunier, S., 2005: Nephronophthisis. Curr. Opin. Genet. Dev.: 15, 324–331.

Saydmohammed, M. et al., 2018: Vertebrate myosin 1d regulates left-right organizer morphogenesis and laterality. Nat. Commun.: 9, 3381.

Schindelin, J. et al., 2012: Fiji: an open-source platform for biological-image analysis. Nat. Methods: 9, 676–682.

Schneider, I. et al., 2019: A dual function of FGF signaling in Xenopus left-right axis formation. Development: 146, dev173575.

Schroeder, T. E., 1970: Neurulation in Xenopus laevis. An analysis and model based upon light and electron microscopy. J. Embryol. Exp. Morphol.: 23, 427–462.

Schürmann, A. et al., 2002: Reduced sperm count and normal fertility in male mice with targeted disruption of the ADP-ribosylation factor-like 4 (Arl4) gene. Mol. Cell. Biol.: 22, 2761–2768.

Schwarz, J. M. et al., 2010: MutationTaster evaluates disease-causing potential of sequence alterations. Nat. Methods: 7, 575–576.

Schwarze, K. et al., 2018: Are whole-exome and whole-genome sequencing approaches cost-effective? A systematic review of the literature. Genet. Med.: 20, 1122–1130.

Schweickert, A. et al., 2007: Cilia-driven leftward flow determines laterality in Xenopus. Curr. Biol.: 17, 60–66.

Schweickert, A. et al., 2000: Pitx2 isoforms: Involvement of Pitx2c but not Pitx2a or Pitx2b in vertebrate left-right asymmetry. Mech. Dev.: 90, 41–51.

Schweickert, A. et al., 2010: The nodal inhibitor Coco is a critical target of leftward flow in Xenopus. Curr. Biol.: 20, 738–743.

Sempou, E. et al., 2018: Candidate heterotaxy gene FGFR4 is essential for patterning of the left-right organizer in Xenopus. Front. Physiol.: 9, 1705.

Seo, J. W. et al., 1992: Abnormal laterality and congenital cardiac anomalies. Relations of visceral and cardiac morphologies in the iv/iv mouse. Circulation: 86, 642–650.

Sepich, D. S. et al., 2011: Wnt/PCP signaling controls intracellular position of MTOCs during gastrulation convergence and extension movements. Development: 138, 543–552.

Session, A. M. et al., 2016: Genome evolution in the allotetraploid frog Xenopus laevis. Nature: 538, 336–343.

Sha, Y.-W. et al., 2017: Novel mutations in CFAP44 and CFAP43 cause multiple morphological abnormalities of the sperm flagella (MMAF). Reprod. Sci.: 26, 26–34.

Shaheen, R. et al., 2014: Mutations in CSPP1, encoding a core centrosomal protein, cause a range of ciliopathy phenotypes in humans. Am. J. Hum. Genet.: 94, 73–79.

Shaheen, R. et al., 2015: Identification of a novel MKS locus defined by TMEM107 mutation. Hum. Mol. Genet.: 24, 5211–5218.

Shapiro, H. A. & Zwarenstein, H., 1934: A rapid test for pregnancy on Xenopus lævis. Nature: 133, 762.

Shi, Z. et al., 2015: Heritable CRISPR/Cas9-mediated targeted integration in Xenopus tropicalis. FASEB J.: 29, 4914–4923.

Shi, Z. et al., 2019: Modeling human point mutation diseases in Xenopus tropicalis with a modified CRISPR/Cas9 system. FASEB J.: 33, 6962–6968.

Shihab, H. A. et al., 2013: Predicting the functional, molecular, and phenotypic consequences of amino acid substitutions using hidden Markov models. Hum. Mutat.: 34, 57–65.

Shibazaki, Y. et al., 2004: Body handedness is directed by genetically determined cytoskeletal dynamics in the early embryo. Curr. Biol.: 14, 1462–1467.

Shimada, Y. et al., 2006: Polarized transport of Frizzled along the planar microtubule arrays in Drosophila wing epithelium. Dev. Cell: 10, 209–222.

Shinohara, K. et al., 2015: Absence of Radial Spokes in Mouse Node Cilia Is Required for Rotational Movement but Confers Ultrastructural Instability as a Trade-Off. Dev. Cell: 35, 236–246.

Shinohara, K. & Hamada, H., 2017: Cilia in Left-Right Symmetry Breaking. Cold Spring Harb. Perspect. Biol.: 9, a028282.

Shiratori, H. et al., 2006: Conserved regulation and role of Pitx2 in situs-specific morphogenesis of visceral organs. Development: 133, 3015–3025.

Shiratori, H. & Hamada, H., 2014: TGFb signaling in establishing left right asymmetry. Semin. Cell Dev. Biol.: 32, 80–84.

Shook, D. R. et al., 2004: Pattern and morphogenesis of presumptive superficial mesoderm in two closely related species, Xenopus laevis and Xenopus tropicalis. Dev. Biol.: 270, 163–185.

Shook, D. R. et al., 2018: Large, long range tensile forces drive convergence during Xenopus blastopore closure and body axis elongation. eLife 7: 115.

Sigg, M. A. et al., 2017: Evolutionary proteomics uncovers ancient associations of cilia with signaling pathways. Dev. Cell: 43, 744–762.

Silva E. et al., 2015: Ccdc11 is a novel centriolar satellite protein essential for ciliogenesis and establishment of left-right asymmetry. Mol. Biol. Cell: 27, 48–63.

Silverman-Gavrila, R. et al., 2011: Rear polarization of the microtubule-organizing center in neointimal smooth muscle cells depends on PKC. Am. J. Phys. Anthropol.: 178, 895–910.

Sinzelle, L. et al., 2006: Generation of trangenic Xenopus laevis using the Sleeping Beauty transposon system. Transgenic Res.: 15, 751–760.

Sironen, A. et al., 2011: Loss of SPEF2 function in mice results in spermatogenesis defects and primary ciliary dyskinesia. Biol. Reprod.: 85, 690–701.

Sive, H. L. et al., 2007: Xenopus laevis Keller Explants. CSH Protoc.

Sive, H. L. et al., 2000: Early Development of Xenopus Laevis: A Laboratory Manual. Cold Spring Harb. Laboratory Press.

Sivadas, P. et al., 2012: A flagellar Akinase anchoring protein with two amphipathic helices forms a structural scaffold in the radial spoke complex. J. Cell Biol.: 199, 639–651.

Skerget, S. et al., 2015: Sperm proteome maturation in the mouse epididymis. PLoS ONE: 10, e0140650.

Slaats, G. G. et al., 2016: MKS1 regulates ciliary INPP5E levels in Joubert syndrome. J. Med. Genet.: 53, 62–72.

Sleigh, M. A., 1981: Primary Ciliary Dyskinisia. Lancet: 318, 476.

Soares, H. et al., 2019: Cilia Distal Domain: Diversity in Evolutionarily Conserved Structures. Cells: 8, 160.

Sohr, A. et al., 2019: Drosophila FGF cleavage is required for efficient intracellular sorting and intercellular dispersal. J. Cell Biol.: 218, 1653–1669.

Song, H et al., 2010: Planar cell polarity breaks bilateral symmetry by controlling ciliary positioning. Nature: 466, 378–382.

Spassky, N. et al., 2005: Adult ependymal cells are postmitotic and are derived from radial glial cells during embryogenesis. Neuroscience: 25, 10–18.

Spassky, N. et al., 2008: Primary cilia are required for cerebellar development and Shh-dependent expansion of progenitor pool. Dev. Biol.: 317, 246–259.

Spéder, P. et al., 2006: Type ID unconventional myosin controls left-right asymmetry in Drosophila. Nature: 440, 803–807.

Spemann, H. & Falkenberg, H. 1919: Uber asymmetrische Entwicklung und Situs inversus viscerum bei Zwillingen und Doppelbildungen. Archiv für Entwicklungsmechanik der Organismen: 45, 371–422.

Srour, M. et al., 2012: Mutations in TMEM231 cause Joubert syndrome in French Canadians. J. Med. Genet.: 49, 636–641.

Srour, M. et al., 2012: Mutations in C5ORF42 cause Joubert syndrome in the French Canadian population. Am. J. Hum. Genet.: 90, 693–700.

Srour, M. et al., 2015: Joubert syndrome in French Canadians and identification of mutations in CEP104. Am. J. Hum. Genet.: 97, 744–753.

Stannard, W. & O'Callaghan, C., 2006: Ciliary function and the role of cilia in clearance. J. Aerosol Med.: 19, 110–115.

Stauber, M. et al., 2017: Identification of FOXJ1 effectors during ciliogenesis in the foetal respiratory epithelium and embryonic left-right organiser of the mouse. Dev. Biol.: 423, 170–188.

Strahl, B. D. & Allis, C. D., 2000: The language of covalent histone modifications. Nature: 403, 41–45.

Stubbs, J. L. et al., 2008: The forkhead protein Foxj1 specifies node-like cilia in Xenopus and zebrafish embryos. Nat. Genet.: 40, 1454–1460.

Su, Q. et al., 2018: Structure of the human PKD1-PKD2 complex. Science: 361, eaat9819.

Sulik, K. et al., 1994: Morphogenesis of the murine node and notochordal plate. Dev. Dyn.: 201, 260–278.

Sunter, J. & Gull, K., 2017: Shape, form, function and Leishmania pathogenicity: from textbook descriptions to biological understanding. Open Biol.: 7, 170165.

Supp, D. M. et al., 1997: Mutation of an axonemal dynein affects left-right asymmetry in inversus viscerum mice. Nature: 389, 963–966.

Supp, D. M. et al., 1999: Targeted deletion of the ATP binding domain of left-right dynein confirms its role in specifying development of left-right asymmetries. Development: 126, 5495–5504.

Suzuki, K. I. T. et al., 2018: A simple knock-in system for Xenopus via microhomology mediated end joining repair. Methods Mol. Biol.: 1865, 91–103

Suzuki, M. et al., 2010: MID1 and MID2 are required for Xenopus neural tube closure through the regulation of microtubule organization. Development: 137, 2329–2339.

Suzuki, M. et al., 2012: Molecular mechanisms of cell shape changes that contribute to vertebrate neural tube closure. Dev. Growth Differ.: 54, 266–276.

Szabó, A. et al., 2016: The molecular basis of radial intercalation during tissue spreading in early development. Dev. Cell: 37, 213–225.

Szabó, A. et al., 2016: In vivo confinement promotes collective migration of neural crest cells. J. Cell Biol.: 213, 543–555.

Szenker-Ravi, E. et al., 2018: RSPO2 inhibition of RNF43 and ZNRF3 governs limb development independently of LGR4/5/6. Nature: 557, 564–569.

Takeda, S. et al., 1999: Left-right asymmetry and kinesin superfamily protein KIF3A: new insights in determination of laterality and mesoderm induction by kif3A-/- mice analysis. J. Cell Biol.: 145, 825–836.

Takeda, S. & Narita, K., 2012: Structure and function of vertebrate cilia, towards a new taxonomy. Differentiation: 83, S4–S11.

Talbot, W. S. et al., 1995: A homeobox gene essential for zebrafish notochord development. Nature: 378, 150–157.

Tallila, J. et al., 2009: Mutation spectrum of Meckel syndrome genes: one group of syndromes or several distinct groups? Hum. Mutat.: 30, E813–E830.

Tanaka, Y. et al., 2005: FGF-induced vesicular release of Sonic hedgehog and retinoic acid in leftward nodal flow is critical for left-right determination. Nature: 435, 172–177.

Tandon, P. et al., 2017: Expanding the genetic toolkit in Xenopus: approaches and opportunities for human disease modeling. Dev. Biol.: 426, 325–335.

Tang, S. et al., 2017: Biallelic mutations in CFAP43 and CFAP44 cause male infertility with multiple morphological abnormalities of the sperm flagella. Am. J. Hum. Genet.: 100, 854–864.

Taulman, P. D. et al., 2001: Polaris, a protein involved in left-right axis patterning, localizes to basal bodies and cilia. Mol. Biol. Cell: 12, 589–599.

Thomas, S. et al., 2012: TCTN3 mutations cause Mohr-Majewski syndrome. Am. J. Hum. Genet.: 91, 372–378.

Thompson, H. et al., 2012: The formation and positioning of cilia in Ciona intestinalis embryos in relation to the generation and evolution of chordate left-right asymmetry. Dev. Biol.: 364, 214–223.

Tingler, M. et al., 2014: Symmetry breakage in the frog Xenopus: role of Rab11 and the ventral-right blastomere. Genesis: 52, 588–599.

Tingler, M et al., 2018: A conserved role of the unconventional myosin 1d in laterality determination. Curr. Biol.: 28, 810–816.

Tisler, M. et al., 2016: Cilia are required for asymmetric nodal induction in the sea urchin embryo. BMC Dev. Biol.: 16, 28.

Tisler, M. et al., 2017: Leftward flow determines laterality in conjoined twins. Curr. Biol.: 27, 543–548.

Tisler, M. et al., 2017: Xenopus, an ideal model organism to study laterality in conjoined twins. Genesis: 55, e22993.

Tolg, C. et al., 2010: RHAMM promotes interphase microtubule instability and mitotic spindle integrity through MEK1/ERK1/2 activity. J. Biol. Chem.: 285, 26461–26474.

Tolg, C. et al., 2014: Hyaluronan and RHAMM in wound repair and the “cancerization” of stromal tissues. Biomed. Res. Int.: 2014, 103923.

Toyoizumi, R. et al., 2005: Xenopus nodal related-1 is indispensable only for left-right axis determination. Int. J. Dev. Biol.: 49, 923–938.

Tözser, J. et al., 2015: TGF-Signaling Regulates the Differentiation of Motile Cilia. Cell Rep.: 11, 1000–1007.

Tuz, K. et al., 2014: Mutations in CSPP1 cause primary cilia abnormalities and Joubert syndrome with or without Jeune asphyxiating thoracic dystrophy. Am. J. Hum. Genet.: 94, 62–72.

Tyanova, S. et al., 2016: The Perseus computational platform for comprehensive analysis of (prote)omics data. Nat. Meth.: 13, 731–740.

Ueno, N. & Greene, N. D. E., 2003: Planar cell polarity genes and neural tube closure. Birth Defects Res. C Embryo Today: 69, 318–324.

Urbanska, P. et al., 2018: Ciliary proteins Fap43 and Fap44 interact with each other and are essential for proper cilia and flagella beating. Cell. Mol. Life Sci.: 100, 2008.

Valente, E. M. et al., 2010: Mutations in TMEM216 perturb ciliogenesis and cause Joubert, Meckel and related syndromes. Nat. Genet.: 42, 619–625.

Vandenberg, L. N. & Levin, M., 2009: Perspectives and open problems in the early phases of left-right patterning. Semin. Cell Dev. Biol.: 20, 456–463.

Vandenberg, L. N. & Levin, M., 2010: Consistent left-right asymmetry cannot be established by late organizers in Xenopus unless the late organizer is a conjoined twin. Development: 137, 1095–1105.

Vandenberg, L. N. & Levin, M., 2010: Far from solved: A perspective on what we know about early mechanisms of left-right asymmetry. Dev. Dyn.: 239, 3131–3146.

Vandenberg, L. N. & Levin, M., 2013: A unified model for left-right asymmetry? Comparison and synthesis of molecular models of embryonic laterality. Dev. Biol.: 379, 1–15.

Vaser, R. et al., 2016: SIFT missense predictions for genomes. Nat. Protoc.: 11, 1–9.

Vasudevan, K. K. et al., 2015: FAP206 is a microtubule-docking adapter for ciliary radial spoke 2 and dynein c. Mol. Biol. Cell: 26, 696–710.

Vernet, N. et al., 2012: Spermatid development in XO male mice with varying Y chromosome short-arm gene content: evidence for a Y gene controlling the initiation of sperm morphogenesis. Reproduction: 144, 433–445.

Vernet, N. et al., 2016: Mouse Y-encoded transcription factor Zfy2 is essential for sperm head remodelling and sperm tail development. PLoS ONE: 11, e0145398.

Vick, P. et al., 2009: Flow on the right side of the gastrocoel roof plate is dispensable for symmetry breakage in the frog Xenopus laevis. Dev. Biol.: 331, 281–291.

Vick, P. et al., 2018: An early function of polycystin-2 for left-right organizer induction in Xenopus. iScience: 2, 76–85.

Vij, S. et al., 2012: Evolutionarily ancient association of the FoxJ1 transcription factor with the motile ciliogenic program. PLoS Genet.: 8, e1003019.

Viotti, M. et al., 2012: Role of the gut endoderm in relaying left-right patterning in mice. PLoS Biol.: 10, e1001276.

del Viso, F. et al., 2016: Congenital Heart Disease Genetics Uncovers Context-Dependent Organization and Function of Nucleoporins at Cilia. Dev. Cell: 38, 478–492.

del Viso, F. & Khokha, M., 2012: Generating diploid embryos from Xenopus tropicalis. Methods Mol. Biol.: 917, 33–41.

Vizcaíno, J. A. et al., 2016: 2016 update of the PRIDE database and its related tools. Nucleic Acids Res.: 44, D447–D456.

Vladar, E. K. et al., 2012: Microtubules enable the planar cell polarity of airway cilia. Curr. Biol.: 22, 2203–2212.

Vladar, E. K. & Stearns, T., 2007: Molecular characterization of centriole assembly in ciliated epithelial cells. J. Cell Biol.: 178, 31–42.

Vonica, A. & Brivanlou, A. H., 2007: The left-right axis is regulated by the interplay of Coco, Xnr1 and derrière in Xenopus embryos. Dev. Biol.: 303, 281–294.

de Vries, W. N. et al., 2000: Expression of Cre recombinase in mouse oocytes: a means to study maternal effect genes. Genesis: 26, 110–112.

Walck-Shannon, E. & Hardin, J., 2014: Cell intercalation from top to bottom. Nat. Rev. Mol. Cell Biol.: 15, 34–48.

Walentek, P. et al., 2012: ATP4a Is Required for Wnt-Dependent Foxj1 Expression and Leftward Flow in Xenopus Left-Right Development. Cell Rep.: 1, 516–527.

Walentek, P. et al., 2013: Wnt11b is involved in cilia-mediated symmetry breakage during Xenopus left-right development. PLoS ONE: 8, e73646.

Walentek, P. et al., 2014: A novel serotonin-secreting cell type regulates ciliary motility in the mucociliary epidermis of Xenopus tadpoles. Development: 141, 1526–1533.

Walentek, P. & Quigley, I. K., 2017: What we can learn from a tadpole about ciliopathies and airway diseases: using systems biology in Xenopus to study cilia and mucociliary epithelia. Genesis: 55, e23001.

Wallingford, J. B., 2005: Neural tube closure and neural tube defects: studies in animal models reveal known knowns and known unknowns. Am. J. Med. Genet. C Semin. Med. Genet.: 135C, 59–68.

Wallingford, J. B. & Harland, R. M., 2002: Neural tube closure requires Dishevelled dependent convergent extension of the midline. Development: 129, 5815–5825.

Wallingford, J. B. et al., 2002: Convergent extension: the molecular control of polarized cell movement during embryonic development. Dev. Cell: 2, 695–706.

Wallingford, J. B. et al., 2013: The continuing challenge of understanding, preventing, and treating neural tube defects. Science: 339, 1222002.

Wallmeier, J. et al., 2019: De Novo Mutations in FOXJ1 Result in a Motile Ciliopathy with Hydrocephalus and Randomization of Left/Right Body Asymmetry. Am. J. Hum. Genet.: 105, 1030–1039.

Wang, K. et al., 2010: ANNOVAR: functional annotation of genetic variants from high-throughput sequencing data. Nucleic Acids Res.: 38, e164.

Wang, L. et al., 2017: Epigenetic regulation of left–right asymmetry by DNA methylation. EMBO J.: 36, 2987–2997.

Wang, Y. & Nathans, J., 2007: Tissue/planar cell polarity in vertebrates: new insights and new questions. Development: 134, 647–658.

Watanabe, T. et al., 2004: Interaction with IQGAP1 links APC to Rac1, Cdc42, and actin filaments during cell polarization and migration. Dev. Cell: 7, 871–883.

Weidemann, M. et al., 2016: CFAP157 is a murine downstream effector of FOXJ1 that is specifically required for flagellum morphogenesis and sperm motility. Development: 143, 4736–4748.

Wheway, G. et al., 2015: An siRNA-based functional genomics screen for the identification of regulators of ciliogenesis and ciliopathy genes. Nat. Cell Biol.: 17, 1074–1087.

Wolf, E. et al., 1997: MultiCoil: a program for predicting two- and threestranded coiled coils. Protein Sci.: 6, 1179–1189.

Womble, M. et al., 2018: The left-right asymmetry of liver lobation isgenerated by Pitx2c-mediated asymmetries in the hepatic diverticulum. Dev. Biol.: 439, 80–91.

Wood, W. B., 1991: Evidence from reversal of handedness in C. elegans embryos for early cell interactions determining cell fates. Nature: 349, 536–538.

Wright, C. F. et al., 2018: Making new genetic diagnoses with old data: iterative reanalysis and reporting from genome-wide data in 1,133 families with developmental disorders. Genet. Med.: 20, 1216–1223.

Wuhr, M. et al., 2014: Deep proteomics of the Xenopus laevis egg using an mRNA-derived reference database. Curr. Biol.: 24, 1467–1475.

Wuhr, M. et al., 2015: The nuclear proteome of a vertebrate. Curr. Biol.: 25, 2663–2671.

Yachie, N. et al., 2016: Pooled-matrix protein interaction screens using Barcode Fusion Genetics.Mol. Syst. Biol.: 12, 863.

Xiao, Q. et al., 2017: The many postures of noncanonical Wnt signaling in development and diseases. Biomed. Pharmacother.: 93, 359–369.

Yan, X. et al., 2006: A complex of two centrosomal proteins, CAP350 and FOP, cooperates with EB1 in microtubule anchoring. Mol. Biol. Cell: 17, 634–644.

Yániz, J. L. et al., 2015: Computer assisted sperm morphometry in mammals: a review. Anim. Reprod. Sci.: 156, 1–12.

Ybot-Gonzalez, P. et al., 2007: Convergent extension, planar-cell-polarity signalling and initiation of mouse neural tube closure. Development: 134, 789–799.

Yoshiba, S. et al., 2012: Cilia at the node of mouse embryos sense fluid flow for left-right determination via Pkd2. Science: 338, 226–231.

Yoshiba, S. & Hamada, H., 2014: Roles of cilia, fluid flow, and Ca2þ signaling in breaking of left-right symmetry. Trends Genet.: 30, 10–17.

Yoder, B. K. et al., 2002: Polaris, a protein disrupted in orpk mutant mice, is required for assembly of renal cilium. Am. J. Physiol. Renal Physiol.: 282, F541–F552.

You, Y. & Brody, S. L., 2013: Culture and differentiation of mouse tracheal epithelial cells. Methods Mol. Biol.: 945, 123–143.

Yuan, S. et al., 2015: Intraciliary calcium oscillations initiate vertebrate left-right asymmetry. Curr. Biol.: 25, 556–567.

Yu, X. et al., 2008: Foxj1 transcription factors are master regulators of the motile ciliogenic program. Nat. Genet.: 40, 1445–1453.

Zaidi, S. et al., 2013: De novo mutations in histone-modifying genes in congenital heart disease. Nature: 498, 220–223.

Zaghloul, N. A. & Katsanis, N., 2009: Mechanistic insights into Bardet-Biedl syndrome, a model ciliopathy. J. Clin. Invest.: 119, 428–437.

Zariwala, M. A. et al., 2007: Genetic defects in ciliary structure and function. Annu. Rev. Physiol: 69, 423–450.

El Zein, L. et al., 2009: RFX3 governs growth and beating efficiency of motile cilia in mouse and controls the expression of genes involved in human ciliopathies. J. Cell Sci.: 122, 3180–3189.

Zhao, H. et al., 2013: The Cep63 paralogue Deup1 enables massive de novo centriole biogenesis for vertebrate multiciliogenesis. Nat. Cell Biol.: 15, 1434–1444.

Zhang, M. et al., 2004: Foxj1 regulates asymmetric gene expression during left-right axis patterning in mice. Biochem. Biophys. Res. Commun.: 324, 1413–1420.

Zhang, S. & Mitchell, B. J., 2016: Basal bodies in Xenopus. Cilia: 5, 2.

Zhang, Y. et al., 2012: KLC3 is involved in sperm tail midpiece formation and sperm function. Dev. Biol.: *366*, 101–110.

Zheng, H. et al., 2007: Lack of Spem1 causes aberrant cytoplasm removal, sperm deformation, and male infertility. Proc. Natl. Acad. Sci. USA: 104, 6852–6857.

Zhu, L. et al., 2019: Rsph9 is critical for ciliary radial spoke assembly and central pair microtubule stability. Biol. Cell: 111, 29–38.

Ziętkiewicz, E. et al., 2012: Mutations in radial spoke head genes and ultrastructural cilia defects in East-European cohort of primary ciliary dyskinesia patients. PLoS ONE: *7*, e33667.

Author's contribution

CFAP157 is a murine downstream effector of FOXJ1 that is specifically required for flagellum morphogenesis and sperm motility

Study design and all *Xenopus* experiments.

The evolutionary conserved FOXJ1 target gene *Fam183b* is essential for motile cilia in Xenopus but dispensable for ciliary function

Study design and all *Xenopus* experiments.

CFAP43 modulates ciliary beating in mouse and *Xenopus*

Study design, *cfap43* expression analysis, generation and analysis of *foxj1* gain of function, *foxj1* crispants and *cfap43* morphants (in parts, initial experiments).

The FOXJ1 target *Cfap206* is required for sperm motility, mucociliary clearance of the airways and brain development

Study design, *cfap206* expression analysis, generation and analysis of *foxj1* gain of function, *foxj1* crispants, *cfap206* morphants and *cfap206* crispants (in parts, not including epidermal flow analysis).

A Conserved Role of the Unconventional Myosin 1d in Laterality Determination

Generation and analysis of *myo1d* crispants.

***Situs inversus* and heterotaxy: the novel peptidase *tout de travers* (*TDT*) drives laterality development**

Study design and all *Xenopus* experiments.

hmmr* mediates anterior neural tube closure and morphogenesis in the frog *Xenopus

Molecular cloning of *hmmr* deletion constructs and parallelized generation of *hmmr* morphants (in parts).

The Frog Xenopus as a Model to Study Joubert Syndrome: The Case of a Human Patient With Compound Heterozygous Variants in *PIBF1*

Study design and all *Xenopus* experiments.

Vertebrate Left-Right Asymmetry: What Can Nodal Cascade Gene Expression Pattern Tell Us?

Data mining (in parts) and meta-analysis (in parts).

The Power of Strain: Organizing Left-Right Cilia

Conceptualization (in parts) and figure design.

Animal left-right asymmetry

Conceptualization (in parts) and figure design.

***Xenopus*: An Undervalued Model Organism to Study and Model Human Genetic Disease**

Conceptualization (in parts), figure design and all experiments.

Mechanical strain, novel genes and evolutionary insights: news from the frog left-right organizer

Conceptualization (in parts) and figure design.

_____ _____

Place and Date Signature (Prof. Dr. Martin Blum)

Curriculum vitae

Name:	Tim Ott
Date of birth:	17.03.1988
Place of birth:	Pforzheim, Germany
Place of residence:	Stuttgart, Germany
Nationality:	German

Education and Scientific Career

1995–2008	Primary and High-School in Pforzheim, Germany
2008–2014	Study of Biology at the University of Hohenheim, Germany
	B.Sc. and M.Sc. Thesis in the Group of Prof. Dr. Martin Blum
Since 2014	Doctoral student at the University of Hohenheim, Germany in the Group of Prof. Dr. Martin Blum
	Funded (2 years) by the Landesgraduiertenförderung of Baden-Württemberg
2014	Visiting Researcher (3 month) at The Hebrew University of Jerusalem, Israel in the Group of Prof. Dr. Abraham Fainsod
	Funded by the Landtag of Baden-Württemberg

Qualifications

06/2012	Seminar 2From Concept to Publication", Hohenheim, Germany
06/2013	Zeiss Workshop "Digital Imaging with AxioVision", Tübingen, Germany
03/2014	Seminar "Fortbildung in der Tierpflege für Kleinsäuger und Aquatische Vertebraten", Hohenheim
07/2014	Seminar "Haltung von Fischen und Fröschen in tierexperimentellen Einrichtungen", Ulm, Germany
09/2014	Laboratory Animal Course Category B, Hohenheim, Germany
12/2015	Seminar "Modellorganismus *Xenopus laevis*", Hohenheim
08/2017	Genome Editing Workshop, Woods Hole, USA
	Funded by Boehringer Ingelheim Funds

03/2018	Seminar “Erkrankungen bei Maus, Ratte und Kaninchen”, “Ersatz und Ergänzungsmethoden” und „Planung und Durchführung von Tierversuchen“, Hohenheim, Germany
09/2019	Seminar „Aquatische Modellsysteme”, Ulm, Germany

Conference Participations

03/2013	International Joint Meeting DZG and GfE, Heidelberg, Germany
04/2013	Xenopus Regio Meeting, Hohenheim, Germany
06/2013	COS Symposium, Heidelberg, Germany
10/2013	1. Deutsches Xenopus-Meeting, Hohenheim, Germany
05/2015	Wnt Symposium, Heidelberg, Germany
10/2015	2. Deutsches Xenopus-Meeting, Karlsruhe, Germany
10/2015	9ème Meeting Cils, Flagelles et Centrosomes, Straßburg, France
08/2016	16th International Xenopus Meeting, Kolimvari, Greece
06/2017	European Amphibian Club 2017, Rennes, France
12/2018	3. Deutsches Xenopus Meeting, Hohenheim, Germany
02/2019	Gordon Research Seminar: Cilia, Mucus and Mucociliary Interactions, Castelvecchio Pascoli, Italy
02/2019	Gordon Research Conference: Cilia, Mucus and Mucociliary Interactions, Castelvecchio Pascoli, Italy
06/2019	European Amphibian Club 2019, Lutherstadt-Wittenberg, Germany
10/2019	6th Tri-Regional stem cell and developmental biology meeting, Illkirch, France

_____ _____

Place and Date Signature

Danksagung

Ich danke:

- Prof. Dr. Martin Blum für das Vertrauen, die Unterstützung und für die Freiheiten, die ich während der gesamten Promotion genießen durfte;
- Prof. Dr. Heinz Breer für seine Bereitschaft diese Arbeit zu begutachten und auch Teil meiner Prüfungskommission zu sein;
- Dr. Kerstin Feistel, Prof. Dr. Axel Schweickert und Dr. Philipp Vick für die vielen wissenschaftlichen Debatten;
- meinen Kollegen bzw. Freunden insbesondere Jennifer Kreis, Dr. Matthias Tisler, Melanie Tingler, Dr. Cathrin Hagenlocher, Matthias Kästle, Anna Iwanska, Fee Wielath, Saskia Lutz, Agnes Fietz und Verena Andre die ich alle nicht mehr missen möchte;
- Magdalena Brislinger, Anna Janz und Franziska Wetzel, bei denen mir die Betreuung so viel Spaß wie bei sonst keinem gemacht hat;
- Dr. Silke Schmalholz und Susanne Bogusch, die in jeder Situation nicht nur für mich, sondern für alle im Labor da waren.